Solar System Ice microphysics

Guillaume Cruz-Mermy

université PARIS-SACLAY

Solar System ice microphysics

Microphysique des glaces du système solaire

Thèse de doctorat de l'université Paris-Saclay

École doctorale n° 579, Sciences Mécaniques et Energétiques, Matériaux et Géosciences (SMEMaG)
Spécialité de doctorat : Structure et évolution de la Terre et des autres planètes
Graduate School : Géosciences, Climat, Environnement, Planètes
Référent : Faculté des sciences d'Orsay

Thèse préparée dans l'unité de recherche GEOPS (Université Paris-Saclay, CNRS), sous la direction de **Frédéric SCHMIDT**, Professeur

Thèse soutenue à Paris-Saclay, le 9 décembre 2022, par

Guillaume CRUZ-MERMY

Composition du jury

Membres du jury avec voix délibérative

François COSTARD Directeur de recherche, CNRS, GEOPS, Orsay	Président
Thierry FOUCHET Professeur, Sorbonne Université, LESIA, Meudon	Rapporteur & Examinateur
Bernard SCHMITT Directeur de recherche, IPAG, Grenoble	Rapporteur & Examinateur
François POULET Astronome, IAS, Orsay	Examinateur
Ann Carine VANDAELE Directrice de recherche, BIRA-IASB, Bruxelles	Examinatrice

THESE DE DOCTORAT

NNT : 2022UPASJ027

université PARIS-SACLAY

ÉCOLE DOCTORALE
Sciences mécaniques et énergétiques, matériaux et géosciences (SMEMAG)

Titre : Microphysique des glaces du système solaire
Mots clés : Glaces, Spectroscopie infrarouge, Transfert radiatif, Mars, Europe

Résumé : Ce travail de recherche porte sur la caractérisation microphysique des glaces présentes en surface de différents corps planétaires. Étudier l'état microphysique de la glace consiste à caractériser les propriétés chimiques et structurales telles que la proportion en volume des composants, la taille de leurs grains, la porosité ou encore la rugosité de surface. Ces propriétés permettent alors de comprendre le mode de formation et les processus gouvernant l'évolution temporelle de ces surfaces. A l'issu de cette thèse, deux objets ont fait la cible de ces investigations : Mars et Europe, un satellite de Jupiter. Pour ce faire nous utilisons les principes physiques décrivant les interactions entre la lumière et la matière et notamment le cadre théorique du transfert radiatif. Les équations du transfert de rayonnement permettent de modéliser les phénomènes d'absorption, de réflexion et de diffusion de la lumière lors de son interaction avec les matériaux de la surface. Ce travail est organisé en trois parties distinctes. La première partie est consacrée à la description du transfert de rayonnement, les concepts et grandeurs physiques importantes sont définis pour aboutir à quelques exemples de modèles couramment utilisé par la communauté scientifique. Le modèle utilisé dans ce travail, dit modèle spectro-photométrique de Hapke, est largement décrit. Les avantages de cette approche résident dans le fait que ce modèle est analytique et qu'il est facilement inversible. L'inversion d'un modèle physique consiste en son utilisation pour remonter aux paramètres physiques permettant de reproduire le plus fidèlement possible une donnée, dans notre cas une observation de la surface. Les concepts et méthodes d'inversions sont également présentés dans cette partie. Une comparaison entre différentes méthodes d'inversion est proposée pour aboutir à la sélection des méthodes les plus adaptées aux problèmes rencontrés. La seconde partie est dédié à la caractérisation de la surface d'Europe. Le contexte scientifique dresse le bilan des connaissances actuelles concernant les propriétés de la surface et aboutit sur les questions demeurant en suspens : quelle est la composition chimique de la surface ? Comment varie t'elle d'une structure géologique à l'autre ? Quels processus favorisent cette composition ? Pour répondre à ces questions nous utilisons les données obtenues par le spectro-imageur NIMS au cours de la mission Galileo. Nous avons combiné le modèle de Hapke et une approche d'inversion bayésienne pour tester, pour la première fois, un très grand nombre de représentations différentes de la surface à partir de 15 composés chimiques qui ont été proposés à ce jour par des études précédentes. Nous montrons qu'il existe une multitude de représentations différentes de la surface produisant un ajustement similaire aux données. La troisième partie est consacré à l'étude des glaces de Mars via l'utilisation des données de la mission récente ExoMars-TGO et notamment du spectromètre infrarouge NOMAD. L'acquisition des premières données de la missions coïncident avec le début de ce travail de thèse, c'est pourquoi un travail de calibration instrumentale a été nécessaire. Une méthode de calibration des données du canal nadir de NOMAD a été proposée et publiée. Une première analyse des données permet de mettre en évidence la capacité instrumentale à détecter des glaces de surfaces. Ces données permettront ensuite d'entreprendre un travail de caractérisation et de suivi temporelle des propriétés microphysiques de la glace sur Mars.

université PARIS-SACLAY

ÉCOLE DOCTORALE
Sciences mécaniques et énergétiques, matériaux et géosciences (SMEMAG)

Title : Microphysics of Solar System ices
Keywords : Ices, near-infrared spectroscopy, Radiative transfer, Mars, Europa

Abstract : This research work focuses on the microphysical characterization of ice present on the surface of different planetary bodies. Studying the microphysical state of the ice consists in characterizing the chemical and structural properties such as the volume proportion of the components, the size of their grains, the porosity or the surface roughness. These properties allow us to understand the formation mode and the processes governing the temporal evolution of these surfaces. At the end of this thesis, two objects were the target of these investigations : Mars and Europa, a satellite of Jupiter. To do so, we use the physical principles describing the interactions between light and matter and in particular the theoretical framework of radiative transfer. The radiation transfer equations allow to model the phenomena of absorption, reflection and scattering of light during its interaction with the surface materials. This work is organized in three distinct parts. The first part is devoted to the description of radiation transfer, the concepts and important physical quantities are defined to lead to some examples of models commonly used by the scientific community. The model used in this work, the so-called spectro-photometric Hapke model, is widely described. The advantages of this approach lie in the fact that this model is analytical and easily invertible. The inversion of a physical model consists in using it to find the physical parameters allowing to reproduce as accurately as possible a data, in our case an observation of the surface. The concepts and methods of inversions are also presented in this section. A comparison between different inversion methods is proposed to select the most suitable methods for the problems encountered. The second part is dedicated to the characterization of the surface of Europa. The scientific background gives an overview of the current knowledge about the properties of the surface and ends with the remaining questions : what is the chemical composition of the surface ? How does it vary from one geological structure to another ? What processes promote this composition ? To answer these questions we use the data obtained by the NIMS spectro-imager during the Galileo mission. We have combined the Hapke model and a Bayesian inversion approach to test, for the first time, a very large number of different representations of the surface from 15 chemical compounds that have been proposed so far by previous studies. We show that there is a multitude of different surface representations that produce a similar fit to the data. The third part is devoted to the study of the ices of Mars via the use of the data of the recent ExoMars-TGO mission and in particular the NOMAD infrared spectrometer. The acquisition of the first data of the mission coincides with the beginning of this thesis, so an instrumental calibration work was necessary. A calibration method for the NOMAD nadir channel data has been proposed and published. A first analysis of the data allows to highlight the instrumental capacity to detect surface ice. These data will then allow to undertake a work of characterization and temporal follow-up of the microphysical properties of the ice on Mars.

Avant-propos

Ce manuscrit de thèse a été rédigé en anglais avec le logiciel Lyx (https://www.lyx.org/) et contient des liens hypertextes internes et externes. Ce choix est motivé par deux raisons principales, la première étant que des articles scientifiques sont présents au sein de certains chapitres de ce document j'ai donc choisi d'assurer la cohérence du manuscrit en conservant la même langue. La seconde tient dans le fait que cette thèse s'inscrit dans la recherche en sciences planétaires et que cette discipline implique souvent des collaborations avec des scientifiques à l'international, j'ai souhaité que ce travail soit accessible au plus grand nombre.

Foreword

This thesis manuscript has been written in English with the Lyx software (https://www.lyx.org/) and contains internal and external hyperlinks. This choice is motivated by two main reasons, the first one being that scientific articles are present within some chapters of this document, so I chose to ensure the coherence of the manuscript by keeping the same language. The second reason is that this thesis is part of the research in planetary sciences and that this discipline often implies collaborations with international scientists, I wanted this work to be accessible to the largest number of people.

Financement

Le travail présenté dans ce manuscrit a été co-financé par le programme « PhD studentships » de l'Agence Spatiale Européenne (id : I-2019-01294).

Nous souhaitons remercier l'Institut National des Sciences de l'Univers (INSU), le Centre National de la Recherche Scientifique (CNRS) et le Centre National d'Etudes Spatiales (CNES) par le Programme National de Planétologie qui nous a permis d'assister à des conférences internationales.

Nous remercions également Europlanet pour leur soutien dans la participation à l'European Planetary Science Congress de 2019.

Funding

The work presented in this dissertation was co-funded by the European Space Agency (ESA) PhD studentships programme (idea : I-2019-01294).

We acknowledge support from the Institut National des Sciences de l'Univers (INSU), the Centre National de la Recherche Scientifique (CNRS) and Centre National d'Etudes Spatiales (CNES) through the Programme National de Planétologie to attend conferences.

We also acknowledge support from Europlanet for participating at the European Planetary Science Congress 2019.

Remerciements

En commençant ce travail de recherche il y a trois ans je m'étais imaginé qu'une thèse c'était surtout un projet très personnel que l'on réalise majoritairement seul. J'ai très rapidement compris que j'avais tort et alors que j'achève cet exercice par l'écriture de ces lignes j'ai pleinement conscience qu'il s'agit d'une formidable aventure collaborative ponctuée par des rencontres très enrichissantes. Il est donc important pour moi de prendre le temps de remercier toutes les personnes impliquées, professionnellement et/ou personnellement, dans ce travail d'équipe.

Cloé, ma partenaire de toujours, sache que sans toi je n'aurais jamais réussi à réaliser ce rêve d'enfant. Je n'ai pas les mots pour te dire à quel point je suis reconnaissant et admiratif de ta patience, bienveillance et bonne humeur perpétuelle. Merci infiniment de m'avoir poussé à reprendre les études et d'avoir partagé ce chemin avec moi. Merci pour ton soutient indéfectible qui m'a permis d'affronter sereinement les différentes épreuves survenues pendant ce projet. Ce travail t'es entièrement dédié.

Je tient à remercier tout particulièrement mon directeur de thèse, Frédéric, sans qui ce travail de recherche n'aurait pas eu lieu. Tout d'abord, merci de m'avoir fait découvrir le laboratoire GEOPS, l'équipe du bâtiment 509 et le transfert radiatif au cours de mes stages de master 1 & 2. Ces premières expériences de travail m'ont très rapidement confortés dans ma volonté de poursuivre en thèse avec toi. Merci d'avoir cru en moi et d'avoir accepté de travailler avec moi pendant 3 ans. Merci de ta patience, ton soutient, ta pédagogie et ta détermination sans failles jusque dans les moments les plus difficiles. Sache que je suis très admiratif de ta personne et que c'est une grande fierté pour moi d'avoir été ton jeune padawan !

Je souhaite remercier les membres de mon jury de thèse qui ont accepté d'évaluer ce travail. Tout d'abord mes rapporteurs, Thierry Fouchet et Bernard Schmitt, pour leurs suggestions pertinentes sur l'amélioration du manuscrit. Merci également à mes examinateurs, François Costard, François Poulet et Ann Carin Vandaele pour vos remarques lors de la soutenance.

Je remercie François Andrieu et Thomas Cornet pour leur forte implication dans ce travail de recherche. François, merci d'avoir consacré du temps sur les questions de l'implantation numérique et sur les interprétations physiques des résultats et plus généralement, merci pour tous ces bons moments au laboratoire comme en mission (elle est claquée au sol cette chambre d'hôtel !). Thomas, merci de ton temps et de ton dynamisme tout au long de ce projet, j'ai fortement apprécié travailler avec toi et j'espère que nous aurons l'occasion de collaborer à nouveau. Merci de m'avoir accueil lors de ma visite à l'ESAC et de m'avoir indiqué les bonnes brasseries de Madrid.

Un grand merci à Ian Thomas et l'ensemble de l'équipe NOMAD. Ian, merci d'avoir pris le temps de m'expliquer les nombreuses particularités de LNO et de m'avoir impliqué dans la calibration de cet instrument. Merci de ton accueil chaleureux lors de mes visites à Bruxelles !

Merci a Matthieu Vincendon pour nos discussions enrichissantes et tes remarques pertinentes lors des comités de suivi de thèse.

Ces trois années au laboratoire GEOPS s'accompagnent de formidable moments de convivialité et de franche rigolade au sein du bâtiment 509 (et parfois 504, quand il y a de la place). François C., Laure, Hélène, Julien, Antoine, Sylvain, Claire, Aurélie, Valérie, Fred B., merci de votre accueil, votre soutient, vos conseils et merci pour ces formidables repas et autres évènements insolites que nous avons partagé ensemble. J'en profite pour remercier les footeux du jeudi soir (en particulier Xavier et sa frappe légendaire) avec qui j'ai pu décompresser à de nombreuses occasions. Un grand merci à Mylène et Georgette, les capitaines du navire, qui ont toujours su rester patiente face à ma phobie administrative.

Un laboratoire c'est aussi des doctorants et j'ai eu la chance de débuter ma thèse en très bonne compagnie. Axel, merci de m'avoir pris sous ton aile à mon arrivé, merci de ton temps, tes conseils, ta bonne humeur et surtout, merci d'avoir pris un hôtel avec piscine à Grenade. Inès, merci d'avoir été la grande soeur qui a su me rassurer et me donner confiance tout au long de ce projet, merci aussi pour tes

conseils et ton implication dans ce travail. Elodie, merci pour ton accueil et ces nombreuses pauses café dans ton bureau.

Et puis ce fût à mon tour d'être l'ainé et j'ai eu la chance d'être rejoint par deux formidables personnes, mes 'wingmen' Cyril et Léo, sans qui cette fin de thèse n'aurait clairement pas été la même. Cyril, merci pour tous ces moments de débats intenses et discussions animées sur le basket et nos autres passions communes (Brann c'est plus ce que c'était) et merci de ton soutient dans cette dernière année de thèse ! J'espère que tu réaliseras ton rêve d'être quaterback #1 (Estos son Reebok o son Nike ?). Léo, mon covoit' ecolo favoris, merci de ton enthousiasme, de ta bonne humeur quotidienne et également de ton soutient lors de ma dernière année. Un grand merci à vous deux de m'avoir accompagné à mes nombreuses pauses café en extérieur et surtout merci infiniment de m'avoir soulagé dans l'organisation de la soutenance. Je vous souhaite le meilleur pour la suite !

Je souhaite évidemment remercier mes parents qui m'ont toujours soutenu dans mon parcours académique et mes choix d'orientation. Merci de m'avoir permis de faire des études de géologie (pratique lorsque l'on finit dans un laboratoire de géologue !), merci infiniment pour votre soutient, vos encouragements et votre amour dans les bons comme dans les moments plus difficiles.

Merci également à ma belle famille, Pierre, Valérie, Lola, Karine, François, Françoise et Jacques, pour m'avoir accueilli à bras ouverts dans cette famille au sens critique affuté, pour tous ces formidables moments de décompression dans la campagne Picarde (ou pluie-carde ?) et pour ce Noël tarantinesque.

Merci à toute ma famille pour vos mots et vos encouragements dans cette étape.

Merci à mon 'crew', vous êtes les meilleurs et vous le savez ! Claire, Julia, Constance, Miguel, Kress, Valérian, P.A., Luc, Lambert. Merci de votre soutient depuis tant d'années, quel chance d'avoir autant de frères et soeurs quand on est fils unique.

Merci à tous les copains que j'ai croisé avant et pendant cette aventure, qui m'ont témoigné du soutient et m'ont fait vivre de très bons moments souvent nécessaires ! Nicolas, Léo, Maryse, Eric, Flo, Lauryne, Jeanne, Pierre, Dorian, Lara, Lucie, Milan, Virgile, Morgane, Malik & Julien, et bien évidemment, Ska & Karum.

Merci aux stagiaires de passage dans le laboratoire, en particulier Jean (et tes questions pièges) et Killian (et tes dunks).

Enfin merci à vous, lecteurs francophones de remerciements, de votre intérêt pour ce manuscrit.

Synthèse

Le travail effectué au cours de cette thèse est présenté dans ce manuscrit rédigé en anglais. En accord avec la réglementation de l'Université Paris Saclay et de l'école doctorale SMEMaG, une synthèse de ce travail rédigée en français est présentée ci-dessous, pour le lecteur francophone qui le souhaite. Bonne lecture.

Contexte général

Dans les sciences planétaires, le terme de « glace » désigne l'ensemble des molécules volatiles susceptibles de condenser sous forme de solides purs, de mélanges de solides, d'hydrates ou de clathrates hydratés (B. Schmitt, 1995). Dans le système solaire on rencontre principalement des glaces d'eau (H_2O), de dioxyde de carbone (CO_2), de monoxyde de carbone (CO), de méthane (CH_4), de dioxyde de soufre (SO_2), d'ammoniac (NH_3) et de diazote (N_2). Ces glaces constituent une masse importante du système solaire externe et représentent un matériel primordial dans la formation et l'évolution de nombreux corps planétaires, depuis le coeur des planètes géantes et leurs satellites jusqu'aux vastes réservoirs de comètes formant le nuage de Oort. Ces glaces sont également impliquées dans l'apport de volatiles sur les planètes du système solaire interne si bien que l'on retrouve aujourd'hui des glaces stables en surface des corps planétaires, même aux endroits les plus proche du Soleil comme sur Mercure (Harmon and Slade, 1992). Les glaces sont au coeur de processus actifs se produisant en surface ou dans l'atmosphère d'une grande majorité d'objets du système solaire (Clark et al., 2012). Etudier les glaces du système solaire et caractériser leurs propriétés physico-chimiques permet de comprendre les processus gouvernant l'évolution des corps planétaires investigués.

La très grande majorité des glaces identifiées dans le système solaire provient d'observations télescopiques et des données issues des missions spatiales. Pour cette raison, il s'agit principalement de glace présente en surface des corps planétaires. L'espèce chimique la plus détectée est la glace d'eau mais l'on identifie une très grande variété d'autres glaces, sous formes pures ou bien mélangées à la glace d'eau (Clark et al., 2012). Une approche courante pour détecter et caractériser les glaces de surface est via l'étude de la lumière réfléchie (spectroscopie en réflectance) ou thermalement émise (spectroscopie en émission) par la surface d'un corps planétaire. En effet, les propriétés optiques des glaces varient significativement avec la longueur d'onde (particulièrement dans le proche infrarouge) ce qui permet notamment de préciser la composition chimique de la surface étudiée. La comparaison des observations de surface avec les spectres de glaces pures obtenus en laboratoire a ainsi permis une première identification de ces glaces.

Les spectres (variation de la quantité de lumière réfléchie en fonction de la longueur d'onde) dans le proche-infrarouge (0.7 - 5 μm) des surfaces observées témoignent de l'interaction entre la lumière et une surface complexe (généralement constitué d'un mélange de composés chimiques) d'extension spatiale variable, allant d'observations hémisphériques avec une résolution spatiale de quelques centaines de kilomètres par pixel à des observations plus localisées de quelques centaines de mètres par pixels. Une approche commune pour étudier ces surfaces a été de considérer que le spectre résultant est la combinaison linéaire de plusieurs spectres de corps purs. Toutefois, il existe plusieurs limites à cette approche. La première est qu'elle n'est pas représentative des effets non linéaires du transfert de rayonnement dans une surface complexe telles que les régolithes planétaires. Ainsi, les spectres observés sont le résultat de processus complexes impliquant réflexion, absorption et diffusion du rayonnement incident qui est fonction des propriétés physiques de la surface telle que sa rugosité, sa porosité ou la taille des grains du milieu. De plus, cette approche de démélange linéaire ne permet pas de caractériser finement les propriétés physiques de la glaces et donc de comprendre les processus géologiques les impliquant. Un modèle de transfert radiatif plus réaliste intégrant les propriétés physiques de la surface et les effets non-linéaires du transfert de rayonnement est nécessaire pour conduire une caractérisation des propriétés microphysiques des glaces de surface.

Les travaux présentés dans cette thèse portent sur la spectroscopie des surfaces de Mars et d'Europe à partir de modèle de transfert radiatif et de spectres en réflectance dans le proche-infrarouge. Ces deux objets sont significativement différents mais témoignent tous deux de processus géologiques actifs en surface impliquant des glaces ce qui en font des cibles pertinentes pour cette étude. De plus, une grande quantité de données dans le proche-infrarouge sont disponibles, facilitant ce travail. A partir d'un modèle de transfert radiatif réaliste nous cherchons à déterminer les propriétés microphysiques (proportions volumiques des espèces chimiques, tailles des grains, rugosité de la surface) de ces glaces. Un suivi temporel de ces propriétés peut ainsi permettre de comprendre les processus gouvernant leur formation et évolution. Ainsi, ce travail est organisé en trois parties. La première partie s'attache à décrire les méthodes employées, les concepts théoriques du transfert de rayonnement et le modèle de transfert radiatif utilisé. Un point clé de ce travail réside dans le concept d'inversion, c'est à dire l'estimation du jeu de paramètres idéal pour reproduire une observation à partir d'un modèle physique. Une comparaison entre différentes stratégies d'inversion permet de sélectionner la méthode la plus adaptée aux problèmes posés. La seconde partie présente une application de ces méthodes pour la caractérisation de la surface d'Europe à partir des données du spectro-imageur NIMS de la mission Galileo. Un contexte scientifique dédié est présenté ainsi que la réalisation d'une première étude sur la sélection des composés chimiques les plus pertinents pour la surface d'Europe. Enfin, la dernière partie est consacrée à l'étude des glaces martiennes avec les données de l'instrument NOMAD de la mission ExoMars Trace Gas Orbiter. L'utilisation de ces données nécessite le développement d'un modèle de calibration qui est présenté puis la conduite d'une première investigation sur la capacité de détecter des glaces avec l'instrument NOMAD.

Transfert radiatif dans les glaces

Concepts et modèles

Lorsqu'un rayonnement électromagnétique (ou un photon) interagit avec un milieu matériel tel qu'une surface ou un atmosphère, il peut être absorbé ou dévié (diffusé, diffracté ou réfracté) par le milieu. Le transfert radiatif est la théorie cadre pour décrire ces interactions en les quantifiant, on parle alors de transfert d'énergie dans la matière. Ces interactions dépendent de la longueur d'onde de la lumière mise en jeu mais aussi des propriétés physiques de la surface. Dans le cas d'une surface granulaire, ce sont principalement les tailles, agencements et compositions des grains qui interviennent. La plupart des surfaces observées peuvent être considérées comme granulaires (Hapke, 1993) et il est donc nécessaire de considérer la propagation de la lumière dans des milieux non uniformes. Au cours de cette propagation l'absorption du rayonnement par la matière peut se produire par des mécanismes de rotations moléculaires, vibrations moléculaires, vibrations du réseau cristallin ou par transition électronique. Ces absorptions sont directement reliées aux propriétés optiques des matériaux et notamment à leurs indices de réfractions complexes ($n+ik$). L'utilisation de ces propriétés optiques (que l'on nommera constantes optiques dans ce manuscrit) apparait comme nécessaire pour décrire finement les transferts de rayonnements dans une surface granulaire. Un autre aspect gouvernant la propagation de la lumière est la diffusion. Celle-ci peut-être simple ou multiple et son intensité peut varier en fonction de l'angle avec lequel la surface est observée. Ce phénomène est également relié aux propriétés physiques de la surface telles que sa composition, la taille des grains et la structure interne des particules (Hapke, 1993). Les paramètres d'albédo de diffusion simple et de fonctions de phase décrivent l'intensité et la directivité de la diffusion à l'échelle d'un grain.

Lorsqu'on traite un milieu complexe tel que le régolithe planétaire, on cherche à décrire la quantité d'énergie renvoyée par la surface vers le détecteur et on considère deux quantités : la contribution spéculaire (la lumière est réfléchie dans une seule direction, symétrique à la direction incidente du rayonnement) et la contribution diffuse (l'énergie qui n'est pas directement réfléchie mais est redistribuée dans l'espace après interaction avec la surface). A partir de cette dernière, deux champs d'investigations se distinguent. Le premier est la spectroscopie en réflectance qui désigne la quantité de lumière réfléchie par la surface en fonction de la longueur d'onde à une géométrie précise. A partir des interactions lumière-

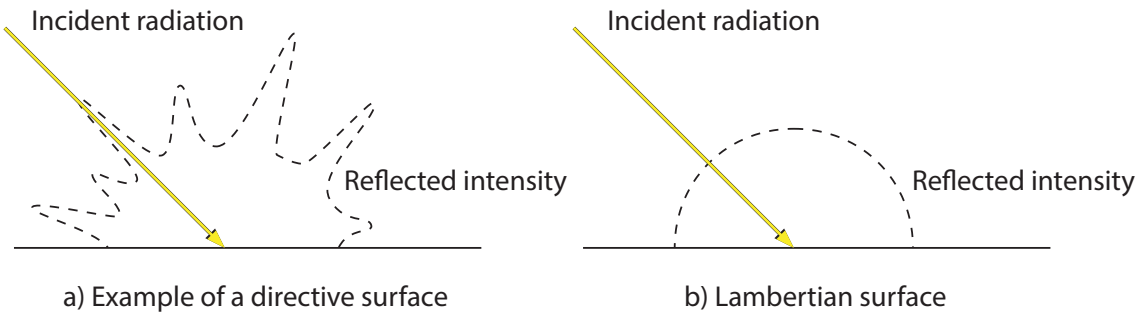

FIGURE 1 : Directivité d'une surface. (a) une surface complexe ou l'intensité du rayonnement dépend de l'angle avec lequel la surface est observée. (b) surface lambertienne : l'intensité du rayonnement est la même dans toutes les directions. En fait, le comportement d'une surface dépend aussi de l'échelle à laquelle elle est observée : si le champ de vision est plus petit que la dimension d'une facette de la surface orientée aléatoirement, elle apparaîtra spéculaire, sinon elle aura tendance à apparaître lambertienne (figure adaptée d'après (Andrieu et al., 2015)).

matière il est possible de remonter aux propriétés physiques de la surface telles que sa composition ou la taille de ses grains. La seconde est la photométrie qui désigne l'étude de la quantité de lumière réfléchie en fonction de la géométrie d'observation à une longueur d'onde particulière. La distribution angulaire de l'intensité de la lumière réfléchie donne accès aux propriétés physiques telles que la taille et formes des grains, la rugosité et la porosité de la surface. Ce travail se concentre sur la spectroscopie en réflectance. La contribution diffuse est non-négligeable lorsque l'on étudie les surfaces planétaires car elles sont rarement lambertiennes (rayonnement isotropes) et l'intensité de la lumière diffusée est très souvent orientée selon quelques directions préférentielles (voir fig. 1). Ainsi, pour décrire la quantité de lumière réfléchie (réflectance) d'une surface il est important d'intégrer la géométrie de l'observation, à savoir l'angle incident, l'angle émergent, l'angle azimutal et l'angle de phase.

A partir de ces considérations, une équation de transfert de rayonnement à travers un milieu optiquement inactif (pas de sources internes) diffusant, absorbant continuellement et éclairé par un flux électromagnétique a été proposé par *Chandrasekhar* en 1960 (Chandrasekhar, 1960). C'est l'équation du transfert radiatif qui intègre les phénomènes d'absorptions et de diffusions simples et multiples du rayonnement. A partir de cette équation, un très grand nombre de modèles de transfert radiatif ont vu le jour, chacun reposant sur des hypothèses différentes et intégrant d'autres effets du transfert de rayonnement. Parmi eux, nous pouvons citer les algorithmes de « traçage de rayons » (Chang et al., 2005; Pilorget et al., 2013) ou encore les méthodes numériques pour résoudre l'ensemble des solutions nombreuses et complexes du transfert radiatif (Stamnes et al., 1988; Grynko and Shkuratov, 2003; Shkuratov et al., 2003, 2005; Grynko and Shkuratov, 2007; Shkuratov et al., 2007). Ces approches, bien que couteuses en temps de calcul permettent des simulations très précises des spectres en réflectance mais reposent sur des hypothèses non réalistes dans le cas des surfaces planétaires, comme l'hypothèse du « champ lointain » dans laquelle les diffuseurs (les grains du milieu) sont supposés ne pas être en contact les uns avec les autres. Une autre approche réside sur le développement de formulation analytique ou semi-analytique en combinant des fonctions empiriques et semi-empiriques. Ceci implique que les modèles ne fournissent pas la solution exacte mais plutôt une approximation raisonnable. Il faut ainsi faire l'hypothèse que les propriétés radiatives du milieu peuvent être décrites statistiquement par leurs propriétés moyennes locales d'absorption et de diffusion (Kubelka, 1948; Hapke, 1981; Shkuratov et al., 1999) et par les paramètres photométriques tels que la rugosité, la porosité, la taille des grains, l'albédo de diffusion simple et la fonction de phase. Ce type de modèle a été privilégié dans ce travail de thèse, notamment le modèle DISORT (Stamnes et al., 1988) et le modèle de Hapke (Hapke, 1993)

Le modèle de DISORT (Stamnes et al., 1988) utilise la méthode discrète des ordonnées pour résoudre numériquement le transfert de rayonnement dans un milieu plan-parallèle diffusant, absorbant et

émettant. Ce modèle peut être utilisé lorsque plusieurs couches verticales hétérogènes sont considérées et il est possible d'intégrer la géométrie d'observation. Les paramètres principaux du modèle sont le nombre de couches considérées, les propriétés optiques de chaque couche (albédo de diffusion simple, épaisseur optique, fonction de phase), les propriétés de la surface (albédo, photométrie) et les propriétés géométriques (angle incident, émergent et azimutal). Ce modèle a notamment été utilisé pour investiguer la contribution des aérosols de l'atmosphère martien dans les spectres en réflectance observés par l'instrument NOMAD.

Le modèle photométrique de Hapke (Hapke, 1993) a été fréquemment utilisé en sciences planétaires et constitue le socle de ce travail. Ce modèle repose sur plusieurs hypothèses facilitant la résolution de l'équation du transfert radiatif. La première est que les propriétés radiatives peuvent être décrites statistiquement à partir des propriétés moyennes locales d'absorption et de diffusion. La seconde est que l'interaction entre un rayon incident et une particule isolée est décrite par l'albédo de diffusion simple (ω) et la fonction de phase ($P(g)$). La diffusion multiple est intégrée séparément. Enfin, le modèle intègre la rugosité de la surface (S) et l'effet d'opposition ($B(g)$) à faible angle de phase comme contribution à la diffusion de la surface et néglige les effets de la diffraction. La réflectance bi-directionnelle de la surface (r) à une longueur d'onde donné suit :

$$r(\mu_0,\mu,g) = \frac{\omega}{4\pi}\frac{\mu_0}{(\mu_0+\mu)}\left\{[1+B(g)]\,P(g)+H(\mu_0)H(\mu)-1\right\}S(\mu_0,\mu,g) \quad (1)$$

Où μ_0 est le cosinus de l'angle incident, μ le cosinus de l'angle émergent et g est l'angle de phase. Dans ce travail, nous considérons une fonction de phase de type Henyey-Greenstein à deux paramètres (Henyey and Greenstein, 1941).

A partir de ce modèle (équation 1) il est possible de simuler un spectre en réflectance d'une surface en fixant un certain nombre de paramètres : la géométrie d'observation, la fonction de Phase (paramètres b et c contrôlant l'isotropie et la direction du lobe de diffusion), la rugosité de la surface, la proportion volumique des composés formant le milieu et la taille de leurs grains. Les deux derniers sont reliés à la composition de la surface. Lorsque l'on considère une surface pure (un seul constituant) alors l'abondance volumique vaut 1 et seule la taille des grains intervient. A partir de deux composés, on suppose que la surface est composée de grains mélangés de manière homogène dans un mélange intime, et donc que la lumière traverse différents milieux. Chaque composé possède une abondance volumique propre et la somme des abondances vaut 1. La composition de la surface intervient à travers l'albédo de diffusion simple qui intègre les propriétés optiques des matériaux. Ainsi, les constantes optiques des matériaux considérés doivent être connues sur une même gamme de longueur d'onde pour intégrer différents composés dans le calcul d'un spectre en réflectance d'une surface. Ces constantes optiques sont mesurées en laboratoires et sont désormais disponibles pour un très grands nombre de glaces à travers les bases de données en ligne (SSHADE (Schmitt et al., 2017a)) ou dans les articles correspondants (Schmitt et al., 1998; Mastrapa et al., 2009; Quirico and Schmitt, 2018; Dalton and Pitman, 2012). Un exemple de spectres de surfaces estimés à partir du modèle de Hapke est présent fig. 2. Ces calculs sont généralement faits à la résolution spectrale des constantes optiques qui est plus élevée que la résolution spectrale des instruments observant les surfaces. Il faut donc intégrer la réponse spectrale de l'instrument lorsque l'on cherche à reproduire une observation à partir de ce modèle.

Inversion

Les modèles physiques tels que le modèle photométrique de Hapke (Hapke, 1993) sont utilisés pour faire des prédictions à partir de théories et concepts et d'une description complète du système. Ce problème de la prédiction d'une mesure est nommé le modèle direct. Par opposition, le problème visant à prédire les paramètres du modèle qui décrivent le système à partir d'une mesure est appelé le problème inverse. En sciences planétaires cette approche est très répandue car l'objectif est précisément de déterminer les propriétés d'un objet (ici une surface composée de glace) à partir des données récoltées par les observations (ici des spectres en réflectance).

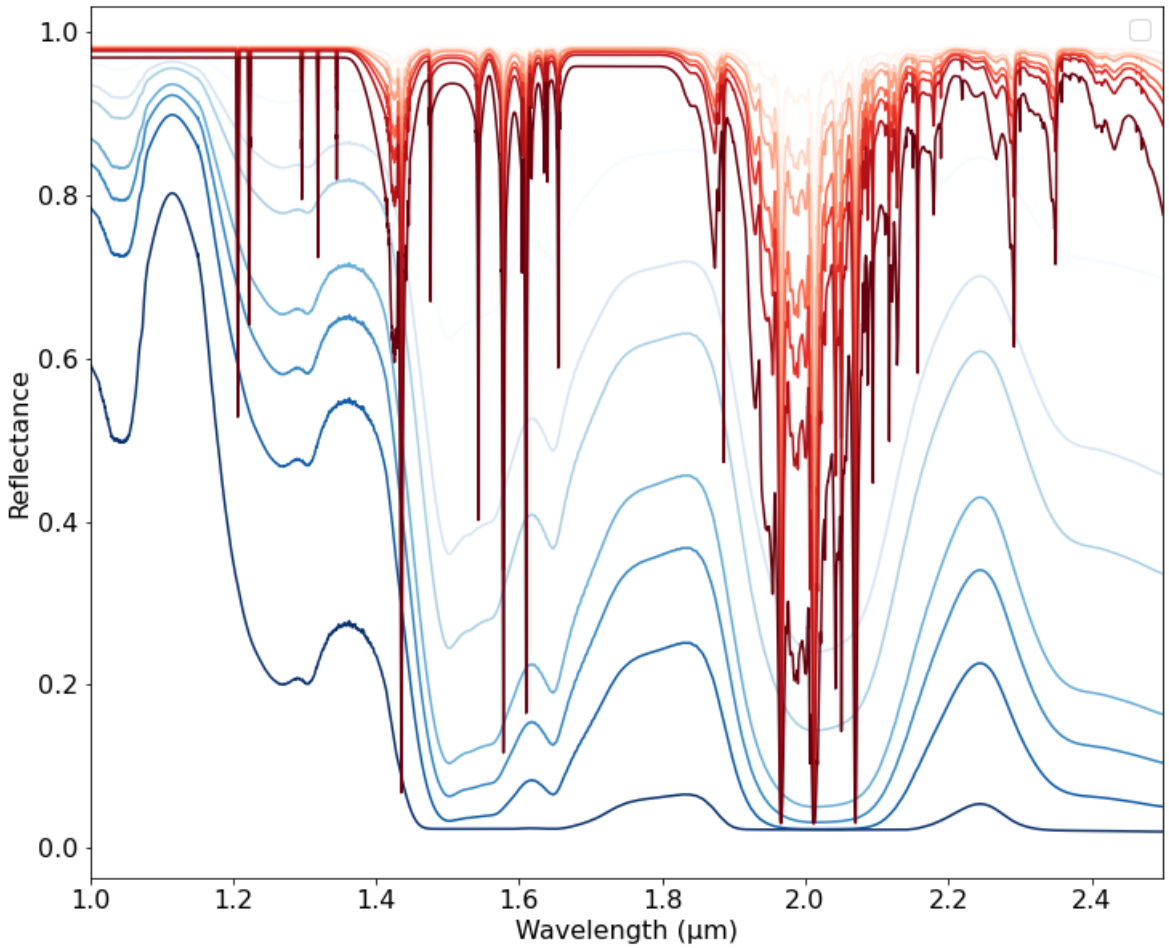

FIGURE 2 : Spectres en réflectance d'une surface granulaire faite de glace d'eau pure à 140-145K (Schmitt, 2020) (nuances de bleu) et de glace de CO_2 pure à 179K (Schmitt et al., 1998) (nuances de rouge) pour différentes tailles de grains (10, 50, 100, 300, 500, 1000 and 5000 μm (du clair au sombre) et considérant un angle incident de 55°, un angle émergent de 35° et angle azimutal de 180°. Les paramètres de fonctions de phases sont fixés à 0.5 pour *b* (paramètre d'asymétrie) et *c* (fraction rétro-diffusée) impliquant aucune direction préférentielle dans le régime de rétrodiffusion. La rugosité de la surface est de 2°. Les deux glaces ont un comportement spectral très différent. La glace d'eau est globalement sombre à ces longueurs d'ondes avec des bandes d'absorption très larges et une pente générale dans le continuum. La glace de CO_2 a un continuum très plat et brillant marqué par de nombreuses et étroites bandes d'absorptions au sein desquelles la réflectance diminue drastiquement. A mesure que la taille des grains augmente, les bandes d'absorptions de la glace d'eau deviennent très larges et finissent par disparaitre au sein d'un continuum global de très faible réflectance alors que les bandes de la glace de CO_2 s'approfondissent et s'élargissent légèrement mais le continuum conserve une réflectance élevée.

Pour ce travail de thèse, le problème inverse est de trouver le meilleur ensemble de paramètres du modèle de Hapke pour reproduire une observation de la surface. Il existe plusieurs difficultés lorsque l'on entreprend cet exercice. La première provient du fait que les paramètres estimés peuvent ne pas correspondre au vraies propriétés de la surface que l'on cherche à caractériser. Ceci peut provenir des non-linéarités présentes dans le modèle initial qui engendre une multi-modalité dans la forme des solutions (Tarantola, 2005). La seconde provient du fait qu'une incertitude est toujours associée aux données utilisées et qu'une mauvaise estimation ou prise en compte de ces incertitudes peuvent rapidement biaiser les résultats du modèle inverse. Ainsi, il convient que le choix de la stratégie d'inversion est dépendant du problème et qu'un compromis entre une estimation réaliste et un temps de calcul raisonnable doit être fait.

Plusieurs stratégies d'inversions existent et sont très bien documentées à ce jour. Depuis les méthodes de régression linéaires et de moindres carrés jusqu'aux méthodes plus complexes d'inférences bayesiennes. Dans cette thèse, nous avons sélectionné deux approches fondamentalement différentes que nous avons comparées via un jeu de données utilisées dans ce projet de recherche : une méthode d'optimisation non-linéaire par descente de gradient (Byrd et al., 1995; Zhu et al., 1997) et une approche par inférence bayesienne (Fernando et al., 2013; Schmidt and Fernando, 2015; Fernando et al., 2016; Cubillos et al., 2016).

La méthode d'optimisation par descente de gradient est une méthode itérative qui permet de converger vers une solution qui minimise la fonction de coût. Dans notre cas la fonction de coût désigne la qualité de l'ajustement entre le spectre simulé et le spectre observé et est fonction des paramètres du modèle de Hapke. A chaque itérations, une nouvelle fonction de coût est évaluée depuis l'espace des paramètres, le gradient agit comme un « compas » orientant l'optimisation dans l'espace des paramètres. La direction favorisant une descente plus abrupte du gradient est favorisée pour converger vers la solution finale. Un algorithme utilisant cette méthode (Byrd et al., 1995; Zhu et al., 1997) a été favorisé pour la calibration de l'instrument NOMAD (voir chap. 8). L'avantage de cette approche est que la solution est obtenue pour un temps de calcul très raisonnable. L'inconvénient est que ce type de méthode peut facilement converger vers un minimum local, particulièrement lorsque le modèle physique présente des non-linéarités et des corrélations fortes entre ces paramètres.

Les méthodes d'inférences bayesiennes sont de plus en plus utilisées en sciences planétaires (Fernando et al., 2013; Schmidt and Fernando, 2015; Fernando et al., 2016; Schmidt and Bourguignon, 2019; Belgacem et al., 2020, 2021; Mishra et al., 2021b,a; Harrington et al., 2022; King et al., 2022) car elles permettent de s'affranchir des problèmes de non-unicité des solutions tout en intégrant correctement les incertitudes associées aux données. Ces méthodes reposent sur les probabilités conditionnelles formalisées par le théorème de Baye. Ce théorème relie la probabilité conditionnelle du paramètre m connaissant la donnée d (nommé la probabilité *a posteriori*) à la probabilité conditionnelle du même paramètre sans connaissance de la donnée (nommé probabilité *a priori*). La connaissance est mise à jour depuis l'antérieur au postérieur en utilisant la probabilité conditionnelle que les données se produisent si le paramètre m est vrai (nommé la vraisemblance ou « Likelihood » en anglais). Ces méthodes reposent sur deux aspects fondamentaux. Le premier est l'intégration d'une connaissance *a priori* réaliste permettant de décrire les incertitudes associées aux données mais aussi l'état des connaissances sur les paramètres à estimer. Dans notre cas ces paramètres sont reliés au modèle de Hapke et représentent les propriétés microphysiques de la surface (proportions volumiques, taille des grains et rugosité de la surface). Ces connaissances sont fonctions des données utilisées et donc de l'objet investigué. Nous considérons ici une distribution uniforme de Dirichlet (Lapotre et al., 2017) pour décrire les proportions volumiques et garantir la somme à 1 des abondances estimées. Nous considérons une distribution log-uniforme pour les tailles de grains entre 10 et 10^5 μm, la limite basse étant imposée par les considérations de l'optique géométrique (la taille des grains doit être plus grande que la longueur d'onde). Pour la rugosité macroscopique nous considérons une distribution uniforme entre 0° et 45° telle que théoriquement prévue par Hapke (Hapke, 1984). Un second aspect des méthodes bayesiennes est la définition d'un échantillonneur des distributions de probabilité *a priori*. Pour ce faire, une approche courante est l'utilisation des méthodes Markov Chain Monte Carlo (MCMC). Ces méthodes reposent sur la construction d'un

« marcheur » qui échantillonne de façon aléatoire l'espace des paramètres pour créer une séquence de différents paramètres appelé une « chaîne ». Une propriété importante de la chaîne est que sa densité d'échantillon est proportionnelle à la fonction de densité de probabilité (Probability Density Function ou PDF) postérieur. A partir de ce concept, différents algorithmes ont été développés utilisant des « marcheurs » permettant l'exploration d'espaces de paramètres plus ou moins complexes.

Dans ce travail de recherche nous avons comparé un algorithme de descente de gradient (Byrd et al., 1995; Zhu et al., 1997) et deux méthodes d'inversions bayesiennes basées sur deux méthodes d'échantillonnages différentes. La première est une adaptation de l'algorithme très connu de Metropolis-Hasting (Metropolis et al., 1953; Hastings, 1970) basé sur une exploration de l'espace des paramètres par pas aléatoires. Une version de cet algorithme a été adapté et utilisé dans le passé pour la détermination des paramètres de Hapke (Fernando et al., 2013; Schmidt and Fernando, 2015; Fernando et al., 2016) et a été révisé depuis (Schmidt and Bourguignon, 2019). La seconde est basée sur une méthode MCMC d'évolution différentielle avec une proposition « Snooker » (Braak, 2006; ter Braak and Vrugt, 2008) disponible librement sous licence Python (Cubillos et al., 2016). Cet algorithme repose sur la construction de chaînes MCMC parallèles facilitant la convergence et permettant d'explorer un espace des paramètres plus complexe. Deux cas d'études ont été investigués : l'inversion des paramètres de Hapke sur un seul spectre et l'inversion des paramètres de Hapke sur une image hyperspectrale complète (plusieurs milliers de spectres). Deux aspects importants sont considérés, l'estimation finale de la solution et le temps de calcul.

Ce travail a permis de sélectionner la méthode d'inversion la plus adaptée aux objectifs établis pour ce travail de recherche, à savoir la caractérisation des propriétés microphysiques de la surface à partir du modèle de Hapke. Il apparait que la très forte non-linéarité et les corrélations entre les paramètres forcent l'utilisation des méthodes bayesiennes pour correctement estimer les paramètres du modèle. Bien que les méthodes classiques d'optimisation peuvent converger vers un minimum global elles sont fortement dépendantes de l'initialisation et ne rendent pas compte des distributions complexes que peuvent prendre les solutions (voir fig. 3). Les méthodes bayesiennes ont un prix couteux en temps de calcul mais permettent de correctement rendre compte de la forme de la solution, ce qui évite les biais dans l'interprétation des résultats. Face à la très grande dimensionnalité que peut prendre le problème inverse il apparait que les méthodes MCMC d'évolution différentielle avec une proposition « Snooker » (Braak, 2006; ter Braak and Vrugt, 2008) sont plus robustes que les échantillonneurs de type Metropolis-Hasting.

Microphysique de la surface d'Europe

Contexte scientifique

Europe est la plus petite et la plus brillante des quatre lunes galiléennes. Sa surface est majoritairement composée de glace d'eau et est profondément marquée par de grands linéaments traversant le satellite sur plusieurs milliers de kilomètres. Le très faible nombre de cratères observés (Moore, 2001) font de sa surface la plus jeune des trois satellites de glace avec un âge estimé à environ 50 millions d'années (Pappalardo et al., 1999). Europe est verrouillé par effet de marée avec Jupiter ce qui implique qu'un hémisphère est constamment orienté face à Jupiter. Les très fortes forces de marées imposées par la géante gazeuse sont à l'origine d'un chauffage interne qui serait par ailleurs impossible au regard de la faible taille du satellite. Ainsi, les premières données du champs de gravité par la mission Galileo ont révélé que la lune était totalement différentiée avec un noyau solide en fer, un manteau rocheux et une couche d'eau d'environ 80 km d'épaisseur (Anderson et al., 1998b). De plus, les données du magnétomètre ont révélé la présence d'un champ magnétique induit pouvant s'expliquer par la présence d'une couche conductive en profondeur (Khurana et al., 1998) tel qu'un océan global d'eau salée. Ces particularités ont rapidement provoqué un grand engouement pour l'étude du satellite et de son habitabilité car Europe regroupe les ingrédients propices à l'émergence de la vie : de l'eau, de l'énergie et les éléments chimiques favorables à la présence de matière organique (C, H, N, O, P, S) à l'interface manteau/océan.

La surface d'Europe est marquée par une grande variété de morphologies qui ont été regroupées en

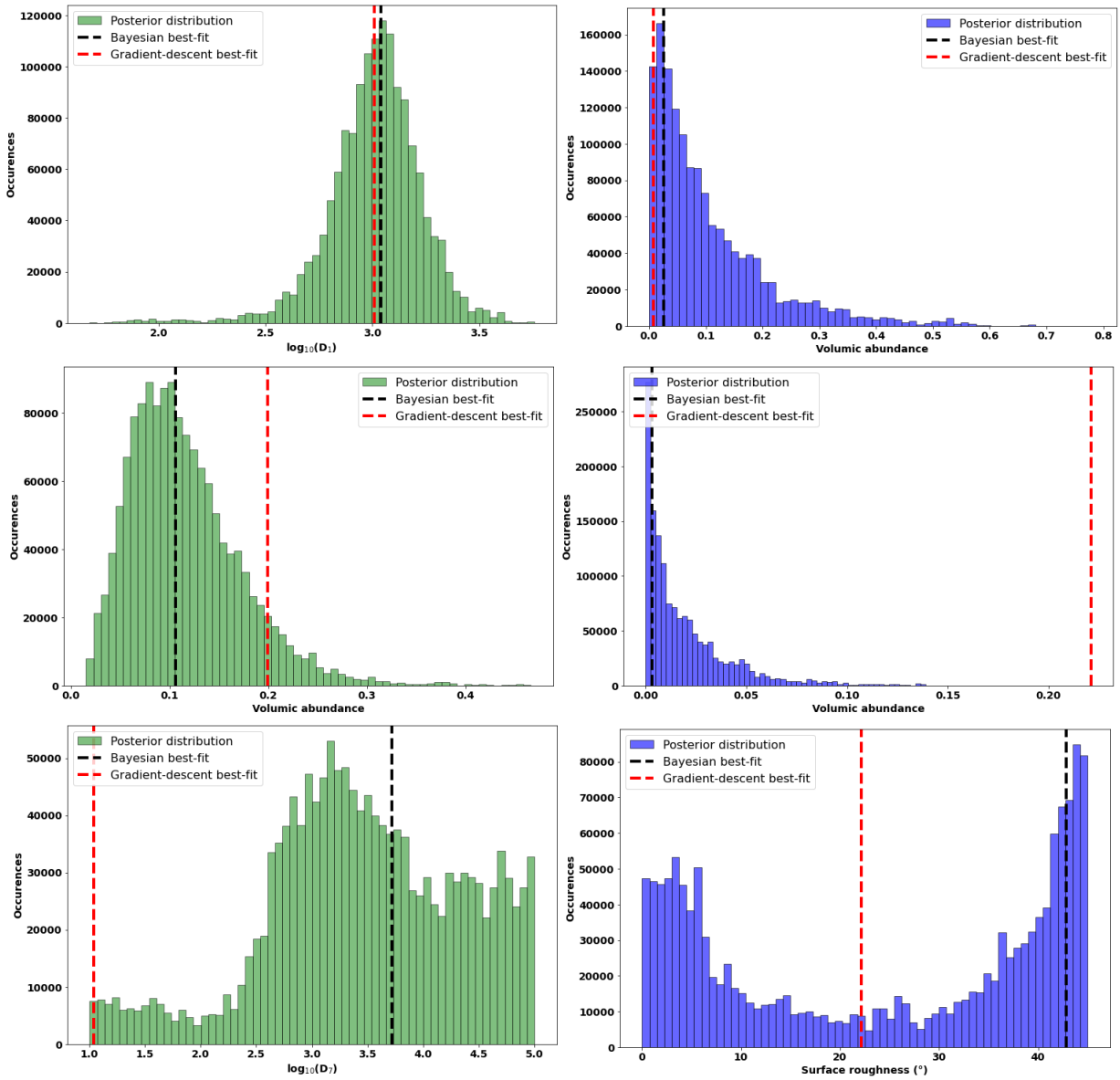

Figure 3: Comparaison des méthodes d'inversion bayésiennes et d'optimisation par descente de gradient. Ces quelques exemples de distribution postérieure estimés par la méthode bayésienne illustrent les variétés de formes de solutions que peuvent prendre les paramètres de Hapke. Le «meilleur ajustement» (lignes pointillées en noir et rouge) correspondent au meilleur ensemble de paramètres estimés par les deux méthodes. Quand les distributions postérieures sont simples (en haut) les deux algorithmes trouvent des solutions équivalentes. Mais ceci n'est pas toujours vrai (au milieu) et parfois les méthodes par descente de gradient estiment des solutions très peu probables au sens bayésien. Lorsque les distributions se complexifient (en bas), les méthodes classiques échouent et le «meilleur ajustement» n'a plus la même signification tant la solution est complexe.

plusieurs ensembles : les rides et bandes, les chaos, les lenticulae, les cratères, les dépôts sombres et les plaines lisses (voir fig. 4) . Chacune de ces morphologies comprend des déclinaisons de tailles et formes diverses (Lucchita and Soderblom, 1982; Geissler et al., 1998; Greeley et al., 2000). La majorité des observations provient de la mission Galileo qui n'a effectué que quelques survols de la lune à des distances variées impliquant une couverture non-homogène de la surface et des résolutions spatiales très différentes, compliquant parfois leurs identifications. Toutefois cette diversité de morphologies et le faible nombre de cratères identifié ont rapidement suggéré l'idée de processus favorisant un resurfaçage actif du satellite, du moins à l'échelle des temps géologiques.

La composition de la surface a été largement étudiée par télescopie depuis la Terre et son orbite mais également par différentes missions spatiales et notamment par la mission Galileo et son spectro-imageur NIMS (Carlson et al., 1992). Un très grand nombre de composés chimiques ont été identifiés et confirmés par la suite. D'abord la glace d'eau a été rapidement identifiée (Kuiper, 1957; Harris, 1961) sous forme cristalline et amorphe (Ligier et al., 2016; Mishra et al., 2021a; King et al., 2022). La majorité des débats porte sur la nature des composés associés à la glace d'eau, des composés hydratés tels que les sulfates de magnésium et sodium ont été proposés (McCord et al., 1998; Dalton, 2007) ainsi que l'acide sulfurique (Carlson et al., 2002, 2005). Plus récemment des chlorinates hydratés ont également été suggérés (Brown and Hand, 2013; Hanley et al., 2014; Trumbo et al., 2020). Enfin, des composés mineurs tels que les oxydants (Carlson et al., 1999a; Trumbo et al., 2019). Bien qu'il n'existe pas de consensus sur la composition actuelle de la surface, ces études témoignent d'une grande diversité de compositions chimiques traduisant des processus complexes pouvant varier significativement d'une localisation à l'autre.

Ces morphologies et compositions de la surface lèvent le voile sur la nature des processus physico-chimiques affectant la surface. Deux catégories distinctes de processus peuvent-être définies : les phénomènes exogènes et endogènes.

Les processus exogènes désignent l'ensemble des phénomènes provenant de l'environnement extérieur du satellite. Ce dernier est profondément influencé par l'environnement magnétique et gravitationnel de Jupiter. Le bombardement intense par un plasma de haute énergie composé d'électrons et de protons (Pospieszalska and Johnson, 1989; Carlson et al., 1999b; Greeley et al., 2000; Cooper, 2001) provenant de la magnétosphère de Jupiter et arrachant des atomes d'oxygène et de souffre de l'atmosphère de Io favorise la mise en place d'un cycle du soufre radiolytique (Carlson et al., 2002, 2005) qui affecte profondément la chimie de la surface. Ceci combiné à la présence de sulfates permet la production *in situ* d'acide sulfurique hydraté sur l'hémisphère arrière. Un autre phénomène extérieur affectant la structure et composition de la surface est le bombardement de météorites et micro-météorites. Le fort champ gravitationnel de Jupiter favorise un flux plus important sur l'hémisphère avant. Ces impacts peuvent amorphiser la glace et également l'enrichir en impuretés et favoriser une composition chimique complexe.

Les processus endogènes regroupent l'ensemble des phénomènes provenant de l'environnement interne du satellite. Sur Europe ces processus désignent principalement les interactions entre les réservoirs profonds d'eau liquide (océan global ou réservoirs plus locaux en subsurfaces). Dû au fort gradient de température entre la surface (100K) et l'océan (273K) de la convection est supposée se produire dans la croûte de glace (Tobie, 2003) favorisant un mélange et un apport d'éléments chimiques en profondeur vers la surface. La possibilité que du liquide ou du gaz soit remonté en direction de la surface a favorisé l'émergence de modèle de « cryovolcanisme » (Geissler, 2015). Un très grand nombre de modèles tentent à ce jour de démontrer cette possibilité (Fagents, 2003; Figueredo, 2002; Miyamoto et al., 2005; Quick et al., 2013; Quick and Marsh, 2016; Lesage et al., 2020, 2022) afin d'expliquer les morphologies observées. Ainsi, les chaos, rides, lenticulae sont notamment proposés comme morphologies témoins de processus cryovolcanique à l'origine d'apport de matériel et de resurfaçage. En revanche, la composition des cryolaves n'est pas contrainte car les modèles reposent sur des hypothèses de compositions chimiques de l'océan au cours de la formation et de l'évolution du satellite (Kargel, 1991, 1992; Barr and Canup, 2008). Néanmoins, les modèles suggérant une évolution à partir de matériaux comparables à ceux d'une chondrite carbonée prédisent la précipitation d'une grande quantité de sulfates de magnésium et de sodium dans l'océan, ce qui est cohérent avec la détection de ces sulfates en surface. Toutefois, la

FIGURE 4 : Image colorisée d'Europe obtenue par la sonde Galileo (NASA) combinant différentes images. La zone présente différentes morphologies : rides, bandes, chaos et lenticulae. Les zones blanches sont supposément plus riches en glace d'eau et les zones rougeatres sont de la glace d'eau mélangée à d'autres composés. Crédit : NASA/JPL-Caltech/SETI Institute.

composition de la surface telle qu'observée à ce jour est le résultat d'une combinaison complexe entre processus endogènes et exogènes si bien que la composition de l'océan ne peut pas être contrainte qu'à partir de la composition de la surface.

Europe est au centre des futurs missions spatiales ESA/JUICE et NASA/EuropaClipper qui apporteront leurs lots de réponses à l'aide des instruments plus performants. En attendant, il est nécessaire de pousser les investigations de la surface pour désigner des futures cibles d'intérêts de ces missions. Les études précédentes ont révélées de premières informations concernant la structure et composition de la surface. Cependant, plusieurs limites existent à ces études. La première réside dans l'utilisation de modèle de mélange linéaire (Carlson et al., 2005; Dalton, 2007; Ligier et al., 2016; King et al., 2022) ou de comparaison spectrale entre les données et les spectres théoriques obtenus en laboratoire (Dalton et al., 2005; Hanley et al., 2014) ce qui ne permet pas d'investiguer finement les propriétés des glaces (voir sec.). De plus, ces études utilisent des données à faibles résolutions spatiales provenant d'observation télescopique (Ligier et al., 2016; King et al., 2022) ne permettant pas d'investiguer des morphologies caractéristiques. Certains travaux utilisant un modèle de transfert radiatif plus réaliste existent mais se limitent à quelques spectres d'Europe (Mishra et al., 2021b,a). Enfin, la plupart des études utilisant les données NIMS sous-estiment les incertitudes associées aux données et leurs calibrations (Carlson et al., 1992)

Nous proposons donc de conduire une étude des propriétés microphysiques de la glace d'Europe via l'utilisation d'un modèle de transfert radiatif réaliste. Les données de l'instrument NIMS permettent de résoudre certaines des morphologies importantes d'Europe (linéaments, cratères, chaos) avec une résolution spatiale de quelques kilomètres par pixel. L'inversion de ces données peut ainsi révéler la composition et texture de glace afin de comprendre la nature des processus géologiques responsables des morphologies observées. Les questions investiguées sont : Quel est la véritable composition de la surface sur ces zones et comment sélectionner les meilleurs composés chimiques parmi tous ceux suggérés jusqu'à présent ? Peut-on différencier ces composés avec les données NIMS ? Si oui, combien de composés sont nécessaires pour reproduire les observations faites par NIMS ? Comment sont les propriétés des glaces au sein d'un linéament ou d'un cratère et ses alentours ? Existe-t-il une corrélation entre ces propriétés et les morphologies ? Certaines de ces questions font l'objet d'un premier travail réalisé dans cette thèse.

Sélection des composés chimiques pour l'étude de la surface

Nous avons investigué la question de la composition chimique d'Europe à partir des données de Galileo/NIMS. Pour ce faire, nous avons sélectionné un spectre d'un linéament sombre (crossing of *Rhadamanthys Linea* et *Harmonia Linea*) provenant d'une observation à haute résolution spatiale de l'hémisphère arrière anti-Jovien (16.5°-21° Nord, 155°-165° Est). Ce spectre combine une résolution spectrale correcte sur la gamme $1 - 2.5\ \mu$m et montre des bandes d'absorption de l'eau très distordues, caractéristique d'une composition chimique complexe.

Nous utilisons le modèle photométrique de Hapke (Hapke, 1993) pour simuler le transfert de rayonnement couplé à une méthode d'inversion bayésienne robuste (Cubillos et al., 2016) pour estimer les paramètres du modèle (voir sec.). Nous avons sélectionné une liste de 15 espèces chimiques incluant certaines suggérées par les études précédentes (glace d'eau cristalline et amorphe, sulfates hydratés de magnésium et de sodium, acide sulfurique hydratée, chlorinate) et avons ajouté d'autres composés non intégrés jusqu'à présent (magnétite et sulfate d'ammoniac). Il n'est pas raisonnable de considérer toutes ces espèces au sein d'une seule inversion spectroscopique car cela garantirait un surajustement des données et ne permettrait pas d'interpréter les propriétés microphysiques. C'est pourquoi nous cherchons à déterminer le nombre de composés idéal pour reproduire cette observation de la surface et de sélectionner les meilleurs composés parmi cette liste. Nous avons donc testé, pour la première fois, toutes les combinaisons de 3, 4 et 5 composés parmi les 15 disponibles et déterminons, pour chacune de ces combinaisons, les paramètres du modèle de Hapke permettant d'ajuster le plus fidèlement l'observation NIMS.

La force de cette approche réside dans le fait que l'incertitude sur la calibration radiométrique abso-

lue de l'instrument pouvant atteindre 10% (Carlson et al., 1992) est correctement pris en compte dans l'estimation des solutions. Face au très grand nombre de combinaisons testées (plus de 5000) le nombre de résultats à analyser explose (à chaque combinaison est associé 7 à 11 paramètres estimés et leurs fonctions de densité de probabilité postérieur) c'est pourquoi nous utilisons des indicateurs statistiques sur la qualité des ajustements. Nous distinguons ainsi deux scénarios : un cas pessimiste où le ratio signal-sur-bruit (SNR) est faible et donc l'incertitude sur le niveau du spectre est élevée (10%) et un cas optimiste ou le SNR est élevé et donc les incertitudes sur les données sont faibles (1%). Nous montrons ainsi que dans le scénario pessimiste, la totalité des combinaisons testées est acceptable en terme de qualité de l'ajustement aux données. Bien que certaines combinaisons semblent produire de meilleurs ajustements, il n'est pas possible de trancher au vue de la très grandes incertitude sur les données.

Lorsque l'on considère un scénario optimiste et donc un SNR élevé, nous montrons qu'il n'y a aucune combinaison de 3 composés permettant de reproduire correctement la donnée NIMS. Il existe 21 et 153 combinaisons de 4 et 5 composés produisant des ajustements très corrects mais non discernables par les données NIMS (voir fig. 5). Ce premier constat implique qu'il n'est pas possible de facilement discriminer parmi tous ces composés car ils sont tous susceptibles d'être représentatifs de la surface. Il apparait que seulement 4 composés soient nécessaires pour décrire un des spectres les plus singuliers de la surface mais les ajustements sont de meilleures qualités en utilisant 5 composés. Intégrer plus de composés au mélange prend le risque de surajuster l'observation et empêcherait toutes interprétations des propriétés microphysiques.

Afin de discuter des composés les plus pertinents parmi ces nombreuses combinaisons acceptables, nous comparons à l'aide d'indicateurs l'ensemble de ces résultats. Nous discutons la qualité des ajustements et la contribution spectrale des composés lorsqu'ils sont inclus et exclus du mélange sur l'ensemble des combinaisons testées. Nous incluons également la distribution des composés au sein des 21 et 153 meilleurs ajustements et comparons les proportions numériques des composés correspondants. La proportion numérique permet de relier la proportion volumique et la taille des grains estimés au sein d'un même indicateur décrivant optiquement le milieu. Ainsi, une abondance numérique élevée indique un milieu dominé spectralement par un certain composé alors qu'une abondance numérique faible témoigne d'une contribution moins importante. Ceci permet de donner une représentation du milieu granulaire estimé par les inversions. Il apparaît qu'un même composé peut ainsi avoir des proportions numériques très variées entre deux combinaisons différentes et produire des ajustements similaires. Ce résultat montre à quel point le transfert de rayonnement dans les glaces n'est pas linéaire et certains paramètres comme les tailles des grains peuvent contribuer fortement à l'ajustement des données.

Ces différents critères ont permis de classer les composés chimiques testés. Ainsi, pour cette observation d'Europe l'acide sulfurique hydraté et la glace d'eau semblent absolument nécessaires, ce qui est en accord avec les études précédentes (Ligier et al., 2016; Mishra et al., 2021a; King et al., 2022). Parmi les composés mineurs, les sulfates hydratés sont retenus dans un plus grand nombre de combinaisons mais il n'est pas possible de les discriminer via les données NIMS à ces longueurs d'ondes, d'autant plus lorsque leurs compositions chimiques sont proches. Des contraintes extérieures sont nécessaires pour préciser la composition chimique de la surface d'Europe. Ce même exercice conduit sur une autre observation produirait des résultats similaires, et donc il n'est pas possible de précisément contraindre la composition et les propriétés microphysique de la surface d'Europe avec NIMS. Ces contraintes pourront venir d'autres instruments ou de données à plus hautes résolutions spectrales, sur une plus grande gamme spectrale et un SNR plus élevé.

Une autre approche envisageable est de caractériser les proportions relatives des « familles chimiques » en sélectionnant un composé représentatif de chaque ensemble chimique (un sulfate hydratée, un chlorinate, etc...). Un tel mélange comporterait plus de 5 composés et prendrait le risque de surajuster les données. Néanmoins, en faisant l'impasse sur une caractérisation précise des propriétés microphysiques, il sera possible de discuter des abondances relatives de ces différents sels et éventuellement mettre en exergue des corrélations spatiales avec les morphologies.

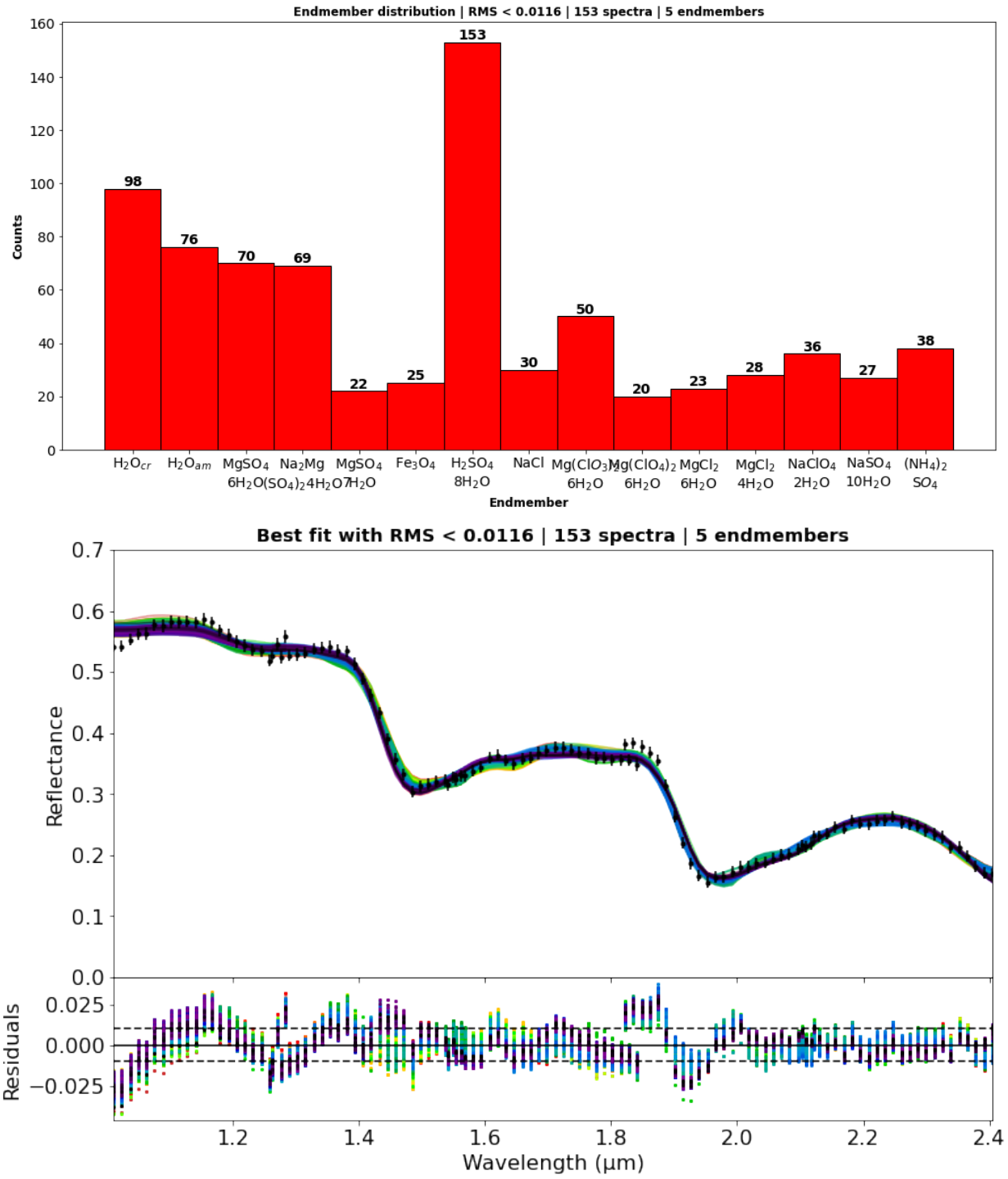

FIGURE 5 : Sélection des composés chimiques pour Europe : les 153 combinaisons de composés chimiques retenus dans le cas du scenario optimiste sur le SNR des données NIMS. (haut) : distribution de ces composés dans les combinaisons retenues. L'acide sulfurique hydraté et la glace d'eau (soit sous forme cristalline, soit amorphe, soit les deux ensemble) sont toujours utilisés. Les autres composés ont des distributions plus variables mais il existe plusieurs combinaisons utilisant chacune de ces espèces chimiques. (bas) : les meilleurs ajustements estimés par l'inversion bayesienne pour ces 153 combinaisons. Bien que des différences soient discernables il n'est pas possible de discriminer parmi tous ces ajustements au regard des incertitudes sur les données NIMS.

Les glaces de Mars avec ExoMars Trace Gas Orbiter

Contexte scientifique

Mars est la quatrième planète du système solaire et orbite à environ 1.52 Unités Astronomiques (UA) du Soleil. Son observation remonte à l'antiquité avec la mise en évidence de son mouvement rétrograde dans le ciel par l'astronome Egyptien Senenmut 1500 ans avant notre ère. Depuis, notre compréhension de la planète rouge n'a cessé de croître principalement grâce aux divers instruments à bord des très nombreuses missions spatiales. Mars est environ deux fois plus petite que la Terre avec un rayon équatorial de 3396 km mais possède une inclinaison similaire (environ 25°) ce qui lui confère un cycle annuel des saisons. Du fait de sa forte excentricité les saisons sont plus prononcées dans l'hémisphère Sud qui connait des hivers longs et froids et des été courts et chaud. Sa surface présente une dichotomie importante, les terrains de l'hémisphère Nord sont majoritairement des plaines de basses altitudes faiblement cratérisées et donc plus jeunes alors que l'hémisphère Sud est composé de hauts plateaux fortement cratérisés, témoins d'un âge très ancien.

Mars possède une atmosphère très ténue avec une pression de surface variant de 3 à 12 mbar majoritairement composée de CO_2 (96%). Cependant, cette atmosphère joue un rôle significatif sur le climat martien et affecte également la surface. La circulation atmosphérique martienne est principalement contrôlée par le cycle du CO_2(Leighton and Murray, 1966). En effet, durant les hivers locaux la température de surface atteint la température de condensation du CO_2(140K) ce qui favorise la condensation en surface d'une fraction du gaz atmosphérique sous forme de glace de CO_2. Ceci entraine des variations drastiques de pression de l'ordre de 30% de la pression atmosphérique totale. Ce phénomène produit un gradient latitudinal de pression qui permet la formation d'une cellule de Hadley (Forget et al., 1999) dont la branche ascendante commence dans l'hémisphère d'été et transporte les composants atmosphériques vers l'hémisphère d'hiver. Puis l'air redescend et se dirige vers l'hémisphère d'été provoquant de forts vents de surface et chargeant l'atmosphère en poussière du régolithe. Au cours des printemps locaux, la température remonte et la glace de CO_2ce sublime ce qui augmente la pression atmosphérique et stoppe la circulation de la cellule de Hadley jusqu'au prochain hiver. Cette cellule change de direction à chaque équinoxe (Forget et al., 1999) et est directement corrélée aux variations de pressions annuelles mesurées. Ce cycle est particulièrement visible sur les calottes polaires Nord et Sud et le développement de dépôts saisonniers jusqu'à des latitudes très basses (50°).

En plus des glaces permanentes et saisonnières de CO_2, des glaces d'eau ont été identifiées sur Mars. La calotte polaire résiduelle Nord est majoritairement composée de glace d'eau (Phillips et al., 2008) alors que la calotte résiduelle Sud est composée principalement de glace de CO_2 surmontant une couche d'une centaine de mètres de glace d'eau quasi-pure (Kieffer, 1979). Un autre réservoir important en glace d'eau est la subsurface martienne dont les mesures par des spectromètres à neutron ont révélé un sous-sol riche en hydrogène avec des proportions variant de 2 à 70% (Feldman, 2004).

Les poussières de l'atmosphère martienne jouent également un rôle important sur les processus de surface. Les forts vents générés par la circulation atmosphérique permettent le transport de ces poussières et leurs interactions avec les surfaces glacées. Ce transport peut se faire à différentes échelles, depuis le simple tourbillon de poussière à la tempête généralisée sur toute la planète. Ces poussières ont des propriétés optiques favorisant une forte absorption du rayonnement solaire visible qu'elles restituent sous formes de chaleurs dans l'atmosphère. Ce sont également de très bon diffuseurs empêchant ainsi le rayonnement d'atteindre la surface. Ceci peut accroître le contraste thermique entre la surface et l'atmosphère et renforce la circulation. C'est cet effet de rétroaction positif qui permet le déclenchement de tempêtes régionales et globales.

Plusieurs morphologies observées sont associées à la présence de glaces saisonnières de CO_2 et d'eau. Certaines d'entre elles comme les spiders (voir fig. 6) sont associées à des processus actifs se produisant chaque année au cours d'une certaine saison. Ces structures aranéiformes sont associées à la présence de glace de CO_2 transparente laissant apparaitre la surface plus sombre sous-jacente et sont souvent corrélées avec la présence de dépôts sombres surmontant cette dernière. Pour expliquer ces morphologies le modèle de jet de gaz froid (Piqueux, 2003; Kieffer et al., 2006) est proposé. Ce modèle

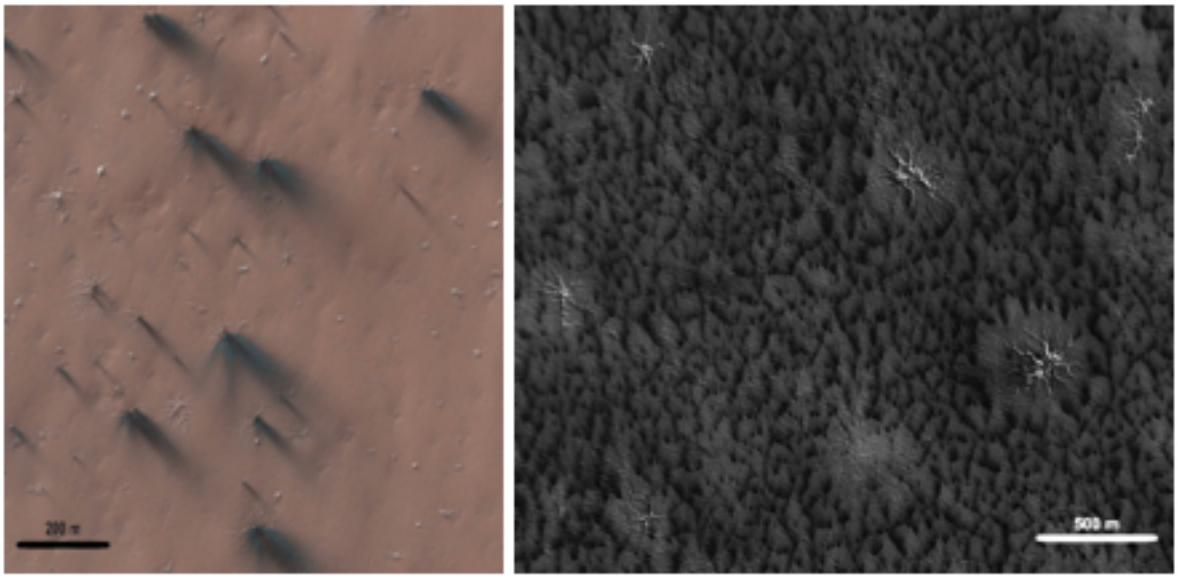

FIGURE 6 : Les « spiders » sont parfois associés aux dépôts sombres (à gauche) et parfois entourés par des dépôts sombres (droite). Ces images ont été prises au cours du printemps Sud à hautes latitudes (85-87°S).

repose sur les propriétés optiques de la glace de CO_2 qui est transparente dans les longueurs d'onde du visible et absorbe ainsi très peu le rayonnement incident, qui atteint le régolithe sous-jacent. Ce dernier absorbe une portion significative du rayonnement qu'il restaure sous forme de radiation thermique dans l'infrarouge à des longueurs d'onde où la glace de CO_2 est fortement absorbante. La glace commence donc à se sublimer par le dessous formant des poches de gaz de CO_2. Lorsque la pression dans la poche de gaz excède le poids de la couche il y a rupture et le gaz et les poussières sont rapidement éjectés en surface. Les poussières peuvent alors se redéposer sous forme de dépôts sombres en surface de la glace. Bien que ce modèle soit supporté par des études thermiques, dynamiques et mécaniques montrant sa cohérence avec les observations (Thomas et al., 2011) il existe plusieurs problèmes à ce sujet. Le premier est que ces jets n'ont jamais été observés directement. De plus, le modèle n'explique pas les variations spatiales observées à des échelles très locales.

Ainsi, une étude fine des propriétés microphysiques peut permettre de comprendre plus amplement ce phénomène. Quel est l'état de la glace de CO_2 à ces localisations (Andrieu et al., 2018) ? Quel est le rôle des impuretés de glace d'eau et/ou de poussière dans ce phénomène ? Existe-t-il un seuil de proportion volumique des impuretés pour empêcher ou déclencher ce processus ? Existe-t-il un lien avec d'autres morphologies actives comme les écoulements sombres (Pasquon et al., 2016; Portyankina et al., 2019) ? Si ce phénomène est réel, alors il joue un rôle important dans la dynamique atmosphérique martienne comme agent de transport de la poussière et peut représenter le phénomène géomorphologique le plus actifs de Mars (Piqueux and Christensen, 2008).

Avec l'arrivée de la mission ExoMars Trace Gas Orbiter (TGO) en orbite autour de Mars en 2018 nous avons pour la première fois accès à des observations de la surface de Mars à des heures locales très variées (Vago et al., 2015), allant de très tôt dans la matinée à tard dans l'après-midi. A son bord plusieurs instruments dont la suite de spectromètre NOMAD (Vandaele et al., 2015; Neefs et al., 2015) et son canal nadir LNO (Limb and Nadir Occultation). Cet instrument opère sur la gamme $2.3 - 3.8\ \mu$m avec un pouvoir de résolution de 10000 ce qui permet d'accéder à une très haute résolution spectrale, idéal pour une caractérisation des propriétés microphysiques de la glace. Le principal inconvénient étant la faible résolution spatiale (empreinte au sol de quelques dizaines de kilomètres) ne permettant pas de résoudre directement les morphologies. Néanmoins, l'orbite très basse de la mission assure une rapide couverture globale de la planète et peut permettre un suivi temporel des propriétés de surfaces. Cette unique combinaison d'observations à des latitudes, heures locales et saisons très variées est prometteuse

pour la compréhension des processus saisonniers martiens.

Calibration de NOMAD/LNO

L'utilisation des données du spectromètre NOMAD/LNO a d'abord nécessité de travailler sur une calibration spectro-photométrique de l'instrument. Pour ce faire, deux approches existent. La première développée par (Thomas et al., 2022) consiste en l'utilisation des observations du Soleil faites par LNO pour directement calibrer les données nadir de l'instrument. En utilisant plusieurs observations à des températures instrumentales différentes et une méthode d'interpolation linéaire un spectre synthétique fonction de la température est généré pour calibrer les observations nadirs. Cette approche à l'intérêt d'être proche des données et n'efface aucune information contenue dans le spectre lors de la calibration. En revanche, elle repose sur l'hypothèse que l'instrument est stable temporellement et que seule la température est responsable des effets instrumentaux. Si d'autres effets existent ils ne sont, par conséquents, pas intégrés et peuvent produire des biais dans les données nadir calibrées.

Une seconde approche a été proposée au cours de ce travail de recherche pour calibrer l'instrument NOMAD (Cruz-Mermy et al., 2022). Cette approche repose sur des considérations théoriques et se veut complémentaire à la première méthode (Thomas et al., 2022). Pour ce faire, un modèle de calibration a été développé visant à simuler les effets instrumentaux sur un spectre solaire synthétique à haute résolution spectrale. La comparaison entre les observations du Soleil par LNO et les simulations permettent de calibrer l'instrument. Un spectre solaire synthétique à haute résolution spectrale sur la même gamme de longueur d'onde est donc nécessaire. Un tel spectre n'étant pas disponible (Fiorenza and Formisano, 2005) nous avons développé les étapes de construction d'un spectre solaire synthétique. Nous avons combiné le spectre solaire en irradiance de Kurucz (Chance and Kurucz, 2010) au spectre en transmittance de ACE-FTS (Hase et al., 2010) à très haute résolution spectrale. Nous avons convertit le spectre aux unités de radiance spectrale et comparé notre produit avec le modèle Planetary Spectrum Generator (PSG) (Villanueva et al., 2018) pour assurer la cohérence du résultat.

A partir de ce spectre solaire synthétique nous avons simulé les effets instrumentaux de NOMAD pour reproduire les observations du Soleil par LNO. Ce spectromètre est un instrument complexe et atteint une très haute résolution spectrale en observant qu'une petite partie de la gamme spectrale que l'on nomme « ordre de diffraction ». La gamme spectrale totale est ainsi découpée en une centaine d'ordres de diffractions. Les principaux composants optiques intervenants dans la génération du spectre final sont le cristal AOTF (Accousto-Optic Tunable Filter), le réseau de diffraction et le détecteur. Le cristal AOTF permet de filtrer la gamme spectrale en ne laissant majoritairement passer qu'une faible gamme de longueurs d'ondes (l'ordre principal observé et quelques ordres adjacents). Le réseau de diffraction permet ensuite d'atteindre la très haute résolution spectrale. Le détecteur composé de 256 pixels dans la direction spatiale et 320 spectels dans la direction spectrale recueille cette lumière diffractée correspondant sur les longueurs d'ondes de l'ordre observé. La complexité réside dans le fait que chacun de ces composants contribuent à la forme finale du spectre et qu'il faut donc parfaitement les intégrer pour calibrer l'instrument.

Nous avons proposé un modèle de calibration qui intègre ces différents effets. Nous intégrons la calibration spectrale (concordance entre le numéro du pixel sur le détecteur et la longueur d'onde), la fonction de transfert de l'AOTF (une fonction de type sinus-cardinal carré et une fonction gaussienne), la fonction « d'éclat » du réseau (ou Blaze Function) et la réponse spectrale de l'instrument (Instrument Line Shape). Par une méthode d'optimisation non-linéaire de type descente de gradient (voir sec.) nous estimons les paramètres de calibration spectrale (décalage en longueur d'onde et résolution spectrale) et les paramètres des fonctions instrumentales de l'AOTF (intensité, largeur à mi-hauteur, décalage en longueur d'onde) permettant le meilleur ajustement entre les spectres simulés et les spectres observés par LNO. Ceci ne permettant pas d'intégralement rendre compte des formes très variées que peut prendre un spectre NOMAD nous avons inclus une étape de correction du continuum sur les spectres simulés et observés. Ceci permet de gommer les effets instrumentaux mal estimés en conservant le niveau absolu du spectre (ce qui est primordial pour une calibration photométrique) ainsi que la reproduction des fines bandes d'absorptions solaires. Une fois l'ajustement réalisé, une comparaison directe fournit le facteur de

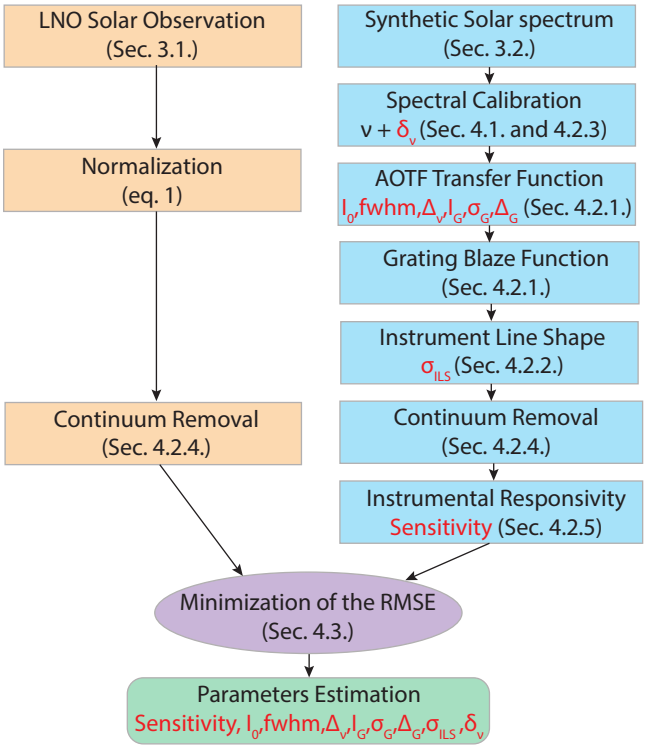

FIGURE 7 : Diagramme résumant les différentes étapes du modèle de calibration. Les paramètres estimés par l'inversion sont indiqués en rouge. (d'après (Cruz-Mermy et al., 2022)).

calibration permettant la conversion entre les nombres digitaux mesurés par le détecteur et une véritable valeur de radiance spectrale pouvant être convertie en réflectance. Le schéma de la méthode est illustré fig. 7.

Les résultats de la calibration ont permis de déduire les courbes de sensibilité instrumentales et ont montré une corrélation au premier ordre avec la température. Une augmentation de la température entraine une baisse de la sensibilité instrumentale. En corrigeant cet effet nous avons pu montrer que l'instrument est stable temporellement validant ainsi l'approche proposée par (Thomas et al., 2022). Les paramètres estimés par l'inversion ont également montré une corrélation entre le décalage en longueur d'onde de la calibration spectrale et la température et indiquent une valeur de 0.75 pixels par degré, cohérente avec les valeurs de 0.71 et 0.83 reportées par (Liuzzi et al., 2019) and (Thomas et al., 2022). Cette approche permet également de calibrer quelconques observations nadirs. Une comparaison sur plus de 130000 spectres de l'ordre 189 montrent que les deux méthodes sont cohérentes avec moins de 3% de différences, validant respectivement les deux approches.

Détection des glaces avec NOMAD/LNO

L'utilisation des données NOMAD/LNO pour étudier les glaces de surface de Mars nécessite de prendre en compte plusieurs facteurs. Le premier est que l'instrument est optimisé pour l'étude de l'atmosphère et des fines bandes d'absorptions produites par les gaz. Dans le cas des glaces de CO_2 les bandes d'absorptions sont plus larges et peuvent s'étendre sur plusieurs ordres de diffractions. De plus la sensibilité instrumentale n'est pas constante sur toute la gamme spectrale et donc certains ordres de diffractions ne sont pas utilisables en raison du trop faible ratio signal-sur-bruit (SNR). La calibration instrumentale a révélé que les 50 premiers pixels du détecteur ne sont pas utilisables car trop bruités ce qui réduit également le nombre d'ordres utilisables. Enfin, il faut également sélectionner un ordre peu affecté par les absorptions atmosphériques pour garantir un signal spectroscopique provenant de la surface.

Nous avons donc simulé des spectres en transmittance atmosphérique à la résolution de NOMAD

via le modèle de transfert radiatif Planetary Spectrum Generator (PSG) (Villanueva et al., 2018). Nous avons également simulé des spectres en réflectance d'une surface composée d'une lame de glace de CO_2 à la résolution de NOMAD via un modèle de transfert radiatif (Andrieu et al., 2015) adapté depuis le modèle de Hapke (Hapke, 1993). Ceci a permis de mettre en évidence la possibilité de détecter un signal spectroscopique de glace de CO_2 dans les données des ordres 189, 193 et 194 de l'instrument NOMAD/LNO. En raison du plus grand nombre de données des ordres 189 et 193 nous avons entamé une première analyse de l'ensemble des observations relatives à ces deux ordres.

Pour s'assurer de la consistance des données calibrées nous avons comparé les spectres en réflectance des données NOMAD avec les données du Mars Global Surveyor (MGS) Thermal Emission Spectrometer (TES) (Christensen et al., 2001). Ces données correspondent à l'albédo bolométrique global obtenu à partir des observations sur une large gamme spectrale combinant les données visibles et proche infrarouge ($0.3 - 2.9$ μm) et les données à larges bandes dans l'infrarouge thermique ($5.1 - 150$ μm). La résolution spatiale initiale étant plus haute que celle de NOMAD (8 pixels par degré contre 1 pixel par degré) les données TES ont été dérésolues. Une comparaison des deux produits montre un bon accord sur les variations à grande échelle spatiale de la réflectance. Les données NOMAD montrent une réflectance significativement plus haute que les données TES. Cet effet peut être lié aux contributions par les aérosols dont TES est corrigé. Pour valider cette hypothèse nous avons utilisé le modèle DISORT (Stamnes et al., 1988) et une paramétrisation des propriétés optiques des aérosols (Vincendon et al., 2007) pour simuler les effets radiatifs des aérosols à partir des paramètres de profondeur optique, de fonction de phase, d'albédo de diffusion simple, d'albédo de la surface et de la géométrie d'observation. Ceci montre notamment que le principal effet des aérosols est d'éclaircir les surfaces sombres et d'assombrir les surfaces claires. Ce constat est en parfait accord avec les différences observées entre NOMAD et TES. Les réflectances de NOMAD correspondent aux valeurs observées au sommet de l'atmosphère et apparaissent plus élevées (donc une surface plus claire) que les valeurs de réflectance de surface telles qu'observées par TES corrigé de l'atmosphère.

Nous avons défini un critère de profondeur de bande pour calculer l'intensité des absorptions de la glace de CO_2 sur l'ensemble des données des ordres 189 et 193. Puisqu'un ordre permet de résoudre intégralement une bande d'absorption, nous pouvons précisément contraindre la valeur de réflectance dans le continuum et au fond de la bande d'absorption. A partir de cartes de latitude-longitude, latitude-longitude solaire et latitude-heures locales nous avons pu identifier un nombre significatif d'absorptions. Un exemple est donné fig. 8 montrant la détection de calotte saisonnière Sud au cours du printemps local avec l'ordre 193. D'autres profondeurs de bandes importantes ont été identifiées à des latitudes plus faibles (équatoriales) et des heures locales très variées. Ces données nécessitent de plus amples investigations pour permettre de distinguer un vrai signal spectroscopique d' un artefact provenant de la calibration instrumentale. De plus, une correction atmosphérique pour intégrer la contribution des aérosols est indispensable avant toutes analyses spectroscopiques plus fines.

Conclusion générale

Au cours de ce projet de recherche nous avons entamé un travail de caractérisation des propriétés microphysiques de glaces présentes en surface de Mars et d'Europe. Pour ce faire nous utilisons des observations des surfaces aux longueurs d'ondes du proche infrarouge issues des missions spatiales. Pour rigoureusement extraire les propriétés de surface de ces observations nous utilisons les concepts de spectroscopie infrarouge et de transfert de rayonnement dans les milieux complexes que forment les régolithes planétaires.

Dans un premier temps, nous avons défini les concepts théoriques décrivant les interactions entre un rayonnement électromagnétique et un milieu matériel. Parmi les différents modèles utilisés en planétologie nous avons sélectionné le modèle photométrique de Hapke car sa formulation analytique le rend facilement inversible et garantit une approximation réaliste des solutions du transfert radiatif. Une revue des méthodes d'inversions a permis de définir la stratégie d'inversion de données de spectroscopie en réflectance. Il apparait que les méthodes robustes d'inférences bayesiennes sont les plus adaptées à la

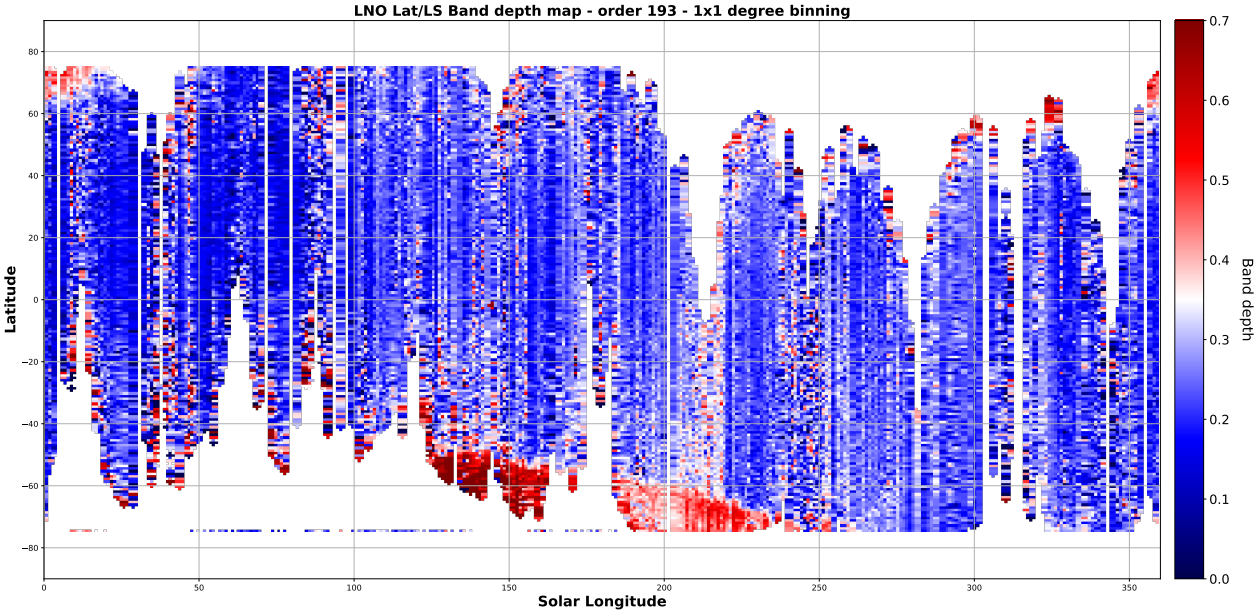

FIGURE 8 : Carte latitude-longitude solaire (époque de la saison) de la profondeur de bande de la glace de CO_2 estimée avec les données de l'ordre 193 de NOMAD/LNO. La profondeur de bande est particulièrement élevée à la fin de l'hiver et au cours du printemps de l'hémisphère Sud, cohérent avec la présence de la calotte saisonnière de glace de CO_2.

très forte non-linéarité du modèle de Hapke et aux corrélations existant entre les paramètres.

Dans un second temps nous avons directement appliqué ces méthodes à l'analyse de la surface d'Europe. Nous avons ainsi montré qu'il n'était pas possible de déterminer précisément la composition de la surface d'Europe avec les données de l'instrument NIMS à bord de la mission Galileo. Des contraintes extérieures sont nécessaires pour permettre une investigation précise des propriétés microphysiques de la surface.

Enfin nous avons investigué la possibilité d'étudier les glaces de surface de Mars avec l'instrument NOMAD/LNO à bord d'ExoMars Trace Gas Orbiter. Le développement d'un modèle de calibration a permis une première analyse des données nadir de quelques ordres de diffractions. La détection de signal spectroscopique associé aux glaces de CO_2 à des latitudes et saisons cohérentes avec la présence de la calotte saisonnière confirme la possibilité d'utiliser NOMAD pour étudier les glaces de surface. De futurs travaux impliquant la correction atmosphérique des aérosols sont nécessaires avant d'entreprendre une analyse plus fine des propriétés microphysiques.

De nombreuses perspectives sont envisagées à la suite de ce travail. L'observation d'Europe par l'instrument NIRSpec du James Webb Space Telescop à très haute résolution spectrale offre la possibilité de contraindre la composition de la surface. Ces données auront un ratio signal-sur-bruit élevé sur une gamme spectrale plus grande que NIMS, ce qui facilitera la distinction des composés chimiques. Un retour aux données NIMS sera alors possible pour entreprendre une caractérisation des propriétés microphysiques. Concernant les surfaces martiennes l'utilisation des données NOMAD semble prometteuse pour l'étude des glaces. Les potentielles détections spectroscopiques à différentes heures locales et des latitudes équatoriales sont à confirmer. Une confrontation de ces observations à très haute résolution spectrale avec d'autres jeux de données à plus haute résolution spatiale (instrument CRISM) peut permettre de préciser le processus de jets de gaz de froids et de dépôts sombres. Enfin des perspectives plus générales sont également envisagées. Les méthodes développées au cours de ce projet de recherche sont applicables à toutes observations de surfaces glacées par spectroscopie en réflectance. Ainsi, une caractérisation des propriétés microphysiques des glaces de Ganymède, Callisto, Titan, Encelade ou Pluton est réalisable.

Contents

General introduction

Usually, the term «ice» refers to the solid state of water that is frequently found on Earth when the temperature falls below 0°C at standard atmospheric pressure. In planetary sciences this same term designates moderately-to-highly volatile molecules in their solid state either as pure solids, solid mixtures, hydrates or clathrate hydrates (B. Schmitt, 1995). In the solar system this mostly includes water (H_2O), carbon dioxide (CO_2), carbon monoxide (CO), methane (CH_4), sulfur dioxide (SO_2), ammonia (NH_3) and nitrogen (N_2). The distribution of ice in the solar system is directly related to its temporal evolution (de Pater and Lissauer, 2014). When the cold interstellar cloud of dihydrogen (H_2), helium (He) and dust collapsed into a rotating proto-Sun surrounded by a rotating primordial nebula, the temperature was then too high to allow the formation of ice. As the nebula begins to cool, different elements condensed into grains or ices depending on their condensation temperature (B. Schmitt, 1995). The «frost line» designates the line between the area where rock and metals condense and the area where carbon and ice grains condense. While the exact location of the frost line is not constrained, a common estimate places it near 4 AU (Prockter, 2005). This imply that few ices were initially formed in the inner solar system while it represents a large fraction of the mass of the outer solar system (B. Schmitt, 1995). Thus, the ice represents a primordial material in the formation and evolution of various planetary bodies from the cores of giant planets (Jupiter, Saturn, Uranus and Neptune) and their icy satellites to the vast and diffuse shell of comets that is the Oort cloud. The progressive cooling of the nebula then allowed comets and meteorites to enrich the inner solar system with volatile. Ices could also trap gases or organic matter from the outer solar system. The evolution, cooling and differentiation of planets have then favoured the stability of the ice, in depth as well as on the surface, even in the places closest to the Sun as on Mercury (Harmon and Slade, 1992). Today, ices drive atmospheric and geologic processes on several objects spanning the solar system (Clark et al., 2012). We can see that studying and characterizing the properties of these ices is important as they inform on the history of the investigated planetary bodies but also because they are closely related to the notion of habitability and the emergence of life.

The majority of ices identified from telescopic observations and space missions are surface ices. The most dominant is water ice but there is a wide variety of other species forming either pure ices or mixtures with water ice (Clark et al., 2012). When in their pure states, ices can exist in crystalline or amorphous forms with a large number of structural configurations depending on their thermal and irradiation history. When mixed, ice traps molecules that may be randomly present in the matrix or substitute a chemical bond to form complex structures such as hydrates (Clark et al., 2012). Another important structure is clathrates in which the crystalline forms of the ice produce a cage around a trapped ,almost free, molecule. The physico-chemical properties of these ices provide key information to understand the processes involved in the evolution of planetary surfaces. These ices and their different structures exhibit singular and characteristic optical properties which allow to differentiate them. Thus, a common approach to characterize the ice properties is through reflectance and/or thermal emission spectroscopy. Combining spectroscopic observations of planetary surface and laboratory measurements have allowed the identification of various ices in different crystalline forms. However, in order to give a per-

fect account of the observations and to differentiate among the very numerous crystalline structures and chemical forms, one has to use a realistic radiative transfer model that correctly account for the microphysical properties of the surface such as volume abundance, grain size, porosity and surface roughness and integrates the highly non-linear effects of multiple scattering when light interacts with a complex medium such as a planetary regolith (the surface layer generally loose). Completing this was difficult until now because it required to synthesize and measure the optical properties of a very large number of ices at different temperatures, which is very difficult to do in laboratory. In addition, the large computational resources required to use accurate radiative transfer models have greatly limited the investigations. Fortunately, our theoretical knowledge from laboratory measurements are constantly evolving, the same applies to computer resources.

The work presented in this document aims to clarify the microphysical properties of surface ices using near-infrared reflectance spectroscopy and by focusing on two main bodies: Mars and Europa. Although these two bodies are fundamentally different, they both show evidence of active geological processes involving different types and forms of ice. In addition, these bodies have been the subject of numerous observations and space missions providing a very large number of available data, which will continue to grow with future space missions. It makes these two bodies relevant choices to study, especially to understand the temporal evolution of these active processes and the impact on ice properties. Since we focus on the use of near-infrared reflectance spectroscopy, the method used is similar for both objects. That is why this document is built in three distinct parts.

The first part of this PhD (see part.I) is dedicated to the presentation of the method for radiative transfer in icy surfaces. Radiative transfer concepts and important physical quantities are defined to lead to some examples of commonly used model by the planetary sciences community. The model used in this work, known as the «Hapke photometric model», is widely described. The advantages of this approach lie in the fact that this model is analytical and easily invertible. The inversion of a physical model consists in using it to find the physical parameters allowing to reproduce as accurately as possible a data, in our case an observation of the surface. The concepts and methods of inversions are also presented in this section. A comparison between different inversion methods is proposed to select the most suitable methods for the problems encountered in this work.

The second part (see part. II) shows an application to the case of Europa. The scientific background describes the current knowledge of the icy surface and points to questions remaining unanswered and which are the subject of a first investigation.

The third part (see part. III) illustrates the beginning of a project dedicated to the study of the ices of Mars via the use of data from the recent ExoMars-TGO mission and in particular the NOMAD infrared spectrometer. The acquisition of the first data of the mission coincides with the beginning of this PhD research project, this is why an instrumental calibration work was necessary. A calibration method for the NOMAD nadir channel data is described. A first analysis of the data is also presented to highlight the instrumental capacity to detect surface ice.

Finally, general conclusions (see chap. 10) will be given and perspectives considered as a continuation of this work will be proposed.

Part I

Methods for radiative transfer in icy surfaces

The study of planetary surfaces refers to all the disciplines that aimed at characterizing and understanding the evolution of the physico-chemical processes governing the evolution of a surface over different time scales. As the last solid envelope of a planet, they represent our first and best witnesses to complex geological events and the interactions between internal and external processes at the origin of their evolution. The great diversity of morphologies observed on the surface of the same planet but also between different bodies of the solar system is sufficient to understand the interest and the difficulty of investigating such processes. On Earth, our understanding of the surface is greatly facilitated by the possibility of carrying out field studies, the samples thus collected and analysed in laboratory bring strong constraints to the geological models. When moving to other planetary bodies, such in situ studies are currently very limited because they are difficult and expensive to carry out. Today, only a few lander have reached the surface of the Moon, Mars, Venus, Titan and smaller bodies such as asteroids, drastically increasing our geological knowledge of a very localized area. Although more and more future missions integrate such landers our overall understanding of planetary surfaces comes from remote-sensing techniques and almost all space missions carry a passive or active remote-sensing instrument.

Passive remote-sensing instruments usually measures ambient electromagnetic radiations, such as sunlight, after its interaction with a physical media like an atmosphere or a surface. When studying planetary surfaces this techniques has been widely used because the light-matter interactions is strongly wavelength (i.e. frequency) dependents and it is thus possible to probe different physical properties of the surface depending on the wavelength at which it is observed. This gives rise to a wide variety of instruments, from the short-wavelength (high-frequency) ultraviolet spectrometers to the long-wavelength (low frequency) radar measurements through the classic visible and near-infrared imagers and spectro-imagers. To properly analyze the remote-sensing data one has to integrate the physical phenomenon of energy transfer that occurs when light encounter a physical medium. Such interactions are described with the radiative transfer principle which integrate the processes of absorption, emission and scattering occurring within a planetary surface.

This thesis focus on the microphysical characterization of icy surfaces through the use of passive remote-sensing instruments and will therefore be based on the radiative transfer principles. This part is intended to focus on the method. A first chapter (see chap. 1) gives general introduction to important radiative transfer concepts and quantities will be given, followed by an overview of the models used. A second chapter (see chap. 2) will describe the concept of the model inversion, from theoretical consideration to concrete examples and tests of different inversion strategies directly applied to the problems encountered in this research work . This part is therefore common to the following two and will serve as a basis for understanding the approaches developed. Scientific results on Europa and Mars will be present in the corresponding parts.

Chapter 1

Radiative transfer

Example of a radiation transfer with the Pink Floyd logo: incident white light on a prism produce by refraction a beam with a color gradient, characteristic of the dispersion of the medium, namely the variation of optical properties as a function of wavelength. (Credit: Harvest Records/Capitol Records/Hipgnosis/George Hardie)

When electromagnetic radiation (or a photon) interacts with a material medium, such as a surface or an atmosphere, it can be absorbed or deflected (diffused, diffracted or refracted) by the medium. The radiative transfer is the framework theory allowing to describe these interactions by quantifying them, we then speak of "energy transfer" into matter.

1.1 Radiative transfer quantities

This section aim at introducing the basis of light-matter interactions as well as geometric and radiometric quantities related to the radiative transfer equation and its resolution which are necessary to understand the model used in this study.

1.1.1 Light-matter interaction in an isolated grain

When light interact with an object such as an isolated grain, the transition from the medium in which the incident light propagates and the grain forms an optical interface called "dioptre" due to the change of the optical index of the medium. At the interface level, four interactions can be considered :

- Reflection : the light is reflected by the interface
- Transmission : the light is transmitted following the phenomena of refraction, it may occur one, two or several times according to the optical geometry laws (Snell-Descartes)
- Absorption : a part of the incoming light is absorbed by the medium. The Beer-Lambert law is a theoretical relation that describe this phenomena in a isotropic homogeneous absorbent medium. For a given wavelength :

$$I = I_0 \exp(-\alpha x) \tag{1.1}$$

Where I is the intensity of the output radiation, I_0 is the intensity of the input radiation, α is the absorption coefficient of the medium and x the length of the optical path. The absorption coefficient depends on the wavelength (λ) and the imaginary part of the refractive index (k), also known as the extinction coefficient, of the material passed through, the relation of which is as follows :

$$\alpha = \frac{4\pi}{\lambda} k \tag{1.2}$$

With $\tau = \alpha x$, the optical depth or thickness, one can see the Beer-Lambert law to characterize the attenuation of the radiation through a medium of optical depth τ:

$$I = I_0 \exp(-\tau) \tag{1.3}$$

- Diffraction : part of the radiation can be diffracted, in the case of a compact medium (grains in contact) composed of irregular grains, larger than the wavelength, this component can be considered negligible (Hapke, 1993).

All these interactions depend on the wavelength considered but also on the physical properties of the object. For a granular object it is mainly the size, the arrangement and the grains composition. For *B. Hapke*, most of the observed surface can be considered as a granular medium, which imply that it is necessary to "consider the scattering and propagation of light within nonuniform media".

1.1.1.1 The light absorption mechanism

The absorption of light by matter occur in several ways depending on the wavelength of the light and the energy of the interaction. The different types of absorption mechanism are :

- Rotation : In a gas or liquid a molecule is able to rotate freely and its electric dipole moment will change its orientation under the application of an electric field. In a solid a molecule will have several stable orientations that may flip from one to another under the application of a electric field. This is described by their dielectric constant, a higher dielectric constant will means that molecules have time to rotate. Rotational spectroscopy is mainly applied in the microwave and far infrared wavelength ranges.

- Molecular vibration : chemical bonds of a molecule may stretch or bend with a characteristic frequency (at a discrete energy level). When an incoming light radiation of a specific frequency (i.e. energy) reach a molecule whose characteristic frequency match the radiation frequency, the molecule will convert the light's energy into vibration. There are multiple vibrational modes depending on the number of atoms considered : a linear molecule with N atoms will have $3N-5$ degrees of freedom while a nonlinear molecule will have $3N-6$. Vibrational frequencies are usually found in the mid-infrared wavelength ranges and vibrational spectroscopy can be used when it involve a change in dipole moment of the molecule. Typically, in the case of a linear molecule such as CO_2 the symmetric stretching vibrations do not absorb the infrared radiation because the dipole moment does not change while the asymmetric stretching vibrations changes the dipole moment and absorption occurs.

- Lattice vibration : Ions in a solid lattice may vibrate around their equilibrium positions. The acoustical branch is one type of vibration for which no net dipole moment is produced, it describes the propagation of shear and pressure waves. The optical branch is the second type of vibration for which positive and negative ions move out of phase and create a net dipole moment, meaning that electromagnetic waves can be absorbed or emitted. Lattice vibrations absorptions mainly occurs in the thermal infrared wavelength ranges.

- Electronic transition : when an electron moves from a lower to a higher energy state (such as the "jump" from the valence band to the conduction band in a solid), it leaves behind a positively-charged hole that may induce absorption of incoming radiation. This mainly occurs in the ultraviolet, visible and near-infrared wavelength ranges.

When light is absorbed by a material according to one of the mechanism described above, a decrease of the light's intensity as function of wavelength is observed. This is called an "absorption band" whose shape and depth is usually related to the physical properties of the material. This phenomena can be explained using the complex refractive index $\underline{n}$ as follow :

$$\underline{n} = n + ik \tag{1.4}$$

Where n, the real part, is related to the phase velocity of the electromagnetic wave in the medium and k, the extinction coefficient is related to the damping of the oscillation amplitude of an incident electric field in the medium. According to Maxwell's equations on electromagnetic theory, the speed of light in vacuum is related to the permittivity of free space ε_0 which describes the resistance by the medium to a flow of charge and the permeability of free space μ_0 which describes the production of a magnetic field by a moving electric charge :

$$c = \frac{1}{\sqrt{\varepsilon_0 \mu_0}} \tag{1.5}$$

When radiation propagate through a medium, the light velocity (V) changes due to the change of relative permittivity (ε_r) and permeability (μ_r), using the complex refractive index, one can write :

$$\underline{n} = \sqrt{\varepsilon_r \mu_r} \tag{1.6}$$

And the velocity through the medium can be expressed as follow :

$$V = \frac{c}{\underline{n}} \tag{1.7}$$

Using this, one can write the expression of the electric field E of a plane wave of frequency ν that propagates through a medium with a velocity V in a direction along x :

$$E = E_0 \exp\left(i2\pi\nu\left[t - \frac{x}{V}\right]\right) \tag{1.8}$$

Where E_0 is the incident electric field and the term $i2\pi\nu\left[t - \frac{x}{V}\right]$ is the displacement at time t after a disturbance created by the electric field located on x along the propagation. Using eq. 1.4 and 1.7, one can write :

$$\frac{1}{V} = \frac{n}{c} + \frac{ik}{c} \tag{1.9}$$

Using eq. 1.9 in eq. 1.8 gives :

$$E = E_0 \exp(i2\pi\nu t) \exp(\frac{-i2\pi xn}{c}) \exp(\frac{-2\pi\nu kx}{c}) \tag{1.10}$$

The last term $\frac{-2\pi\nu kx}{c}$ is the measure of the extinction coefficient k as the radiation propagate through the medium. When expressing the power P of an incident wave through a medium as follow :

$$P = \sigma_c . E^2 \tag{1.11}$$

With σ_c the conductivity of the medium. Using the extinction coefficient, the fraction of incident power that has propagated from initial position to a distance x is given by :

$$\frac{P(x)}{P(0)} = \frac{\sigma . E^2(x)}{\sigma . E^2(0)} = \exp(\frac{-4\pi\nu kx}{c}) \tag{1.12}$$

From which we derive the absorption coefficient α:

$$\alpha = \frac{4\pi\nu k}{c} \tag{1.13}$$

Please note that using the velocity of light in a vacuum $c = \nu.\lambda$ in eq. 1.13 gives the relation expressed in eq. 1.2 from which the Lambert's law (eq. 1.3) is derived. The optical properties of a medium describe the behaviour of incident radiation as it passes through the medium, namely the change of velocity and the attenuation of incident energy. The real part n and imaginary part k of the refractive index are both wavelength dependents and are not independent. Using mathematical relations such as the *Kramers-Kronig* relations (Lucarini et al., 2005), one can empirically determine the imaginary part if the real part is known (and vice versa). Otherwise, n and k can be determined using precise measurement of transmission spectra through a medium. In this study we will use the term "optical constant" to refer to the complex refractive index of materials. Optical constants are used as inputs in radiative transfer modelization, details and illustration can be found in subsec. 1.3.1.

1.1.1.2 The extinction

The extinction refers to the phenomena of absorption and scattering that occurs when a wave interact with a particle. To describe such effect we use the cross section σ that express the effective interaction surface projected orthogonally to the source which gives the probability of a diffusion or absorption event. With σ_E, σ_A and σ_S respectively the cross section of extinction, absorption and scattering and σ_G

the effective geometrical cross section *B. Hapke* (Hapke, 1993) derives the efficiency factors Q_E, Q_A and Q_S as follows :

$$Q_{E,A,S} = \frac{\sigma_{E,A,S}}{\sigma_G} \tag{1.14}$$

With $\sigma_E = \sigma_A + \sigma_S$. In the case of a granular dense media, diffraction may be ignored in Q_A, and Q_S (Hapke, 1993).

1.1.1.3 The single scattering albedo

The single scattering albedo ω describes the ratio between the scattered energy and the energy that interacts with an isolated particle as a function of the incident angle and the wavelength. It depends on the composition, grain size and the internal structure of the particle. According to *B. Hapke* (Hapke, 1993):

$$\omega = \frac{Q_S}{Q_E} = \frac{Q_S}{Q_S + Q_A} \tag{1.15}$$

With Q_E, Q_A and Q_S defined in subsec. 1.1.1.2. The single scattering albedo varies between 0 (the radiation is fully absorbed) and 1 (the radiation is fully scattered). In the optical geometry configuration (grain size are larger than the wavelength) and in a dense granular medium diffraction is ignored so $Q_E = 1$ and $\omega = Q_S$. The diffuse efficiency Q_S of an isolated grain is proposed by *B. Hapke* (Hapke, 2012) as follows :

$$Q_S = S_E + \frac{(1-S_E)(1-S_i)}{1-S_I\Theta}\Theta \tag{1.16}$$

Where S_E and S_I are respectively the total external and internal reflection coefficients, corresponding to the integration of Fresnel coefficients over all possible geometries for the considered isolated grain. Θ is the internal transmission factor described by *B. Hapke* (Hapke, 2012) as follows :

$$\Theta = \frac{r_i + \exp(-\sqrt{(\alpha \times (\alpha+s)}\overline{D})}{1 + r_i + \exp(-\sqrt{(\alpha \times (\alpha+s)}\overline{D})} \tag{1.17}$$

With $\overline{D}$ the mean diameter of a particle, α is the absorption coefficients (see eq. 1.2), s is the scattering coefficients (if $s = 0$ then there is no internal scatterer in the medium) and r_i the bi-hemispherical reflectance of a semi-infinite medium defined by *B. Hapke* (Hapke, 1993) as follow :

$$r_i = \frac{1 - \sqrt{\frac{\alpha}{\alpha+s}}}{1 + \sqrt{\frac{\alpha}{\alpha+s}}} \tag{1.18}$$

1.1.1.4 The Phase function

The phase function $P(g)$ describes the angular distribution of the scattered light as a function of the phase angle g. It can be seen as the probability of an incoming photon to be deviated from its incident direction when it interacts with a particle. The integration of such function over the entire space gives :

$$\frac{1}{4\pi}\int_0^{4\pi} P(g).d\Omega = 1 \tag{1.19}$$

In the case of an isotropic diffusion, the phase function is constant. However, diffusion is rarely isotropic and several complex functions were used to describe the diffusion in various situation.

1.1.1.4.1 The Rayleigh scattering Rayleigh scattering happens for particle much smaller than the incident light wavelength. The smaller the particle the stronger is the scattering (proportional to λ^4 (Shepard, 2017)). in such condition, the Rayleigh phase function is defined as follow :

$$P(g) = \frac{3}{4}(1+\cos^2(g)) \tag{1.20}$$

1.1.1.4.2 The Mie scattering The Mie scattering theory describes the light scattering for isolated spherical particles whose size is comparable or larger to the incident light wavelength. Solving the Maxwell's equation in such condition gives a series of spherical wave functions that describe the amount of energy scattered in a certain direction. This works well for an isolated particle but becomes hard to solve when dealing with complex media such as a planetary surface. The advantage of the theory is that its applicable to larger particle and the theory converge to the limit of geometric optics for large particles.

1.1.1.4.3 Legendre polynomial According to *B. Hapke* (Hapke, 1981), two-terms Legendre polynomials may be used to approximate the particle phase function as follow :

$$P(g) = 1 + b.\cos(g) + c.(1.5\cos^2(g) - 0.5) \tag{1.21}$$

Where b describes the forward and backward scattering magnitude and c the width of the diffusion lobe.

1.1.1.4.4 1-term Henyey-Greenstein function (HG1) This is an empirical function (Henyey and Greenstein, 1941) initially used for the study of interstellar dust using the asymmetry parameter b to describe the forward and backward scattering :

$$P_{HG1}(g) = \frac{1-b^2}{(1+2b\cos(g)+b^2)^{\frac{3}{2}}} \tag{1.22}$$

With b varying between -1 (mainly backward scattering) and $+1$ (mainly forward scattering) describing the asymmetry parameter of the lobe, a value of $b = 0$ meaning that the scattering is isotropic.

1.1.1.4.5 2-term Henyey-Greenstein function (HG2) This function is similar to the HG1 phase function but integrate the isotropy of the diffusion :

$$P_{HG2}(g) = \frac{1-c}{2}\frac{1-b^2}{(1+2b\cos(g)+b^2)^{\frac{3}{2}}} + \frac{1+c}{2}\frac{1-b^2}{(1-2b\cos(g)+b^2)^{\frac{3}{2}}} \tag{1.23}$$

With b being the asymmetry parameter describing the isotropy of the diffusion lobe ($b < 0.5$: larger lobe, $b > 0.5$ narrow lobe) and c the backscattering fraction describing the forward ($c < 0.5$) and backward ($c > 0.5$) behaviour of the particles.

1.1.1.4.6 the 2-term 3-parameter Henyey-Greenstein function (HG3) This is a complexification of the HG2 function using 2 asymmetry parameters :

$$P_{HG3}(g) = (1-c)\frac{1-b_1^2}{(1+2b_1\cos(g)+b_1^2)^{\frac{3}{2}}} + c\frac{1-b_2^2}{(1+2b_2\cos(g)+b_2^2)^{\frac{3}{2}}} \tag{1.24}$$

With b_1 and b_2 respectively describing the the width of the forward and backward scattering of the lobe and c the backscattering fraction.

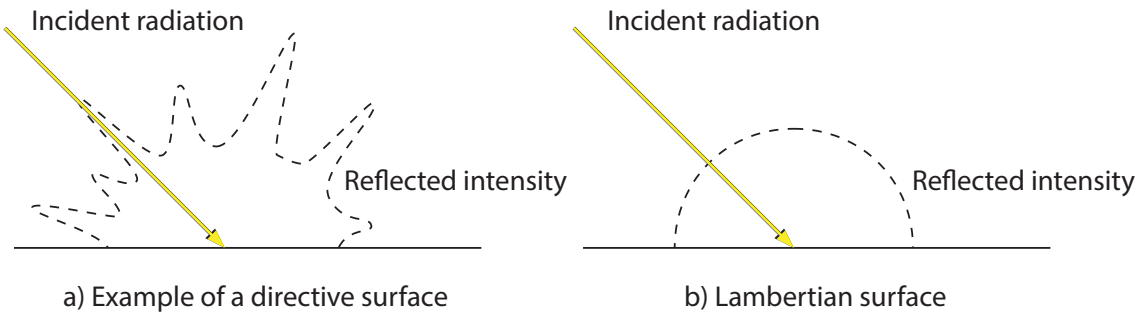

Figure 1.1: Directivity of a surface. (a) A complex surface where the radiation intensity depends on the angle at which the surface is observed. (b) Lambertian surface : the intensity of the radiation is the same in every directions (modified from (Andrieu et al., 2015)).

1.1.2 Light-matter interaction in a surface

When dealing with a complex medium such as a planetary regolith we aim at describing the amount of energy returned by the surface toward the detector and we consider two quantities :

- The specular contribution : light is reflected in a single direction, symmetrical to the incident radiation with respect to the normal (azimuthal angle equal to 180°) with an emergent angle equal to the incident angle according to Snell-Descartes's Law.

- The diffuse contribution : the amount of energy which was not directly reflected toward the external medium at the first interface. This diffuse energy is redistributed in space after the interaction with the surface and this amount of energy is a function of the medium physical properties (composition, grain size, roughness...).

From the diffuse contribution, two fields of study are to be considered :

- Reflectance spectroscopy is the study of the amount of light reflected by a medium as a function of wavelength at a given geometry. It is based on the light-absorption mechanism (see subsec. 1.1.1.1) in order to characterise the physical properties of the medium such as its composition through the study of the absorption bands.

- Photometry is the study of the amount of light reflected at various geometrical conditions for a given wavelength. The angular distribution of the light called the "photometric function" or "scattering function" depends on the surface composition and the physical properties of the materials composing the surface such as the grain size and grain shape, the roughness or the compacity of the regolith. When looking at the angular distribution, two boundaries are to be considered. First are the "specular" surfaces corresponding to a smooth surface that act as a perfect mirror for which only the specular contribution exist. Second are the "lambertian" surfaces for which the outgoing radiation from the surface does not depend on the incident angle but only from the incident flux per unit of surface. In this case the intensity of the radiation is the same in all directions (isotropic). In reality planetary regolith are rarely lambertian and the intensity of the scattered radiation is often directed according to one or more preferential directions (see Fig. 1.1). In fact, behaviour of a surface also depends on the scale at which it is observed : if the field of view is smaller than the dimension of a randomly oriented facet of the surface then it will appear specular, otherwise it will tend to appear Lambertian.

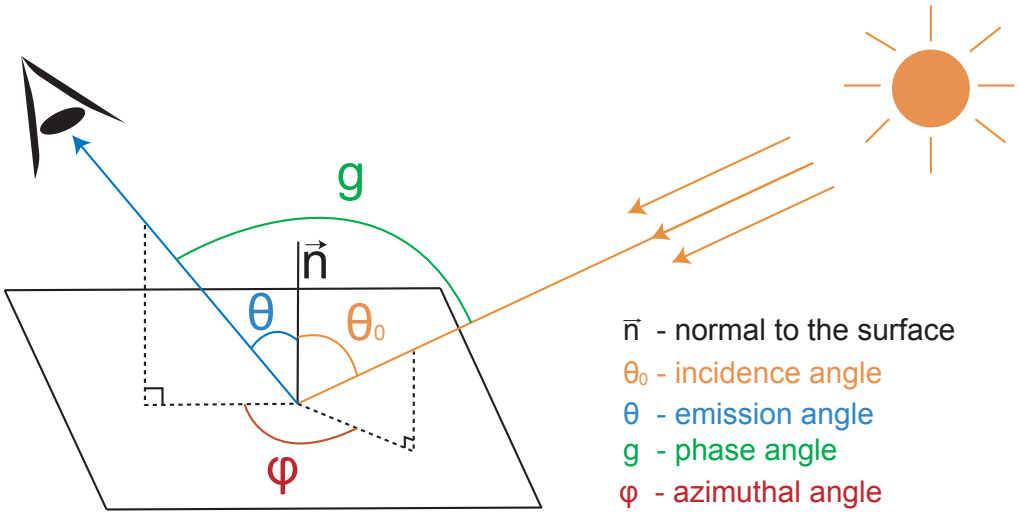

Figure 1.2: Definition of the geometry of observation angles (modified from (Belgacem et al., 2020)).

1.1.2.1 Geometric quantities

To describe the reflectance of a surface, one has to consider the following geometric conventions (see fig. 1.2):

- The solar incident angle θ_0 is the angle between the normal to the surface (the zenith) and the direction of the incoming radiation from the source (usually the Sun) :
- The emergent angle θ is the angle between the normal to the surface and the direction of the observer (usually the detector). For a Nadir configuration $\theta = 0°$.
- The relative azimuthal angle φ is the angle between the relative position of the source and the observer projected onto the surface.
- The phase angle g is the angle between the direction of illumination and the observer. It is used for the characterisation of the scattering effect (see subsec. 1.1.1.4) and is defined using the 3 previous angle as follow :

$$\cos(g) = \cos(\theta_0) \times \cos(\theta) + \sin(\theta_0) \times \sin(\theta) \times \cos(\varphi) \tag{1.25}$$

For practical reasons, the following notations is commonly adopted : $\mu_0 = \cos(\theta_0)$ and $\mu = \cos(\theta)$ respectively the cosine of the incident and emergent angle.

1.1.2.2 Radiometric quantities

We define here several radiometric quantities useful for the understanding of the radiative transfer equation described hereafter (see sec. 1.2.1).

Light flux The light flux F is the total power received or emitted by a surface integrated over the entire space, expressed in W $(J.s^{-1})$.

1.1.2.2.1 Irradiance Irradiance E is the light flux dF received per unit area d^2S integrated over the entire spectrum, expressed in $W.m^{-2}$

$$E = \frac{dF}{d^2S} \tag{1.26}$$

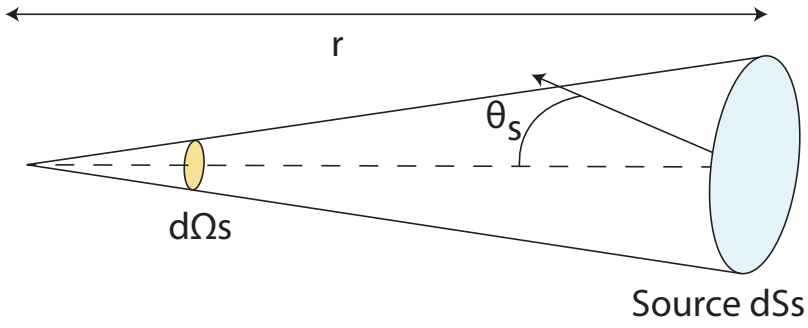

Figure 1.3: Definition of solid angle $d\Omega_s$.

The spectral irradiance E_λ is the same quantity but express per unit of wavelength ($W.m^{-2}.nm^{-1}$).

$$E_\lambda = \frac{dF}{d^2S.d\lambda} \tag{1.27}$$

We usually distinguish the illumination E which describes the light flux received F_i from the emittance M which describes the light flux emitted F_E. In practice the expression of E and M are the same, it is a simple convention to separate the received and emitted flux.

1.1.2.2.2 Solid angle In the case of small solid angle, one can define the solid angle Ω as the directions covered to observe a surface S at a distance D:

$$\Omega = \frac{S}{D^2} \tag{1.28}$$

In the case of a disk, the solid angle is conical and one can define the solid angle Ω as a function of its half aperture α:

$$\Omega = 2\pi \times (1 - \cos(\alpha)) \tag{1.29}$$

1.1.2.2.3 Radiance Radiance L is the light flux received by a surface per unit solid angle $d\Omega_s$ around a direction θ per unit project area dS. The SI unit for radiance is $W.m^{-2}.sr^{-1}$:

$$L_\Omega = \frac{dF}{d\Omega_s.dS.\cos(\theta)} = \frac{dE}{d\Omega.\cos(\theta)} \tag{1.30}$$

Where $S.\cos(\theta)$ is the projected area in m^2 (with θ the incidence/emergent angle) and Ω_s is the solid angle, defined by :

$$d\Omega_s = \frac{dS_s.\cos(\theta_s)}{r^2} \tag{1.31}$$

Figure 1.3 illustrates the definition of solid angle.

The quantity $d^2G = d\Omega_s.dS.\cos(\theta)$ is often used to expressed the throughput of the detector to characterises how "spread out" the light is in area and angle in m^2/sr.

Radiance is a function of viewing direction, depending on incidence angle θ through $\cos(\theta)$ and azimuth angle through $\frac{d\varphi}{d\Omega_s}$. For a Lambertian surface, $\frac{dF}{d\Omega_s.dS}$ is proportional to $\cos(\theta)$ and L is isotropic. When estimating the radiance emitted by a source, dS refers to an area on the surface of the source and $d\Omega_s$ to the solid angle into which the light is emitted. When estimating the radiance received by a detector, dS refers to an area on the surface of the detector and $d\Omega_s$ to the solid angle subtended by the source as viewed from the detector.

We define the spectral radiances as the same quantity but expressed per unit of wavelength ($W.m^{-2}.nm^{-1}$) over the spectrum, similarly to spectral irradiance :

$$L_\lambda = \frac{dL}{d\lambda} = \frac{dE_\lambda}{d\Omega_s.\cos(\theta)} \tag{1.32}$$

1.1.2.3 Reflectance

When reaching a surface, part of the incident radiation may be reflected by the surface. The term reflectance is used to describe how the light is reflected and scattered by the surface. Hereafter are the different reflectance commonly used in surface planetology.

1.1.2.3.1 Bidirectional reflectance It is the ratio between the radiance L emitted by the surface in the direction of the observer over the incident solar flux coming from the collimated direction of the light source πF as follow :

$$r = \frac{L}{\pi F} \tag{1.33}$$

1.1.2.3.2 Radiance factor The radiance factor r_f is defined as :

$$r_f = \frac{L}{F} = \pi.r \tag{1.34}$$

For a perfect Lambertian surface, the radiance factor is simply :

$$r_{f,Lambert} = \cos(\theta_0) \tag{1.35}$$

1.1.2.3.3 Bidirectional reflectance distribution function This function, often called "BRDF", describes how a surface scatters the light it received, it is define as :

$$r_{BRDF} = \frac{r}{\cos(\theta_0)} = \frac{L}{\pi F \cos(\theta_0)} \tag{1.36}$$

The BRDF verify these properties :

1. positivity : $r_{BRDF}(\theta_0, \theta) \geq 0$
2. energy conservation : the reflected flux integrated over the hemisphere is less than or equal to the incident flux
3. reciprocity : $r_{BRDF}(\theta_0, \theta) = r_{BRDF}(\theta, \theta_0)$

1.1.2.3.4 Reflectance factor The reflectance factor r_c is defined as :

$$r_c = \pi r_{BRDF} = \pi \frac{r}{\cos(\theta_0)} \tag{1.37}$$

For a Lambertian surface, the reflectance factor is equal to 1. Finally, the reflectance factor can be seems as the comparison between the reflectance of a surface and the reflectance of a Lambertian surface :

$$r_{BRDF} = \frac{r_c}{r_{c,Lambert}} \tag{1.38}$$

1.1.2.3.5 Lommel-Seeliger model The Lommel-Seeliger model is based on a simple model of diffuse reflection in which the scattering is isotropic. The bidirectional reflectance distribution function follows:

$$r = \frac{\omega}{4\pi} \frac{\mu_0}{\mu_0 + \mu} \tag{1.39}$$

1.1.2.3.6 Albedos The albedo is a term often used to describe the reflecting power of a surface. It is a definition close to reflectance but whose meaning varies from one field of study to another. Here are the different albedos commonly used :

- The normal albedo A_n is the ratio between the radiance of surface observed at phase angle equal to 0 normalised by the the radiance of a lambertian surface illuminated and observed at Nadir configuration ($\theta_0 = \theta = 0°$). It is commonly used to characterise planetary surfaces.
- The geometrical albedo A_g is the ratio between the radiance of a planet at phase angle equal to 0 and the radiance of a lambertian disk of the same diameter and at the same distance as the illuminated planet and observed according to its normal. It corresponds to the normal Albedo weighted by the area of the illuminated surface of the planet.
- The Bond albedo A_{Bond} also called "spherical albedo" is the ratio between the total energy reflected by a planet and the total energy received at a given wavelength, varying between 0 and 1.
- The bolometric albedo A_b is the Bond albedo integrated over the entire spectral range and weighted by the energy of the Sun.

1.2 Radiative transfer

1.2.1 The radiative transfer equation

In 1960 *Chandrasekhar* (Chandrasekhar, 1960) proposed an equation to describe the transport of energy when electromagnetic radiation passes through a parallel plane layer of an optically inactive material (without internal source) diffusing and absorbing continuously, illuminated from above by a light flux F. The first application was to understand this energy transport in the atmosphere of a star and was then adapted for the propagation of light in atmosphere of planetary bodies. The radiance L of such medium is based on the photon transport equation which describes the energy conservation within the layer. It considers that the radiance variation is caused by absorption or scattering in multiple directions (extinction) or a contribution from various directions (multiple scattering) including the source itself (single scattering). By making the local energy balance of the electromagnetic field at a point referred to the normal area unit, within the unit solid angle and between two layer of optical depth τ and $\tau + d\tau$, *Chandrasekhar* proposed :

$$\mu \frac{\partial L(\tau,\mu,\varphi)}{\partial \tau} = L(\tau,\mu,\varphi) - \frac{F}{4\pi}\exp(-\frac{\tau}{\mu_0})P(g) - \frac{1}{4\pi}\int_{-1}^{1}\int_{0}^{2\pi} \omega P(g) L(\tau',\mu',\varphi') d\mu' d\varphi' \tag{1.40}$$

With μ_0, μ and φ the geometrical configuration described subsec.1.1.2.1, $P(g)$ the phase function (see subsec. 1.1.1.4) and ω the single scattering albedo (see subsec. 1.1.1.3). This equation describes the variation of the radiance L along a given direction of propagation, the first term ($L(\tau,\mu,\varphi)$) describes the extinction of the radiation, the second term $\left(\frac{F}{4\pi}\exp(-\frac{\tau}{\mu_0})P(g)\right)$ refers to the single scattering of the reduced incident radiation and the third term $\left(\frac{1}{4\pi}\int_{-1}^{1}\int_{0}^{2\pi} \omega P(g) L(\tau',\mu',\varphi') d\mu' d\varphi'\right)$ describes the multiple scattering from multiple directions. In 1962, *Twersky* (Twersky, 1962) showed that this equation can be linked to Maxwell equations of electromagnetism with three main assumptions :

- Light scattering is always forward (multiple scattering from impacted particle must be negligible)
- All particles interactions are made with a plane wave, also called the "far field" hypothesis.
- Scattering occurs in a tenuous medium, typical size of scatterers is small compared to the typical distance between two scatterers

In the case of a planetary regolith, neither of these three assumptions can be verified, especially the far field hypothesis because particles are very often in contact with each other. Moreover some important and complex effects are not accounted for such as the opposition effect or the macroscopic roughness which will be described later.

These considerations have led the development of various model to describe the complex behaviour of light in interaction with a complex medium such as a planetary regolith. Two kind of approach were developed, the first one is based on the development of exact solutions by numerical resolution. For instance the "ray-tracing' algorithms combining the geometrical optic and Monte Carlo algorithm to simulate the path of a large number of photons in a defined medium and thus estimate the bidirectional reflectance of a surface (Chang et al., 2005; Pilorget et al., 2013). The main advantage is the precision of the methods by studying the statistical behaviour of a very large number of path. Also various numerical approaches has been develop to reach the radiative transfer solution (Stamnes et al., 1988; Grynko and Shkuratov, 2003; Shkuratov et al., 2003, 2005; Grynko and Shkuratov, 2007; Shkuratov et al., 2007). However these approaches require a very long computation time and rely on hypotheses such as the far-field assumption, which turns out to be wrong in the case of a planetary regolith. A second approach is the development of an analytical or semi-analytical formulation by combining empirical and semi-empirical functions. This imply that the modelization will not give an exact solution but rather a reasonable approximation. This is achieved by considering that the radiative properties of the considered media can be described statistically using the average local absorption and diffusion properties (Kubelka, 1948; Hapke, 1981; Shkuratov et al., 1999) and several photometric parameters such as the roughness, compacity, grain size, single scattering albedo and phase function. Several analytical model have been developed such as in increasing complexity order: the Lambert law (*Lambert, 1760*), the Minnaert law (Minnaert, 1941), the Lommel-Seeliger law (Hapke, 1993, 2012), the Lunar-Lambert law (Meador and Weaver, 1975) and the Hapke model (Hapke, 1993). The latter forms the basis of the work undertaken here and is described below (see subsec. 1.2.3). Hereafter, we will describe more into details the approaches used during this PhD: DISORT and Hapke.

1.2.2 DISORT model

The DISORT model (Stamnes et al., 1988) uses the discrete ordinate method to solve numerically the transfer of monochromatic radiation in a scattering, absorbing and emitting plane parallel medium with a specific bidirectional reflectivity at the lower boundary (the surface). This model can be used for any vertically heterogeneous layered and diluted media with little effect of compactness and where scatterers are far from each other, such as an atmosphere filled with aerosols.. The main advantages of this approach is that DISORT can solve a wide variety of layers independently of each others following the "discrete-ordinate" method. The final solution is based on a particular sum of the layers's solutions. Moreover, multiple geometries can be used as the model follow the two-stream approximation : an incident angle and an emergent angle. Also, surface photometric effects can be accounted with the possibility to add directionality following Hapke's bidirectional model.

The main DISORT entries are :

- The number of layer
- Optical properties for each layer:
  - The wavelength is implicitly given. It is actually not a parameter of DISORT but since all following quantities change with wavelength, wavelength can be considered as a parameter
  - The single-scattering albedo (SSA)
  - Optical thickness. As a reminder, a layer with an optical thickness τ has a transmittance of $e^{-\tau}$
  - The phase function of the aerosols with the asymmetry parameters
- Surface boundary properties:

  - The surface properties : albedo, photometry (Lambert's law / Hapke's BRDF)

- Geometry properties:
  - The illumination condition top of the atmosphere (TOA) : incident angle
  - The observation condition : emergence angle, azimuthal angle

Recent work (Gabasova, 2021) have used the DISORT model to estimate the surface composition of Pluto. In this PhD, we will use it to estimate the surface reflectance of Mars from the measured reflectance top of the atmosphere and the estimated aerosols optical thickness.

1.2.3 The Hapke model

Among the different model used in surface Planetology, the Hapke photometric model (Hapke, 1993, 2012) has been widely used to estimate the bidirectional reflectance of airless regolith surfaces. The model is based on the radiative transfer equation (Chandrasekhar, 1960) but several assumptions are made in order to simplify its resolution. First, the model considers that the radiative properties inside a media can be described statistically by using local mean properties of scattering and absorption. It consider the interaction between an incident beam and an isolated particle using the single-scattering albedo (ω) and the particle phase function ($P(g)$). Multiple scattering (Ambartsumian-Chandrasekhar H functions) is handled independently. Moreover, the model integrates the surface scattering contribution with the opposition effect ($B(g)$) seen at low phase angle and the macroscopic roughness (S), and removes the diffraction contribution from the single scattering. The bidirectional reflectance (r) at a given wavelength follows (Hapke, 2012):

$$r(\mu_0,\mu,g) = \frac{\omega}{4\pi}\frac{\mu_0}{(\mu_0+\mu)}\left\{[1+B(g)]P(g)+H(\mu_0)H(\mu)-1\right\}S(\mu_0,\mu,g) \tag{1.41}$$

Where μ_0 is the cosine of the incident angle i, μ is the cosine of the emission angle e and g is the phase angle. The single scattering albedo ω is described in subsec. 1.1.1.3 and the particle phase function $P(g)$ is described in subsec.1.1.1.4, we consider here the two-parameters Henyey-Greenstein function (Henyey and Greenstein, 1941) (see subsec. 1.1.1.4.5).

1.2.3.1 Multiple scattering

While the single scattering albedo describes the scattering of light by one particle before it goes back to the observer, multiple scattering occur when light is scattered repeatedly by several particles before being observed. The more multiple scattering occur, the more light returning to the observer tends to be isotropically distributed resulting in a behaviour close to the isotropic scattering case. Thereby the single scattering term mostly describes the anisotropy effects. According to (Hapke, 2002), an approximation of the multiple scattering function H below 1% of the exact solution follows:

$$H(x) \approx \frac{1}{1-\omega\left[r_0+\frac{1-2r_0x}{2}\ln(\frac{1+x}{x})\right]} \tag{1.42}$$

Where $r_0 = \frac{1-\sqrt{1-\omega}}{1-+1-\omega}$.

1.2.3.2 Opposition effect

At low phases angle (close to 0°) a surge of brightness in diffused light is observed and can be related to two distinct contributions: the Shadow Hiding Opposition Effect (SHOE) and the Coherent Backscattering Opposition Effect (CBOE). The first one describes the effects of shadows casted by the particles from the granular medium, when reaching the opposition geometry (the illuminating source is perfectly behind the observer and aligned with the target) the shadows are no longer visible. Such effect depends

on particle size and their distribution. The second one describes the constructive interference of photons diffused in opposite direction along the same path after multiple scattering (Hapke et al., 1998). This effect is also dependent on particle size and distribution but also on wavelength. A formulation of the opposition surge has been proposed by (Hapke, 1986) and follows:

$$B(g) = \frac{B_0}{1 + \frac{1}{h}\tan(\frac{g}{2})} \tag{1.43}$$

Where B_0 is the amplitude of the shadow hiding opposition effect which describe the transparency of the particle (a high value imply that all the light is diffused and the particle appears opaque) and h is the width of the opposition surge which is strongly related to porosity, the more compact and uniform the particles are the higher the value of h (Hapke, 1993):

$$h = -\alpha \langle \alpha \rangle \ln \frac{p}{2(1-p)} \tag{1.44}$$

Where α is the extinction coefficient (see subsec.1.1.1.2), $\langle \alpha \rangle$ is the mean particle radius and p is the porosity.

1.2.3.3 Macroscopic roughness

The surface roughness is accounted by considering that the observed surface is made by a multitude of unresolved facets N, with $N >> 1$, whose orientation follows a probability density $a(\vartheta, \zeta)$ where ϑ is the zenith angle between the facets' normal and the local vertical direction, and ζ is the azimuthal angle. By assuming that a is uniform according to ζ and considering a Gaussian distribution of altitudes, *B. Hapke* (Hapke, 1984) proposed :

$$a(\vartheta) = \frac{2}{\pi \tan^2 \bar{\theta}} \exp(-\frac{\tan^2 \vartheta}{\pi \tan^2 \bar{\theta}}) \sec^2 \vartheta sin\vartheta \tag{1.45}$$

With :

$$\tan \bar{\theta} = \frac{2}{\pi} \int_0^{\frac{\pi}{2}} a(\vartheta) \tan \vartheta d\vartheta \tag{1.46}$$

The angle $\bar{\theta}$ represents the surface roughness and characterizes the distribution of the unresolved facets' orientations. It is also referred as the 'mean slope angle'. The complete description of the equations leading to the parameter $a(\vartheta)$ in the shadowing function S is present in Hapke (1984).

This expression of the Hapke model does not account for the opposition effect due to coherent backscattering (CBOE) and assumes that multiple scattering are isotropic. This assumption is debatable (Shkuratov et al., 2013; Hapke, 2013) but the fact that this model can be computed extremely rapidly due to its analytical formulation makes it very adequate for data analysis and massive inversion. The whole formulation details of the model is available in (Hapke, 2012). Such model has been widely used and works well when dealing with a granular homogeneous media at mesoscopic scale. From this model, several cases were developed (Andrieu et al., 2015) for a compact layer containing spherical inclusions homogeneously distributed in the matrix and overlaying an optically thick granular medium. In this work we will consider the surface as a simple granular medium and therefore we consider only the Hapke model in our simulation. Thus, when mentioning the microphysical properties of the surface we refer to the macroscopic roughness, particles volumetric abundances and grain size and porosity as described in the Hapke model.

1.3 Numerical implementation

The Hapke model (subsec. 1.2.3) is used to generate reflectance spectrum and investigate microphysical properties of the surface. Computation of reflectance spectrum using this model requires parameters that needs to be described, instrumental effects that needs to be taken into account when comparing simulation with real data, and also involves a computation time aspect that is important to consider when treating massive amount of data, as in the case of space mission data. This section will address these questions of the numerical implementation of the Hapke's model, from the direct model simulation, the integration of the instrumental spectral response and the computation time optimisation. We will illustrates these questions by considering two cases representative of the surface of Europa and Mars: a granular medium composed of pure water ice and pure CO_2 ice. We will use the Galileo/NIMS instrument to illustrate the instrumental effects on these spectra. Although such instrument only concerns the Europa part of this PhD, such classical radiative transfer problem is adaptable to all spectra.

1.3.1 Simulation

Reflectance spectrum are generated from the Hapke model using eq. 1.41, its numerical implementation was made under the *Python* programming language. Several keys parameters need to be defined in order to compute a reflectance spectrum. Since we consider a semi-infinite granular medium the porosity is not involved and will not be a microphysical parameter investigated here. Important parameters are:

- Observational geometry: incidence, emission and azimuth angles
- The particle phase function: values of coefficients b and c of eq. 1.23
- Surface roughness: mean slope angle $\bar{\theta}$ from eq. 1.46
- Volumetric abundances of the compounds
- Grain-size diameter of the compounds

The last two are key parameters that are related to surface composition. When considering a pure granular medium made of only one compound then the volumetric abundance is 100% and one has to define the grain size of the compound. For a surface with more compounds mixed together we consider that the different particles are mixed homogeneously in an intimate mixture, thus the light is penetrating through different material particles. An equivalent material has a single-scattering albedo ω defined as the volume average of different species in the mixture:

$$\omega_{vol} = \frac{\sum_i M_i \sigma_i Q_i}{\sum_i M_i \sigma_i} \tag{1.47}$$

Where M_i is the number of particles of a species i per unit volume. This can be converted to a number density fraction (or abundance) X_i following $X_i = M_i / \sum M_i$. σ_i and Q_i are respectively the geometrical cross-section and the scattering efficiency of a particle of type i. The grain radius r_i not only appears in its geometrical cross section $\sigma_i = \pi r_i^2$ but also in the scattering efficiency Q_i along with its complex optical index $n_i + ik_i$ (**?**) (see subsec. 1.1.1.3). This makes the single-scattering albedo a major parameter of the model as it controls the abundances, grain sizes and absorption coefficients of each compounds. Thus, the optical properties of a compound such as their optical index are mandatory to compute any reflectance spectrum. Measurements of the real and imaginary part of the complex refractive indices are usually made in laboratory or can be derived from reflectance measurement using analytical radiative transfer model such as the Shkuratov model (Shkuratov et al., 1999). Optical constants measurements of a wide variety of materials are more and more available through online database (Schmitt et al., 2017a,b) or within the literature in dedicated papers (such as (Mastrapa et al., 2009) for crystalline water ice). As illustrated figure 1.4, different measurements of the same material may gives different values of the refractive index and extinction coefficient that can be related to a measurement uncertainties, the

experimental conditions or the difference of spectral resolution between two instruments. Also, optical constants are subject to change with temperature. It is important to note that optical constants measured in laboratory are not perfect fundamental data but are extracted from reflectance spectra under numerous hypothesis. Moreover, these measurements are often made on materials processed into powder with a grain size distribution that is not perfectly constrained. This leads to uncertainties regarding the absolute value of the optical constants (Douté et al., 2007). These uncertainties can therefore be propagated in the quantities estimated by the radiative transfer models using them. It is difficult to access estimates of these uncertainties and it is sometimes necessary to compare different data sets of the same material to realize this, as evidenced fig. 1.4 for the crystalline water ice. However, these measurements are difficult to perform for more complex materials because they require the synthesis of pure compounds and to date there are very few different measurements of such materials. One of the major assumptions made in this work is to consider that the optical constants used have no associated uncertainties.

Simulation of a surface with multiple compounds requires to have the optical constants of each compound at the same spectral resolution on the same spectral range which limits the use of multiple compounds together. This aside, using such data and fixing the parameters defined above, one can simulate a reflectance spectrum of an airless granular surface. An example is given figure 1.5 for two granular surfaces: one made of pure crystalline water ice and one made of pure CO_2 ice. Laboratory instruments generally have higher spectral resolution than instruments on board space missions. When trying to reproduce an actual spaceborne observation using this model, one has to integrate the spectral response of the instrument . This will be developed in next subsection. Moreover, computation at high spectral resolution can take time, it is possible to lower the initial resolution without losing much information in the final spectrum to optimise the computation time. This will be addressed in subsec.1.3.3

1.3.1.1 Band list of relevant compounds for icy planetary surfaces

This research project focuses on the study of the icy surfaces of Mars and Europa and therefore will rely on the use of optical constants of relevant pure materials. For the Martian case it is mainly water and CO_2 ice that we consider but for Europa the list of compounds extends to hydrated salts and clathrates. The complete list of optical constants used in this work (with their corresponding references) can be found in chapter 4 (table 1). An illustration of their extinction coefficients k is also made in chapter 4 (figure 2) on the 1.0 - 2.5 μm range to highlights the position of their absorption bands. The spectral position of the center of the main absorption bands of these materials in the 1.0 - 2.5 μm range is given table 1.1.

From this table we can note that these materials have absorption bands at common wavelengths. This is due to the fact that their chemical compositions are close and therefore these species will have a similar spectral behaviour. This is particularly true for the sulfated and chlorinated compounds. Moreover, most of these species are either hydrates or clathrates-hydrates and therefore have a high water content. This involves strong absorptions at the same wavelengths than the main absorption bands of pure water ice, either in crystalline or amorphous state. For these hydrated materials, the absorption bands will appear altered in width and intensity, and the center of the band will sometimes be slightly shifted in wavelength. We can see from this table the complexity that can occur when trying to differentiate these compounds from the positions of their main absorption bands. This topic is covered extensively in chapter 4 in which these hydrated compounds are used to investigate the surface composition of Europa.

CO_2 ice stands out among these materials and is easily distinguishable. We can see from figure 1.5 that such material have many absorption bands, often narrow and deep. The bands at 2.29 and 2.35 μm listed in the table correspond to the two bands used in this work for the study of Mars surface ices with the NOMAD instrument (see chapter 9).

1.3.2 Spectral response of the instrument

An optical system such as a spectrometer or a spectro-imager records light through its optical system, characterised by its impulse response, or transfer function. Such impulse response is usually known as the Point Spread Function (PSF) when dealing with imaging system and refers to the spatial blurring of

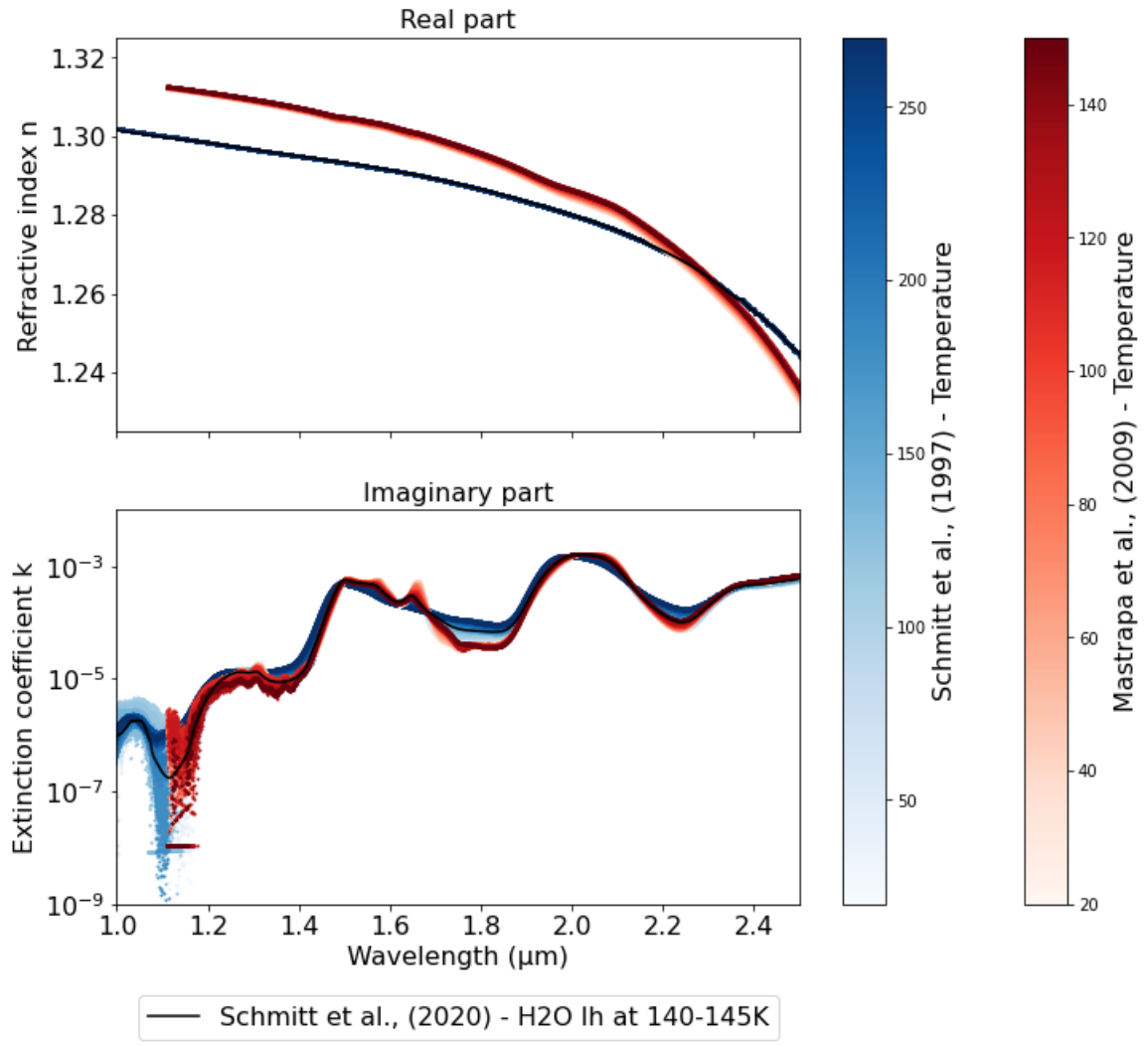

Figure 1.4: Optical constants of crystalline water ice from 3 different measurements on the 1.0 - 2.5 μm range: 20 to 293K (from (Schmitt et al., 1998)) in shades of blue, 20-150K (from (Mastrapa et al., 2009)) in shades of red and at 140-145K (from (Schmitt, 2020)) in black. Global variations are consistent between the three datasets but significative differences can be observed, in this case temperature variations are small compare to the differences between two measurements (especially between the blue and red points). Also the red and blue data are noisier in the 1.0 - 1.2 μm range compare to the black line which makes their use irrelevant in this spectral region.

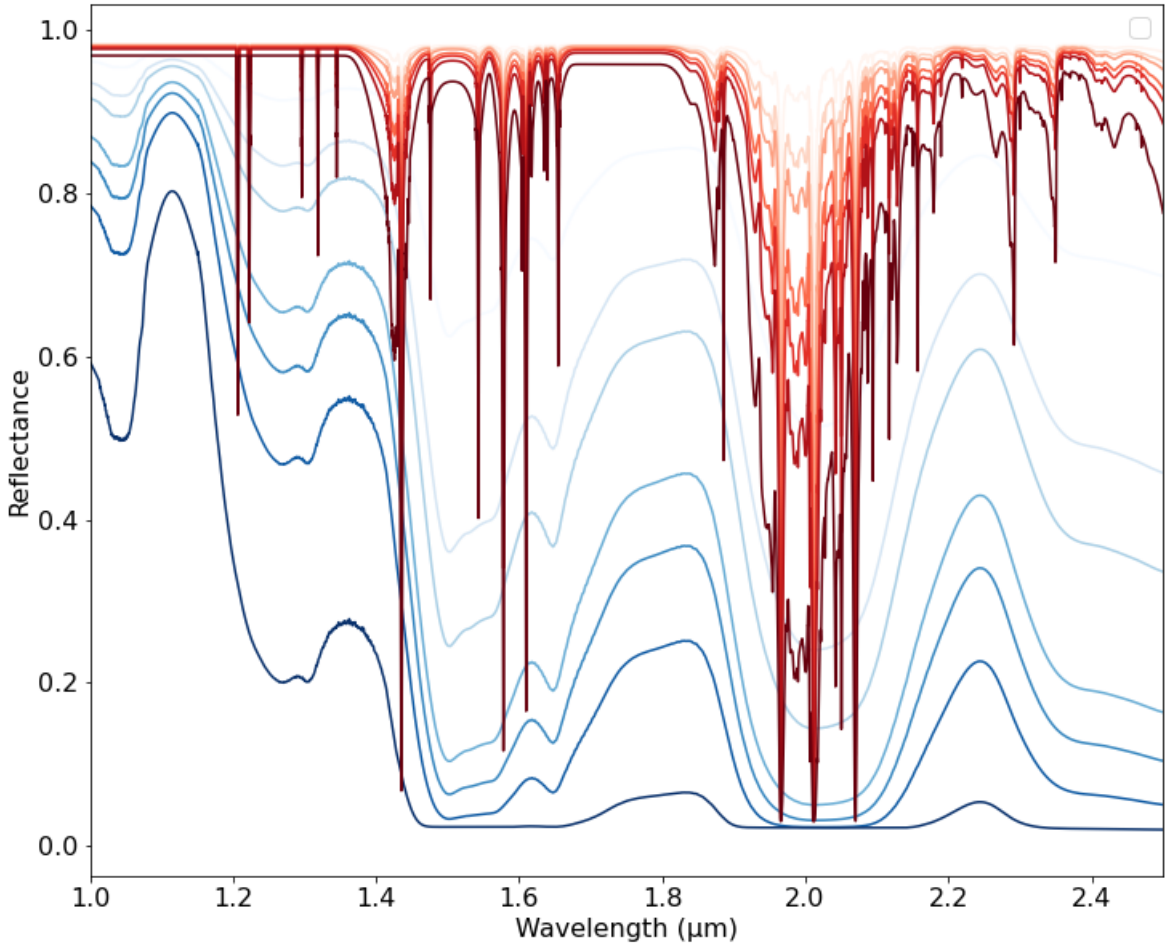

Figure 1.5: Modelled reflectance spectra of pure water ice at 140-145K (from (Schmitt, 2020), shades of blue) and CO_2 ice at 179K (from (Quirico and Schmitt, 2018), shades of red) with varying grain-size: 10, 50, 100, 300, 500, 1000 and 5000 μm (from lighter to darker colours). Simulation in the 1.0 - 2.5 μm wavelength range computed with optical constants at native high spectral resolution using the Hapke model (see subsec. 1.2.3). The parameters are: incidence angle of 55°, emission angle of 35°, azimuth angle of 180°, phase function asymmetry parameter $b = 0.5$ and backscattering fraction $c = 0.5$ implying no preferential distribution regime for the backscattering, surface roughness: mean slope angle of 2°, . The spectral resolution varies between 4.3×10^{-5} and 3.0×10^{-4} μm for water ice and 4.9×10^{-5} and 3.5×10^{-4} μm for the CO_2 ice. Two ices spectrum are very different: water ice is darker with a slope in the continuum and large absorption bands while CO_2 ice has a bright and flat continuum with thin absorption bands in which reflectance drastically falls. With increasing grain-size, water ice absorption bands become larger and eventually disappear within a low reflectance continuum while CO_2 ice bands become deeper and slightly larger but the continuum level remains high.

Chemical compound	Name	Main absorption bands position (μm)
$H_2O_{Cr.}$	Crystalline water ice	1.05 ; 1.3 ; 1.5 ; 2.0 ; 2.45
$H_2O_{Am.}$	Amorphous water ice	1.05 ; 1.3 ; 1.5 ; 2.0 ; 2.45
$MgSO_4.6H_2O$	Magnesium sulfate : Hexahydrite	1.5 ; 1.95 ; 2.45
$MgSO_4.7H_2O$	Magnesium sulfate : Epsomite	1.47 ; 1.7 ; 1.95 ; 2.43
$Na_2Mg(SO_4)_2.4H_2O$	Sodium magnesium sulfate : Bloedite	1.25 ; 1.5 ; 1.65 ; 1.95 ; 2.43
$Na_2SO_4.10H_2O$	Sodium sulfate : Mirabilite	1.23 ; 1.47 ; 1.78 ; 1.95 ; 2.47
$H_2SO_4.8H_2O$	Sulfuric Acid Octahydrate	1.25 ; 1.5 ; 1.97
$Mg(ClO_3)_2.6H_2O$	Magnesium chlorate	1.2 ; 1.5 ; 1.75 ; 1.97 ; 2.43
$Mg(ClO_4)_2.6H_2O$	Magnesium perchlorate	1.17 ; 1.43 ; ; 1.97 ; 2.43
$MgCl_2.4H_2O$	Magnesium chloride tetrahydrate	1.2 ; 1.45 ; 1.76 ; 1.97 ; 2.43
$MgCl_2.6H_2O$	Magnesium chloride hexahydrate	1.2 ; 1.45 ; 1.83 ; 1.97 ; 2.43
$NaClO_4.2H_2O$	Sodium perchlorate	1.2 ; 1.45 ; 1.76 ; 1.97 ; 2.43
$(NH_4)_2SO_4$	Ammonium sulfate : Mascagnite	1.05 ; 1.33 ; 1.57 ; 2.2
CO_2	Carbon Dioxide	1.43 ; 1.54 ; 1.58 ; 1.61 ; 1.87; 2.0 ; 2.29 ; 2.35

Table 1.1: Absorption bands list of relevant materials for planetary icy surfaces used in this work on the 1.0 - 2.5 μm range.

the point objects or as the Instrument Line Shape (ILS) when dealing with spectrometer and refers to the spectral spreading of the recorded spectrum. Such spectral response function must be taken into account to avoid potential bias when comparing any simulated spectrum to an observation. We will illustrate this effects using the Galileo/NIMS instrument hereafter but these considerations are more general.

Measurement of any spectrometer instrument are recorded by "spectral channel" or "spectel" noted here R^n_{NIMS} in unit of reflectance and n denotes the ID number in the spectral domain (from $n = 1$ at $\lambda = 0.7016$ μm, to $n = 360$ at $\lambda = 5.2326$ μm). NIMS is a complex instrument, and this wavelength sampling is changing trough time, due to the ageing of the instrument but also to different instrumental configuration.

For each spectral channel n, one can define the corresponding spectral response of the instrument $S^n_{NIMS}(\lambda)$, centered in wavelength λ_n. Figure 1.6 shows the spectral response of NIMS. The spectral bandpass response has been measured in the laboratory before the launch. It has been designed to follow a triangular response function (Carlson et al., 1992) spanning the channel width of about 0.0250 μm. We approximate it with a Gaussian function with a standard deviation is defined as follow : $\sigma = \frac{fwhm}{2\sqrt{2\ln 2}}$.

$$S^n_{NIMS}(\lambda) = \mathscr{G}(\lambda_n, \sigma) \tag{1.48}$$

Please note that the spectral response is normalised such as $\int S_{NIMS}(\lambda)d\lambda = 1$. We will assume here that the width of the spectral response is constant for all the lifetime of the instrument. The center wavelength is subject to change (Carlson et al., 1992) and is given as a metadata in the PDS archive .

The observed reflectance for the spectel n is thus:

$$R^n_{NIMS} = \int R(\lambda).S^n_{NIMS}(\lambda)d\lambda \tag{1.49}$$

The reflectance spectra $R_{NIMS}(\lambda)$ is the collection of all spectels $\{R^n_{NIMS}\}$.

1.3.3 Computation time optimisation

Among the input parameters of the model, the spectral resolution of the chosen optical constants defines the spectral resolution of the reflectance spectra $R(\lambda)$ at model output. It also impacts the computation time (higher resolution means longer computing time). We need to reduce the computation time without degrading too much the optical constants to avoid losing information. The main issue is that initial optical constants are usually sampled at constant wavenumber interval while the NIMS data are sample

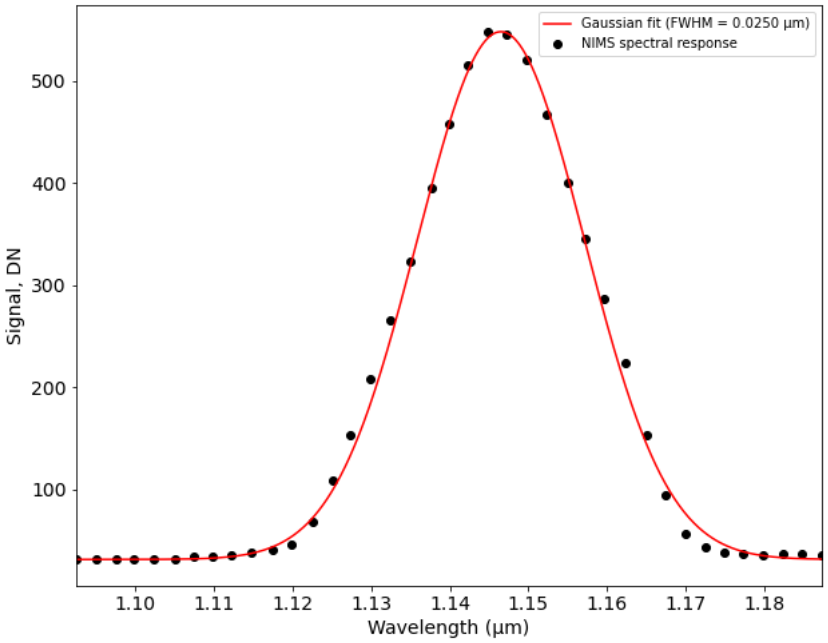

Figure 1.6: Spectral bandpass response of NIMS from (Carlson et al., 1992). The ideal response is expected to be triangular, here we fit it with a Gaussian function with a full-width-at half-maximum of about 0.0250 μm.

at constant wavelength interval. To encompass this sampling difference while reducing the spectral resolution we propose the following solution :

1. We define λ_m the wavelengths that will be used for the computation of the reflectance in the model. We also define a constant wavelength step size $\Delta\lambda_m$. This width is defined as the smallest sampling step of the instrument ($\Delta\lambda_m = \min\Delta\lambda_n$). The corresponding wavelength vector is sampled as follows:
$$\lambda_m = \min(\lambda_n) + k \times \Delta\lambda_m,\ k \in \left[\!\left[0, \frac{\max(\lambda_n) - \min(\lambda_n)}{\Delta\lambda_m}\right]\!\right] \tag{1.50}$$
This equation will be altered by a sampling step factor K defining a resampled wavelength vector grid:
$$\lambda_m = \min(\lambda_n) + k \times \frac{\Delta\lambda_m}{K},\ k \in \left[\!\left[0, \frac{\max(\lambda_n) - \min(\lambda_n)}{\frac{\Delta\lambda_m}{K}}\right]\!\right] \tag{1.51}$$

2. For each λ_m we compute the resampled optical constants using a convolution with a Gaussian kernel:
$$\underline{n}(\lambda_m) = \int \underline{n}(\lambda).\mathcal{G}(\lambda_m, \sigma_m)d\lambda \tag{1.52}$$
The width of the Gaussian function σ_m depends on the actual stepping size:
$$\sigma_m = \frac{\Delta\lambda_m}{K} \tag{1.53}$$

3. We used the radiative transfer model to compute the reflectance spectrum $R(\lambda_m)$. Eq 1.49 is then adapted to convert the spectra to the NIMS spectral resolution:
$$R^n_{NIMS} = \int R(\lambda_m).S^n_{NIMS}(\lambda_m)d\lambda_m \tag{1.54}$$

Method	Max. Rel. Err. (%)	Time (s)	Resolution (nb. of wavelength)
Initial resolution (reference)	-	0.096	17827
Opt. Cst. convolved with NIMS	8.09	0.003	319
Resampling x1	1.02	0.005	599
Resampling x2	0.539	0.009	1195
Resampling x4	0.417	0.013	2388
Resampling x10	0.392	0.044	5967
Resampling x20	0.390	0.074	11931

Table 1.2: Comparison of the resampling method with the computation at initial spectral resolution then convolved with the NIMS response. The maximum relative error between the reference spectra and optimized spectra indicates the quality of the fit. One can see that the resampling x2 method (scaling factor $K = 2$) allows a maximum relative error below 1% while guaranteeing a low computation time (10 times faster that with initial resolution).

Method	Max. Rel. Err. (%)	Time (s)	Resolution (nb. of wavelength)
Initial resolution (reference)	-	0.0762	13060
Opt. Cst. convolved with NIMS	48.36	0.0011	100
Resampling x1	21.86	0.0012	103
Resampling x2	15.05	0.0020	204
Resampling x4	8.19	0.0021	405
Resampling x10	2.44	0.0149	1009
Resampling x20	0.82	0.0161	2015

Table 1.3: Comparison of the resampling method with the computation at initial spectral resolution then convolved with the NIMS response. The maximum relative error between the reference spectra and optimized spectra indicates the quality of the fit. Here the resampling x20 method (scaling factor 20) is enough to reach a maximum relative error below 1%, however the computation time remain low (5 times faster than with initial resolution).

1.3.4 Results on water ice spectrum

Figure 1.7 shows several test of resampling method with different scaling factor K (see Eq. 1.50 to 1.53). The maximum value of relative error between the spectrum computed at initial spectral resolution of the optical constants then convolved with the NIMS response function (no intermediate resampling) and the test with different resample is given table 1.2 along with the estimated computation time.

1.3.5 Results on CO_2 ice spectrum

Figure 1.8 shows several test of resampling method with different scaling factor K (see Eq. 1.50 to 1.53).. The maximum value of relative error between the spectrum computed at initial spectral resolution of the optical constant then convolved with the NIMS response function (no intermediate resampling) and the test with different resample is given table 1.3 along with the estimated computation time.

1.3.6 Conclusion

The Hapke model has been implemented to generate reflectance spectrum of a surface from a set of parameters as defined in subsec. 1.3.1. Optical constants of the considered compounds are important inputs because they are involved in the single scattering albedo which is a key optical property of the model. Such data generally acquired in laboratory have higher spectral resolution than spaceborne instruments.

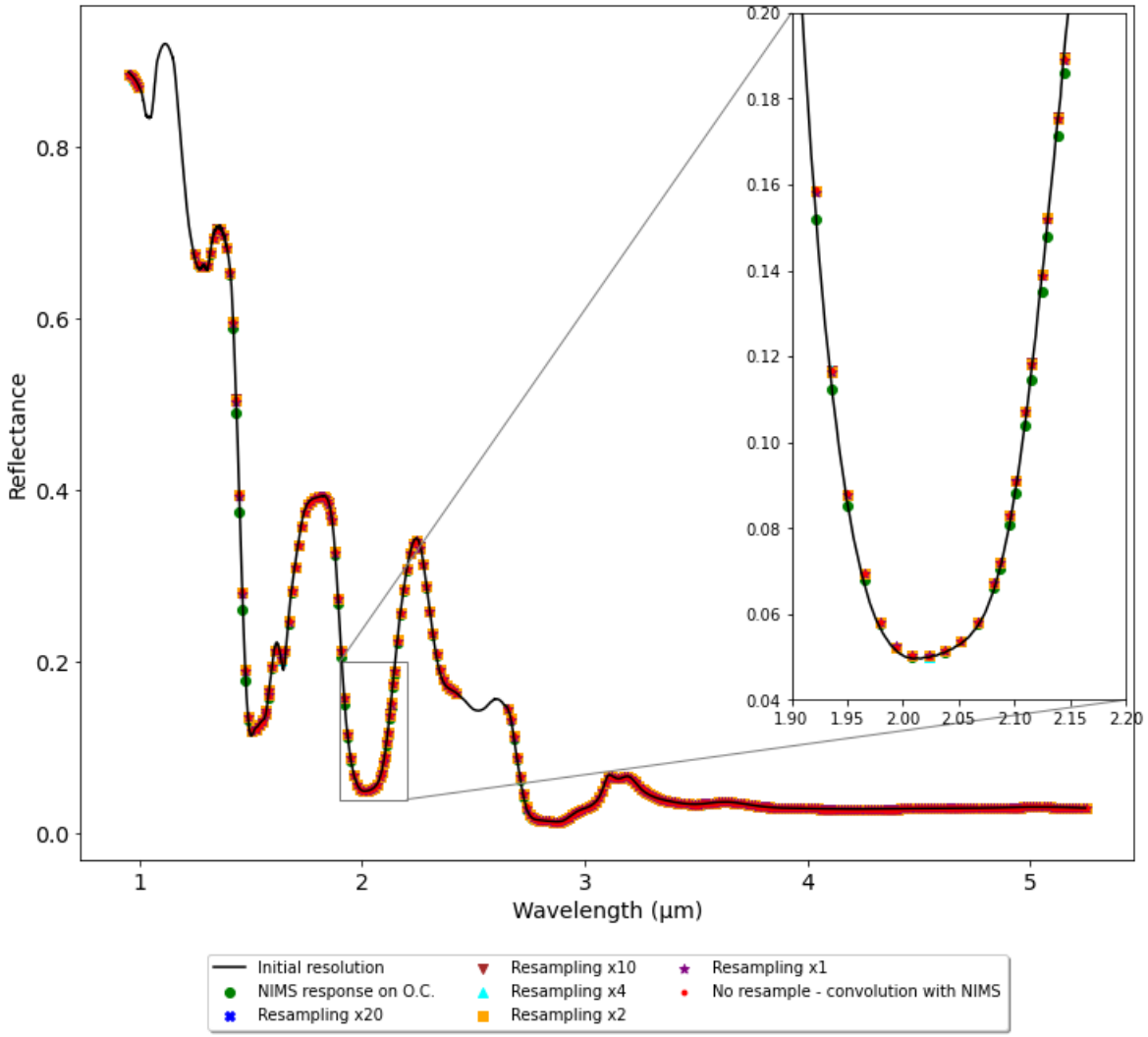

Figure 1.7: Illustration of the resampling method for a water ice dominated spectrum: the initial reference spectra at the very high spectral resolution of the optical constants (black line) and the different test conducted in this study. The red point markers are the reference spectra convolved with the NIMS response and represent our target (Eq. 1.49). The green circle are the optical constants directly convolved with the NIMS response before computation of the spectrum. This is the worst case. Other markers are the resampling method respectively with $K = 1, 2, 4, 10, 20$ (see Eq. 1.50 to 1.53). Most of the points overlap which prevents to distinguish the best fit. The maximum relative error is given in tab. 1.2 along with the respective computation time. The resampling x2 method (orange square) seems to be the best compromise here.

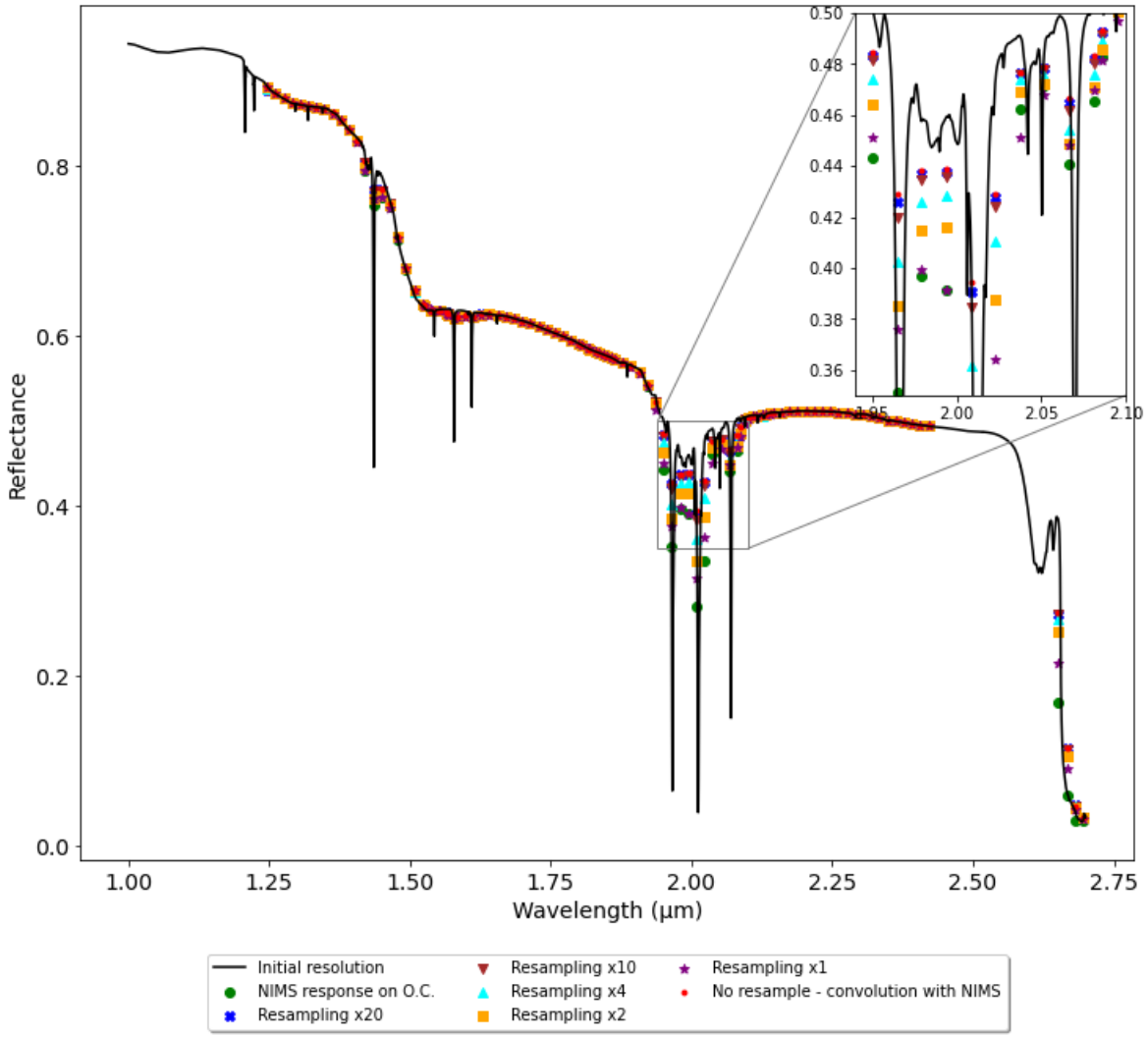

Figure 1.8: Illustration of the resampling method for a CO_2 ice dominated spectrum: the initial reference spectra at the very high spectral resolution of the optical constants (black line) and the different test conducted in this study. The red point markers are the initial reference spectra convolved with the NIMS response and represent our target (Eq. 1.49). The green circle are the optical constants directly convolved with the NIMS response before computation of the spectrum. This is the worst case. Other markers are the resampling method respectively with $K = 1, 2, 4, 10, 20$ (see eq. see Eq. 1.50 to 1.53). Within the continuum the fit is good no matter the resampling method, however on can see that within the band only the resampling x20 method (blue cross) reproduce what is theoretically expected with the red markers. The maximum relative error is given tab. 1.3 along with the respective computation time.

This is is related to the instrumental transfer function and it must be accounted for when trying to compare a simulated spectrum with an observation. Doing so considerably lowers the initial resolution and reduces drastically the computation time but also degrades the theoretical shape of the initial spectrum which can lead to loss of information. We show from two distinct examples with water ice and CO_2 ice that this loss of information depends on the shape of the initial spectrum and especially the width and depth of the absorption bands.

With large absorption bands such as the water ice spectrum, the maximum relative error between the initial spectrum and the spectrum convolved with the spectral response function is below 10% but such differences reflect above all a difference in the absolute level and only marginally affects the shape of the absorption bands. With narrow and deep absorption bands such as the CO_2 ice spectrum the maximum relative error almost reached 50% which is significantly high. Differences mainly occur within the absorption bands where not only the level but also the width and depth of the bands are no longer consistent with the initial computation at high resolution. In an attempt to find a compromise between little loss of information and a reasonable computation time we propose to carry out a spectral resampling after accounting for the spectral response of the instrument. The resampling factor strongly depends on the considered compounds and therefore on the shape of the initial optical constant spectrum at high resolution. For a water ice dominated spectrum, a resampling factor of 2 is enough to lower the maximum relative error below 1% for a computation time 10 times lower than for the initial resolution. For a CO_2 ice dominated spectrum, a resampling factor of 20 is required to lower the maximum relative error below 1% for a computation time almost 5 times lower than for the initial resolution.

When studying Europa with the NIMS instrument, the spectral response of the instrument is included along with a resampling factor of 2 as the surface is mostly composed by water ice and other compounds without narrow absorption bands which ensure that very little information are lost while ensuring a fast computation time. When using the NOMAD instrument to study the martian surface, which is dominated by CO_2 ice, we include the corresponding spectral response but since the very high spectral resolution of the instrument is close to the initial resolution of the optical constants a resampling step is no longer necessary.

Chapter 2

Inversion

'*Bayesians address the question everyone is interested in by using assumption no-one believes, while frequentists use impeccable logic to deal with an issue of no interest to anyone'.* From Louis Lyons in (Lyons, 2007)

Physical model are build to make predictions through theories and concepts such as presented in the previous chapter for radiative transfer. Using the Hapke model for instance, and giving a complete description of the system, one can predict the outcome of a measurements. The problem of predicting a measurements is called the direct model or forward model . Oppositely, the problem of using actual measurements to predict the values of the model's parameters that describe the system is called the inverse problem. This chapter focuses on describing the concept behind inverse modelling and give some examples and comparison between well-known inversion methods adapted to the data used in this work. It is largely based on the very pedagogic documents of Tarantola (Tarantola, 2005) and Trotta (Trotta, 2017). This will establish the necessary theoretical basis to understand inversions made in part 2 and 3 of this manuscript.

2.1 Data assimilation / inversion concept

The inverse problem fits into the concept of the 'state of information' over a parameter or a set of parameters. The general idea is to use any a priori information on model parameters to describe a set of parameters forming the data with the associated uncertainties. The theory behind inverse problems is complex therefore the details will not be developed here, some key concepts and inversion methods will be presented. For more information and background the reader is referred to (Tarantola, 2005) who gives a very complete description of the theory. First we need to define a few important terms:

- d is the data vector and d_i are each individual points in d
- F is the forward model
- m is the vector of model parameters
- $\dot{m}$ is the vector of estimated parameters
- $\dot{d} = F(\dot{m})$ is the vector of the fit values produced by the model and the estimated parameters

The application of F is the forward problem. The inverse problem is to find the best model to reproduce the data d. In the case of analytical models, such as the Hapke model, it is similar to finding the best set of parameters of the given model for which $F(m)$ is closest to d. As well stated by (Tarantola, 2005) : 'While the forward problem has a unique solution, the inverse problem does not'. Multimodality of the solution or local minima can occur, especially when forward model are highly non-linear. This is why any a priori information on the model parameters as well as the representation of the data uncertainties must be properly taken into account. This led to the conclusion that the parameters obtained from the inversion of the data are not necessarily equal to the true parameters that one seek.

Apart from estimating the consistency between the estimated model parameters $\dot{m}$ and the data d one has to investigate the relation between the estimated model parameters and the true model parameters m. Such step is called the appraisal problem and determines what properties of the true model parameters are recovered and what errors are attached to it. There can be several reasons why the estimated model parameters differs from the true model parameters: (i) first it is due to the non-uniqueness of the inverse problem that may imply several model parameters to fit the data but also because (ii) there are always uncertainties and errors attached to the data so the estimated model parameters are affected by these uncertainties and errors. Error propagation is a major aspect of the inverse problem.

The inverse problem is largely model dependent and fundamentally different for discrete models with finite number of degrees of freedom and for continuous models with infinite degrees of freedom (Snieder and Trampert, 2003). Moreover, the model appraisal problem is mostly explicitly well-solved for linear inverse problems. Even though many inverse problems are not really linear, they can be linearised with realistic approximation (Snieder and Trampert, 2003).

2.2 Simple linear model estimation

In the case of a finite-dimensional model, meaning that the model can be characterised by a finite number of parameters, one can write $d = F(m)$ as a series of n equations. Such linear system can be re-written using the matrix formulation $F(m) = Am$.

Every acquisition also induces a measurement error. According to an additive noise process, the data can be expressed as:

$$d = F(m) + e = Am + e \tag{2.1}$$

Where m are the model parameters, d is the data vector and e is the error vector (usually a random gaussian process, with zero mean) associated to the data. From the data an estimate of the model parameters can be made and will be, in practice, different from the true model parameters. Let's denote $\dot{m}$ the estimated model parameters. A general inverse operator that links the data to the estimated model parameters follows:

$$\dot{m} = A^{-g} d \tag{2.2}$$

Where the operator A^{-g} is called the generalised inverse of the matrix A (Snieder and Trampert, 2003). If A is a square matrix then this terms is equals to A^{-1}. From eq. 2.1 and 2.2 one can write the relation between the estimated model parameters and the true model parameters:

$$\dot{m} = A^{-g} Am + A^{-g} e \tag{2.3}$$

The matrix $A^{-g}A$ is called the resolution kernel. This expression can be rewritten as follow:

$$\dot{m} = m + (A^{-g}A - I)m + A^{-g} e \tag{2.4}$$

Where I is the identity matrix. The terms $(A^{-g}A - I)m$ describes the linear combinations of the true model parameters, different from identity. The last term $A^{-g}e$ describes how the errors are mapped onto the estimated model parameters. Statistical analysis are needed to describe the errors in the estimated model. For uncorrelated data d_j with standard deviation σ_{d_j} the standard deviation $\sigma_{\dot{m}_i}$ of the estimated model parameters $\dot{m}_i$ follows :

$$\sigma^2_{\dot{m}_i} = \sum_k (A^{-g}_{ik} \sigma_{d_k})^2 \tag{2.5}$$

In the ideal case, the estimated model parameters equals the true model parameters and so $\dot{m} = m$ and the term $A^{-g}A$ in eq. 2.4 is equal to the identity matrix I. This means that for perfectly resolved model parameters the resolution matrix is the identity matrix :

$$R \equiv I \equiv A^{-g}A \tag{2.6}$$

2.3 Least-square estimation

In the case where the number of independent data is larger than the number of unknowns parameters the system $F(m) = Am$ cannot be always satisfied for any given model parameters m because of the uncertainties and errors in the data d. A way of estimating the model parameters is to look for the differences between the data and the simulated data measured by the L_2-norm:

$$\chi^2 = \|d - Am\|^2 \tag{2.7}$$

Where χ^2 is the square error, also called cost function. The estimated parameters $\dot{m}$ that gives the best fit to the data, is the one that minimises χ^2:

$$\dot{m} = \arg\min \chi^2(m) \tag{2.8}$$

For the case of n independent linear equations the matrix $A^T A$ is an invertible square matrix, it has been shown that the least-square solution S is given by:

$$\dot{m} = (A^T A)^{-1} A^T d \tag{2.9}$$

Where $(A^T A)^{-1} A^T$ is called the pseudo-inverse of the matrix A. If A is a square matrix then this terms is simplified to A^{-1}.

2.4 Nonlinear optimisation : gradient descent

When trying to fit a model function $F(m)$ of parameters m to a set of data points d a convenient way is to define a measure of the goodness of fit as the sum of the weighted squares of the errors (named the chi-squared error criterion χ^2) between the data and the model function:

$$\chi^2(m) = \sum_k \left[\frac{d_j - F(m)_k}{\sigma_{d_k}} \right]^2 \tag{2.10}$$

This scalar value measures the goodness of fit, the lower this value is the better the fit of the model to the data is. The solution is when the chi-squared error is minimised.

This expression can be written in matrix form:

$$\chi^2(m) = (d - F(m))^T W (d - F(m)) \tag{2.11}$$

With W the diagonal weighting matrix $W_{jj} = 1/\sigma_{d_j}^2$, using σ_d as the measurement error of data d.

When developed:

$$\chi^2(m) = d^T W d - 2 d^T W F(m) + F(m)^T W F(m) \tag{2.12}$$

If the model function $F(m)$ is a nonlinear function of m then the minimization must be carried out iteratively where the goal is to find a perturbation h to the parameters m that reduces χ^2. A typical iterative method is the gradient descent method (Byrd et al., 1995; Zhu et al., 1997).

The gradient descent method (or steepest descent method) is an iterative minimization method that updates parameters values in the opposite direction to the gradient of χ^2. The gradient act as a 'compass' toward the downhill direction. The gradient of the chi-squared objective function is:

$$\frac{\partial}{\partial m} \chi^2 = -2(d - F(m))^T W J \tag{2.13}$$

Where $J = \partial F(m)/\partial m$ is the $m \times n$ Jacobian matrix representing the local sensitivity of the model function $F(m)$ to variation in the parameters m.

At each step, one can define the direction of steepest descent h by:

$$h = \alpha J^T W (d - F(m)) \tag{2.14}$$

Where the positive scalar α controls the length of the step in the downhill direction at each iteration. Lower steps will require many iterations until the objective function is minimised while larger steps take the risk of missing the minimum.

Similar approach such as the Gauss-Newton method were developed in which the χ^2 is reduced by assuming that the least squares function is locally quadratic so the goal is to find the minimum of this quadratic in one step. The Levenberg-Marquart method is another well-known approach that combines the gradient descent method (when the parameters are far from their optimal value) and the Gauss-Newton method (when the parameters are close to their optimal value). Such algorithm was often used in photometry and spectroscopy when trying to estimate model parameters of non-linear models.

The main issues of such methods is that it could easily converge toward a local minimum and this strongly depends on the initialization vector of parameters m_0. Also for model with large amounts of parameters m and for problems with complex solution (multimodality), the uncertainties on the estimated parameters is hard to estimate.

2.5 Bayesian inference approach

Previous methods are well suited for linear model with few independent parameters because it can gives a good estimation of the solution for a reasonable computation time. However, when dealing with strong nonlinear model with correlated parameters one would take the risk of missing the best possible solution by reaching a local minimum (in the least-square minimum sense) or missing multiple solutions when multimodality occurs. Also uncertainties may not only be associated to the data but may also concern the relationship between quantities in the model, the completeness of the model itself or unmodelled systematics. For these reasons it is difficult with previous methods to have a realistic estimation of these uncertainties. Bayesian inferences overcome these problems by using conditional probabilities on what has actually occurred and what can be learnt about the underlying distributions from the observed data (Trotta, 2017). It allows to deal with a high number of parameters in the forward modelling, it ensures that relevant prior information are accounted for in the final inference and look for non-unique solutions while statistically constraining the model parameters. the main difference is that solutions are expressed in the form of probability density function (PDF) which gives a more complete understanding of the solution. For these reasons Bayesian approaches are more and more common in planetary surface studies (Fernando et al., 2013; Schmidt and Fernando, 2015; Fernando et al., 2016; Schmidt and Bourguignon, 2019; Belgacem et al., 2020, 2021; Mishra et al., 2021b,a; Harrington et al., 2022; King et al., 2022).

In this section, generalities about bayesian methods will be provided along with examples of two sampling methods that has been used in this PhD work. Elementary notions about probabilities are required to fully understand bayesian statistics such as the notion of probability, distributions and random variables that will not be described here. For these notions we refer the reader to (Trotta, 2017) who wrote a very complete synthesis around the bayesian methods adapted to physical problems.

2.5.1 The Baye's theorem

Baye's theorem links the conditional probability of the parameter m_i knowing the data (the posterior probability) to the conditional probability of the same parameter without knowing the data d (the prior probability), updating our knowledge of the parameter from the prior to the posterior using the conditional probability of the data occurring given the parameter m_i is true (the likelihood) (Trotta, 2017):

$$p(m_i \mid d) = \frac{p(d \mid m_i)p(m_i)}{p(d)} \tag{2.15}$$

Where $p(m_i \mid d)$ is the a posteriori probability density function which describe the state of information on the parameter m_i conditioned on the measurements d. $p(m_i)$ is the a priori information we have on the parameters, such as the initial information we believe and the mathematical intervals of definition in which we expect the parameters to fall. $p(d)$ is a normalising function, also called the 'evidence' or 'marginal likelihood' (Trotta, 2017). It represents the state of null information (Tarantola and Valette, 1982).

The function $p(d \mid m)$ for all parameters is the likelihood function $\mathscr{L}$, also known as the probability of the data d given a value of the parameter m_i:

$$\mathscr{L} = p(d \mid m) \tag{2.16}$$

The likelihood function describes the joint probability of the observed data as a function of the parameters of the chosen model. By assuming that the noise within the data is Gaussian and independent the likelihood function can be expressed by:

$$\mathscr{L}(m) = \sum_{k=1}^{n} \frac{1}{\sqrt{2\pi\sigma_k^2}} \exp\left(-\frac{[d_k - F(m)_k]^2}{2\sigma_k^2}\right) \tag{2.17}$$

Where n is the number of data points (in the case of spectroscopic studies, the comparison is made between a simulated and an observed spectra so this refers to the number of spectral channels, i.e. the number of wavelengths/wavenumber), σ_k is the standard deviation of the data and $F(m)_k$ is the k-th simulated data point using the forward model F. Similarly, using the matrix expression the likelihood follows:

$$\mathscr{L} = \frac{1}{\sqrt[n]{2\pi}\sqrt{|\Sigma|}} \exp\left(-\frac{1}{2}((d_k - F(m)_k)^T \Sigma^{-1}(d_k - F(m)_k)\right) \tag{2.18}$$

Where Σ is the covariance matrix associated to the data d.

2.5.2 A priori information

The prior function $p(m_i)$ in equation 2.15 describes the a priori knowledge on the parameters m_i . In this study, the forward model used is the Hapke model so the unknown parameters are the one describing the microphysical properties of the surface:

- The abundances X_i of each considered compound i
- The grain-size diameter D_i of each considered compound i
- The macroscopic surface roughness $\bar{\theta}$

The a priori information on these parameters are mostly their distributions and their mathematical intervals of definition. Such information may comes from previous scientific results or out of pure theory. Commonly, when there are no particular prior beliefs about a parameter it is common to use uniform distribution as they are uninformative, which leads the data to drive the solution(Tarantola and Valette, 1982).

The abundances parameters X_i are a particular case since they are not independent because they must respect the sum to one principle ($\sum X_i = 1$). When considering more than one compound this principle reduce the dimensionality by one because the abundance of the last compound can be deduced with the sum of the others. To respect this important constraint we use a Dirichlet prior defined from $X_i^{'}$ uniform distribution over $[0,1]$, which also describes the state of no information for n_p linked parameters(Lapotre et al., 2017):

$$p(X_i) = Diri(X_i) = \frac{\log(X_i')}{\sum_i^{n_p} \log(X_i')}, X_i' \in Unif[0,1] \tag{2.19}$$

For the grain size parameters D_i, we use a log-uniform distribution between D_{min} and D_{max}:

$$p(D_i) = \log\left(D_{min} + D_i'(D_{max} - D_{min})\right), D_i' \in Unif[0,1] \tag{2.20}$$

The lower boundary D_{min} was set to 10 microns so that we respect the geometric optic regime which imply that the grain size must be greater than IR wavelength range we explore, this study is made using near-infrared (NIR) data in the typical $1-5\mu m$ wavelength range. The higher boundary D_{max} is set to 10^5 microns in order to explore a large parameter space but also to prevent a too strict constraint on a poorly known a priori parameter.

For the macroscopic surface roughness parameter $\bar{\theta}$ we assume a uniform distribution between $\bar{\theta}_{min}$ and $\bar{\theta}_{max}$:

$$p(\bar{\theta}) = \bar{\theta}_{min} + \bar{\theta}'(\bar{\theta}_{max} - \bar{\theta}_{min}), \bar{\theta}' \in Unif[\bar{\theta}_{min}, \bar{\theta}_{max}] \tag{2.21}$$

We set $\bar{\theta}_{min} = 0°$ and $\bar{\theta}_{max} = 45°$ as theoretically expected (Hapke, 1984). Recent photometric studies of Europa's surface have shown that the macroscopic roughness range from 6° to 27° (Belgacem et al., 2020).

The other a priori knowledge is related to the data. In this spectroscopic studies the data comes from spectrometer and spectro-imager so data are in the shape of a collection of spectra or hyperspectral images. Their uncertainties are mostly related to the instrumental noise (thermal noise, detector current noise, radiation noise) and also to the absolute calibration of the instrument which may affects the absolute level of the data. Such informations may be found from ground and in-flight calibration studies carried out before and during the mission. This uncertainties may change through time or across the different data points d_k of the same observation so one has to be careful to properly account for such varying uncertainties from one dataset to another. Such a priori is reflected by the covariance matrix the likelihood equation 2.18, the general case is to consider that all data points (all spectral channels within one spectrum) are assumed to be independent and their uncertainties can be described as Gaussian. In such case, the observed values is their mean and their uncertainties is represented by their standard deviation σ_n. This results in a diagonal covariance matrix:

$$\Sigma = \begin{pmatrix} \sigma_1^2 & 0 & 0 & 0 \\ 0 & \sigma_2^2 & 0 & 0 \\ 0 & 0 & ... & 0 \\ 0 & 0 & 0 & \sigma_n^2 \end{pmatrix} \tag{2.22}$$

2.5.3 A posteriori sampling : Markov Chain Monte Carlo methods

A crucial point of the bayesian approach is the sampling of the a posteriori probability distributions. A well-known and efficient approach is the Markov Chain Monte Carlo (MCMC) sampling methods. The purpose of such algorithm is to use 'walkers' that randomly sample the parameter space to create a sequence of different parameters values called a chain. An important property of the chain is that the density of samples is proportional to the posterior PDF (Trotta, 2017) which allows to construct the posterior distribution. The chain is composed by a sequence of random variables such that the probability of the $(n+1)$-th element in the chain only depends on the value of the n-th element (Trotta, 2017). The generation of each element is described by a transition probability $T(m^{(n)}, m^{(n+1)})$ giving the probability of moving from $m^{(n)}$ to $m^{(n+1)}$ in the parameter space :

$$p(m^{(n)} \mid d) T(m^{(n)}, m^{(n+1)}) = p(m^{(n+1)} \mid d) T(m^{(n+1)}, m^{(n)}) \tag{2.23}$$

This is called the 'detailed balance condition' (Trotta, 2017) and describes that the ratio of transition probabilities is inversely proportional to the ratio of the posterior probabilities at the two points. A key parameter of Markov Chains is that they converge to a stationary state where each elements of the chain are samples from the posterior PDF. When N elements have been generated, an estimate of the parameters can be done. For example the posterior mean $E(m_i)$ follows:

$$E(m_i) = \int p(m_i \mid d) m_i dm_i \approx \frac{1}{N} \sum_{n=0}^{N-1} m_i^{(n)} \tag{2.24}$$

Results of the inferences can be given using the marginal probability of m_i by integrating out all other parameters from the posterior (Trotta, 2017), for instance for m_1:

$$p(m_1 \mid d) = \int p(m \mid d) dm_2 .... dm_n \tag{2.25}$$

Similarly, pairwise posterior distribution between two parameters can be made to highlight potential correlations, for instance for m_1, m_2:.

$$p(m_1, m_2 \mid d) = \int p(m \mid d) dm_3 .... dm_n \tag{2.26}$$

Several algorithms were developed to build a chain to sample the posterior distribution. Recent approach has been dedicated to accelerate the convergence of the chain or to efficiently samples complex parameters space with high dimensionality. The choice of the 'walkers' (and therefore of the algorithm) is 'problem-dependent' so the following will present two examples of samplers that wee tested in this study : a Metropolis-Hastings algorithm (Metropolis et al., 1953; Hastings, 1970) and a Differential Evolution Markov Chain algorithm (Braak, 2006).

2.5.3.0.1 Metropolis-Hasting algorithm The Metropolis-Hastings algorithm (Metropolis et al., 1953; Hastings, 1970), described in (Mosegaard and Tarantola, 1995)(Trotta, 2017) (also used and optimised in (Fernando et al., 2013; Schmidt and Fernando, 2015; Fernando et al., 2016; Schmidt and Bourguignon, 2019; Belgacem et al., 2020, 2021)) is a well-known adaptation of the classical MCMC approach in which the candidate element $m^{(c)}$ of the chain is drawn from the proposal distribution $q(m^{(0)}, m^{(c)})$. The proposal distribution can be of any form such as a Gaussian of fixed width and centred around the current point. The general steps of the algorithm are:

1. Start from a random point $m^{(0)}$ and its associated posterior probability $p_0 \equiv p(m^{(0)} \mid d)$
2. Propose a candidate point $m^{(c)}$ by drawing from the proposal distribution
3. Evaluate the posterior at the candidate point: $p_c = p(m^{(c)} \mid d)$
4. Accept the candidate point with probability $\alpha = \min(\frac{p_c}{p_0}, 1)$
5. If the candidate point is accepted it is added to the chain and move there, otherwise duplicate the old point in the chain. Go back to (2).

The accept/reject step can also be performed by generating a random number u from the uniform distribution $[0,1]$ and accepting the candidate sample if $u < \alpha$ and rejecting it otherwise. If the candidate sample has a larger posterior than the previous one it is always accepted.

The convergence of the chain is evaluated using the 'acceptance rate' which describes the number of accepted jumps to the total number of likelihood evaluations. An acceptance rate of about 25% relates an optimal choice of the proposal distribution (Trotta, 2017). The choice of the proposal distribution is important for efficient exploration of the posterior, if the scale of the proposal distribution q is small compare to the target distribution the algorithm will spend too much time locally while if the scale is too high the chain can stay close to initialization as the jumps will be rejected, both cases lead to a poor exploration of the parameter space. Such algorithm can be easily adaptable to the problem by randomly exploring far or close neighbourhood from point to point, this will be shown in subsec. 2.6.

2.5.3.0.2 Differential Evolution Markov Chain The Differential Evolution Markov Chain (DE-MC) is another adaptation of the MCMC algorithm in which multiple chains are run in parallel (Braak, 2006; ter Braak and Vrugt, 2008). The information of the past of each chain is used to generate appropriate jumps within the parameter space. It has been shown that such approach outperformed a classical sampler in a nonlinear mixed effects model (ter Braak and Vrugt, 2008) by using only few parallel chains. This algorithm is implemented in Python in the MC3 package (Cubillos et al., 2016).

The convergence of the chains is monitored using the Gelman-Rubin test (Gelman and Rubin, 1992). The idea of the test is that at each step of the iterative simulation a distributional estimate and an estimate of how much sharper this distributional estimate might become if the simulation were continued indefinitely (Gelman and Rubin, 1992), for each individual parameter. It first discard the "burnin" period corresponding to the initialization and the first samples expected to be far away from the solution. Then, it computes the the "potential scale reduction factor" R by comparing the current inter-chain variance estimate $\hat{V}$ to the intra-chain variance W as follows :

$$R = \sqrt{\frac{\hat{V}}{W}} \tag{2.27}$$

The potential scale reduction R must tend to unity to states that convergence has been reached. This imply that evaluating more samples will not change the distribution of the parameters. Commonly it is considered that values close to 1.01 indicates convergence and that values above 1.2 for any of the model parameters should indicate non convergence (Gelman and Rubin, 1992) or require a longer burnin period. Such test can be conducted at any step, typically it is computed every 10% of the total MCMC iterations. An application of such algorithm will be shown in subsec. 2.6.

2.5.4 Estimators

From the solution (i.e.: the a posteriori PDF) several estimators can be computed:

- The maximum a posteriori probability (MAP), or 'best fit': $\dot{m}$
- The mean, simply computed from the average of the sample in the chain
- The standard deviation
- The maximum likelihood $\mathscr{L}$

If the a priori information is a uniform distribution function then the MAP and the maximum likelihood estimators are equivalent.

To evaluate the solution, one can also define the goodness of fit using a Root Mean Square (RMS) deviation, defined by:

$$RMS = \sqrt{\frac{\sum_k \left(d - F(\dot{m})\right)^2}{N_k}} \tag{2.28}$$

Where d is the data, $F(\dot{m})$ is the best fit, $\dot{m}$ is the corresponding parameters, N_k is the number of data points (i.e. number of wavelengths). Such definition did not take into account the data uncertainties. To account for this one can use the normalised root mean square deviation (in the case of independent variables with a homogeneous noise dispersion σ_N):

$$NRMS = \frac{RMS}{\sigma_N} \tag{2.29}$$

2.6 Inversion methods comparison

This section will be devoted to the comparison of some inversion methods among the one mentioned above. First an overview of the selected methods will be given, then the comparison will be made on two separate cases, on a single spectrum of a selected hyperspectral image and on an entire hyperspectral image. The results of these two tests will serve as guidelines for the choice of the method and therefore of the inversions made in part 2 and 3 of this work.

2.6.1 Algorithm

For each of the inversion methods presented above there are a large number of different algorithms, each suitable for particular types of problems. Here we present either an already functional algorithm which has been directly used or an adaptation of an already existing algorithm to the problem treated here.

The L-BFGS-B algorithm The 'L-BFGS-B' method (Byrd et al., 1995; Zhu et al., 1997) is a gradient descent algorithm made for solving large nonlinear optimisation problems with bounds constraints available under Python 'scipy.optimize' package. Such algorithm is a great choice for the method comparison because it is easily implementable but also because of the possibility of defining boundaries for the parameter space. This makes the inversion faster and comparable to Bayesian methods in which we

define an a priori on the parameters, such as their boundaries. Since the parameters we are fitting for are the microphysical properties of the surface, using a bound-constrained minimization ensures that the algorithm respect the positivity of each parameter but also the sum to one for the abundances. Using the gradient descent approach (see sec. 2.4) the algorithm start from an initialization vector (which can be chosen randomly or set manually) and will look for the set of parameters that minimise the root-mean-square deviation (see eq. 2.28) between the data (the observed spectrum) and the simulated spectrum with the Hapke model and the estimated parameters. For each minimization performed, a unique set of parameters is returned with only one estimate per parameter. Some convergence and hyper-parameters must be set:

- The boundaries of each parameters to evaluate
- The parameter 'gtol' defines the norm of the projected gradient. It serves as an indicator to stop the minimization when the maximum of the projected gradient is less or equal to 'gtol'.
- The parameter 'jac' defines the method to compute the descent direction, based on gradient vector and jacobian. It is often used to select a finite difference scheme for numerical estimation of the gradient with a relative step size.
- The parameter 'eps' defines the absolute step size used for numerical approximation of the jacobian via forward differences.
- The parameter 'maxfun' defines the number of function evaluations (this includes the actual sampling points but also all gradient/jacobian estimation)
- The parameter 'maxiter' defines the maximum number of iteration

The values set for these hyper-parameters will change from case to case and will be given when comparing methods below (see subsec.2.6.2 and 2.6.3).

Adaptation of the Metropolis-Hasting algorithm We use an adaptation of the Metropolis-Hasting algorithm (see par.2.5.3.0.1) that has been developed to estimate the Hapke parameters with hyperspectral data (CRISM instrument) on Mars (Fernando et al., 2013; Schmidt and Fernando, 2015; Fernando et al., 2016) and has been revised since (Schmidt and Bourguignon, 2019). The sampling strategy of the MCMC bayesian approach is very important to reach efficiently the convergence of the chain. In the classical Metropolis-Hasting the exploration of the parameter space is based on the selection of a candidate for the next iteration from a proposal distribution and on a probabilistic step of acceptance or rejection of the selected candidate. The adaptation of such algorithm proposed here consists of adding sampling steps that modify the proposal distribution of the next candidate points to evaluate in order to randomly explore the far, close or very close neighbourhood of the current point. The random sampling is described in figure 2.1. An alternative case was also developed to add a fourth option in which only 1 parameter is changed. The subsequent algorithm is shown figure 2.2. To speed up the convergence, we used either 3 (cases 1-3) or 4 cases from:

1. Random sampling over the full possible domain of all parameters
2. Random sampling close to previous sample. The step is set here to $1/20$th of the full domain around the previous sample
3. Random sampling very close to previous sample. The step is set here to $1/500$th of the full domain around the previous sample
4. Random sampling relative to previous sample, close to it but moving a single parameter only. The step is set here to $1/10$th of the full domain around the previous sample.

The convergence and hyper-parameters to define are :

Algorithm 2 MCMC random sampling - 3 cases

$Case \leftarrow Unif$
while $Redo \neq True$ **do**

  if $case \leq 1/5$ **then** ▷ Full domain
    $p[1] \leftarrow Unif(1) * 45$
    $p[2-5] \leftarrow Dirichlet(4)$
    $p[6-9] \leftarrow 10 * *(Unif(4) * 4 + 1)$

  else if $case > 1/5$ and $case \leq 3/5$ **then** ▷ Far 1/20th
    $p[1] \leftarrow p_{old}[1] + UnifScal(1) * 2$
    $nbhood = 0.2$
    $p[2-5] \leftarrow p_{old}[2-5] - nbhood/4 + Dirichlet * nbhood$
    $p[6-9] \leftarrow 10 * *(log10(p_{old}[6-9]) + UnifScal(4) * 0.2)$

  else ▷ Close 1/500th
    $p[1] \leftarrow p_{old}[1] + UnifScal(1) * 0.1$
    $nbhood = 0.005$
    $p[2-5] \leftarrow p_{old}[2-5] - nbhood/4 + Dirichlet * nbhood$
    $p[6-9] \leftarrow 10 * *(log10(p_{old}[6-9]) + UnifScal(4) * 0.01)$
  end if
  if p is in the domain **then**
    $Redo \neq False$
  end if
end while

Figure 2.1: Algorithm of the Bayesian MCMC approach based on the Metropolis-Hasting rule, modified from (Schmidt and Bourguignon, 2019). Here 3 cases are made to explore the far, close and very close neighbourhood of the current iteration.

- The total number of MCMC samples to compute
- The number of 'burned-in' (removed) iterations at the beginning of each chain
- The starting point of the MCMC chain is computed randomly

The convergence of the chain is monitored via the final acceptance rate. The best model is evaluate via the maximum of the likelihood, which is similar to looking for the minimum root-mean-square deviation as in the gradient-descent approach.

mc3: Multi-Core Markov Chain Monte Carlo algorithm The Multi-Core Markov-Chain Monte Carlo (called 'mc3' hereafter) (Cubillos et al., 2016) is an open-source python library that includes several sampler algorithms. Recent radiative transfer simulations (Harrington et al., 2022) using this algorithm have shown promising results. Among the different samplers, the Differential Evolution MCMC with Snooker proposal (DEMCz) (Braak, 2006) was chosen because it is well suited for nonlinear model with potential multimodal distribution in the parameters, such as the Hapke model in an intimate mixing scenario, but also because of its speed of calculation and convergence. More details of this algorithm can be found in (Braak, 2006) and (ter Braak and Vrugt, 2008). The exploration of the parameter space is made by running several chains in parallel and performing 'jumps' from differences of pairs past states. The convergence and hyper-parameters to define are:

- The stepping behaviour of the fitting parameters over the parameter space
- The total number of MCMC samples to compute
- The number of parallel chains to use

Algorithm 1 MCMC random sampling - 4 cases

$Case \leftarrow Unif$
while $Redo \neq True$ **do**

  if $case \leq 1/7$ **then** ▷ Full domain
    $p[1] \leftarrow Unif(1) * 45$
    $p[2-5] \leftarrow Dirichlet(4)$
    $p[6-9] \leftarrow 10 * *(Unif(4) * 4 + 1)$

  else if $case > 1/7$ and $case \leq 3/7$ **then** ▷ Far 1/20th
    $p[1] \leftarrow p_{old}[1] + UnifScal(1) * 2$
    $nbhood = 0.2$
    $p[2-5] \leftarrow p_{old}[2-5] - nbhood/4 + Dirichlet * nbhood$
    $p[6-9] \leftarrow 10 * *(log10(p_{old}[6-9]) + UnifScal(4) * 0.2)$

  else if $case > 3/7$ and $case \leq 5/7$ **then** ▷ Close 1/500th
    $p[1] \leftarrow p_{old}[1] + UnifScal(1) * 0.1$
    $nbhood = 0.005$
    $p[2-5] \leftarrow p_{old}[2-5] - nbhood/4 + Dirichlet * nbhood$
    $p[6-9] \leftarrow 10 * *(log10(p_{old}[6-9]) + UnifScal(4) * 0.01)$

  else ▷ Far - 1 parameter
    $ParamID \leftarrow fix(Unif * 9)$
    if $ParamID = 0$ **then**
      $p[1] \leftarrow p_{old}[1] + UnifScal(1) * 5$
    else if $ParamID \geq 1$ and $ParamID < 4$ **then**
      $p[ParamID] \leftarrow p_{old}[ParamID] + UnifScal(1) * 0.5$
      $p[\neg ParamID] \leftarrow p_{old}[\neg ParamID]/sum(p_{old}[\neg ParamID]) * (1 - X[ParamID])$
    else
      $p[ParamID] \leftarrow 10 * *(log10(p_{old}[ParamID]) + UnifScal(4) * 0.5)$
    end if

  end if
  if p is in the domain **then**
    $Redo \neq False$
  end if
end while

Figure 2.2: Algorithm of the Bayesian MCMC approach based on the Metropolis-Hasting rule, modified from (Schmidt and Bourguignon, 2019). Here 4 cases are made to explore the far, close and very close neighbourhood of the current iteration as well as the close neighbourhood of only one parameter.

- The number of 'burned-in' (removed) iterations at the beginning of each chain
- The thinning factor TF (decimation, by keeping only one over TFth sample). This is mostly used to reduce the memory usage to store only a few samples of the chain.
- The starting point of the MCMC chain is computed randomly

The convergence of the algorithm is monitored with the Gelman-Rubin test (see par. 2.5.3.0.2, eq. 2.27). The algorithm returns the posterior distribution of the parameters and the associated 'chi-square' value (see eq. 2.10). The best model evaluation corresponds to the set of parameter for which the maximum of likelihood is obtained.

2.6.2 Test case n°1: single spectrum

In this case we will illustrate a comparison between the 3 algorithms presented in subsec. 2.6.1 on an inversion of a single spectrum. The data and independent parameters common to the 3 algorithms will be detailed and the results will be illustrated with each model best fit and pairwise posterior distribution of the estimated parameters.

2.6.2.1 Dataset

As an example, we consider an observation of a bright region of the Trailing Anti jovian hemisphere of Europa from the Galileo/NIMS instrument, a NIR spectro-imager. The observation name is '14e006ci' and we selected one spectrum from the collection of spectra forming the hyperspectral image. The spectrum is first shown in figure 2.3. To test the numerical solutions of these 3 algorithms we consider the Hapke model and we seek to estimate the microphysical properties of the surface which are abundances of the considered compounds, their grain sizes and the macroscopic roughness of the surface. We consider a surface made of 4 compounds: crystalline water ice, hexahydrite (hydrated magnesium sulphate), magnetite and sulphuric acid octahydrate. The relevance of this choice of compounds is not discussed here, it is a naïve case in which we only looking to compare methods and results, more detail concerning the NIMS instrument, data and compounds selection attached to the study of Europa are present in part 2 of this work.

The data required to perform direct model simulation, in any of the 3 algorithm tested are:

- Observation data: the reflectance spectrum d of a bright surface of Europa
- Wavelength of the data on which we estimate the simulated spectrum and the corresponding number of spectels
- Optical constants (n and k) of each compound with which we simulate the spectrum, here we consider 4 compounds
- Geometrical condition of the observation: the incidence (43.7°), emission (49.0°) and azimuth (69.5°) angles
- Uncertainties on the data: the error is assumed to be gaussian with a standard deviation at 10% with a minimum at 0.01 in reflectance

From this data and the model parameters m, one can simulate a synthetic spectrum s following:

$$s = F(m) \tag{2.30}$$

Each element of spectrum s is note s_i. The goal is to estimate the best of parameters m so that the simulated spectrum fit the data d. The parameters m integrates the surface roughness (1 parameter), the abundances (4 parameters) and the grain size (4 parameters) for a total of 9 parameters to estimate. Since the abundances are linked together with the sum to one principle, the number of dimension of

the parameter space is $9-1=8$. The a priori knowledge on these parameters is their mathematical domain of definition (or boundaries of the parameter space) which are define in subsec. 2.5.2. For an easier comparison between the results, the goodness-of-fit for the best-fit estimated by each algorithm will be estimate using the root-mean-square deviation (see eq. 2.28). Because some optical constants of the compounds considered here are not available beyond 2.5 μm the wavelength range we consider is $0.95-2.5$ μm divided in 103 spectral channels (or spectels).

2.6.2.2 Results from the L-BFSG-B algorithm

Using the L-BFGS-B algorithm one can perform a minimization of the root-mean-square deviation between the observation and the simulated spectrum to find the best set of parameters m. To simplify the numerical implementation, we normalize all parameters in the $[0,1]$ range and convert them into real value when computing F. As an initialization, we set of all random values between 0 and 1 for each of the 9 parameters. Each parameter is then converted to its real value for the forward model considering their prior knowledge: the roughness follows a uniform linear law between 0° and 45° , the abundances follow a Dirichlet prior to ensure the sum to one and the grain size follows a log-normal law between 10 and $100,000$ μm. The hyper-parameters related to the L-BFGS-B algorithm (see par. 2.6.1) were set as follows:

- Boundaries were set to $[0,1]$. A small exception is made for the abundances as the minimum value was set at 1×10^{-10} instead of 0. This was made to prevent error during sum-to-one transformation from the randomly drawn initialization. This should no affect drastically the results as we expect a negligible impact from an abundance of 1×10^{-10} on the simulated spectrum.
- 'gtol' was set at 1×10^{-14}
- 'jac' was set to None meaning that we do not use a finite difference scheme for numerical estimation of the gradient with relative step size
- 'eps' was set to 1×10^{-9}
- 'maxfun' was set to 2×10^{4}
- 'maxiter' was set to 2×10^{3}

A typical results from a single random initialization is given Fig. 2.3. In this case the estimated RMS error is 0.0133. The algorithm stopped after 1480 iterations for a computation time of about 30 sec (on a 2.9 GHz Intel Core i7 dual core with 16 GB of RAM). This imply that there are 1480 evaluations of the RMS to reach the "best" solution. Although the fit is acceptable, the algorithm gives a unique solution for each parameter which does not give a clear representation of the solution error distribution and the potential correlation between parameters. Using the full RMS and parameters collection estimated during the gradient descent would give a more accurate representation of the solution. However, a single initialization only gives about a thousand estimate, which is too small to be representative.

In the need to be able to compare the gradient-descent algorithm with the bayesian approach we decided to perform several successive minimizations with random initialization each time. As a result, we will be able to have a clear representation of the topography of the solution. If there is only one minima in the parameter space, then the gradient would point toward it no matter the initialization. If the solution is more complex (local minima, multimodality) then 1000 random initializations should be enough to map such solution as we expect. Different local gradients should point toward different local minima from one initialization to another. A key aspect to entirely map the solution is to keep all estimated parameters and their associated RMS deviation during the descent until convergence. This collection of model evaluation (usually a thousands estimate per minimization) times the number of random initializations (1000 here) should provide enough information to estimate the full shape of the posterior probability density function.

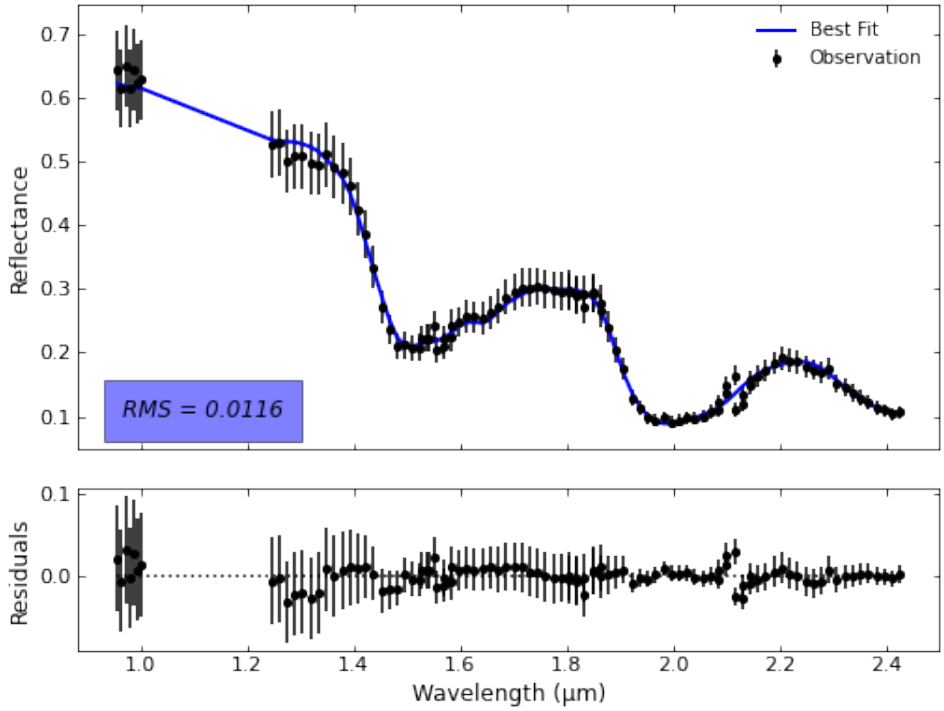

Figure 2.3: Best-fit (in blue) to the data (in black) from a random initialization using the 'L-BFGS-B' gradient-descent minimization. The data uncertainties are shown as black vertical line at each spectel. The RMS error is 0.0116. The solution of the estimated parameters is: 39.87° for the roughness, 5.4% of crystalline water ice with a grain size of 4.06×10^2 μm, 6.35×10^{-4}% of hexahydrite with a grain size of 1.825×10^3 μm, 85.2% of magnetite with a grain size of 1.0×10^5 μm and 9.3% of sulfuric acid octahydrate with a grain size of 58 μm. The computation time is 27.93 seconds on a 2.9 GHz Intel Core i7 dual core with 16 GB of RAM.

The best fit and all the collection of computed parameters from 1000 random initializations is shown in Fig. 2.4. The computation time is about 8 hours (on a 2.9 GHz Intel Core i7 dual core with 16 GB of RAM). One can see that the best-fit RMS is lower than for a single random initialization (see fig. 2.3) although the two fits are visually substantially identical.

To produce the pairwise posterior distribution plot (also called 'corner' plot hereafter) and make it comparable to the Bayesian approach, we had to redefine a "likelihood" for each sampling, that takes into account the uncertainty on the data. Since errors are assumed to be Gaussian with a standard deviation σ_i at 10% with a minimum at 0.01 in reflectance we can define the weighted Root Mean Square error:

$$wRMS = \sqrt{\frac{1}{N}\sum_i \frac{(d_i - s_i)^2}{\sigma_i^2}} \tag{2.31}$$

The likelihood is defined as follow:

$$\mathscr{L} = C \times \exp\left(-\frac{1}{2} \times \sum_i \frac{(d_i - s_i)^2}{\sigma_i^2}\right) \tag{2.32}$$

Using eq. 2.31 and 2.32 we can rewrite:

$$\mathscr{L} = C \times \exp\left(-\frac{1}{2} \times wRMS^2 \times N\right) \tag{2.33}$$

The constant C could be difficult to estimate analytically. It must be normalised so that the likelihood is a probability (integral of likelihood over the whole parameter domain is equal to one) and thus must follow:

$$C = \int_p \mathscr{L} \tag{2.34}$$

In practice this normalisation can be approximated by the computed samples. The function $\mathscr{L}$ is the likelihood of a simulated spectrum s, computed from a set of parameter m. The 'best-fit' is the set of parameter $\dot{m}$ for which the weighted RMS $wRMS$ is minimum and the likelihood is maximum. From eq. 2.31 and 2.33 we converted the RMS vector estimated during the 1000 gradient descents into a likelihood vector. Then, each likelihood values were normalised with the sum of all likelihood values to define a "frequency" vector representing the probability of the solution. This frequency vector was finally used to weight each parameter and to build the histogram and pairwise distribution of the corner plot. Thus each single iteration of the parameter vector is considered with regard to the value of the likelihood in a similar way to the Bayesian approach. The difference here is that the sampling is NOT following the a posteriori PDF.

Fig. 2.4 shows the narrow "valleys" in the space of two parameters and therefore the correlations between these parameters. However, it can be seen that the approach is naive because all the parameter space was explored, region far and close to the best fist almost equally. Nevertheless, these results is a good starting point for comparison with Bayesian methods.

2.6.2.3 Results from the MCMC with Metropolis-Hasting rules

With the dataset described in section 2.6.2.1 we perform a MCMC bayesian inversion using the adapted Metropolis-Hasting sampler described in section 2.6.1. We tested both the 3 and 4 cases random sampling to generate a MCMC chain made of 1×10^6 samples. Best-fit and posterior distribution of the parameters are shown fig. 2.5 for the 3 cases random sampling and fig. 2.6 for the 4 cases random sampling. For each test the computation time is about 1 hour. The acceptance rate is respectively 0.217 and 0.288 which is around the value of 25% which testifies to a relevant choice for the proposal distribution. The second case seems to have a higher acceptance rate which indicates the relevance of including a fourth step to move only one parameter in the exploration strategy.

Looking at the results from the 3 cases (fig. 2.5) it is clear that the algorithm explored less parameter space than the naive gradient-descent with random initialization. This is inherent in the formalism of the Metropolis-Hasting rule as the candidate point with a lower likelihood will automatically be rejected, which strongly constrains the space to explore. However, it is easy to observe that the explored parameter space has a higher posterior density than the one estimate with the gradient-descent algorithm. Valleys with preferential directions showing correlations between parameters are observed whereas the gradient-descent method only returned very narrow and pseudo-circular valleys. This is due to the better consideration of the data uncertainties in the bayesian approach unlike gradient-descent methods where the uncertainty was considered a posteriori, when artificially creating a 'likelihood' chain from the RMS chain. We can note that the best-fit RMS from the gradient-descent with 1000 random initializations method is lower than the RMS estimated with this case, which underlines the effectiveness of the gradient-descent methods at finding the exact position of the minimum. Although the random sampling with 3 cases has significantly improved the posterior PDF estimation of the parameters. The exploration may be not totally completed since the PDF is quite noisy.

When adding a fourth step in the sampling process (see fig. 2.6) we can clearly notice a significant improvement in the exploration of the parameter space and in the posterior distribution of the parameters. Strong correlations between parameters are visible when it was unclear with the previous case. While some valleys appears, some remained as confined and narrow as observed in the previous case. This fully demonstrate the contribution of the fourth case in the sampling step of the candidate point. The acceptance rate of 0.288 shows that the proposal distribution of the candidate point is optimal. The

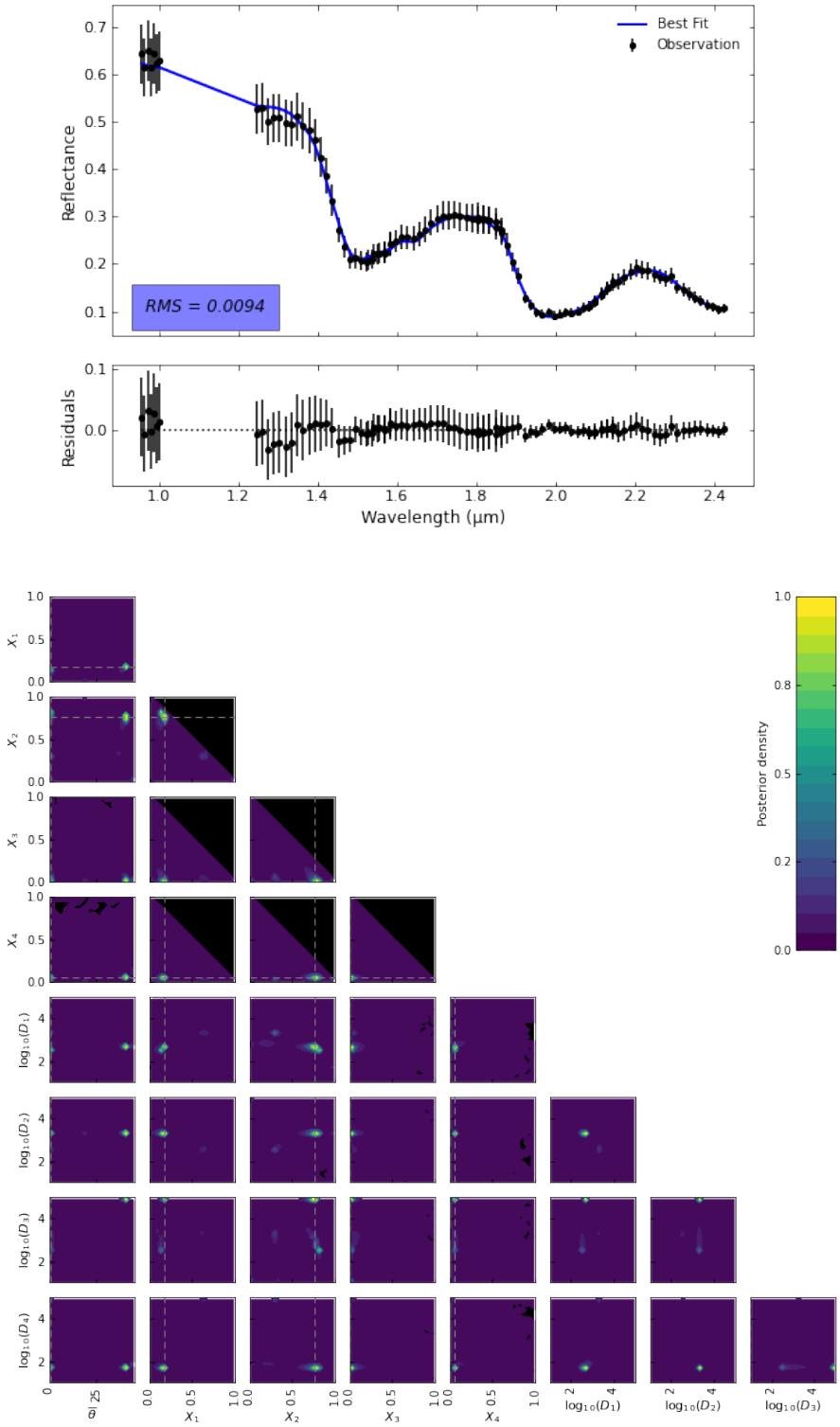

Figure 2.4: Results from 1000 random initialization using the 'L-BFGS-B' gradient-descent minimization. (top): Best-fit (in blue) to the data (in black). The data uncertainties are shown as black vertical line at each spectel. The RMS error is 0.0094. (bottom): Pairwise posterior distribution of each estimated parameters. The best-fit parameters are: 39.87° for the roughness, 17.6% of crystalline water ice with a grain size of 4.06×10^2 μm, 76.25% of hexahydrite with a grain size of 1.82×10^3 μm, 6.10×10^{-10}% ~~of magnetite with a grain size of 1.0×10^5 μm and 6.10% of sulfuric acid octahydrate with a grain size~~ of 58.38 μm.

best-fit RMS is 0.0095 which is similar to the best-fit solution estimated by the gradient-descent method and clearly tends to favour the bayesian approach. This case shows that complex distribution can be handled more easily than the 3 random sampling case and the gradient-descent method. However, when the solution is unimodal forming a narrow valley around the solution, both the gradient-descent method and the 3 random sampling case can be efficient.

2.6.2.4 Results from the mc3: DEMCz algorithm

Using the Differential Evolution MCMC with snooker proposal (DEMCz) algorithm described in section 2.6.1 and the independent parameters described sec. 2.6.2.1 we perform a similar inversion to estimate the microphysical parameters of the model. For the comparison to be relevant we used the same number of total samples evaluated in the chain as for the MCMC with Metropolis-Hasting rules, i.e. 1×10^6 samples. The difference lies in the fact that this algorithm runs multiple chain in parallel to speed up the convergence. The computation time is also close to 1 hour.

The estimated best-fit and posterior distribution of the parameters are shown fig. 2.7. Looking at the best-fit RMS one can see that the estimated solution is equivalent to that found by the MCMC with 4 random sampling steps and the gradient-descent with 1000 random initializations with a value of 0.0095. The value of the parameters associated to this best-fit are described in the caption of fig. 2.7. When comparing all best-fit solutions of the 3 algorithms we see that the orders of magnitude of the estimated parameters are respected from one solution to another although the exact values vary. This happens because there are no overly complex solutions involving multimodality but rather more or less unimodal solutions with complex shape. This leads to a good estimation of the shape of the solution by Bayesian methods, the estimated numerical value of the best-fit depends on the numerical resolution of the sampler and of the sampling method itself. This reinforces the confidence that one can have in the classic gradient-descent methods to find the best solutions of simple distribution but shows that a single solution does not exist, but rather a set of parameters that influence each other with strong correlations. This is evidenced by the posterior distribution of the parameters. Some similarity with the MCMC with 4 random sampling steps are visible but the estimated valleys appear larger and better constrained in this case, also the algorithm has explored a much wider parameter space. This algorithm seems to be the most efficient for the problem investigated with a similar computation time as for the MCMC with Metropolis-Hasting rules, an equivalent best-fit RMS and a better exploration and estimation of the parameters posterior distribution.

2.6.3 Test case n°2: hyperspectral image

In this case we will consider an hyperspectral image made of multiple spectra and we will estimate the same microphysical parameters as for the previous case (see subsec. 2.6.2) using 2 methods: the gradient-descent algorithm and the Differential Evolution MCMC algorithm. The comparison of the two approaches will show the effectiveness of the methods when moving from a single spectrum to a collection of spectra where not only a good estimate of the solutions are required but also a reasonable computation time.

2.6.3.1 Dataset

Dataset related to the direct model are similar to the one described in section 2.6.2.1 of the test case number 1 (see. 2.6.2), only the data change as we now consider an entire hyperspectral image of Europa from the Galileo/NIMS instrument. The corresponding image is shown fig. 2.8 along with the collection of spectra. In this case, for each of the 3441 spatial pixel correspond a spectrum with a collection of wavelengths as well as a specific value of the incidence, emission and azimuth angles. Note that the number of wavelengths channels (or spectels) may change from one spectrum to another across the image as some detectors sometimes measured abnormal reflectance values of -99999 which have been transformed to *NaN* so that we prevent the algorithm from fitting outliers. The uncertainties on

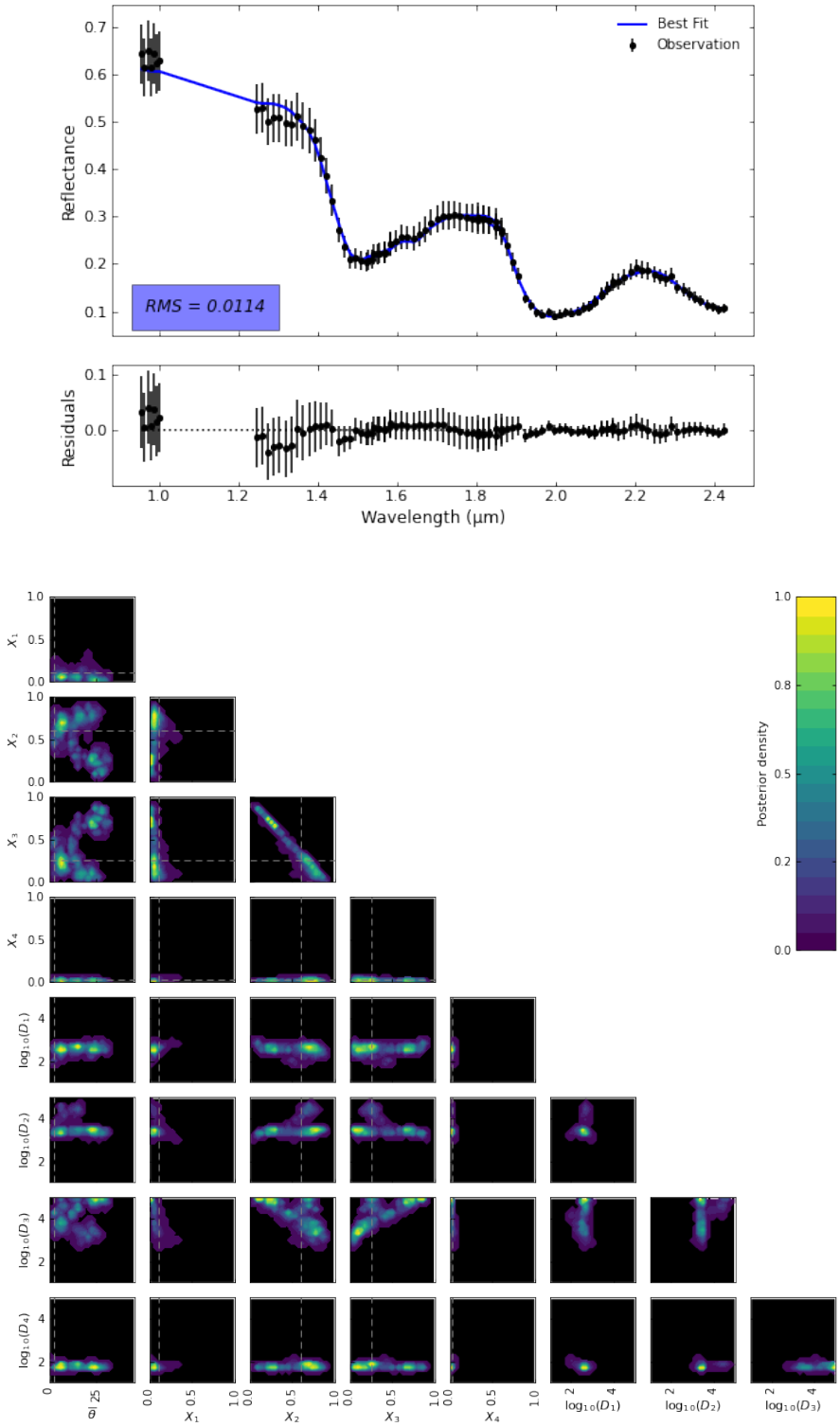

Figure 2.5: Results from the adapted MCMC Metropolis-Hasting algorithm when considering 3 random sampling steps as described par. 2.6.1. (top): Best-fit (in blue) to the data (in black). The RMS error is 0.0114. The data uncertainties are shown as black vertical line at each spectel. (bottom): Pairwise posterior distribution of each estimated parameters. The acceptance rate is 0.217. The best-fit parameters are: 2.83° for the roughness, 10.9% of crystalline water ice with a grain size of 4.16×10^2 μm, 60.1% ~~of hexahydrite with a grain size of 2.237×10^3 μm, 25.12% of magnetite with a grain size of 5.0×10^4~~ μm and 3.74% of sulphuric acid octahydrate with a grain size of 57.17 μm.

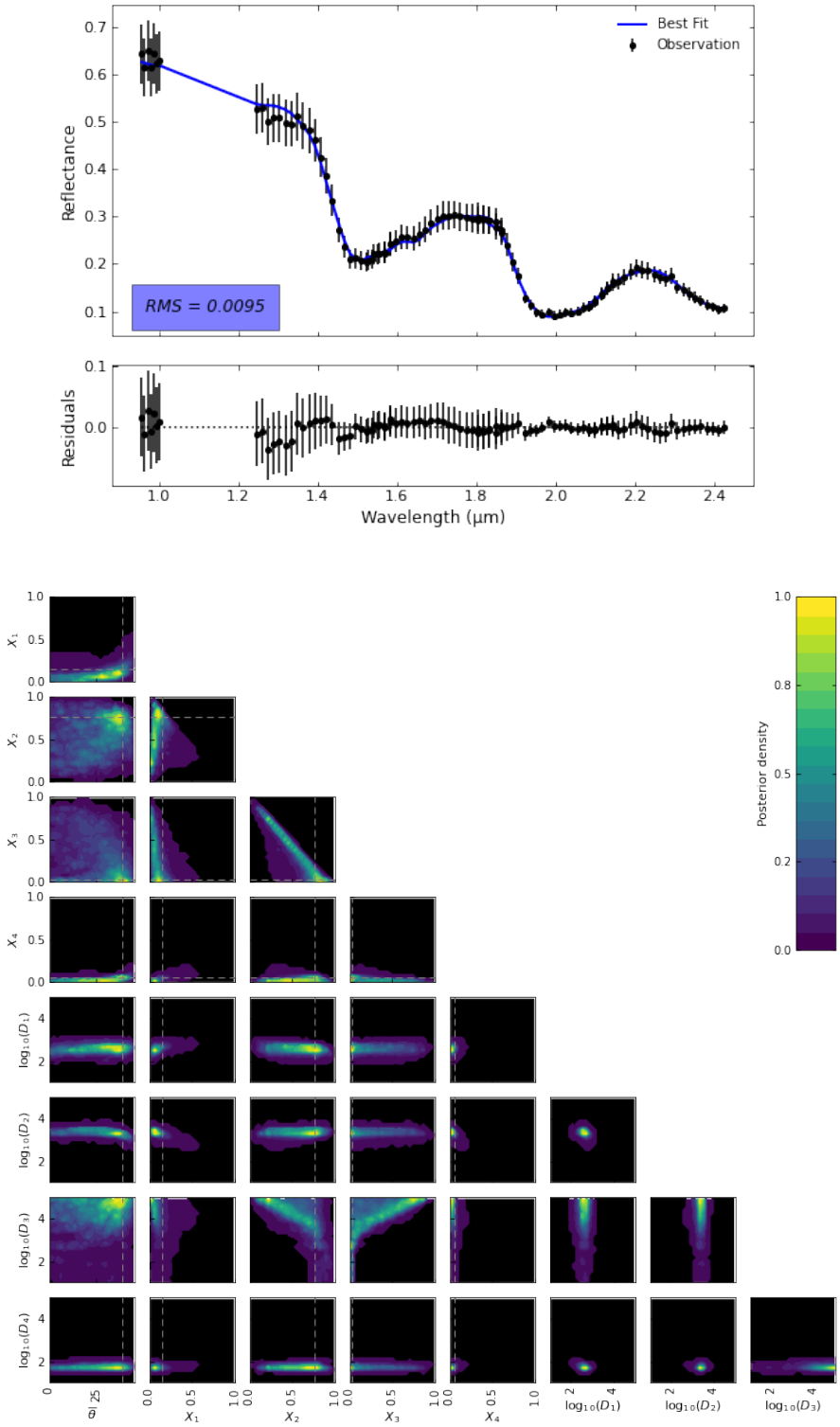

Figure 2.6: Results from the adapted MCMC Metropolis-Hasting algorithm when considering 4 random sampling steps as described par. 2.6.1. (top): Best-fit (in blue) to the data (in black). The RMS error is 0.0095. The data uncertainties are shown as black vertical line at each spectel. (bottom): Pairwise posterior distribution of each estimated parameters. The acceptance rate is 0.288. The best-fit parameters are: 38.37° for the roughness, 15.6% of crystalline water ice with a grain size of 3.98×10^2 μm, 75.8% ~~of hexahydrite with a grain size of 2.017×10^3 μm, 3.24% of magnetite with a grain size of 1.53×10^4~~ μm and 5.33% of sulphuric acid octahydrate with a grain size of 58.46 μm.

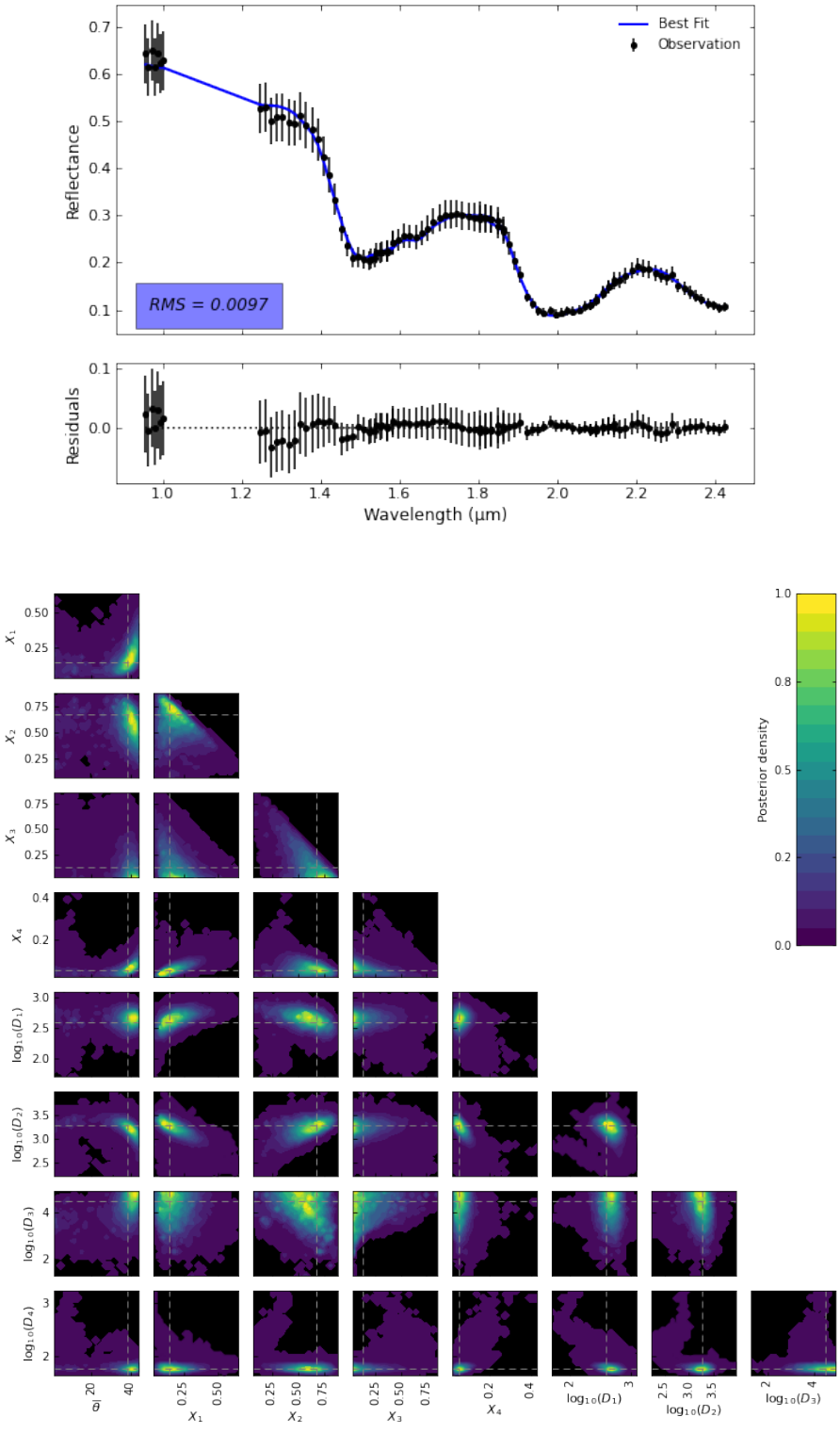

Figure 2.7: Results from the mc3:DEMCz algorithm as described par. 2.6.1. (top): Best-fit (in blue) to the data (in black). The RMS error is 0.0095. The data uncertainties are shown as black vertical line at each spectel. (bottom): Pairwise posterior distribution of each estimated parameters. The convergence monitored by the Gelman-Rubin test indicate that all parameters fall below the threshold value of 1.01, indicating convergence. The best-fit parameters are: 38.69° for the roughness, 14.43% of crystalline ~~water ice with a grain size of 3.91×10^2 μm, 68.06% of hexahydrite with a grain size of 1.89×10^3 μm,~~ 12.30% of magnetite with a grain size of 3.15×10^{-1} μm and 5.19% of sulphuric acid octahydrate with a grain size of 59.92 μm.

the data is similar to case number 1 as it is the same instrument, the error is assumed to be gaussian with a standard deviation at 10% of the reflectance with a minimum at 0.01 in reflectance . Here we will consider the surface as an intimate mixing of 7 compounds: crystalline and amorphous water ice, hexahydrite (hydrated magnesium sulphate), sulphuric acid octahydrate, magnesium chloride, mirabilite (hydrated sodium sulphate) and mascagnite (ammonium sulphate). Therefore, for each compound we consider their optical constants (n and k). With the surface roughness (1 parameter), the abundances (7 parameters link by the sum to one principle) and the corresponding grain size of each compound (7 parameters) the number of dimension of the parameter space is $15-1=14$.

2.6.3.2 Data clustering

We want to estimate the microphysical properties of the surface by performing an inversion of the Hapke model on the 3441 spectra of the image. We saw from test case number 1 (see subsec. 2.6.2) that bayesian approach using either the DEMCz or the MCMC with Metropolis-Hasting rules would give a good estimate of the parameters posterior distribution while properly accounting for the data uncertainties but at the cost of high computation time. Also, we have seen that gradient-descent methods using the bound-constrained L-BFGS-B algorithm could give a good estimate of the best-fit solution in a very fast computation time but takes the risk of getting trapped in a local minimum and will not give the full shape of the solution with the associated uncertainties. Also, this method is really initialization dependent. We tested a naive gradient-descent approach and found that the results map was not coherent.

To solve this problem, we want to test if a compromise between the 2 approaches is possible. A first solution would be to perform a bayesian inversion of a synthetic spectrum made by the mean of all spectra (or by taking the spectrum closest to the mean of all spectra) and use the best-fit solution to initialise the gradient-descent algorithm so that we avoid local minimum and guarantee the robustness of the solutions estimated by the minimization. The subsequent results would be interpreted with regard to the posterior distribution estimated by the bayesian solution. Two major problems can arise from this, first we saw from test case number 1 that even for a single spectrum with lower dimensionality of the parameter space the solution can be very complex and this strategy would erase such complexity. Second, looking at the collection of spectra from fig. 2.8 one can see that there is a significant spectral variability across the dataset which translates a variation of the microphysical properties, using a single initialization would very often results in either a bad estimation of the solutions or miss the global solution while remaining stuck in a local minimum. However we can notice that data can be organised according to spatial and spectral coherence. This imply that some areas appear similar and therefore the microphysical properties must be close.

Based on this observation we propose to perform a data clustering on all pixel of the image to group data according to their spectral similarities. We used the 'k-means' clustering approach that aims to partition n observations x_i into k clusters in which each observation belongs to the cluster with the nearest mean μ_k, also called the cluster centre or cluster centroid (Lloyd, 1982). The 'k-mean' algorithm follow a minimization problem called the 'Expectation-Maximization' in which the Expectation step is assigning the data points to the closest cluster and the Maximization step compute the centroid of each cluster. First, let's considers the objective function J as follow:

$$J=\sum_{i=1}^{m}\sum_{k=1}^{K} w_{ik}\left\|x_i-\mu_k\right\|^2 \tag{2.35}$$

Where $w_{ik}=1$ for data point x^i if it belongs to cluster k, and 0 otherwise. μ_k is the centroid of the cluster x^i. First, the algorithm minimise the objective function J with reference to w_{ik} and treat μ_k fixed to update cluster assignment:

$$\frac{\partial J}{\partial w_{ik}}=\sum_{i=1}^{m}\sum_{k=1}^{K}\left\|x_i-\mu_k\right\|^2 \tag{2.36}$$

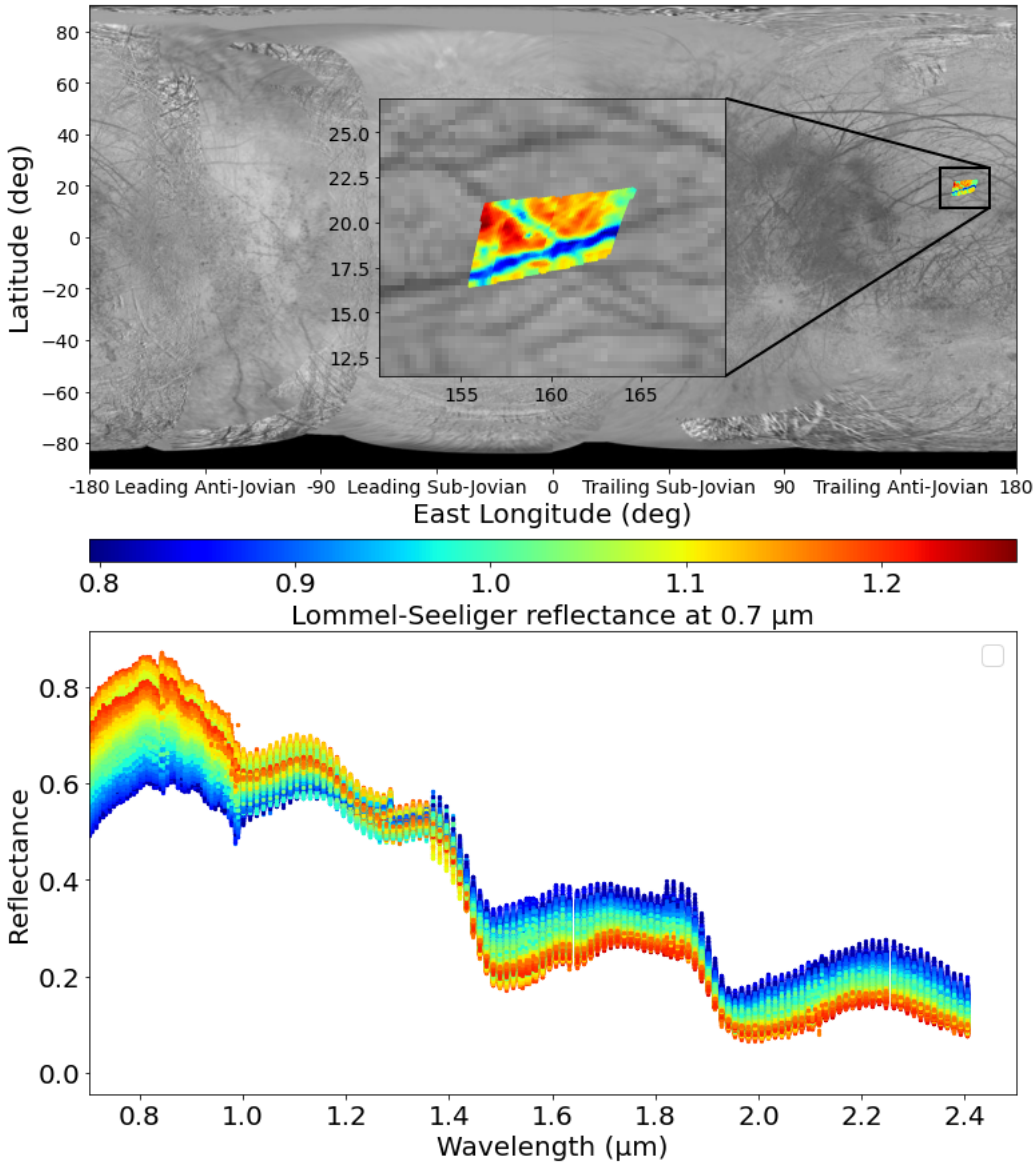

Figure 2.8: Dataset of the test case n°2: hyperspectral image 'e6e007ci' from the Galileo/NIMS instrument showing 'Harmonia Linea', a dark lineament of the Trailing Anti Jovian hemisphere. The color represents the reflectance at 0.7 μm normalized using the Lommel-Seeliger law. At these visible wavelengths the dark lineaments (in blue) are easily identifiable among the surrounding brighter plains (in yellow to red). For each pixel of the image corresponds a spectrum represented on the bottom plot (the spectra colors match the colorcode of the image).

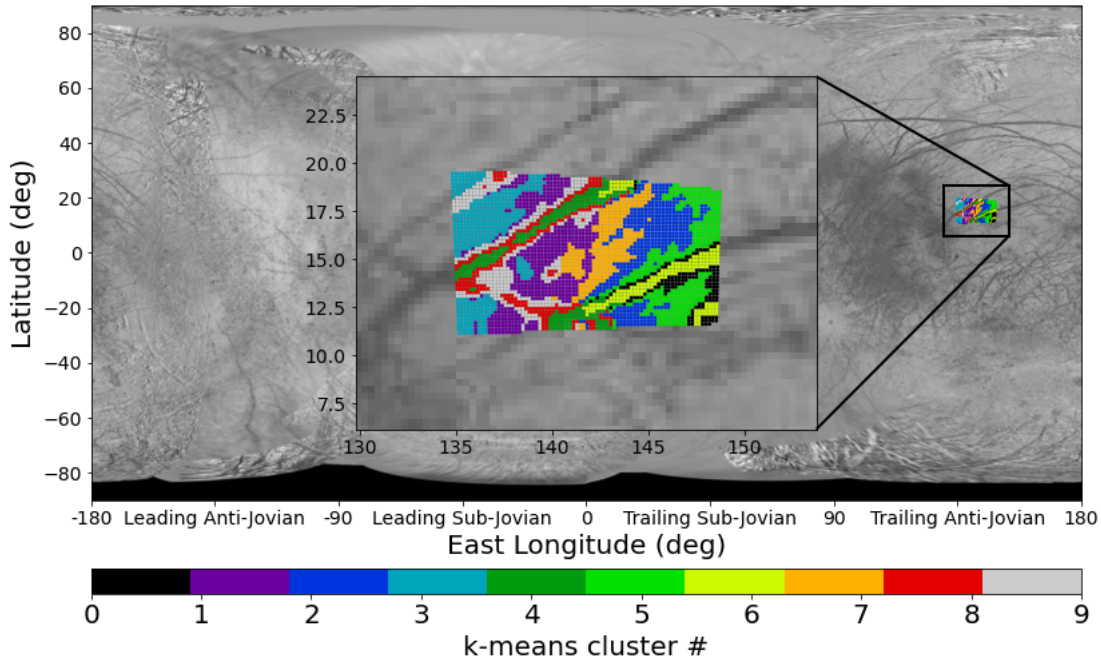

Figure 2.9: Cluster map with $K = 10$ classes estimated with the 'k-means' algorithm.

$$w_{ik} = \begin{cases} 1, & if\, k = \arg\min \left\| x_i - \mu_j \right\|^2 \\ 0, & otherwise \end{cases} \tag{2.37}$$

This will assign the data point x_i to the closest cluster according to its sum of squared distance from cluster's centroid. Then the algorithm minimize J with reference to μ_k and treat w_{ik} fixed. This step recomputes the centroids after the cluster assignments from previous step:

$$\frac{\partial J}{\partial \mu_k} = 2 \sum_{i=1}^{m} w_{ik}(x_i - \mu_k) = 0 \tag{2.38}$$

$$\mu_k = \frac{\sum_{i=1}^{m} w_{ik} x_i}{\sum_{i=1}^{m} w_{ik}} \tag{2.39}$$

Which recomputes the centroid of each cluster to reflect the new assignments. The k-means is an iterative algorithm which works as follows:

1. Specify the number of clusters K

2. Randomly initialise the centroids

3. Keep iterating until there is no change to the centroids

As for many iterative algorithms with random initialization, different initialization could lead to different clusters as the algorithm could be stuck in a local optimum which is different from the global optimum. Generally we overcome this problem by doing several random initializations and taking the solution for which the squared distance is the lowest. We used an implementation of this approach from the open source 'scipy.cluster.vq' in Python programming language by considering a number of 10 clusters. Figure 2.9 shows the cluster map estimated with the 'k-means' algorithm.

2.6.3.3 Initialization

From the clustering step we define x_k^+ and x_k^- which are respectively the most and least representative spectrum of the k-th class, with k ranging from 0 to 9. x_k^+ is automatically returned by the 'k-means' algorithm as it correspond to the centroid of the class. x_k^- is defined as the spectrum within the class k for which the squared distance with the centroid is maximum. On each of these 20 spectra we perform a bayesian inversion using the DEMCz algorithm (see par. 2.6.1) similar to what have been done in case number 1 (see sec. 2.6.2.4). To account for a higher dimensionality of the parameter space and ensure convergence of the chains we consider a total number of samples of 1.5×10^6. For each spectra x_k^+ and x_k^- of the classes, the solutions estimated are similar to what is presented in the single spectrum case (see fig. 2.7): a set of best-fit parameters and their posterior distribution.

The best-fit solution of the x_k^+ spectra is used as initialization parameters for the gradient-descent algorithm performed on all spectra of the corresponding cluster. Thus a comparison between the estimated parameters from the gradient-descent method and the bayesian method will be possible on both spectra x_k^+ and x_k^- for each cluster. We expect strong similarities between the parameters estimated by the two approaches for x_k^+ because the initialization falls within a minimum, the gradient-descent method should stay close to this solution. In contrast, the comparison on the least representative spectrum of the cluster x_k^- will reveal the robustness of the gradient-descent method as one would expect significative differences between x_k^+ and x_k^+ , so the initialization should be far from the optimal solution.

Using the gradient-descent algorithm we performed the minimization of the root-mean-square deviation on the 3441 spectra of the image.

2.6.3.4 Results

Considering the 10 classes made from the clustering step, each with a class best and worst representative (x_k^+ and x_k^-) and the 15 parameters estimated by each of the two inversion methods, the amount of analysable data is considerable. It is not possible to simply illustrate these 600 results individually. Rather than looking at the quality of the fit, which is expected to be good enough based the observed results on a single spectrum (see subsec. 2.6.2), it is more interesting to look at the estimated posterior distribution by the Bayesian approach for one parameter and compare it to the best-fit solution estimated by the gradient-descent method. Thus, the consistency of the results can be validated via the relevance of the solution within the shape of the posterior distribution.

Figure 2.10 depicts different scenarios which account for the varieties in the shape of the posterior distribution of some estimated parameters with the DEMCz algorithm. In these examples the distribution of only one parameter among the 15 estimated taken either on the best class representative (x_k^+, in green) or on the worst class representative (x_k^-, in blue) of a single cluster is shown. Each example illustrates a different parameter taken from a different cluster in order to demonstrate the generality of the conclusions. Looking at the results it can be noted that:

- When the parameter shows a fairly tight unimodal posterior distribution and the gradient-descent approach is initialized with the best-fit solutions of the bayesian method (fig.2.10, top left) then the gradient-descent method solution is very consistent with both the bayesian best-fit and posterior distribution. But, as evidence fig. 2.10 (middle, left) this is not always true as the gradient-descent best-fit falls on the edges of the distribution.

- Unimodal distributions of the solutions give similar best-fit by the two approaches even for the class least representative initialized from the best-fit solution of the class best-representative as shown fig. 2.10 (top, right) as long as the differences between the two data do not involve significant changes in the solutions as evidenced fig. 2.10 (middle, right), even for tight unimodal distributions. In this case the gradient-descent algorithm stay trapped in the local minimum (probably near the initialization) that the bayesian considers improbable.

- More complex distribution are poorly managed by the gradient-method as evidenced fig. 2.10 (bottom, left) in which the best-fit solution of the gradient-descent method falls near the bounds

of the parameter space although initialise near the maximum of the distribution, but also fig. 2.10 (bottom, right) in which the best-fit solution of the gradient-descent falls perfectly in the middle of the bimodal solution at the least likely place.

Although one must remain cautious when interpreting marginal 1D posterior distribution because it illustrates only a small part of the true shape of the solution, in which the 14 remaining dimensions are folded on this one. This explains why the bayesian 'best fit' does not always fall on the maximum of the distribution (which would define the most 'probable' solution). The demon of dimensionality should also be the reason for the trapping of gradient-descent algorithm in a local minimum that the bayesian does not even consider as a solution.

Nevertheless these few examples allow us to draw several conclusions. First, although the clustering step can save computation time by performing only few estimate with the bayesian approach it is easy to miss the global 'best fit' solution. This is the case for the class least representative spectra x_k^- but more unexpectedly also for the class best representative one x_k^+. This is due to the nonlinearity and high dimensionality of the problem which does not make the gradient-descent method an efficient exploration strategy. Increasing the number of cluster won't even help because it could produce bias when interpreting all solutions of the same cluster and would also require more bayesian to be performed as verification step, which is irrelevant.

Second, complex posterior distributions may occurs in which the best-fit solution no longer make sense, especially as initialization of the gradient-descent approach that will very certainly remain stuck in a local minimum. These distributions demonstrate either strong correlation between the model parameters or a too weak constraint on the data. Interpreting distributions requires other estimators than the best-fit solution (such as the mean and standard deviation of the distribution, skewness or the kurtosis). Having access to the posterior PDF it is one of the major advantages of MCMC Bayesian methods that more conventional methods cannot do.

2.7 Conclusion

In this chapter we covered the theoretical notions behind inverse problems and modelling. Some examples of well-known methods from the linear model estimation and least-square regression to the gradient-descent and bayesian framework were presented. A key point of the inverse problem is that the choice of the methods is problem-dependent as some approaches will fail at finding the global minimum of the solution, especially when dealing with highly nonlinear model with high dimensionality of the parameter space. In this work we mainly focus on characterising the microphysics of icy surfaces through the use of the Hapke model as a forward model. Such model is complex due to the highly non linear effects of the radiative transfer and the dimensionality of the parameter space quickly raise when adding more compounds to the mixing. In order to find the appropriate approach that combines a realistic estimation of the parameters and a reasonable computation time we described and compared two distinct approaches, a classical minimization of the cost-function through the gradient-descent algorithm and a MCMC Bayesian framework through different kind of sampling methods. The comparison was made on two cases representative of the problems encountered in this work: an estimation of the optimum parameters on a single spectrum and on a whole hyperspectral image with many spectra.

Results have shown that in some cases, when the dimensionality of the problem is not too high and the shape of posterior distribution of the solution is relatively simple with very little or no local minimum the gradient-descent algorithm is well-suited as it gives a good estimate of the best-fit solution for a fast computation time. Such approach will be used for the instrumental calibration of the NOMAD instrument (see chap. 8) when trying to find the optimal set of parameters that describes the instrumental functions where strong nonlinearity and correlations are not expected.

When trying to estimate the microphysical properties of the surface through radiative transfer modelling such approach is no longer adapted because of the strong nonlinearity in the model which translates into complex posterior distribution and correlations. In such case the 'best-fit' solutions matters very little but the whole distribution gives a complete description of the state of the solution and should be preferred.

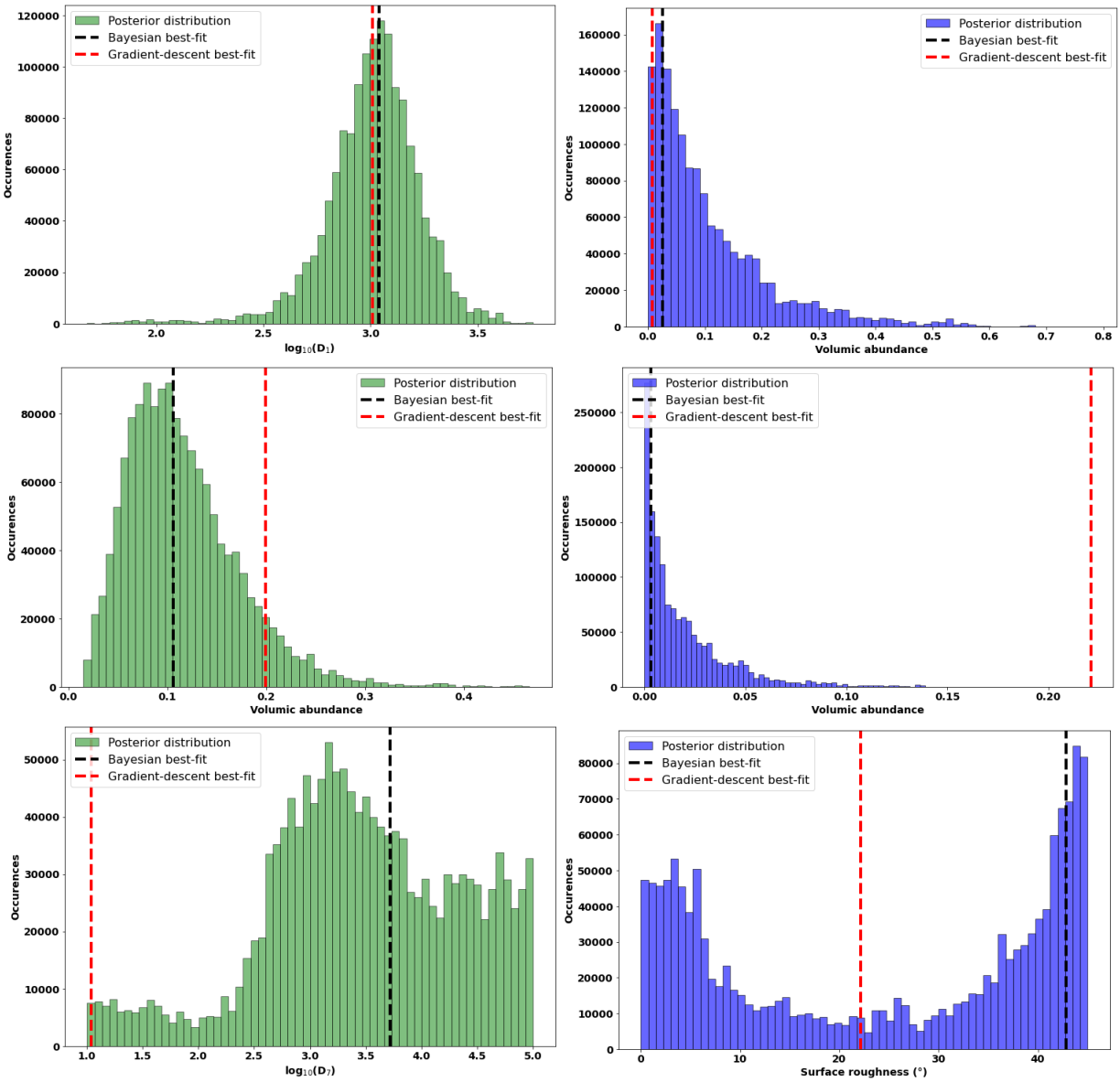

Figure 2.10: Inversion comparison between the Bayesian and the gradient-descent methods: example of 6 parameters for a particular cluster, representative of the full results. The black dashed line is the Bayesian best-fit solution and the red dashed line is the gradient-descent best-fit solution. The histograms represents the a posteriori results from the Bayesian MCMC. The left plots shows a comparison on a best representative spectrum of a cluster (x_k^+ or cluster centroid) while the right plots shows a comparison made on a worst representative spectrum of a cluster (x_k^-). One can clearly observe in the upper plots that both methods seem consistent in some cases. In the middle and lower plots, the gradient-descent and bayesian approach are clearly incompatible, demonstrating that gradient-descent should be discarded for this problem.

Of all algorithm tested here, only the MCMC Bayesian framework with a dedicated sampling methods (like the Differential Evolution Markov Chain algorithm) was robust enough to efficiently sample the true shape of the solution. Although the computation time is high when considering a whole hyperspectral image with several thousand of spectra it is preferable to ensure a Bayesian inversion of all spectra rather than trying to save time with intermediate steps (like clustering/gradient descent) that could give wrong estimate or produce bias in the final results. Such approach will be used for the microphysical characterisation of Europa's surface (see chap. 4).

Part II

Microphysics of Europa's surface

This part presents a direct application of the method presented in part. I for the microphysical characterization of Europa's surface. A first chapter (see chap. 3) is devoted to the description of the Galilean system, then a more detailed review of our knowledge about Europa is made including its interior, its surface and the important coupling with its external environment. The observed morphologies, surface properties and processes invoked to explain these observations are developed in order to defined the unanswered questions. A second chapter (see chap. 4) is dedicated to the question of the surface composition of Europa. It will discuss the selection of the best chemical compounds for the characterization of Europa's surface. This work was the subject of a publication in which the method is carefully described. A direct application to a Galileo/NIMS observation of Europa provides clear answers to the question raised. The conclusions of this work are summarized in the last chapter (see chap. 5), important perspectives that will be the subject of future work are developed at the same time.

Chapter 3

Context

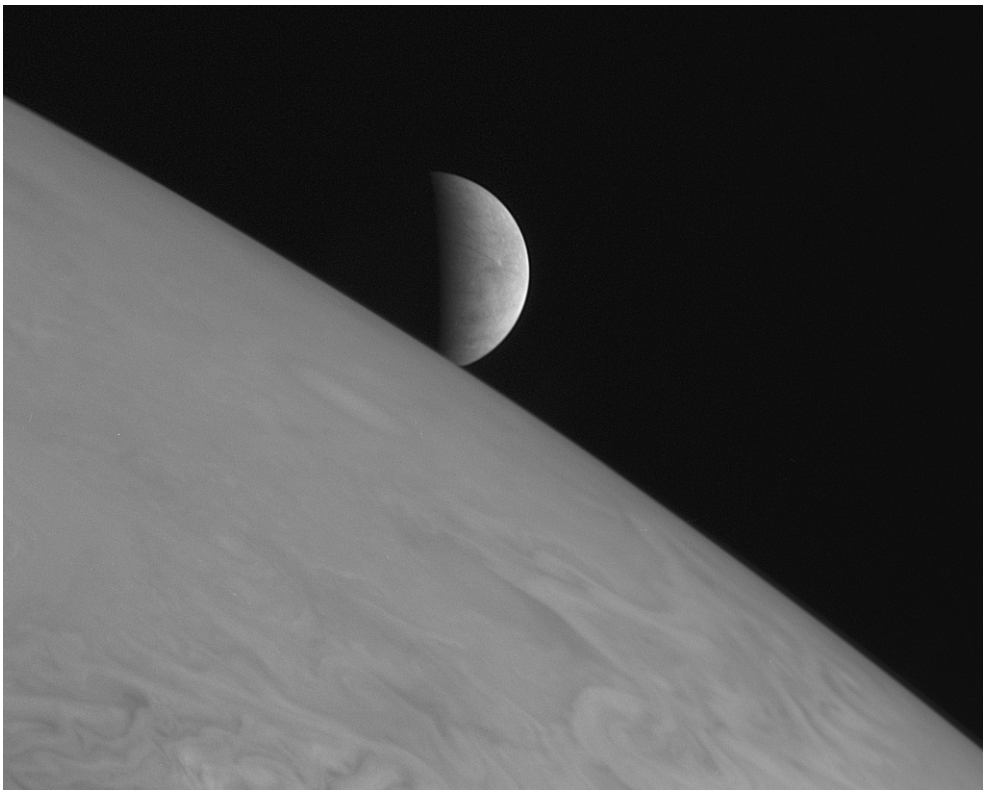

Europa rising above Jupiter's cloud. This image was taken by the long Range Reconnaissance Imager (LORRI) on board the New Horizons spacecraft on February 28, 2007. (credit NASA/Johns Hopkins University Applied Physics Laboratory/Southwest Research Institute)

This chapter presents the current state of knowledge on Jupiter's system and its icy moon Europa which is necessary for the understanding of the work undertaken. The entire literature relating to the Jovian system will not be covered but we focus on the key elements composing it. Then we will focus on a more complete description of Europa, from the observed morphologies to the processes at their origins. We will also give few informations regarding its past and future exploration with an emphasis on the Galileo mission because this work is based on data from one of the instruments. We will end with the outstanding questions and the motivations for conducting a spectroscopic study of Europa.

3.1 The Jovian system

The Jovian system designates the planet Jupiter and all surrounding objects affected by its gravitational influence. This region is called the 'Sphere of influence' and it includes the numerous moons of Jupiter but also its ring system. Another important component of the Jovian system is the massive magnetosphere of Jupiter.

3.1.1 Jupiter

Jupiter is the fifth planet of the solar system orbiting at about 5.2 Astronomical Units (AU) from the Sun and also the largest and most massive. Its period of revolution around the Sun is 12 years but its rotation period is the shortest of the Solar system with a value of about 10 hours. As evidenced fig. 3.1, its massive atmosphere is separated in various latitudinal cloud bands evolving in differential rotation, each at their own speed producing turbulences and storms such as the famous 'Great Red Spot', a giant anticyclone whose size is twice the diameter of the Earth. Jupiter's composition is similar to the Sun with mostly hydrogen and helium accounting for more than 87% by mass (Guillot et al., 2004) but while the Sun only has 2% of its mass in heavy elements Jupiter has between 3 and 13%. The exact amount and distribution of these heavy elements in the planets are keys to understand the formation of Jupiter and the Solar System (Guillot et al., 2004). Its interior is not well constrained but the relatively warm conditions (around 20000K) imply that its interior is mostly fluid (Guillot et al., 2004)with a dense rock and ice core in its center. With a cooling rate of about 1K per million year and a contracting rate of about 3 cm per year (Guillot et al., 2004) a significant intrinsic energy flux drives convection in most parts of the helium enriched metallic hydrogen envelop but also in the external helium depleted molecular hydrogen layer, which tends to homogenize its interior.

3.1.2 Gravity field and tidal forces

Due to its important mass, Jupiter has a strong gravitational field interacting with any body orbiting in its sphere of influence. In a planet-satellite system the gravitational forces are directed toward the barycenter of the system and its intensity varies with the distance between its application point and the barycenter (on a $1/r^2$ dependency) implying that they are stronger at the point closest to Jupiter and weaker at the furthest. Its counterbalance, the centrifugal force due to the rotation of the satellite around the planet, tends to push the two bodies apart. If the system is in equilibrium the two forces compensate each other. Unlike the gravitational force the centrifugal force is equal at each point of the satellite creating an imbalance at the origin of the tidal forces. Such force therefore depends on time, latitude and longitude creating a bulging on the satellite-planet axis.

Tidal forces implies tidal stresses on the satellites whose distribution and intensity may vary from one satellite to another depending on the physical properties of the materials involved. As a consequence of the tidal deformations the stresses can be stored elastically, relieved through material failure or relaxed away viscously (Wahr et al., 2009). In the case of icy satellites, viscous effects are likely to play an important role in the stress environment of ice layers (Wahr et al., 2009) because the melting point of ice is much lower than the one of silicates. Tidal heating is also an important effect to consider as it can promote the melting of a material and this is expected to have play an important role in the histories of many icy bodies (Wahr et al., 2009). The presence of a subsurface ocean would decouple the icy shell

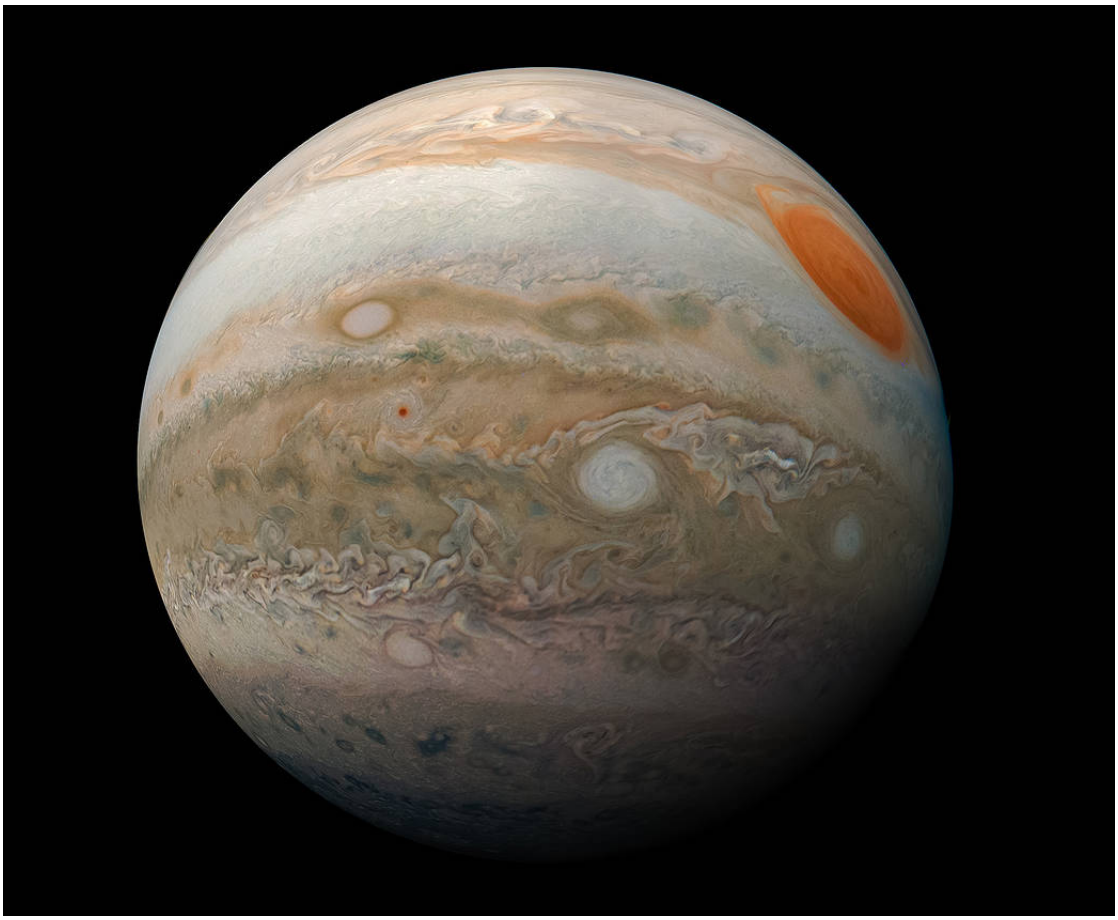

Figure 3.1: Color-enhanced view of Jupiter's Great Red Spot and turbulent southern hemisphere captured by NASA's Juno spacecraft. Credits: NASA/JPL-Caltech/SwRI/MSSS/Kevin M. Gill.

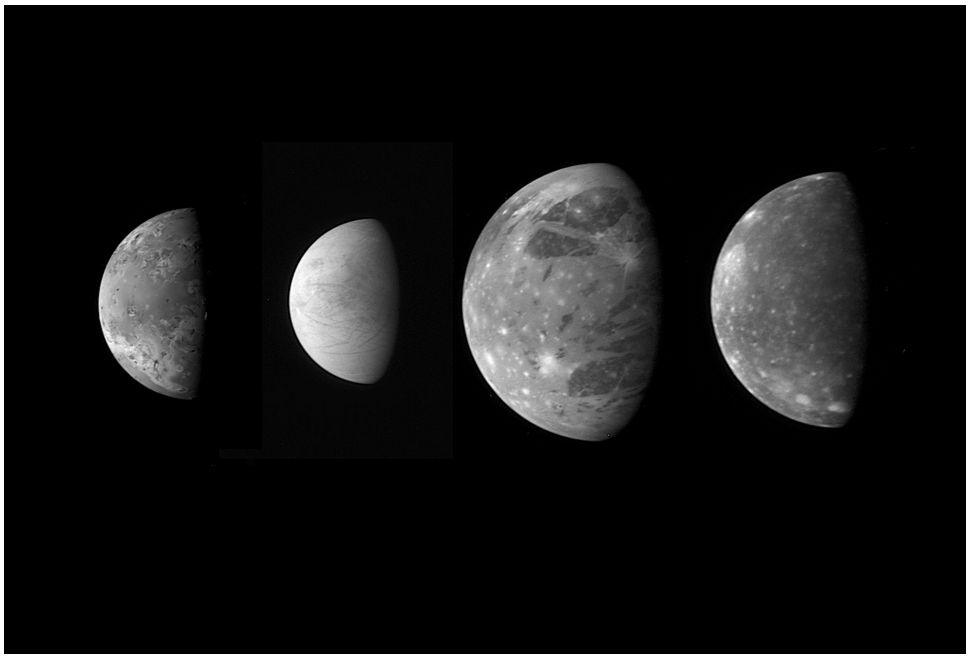

Figure 3.2: The Galilean moons, from left to right: Io, Europa, Ganymede and Callisto. This montage was made with images taken by the Long Range Reconnaissance Imager (LORRI) on the New Horizons spacecraft during its flyby of Jupiter in February 2007 (credits NASA/Johns Hopkins University Applied Physics Laboratory/Southwest Research Institute).

	Io	Europa	Ganymede	Callisto
Mean distance to Jupiter (km)	421,800	671,000	1,070,000	1,883,000
Orbital period (Earth days)	1.769	3.55	7.12	16.69
Mean radius	1821	1561	2631	2410
Density (g.cm^{-3})	3.528	2.989	1.942	1.834
Surface's age (Years)	$1.9-3.6\times10^5$	$\approx 50\times10^6$	$\approx 2\times10^9$	$>4\times10^9$
Magnetic field	Induced	Induced	Internal + Induced	Induced
Surf. Temp. (min/mean/max in K)	90/110/130	50/102/125	70/110/152	80/134/165
Geometric Albedo	0.63	0.68	0.44	0.19

Table 3.1: Principal characteristics of the Galilean moons (from (de Pater and Lissauer, 2014)).

from materials in depth and the amplitude of the deformation induced by tidal forces would be smaller. Since tidal force is less important as the distance with Jupiter increase, the amplitude of tidal heating and the consequences on the internal structure will change from one satellite to another.

3.1.3 The Galilean moons

Jupiter has a total of 79 known natural satellites, 4 of them are embedded within its faint and tenuous rings and the 75 others orbiting further away. The four major satellites closest to the ring system are the Galilean moons named after Galileo Galilei who in 1610 first observed three of the four moons. These satellites are named Io, Europa, Ganymede and Callisto (in order of proximity to Jupiter) and they account for 99.997% of the total mass of all satellites. Although they were formed with the same initial material they evolved very differently as evidenced by their sizes and the state of their surface on fig. 3.2 and are today a fine example of the diversity of processes responsible for the evolution of a planetary body. The main characteristics of the moons are summarized table 3.1.

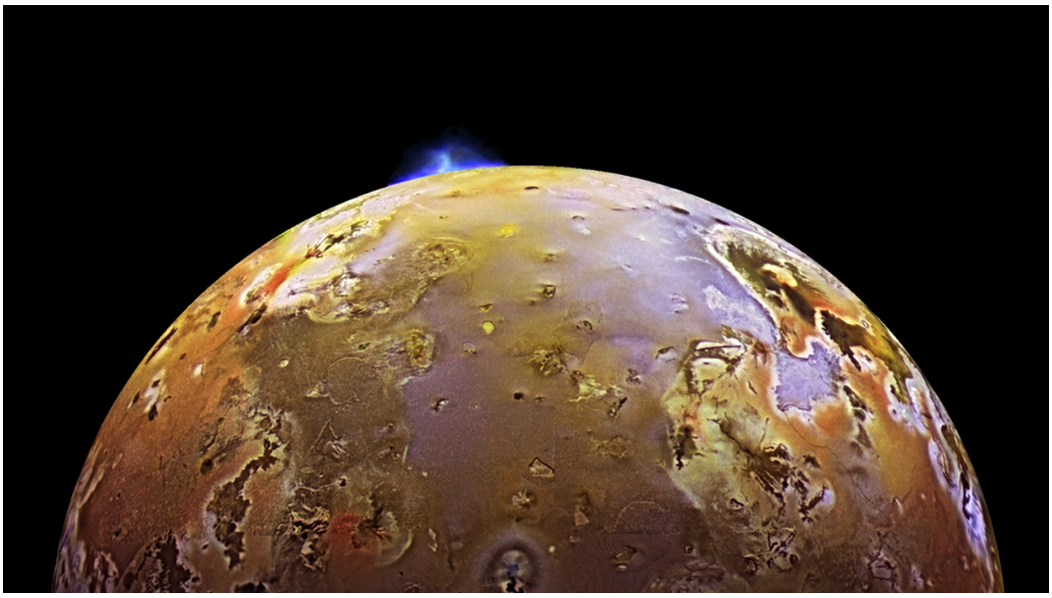

Figure 3.3: Volcanic eruption on Io caught by the NASA's Galileo spacecraft. Credits: NASA/JPL/DLR

3.1.3.1 Io

Io is the closest Galilean moon to Jupiter and the second smallest. It is locked in a $1:2:4$ resonance with Europa and Ganymede, called the Laplace resonance, implying that it finishes 2 rotations around Jupiter when Europa finishes one and finishes 4 rotations around Jupiter when Ganymede finishes one. This resonance prevents the three moons to have circular orbits which maintains strong tidal forces produced by Jupiter. Since Io is the closest these tidal dissipation produces an important internal heat source (Hussmann and Spohn, 2004) that drives continuous volcanic activity at the surface. Such activities mostly imply sulfur compounds that gives Io's surface its characteristic yellowish color (see fig. 3.3). Gases expelled during volcanic activities feed a thin atmosphere continuously stripped by Jupiter's magnetosphere, this phenomenon plays an important role in the Jovian system and will be discussed in section 3.1.4. With a thin atmosphere the surface temperature remains cold enough (see tab. 3.1) so that SO_2 ices condense and occupy a large majority of the surface (McEwen, 1988; Carlson et al., 1997), although unevenly distributed (Douté et al., 2004). Other materials related to volcanism are present including silicates, sulfur and sulfur dioxide (Carlson et al., 1997). This constant renewal of Io's surface explains the fact that no crater was observed making it the youngest surface of the entire Solar System with an estimated age of about $1.9 - 3.6 \times 10^5$ years.

3.1.3.2 The icy Galilean moons

The remaining three moons are called the Icy Galilean moons because their surface is mostly covered by water ice. They represent targets of interest for space agencies and the scientific community because the tidal heating imposed by Jupiter may be responsible for the presence of a global liquid water ocean underneath their surface making them ideal candidates for the search of life in the solar system. In this section some general informations about the three moons will be given on both their surfaces and interiors. Since this work focus on Europa's surface characterization a more exhaustive review of knowledge about the satellite is given in sec. 3.2.

3.1.3.2.1 Europa Europa is the smallest and brightest Galilean moon with a visual geometric albedo of 0.68. The surface is mostly water ice mixed with non-ice materials and is deeply marked by lineaments sometimes reaching several thousands kilometers in length (see fig. 3.4). The very limited number of craters (Moore, 2001) makes it the youngest surface of the three icy Galilean moons with an estimated age

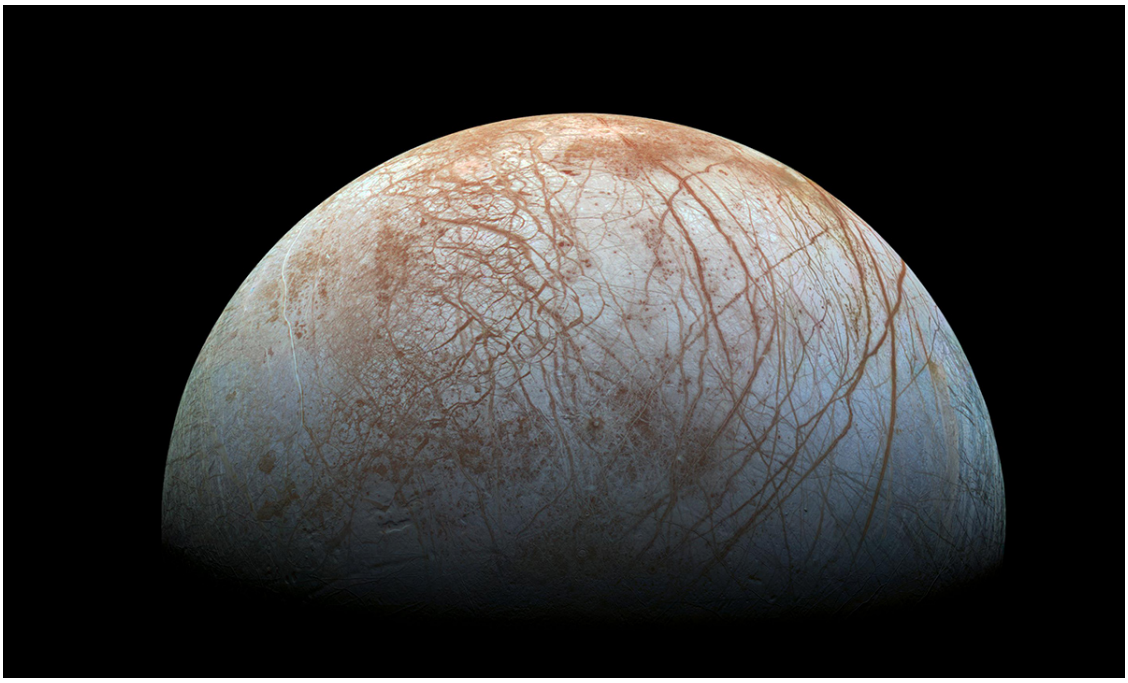

Figure 3.4: Color view of Europa from NASA's Galileo spacecraft. The initial mosaic of images taken through the near-infrared, green and violet filters was reprocessed and assembled into a realistic color view of the surface. The white and blue areas contain mostly pure water ice whereas reddish and brownish areas include more non-ice components. The long, linear ridges and disrupted terrains are correlated with the non-ice materials. The surface is lightly craterised implying active resurfacing processes

of about 50 Myrs (Pappalardo et al., 1999). Europa is tidally locked to Jupiter, meaning that one hemisphere is constantly facing Jupiter, the sub-jovian hemisphere, and one hemisphere constantly opposed to Jupiter, the anti-Jovian hemisphere. Similarly, we distinguish the 'leading' hemisphere which faces the direction of Europa's orbit, in the direction of the velocity vector, and the 'trailing' hemisphere, facing the opposite direction. Europa shows a hemispherical dichotomy as the leading hemisphere appears about 37% brighter than the trailing hemisphere (Spencer, 1987). The reason behind this observation are discussed later in sec. 3.2.

The Galileo mission has revealed much about the internal structure of Europa, first the gravity measurements have shown that the moon is completely differentiated with a solid iron core, a rocky mantle and a water layer of at least 80 km thick (Anderson et al., 1998b). In addition, the magnetometer has monitored the evidence of an induced magnetic field which can be explained by the presence of a conductive layer beneath the surface (Khurana et al., 1998), such as a global liquid salted water ocean. The internal structure of Europa is represented fig. 3.7.

It has been shown that the decay of radioactive isotopes trapped during its accretion cannot generate enough heat to maintain this global ocean in a liquid state until the present time (Reynolds and Cassen, 1979; Cassen et al., 1979). So, another heat source must be invoked to guarantee the stability of the ocean over geological time. Similarly to Io, the tidal forces induced by Jupiter and the Laplace resonance between the moons produce enough tidal heating to maintain the subsurface ocean in a liquid state (Cassen et al., 1979). With a non zero eccentricity of 0.001 the sub-jovian hemisphere slightly vary on the quasi-synchronous orbit producing 'librationnal tide' (Hoppa et al., 1999; Robert T. Pappalardo, 2009; Wahr et al., 2009) that have been linked to the formation of geological features on the surface, such as bands and cycloid ridges (see sec. 3.2). Such tides could also produce enough heating to produce volcanism at the rocky mantle/ocean interface in depth (Robert T. Pappalardo, 2009) and would promote the exchange of materials between the two layers.

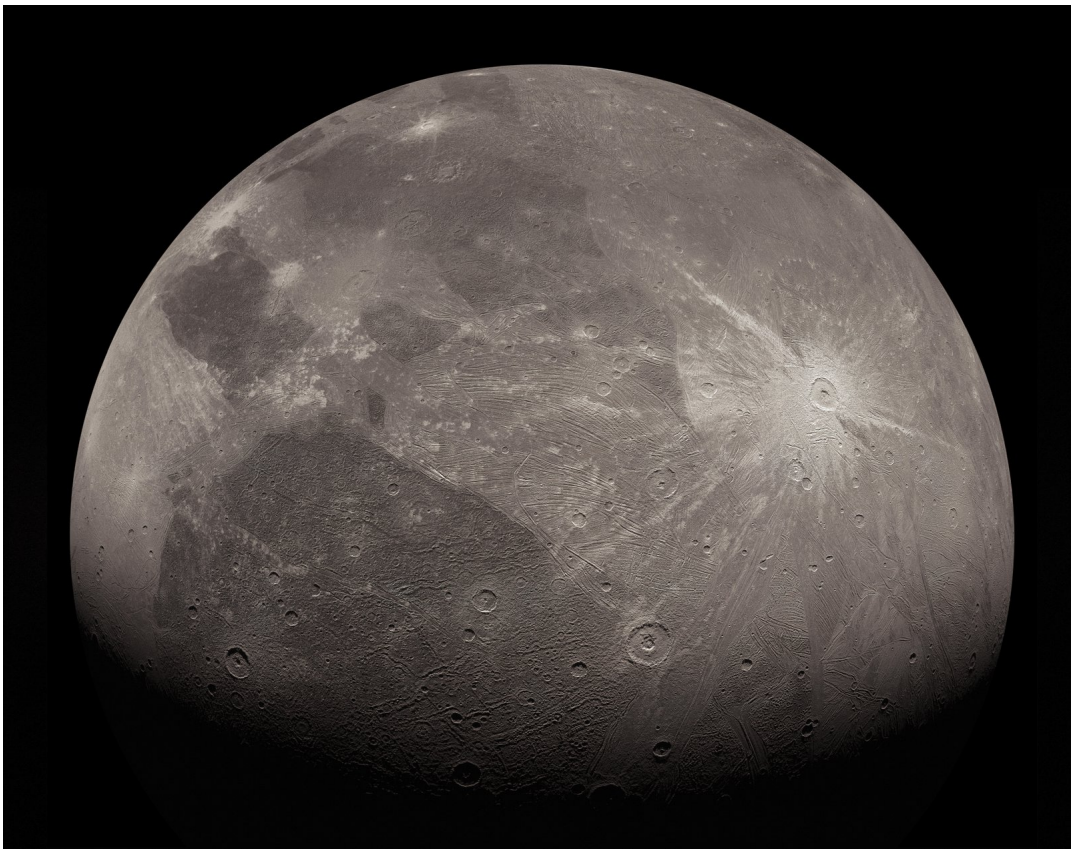

Figure 3.5: Enhanced image of Ganymede obtained by the JunoCam imager aboard NASA's Juno spacecraft. The image highlight the craters, dark and bright terrains and long structural features possibly related to a tectonic activity. Credit: NASA/JPL-Caltech/SwRI/MSSS/Kalleheikki Kannisto © CC BY

3.1.3.2.2 Ganymede Ganymede is the largest and most massive satellite of the entire Solar System and the third of the Galilean moons. Its surface is made of dark regions saturated with craters and brighter younger terrains crossed by ridges and grooves as shown fig. 3.5. Similarly to Europa, Ganymede is tidally locked with Jupiter and some differences between the leading and trailing hemisphere were observed but not as pronounced as on Europa.

Gravity measurements have revealed that Ganymede is entirely differentiated with an iron core, a rocky mantle and an ice shell of about 800 km (Anderson et al., 1996). The core is thought to have temperature exceeding 1300 K (Anderson et al., 1996) which is hot enough to be liquid. The convection of the liquid iron core produces a magnetosphere making Ganymede the only natural satellite to generate its own magnetic field. The interactions between Jupiter's magnetosphere and Ganymede are thought to influence surface features and produce aurorae. Measurements by the Galileo's magnetometer also revealed the presence of induced magnetic field around Ganymede which suggest the presence of a global liquid ocean inside the ice shell (Kivelson et al., 2002). So, the ocean is not in direct contact with the rocky mantle but separated by hundred of kilometers of high-pressure ice which imply that a strong thermal gradient must exist inside Ganymede's ice shell to allow the presence of a liquid layer. The phases of ice would change as the depth increase to accommodate the temperature-pressure variations and could also change with salt concentrations. The internal structure of Ganymede is shown fig. 3.7.

3.1.3.2.3 Callisto Callisto is the furthest and the second-largest Galilean moon. Due to its important distance with Jupiter, it does not participate in the resonance in which the three inner Galilean satellites are locked. The surface shows no sign of internal activity and is heavily cratered as evidenced fig. 3.6. From the crater distribution the age fo the surface was estimated between 3.9 and 4.3 Gyrs making it the oldest of the Solar System.

Figure 3.6: Global color image of Callisto obtained by NASA's Galileo spacecraft. The surface is uniformly cratered (bright spots) among dark terrains testifying a long history of impacts which have profoundly modified its surface from ice-rich areas to highly eroded, ice-poor materials. Credit: NASA/JPL/DLR

Gravity measurements have shown that Callisto was partially differentiated (Anderson et al., 1998a) with two possible scenarios: a differentiated rock-metal core and an outer layer of ice or the whole interior is an inhomogeneous mixture of rock and ice (Anderson et al., 1998a). The magnetometer on board Galileo also revealed the presence of an induced magnetic field suggesting that a conductive layer in depth is present, similarly to Europa and Ganymede, such as a global water ocean (Khurana et al., 1998). The internal structure of Callisto is shown fig. 3.7.

3.1.4 The magnetosphere

Convection in the deep layer of liquid metallic hydrogen in Jupiter's internal structure creates a massive magnetic field in the Jovian system. The resulting magnetosphere strongly affects any object orbiting Jupiter, especially the nearest bodies. It can be divided into three parts: the inner, middle and outer magnetosphere. In the inner magnetosphere are the inner small satellites (Metis, Adrastea, Amalthea and Thebe) and most of the ring system. In the middle magnetosphere are the Galilean moons and especially Io who plays a major role in the Jovian system through its interaction with the magnetosphere. Being the most active body of the entire Solar System Io continuously emits huge amounts of sulfur dioxide through volcanic events. Most of the eruption products are dissociated and ionized by electron impacts from the magnetosphere of Jupiter producing ions of sulfur and oxygen (Cooper, 2001). This result

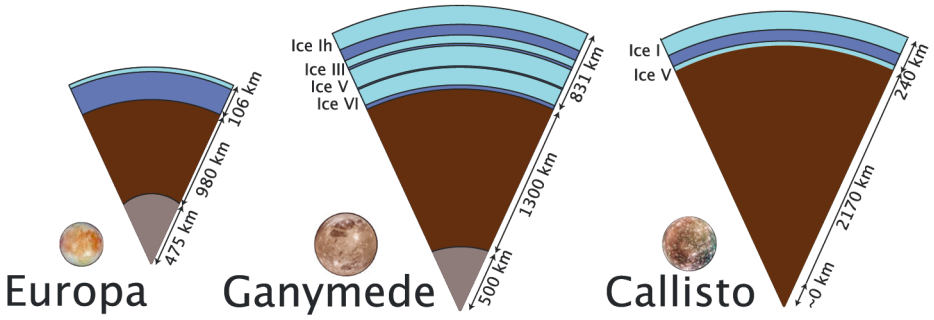

Figure 3.7: Interior structures of Europa, Ganymede and Callisto (from (Vance et al., 2018))

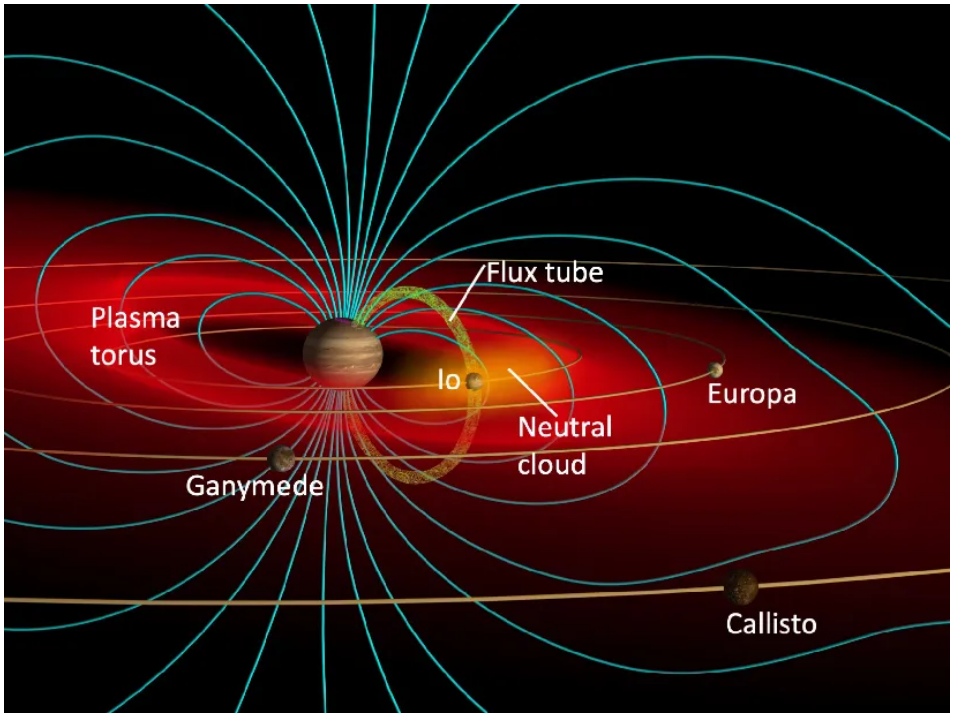

Figure 3.8: Illustration of Jupiter's magnetosphere showing the magnetic field lines, Io plasma torus and the three icy Galilean moons. Credit: John Spencer, Southwest Research Institute

in a 'plasma torus' of charged particles encircling Jupiter along the orbit of Io (see fig. 3.1.4). While this plasma torus has little influence in the outer magnetosphere, it strongly affects the moons orbiting close to Io in the middle magnetosphere. It has been shown that the charged particles strongly affect the surface composition of the icy Galilean satellites, especially Europa and Ganymede for which they are preferentially implemented in the trailing hemisphere and is thought to be responsible of the terrain's darkening producing the observed hemispherical dichotomy of the reflectance. This continuous bombardment of energetic particles causes radiolysis (Carlson et al., 1999b)of water ice and other chemical compounds present at the surface, it breaks water into oxygen and hydrogen which in turns can form complex chemistry.

3.2 The surface of Europa

Europa's surface shows sign of activity in the icy crust that can be related to either internal or external processes. With a silicated mantle in direct contact with a subsurface ocean protected by a thick ice shell and an internal source of heating provided by the strong tidal forces from Jupiter, Europa holds the minimum requirements for the emergence of life: stable liquid water, building blocks of organic

material (C, H, N, O, P, S) and a source of energy. For these reasons, Europa was quickly a priority candidate for space exploration, from Earth-based telescopic observation to dedicated space missions, bringing more and more informations on the moon's habitability potential. In this section, we review the major knowledge we have of the state of the surface which will then allow to highlight the outstanding questions remaining, some of which will constitute the objectives of this work. We go through the main geological and geomorphological features observed on the surface to the chemistry responsible for its composition. We will end by describing the processes potentially occurring at the surface and their link with the chemical composition of the surface.

3.2.1 Geomorphology

Surface features were first mapped and described by (Lucchita and Soderblom, 1982) using Voyager images. They show that Europa has little topographic relief with a variety of smooth and textured terrains of different spectral properties (Greeley et al., 1998). We distinguish the plains, generally brighter and relatively smooth, transected by linear features (Greeley et al., 2000) from the mottled terrains characterized by low albedo and large-scale roughness with pits and hummocky topography (Lucchita and Soderblom, 1982). Then, the Galileo images provided extensive knowledge with higher resolution images up to a few meters per pixel (Belton and Team, 2000) allowing to decipher more complex structures. Below we describe the main geologic and geomorphologic features as classified by (Greeley et al., 2000).

3.2.1.1 Ridges and Bands

Ridges are the moon's most ubiquitous landforms (Greeley et al., 2000) and can come in different morphological shapes on very varied spatial extensions, from the simple isolated troughs of few hundred meters to complex ridges with a series of subparallel features of few hundred kilometers (Greeley et al., 2000) (see fig. 3.9). Some areas are filled with overlapping ridges and were named 'ridged plains' and occupy a large part of the surface (see fig 3.14). The most common form is the double ridges pair with a medial trough whose width can reach up to 2 km (Greeley et al., 2000). An evolutionary transition from isolated troughs, to double and triple ridges, to complex ridges (or dilatation bands) has been suggested (Pappalardo et al., 1998b; Greeley et al., 1998; Head and Pappalardo, 1999) to explain this diversity as shown fig. 3.10. Some ridges which have cycloidal appearance that has been interpreted as the consequences of the application of a periodic force whose direction varies over time (Greeley et al., 1998; Hoppa et al., 1999; Wahr et al., 2009) which coincides with the action of tidal forces by Jupiter.

The evidence of old ridges interspersed by younger ridges, strike-slip motion along pre-existing double ridge and pull-apart band margins have suggested a potential plate-like tectonics occurring within the icy shell. The processes behind the ridges formation is still debated and probably regroup several complex mechanisms most of which involve a connection with the subsurface ocean. Among the proposed mechanisms are the tidal pumping (Greenberg et al., 1998) in which double ridges are made by successive opening and closing of a crack following the diurnal tide cycles. Ridges could also be compressional structures (Sullivan et al., 1998) allowing liquid water to rise from depth. Linear diapirism (Head and Pappalardo, 1999) has been proposed suggesting that double ridges are made in response to cracking and diapiric rise of warm ice. Another mechanism is the shear heating (Gaidos and Nimmo, 2000) induced by diurnal tides generating heating in the sub-surface, which can partially melt the ice and create ridges and troughs. More recent work invoke the propagation of shallow water sills (Craft et al., 2016; Culberg et al., 2022) that could be frequently filled by the ocean.

3.2.1.2 Chaos

Chaos were defined as large areas where the surface is split into different pieces of varying size, separated from each other by a relatively smooth matrix and often of lower topography (Greeley et al., 2000) (see Fig. 3.11). The blocks generally come from pre-existing ridged plains that have shifted within a matrix of hummocky materials (Carr et al., 1998). Two types of chaos are distinguished (Greeley et al., 2000),

Figure 3.9: Colorized image of Europa from the NASA's Galileo spacecraft combining clear-filter gray-scale data from one orbit and a low-resolution color data taken on a different orbit. The image shows various morphologies and sizes of fractures, ridges and reddish bands. The blue-white terrains are supposed to be mostly pure water ice and the reddish areas are water ice mixed with non-ice materials. Credit: NASA/JPL-Caltech/SETI Institute .

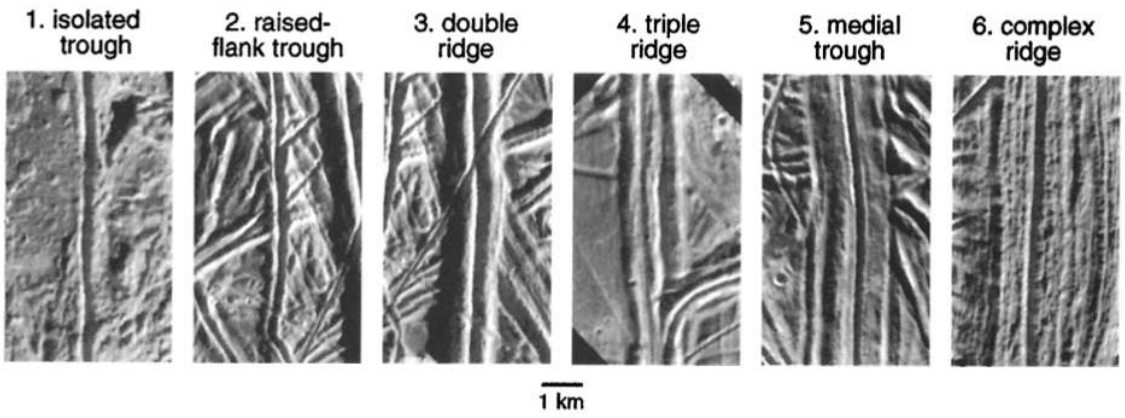

Figure 3.10: A classification scheme of Europan ridges and troughs (from (Head and Pappalardo, 1999), after (Pappalardo et al., 1998b)).

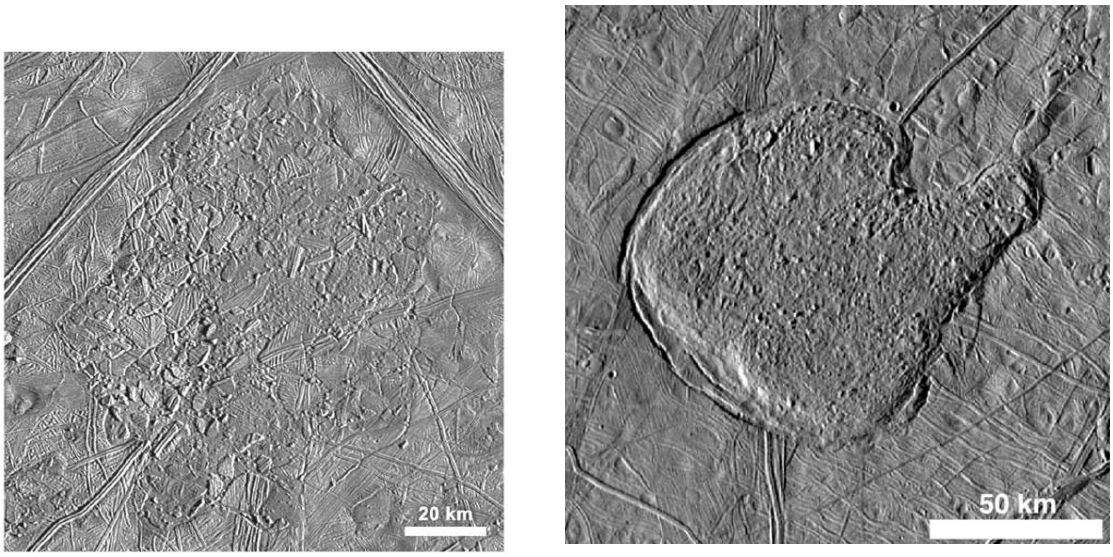

Figure 3.11: Two examples of chaotic terrains. (left): 'Platy chaos' of the Conamara chaos region, previous ridged terrains constitutes the blocks of the chaos in a relatively smooth matrix. (image mosaic made by (Collins et al., 2000)). (right): High resolution image (about 230m per pixel) showing the 'knobby chaos' called Murias Chaos (from (Fagents, 2003)).

the 'platy chaos' in which entire blocks of the pre-existing surface have been shifted from their original position but are still recognisable as opposed to 'knobby chaos' in which fragments of the old surface cannot be correctly identified. The establishment of these morphologies can be explained by several mechanisms. It was first proposed that plumes of warm ice could rise by diapirism (Greenberg, 1999) or it could be related to percolation phase transition, brine mobilisation and migration from a liquid water reservoir in depth (Head and Pappalardo, 1999). Recent mechanical modelling proposes that a reservoir freezing could be at the origin of small chaos (Lesage et al., 2020, 2022). If so, chaos would be area of amplified heat flow that would promote local melting (Carr et al., 1998) even close to the surface, or that brines are admixed in the crust of Europa and lower the eutectic temperature of the ice.

3.2.1.3 Lenticulae

Lenticulae designates domes, pits and spots (see fig. 3.12) with a vertical extension up to a few hundred meters (Greeley et al., 2000) often associated to chaos and smooth dark plains. These morphologies generally have a lobed shape with a diameter of about 10 km (Pappalardo et al., 1998,b) and could be consistent with a diapiric origin through the solid-state convection of Europa's icy shell (Rathbun et al., 1998) or small members of a continuous size distribution of chaos areas (Greenberg, 1999). Recent work have also proposed reservoir of subsurface liquid water that would create a depression if the underlying lithosphere is thin enough, a bulge would appear when the water freezes (Manga and Michaut, 2017). The close proximity with chaos suggest similar formational processes for lenticulae and must therefore involve a heat source in depth to either promote the rise of plume or the melting of the ice.

3.2.1.4 Crater

Europa shows a limited number of craters with only 16 complex craters identified (Moore, 2001) implying a relatively young age of the surface and therefore that there are active processes at the origin of resurfacing. Although the surface is lightly cratered, the observed impact shows a variety of morphologies and a wide range of sizes (Moore, 2001). Crater morphology is strongly influenced by the target's material properties and near-surface structure (Moore, 2001) and reveal much on the subsurface physical properties. The Solid State Imager (SSI) on board Galileo spacecraft has revealed much information

Figure 3.12: Round, reddish spots known as ‘Lenticulae’ each about 10 km across captured by NASA’s Galileo spacecraft. This enhanced colour image was obtained from the combination of a clear-filter grayscale data from one orbit and a low-resolution color data taken on a different orbit. Credit: NASA / JPL / University of Arizona / University of Colorado.

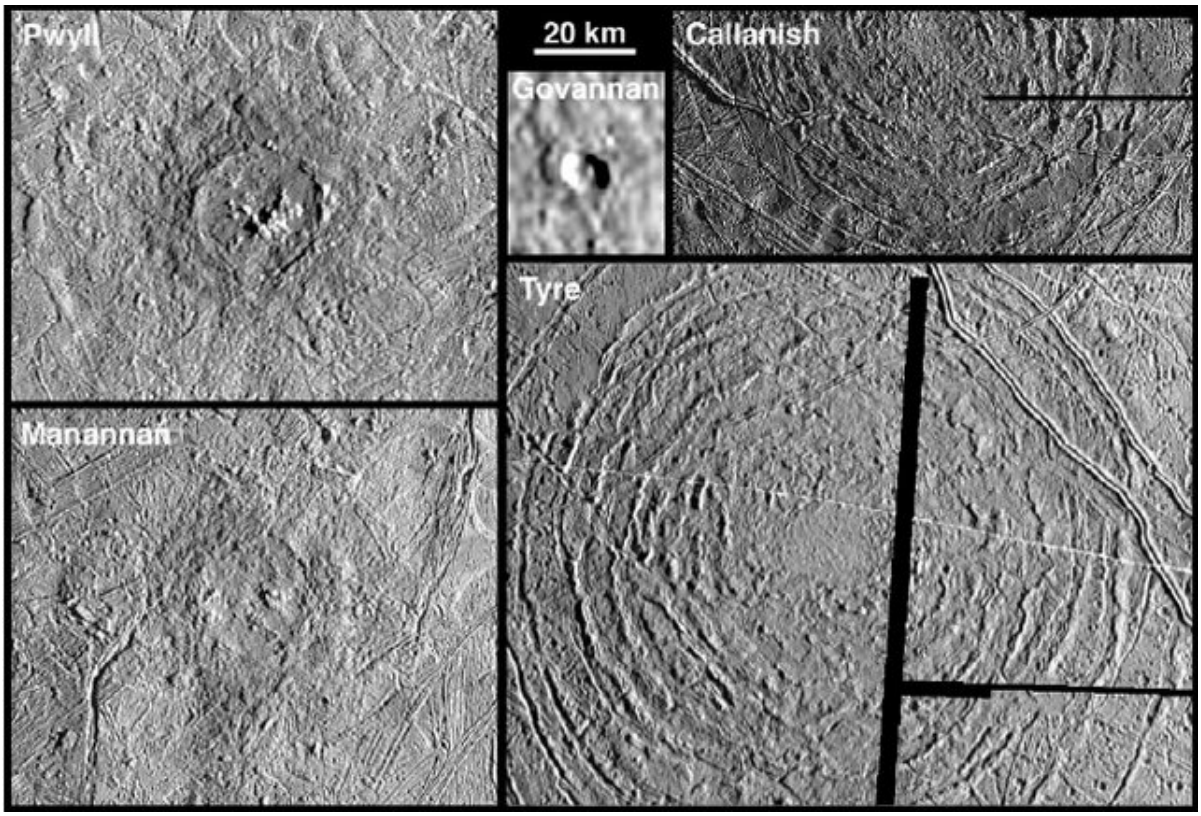

Figure 3.13: Europa's largest impact craters Pwyll and Manannan and the multi-ring structures Callanish and Tyre. (from (Pappalardo, 2010)).

on the icy shell. For instance, large diameter craters such as Pwyll (26 km) and Manannan (23 km) shown fig. 3.13 had transient crater depth between 3 and 6 km implying a transported material to the surface from a depth not greater than 2 km (Moore, 2001). Some europan craters such as Pwyll have dark and red materials observed around them, in the form of ejecta, suggesting that the source of such dark materials is within a few kilometers of the surface. Also, the small depth-to-diameter ratio of Pwyll indicate an isostasic adjustment of large-scale topography (Moore, 2001) which is favoured by a warm ice at depth. Other morphologies such as the Tyre and Callanish craters (see fig. 3.13) show radially arrayed chains of pits interpreted as secondary craters surrounding the feature. This morphology could be the consequence of impact into target materials mechanically weak at depth (Moore, 2001) such as a low viscosity substrate. They also note that one cannot distinguish between the presence of a purely liquid layer or brine-rich zone associated with convecting ice (Moore, 2001).

3.2.1.5 Dark deposits

Low albedo deposits are frequently observed closed to ridges and lenticulae (see fig. 3.23a). It has been shown that such deposits only appear around complex ridges and never around simple cracks or troughs (Geissler et al., 1998). They also showed that there older ridges have higher concentrations of dark deposits implying active processes at their origins. Two mechanisms were invoked to explain these deposits (Greeley et al., 1998), it could be the effusion of liquid coming from shallow reservoirs or by an explosive eruption of gases and materials of the icy shell, similar to a geyser. Works from (Quick et al., 2013) have shown that steam plume are possible and could explain the shape and distribution of these deposits as long as the height of the plume remains below 7 km.

3.2.1.6 Smooth Plains

Smooth plains are large areas on which no particular structures are identified, a low macroscopic roughness and generally have a lower albedo than the surrounding terrains (Greeley et al., 2000). They are often associated with ridges as they seem to be delimited by the topographically high structures and fill the topographic hollows (see fig. 3.23c). Mechanisms invoked to explain these morphologies involve the flows of low-viscosity ice (or liquid) on the surface or the local melting of very shall reservoirs (Greeley et al., 2000). The emitted volume has been estimated, enabling a more precise discussion of the formation mechanism (Lesage et al., 2021)

3.2.1.7 Global Geological map

The initial classification of morphological features on Europa by (Lucchita and Soderblom, 1982) defined five primary material units and terrains: plains materials, mottled terrains, craters, band material and 'spots and bands'. From then, complex structures have been identified and the classification has been developed, and will continue to evolve over time thanks to data from future space missions. The morphologies described above are just few examples illustrating the main features identified on the surface, but each of these features can present very complex diversities which reflect the combination of several processes that can vary from one location to another. Higher resolution imageries will surely unveil more morphologies. A recent global geologic map of Europa with the main geomorphological features described above was presented by (Leonard et al., 2018) and is shown fig. 3.14. The map clearly highlights the dominant features on Europa's surface: ridged plains, chaos and lineaments.

3.2.2 Surface composition

Our understanding of the surface composition of Europa was mostly brought by the use of ultraviolet, visible and near-infrared spectroscopy and is constantly evolving. The re-analysis of old data using more realistic models as well as the comparison between the data and spectra of analogous species produced in laboratory under europan conditions brought new evidence of the presence of chemical species on the surface. The surface composition is one of the microphysical property investigated in this work, it is therefore important to make a detailed review of the work already carried out in this topic. Below is a synthesis of the chemical species which have been revealed so far. Suspected processes causing their presence will be given but will be further detailed in the dedicated section (see sec. 3.2.5).

3.2.2.1 Water ice

Water ice has quickly been identified by ground-based spectroscopy (Kuiper, 1957; Harris, 1961) because the similarity between spectra of Europa and those of pure water ice was remarkable, especially when comparing the position and shape of the characteristics absorption bands. A small distortion of the bands were observed, especially for spectra of the trailing side, involving a potential 'non ice' component. This was first reported by (Clark, 1980) but the suspected compounds were not identified. Since, water ice has been constantly identified by many studies involving different instrument(Calvin et al., 1995; Carlson et al., 2005; Ligier et al., 2016; Mishra et al., 2021a; King et al., 2022) so that the presence of water ice is no longer discussed. Nevertheless, questions concerning its texture (crystalline or amorphous), its grain size and volume proportion are still investigated. The first two properties are discussed in sec. 3.2.3. Concerning the volume proportion, some recent work by (Ligier et al., 2016) and (King et al., 2022) using spectral fitting analysis in a linear mixture model of various chemical species and different instruments have started to highlight the distribution of water ice across the surface (see fig 3.15). (Ligier et al., 2016) used observation from the near-infrared SINFONI instrument on the Very Large Telescope (VLT) and a spectral ratio to highlight a dichotomy between the trailing and leading hemisphere. The first show a decrease in the water ice content correlated with the darkening of the surface while the later shows an enrichment of the water ice content. Similarly, (King et al., 2022) produced compositional map of Europa using the near-infrared SPHERE instrument on the VLT using a simplified radiative transfer and

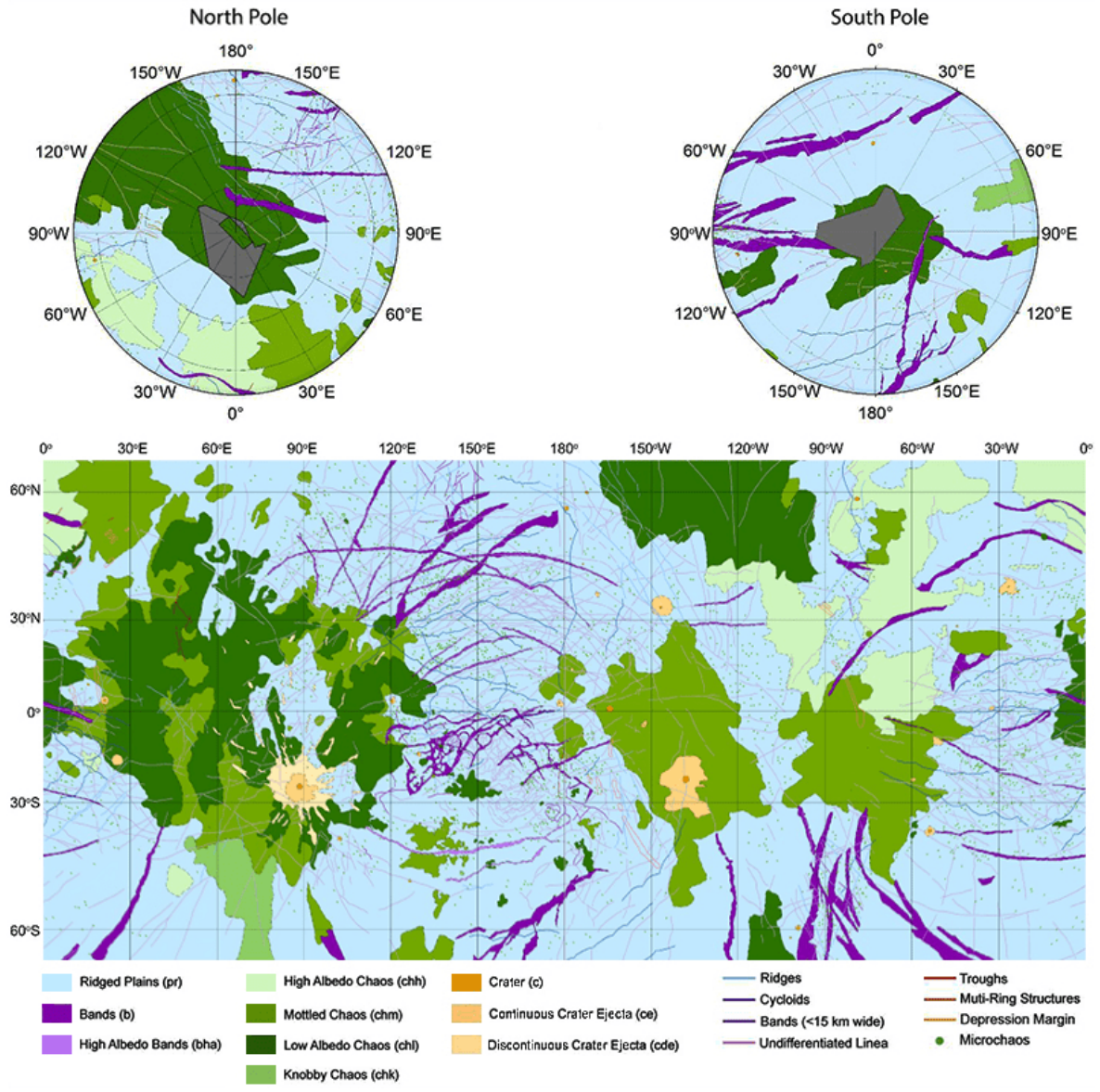

Figure 3.14: Global geologic map of Europa showing the main morphological features. (from (Leonard et al., 2018; Wendel, 2017), Credit:NASA/Erin Leonard, Alex Patthoff, and Dave Senske, build on work by Ron Greeley, Thomas Doggett and Melissa Bunte)

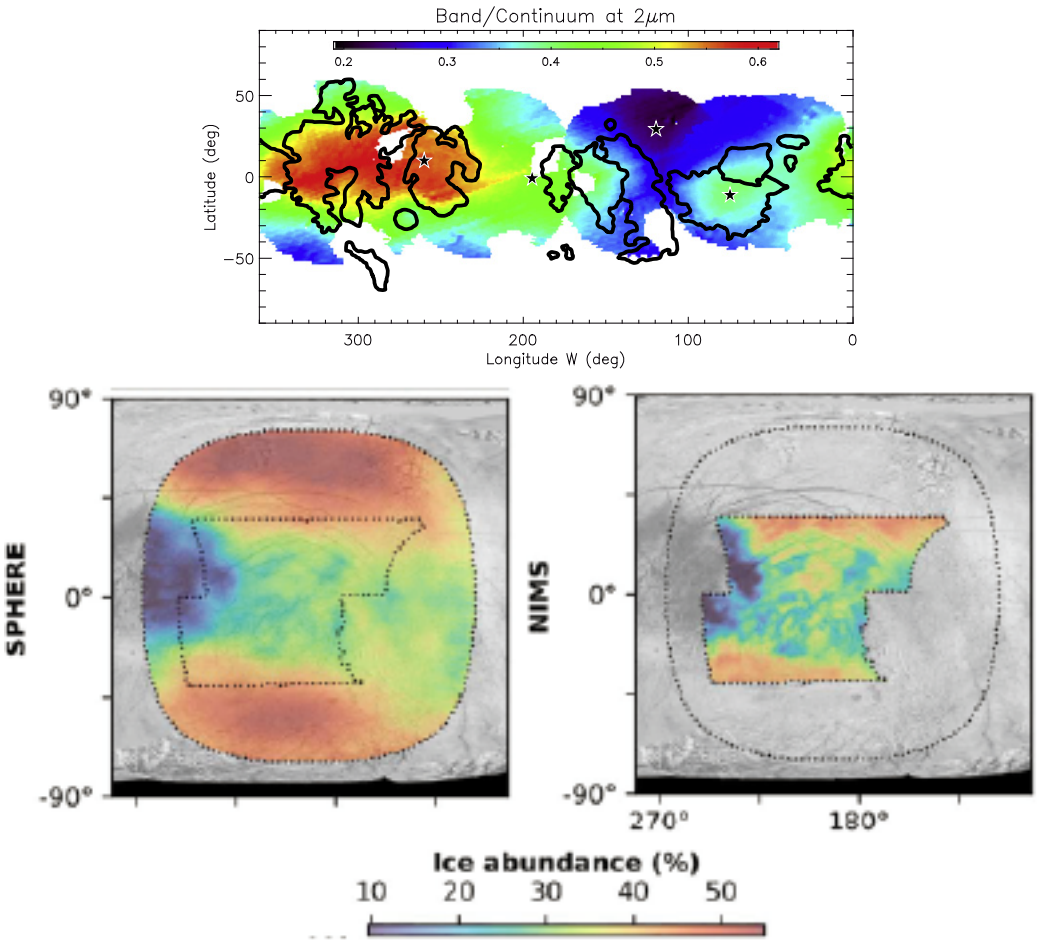

Figure 3.15: Distribution of water ice across the surface of Europa. (Top): water ice distribution from the band/continuum ratio at 2 μm from (Ligier et al., 2016). A lower ratio indicate a higher proportion of water ice (in blue). The map is displayed in equirectangular projection with longitude increase westward. The trailing hemisphere is between 360 and 180 degrees and the leading hemisphere is between 180 and 0 degrees. (Bottom): Water ice volume proportion derived by (King et al., 2022) using the SPHERE and NIMS instrument. The map shows a transition between the trailing and the leading hemisphere highlighting a significative increase of water ice content toward the leading side and the poles.

a Monte Carlo approach. The spatial coverage was limited to a small part of Europa and covered most of the leading and trailing part of the Anti-Jovian hemisphere. They were able to compare their results by performing the same approach with an hyperspectral image of the Galileo/NIMS instrument. Results are consistent with (Ligier et al., 2016) showing a lower proportion of water ice as one approaches the darker trailing hemisphere. They also show a significative increase in water ice toward the poles.

3.2.2.2 Hydrated compounds

Reflectance spectra from the Cooled Grating Array Spectrometer (CGAS) of the NASA Infrared Telescope Facility (IRTF) have clearly identified weak apparent features in the trailing side that do not appear in laboratory spectrum of water ice. Works from (Brown et al., 1988) have highlighted similarities between Europa and solid hydrates and free ice of methane, ammonia and carbon monoxide, leading the way through the search of volatiles on Europa and other icy satellites. With the Galileo/NIMS instrument, the scientific community had access to a greater number of data, at higher spatial resolution, and the highly distorted water absorption bands has been further studied. Two main candidates have been proposed: hydrated salts and hydrated sulfuric acid.

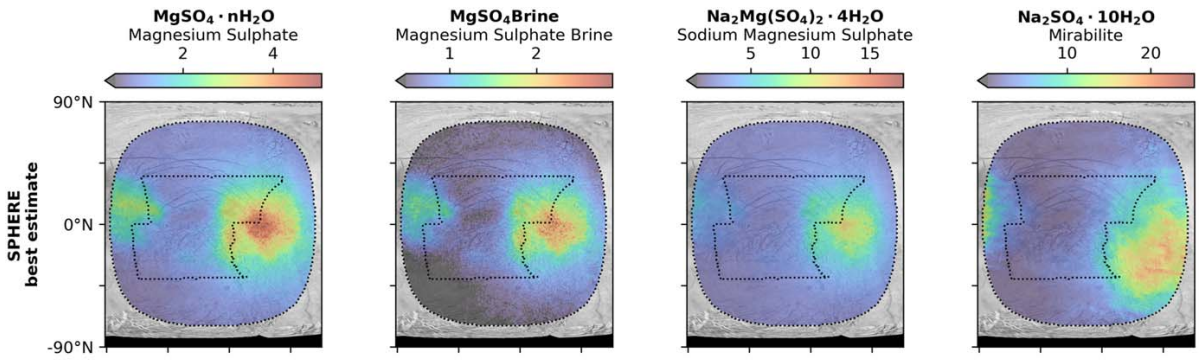

Figure 3.16: Spatial distribution of hydrated sulfate salts (best-estimate abundances, median of the posterior distribution) from (King et al., 2022).

A study by (McCord et al., 1998) has shown that among the hydrated minerals that have been suggested to exist on the surface of icy Galilean satellites, hydrated salts such as magnesium, sodium-magnesium and possible sodium-carbonate sulfates are good candidates. They notice that the H_2O molecule must be strongly active spectrally and closely bound to the host molecule, in numerous slightly different bonding configurations, to explain the strong and multiple distorting effects the host electric potential has on the energy of the absorption bands (McCord et al., 1998). This implies a heavy hydration of the compound involved. Thus, the suspected compound could be in the form of [$MgSO_4$. nH_2O] or [$NaMgSO_4$. nH_2O] or [Na_2SO_4. nH_2O] with n indicating the hydration state. The work by (Dalton, 2007) showed a spectral comparison between some heavily hydrated sulfur-bearing salts obtained in laboratory under europan conditions of pressure and temperature and some NIMS observation of dark terrains. Even though spectra of Hexahydrite ($MgSO_4$. $6H_2O$), Epsomite ($MgSO_4$. $7H_2O$), Bloedite (Na_2MgSO_4. $4H_2O$), Mirabilite (Na_2SO_4. $10H_2O$) seems more appropriate to reproduce dark terrains of Europa than lower hydration states salts they notice that none of these compounds alone were able to account for all the observed spectral features. They added that these hydrated salts appear white in colours while the dark surface takes on a reddish cooler which seems to indicate that no single surface material are expected but rather a mixture of hydrated sulfates with other materials (Dalton, 2007). Using the low temperature optical constants of Hexahydrite, Epsomite, Bloedite and Mirabilite measured in laboratory by (Dalton and Pitman, 2012), a spectral fitting analysis by (King et al., 2022) using a linear mixture model and a MCMC modelling has shown a good adjustment of both the SPHERE and NIMS spectra, the spatial distribution of the estimated volume proportion is shown fig. 3.16. Salts appear correlated with dark terrains and Mirabilite seem the more abundant in the leading hemisphere. They also note that the lower bounds on the abundances of magnesium sulfates are very low and close to zero suggesting that uncertainties and degeneracies between the salt spectra make it not possible to identify any individual magnesium sulfate salts (King et al., 2022). A recent study by (Comodi et al., 2021) showed that the distinction between hydrated sulfates compounds may be tricky because characteristic spectral features are mostly over 4 μm while the usually investigated spectral range goes from 0.8 to 2.5 μm where spectra are dominated by water absorption bands. The origin and processes behind the presence of hydrated sulfates at the surface of Europa are discussed in sec. 3.2.5.

In 1999, Carlson et al. (Carlson et al., 1999b) show that laboratory spectra of frozen sulfuric acid (H_2SO_4) hydrates could also explain some of the spectral features identified in the dark regions of Europa. Its presence would be related to the radiolytic sulfur cycle which will be amply described in sec. 3.2.5. They found that spectrum of sulfuric acid octahydrate ($H_2SO_4.8H_2O$) provides the best match of all sulfuric acid with different hydration levels. Further evidence of sulfuric acid was made by (Carlson et al., 2005) using the measured optical constant of sulfuric acid octahydrate (SAO) and a simple two-component radiative transfer modelling of SAO and water ice to fit Europa's spectra obtained by NIMS. The obtained map is shown fig. 3.17 and shows a strong trailing-hemisphere enhancement with a maximum volume abundance of 90%. Recent works by (Ligier et al., 2016), (Mishra et al., 2021a) and (King

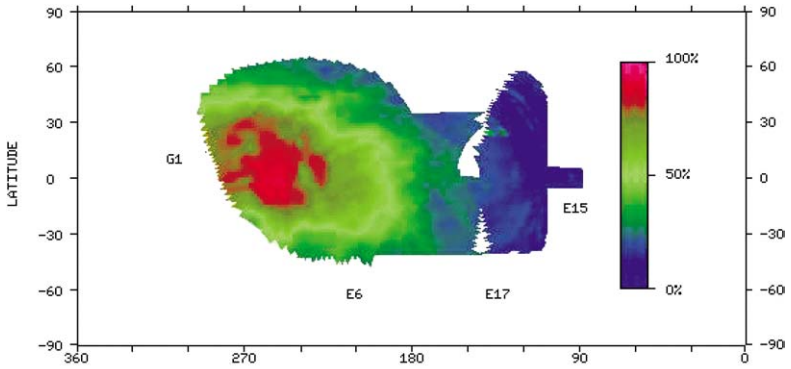

Figure 3.17: Distribution of hydrated sulfuric acid made with Galileo NIMS data from observation made during the G1, E6, E15 and E17 orbits (from (Carlson et al., 2005)). The strong dichotomy between the trailing and leading hemisphere is visible with a volume abundance going from 90% to almost 0%.

et al., 2022) have all included the SAO in their spectral fitting analysis and all show a significant detection of SAO as well as a positive spatial correlation with the dark terrains of the trailing-side. (Mishra et al., 2021a) find volume abundance between 70% and 99% on three spectra of the trailing hemisphere by considering only 3 components (crystalline and amorphous water ice and SAO) while (Ligier et al., 2016) and (King et al., 2022) find abundances up to 70% with much more compounds included in the fitting procedure. These differences can be explained by the choice of the method and the number of compounds included, it is nevertheless clear that SAO is an important compound to consider when studying Europa's surface.

3.2.2.3 Chlorinated compounds

Chlorinated compounds have quickly been suggested at the surface of Europa as they would translate an exchange between the salty sub-surface ocean and the surface. NIMS spectra of the leading hemisphere also show distortion of the water ice absorption bands but not as pronounced as for the trailing-side. An analysis of salts and radiation products on the surface of Europa by (Brown and Hand, 2013) recognised the potential detection of magnesium sulfate salts on the trailing side but they disagree on the interpretation of its origin. While many studies thought that magnesium sulfate salts reflect the composition of the sub-surface ocean and icy shell, they suggest that magnesium sulfate salts are initially brought to the surface as magnesium chloride and are irradiated and transformed into magnesium sulfate after, explaining the correlation with the distribution of SAO and the trailing-side enrichment. Given the relative abundance of sodium, potassium and magnesium they predict that the leading-hemisphere should contain the spectra signature of NaCl, KCl and $MgCl_2$ salts. Similarly to hydrated sulfates, any chlorine salts are expected to be present in a highly hydrated form(Hanley et al., 2014), considering the abundance of water and the low surface temperature. Using reflectance spectra of magnesium chlorate ($Mg(ClO_3)_2.\ 6H_2O$), magnesium perchlorate ($Mg(ClO_4)_2.\ 6H_2O$), Magnesium chloride ($MgCl_2.\ nH_2O$ with $n = 2, 4, 6$), Sodium perchlorate ($Na(ClO_4)_2.\ 2H_2O$) salts measured by (Hanley et al., 2014) under europan conditions, (Ligier et al., 2016) showed that Mg-bearing chlorinated species provided improved spectral fits than magnesium sulfate salts. They also showed a correlation with large-scale geomorphologic units such as chaos and darker areas, favouring an endogenous origin. Recently, (King et al., 2022) showed that chlorine-bearing salts, especially magnesium chloride, seem correlated with geological units such as linae and darker areas, in agreement with (Ligier et al., 2016). Non-zero abundances on the leading-side were also estimated by both studies, favouring a complex chemical mixture rather than a single material. A recent study by (Trumbo et al., 2020) using the ultraviolet Space Telescope Imaging Spectrograph (STIS) of the Hubble Space Telescope (HST) showed a broad absorption near 450nm exclusively located on the leading hemisphere and correlated with chaos terrain. This spectral feature is consistent with the F-bands of irradiated sodium chloride (NaCl) and the spatial correlation (see fig. 3.18) would suggest an

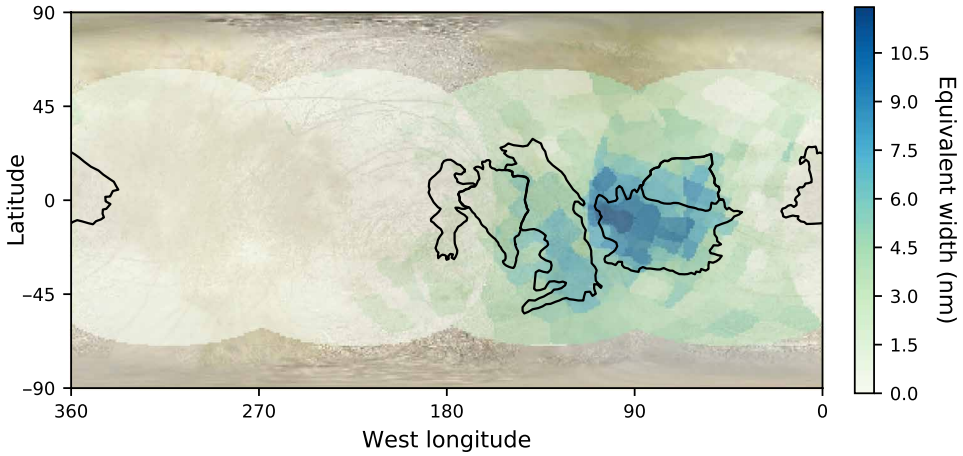

Figure 3.18: Map of the strength of the 450nm absorption suggesting relative enrichment of sodium chloride (from (Trumbo et al., 2020)). Black outlines correspond to large-scale chaos regions. The spatial resolution of the mapped data is about 150km at the sub-observer point. Background image credit: NASA/JPL/Björn Jonsson/Steve Albers.

endogenic origin. Using the Infrared Camera and Spectrograph (IRCS) and adaptive optics on the Subaru telescope, (Tan et al., 2022) investigated the upper limits to the abundances of hydrated Cl-bearing salts. They estimated conservative upper limits of about 10% and up to 17% for Magnesium chloride salts at the 3σ noise levels, which is lower than the abundances retrieved by (Ligier et al., 2016) with values above 20% relative to water ice. Abundance must be interpreted with caution since all those studies used simplified linear mixture. Even though they found no clear absorption features due to hydrated chlorine salts, they suggest that anhydrous Cl-bearing salts (NaCl and $NaClO_4$) or hydrated NaCl would be the major salts if non-ice materials are Cl-bearing salts (Tan et al., 2022).

3.2.2.4 Oxidants

The subsurface ocean in direct contact with the rocky mantle could be an important source of reductants through hydrothermal processes, but as (Trumbo et al., 2019) stated 'the potential habitability of Europa's ocean will likely depend on a complementary supply of oxidants'. Main oxidants that have been detected so far are hydrogen peroxide, dioxygen, carbon dioxide and sulfur dioxide.

Hydrogen peroxide (H_2O_2) was suggested by (Carlson et al., 1999a) to explain spectral features at 3.50 μm in NIMS observation of the leading anti-jovian quadrant. Comparison with laboratory measurements indicate a concentration of about 13% by number, relative to water ice. They proposed that hydrogen peroxide is formed by energetic plasma irradiation of Europa's surface (see sec. 3.2.5). Observation by the Near InfraRed Spectrograph (NIRSPEC) on the Keck II telescope of hemispherical differences of the L-band ($3.16-4$ μm) absorption strength (Hand and Brown, 2013) confirmed previous results on the leading hemisphere and added that almost no hydrogen peroxide was detected during observation of just the trailing hemisphere. Recent work by (Trumbo et al., 2019) using the same instrument as (Hand and Brown, 2013) and adaptive optics system have provided first map of the hydrogen peroxide distribution. The strength of the absorption was mapped at a spatial resolution of about 300km (see fig. 3.19). Results showed higher absorptions at low latitudes on the leading anti-jovian hemisphere, correlated with chaos terrain. A depletion toward higher latitudes was also evidenced.

Clathrate hydrate hosting Carbon dioxide (CO_2), Dioxygen (O_2) and Sulfur Dioxide (SO_2) could be present at the surface and deeper in the icy shell (Hand et al., 2006). If so, it would be an important source of oxidants for the subsurface ocean. A study by (Hand et al., 2006) showed that mixed SO_2-CO_2- O_2 clathrate will be stable throughout the ice shell for thickness of 5km and higher and would also have significative influence on the heat flux through the ice. With a thin O_2 atmosphere (see sec. 3.2.4)

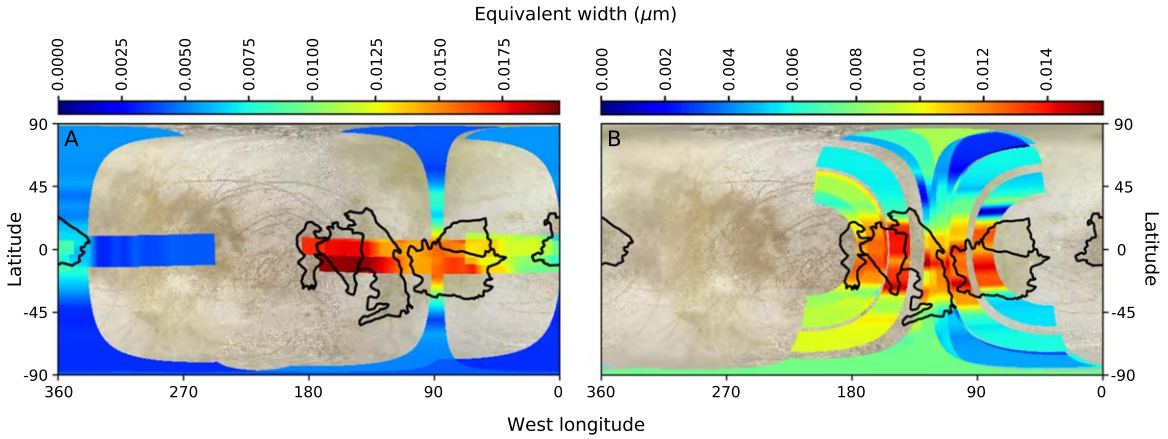

Figure 3.19: Maps of the 3.5μm hydrogen peroxide absorption (from (Trumbo et al., 2019)) splits between the 2016 (A) and 2018 (B) observations.

on Europa, dioxygen was thought to be present at the surface. Work by (Spencer and Calvin, 2002) using ground-based observation showed that molecular oxygen is trapped in the surface ice. Using the same data (Hand et al., 2006) estimated an abundance of $1.2-4.6\%$ O_2 by number relative to water assuming randomly distributed dioxygen molecules. Carbon dioxide abundance has been estimated at 0.0036% by number relative to water by (Hand et al., 2007) using NIMS data of the leading-hemisphere and the CO_2 absorption at 4.26 μm using the observed equivalent width of the band strength at 100K and considering an effective path length through the ice of about 60μm. Even though this result comes from empirical deduction it is one of the only estimate as no comprehensive map of CO_2 was made to this day (Trumbo et al., 2019). As for the sulfur dioxide, it has been first identified by (Lane et al., 1981) using the International Ultraviolet Explorer (IUE) and showed an absorption feature at 280nm in Europa reflectance spectrum that has been interpreted as SO_2. Its surface abundance was estimated at about 0.3% by number relative to water using compositional arguments (Hand et al., 2006). Sulfur is an important compound of the radiolytic cycle on Europa (see sec. 3.2.5) as evidenced by the sulfated compounds highlighted so far. Recent works by (Mishra et al., 2021a) combining the Hapke radiative transfer model and a bayesian inversion framework on three NIMS spectra of the trailing hemisphere showed no evidence of either CO_2 and SO_2 ices but they add that a theoretical analysis revealed that it is unlikely to detect these species in the $1-2.5$ μm NIMS data.

3.2.3 Surface texture

Surface textures parameters interesting for our study are the surface roughness, the crystallinity of the ice and the grain size of the compounds considered. Europa's surface is the smoothest of the icy Galilean moons with an estimate mean slope of about 10° (Domingue et al., 1991; Domingue and Hapke, 1992). Modelling of the sublimation on Europa's surface by (Hobley et al., 2018) showed that meter-scale blade-like water ice structure called 'penitentes' (see fig. 3.20) could be present at equatorial latitudes (see sec.3.2.5.1), drastically increasing the surface roughness. A recent comprehensive photometric study by (Belgacem et al., 2020) using the full collection of Voyager's Imaging Science System (ISS) and New Horizon's LOng Range Reconnaissance Imager (LORRI) with the Hapke radiative transfer model and a bayesian framework revealed a more heterogenous roughness with values ranging from 6° to 27° without clear equatorial trend as predicted by the model.

Water ice exists in both crystalline (hexagonal or cubic) and amorphous phases in the pressure-temperature conditions occurring in the Solar System (Jaccard, 1976) so both phases are expected to occur on the surface of icy satellites. Amorphous water ice transforms into a crystalline structure at a temperature-dependent rate, where the transformation is much faster at warmer temperatures (Berdis et al., 2020). Oppositely, charged-particle bombardment can cause disruption and disorder of the

ice's crystalline structure, producing an amorphous-like structure at a rate dependent on the particle bombardment flux (Cooper, 2001). The ice crystallinity is therefore an indirect tracer of the physical processes that can occur on a surface. A spectral modelling study by (Hansen, 2004) showed that surface ice is predominantly amorphous on Europa with crystalline ice at a few millimeters depth. (Ligier et al., 2016) produced global map of the water ice crystallinity and showed a higher amorphization on the leading-side, which can be explained by the stronger meteoritic flux (see sec. 3.2.5.1) occurring at this location. They also show a strong correlation between amorphous ice and geomorphological units such as chaos. Recent works by (Berdis et al., 2020) using 1D thermophysical model have estimated the full-disk crystallinity of Europa's leading hemisphere and found a crystallinity between 80 and 95% which is inconsistent with the results of (Ligier et al., 2016). In a revisit of three NIMS observations of the trailing-hemisphere using Hapke radiative transfer model and a bayesian framework (Mishra et al., 2021a) found that both forms of water ice are detected, but at varying confidence levels (volume abundance of $0.12\ +0.16/-0.07$ and $0.28\ +0.16/-0.13$). The water ice crystallinity on Europa's surface is still poorly constrained.

Grain size of the ice is important to constrain because it gives information on the physico-chemical processes occurring on the surface. It can be drastically affected by the processes occurring on it, for instance exogenic bombardment (see sec. 3.2.5.1) sputtering the surface may breaks the grains into smaller ones. Oppositely, coarser grains may be the product of thermal growth and reveal endogenic processes (see sec. 3.2.5.2). The retrieval of grain size on Europa was first made indirectly: using laboratory spectra acquired at a particular grain size and linear mixture radiative transfer models, one could estimate surface abundances of compounds assuming a fixed grain size. Recent works by (Ligier et al., 2016) using this approach but combining several water ice spectra at various grain size showed that Europa's surface is largely influenced by small grains between 20 and 200 μm. 1 mm grains are exclusively found in the trailing hemisphere while lower grains are found in the leading hemisphere. Smallest grains (5 μm) was evidenced in a chaos area. Radiative transfer modelling of three NIMS spectra of the trailing hemisphere by (Mishra et al., 2021b,a) revealed an increase of both amorphous and crystalline water ice grain size toward higher latitudes. Nevertheless, this study has estimated a very low packing density (porosity 80%) that seems unrealistic for ice surface.

3.2.4 Exosphere

An atmosphere mostly made up of O_2 was detected (Hall et al., 1995)with the Goddard High Resolution Spectrograph on the Hubble Space telescope. With a surface pressure of about 10^{-11} bar it is rather an exosphere. Exogenic processes (see sec. 3.2.5.1) are thought to be responsible of the dissociation of water into H_2 and O. The lighter molecular hydrogen molecules would escape from Europa relatively easily, leaving behind an enriched oxygen atmosphere.

Na and K were also detected (Brown and Hill, 1996; Leblanc et al., 2002), they can be the consequence of an external contribution by the atmosphere of Io or could be linked to the sputtering of sulfated materials on the surface.

In November and December 2012 the HST spotted an excess of hydrogen and oxygen emissions in the ultraviolet above the southern hemisphere (Roth et al., 2014). These emissions were persistent in the same area over several hours of observation, suggesting atmospheric heterogeneity. Non detection in previous HST images suggested that these emissions were the results of a 200-km-high plume activity. This could be the result of an important endogenic activity occurring in the icy shell, possibly related to the lineaments features.

More recent observations of Europa with the HST in far-ultraviolet revealed a stable water vapour atmosphere but only above the trailing hemisphere of the moon (Roth, 2021) that they interpreted as the consequence of sublimation and preferential sputtering by charged particles of the surface ices, producing this hemispheric difference.

Figure 3.20: Penitentes ice formations at the southern end of Chajnantor plain in chile. Ice blades are perpendicular to the viewing direction, the depressions between these bladed structures have ablated down to the underlying rock surface. Credit: ESO (`https://www.eso.org/public/images/img_1824/`).

3.2.5 Surface Processes

The morphologies (sec. 3.2.1), composition (sec. 3.2.2) and texture (sec. 3.2.5) identified at the surface of Europa are the results of active processes occurring through different timescales. We can easily distinguish two types of processes: endogenic, which may occur in the ocean and/or in the icy crust, and exogenic, i.e. following the influence of external phenomena interacting with surface. The complexity of the global understanding of surface processes lies in the fact that these processes are coupled and can mutually influence each other. In this section we review the main physico-chemical processes occurring at the surface of Europa that have been proposed so far.

3.2.5.1 Exogenic processes

A strong environmental factor for the surface is the intense, high-energy plasma of electrons (e^-) and protons (H^+, O^+ and S^+) (Pospieszalska and Johnson, 1989; Carlson et al., 1999b; Greeley et al., 2000; Cooper, 2001) coming from Jupiter's magnetosphere. The oxygen and sulfur protons are thought to come from SO_2 molecules released from volcanoes on Io, torn by the magnetosphere where they are dissociated, ionized and accelerated before settling on the surface (Brown and Hand, 2013). This radiation flux impacting the surface has two major consequences, first the creation of an exosphere mostly made up of O_2 maintained by the sputtering (Hall et al., 1995) (see sec. 3.2.4), second is the radiolytic sulfur cycle. Radiolysis means the dissociation by chemical decomposition of water in the form of H^+ and OH radicals. The works of (Carlson et al., 1999b) showed that the detection of hydrogen peroxide and sulfur dioxide in the surface suggest that sulfuric acid might be formed on Europa, as it is a common photochemical product in the atmosphere of Earth and Venus. In subsequent works (Carlson et al., 2002), they showed that sulfuric acid hydrates are radiolytically produced from sulfur-bearing surface material as part of global cycle (see fig. 3.21) that include water ice, sulfur, sulfur dioxide and constitute a surface in dynamic equilibrium between continuous production and destruction by radiation-induced chemical reactions (Carlson et al., 1999b,a, 2002, 2005). Their experimental study showed that the cycle time is about 4000 years and that sulfur on the surface would be quickly radiolyzed to acid sulfuric implying that

a sulfur source is needed, such as ion implementation and a briny or acidic ocean. A strong evidence of the importance of the radiolitic sulfur cycle is the spatial correlation between the hydrated sulfuric acid concentration and the typical 'bullseye' feature of darker terrains in the trailing anti-jovian hemisphere (Carlson et al., 2005; Ligier et al., 2016; King et al., 2022) where the particle bombardment is higher (Paranicas et al., 2001) due to Europa's synchronous rotation .

With water ice and highly hydrated materials as part of the surface composition (see sec. 3.2.2), radiolysis is expected to change the chemical composition of the terrains. The dissociation of water molecules produces OH radicals which can recombine to produce hydrogen peroxide and other oxidants. Since H_2 is lost in the process (Trumbo et al., 2019), it creates an important dehydration and an increasingly oxidised surface. If dehydration occurs, it likely affects the hydrate salts such as sulfated compounds. In an experimental study on thermal and radiation stability of hydrated salts mineral (McCord et al., 2001) investigated the long-term stability of hydrated Mg, Na and K-bearing sulfate salts under europan conditions. They showed that Mg-bearing salts, such as epsomite, are stable over geologic time against thermal dehydration and radiolysis whereas natron ($NaCO_3.10H_2O$) and mirabilite appear less stable to dehydration. Na^+ are expected to desorb as a consequence of the sputtering (McCord et al., 2001). This result is well-correlated with the detection of *Na* in the exosphere (see sec. 3.2.4). (McCord et al., 2001) also reported that a small amount of SO_2 is generated from the radiolysis of the salts, providing a potential source for the radiolytic sulfur cycle. This evidence would favours an enrichment of Mg-bearing salts over Na-bearing salts, consistent with the detection on the trailing side of hydrated $MgSO_4$ (McCord et al., 1999; Ligier et al., 2016; King et al., 2022). The origin of Mg sulfates on the surface is still debated, although some believe that it has an endogenic origin as a plausible component of Europa ocean (see sec. 3.2.5.2), other have proposed that $MgSO_4$ is an irradiation product (Brown and Hand, 2013) and that it initially was in the form of $MgCl_2$ through endogenic origins. Even though chlorine ions in Io plasma torus (Küppers and Schneider, 2000) and atomic chlorine in Io's atmosphere were detected, they show small relative abundance which favours an endogenic Cl. If so, (Brown and Hand, 2013)predicted that NaCl and KCl should also be involved. Similarly to Na, K is expected to be unstable to irradiation and will quickly be sputtered off the surface, explaining its detection in the atmosphere (see sec. 3.2.4). With the leading hemisphere being less affected by the sputtering process, one might expect a higher concentration of chlorinated salts on the leading-side (Brown and Hand, 2013). The distribution of chlorinated salts estimated by (Ligier et al., 2016) and (King et al., 2022) fit well with this scenario. If chloride are brought to the surface they also experience irradiation, a work by (Hand and Carlson, 2015) showed that sodium chloride, when exposed to Europa surface conditions, accumulates and traps free electrons by creating anion vacancies in the crystal structure (Trumbo et al., 2019) and causes diagnostic absorption features. This growth of 'color centers' yield a yellow-brown discolouration of the chloride comparable to the one observed on the surface, especially in the ridges and lineaments (see fig. 3.22), providing an elegant argument to the composition of the non-ice materials.

Amorphous water ice are thought to be created from crystalline ice through disruption by particle radiation (Hansen, 2004). Using the NIMS instrument, (Hansen, 2004) showed that there is a balance between radiolytic disruption and thermal ordering of the surface ice. Amorphous ice are expected to be dominant over crystalline form and that crystalline ices are expected at depth of about 1mm. (Ligier et al., 2016) found a higher concentration of amorphous water ice in the leading-side which does not favour the hypothesis of global amorphization on the surface of Europa. But other active processes on the trailing side such as the radiolytic sulfur cycle could provide a heat source to the crystallisation of amorphous ice.

Another important process occurring at Europa's surface is impact gardening. The huge gravity field of Jupiter impose an important meteoritic and micrometeoritic flux in the external environment of the Galilean moons. With a very tenuous atmosphere, much of the impacters reach the surface. Impact gardening would mix the exogenic material into the icy crust. The energy produced by high-velocity impacts could lead to chemical modification of the surface through shock waves, vaporization or light emission (Eichhorn and Grün, 1993; Burchell et al., 1996; Kissel and Krueger, 1987). Small impacters such as chondritic meteorites or comets could also be an important source of material for the surface,

bringing sulfates, carbonates or volatiles. Works by (Zahnle, 2001) using Monte Carlo methods have showed that the cratering rate was expected to be higher on the leading-hemisphere on synchronously rotating satellites, as opposed to the high energy plasma flux. This hemispherical difference could impact either crystallinity of the water ice and its grains-size distribution. (Ligier et al., 2016) showed that Europa was largely influenced by small grains between 20 and 200 μm with a significative increase up to 1mm in the trailing side. Such asymmetry could be explain by small impactors that break the ice into smaller grains in the leading-side, a less intense phenomenon takes place at the poles and on the trailing side favouring coarser grains. However, grain growth can also be the results of metamorphism mechanism. Even though the meteoric impact is on average 10^5 less powerful than the energetic particles impact (Cooper, 2001) it still holds the potential to modify the surface physico-chemical properties. Recent photometric works by (Belgacem et al., 2020) showed a global bright backscattering behaviour of the surface that has been attributed to space weathering that would mix the upper layer of the surface and produce complex particles and aggregates, reinforcing the backscattering behaviour of the surface.

Sublimation of water ice is expected to occur on the icy Galilean moons creating a local depletion of water and subsequent enrichment of surface materials (Zolotov and Shock, 2001). Another effect of the sublimation could occur on Europa: penitente ice (see fig. 3.20). On Earth, the sublimation of massive ice deposits at equatorial latitudes under cold and dry conditions lead to the formation of spiked and bladed textures eroded into the surface of the ice (Hobley et al., 2018), known as penitentes. They are formed by scattering and lensing of light, on and into the ice, under a daily low solar incidence angle such that light strikes the walls of the blades at high angle and illuminates the floor of the pit, favouring sublimation and creation of these features. This leads (Hobley et al., 2018) to suggest that penitente ice could be created on Europa as the maximum zenith angle on any point of the tidally-locked satellite never varies by more than 4°. They found that the sublimation rates in equatorial belt (below 23°) exceeds the erosion rate by space-weathering processes leading to penitentes that could reach 15 m in depth and spaced by about 7.5 m. This results was quickly contested by (Hand et al., 2019) who argued that penitentes results from a specific set of physical conditions that exist on Earth but do not apply to the cryogenic ultrahigh vacuum of Europa's surface. They concluded that penitentes might exist on Europa but their formation cannot be predicted by equations based on Earth-like conditions. Unfortunately, there is not images of Europa with a sufficient resolution to detect meter-scaled features so the presence of penitentes is still uncertain even though (Hobley et al., 2018) argued that such morphologies could explain the radar and thermal data. The formation of penitentes would drastically modify the macroscopic surface roughness but (Belgacem et al., 2020) estimates a photometric roughness with values ranging from 6° to 27° without clear equatorial trend as predicted by the model.

3.2.5.2 Endogenic processes

Endogenic processes designate mechanisms with which the surface is modified through its interaction with internal processes. On Europa, endogenic processes can occurs through the interaction of the subsurface putative ocean with the rocky mantle and/or the icy shell. Some of them can have consequences on the surface properties. A major effect governing the internal structure is the thermal gradient and the thickness of the icy shell. Each layer composing the internal structure of Europa will dissipate the gravitational tides differently depending on the physico-chemical properties of each layer (Tobie, 2003). Estimation of heat generated in the icy layer shows a higher heating than in the ocean or the mantle (Tobie et al., 2005). Due to the strong differences between the surface temperature (around 100K) and subsurface ocean (around 273K) convection was expected to occur within the icy shell, with an uppermost layer of conductive ice to the surface (McKinnon, 1999). It has been shown that the convective plumes of warm ice were submitted to an even higher heating due to their low viscosity (Sotin et al., 2002). Such local heating would promote the presence of liquid subsurface reservoirs within the icy shell. Even though the thickness of the icy shell must have varied over geological time through variation of the internal heat flux, current estimates converge a thickness of about 30 km when considering the convection. The conductive layer is expected to extend up to 10 km below the surface (Pappalardo et al., 1999; Tobie, 2003; Quick and Marsh, 2015). The possibility that gases and liquid-water could reach the

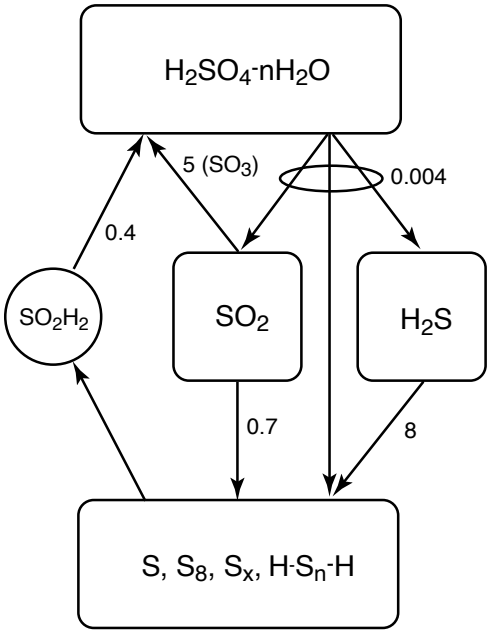

Figure 3.21: The radiolytic sulfur cycle of Europa (from (Carlson et al., 2002)).

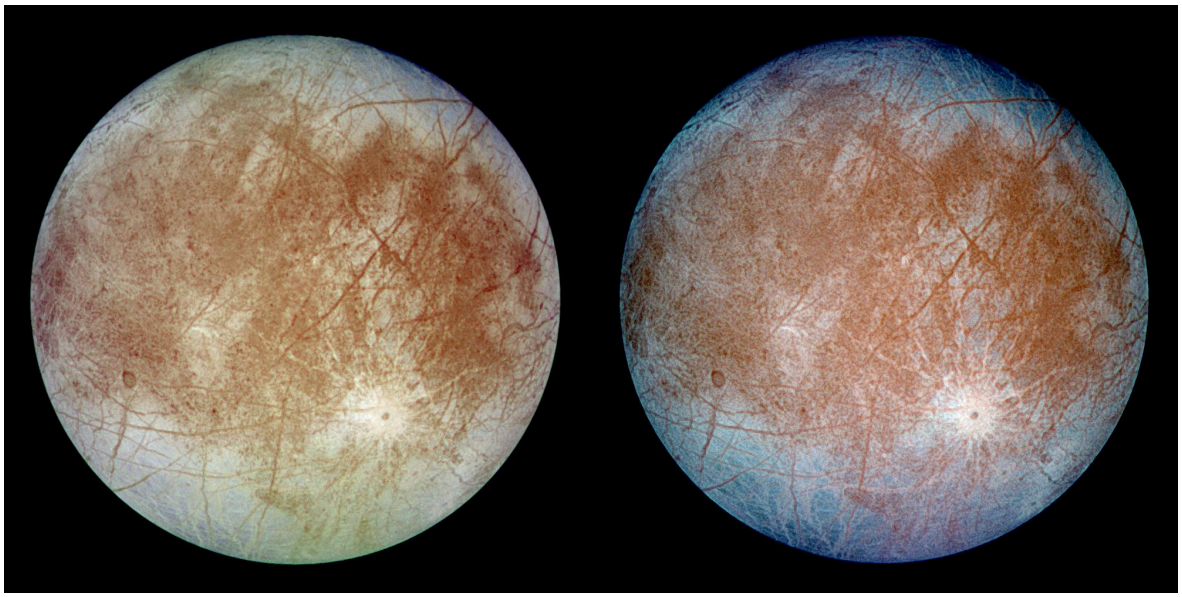

Figure 3.22: Two views of the trailing hemisphere of Europa. The left image shows the approximate natural colour appearance of the moon. The right image is a false-color composite version combining violet, green and infrared images to highlight the difference in surface composition. Blueish areas disitnguish between coarse-grained (dark blue) and fine-grained (light blue) water ice and the dark brown areas are the non-ice materials. Long lineaments and ridges are visible, crosscutting the surface on more than 3000km long. The young Pwyll crater is visible in the lower third of the image, with a dark central spot and bright ejecta. (Credits:NASA/JPL/DLR, `https://europa.nasa.gov/resources/91/natural-and-false-color-views-of-europa/`).

surface through localised subsurface reservoirs or via a connection with the global ocean were quickly invoked by analogy to the volcanic phenomena occurring on Earth. The term 'cryovolcanism' was defined as 'the eruption of liquid or gaseous phases (with or without entrained solids) of water or other volatiles which should normally be in solid form at the surface temperature of the satellite' (Geissler, 2015).

Mechanisms behind cryovolcanism are complex and still debated as they involve many issues regarding the origin of the cryolava, the creation and stability of subsurface reservoirs and their pressurization. Several models have being investigated and will not be cover here, for more detailed information the reader can refer to (Fagents, 2003; Quick and Marsh, 2016; Lesage et al., 2020). In this work, we aim at characterising the surface microphysical properties and therefore we hypothesize that cryovolcanism is a major endogenic process governing the surface morphologies, compositions and textures. Below is a quick review of the potential cryovolcanic processes responsible of the surface morphologies observed on Europa. Then, the implication of the initial composition of the internal ocean on the composition of the cryolava observed at the surface will be covered.

Cryovolcanic processes On Europa several geomorphological features are thought to be the results of a cryovolcanic activity: low albedo deposits not confined by underlying deposits, lenticulae and chaos, smooth plains and low albedo deposits interacting with the underlying terrain (see fig 3.23).

Low albedo deposits not confined by underlying deposits are frequently observed either along ridges and lineaments (fig 3.23, a) or surrounding domes (fig 3.12). These quasi-circular deposits seem to have been deposited without being stopped by the surrounding relief, suggesting explosive activity similar to what is observed on Earth (Fagents, 2003). A study by (Quick et al., 2013) showed that steam plumes of a mixture of gases and particles in an explosive events can explain these deposits. These eruptions could produce plumes of few kilometers height consistent with the size of the deposits. An illustration of the mechanism is shown fig 3.24a.

Chaos (fig 3.11 and 3.23 b) and lenticulae with positive relief (fig 3.12) are generally lobate features with a rough texture significantly different than the surrounding terrains. Their morphological characteristics allowed to suppose an installation by extrusion of a viscous material to cover pre-existing ground without this hindering the expansion of these structures (Miyamoto et al., 2005). Thereby, it has been proposed that these features are the results of the diapirism of viscous ice (Figueredo, 2002; Miyamoto et al., 2005) as illustrated in fig. 3.24 (e). Recent studies by (Quick et al., 2017) showed that the lobate shape of domes can also be explained by the effusion of cryolava on the surface such as the one illustrated fig 3.24 (b and c).

Smooth plains and low albedo deposits confined by underlying and surround deposits (fig 3.23c and d) seem to testify to an effusive cryovolcanic origin. These features are sometimes seen confined around lenticulae (Fagents, 2003). These smooth textures could form as the effusion of a very low viscosity fluid (Miyamoto et al., 2005) or through the local melting due to a warm ice plume in subsurface (Fagents, 2003). The volume of those deposits has been estimated, enabling a more precise discussion of the formation mechanism. These authors demonstrated that the emitted volume is in agreement with a subsurface reservoir freezing (Lesage et al., 2021).

Many of these models partly explain the deposits observed close to lineaments and ridges as the consequence of cryolava flows or explosive venting. Some have also proposed mechanisms to explain the development of ridges itself. (Greenberg et al., 1998) proposed the ridge formation by the tidal pumping of shallow water-filled fractures (see fig. 3.24d) connecting the surface to a global ocean allowing the water to freeze partially during the opening of the ridge and then the compression and upwelling of water during the closing. This mechanism was contested by (Head and Pappalardo, 1999) who proposed the upwelling of a linear diapir to cause flexure of the region marginal to fractures leading to ridges.

Composition of the cryolava The cryovolcanic mechanisms imply a connection between either the internal ocean or subsurface local reservoirs. Thus, the chemical composition of the cryolava should (in part) reflects the composition of the internal ocean. Since the latter is in direct contact with the rocky mantle, the dissolution of minerals in water should change its chemical composition and should

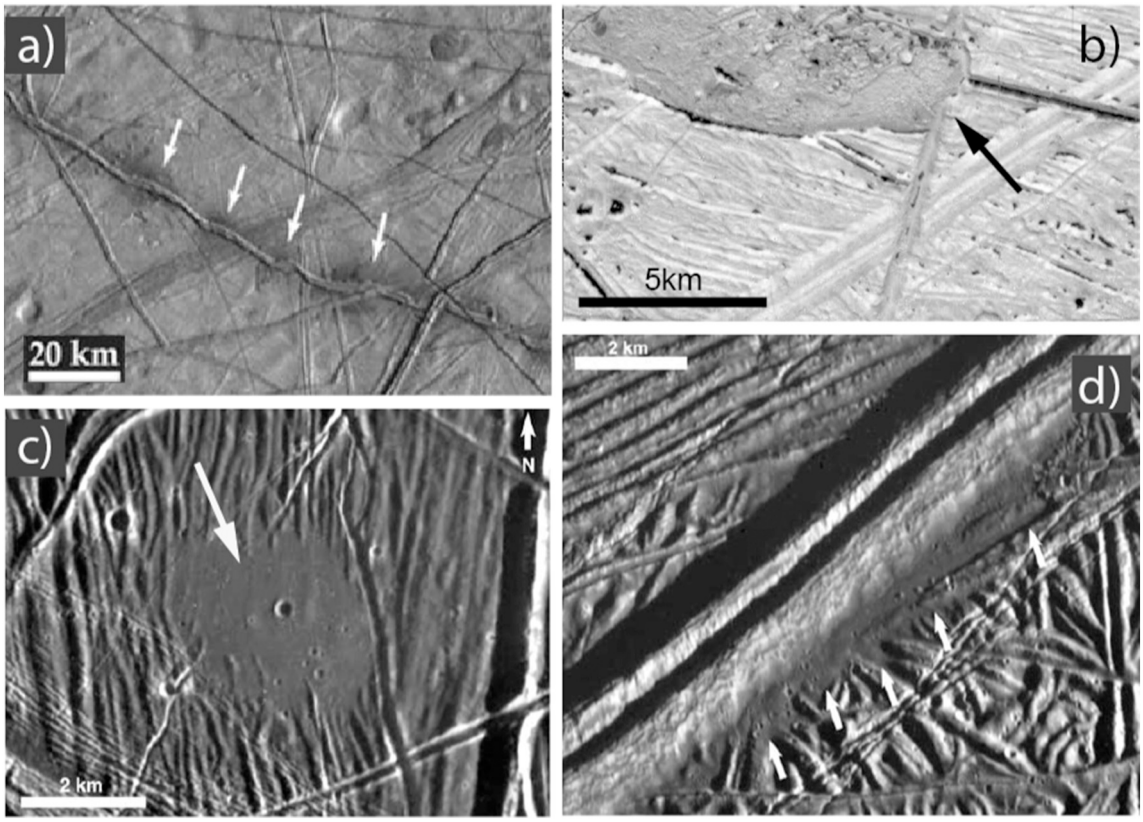

Figure 3.23: Example of Europan surface features showing potential cryovolcanic origins (white and black arrows, from (Lesage et al., 2020)). (a) Low albedo deposits along the double ridge of 'Rhadamanthys linea' ((Quick and Marsh, 2016)). (b) chaos-like feature with a lobate structure. (c) Ciruclar smooth plain deposits ((Fagents, 2003)). (d) Smooth deposits flanking a double ridge ((Fagents, 2003)).

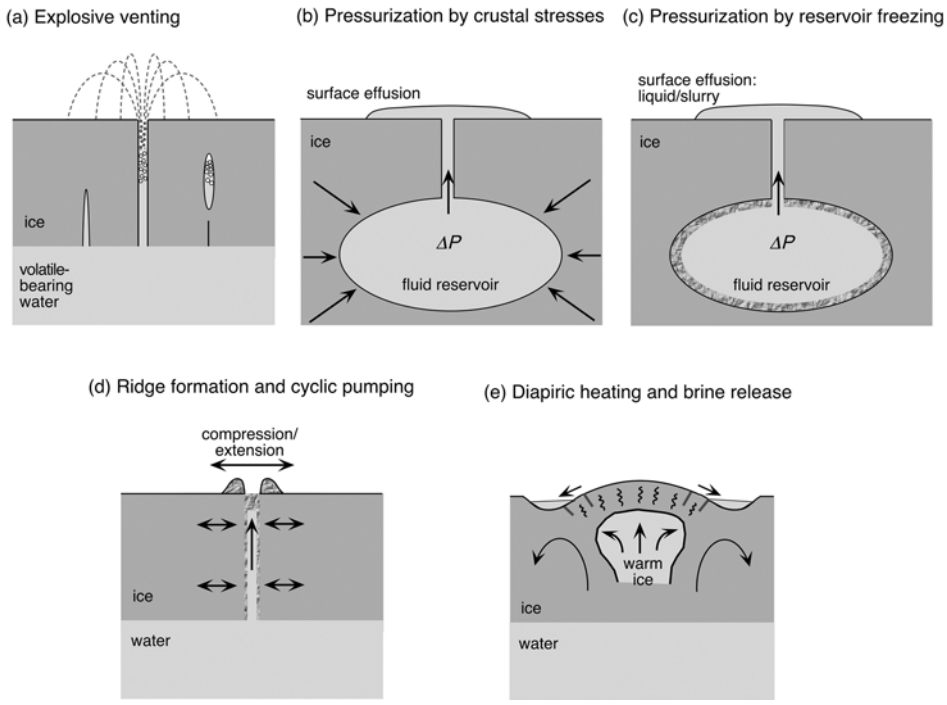

Figure 3.24: Examples of alternative mechanisms for delivering fluid to Europa's surface (from (Fagents, 2003)). (a) exsolution of volatiles and explosive venting. (b) pressurization of fluid reservoir in ice lithosphere by lithospheric stresses. (c) pressurization by partial freezing of liquid reservoir. (d) tidal pumping of slush mixtures ((Greenberg et al., 1998)). (e) ascent of warm ice diapirs leading to melting and release of near-surface brines ((Head and Pappalardo, 1999)).

therefore be reflected in the composition of cryolavas. However, the dissolution stage is only a first step in the history of the ocean, it then freezes to form the icy shell, which could differentiate into an heterogeneous solid layer, may have melted locally to produce cryolava to the surface, which are then altered by the exogenic processes (Kargel et al., 2000) (see sec. 3.2.5.2). Thus, inferring the composition of the inner ocean from surface observations is not trivial. Still, the identification of major chemical species helps to bring constraint on such composition.

The similar masses, quasi-circular and coplanar prograde orbits of the Galilean satellites suggest that they were formed around Jupiter with the same circumplanetary disk (Robert T. Pappalardo, 2009). Formation models of this circumplanetary disk predict that Galilean satellites were formed at least 4 Myrs after the carbonaceous chondrites (Barr and Canup, 2008). This strongly suggests that the initial composition of Europa may be close to carbonaceous chondrites. Primary phases in chondrites are generally similar to terrestrial crustal phases (Kargel, 1991) which includes olivine, pyroxene, feldspars and sulfides. Thus, a significant amount of soluble salts is expected to be produce at the rocky mantle/ocean interface. Works from (Kargel, 1991; Kargel et al., 2000) using chemical-structural models showed that the dissolution of type C1 and C2 carbonaceous chondrites in water produces an important amount of Mg, Na and Ca salts. The very low solubility of carbonate salts $CaSO_4$ suggests that $MgSO_4$ and Na_2SO_4 are the most important solutes. Minor components such as sulfates of K, Ni, Mn and chlorides are also produced. The low cosmic abundance ratio of Cl/S of 0.01 in carbonaceous chondrites suggest little amount of chlorides in the Ocean (Kargel, 1991). This indicates an initial system made of $MgSO_4$- Na_2SO_4-H_2O. Later, laboratory works (Fanale et al., 2001) using a natural sample of carbonaceous chondrite (from a CM meteorite) subject to hot water showed that subsurface aqueous phase on Europa probably consists of a brine made of cations Mg$\sim$ Na > Ca, K, Fe and anions SO_4>> Cl which was in complete agreement with work made by (Kargel, 1991). As the ocean start to freeze during its evolution a salt-rich crust is formed with the crystallisation of water and highly hydrated sulfates. (Kargel, 1991) showed that

the ternary $MgSO_4$- Na_2SO_4- H_2O eutectic liquid has a higher density than the equivalent frozen eutectic mixture, so a solid crust would float on its own liquid making extrusion of brines to the surface possible. As the crust thickens, $MgSO_4$-rich aqueous volcanism would become increasingly difficult. Late-stage differentiation of the crust would favour water and Na_2SO_4- H_2O solutions to be extruded as they are less dense than the $MgSO_4$-rich crust(Kargel, 1991). These results tends to favours a salt-rich crust made of hydrated magnesium and sodium sulfates, with potential extrusion of sodium sulfates and water through cryovolcanism events which is consistent with the detection of both magnesium and sodium sulfates on the surface (McCord et al., 1998, 1999; Ligier et al., 2016; King et al., 2022).

The very low amount of chloride in the ocean predicted by (Kargel, 1991) and (Fanale et al., 2001) do not favour the presence of chlorides in the icy crust during its freezing. However, chlorinated compounds on the surface was evidenced by (Dalton, 2007; Ligier et al., 2016; Trumbo et al., 2020; King et al., 2022) and the very low abundance of Cl in Io's plasma torus suggests that they are endogenic. (Zolotov and Shock, 2001) investigated the salts stability on the surface and their oceanic origin through theoretical model and argued that solutes in the ocean are not a result of leaching from a salt-containing carbonaceous chondrite but rather from the aqueous alteration of anhydrous chondritic material. They suggest that aqueous and possibly hydrothermal alteration during the differentiation of Europa could be the main contributor of the ocean's ionic composition. Their results indicate that freezing of the ocean leads to a gradual change of its composition leading to sequential salt deposition. During the freezing stage, pure water crystallize first and the liquid phase is enriched with salts that crystallize in the following order: $CaSO_4$, Na_2SO_4, $MgSO_4$, KCl, NaCl. This has two majors implications, first magnesium and sodium sulfates would be predominantly formed during the freezing of oceanic water which supports the results obtained by (Kargel, 1991) and (Fanale et al., 2001). They add that highly hydrated salts are stable in ice-bearing surface materials and throughout the icy crust (Zolotov and Shock, 2001), even more than water ice suggesting salt lag deposits through sublimation of the ice on the surface. Second, while hydrated sulfates of magnesium precipitate the liquid phase becomes enriched in Cl and chloride salts of K, Na and Mg can precipitate from deeply fractionated brines (Zolotov and Shock, 2001). If a subsurface liquid reservoirs is formed through local melting, the liquid phase is enriched successively in NaCl, KCl, $MgSO_4$, $Na_2SO_4$and $CaSO_4$ which favours a cryovolcanism of Cl- and Mg-rich eutectic brines. The Cl/S, K/Na and Mg/Ca ratios could be even higher if the oceanic water was fractionated during its upwelling in the icy crust(Zolotov and Shock, 2001). Such results suggest a hydrated magnesium-sodium sulfate-rich crust with potential surface dehydration creating salt lag deposits and extrusion of chlorinated brines through cryovolcanic events, which is consistent with surface detections of hydrated chlorine salts.

Finally, deepwater volcanism at the ocean/mantle interface during early stage of Europa's evolution could have dissolved gases such as CO_2, SO_2 and CH_4 in explosive water volcanism. (Kargel et al., 2000) showed that the $CaSO_4$ of a carbonaceous chondrite, although sparingly soluble in water, would break down and yield free SO_2 or SO_3 fluid in Europa's interior and produce sulfurous volatiles. The SO_2 and S_2 gases that would be generated are consistent with observations of gases venting from Io's volcanic plume (which should have an initial composition close to Europa). $SO_2$and SO_3 would tend to migrate upward and eventually vented into the ocean, reacting with water or ice to form sulfuric acid. Sulfuric acid could accumulate and reach saturation to form hydrate phase (Kargel et al., 2000). While this model fits onto the sulfate salt model, it could also be explained by the endogenic sulfuric acid observed on the surface (Carlson et al., 1999b) as a secondary source feeding the radiolytic sulfur cycle. (Kargel et al., 2000) recognize that the distribution pattern of hydrate is consistent with exogenic modulation of sulfuric acid but argued that this exogenic compositional patterns could be superposed over this endogenic distribution in this ice crust during the freezing of the ocean. Dissolved SO_2 and H_2SO_4 yield a highly acidic ocean and could drive explosive aqueous volcanism (Kargel et al., 2000).

As stated (Kargel et al., 2000), 'realistic chemical-physical evolution scenarios differ greatly in detailed predictions, but they generally call for a highly impure and chemically layered crust. Some of these models could lead also to lateral chemical heterogeneities by diapiric upwellings and/or cryovolcanism'. Combination of both endogenic and exogenic processes can significantly change the surface

composition, making characterisation of ocean composition difficult. Examples of 12 alternatives surface compositions (in agreement with NIMS observation) and implication for Europa's hydrospheric evolution are given by (Kargel et al., 2000).

3.3 Past and future exploration

Since the discovery of Jupiter's moons by Galileo Galilei in 1610 then described as 'three little stars', our understanding of Europa has continued to grow thanks to space missions. This section gives a brief history of past space missions, a focus will be made on the Galileo mission and in particular the NIMS instrument because this work is based on these data. Then, missions at the heart of its future exploration will be discussed.

3.3.1 Past exploration

The exploration of Europa began with the Jupiter flybys by the Pioneer 10 (1973) and 11 (1974) spacecrafts. These two missions provided first images of Europa with a resolution of about 200 km per pixel and took measurements of the gas giant's magnetosphere, radiation belts, magnetic field, atmosphere and interior.

In 1979 the twin Voyager 1 and 2 spacecrafts traveled through the Jovian system during their journey to the outer solar system. They provided more images of the icy surface of Europa with a resolution up to 2 km per pixel. The images revealed a very smooth surface, little cratered and dotted with lineaments of variable size. The first speculations concerning the presence of a global internal ocean possibly containing the ingredients necessary for the emergence of life appear. The question of the habitability of Europa is then open, reinforcing the motivations for its exploration.

The Galileo spacecraft, launched in 1989 by NASA, was the first mission entirely dedicated to the study of the Jovian system. It arrived in 1995 and began its eight year mission orbiting Jupiter and performing numerous close flybys of Europa. The 11 instruments on the orbiter include visible cameras, spectrometer (NIR, UV) magnetometer, photopolarimeter as well as high-energy particles, dust and plasma detectors. The Solid State Imager (SSI) brought images with spatial resolution up to 21 m per pixel, revealing a very wide diversity of morphologies. Most of the current knowledge presented in this chapter comes from this mission, the Near Infrared Mapping Spectrometer (NIMS, see sec.3.3.2) instrument notably allowed a first characterization of the surface's microphysics, i.e. its chemical composition and texture. Since no mission has come so close to Europa so far, the Galileo data are still an important source of knowledge and are constantly reanalysed at the dawn of new models.

Since, some missions have performed far flybys on their way to other targets such as Cassini (2000) and New Horizons (2007) bringing new data. The JUNO spacecraft launched by NASA in 2011 is the most recent space mission targeting the Jovian system. Even though the mission is dedicated to the study of Jupiter observations of the Galilean moons have been planned. The orbiter continues to this day to provide data.

An important source of observational data also comes from Earth-orbiting space telescope, this is particularly the case of the Hubble Space Telescope (HST) instruments which notably observed the first plumes in Europa's atmosphere. The lower spatial resolution of Earth-orbiting space telescope is compensated by a higher spectral resolution and, above all, a much faster deployment than any dedicated space mission to the Jovian system (about 8 years of cruise phase), making this approach still very prolific for years to come.

3.3.2 The Galileo NIMS instrument

The Near Infrared Mapping Spectrometer (NIMS) (Carlson et al., 1992) is a combination of imaging and spectroscopic methods. It covers the $0.68 - 5.2\ \mu$m spectral range and consists of a telescope, with one dimension of spatial scanning, and a diffraction grating spectrometer (see fig. 3.25) both cooled to low temperatures to reduce background photon noise. The operating mode is as follow: the spatial

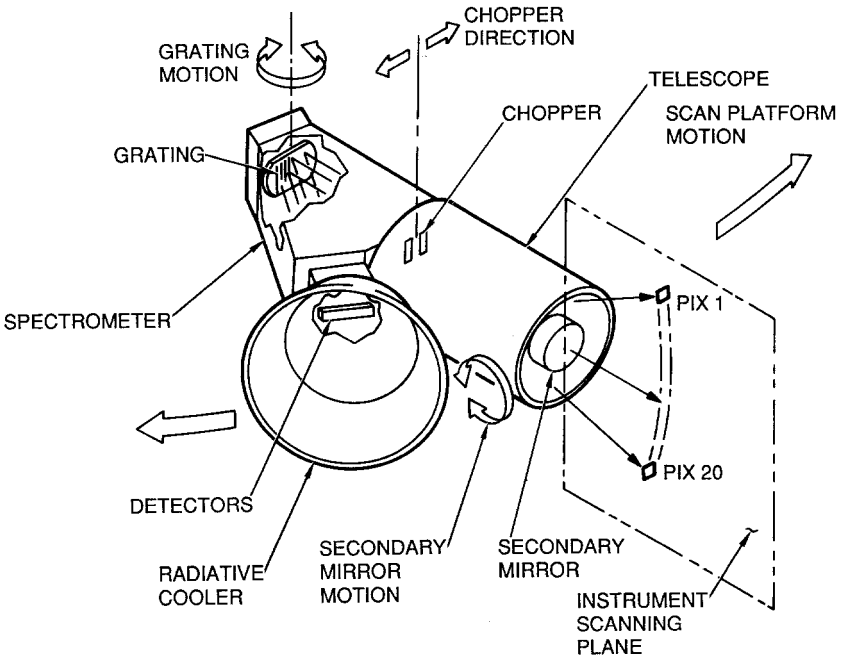

Figure 3.25: Schematic diagram of the instrument and scanning motions (from (Carlson et al., 1992)). Major elements are the cone angle motion of the scan platform (large arrows), The internal 20-position spatial scan produced by the motion of the telescope secondary mirror, an optical chopper to provide dark reference, a diffraction grating spectrometer dispersing the radiation onto the focal plane assembly, a focal plane assembly consisting of 17 individual detectors and optical filters, a passive radiative cooler which cools the focal plane. Signal processing and control electronics are not shown.

scanning is provided by a motion of the telescope secondary mirror, giving 20 contiguous pixels, each with a 0.5×0.5 mrad resolution. The second dimension of spatial scanning is made by a slow rotation of the spacecraft scan platform in the cone direction. During the mirror scan, the grating is set at a fixed angle with a corresponding set of 17 wavelengths striking the 17 individual detectors of the focal plane assembly. When half of the up/down mirror scan is achieved, the grating is stepped to a new setting of 17 wavelengths measured during the second half of the mirror scan. This continues until the whole spectral range is covered, and the spacecraft scan platform slightly moves to observed 20 new contiguous pixels. The instrument calibration was described by (Carlson et al., 1992). The NIMS instrument is expected to have a triangular spectral bandpass response, with a full width at half maximum (FWHM) of 0.025 μm (see fig. 1.6). The first two detectors at shorter wavelengths (0.6887 and 0.6963 μm) have a spectral resolution of 0.0125 μm while it is nearly constant for the other wavelengths ($0.704 - 5.2592$ μm) with a value of 0.025 μm. The spatial resolution will vary according to the distance with which the flyby of the target is achieved. A major concerns of the NIMS data is the noise level uncertainty. It can comes from thermal noise, detector current noise and radiation noise. There is also an uncertainty on the absolute radiometric calibration of the instrument that (Carlson et al., 1992, 2005) have estimated to be up to 10%, which is not insignificant. A current estimate of the signal-to-noise ratio of the NIMS data is between 5 and 50 (Robert T. Pappalardo, 2009) which can be very low, especially beyond $3\mu m$ (Stephan et al., 2008).

3.3.3 Future exploration

Future exploration of Europa and the Jovian system holds great promise with the launch of two space missions: ESA's JUpiter ICy moons Explorer (JUICE) (Grasset et al., 2013) in 2023 and NASA's Europa Clipper (Phillips and Pappalardo, 2014) in 2024.

The JUICE mission is designed to explore Jupiter and the icy Galilean satellites in a three and half

years nominal mission. The spacecraft will make multiple flybys of Ganymede, Callisto and Europa and then go into orbit around Ganymede. The science payload includes a camera, visible and infrared imaging spectrometer, ultraviolet imaging spectrograph, radar sounder, laser altimeter, submillimeter wave instrument, magnetometer, particle and plasma package, radio and plasma wave investigation and radio science package. Although the focus is on Ganymede, the several flybys of Europa should bring helpful additional data to constrain the surface properties. The MAJIS (Moons and Jupiter Imaging Spectrometer) is a visible and near infrared imaging spectrometer is a dual grating spectrometer designed with a VIS-NIR channel from 0.4 to 1.9 μm and an IR channel from 1.5 to 5.7 μm. The expected signal-to-noise ratio will exceed 100 over most of the spectral range and the spatial resolution can reach 65 m per pixel. Such state of the art instrument will allow a finer characterization of the surface microphysics.

The Europa Clipper mission is entirely dedicated to the study of Europa. The spacecraft, in orbit around Jupiter, will make nearly 50 flybys of Europa at altitudes as low as 25 km above the surface. The spacecraft's payload includes a mid to far infrared imaging system, a near infrared spectrometer, a wide and narrow angle visible camera, an ultraviolet spectrograph, a dual-frequency penetrating radar, a magnetometer, a magnetic sounder and a mass spectrometer. The Mapping Imaging Spectrometer for Europa (MISE) is a high-optical-throughput pushbroom imaging spectrometer designed to cover the $0.8-5$ μm spectra range with a 10 nm spectral sampling. The combination of such high spectral resolution with a spatial resolution down to 25 m per pixel will provide key data to characterize local scale surface properties.

The future exploration of Europa will also be done by Earth-orbiting telescope. With the very recent commissioning of the James Webb Space Telescope (JWST) (Clampin, 2008), known as the successor of the Hubble Space Telescope. The HST provided extensive knowledges on Europa and we expect a lot from the observations campaigns of our Solar System, especially for the Galilean icy moons. The near infrared camera NIRCam and Near infrared spectrometer NIRSpec operates both in the $0.6-5$ μm spectral range which is similar to the Galileo/NIMS, JUICE/MAJIS and EuropaClipper/MISE instruments and will allow a cross-comparison between the data. First image of Jupiter with NIRCam instrument (see fig. 3.26) is a great example of the resolution power of the telescope.

3.4 Outstanding questions

In this chapter we have reviewed the current state of knowledge concerning the surface of Europa. We have seen in particular that many studies have succeeded each other to provide answers on the composition of the surface. Although these seem to vary drastically from one hemisphere to another, many authors agree that the surface is mostly made of water ice mixed with highly hydrated compounds (McCord et al., 2001; Carlson et al., 2005; Ligier et al., 2016; Trumbo et al., 2020; King et al., 2022). These hydrated compounds are likely to change from one location to another, according to the geological processes involving them. However, the differentiation between endogenous and exogenous processes, and their influences on the chemical composition of the surface is not clearly understood. It is commonly accepted that the trailing hemisphere is globally more affected by the Jovian magnetosphere, favouring the establishment of a radiolitic sulfur cycle which in turn promotes the presence of sulfuric acid on the surface (Carlson et al., 1999b, 2002, 2005). In contrast, the impact of space gardening on the surface composition of the leading hemisphere is not well constrained. Concerning the internal processes, many physical models try to explain the observed morphologies (Fagents, 2003; Miyamoto et al., 2005; Quick et al., 2013; Lesage et al., 2020, 2022). Most of them involve an exchange of material between the subsurface and the surface via cryovolcanic events. There is no clear connection between these models and the chemical compounds detected so far because the cryovolcanic features are often very localized, explaining a particular morphology, while the spectroscopic studies carried out are often dedicated to few spectra of Europa or from observations with very low spatial resolution covering several hundred square kilometers of the surface, preventing a precise characterization of the surface composition. This clearly limits the understanding of the processes at the origin of the observed morphologies and chemical compounds detected. It appears important to be able to specify the composition of the surface, at

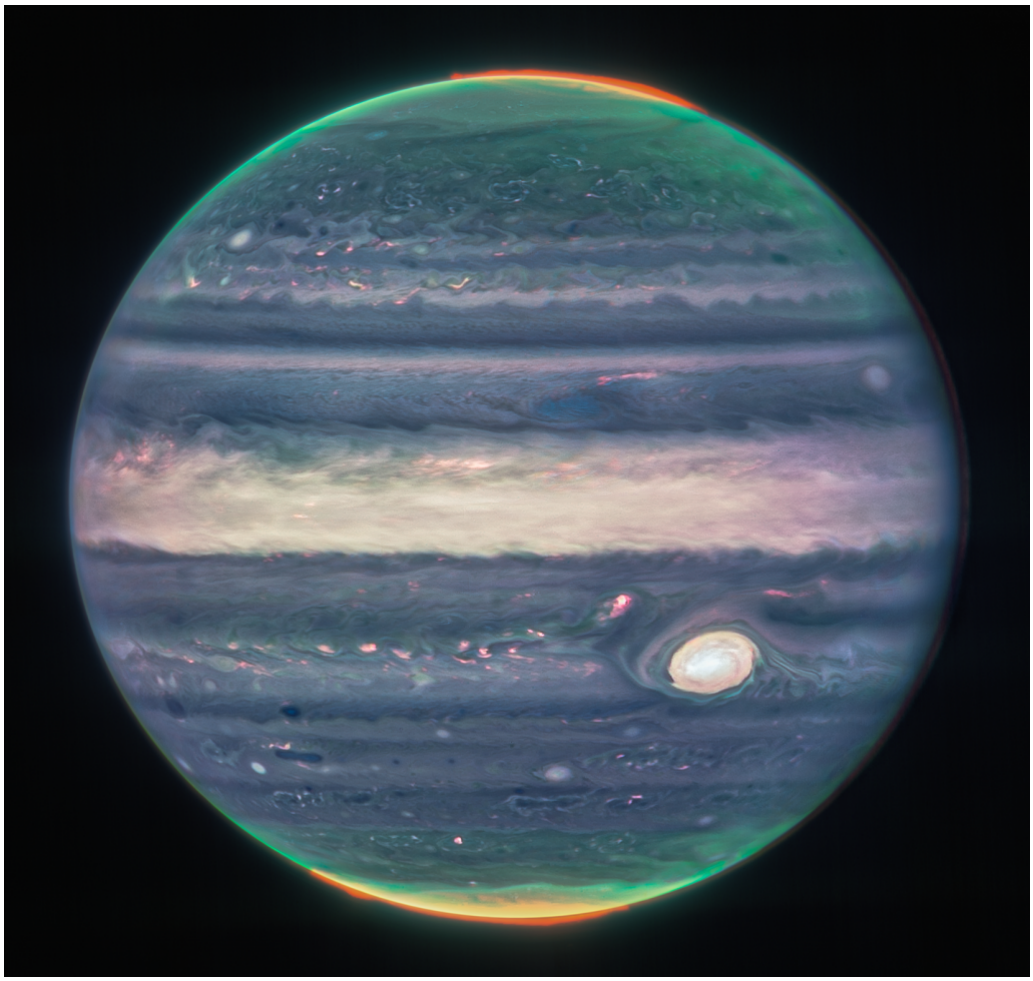

Figure 3.26: Composite image of Jupiter from the JWST NIRCam instrument in three infrared filters: 3.6 (red), 2.12 (green) and 1.5 (blue) μm. Aurorae in the North and South poles (in yellow to orange colours) as the consequence of the interaction between Io plasma torus and the magnetic field lines of Jupiters. Credit: NASA, ESA, CSA, Jupiter ERS Team; image processing by Judy Schmidt.

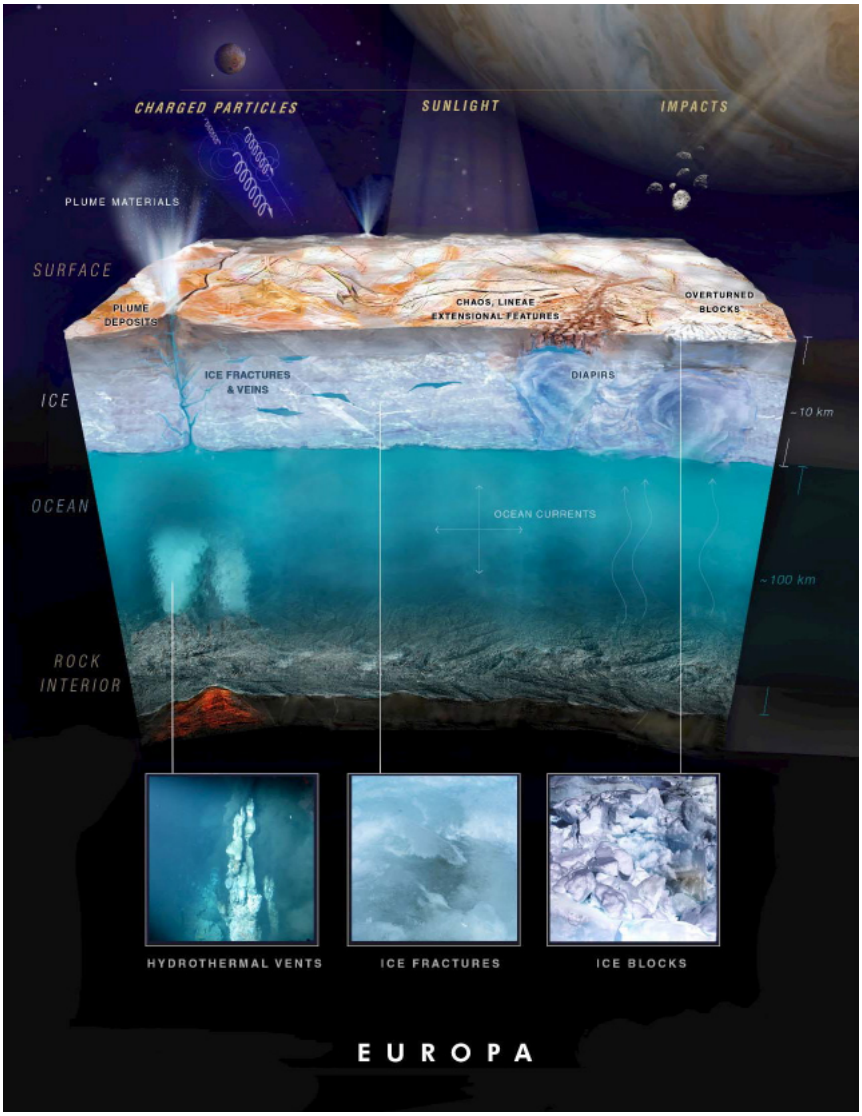

Figure 3.27: An artist view of the endogenic and exogenic processes occurring on Europa and affecting its surface properties. Credit: NASA

the scale of the geomorphological units identified, to not only discriminate between endogenous and exogenous processes, but also to refine the cryovolcanic models. As *Fanale* stated, 'it has been assumed that if the mineralogy of the non-H_2O ice material could be deciphered, the chemical composition of the aqueous phase could be established' (Fanale et al., 2001). While the determination of Europa's surface composition is a major issue, it is clear that the task is not trivial because it is the results of a combination of multiple processes whose form and intensity can vary drastically from one position to another, as illustrated fig. 3.27.

As we have just said, there are several limitations in the spectroscopic studies performed to date. The first is related to the low spatial resolutions of the data that has been used to derive the surface composition. The works from (Ligier et al., 2016) and (King et al., 2022) use observations made by the VLT/SINFONI and VLT/SPHERE instrument with spatial resolutions of about 50 km per pixel, which allows global mapping but does not allow to specify the composition within relevant geomorphological units. Some studies are based on the use of Galileo/NIMS data. Although the mission is old and the instrumental capacity is not as high as that of the VLT (especially concerning the spectral resolution), the close flybys made by the mission allow the use of higher spatial resolution data. However, it has been shown that the radiometric calibration uncertainty of the instrument is high (up to 10%) (Carlson et al., 1992) and such uncertainty was not properly taken into account in these spectroscopic studies (McCord et al., 1998, 1999; Carlson et al., 2005). It is of primary importance to be confident on the absolute photometric level of the data when studying surface properties as a change in the reflectance level could be related to either a different grain size (which will imply a change in the volume abundance retrieved) or to another chemical compounds (which would also affect the estimated abundances of the other compounds). That is why the results from these studies should be treated with caution. Finally, a common point to all these works is the use of a non-realistic radiative transfer model as they are either based on a direct spectral comparison with laboratory spectra (McCord et al., 1998) or from a linear mixture model (Ligier et al., 2016; King et al., 2022). Linear mixture model are based on the principle that the observed spectrum is the results of a linear combination of the spectra of different species. To each species (or endmember) is associated a reflectance spectrum obtained in laboratory at a particular grain size and the linear unmixing method adjust the abundance of each considered species. Although these techniques are easily implemented and allow a first identification of the species involved, they neglect the effects of some microphysical properties such as the grain size. Also, they do not correctly account for the highly non-linear effects of the light path within a planetary regolith due to multiple scattering (Hapke, 2012; Schmidt and Fernando, 2015; Shirley et al., 2016; Mishra et al., 2021a). These approaches are therefore non-suited to a precise understanding of Europa's surface microphysics, especially at the scale of specific geomorphological units in which other microphysical properties are expected to play a significant role, such as the macroscopic roughness or the porosity. Recent works have used a realistic radiative transfer model to constrain Europa's surface composition (Mishra et al., 2021a). Although the radiative transfer model is more appropriate for this problem, the study was limited to only 3 spectra of the trailing hemisphere from a single observation at moderate spatial resolution (39 km per pixel). The selected spectra were not associated to any particular geomorphological units and the signal-to-noise ratio has been greatly overestimated.

We therefore propose to push these analyses by combining Galileo/NIMS data at high spatial resolution (from 1 to 10 km per pixel) with a realistic radiative transfer model (see chap. 1) and a robust inversion method (see chap. 2) to properly account for the calibration uncertainties. As shown fig. 3.28 there are several NIMS observation of both the leading and trailing hemisphere with spatial resolution high enough to resolve geologic units such as craters, chaos and lineaments. Performing realistic radiative transfer modelling on these observation will allow to understand the impact of the physico-chemical processes through the characterization of the ice microphysics. The main questions we wish to investigate are:

What is the true composition of the surface at these locations and how to selected the best chemical compounds among the many suggested? It is clear that such composition is expected to vary within a single observation but also from one observation to another. Moreover, the real composition of the

surface is certainly very complex when reaching very local scales. Can we differentiate different compounds with close chemical composition and approximate a general surface composition from these observations? If so, how many compounds are required to properly reproduce the data by correctly integrating the associated uncertainties?

Are there any other compounds that have not been previously suggested but would produce similar or even better fits to the data? For instance, Ammonia have been quickly suggested to be a potential cryovolcanic liquid (Kargel, 1992) producing thick lobate flows attributable to ammonia-water volcanism. If so, (Kargel, 1992) predicts that a large quantity of ammonium sulfate should have precipitated. The magnesium sulfate largely invoked by previous studies is not stable in aqueous ammonia solution so this would produce areas undersaturated or enriched of either magnesium or ammonium sulfate, implying distinct chemical reservoirs (Kargel, 1992). Recent laboratory data made by (Fastelli et al., 2022) provide reflectance spectra of ammonium sulfates under Europa's surface condition that can help investigate this potentiality.

What is the ice microphysics and how does it vary within a particular geological units? Can we accurately constrain the volume abundance, grain size and surface roughness and is there any spatial correlation with the geomorphological structures? Linking the ice microphysics to the identified structures can provide key answers on the processes involved. How does the composition and grain size vary between the lineaments and the surrounding terrain? How does it vary between two lineaments? What are the ice properties within and outside the craters?

Can we target observation sites of interest for future ESA/JUICE and NASA/EuropaClipper missions? Although the Galileo/NIMS data limit our investigations (low SNR, low spectral resolution, small wavelength-range coverage) can we highlight singular microphysical properties which may reflect active geological processes or testify to the habitable nature of the moon? The study of the surface remains the best window to study the ocean's composition, a fine microphysical analysis of the surface will help at identifying the best areas for future observations by better instruments.

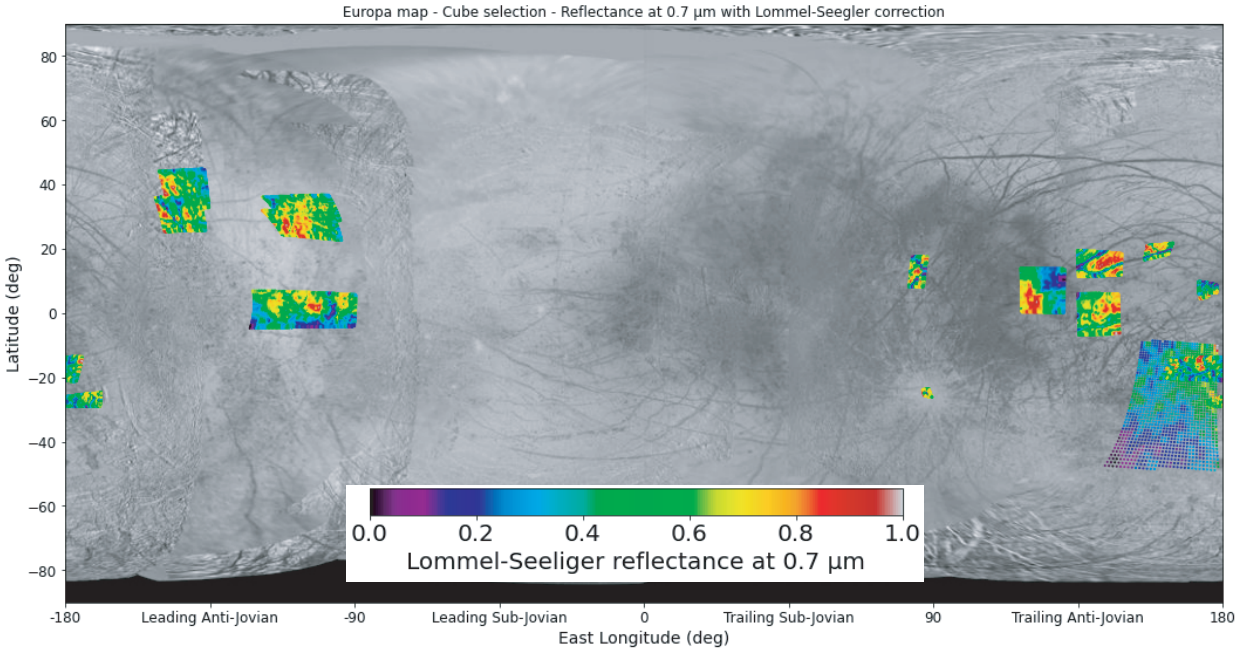

Figure 3.28: Examples of several Galileo/NIMS observation at higher spatial resolution (between 1 and 20 km per pixel). The color represents the reflectance at 0.7 μm (visible wavelength) corrected for the photometric effects with the Lommel-Seeliger law. The background global map of Europa is from the USGS (https://astrogeology.usgs.gov/search/map/Europa/Voyager-Galileo/Europa_Voyager_GalileoSSI_global_mosaic_500m) derived from Galileo and Voyager images, shown in cylindrical projection with a resolution of 500 m.

Chapter 4

Selection of chemical species for Europa's surface using Galileo/NIMS

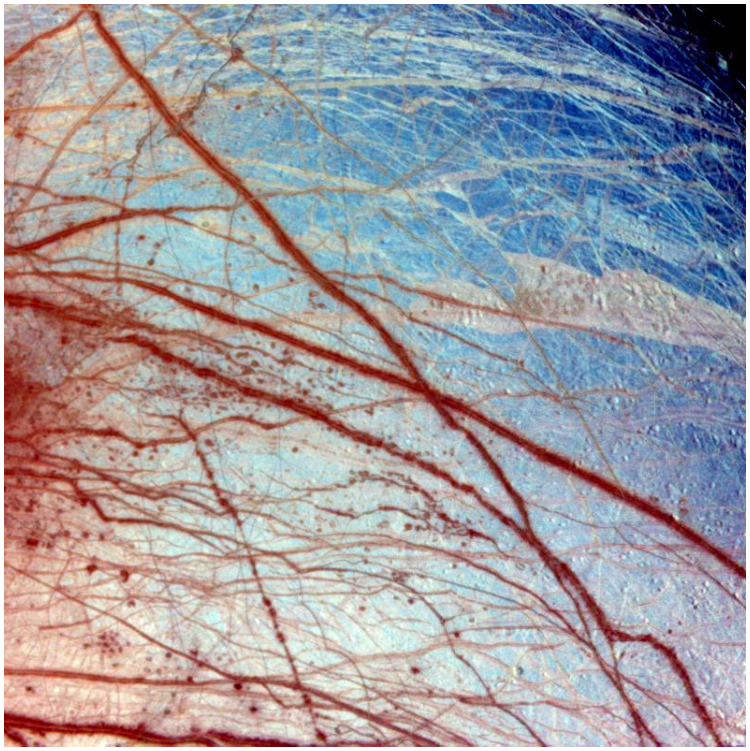

False color images of Minos Linea region on Europa (45N, 221W) seen by the NASA's Galileo spacecraft. The spatial resolution is between 1.6 and 3.3 kilometers per pixel. Triple bands, lineae and mottled terrains appear in brown and reddish colors indicating non-ice materials. Icy plains are shown in shades of blue. Credit: NASA/JPL/University of Arizona.

This chapter focuses on the question of the selection of the best chemical compounds for Europa's surface characterization. We investigated the possibility of using Galileo/NIMS data to discriminate among the chemical compounds proposed so far in the literature and to conduct a study of the micro-physical properties of the surface. To do so we combine the spectro-photometric model of Hapke (see sec. 1.2.3) with a robust inversion method (see sec. 2.6) to test for the first time all combinations of 3, 4 and 5 chemical compounds among 15 relevant candidates. The method, results and interpretations are presented in the following article Cruz-Mermy et al. (2023):

G. Cruz Mermy, F. Schmidt, F. Andrieu, T. Cornet, I. Belgacem, N. Altobelli. Selection of chemical species for Europa's surface using Galileo/NIMS. https ://doi.org/10.1016/j.icarus.2022.115379.

Selection of chemical species for Europa's surface using Galileo/NIMS

G. Cruz Mermy[a,*], F. Schmidt[a,b], T. Cornet[c], I. Belgacem[d], N. Altobelli[d]

[a] *Université Paris-Saclay, CNRS, GEOPS, 91405, Orsay, France*
[b] *Institut Universitaire de France (IUF)*
[c] *Aurora Technology BV for ESA*
[d] *European Space Agency (ESA), European Space Astronomy Centre (ESAC)*

Abstract

Europa's surface shows evidence of active resurfacing which can be explained by either endogenic or exogenic processes. Apart from water ice, several compounds have been proposed to account for the potential complex chemistry that could take place if a connection with the subsurface salty ocean would occur. Previous spectroscopic studies that investigated the surface composition were limited by the number of compounds to consider due to the unavailability of laboratory measurements. We now have access to optical constants and laboratory spectra of synthetic chemical compounds such as hydrated sulfates and chlorinated salts under Europa's surface conditions.

In this study, we test for the first time the relevance of 15 potential endmembers on a Galileo/NIMS observation of a dark lineament of the Trailing Anti-Jovian hemisphere using a realistic radiative transfer modelling and a robust Bayesian inference framework. We consider an intimate mixture of 3, 4 and 5 endmembers and perform a fitting procedure on all possible combinations among the list of 15 compounds in the 1.0 - 2.4 μm spectral range. At the end, 5000 combinations have been tested and analyzed. The parameters we are fitting for are the surface roughness, the volumetric abundances and the grain size. Given the fact that NIMS noise level and absolute calibration are uncertain, we have distinguished two scenarios: assuming a pessimistic signal-to-noise ratio (SNR) of 5 and an optimistic SNR of 50. For each scenario, we use several criteria to highlight the contribution of each endmember and thus identify the most relevant compounds.

We first show that no combinations using only 3 endmembers are able to accurately reproduce the observation. Then, when considering 4 and 5 endmembers together and assuming the SNR=50, there is 21 and 153 combinations that evenly reproduce the observation. From this result, we discuss the relevance of each endmember using criteria such as the Root-Mean-Square (RMS) deviation of the best-fits, the spectral contribution at each wavelength, the occurrences distribution of the selected best-fits and the numerical abundances retrieved by the fitting procedure. By grouping criteria together, we show that only sulfuric acid octahydrate and water ice appear as essential compounds. Then, hydrated sulfates are in general preferred over others compounds. This result is only valid for a lineament of the Trailing Anti-Jovian hemisphere and can be possibly extended to other lineaments in the same hemisphere. However, we show that chlorinated salts but also ammonium sulfate mascagnite ($(NH_4)_2SO_4$), sodium chloride (NaCl) and even magnetite (Fe_3O_4) are not excluded, their contributions from the selected criteria are just less pronounced than hydrated sulfates. Nevertheless, it is clear that it is not possible to correctly distinguish between these endmembers, and even less between endmembers with similar chemical composition, at these wavelengths. We therefore propose for future investigation to either consider a mixture

*Corresponding author
Email address: guillaume.cruz-mermy@universite-paris-saclay.fr (G. Cruz Mermy)

Preprint submitted to Icarus *December 28, 2022*

that would include only one representative of each chemical compound, rather than using all possible endmembers and overfitting the data.

1. Introduction

The surface of Europa is one of the youngest in the solar system. The great diversity of morphologies observed (Greeley et al., 1998) quickly raised the question of the processes responsible for this active resurfacing. The Jovian moon is believed to hide a global liquid water ocean under its ice crust (Pappalardo et al., 1999) which led to the assumptions of exchanges between the surface and the putative subsurface ocean through cryovolcanism and diapirism events. In addition, Europa is exposed to intense space weathering due to the continuous bombardment by electrons and ions from Jupiter's magnetosphere (Carlson et al., 1999) altering the surface by radiolysis. This strongly affects the surface composition as evidenced by the trailing hemisphere which appears darker and redder than the leading hemisphere (Trumbo et al., 2020). The surface therefore appears as the key witness of these internal and external processes. Its characterization is essential to our understanding of Europa over geological times but also of its current habitability.

Our understanding of surface composition has increased significantly mainly through reflectance spectroscopy. First, provided by ground-based telescopic observations, the water absorption bands and their similarity to Europa's spectra were identified. Then, orbital telescopes and spacecrafts (Voyager, Galileo) confirmed the presence of water ice and noticed the unusually broad absorption on the trailing hemisphere pointing toward a potential mixture of water ice and other minerals. Finally, using linear mixture models allowed the detection of several chemical species such as hydrated sulfuric acid (Carlson et al., 1999, 2005) or hydrated sulfates (McCord et al., 1998; Dalton, 2007). Comparison between Galileo Near Infrared Mapping Spectrometer (NIMS) spectra and hydrated chlorine salts spectra acquired from laboratory measurements have also shown similarities (Hanley et al., 2014). Using these spectra, recent studies have shown the relevance of including hydrated chlorine salts in linear mixture model (Ligier et al., 2016; King et al., 2022). Hereafter, we will use the term "endmember" to define a particular chemical compound present in the mixture.

Linear spectral fitting or band depth analysis are great tools to highlight the presence of a compound or a set of species showing chemical similarities. However, to characterize the surface microphysics, such as average grain size, macroscopic roughness, porosity and endmember abundances which are highly degenerated with each other (Mishra et al., 2021a), it is necessary to use a realistic radiative transfer model. Additionally, non-linearity due to grain size is a real limitation of the previous approach. Non-linear radiative transfer, for instance (Hapke, 1993; Douté and Schmitt, 1998), integrates the highly non linear effects of the light path within the regolith due to scattering, which promotes a better estimation of the physical properties. Recent studies using such radiative transfer model with NIMS and Juno/JIRAM observations (Mishra et al., 2021b,a) have shown deeper insights into Europa's surface composition. However, radiative transfer models require optical properties of endmembers acquired in relevant temperature and pressure conditions which greatly limits the number of species that has been considered so far. Fortunately, more and more laboratory spectra of relevant chemical species for icy planetary bodies are available. From an observation spectra and knowing the average grain size and the observation geometry, one can easily derive optical constants using a radiative transfer model (Shkuratov et al., 1999). This approach should be considered as a reasonable approximation, as proposed by Douté et al. (2007) and Andrieu et al. (2018), even if less precise than laboratory experiments. Still, this approach is the only one that allows to extend the list of chemical species to be considered.

In this study, we propose to test a significant number of chemical compounds using a realistic radiative transfer model (Hapke, 1993) in a Bayesian inference framework. Bayesian approaches are more and more common in planetary studies (Fernando et al., 2013; Schmidt and Fernando, 2015; Fernando et al., 2016; Schmidt and Bourguignon, 2019; Belgacem et al., 2020, 2021; Mishra et al., 2021b,a; Harrington et al., 2022; King et al., 2022) due to their efficiency at constraining the model parameters and integrating the associated uncertainties. The approach is intended to be exhaustive so that all endmembers are equally tested. We include all relevant species for which the optical constants were available and added several others by estimating their optical properties from laboratory spectra. Thus, for the first time, we propose to test all potential combinations of 3, 4 and 5 endmembers that include crystalline and amorphous water ice, sulfuric acid-octahydrate, hydrated sulfates, hydrated chlorine salts and pure minerals such as magnetite, sodium chloride and ammonium sulfate for a total of 15 endmembers. We apply this framework on a NIMS spectrum of a dark lineament of the trailing Anti-Jovian hemisphere, which is usually a difficult case to fit due to low albedo.

A major limitation in using infrared spectroscopy data from the NIMS instrument is related to the calibration and noise level uncertainties. A rough estimate of the signal-to-noise ratio of Galileo data is between 5 and 50 (Mishra et al., 2021a). We will prove that with such a flexible constraint on the SNR, many endmembers combinations are acceptable and produce similar adjustements to data. We perform radiative transfer inversion considering the lowest possible SNR (up to 10% uncertainty on the data). We show with one comparison case that considering a higher SNR of 50 produces similar best-fit. With the high number of combinations and therefore results, we use proxies to highlight contributions from each endmember. We show that using the Root-Mean-Square (RMS) deviation as estimator of the quality of the fit we can interpret the results within two distinct scenarios : when considering a pessimistic SNR of 5 or an optimistic SNR of 50. Specific proxies are used as selection criteria in each scenario. The NIMS data and the optical properties of the endmembers are described in Section 2, the forward radiative transfer model, the Bayesian framework and the selection criteria are described Section 3. We discuss the results for the endmembers selection in Section 4.

2. Data selection

2.1. NIMS data

We use data acquired by NIMS (Near Infrared Mapping Spectrometer) during the Galileo Mission. The instrument combines imaging and spectroscopic methods to produce hyperspectral cubes of the Jovian moons. Using a single plane grating with a uniform line spacing and 17 detectors, it covers the 0.7 to 5.2 μm spectral range. The first two detectors at shorter wavelengths ($0.7 - 1$ μm) have a spectral resolution of about 0.0125 μm while for the 15 others it is nearly constant with a value of about 0.025 μm (Carlson et al., 1992). The spectral bandpass response is expected to be triangular (Carlson et al., 1992) with a full width at half maximum (FWHM) of 0.025 μm. As the mission was designed to perform flybys, the spatial resolution varies greatly from one cube to another, which prevents the use of different cubes acquired over the same geographical area in a unique, integrated, spectroscopic study.

2.1.1. Reference spectrum

We focus here on high spatial resolution cubes so that a spectrum coming from a single pixel does not average information of a too large area, which is more suited for investigating micro-physical properties. Given that not many areas on Europa were observed at high resolution, and

most of them land on the trailing side, we selected an observation of the trailing anti-Jovian hemisphere. It has been shown that the continuous bombardment of electrons and ions from Jupiter's magnetosphere strongly affects the surface chemical composition (Carlson et al., 2005) and such phenomenon is more important on the trailing hemisphere. By targeting the potentially most diverse terrain we can test multiple chemical compounds for the surface characterization with the aim of being able to investigate, in the future, the moon as a whole using the same endmembers selection.

We used the hyperspectral cube "e6e007ci" (fig. 1, top) which corresponds to an observation of the well-known crossing of two dark lineaments: *Rhadamanthys Linea* and *Harmonia Linea* between 16.5 and 21°N latitude, and 155 and 165°E longitude. The spatial sampling is nearly constant with a value of 2.178 km per pixel. The observation geometry is as follows: the incident angle varies between 18.5° and 23°, the emission angle varies between 46.8° and 63.5° and the azimuth angle varies between 69.4° and 95.5° making a phase angle that slightly varies between 51.6° and 57.8°. The expected photometric contribution under such configuration is very low (Labarre et al., 2017) making this observation very interesting for spectroscopic analysis.

The 2498 spectra from this observation are shown Figure 1. From the radiance factor (I/F) map at 0.7 μm and the corresponding spectra one can easily recognize two distinct terrains. The first terrain are what we called "bright" regions in which the reflectance in the visible part of the spectrum is high, between 0.65 and 0.8, and where the characteristic water-ice absorption bands in the infrared at 1.5 and 2 μm are deeper. These regions are located between the lineaments. The second terrain are the "dark" area in which the reflectance at 0.7 μm is generally between 0.5 and 0.65. Such area mainly encompasses the lineaments as evidenced by the reflectance map (Figure 1). Although reflectance between 0.7 and and 1.2 μm is lower than brighter terrains, the reflectance at longer wavelengths and especially within the absorption bands at 1.5 and 2 μm are always higher. This spectral pattern makes the distinction between the two areas even more remarkable, where dark terrain appear brighter than bright terrain beyond 1.3 μm.

From this collection of spectra, we selected our "reference spectrum" for this study from the dark terrains (Figure 1, bottom) of *Harmonia Linea*. This choice is primarily driven by the fact that its spectral behavior seems the most distinct from that of a typical water-ice spectrum, making it ideal to test different chemical compounds. Moreover, the geological context of such spectrum makes it very relevant for our approach as one could expect a link in surface composition between the lineaments and the surrounding surface. After all, even though the absorption bands become more and more asymmetrical when approaching darker terrains, the overall shape of the spectra are fairly homogeneous and do not vary drastically between the two regions so we expect to be able to explain these variations with similar chemical compounds.

At last, it represents a good test to challenge the robustness of our inversion algorithm, since spectra from these darker terrains are usually difficult to fit due to low albedo in comparison with pure water ice.

2.1.2. Noise uncertainty

One of the major advantages of Bayesian inferences approach lies in its ability to correctly integrate the uncertainties associated with the data into the *a priori* information, which will be referred to hereafter as the noise uncertainty σ. We define the signal-to-noise ratio (SNR) as :

$$SNR = \frac{r(1\ \mu\text{m})}{\sigma} \tag{1}$$

With r the reflectance of the continuum at 1 μm measured by NIMS. We choose the value at

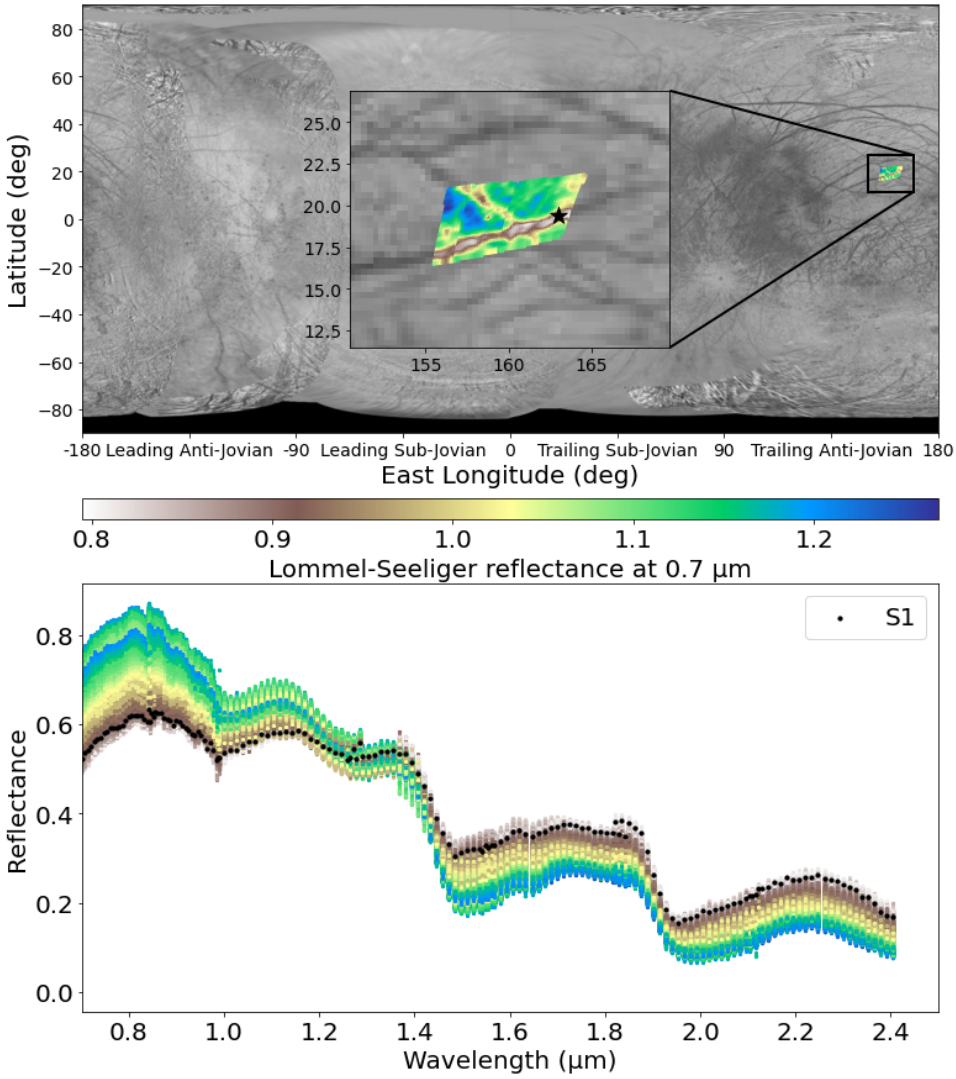

Figure 1: (top) : Europa map with a zoom on cube "e6e007ci" at the Trailing Anti-Jovian hemisphere. The color represents the reflectance at 0.7 μm normalized using the Lommel-Seeliger law (Seeliger, 1884). The location of the "reference spectrum" S1 is shown with a black star. (bottom): The 2498 spectra from the cube. The color code matches the reflectance map so that bright and dark terrains spectra as recognizable. The selected spectrum S1 is shown in black.

1 μm of the reflectance in the continuum as a reference because it is the best constrained portion of the spectra. In our case, the noise uncertainty is related to the NIMS instrument and may includes thermal noise, detector current noise and radiation noise (Carlson et al., 1992). In addition, there is an uncertainty on the absolute calibration of the NIMS instrument which can reach up to 10% (Carlson et al., 1992, 2005). A more recent study suggest an SNR between 5 and 50 (Mishra et al., 2021a). The SNR can vary drastically from one observation to the other, and a precise noise estimation is always very difficult to obtain. One approach is to estimate the noise level from the residuals of the fitted model (Mishra et al., 2021b), but this strategy is model dependent. Also (Mishra et al., 2021b) estimated a large SNR range within one single hyperspectral cube which seems unlikely. This finding forces us to be cautious when analyzing NIMS data. This is why we focus our approach on two distinct axes: a pessimistic scenario in which we expect up to 20% uncertainties on the data, equivalent to a SNR of 5 ($\sigma = 0.116$) and an optimistic scenario in which the SNR is up to 50 ($\sigma = 0.0116$). These values of σ are discussed in later sections for both scenarios (see sec.4.3 and sec.4.4) scenario.

2.2. Spectral library

The key dataset of this approach are the optical constants of the chemical compounds considered, which we will call "endmembers" hereafter (Figure 2). A significant number of potential endmembers have been proposed in the literature to explain Europa's surface composition using water ice and contaminants such as hydrated sulfuric acid (Carlson et al., 2005) or a variety of hydrated salts (McCord et al., 1998; Dalton, 2007; Hanley et al., 2014). The list of endmembers we consider in this study, comprising species from these different chemical groups, is given in Table 1. The library includes water ice in both crystalline (H_2O_{cr})(Schmitt, 2020) and amorphous (H_2O_{am})(Trotta and Schmitt, 2018) phases, hydrated magnesium sulfates: Hexahydrite ($MgSO_4.6H_2O$) and Epsomite ($MgSO_4.7H_2O$)(Dalton and Pitman, 2012), sodium-magnesium sulfate: Bloedite ($Na_2Mg(SO_4)_2.4H_2O$)(Dalton and Pitman, 2012) and sodium sulfate: Mirabilite ($Na_2SO_4.10H_2O$)(De Angelis et al., 2021), hydrated sulfuric acid octahydrate $H_2SO_4.8H_2O$(Carlson et al., 2005), hydrated magnesium chlorate ($Mg(ClO_3)_2.6H_2O$) (Hanley et al., 2014), magnesium perchlorate ($Mg(ClO_4)_2.6H_2O$)(Hanley et al., 2014), sodium perchlorate ($NaClO_4.2H_2O$)(Hanley et al., 2014) and magnesium chloride tetrahydrate ($MgCl_2.4H_2O$)(Hanley et al., 2014) and hexahydrate ($MgCl_2.6H_2O$) (Hanley et al., 2014). We also include pure minerals such as sodium chloride (NaCl)(Querry, 1987), magnetite (Fe_3O_4) (Roush et al., 2021) and Mascagnite ($(NH_4)_2SO_4$)(Fastelli et al., 2022). The last two are not typical endmembers that have been proposed so far for Europa. Although magnetite may be relevant to planetary surfaces, it is introduced here as a dark material to mimic small impurities within the ice. Its extinction coefficient k is high and constant on the spectral range considered here. As for the ammonium sulfate mascagnite, which is not an hydrated sulfate but a non-hydrated mineral, it has not been used in previous spectroscopic studies. It has been suggested that a large amount of ammonium sulfate should be present at the surface in the case of cryovolcanism based on a water-ammonia mixture (Kargel, 1992). If so, the non-stability of ammonia (NH_3) in aqueous $MgSO_4$ solution (and vice versa) implies that some regions will be NH_3-saturated (and depleted in magnesium sulfate) or NH_3-undersaturated (and enriched in magnesium sulfate) and that distinct chemical reservoirs exist (Kargel, 1992). It therefore seems appropriate to include this compound in this study. Moreover, its relevance lies in its spectral behavior where its extinction coefficient shows absorption features at specific wavelengths consistent with NIMS spectra (1.3, 1.6 and 2.1 μm), in addition to being a sulphate compound as for other types of sulfates endmembers proposed so far.

For most endmembers, refractive indices were available from online database (Schmitt et al.,

Endmember	Name	Reference
H_2O(Cr) (140K, refractive indices)	Crystalline water ice	(Schmitt, 2020)
H_2O(Am.) (38K, refractive indices)	Amorphous water ice	(Trotta and Schmitt, 2018)
$MgSO_4.6H_2O$ (120K, refractive indices)	Magnesium sulfate : Hexahydrite	(Dalton and Pitman, 2012)
$MgSO_4.7H_2O$ (120K, refractive indices)	Magnesium sulfate : Epsomite	(Dalton and Pitman, 2012)
$Na_2Mg(SO_4)_2.4H_2O$ (120K, refractive indices)	Sodium magnesium sulfate : Bloedite	(Dalton and Pitman, 2012)
$Na_2SO_4.10H_2O$ (100K)	Sodium sulfate : Mirabilite	(De Angelis et al., 2021)
$H_2SO_4.8H_2O$ (77K, refractive indices)	Sulfuric Acid Octahydrate	(Carlson et al., 2005)
$Mg(ClO_3)_2.6H_2O$ (80K)	Magnesium chlorate	(Hanley et al., 2014)
$Mg(ClO_4)_2.6H_2O$ (80K)	Magnesium perchlorate	(Hanley et al., 2014)
$MgCl_2.4H_2O$ (80K)	Magnesium chloride tetrahydrate	(Hanley et al., 2014)
$MgCl_2.6H_2O$ (80K)	Magnesium chloride hexahydrate	(Hanley et al., 2014)
$NaClO_4.2H_2O$ (80K)	Sodium perchlorate	(Hanley et al., 2014)
NaCl (80K, refractive indices)	Sodium chloride	(Querry, 1987)
Fe_3O_4 (refractive indices)	Magnetite	(Roush et al., 2021)
$(NH_4)_2SO_4$ (100K)	Ammonium sulfate: Mascagnite	(Fastelli et al., 2022)

Table 1: Optical constant dataset of endmembers used in this study. Data are plotted in Figure 2

2017) or within the literature (Querry, 1987; Dalton and Pitman, 2012; Roush et al., 2021). Other compounds such as Mirabilite ($Na_2SO_4.10H_2O$) (De Angelis et al., 2021), Mascagnite ($(NH_4)_2SO_4$) (Fastelli et al., 2022), and hydrated chlorine salts (Hanley et al., 2014) were available as reflectance spectra at a given temperature. For these data, we derive the refractive indices using the Shkuratov model (Shkuratov et al., 1999). It is an analytical radiative transfer model that depends only on four parameters: the filling factor q, the grain-size S, and the optical constants $n + ik$. The main advantage is that it gives an analytical formulation of k knowing the reflectance, q, S and n. The filling factor q was set at 0.5 which corresponds to the typical porosity of a granular medium. The grain size S and the refractive index n are known from laboratory measurements. The cross-compatibility of our forward model described in 3.1 with this method of evaluating k was ensured by re-generating the reflectance spectra that were used to derive the optical constants using our forward model at the same grain size as the experimental dataset. The real and imaginary part of the refractive indices for each endmember is shown Figure 2. Unfortunately, all these laboratory datasets do not cover the entire spectral range of NIMS. We choose to focus on the intersection of all datasets wavelengths range, which limits our study to the 1.0119-2.5 μm range but allows to test all potential combinations of endmembers.

3. Methods

Spectral fitting analysis using a Linear mixing model has been widely used to highlight the presence of chemical species on the surface of Europa (Carlson et al., 2005; Dalton, 2007; Ligier et al., 2016; King et al., 2022). Such approach considers a linear sum of the pure species reflectance, which is only valid in the case of surface areal mixtures within the pixel. It requires laboratory reference spectra obtained under controlled conditions at a specific grain size, which strongly constraints the number of parameters that can be used to describe a surface in the mixture model. Although these methods are great tools to highlight the presence of particular chemical species they do not integrate the highly nonlinear effects of the light path within the planetary regoliths due to scattering. Therefore, to fully understand the surface properties and characterize the ice microphysics, it is necessary to use a realistic radiative transfer model coupled with a robust inversion method.

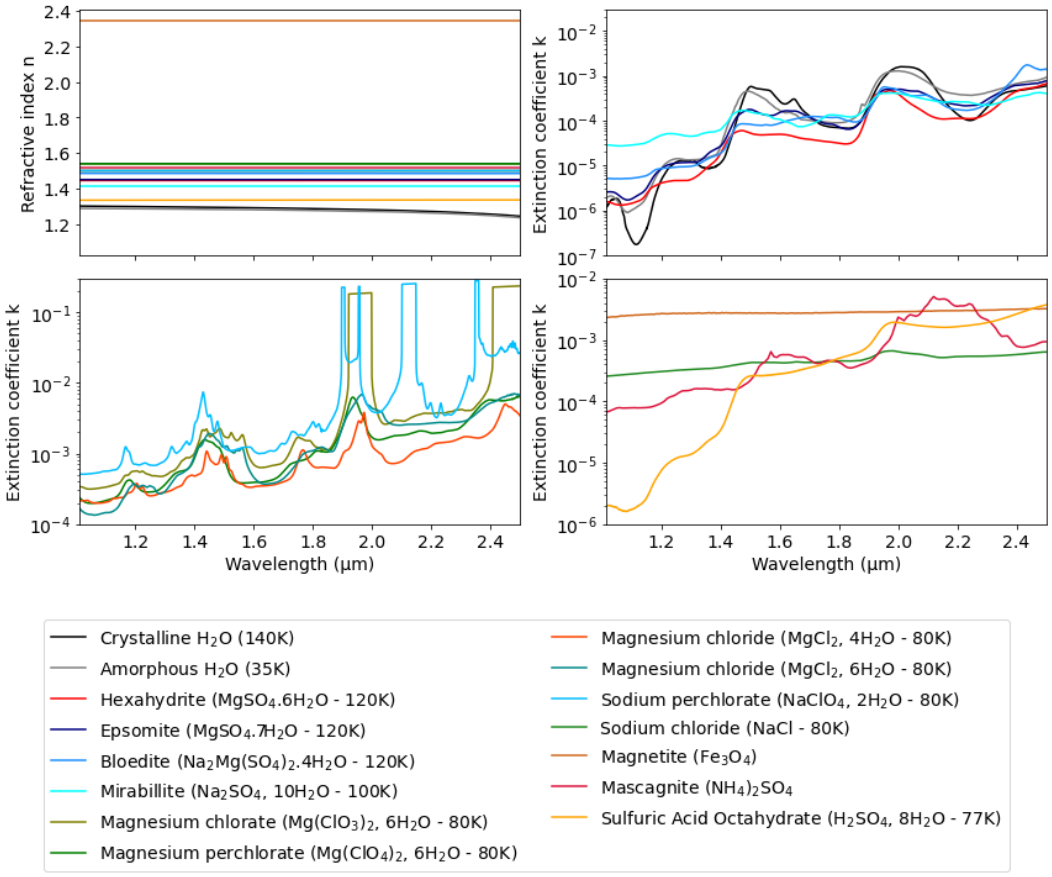

Figure 2: Refractive index n and extinction coefficient k of each endmember considered in this study. Extinction coefficients of water ice and hydrated sulfates (top left panel), magnesium and sodium chlorate, chloride and perchlorate (bottom left panel), sodium chloride (NaCl), magnetite (Fe_3O_4), mascagnite ($(NH_4)_2SO_4$) and sulfuric acid octahydrate (bottom right panel) are plotted separately for clarity. References for each endmember can be found in table 1.

In this study, we use a Bayesian inference framework and a Monte Carlo Markov Chain (MCMC) algorithm. The Bayesian approach are more and more common in planetary studies (Fernando et al., 2013; Schmidt and Fernando, 2015; Fernando et al., 2016; Schmidt and Bourguignon, 2019; Belgacem et al., 2020, 2021; Mishra et al., 2021b,a; Harrington et al., 2022; King et al., 2022) because it gives a complete understanding of the solution in form of probability distribution functions and the associated uncertainties in the entire parameters space. In this Section, we describe the approach of combining the Hapke forward radiative transfer model we use (Section 3.1) and the Bayesian inference framework (Section 3.2) for its application to the selected NIMS reflectance data.

3.1. Forward model

The Hapke model (Hapke, 1993, 2012) has been widely used in planetary sciences to estimate the bidirectional reflectance of airless regolith surfaces. This semi-empirical model is based on the radiative transfer equation (Chandrasekhar, 1960) but several assumptions are made in order to simplify its resolution. First, the model considers that the radiative properties inside a media can be described statistically by using local mean properties of scattering and absorption. It considers the interaction between an incident beam and an isolated particle using the single-scattering albedo (ω) and the particle phase function ($P(g)$). Multiple scattering (Ambartsumian-Chandrasekhar H functions) is handled independently. Moreover, the model integrates the surface scattering contribution with the opposition effect ($B(g)$) seen at low phase angle, and the shadowing function (S), and removes the diffraction contribution from the single scattering. The bidirectional reflectance r at a given wavelength follows (Hapke, 2012):

$$r(\mu_0, \mu, g) = \frac{\omega}{4\pi} \frac{\mu_0}{(\mu_0 + \mu)} \left\{ [1 + B(g)]\, P(g) + H(\mu_0) H(\mu) - 1 \right\} S(\mu_0, \mu, g) \tag{2}$$

Where μ_0 is the cosine of the incidence angle i, μ is the cosine of the emission angle e and g is the phase angle. This expression of the Hapke model does not account for the opposition effect due to coherent backscattering (CBOE) and assumes that multiple scattering is isotropic. This assumption is debatable (Shkuratov et al., 2012; Hapke, 2013; Shkuratov et al., 2013) but the fact that this model can be computed extremely rapidly due to its analytical formulation makes it very adequate for data analysis and massive inversion. The whole formulation details of the model is available in (Hapke, 2012) but we will describe below its main ingredients, relevant to our study.

3.1.1. The single scattering albedo

We consider here that the different particles are mixed homogeneously in an intimate mixture. Thus the light is penetrating through different material particles. An equivalent material has a single-scattering albedo ω defined as a volume average of different species in the mixture:

$$\omega_{vol} = \frac{\sum_i M_i \sigma_i Q_i}{\sum_i M_i \sigma_i} \tag{3}$$

Where M_i is the number of particles of a species i per unit volume. This can be converted to a number density fraction (or abundance) X_i following $X_i = M_i / \sum M_i$. σ_i and Q_i are respectively the geometrical cross-section and the scattering efficiency of a particle of type i. The grain radius r_i of a type i particle not only appears in its geometrical cross section $\sigma_i = \pi r_i^2$, but also in the scattering efficiency Q_i, along with its complex optical index $n_i + \mathrm{i}k_i$ (Andrieu et al., 2015). This makes the volume-averaged single scattering albedo ω_{vol} one of the key parameters in our model, as it depends on the abundances, the grain-sizes and the absorption coefficients of each species.

3.1.2. The particle phase function

The phase function $P(g)$ describe the angular distribution of the scattered light as a function of the phase angle g. It can be seen as the probability of an incoming photon to be deviated from its incident direction when it interacts with a particle. Here we consider a two-parameters Henyey-Greenstein function (Henyey and Greenstein, 1941) because it has been shown to be representative of a wide variety of planetary regoliths, including icy particles on Europa (Hapke, 2012; Mishra et al., 2021b), expressed as follows:

$$P(g) = \frac{1-c}{2}\frac{1-b^2}{(1+2b\cos(g)+b^2)^{\frac{3}{2}}} + \frac{1+c}{2}\frac{1-b^2}{(1-2b\cos(g)+b^2)^{\frac{3}{2}}} \tag{4}$$

With b being the asymmetry parameter describing the isotropy of the diffusion lobe ($b < 0.5$: larger lobe, $b > 0.5$ narrow lobe) and c the backscattering fraction describing the forward ($c < 0.5$) and backward ($c > 0.5$) behavior of the particles. We use the same particle phase function for each species considered with a value of $b = 0$ and $c = 0.5$ implying that there is no preferential distribution regime. Recent studies on the photometric behavior of Europa's surface (Belgacem et al., 2020) shows that b and c can vary significantly even for two close regions and there is no clear evidence of a preferential scattering regime depending on the location at Europa's surface (trailing or leading hemisphere for instance). Unfortunately, the knowledge of Europa's surface particle phase function parameter at the NIMS wavelengths is not known. This is why we decided to fix the phase function for each species with a median value for b and c.

3.1.3. The macroscopic roughness

The surface roughness is accounted in the Hapke model with the shadowing function S (see eq. 2). It considers that the observed surface is made by a multitude of unresolved facets N, with $N >> 1$, whose orientation follows a probability density function $a(\vartheta, \zeta)$ where ϑ is the zenith angle between the facets' normal and the local vertical direction, and ζ is the azimuthal angle. By assuming that a is uniform according to ζ and considering a Gaussian like distribution of altitudes, Hapke (1984) proposed :

$$a(\vartheta) = \frac{2}{\pi \tan^2 \bar{\theta}} \exp(-\frac{\tan^2 \vartheta}{\pi \tan^2 \bar{\theta}}) \sec^2 \vartheta sin\vartheta \tag{5}$$

With :

$$\tan \bar{\theta} = \frac{2}{\pi} \int_0^{\frac{\pi}{2}} a(\vartheta) \tan \vartheta d\vartheta \tag{6}$$

The angle $\bar{\theta}$ represents the surface roughness and characterizes the distribution of the unresolved facets' orientations. It is also referred as the "mean slope angle".The complete description of the equations leading to the parameter $a(\vartheta, \zeta)$ in the function shadowing function S is present in (Hapke, 1984).

3.2. Bayesian inference framework

We use a Monte Carlo Bayesian inference approach in our model. Bayesian statistics offer several advantages when dealing with a high number of parameters in the forward modelling. First, it ensures that relevant prior information is accounted for in the final inference (Trotta, 2017), in order to discard meaningless results. This approach allows exploring a large parameter

space and looking for non-unique solutions while statistically constraining the model parameters. Second, from the collection of parameters generated by the posterior sampler one can get posterior distributions of each parameter that helps to identify possible correlations between parameters.

We used the radiative transfer model from Equation 2 and adjusted the following unknown parameters (noted θ_i hereafter) :

- The abundances X_i of each endmember i (linked with $\sum X_i = 1$)
- The grain-size diameter D_i of each endmember i
- The macroscopic surface roughness $\bar{\theta}$

The fixed parameters of the model are :

- The optical constants of each endmember $(n_i + ik_i)$
- The particle phase function $(P(g))$
- The observational geometry (incidence, emission, and azimuth angles)

We use the refractive indices listed in Table 1 and illustrated in Figure 2 for the optical constants of each considered species. The observation geometry is assumed to be perfectly known from the NIMS data.

3.2.1. Bayes's theorem

We consider the Hapke model (Section 3.1) as a forward model M described by a set of variable parameters θ_i where i is the dimension index of the parameter space. Let d be the data measurements to fit, in our case the NIMS observation shown fig. 1. Bayes theorem links the conditional probability of the parameter θ_i knowing the data (the posterior probability) to the marginal probability of the same parameter without knowing the data (the prior probability), updating our knowledge on the parameter from the prior to the posterior using the conditional probability of the data occuring given that parameter θ_i is true (the likelihood) (Trotta, 2017):

$$p(\theta_i \mid d) = \frac{p(d \mid \theta_i)p(\theta_i)}{p(d)} \tag{7}$$

Where $p(\theta_i \mid d)$ is the a posteriori probability density function which describe the state of information on the parameters θ_i conditioned on the measurements d. $p(\theta_i)$ is the *a priori* information we have on the parameters, such as the mathematical intervals of definition in which we expect the parameters to fall. $p(d)$ is a normalizing constant, also called the "evidence" or "marginal likelihood" (Trotta, 2017), it ensures that the posterior is normalized to unity and follows:

$$p(d) = \int p(d \mid \theta_i)p(\theta_i)d\theta_i \tag{8}$$

$p(d \mid \theta_i)$ is the likelihood function, also known as the probability of the data d given a value of the parameter θ_i. The likelihood is often noted $\mathcal{L}$ and follows:

$$\mathcal{L}(d \mid \theta_i) = p(d \mid \theta_i) \tag{9}$$

The likelihood function describes the joint probability of the observed data as a function of the parameters of the chosen model. We assumed that the noise within the data is Gaussian and independent, thus the likelihood follows:

$$\mathcal{L} = \sum_{k=1}^{n_\lambda} \frac{1}{\sqrt{2\pi\sigma_k^2}} \exp\left(-\frac{[d_k - M(\theta)_k]^2}{2\sigma_k^2}\right) \tag{10}$$

Where n_λ is the number of data points (in our case, the number of spectral channels in the NIMS spectrum), σ_k is the standard deviation of the data at the k data point, i.e. the uncertainty on the absolute reflectance level, d_k is the data at the k data point and $M(\theta)_k$ is the k-th simulated data point using the forward model M. In our inversion framework $\sigma_k = 0.1 \times r(\lambda_k)$ in agreement with the 10% uncertainties (Carlson et al., 1992). To keep realistic uncertainties for low reflectance data we set a minimum value of $\sigma_k = 0.01$.

3.2.2. Prior distribution

The prior function $p(\theta_i)$ in Equation 7 describes the *a priori* knowledge on the parameters we are fitting for, i.e. the physical boundaries of each parameter. Commonly, uniform distribution are preferred because they are uninformative, which leads the data to drive the solution (Mishra et al., 2021b).

For the abundances parameter X_i, we used a Dirichlet prior defined from X_i' uniform distribution over [0,1], which also describes the state of no information for n_p linked parameters:

$$p(X_i) = Dir(X_i) = \begin{cases} \frac{\log(X_i')}{\sum_i^{n_p} X_i'}, & X_i \in [0,1] \\ 0, & otherwise \end{cases} \tag{11}$$

For the grain size, we use a log-uniform distribution :

$$p(\log(D_i)) = \begin{cases} \frac{1}{\log(D_{max}) - \log(D_{min})}, & \log(D_i) \in [\log(D_{max}), \log(D_{min})] \\ 0, & otherwise \end{cases} \tag{12}$$

The lower boundary D_{min} was set to 10 microns in order to cope with the geometric optics regime, which implies that the grain size must be greater than the infrared wavelength range explored (1-2.5 μm domain). The higher boundary D_{max} was set to 10^5 microns in order to explore a large parameter space but also to prevent a too strict constraint on a poorly known *a priori* parameter.

For the macroscopic surface roughness parameter $\bar{\theta}$, we assume a uniform distribution:

$$p(\bar{\theta}) = \begin{cases} \frac{1}{\bar{\theta}_{max} - \bar{\theta}_{min}}, & \bar{\theta} \in [\bar{\theta}_{min}, \bar{\theta}_{max}] \\ 0, & otherwise \end{cases} \tag{13}$$

We set $\bar{\theta}_{min} = 0°$ and $\bar{\theta}_{max} = 45°$ as theoretically expected (Hapke, 1984). Recent photometric studies of Europa's surface in the visible (Belgacem et al., 2020) have shown that the macroscopic roughness ranges from 6° to 27°.

3.2.3. Bayesian posterior sampling

To sample the a posteriori probability distributions we use a Markov Chain Monte Carlo (MCMC) algorithm. The purpose of MCMC algorithm is to use "walkers" that randomly samples the parameter space to create a sequence of different parameters values called a chain. The generation of each element of the Markov chain depends on the value of the previous element, at each steps the posterior probability is evaluated so that the chain converges to a stationary state. One of the key properties of the chain is that its sample density is proportional to the posterior

probability density function (Trotta, 2017), which helps at building the posterior distribution. The choice of the walker (and therefore of the algorithm) is "problem-dependent" as some algorithm will fail to efficiently sample a complex parameter space with non-unique solutions.

We use the Multi-Core Markov-Chain Monte Carlo package (mc3, (Cubillos et al., 2016)), an open-source python library that includes several sampler algorithms, which showed promising results in recent radiative transfer simulations (Harrington et al., 2022). We selected the "DEMC-zs" algorithm with snooker proposal (ter Braak and Vrugt, 2008), which is a differential evolution Markov Chain in which multiple chains are run in parallel independently, and all the past information of each chain is used to generate appropriate jumps in the parameter space. It has been shown that such algorithm outperforms classical algorithms when dealing with non-linear mixed effects models, which is the case in the Hapke photometric model, especially for an intimate mixing scenario. More details about this algorithm can be found in (ter Braak and Vrugt, 2008).

3.2.4. Convergence monitoring: the Gelman-Rubin test

The differential evolution snooker algorithm (ter Braak and Vrugt, 2008) requires to define a number of chains to be built in parallel and a number of samples to be estimate for each parameter. We use 5 chains with a total number of samples of 6×10^5 leading a number of samples per chain of 1.2×10^5 for each combination. This number corresponds to a compromise between a reasonable computation time and a sufficiently large number of samples to allow the exploration of the parameter space. Because the chains are independent, a convergence criterion that monitors both the convergence of each chain (intra-chain), and the overall convergence of the algorithm (inter-chain) must be used. The mc3 library (Cubillos et al., 2016) integrates the Gelman-Rubin test (Gelman and Rubin, 1992), which has such property. At each step of the iterative simulation, a distributional estimate and an estimate of how much sharper this distributional estimate might become if the simulation were continued indefinitely (Gelman and Rubin, 1992) is done, for each individual parameter. In other words, it first discards the period corresponding to the initialisation and the first samples expected to be far away from the solution ("burnin"). Then, it computes the "potential scale reduction factor" R by comparing the current *a posteriori* inter-chain variance estimate $\hat{V}$ to the intra-chain variance W as follows:

$$R = \sqrt{\frac{\hat{V}}{W}} \tag{14}$$

The potential scale reduction R must tend toward unity when the convergence has been reached. This implies that evaluating more samples will not change the *a posteriori* distribution of the parameters. Commonly it is considered that values close to 1.01 indicates convergence and that values above 1.2 for any of the model parameters should indicate divergence (Gelman and Rubin, 1992) or requires a longer burnin period. In the mc3 library the Gelman-Rubin test is computed every 10% of the MCMC exploration. We included a threshold to stop the simulation if the Gelman-Rubin test is below 1.01 for each parameter and the fraction of the total samples evaluated is at least 50% of the total amount expected, i.e. 3×10^5 samples after the burnin period. We chose a burnin period of 5×10^3 samples.

3.2.5. Best-fit

From the chain, we selected the best fit, that is the spectra with the maximum likelihood within our chains (noted $M_{best-fit}$), corresponding to the set of parameters $\theta_{best-fit}$.

3.3. Selection criteria

From the inversion of various combinations of endmembers, we need to evaluate the quality of the fit and also the relevance of the endmembers. Hereafter are described the proxies for that purpose.

3.3.1. Best-fit RMS

Since the noise in NIMS data is not well characterized, we evaluate the best fit by a simple root-mean square deviation (RMS) as follows:

$$RMS = \sqrt{\frac{\sum_{\lambda} \left(d - M_{best-fit}\right)^2}{N_{wvl}}} \tag{15}$$

Where d is the NIMS observation (reference spectrum), $M(\theta_{best-fit}) = M_{best-fit}$ is the reflectance spectrum generated by the forward model using the set of parameters that maximizes the likelihood in the MCMC algorithm and N_{wvl} is the number of spectral channel, i.e. the number of wavelengths. This RMS has the advantage to be independent of the noise level assumption. If the best fit lies within the acceptable SNR level (0.116 for SNR=5 and 0.0116 for SNR=50), we will consider that the combination is acceptable. Thus, in this exercise of selecting the best compounds, a compound appears to be relevant if it is present in a large number of acceptable combinations.

3.3.2. RMS including/excluding endmember

A simple way to estimate the relevance of an endmember is to compare the RMS with and without the presence of an endmember. If the RMS is smaller with than without, the endmember should be considered as relevant. Also the more the RMS decreases including an endmember, the more its relevance.

3.3.3. Improvement factor

Looking only at the RMS may produce bias in the interpretation because by definition the RMS is averaged over all wavelengths. Thus, the RMS is blind to improvements from some endmembers at specific wavelengths. We propose to quantify the spectral contribution of each endmember at each wavelength by another proxy: the "improvement factor" $\iota(\lambda)$:

$$\iota_n(\lambda) = \frac{\langle \mid d(\lambda) - M_{best-fit}(\lambda) \mid \rangle_{without\{E_i\}}}{\langle \mid d(\lambda) - M_{best-fit}(\lambda) \mid \rangle_{with\{E_i\}}} \tag{16}$$

Where d is the reference spectrum, $M_{best-fit}$ is the best fit, $\langle\rangle$ indicates the average for all combinations with/without endmember E_i and $||$ is the absolute value. This proxy computes the ratio of the average absolute differences between the data and all best-fit when the endmember is considered and when it is excluded, at each spectral channel. By design, values above 1 indicates that including the endmember improves on average the quality of the fit at a specific wavelength while values below 1 shows that the quality of the fit increase when excluding the endmember.

3.3.4. Numerical abundances

A last proxy allowing to discriminate possible endmembers would be to compare the corresponding abundances. Volumetric abundances and grain sizes can be strongly correlated as clearly shown in Figure 11. In addition, due to non-linear effects of the radiative transfer, a high volumetric abundance due to a larger grain size may have a very limited effect on the spectra because

the light-matter interaction would mainly occur within and between the endmembers with smaller grain size. To fully encompass that, we use a proxy more related to the spectral signature: the numerical abundances. The numerical abundance X_{num} of an endmember i is defined as numerical fraction of grain in a unit volume:

$$X_{num,i} = \frac{X_i}{D_i^3} \tag{17}$$

Where X_i is the volumetric abundance, and D_i is the grain size (in meters). To guarantee the sum to 1 we normalize Equation 17 by $\sum_i^n \frac{X_i}{D_i^3}$ where n is the number of considered endmembers. This numerical abundance indicates how the granular medium can be represented for each best fit. An endmember with a high numerical abundance would indicate a medium spectrally dominated by this compound while a low numerical abundance would describe a medium in which the compound is spectrally insignificant. Such indicator describes at the granular scale whether the light-matter interactions are numerous (high numerical abundance) or few (low numerical abundance) for each endmember. Endmembers with numerical abundance $<10^{-4}$ should be considered as negligible in the spectra.

4. Results: endmembers selection

We aim at characterizing the surface composition of Europa using the NIMS data and a realistic radiative transfer model to simulate reflectance spectra, described in Section 3.1. Our Bayesian framework exposed in Section 3.2 allows to efficiently sample the large parameter space of our model, which we extend to a list of 15 potential endmembers (Table 1). Among those many endmembers, we aim at finding an ideal number and combination of endmembers to use, by testing all potential combination of compounds, able to reproduce the observations. As an example, adding one compound in this intimate mixture adds two dimensions in the parameter space (one for its abundance, one for its grain size) and leads to higher computation time. We seek to test these combinations with a reasonable computation time but also to respect the principle of Ockham's Razor for which the simplest sufficient assumptions should be preferred. In our approach, this means that adding more and more compounds could definitely improve the fit of the observations, at the expanse of the risk of overfitting the data with an over-complex solution. If a similar fit can be explained with less parameters, then it is preferred. Hence, we limit our study by testing mixtures of 3, 4 and 5 endmembers. At last, the significantly high uncertainty in the data (which is up to 10% (Carlson et al., 1992, 2005)) forces us to be cautious. We therefore discuss the results using a pessimistic scenario with a low SNR of 5 (see subsec. 4.3), and an optimistic scenario with a high SNR of 50 (see subsec. 4.4).

4.1. Compounds combination

The full number of possible combinations is estimated by the k-combinations of n endmembers:

$$\binom{n}{k} = \frac{n(n-1)...(n-k+1)}{k(k-1)...1} = \frac{n!}{k!(n-k)!} \tag{18}$$

In our case $n = 15$ endmembers, and $k = 3, 4, 5$ when considering 3, 4 or 5 endmembers in the combination. This leads to 3 cases that we will refer to hereafter as:

- comb3: 455 combinations for the 3 compounds case with a total of 7 free parameters for each combination (3 abundances, 3 grain sizes, 1 roughness)

- comb4: 1365 combinations for the 4 compounds case with 9 free parameters (4 abundances, 4 grain sizes, 1 roughness)
- comb5: 3003 combinations for the 5 compounds case with 11 free parameters (5 abundances, 5 grain sizes, 1 roughness)

A typical MCMC inversion considering 5 compounds and 6×10^5 samples performed in parallel on a 28 dual core E5-2690 V4 at 2.6GHZ (56 threads) server lasts up to 5 minutes. Adding more compounds to the mixture or doing this thorough exercise on every NIMS spectra would significantly increase the computation time. Our strategy is therefore to investigate all these endmembers combinations on a reference NIMS spectra, which will then allow us to decipher the appropriate endmembers to use for future NIMS inversions at larger scales. Even with this single test combination, the number of simulated spectra to analyze represents $455 + 1365 + 3003 = 4823$ combinations. Such analysis on every single spectra of a NIMS cube and their posterior distribution or pairwise correlation therefore falls beyond the scope of the present study, for which we would rather use relevant criteria to discard or retain important endmembers.

All the spectroscopic studies carried out on Europa's surface show that water ice is the essential compound used to reproduce the observation (Hansen, 2004; Filacchione et al., 2019; Mishra et al., 2021a; King et al., 2022). Testing combinations that exclude this compound could appear pointless. Nevertheless, this seems relevant to us for three reasons. First, this study is intended to be exhaustive so that the tests excluding water ice contain useful information to investigate the role of other endmembers. Second, most of the other endmembers are hydrated materials so that their spectral behavior is not so far from a water ice spectrum, considering the non-linear effects of the radiative transfer one might reproduce the observation using only very little water ice or not at all, and this needs to be investigated as well. Third, the selected observation as reference spectrum lands within the dark lineaments of the trailing hemisphere, an area in which water ice could be not necessarily needed to best fit the spectroscopic data.

4.2. Convergence verification

Results of the Gelman-Rubin test for all comb3, comb4 and comb5 cases, indicating the convergence of the algorithm, are shown on Figure 3. The vast majority of the parameters are below or close to the 1.01 value, as shown by the very high density of points. This density decreases slowly between 1.01 and 1.1, which still gives reasonably acceptable solutions. Few points are close to 1.2, which tends to indicate that a longer burnin period would be required although the chain is close to being considered stationary. This also indicates that in most situations the algorithm has sufficiently explored the parameter space with the available samples, and that any addition of samples to the chain marginally improve the posterior distribution of the parameters. This gives greater confidence on the use of the best fit for the endmembers comparisons.

4.3. Pessimistic SNR

In this section, we will assume a pessimistic SNR of 5 which corresponds to the highest uncertainty on the data (20% of the reflectance value in the continuum at 1 μm).

A typical result using a combination of 5 endmembers is shown in Figure 11 (top). At this low SNR, the noise is high and the uncertainties are large in the parameter space. An interesting result is that all set of combinations are able to fit the reference spectrum, at the given noise level. Instead of studying the full distribution of the parameters, for all combinations, we will focus on the best fit out of the Markov Chain. Next sections will discuss all best-fits in order to pick the most useful endmembers.

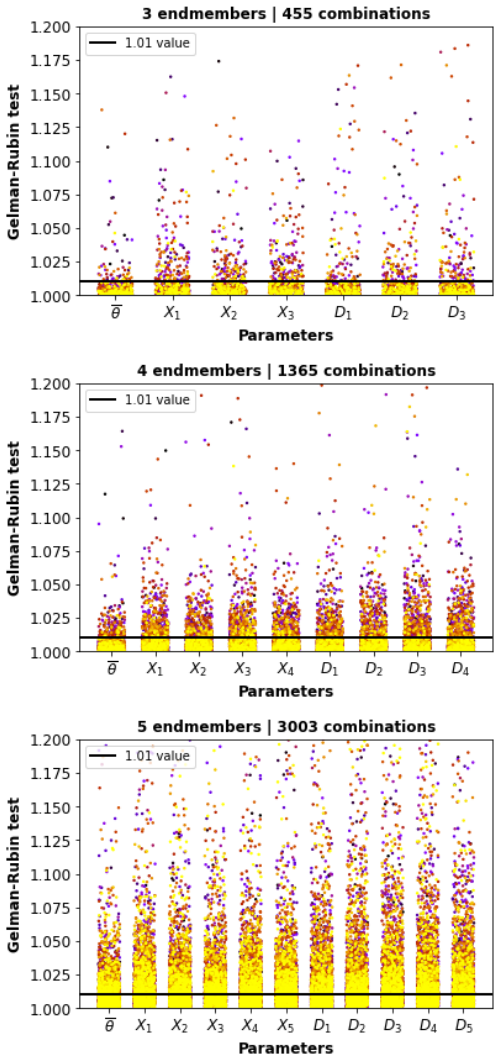

Figure 3: The Gelman-Rubin test for each parameter using a combination of 3 (top), 4 (middle) and 5 (bottom) endmembers. Results are artificially spread horizontally for clarity. The colours are not informative and only represent all combinations, from the first (yellow) to the last (black) and thus indicate that the vast majority are close to or below the 1.01 threshold. The horizontal red line correspond to the value of 1.01 as convergence indicator.

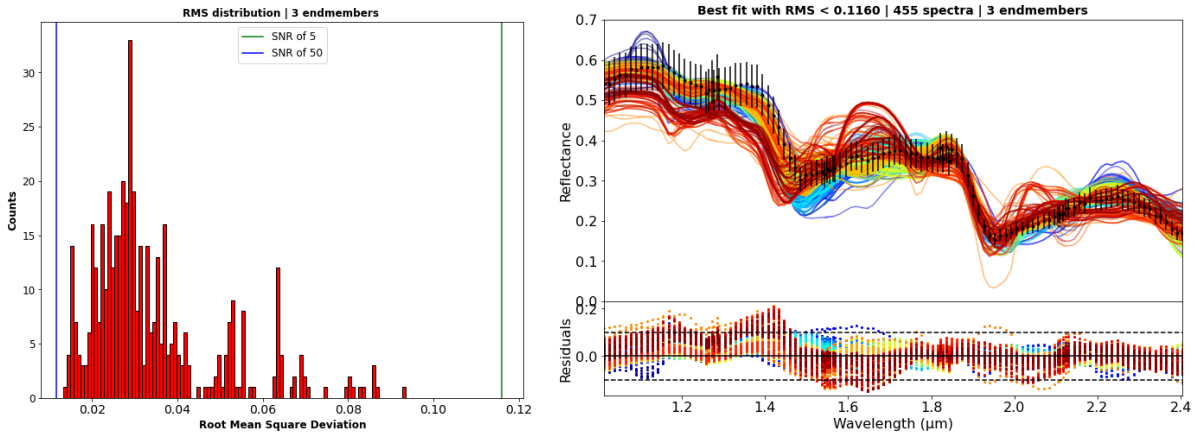

Figure 4: Best-fit RMS analysis of all combinations using 3 endmembers (comb3). (left) : Distribution of all 455 best-fits RMS. The vertical lines indicate the RMS threshold for a SNR of 5 (green) and 50 (blue). (right) : All best-fits (in colour) to the NIMS observation (black dots) for the corresponding combinations that pass the RMS threshold of 0.116 (SNR of 5, 20% uncertainty). Each color represent a single combination.

4.3.1. Best-fit RMS

We compute the RMS using Equation 15 for each best-fit of each case and we look at the RMS distribution (see Figures 4, 5, 6, left). The value of the reflectance at 1 μm in the continuum is 0.58. Using this value we compute a RMS threshold beyond which the best fits are rejected when considering the SNR of 5. This gives a RMS threshold of 0.116 (see figs. 4, 5, 6, left, green vertical line).

A first surprising result is that all of the best fits of each combination of 3, 4 or 5 endmembers are below this RMS threshold. A naive interpretation of this result would lead to the acceptance of all the chemical species tested here because all of them are present in the combinations. However, when looking at all these best fits (see Figures 4, 5, 6, right), one can easily realize that some spectra are very far from the data, despite passing the RMS threshold on average. In addition, residuals are far from typical independent random noise. Nevertheless, the presence of some endmembers in particular combinations seems to produce very good fits as evidenced by the RMS distributions. Assuming a pessimistic scenario on the SNR does not directly highlight the best endmembers. Thus, we will discuss here several proxies to classify the relevance of each endmember.

4.3.2. RMS including/excluding endmember

With a pessimistic scenario on the SNR all combinations of endmembers achieve a best fit that has an acceptable RMS but some endmembers may be more important than others. A first proxy of the contribution of an endmember E_i is to compare (i) all best-fit RMS when the endmember is included ($RMS_{with\{E_i\}}$) with (ii) all best-fit RMS when it is excluded ($RMS_{without\{E_i\}}$). We compare the RMS minima min $\left(RMS_{with\{E_i\}}\right)$, min $\left(RMS_{without\{E_i\}}\right)$ and the RMS averages $< RMS_{with\{E_i\}} >$, $< RMS_{without\{E_i\}} >$ for all 15 endmembers. As an example, for comb3, E_1 (crystalline water ice) is present in 91 combinations and absent in 364 combinations, the average and the minimum of those RMS are considered here. The minimum is relevant to distinguish the best case of combination including/excuding an endmember. The average allows the comparison to be made on all data which is statistically more robust.

Those comparisons are shown Figure 7. First, one can see that the RMS profiles look quite similar for each endmember when considering comb3, comb4 an comb5. In general, the RMS values

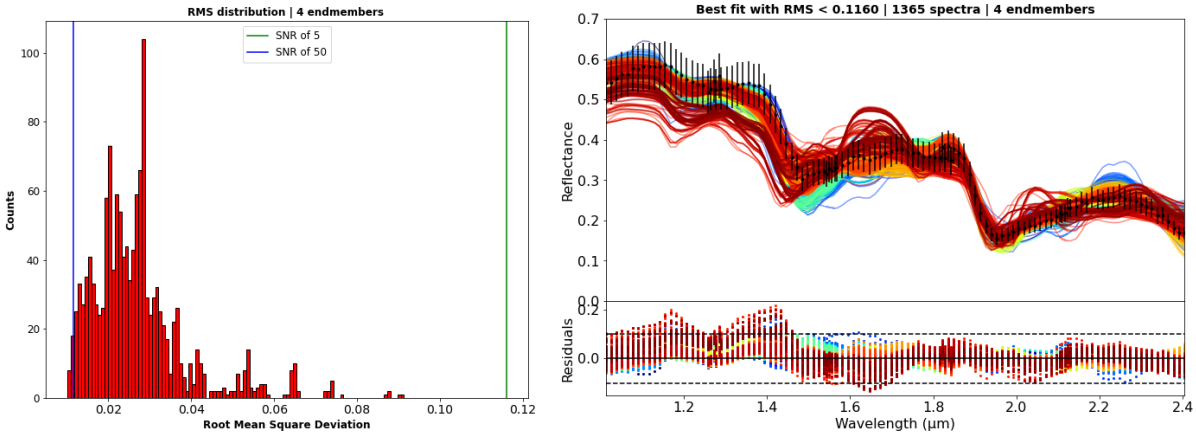

Figure 5: Same as Figure 4 but for a mixture of 4 endmembers (comb4) .

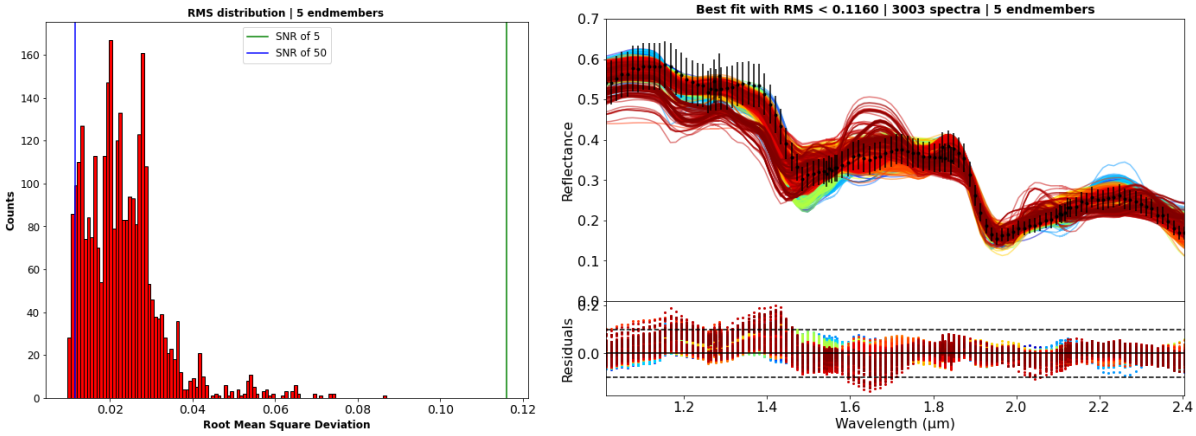

Figure 6: Same as Figure 4 but for a mixture of 5 endmembers (comb5)

decrease as more endmembers are considered in the mixtures, which is an expected result. However, interestingly, for each endmember, there seems to be always at least a combination reaching very low minimum RMS (purple points). Differences between minimum RMS per endmember are very small. Moreover, when looking at the minimum RMS when the endmember is excluded (yellow points), one can see that for most endmembers there is an acceptable combination excluding it and allowing to reach a very low RMS. The average RMS of water ice (both crystalline and amorphous), sulfated compounds (except for Mirabilite $Na_2SO_4.10H_2O$) and Sulfuric Acid Octahydrate (SAO) is lower when included in all 3 cases. Whereas magnetite (Fe_3O_4) and the chlorinated salts shows the opposite pattern. This clearly distinguish two populations: the sulfated compounds and the chlorinated salts. This pattern is not reproduced when looking at the minimum RMS. Of course we cannot compare the 3 cases in similar ways for the minimum RMS because there is at least one combination producing the lowest RMS and we expect that the endmembers used for such combination will have a lower RMS than when they are excluded. And so, going from comb3 to comb5 will result in more endmembers in such configuration. This being, and considering the 3 cases together, only crystalline water ice and SAO have a lower minimum RMS when included. In comb5, hexahydrite ($MgSO_4.6H_2O$) and mirabilite also show a similar result. For the other endmembers, excluding them is often better. Few exceptions are notable when the minimum RMS is similar when included and excluded, this is the case for the magnesium chloride hexahydrate $MgCl_2.6H_2O$ (all 3 cases), hexahydrite, magnesium chlorate ($Mg(ClO_3)_2.6H_2O$), sodium perchlorate ($NaClO_4.2H_2O$) and ammonium sulfate $(NH_4)_2SO_4$) in comb4 and magnetite (Fe_3O_4), sodium chloride (NaCl), sodium perchlorate in comb5.

From this result one can easily discriminate some endmembers assuming that best compounds should produce lower average and minimum RMS when included than when excluded. From such criterion, an endmember is clearly distinguished in the all comb3-4-5 cases: the sulfuric acid octahydrate (SAO) $H_2SO_4.8H_2O$, for which the differences between included and excluded are increasingly significant when adding more endmembers. Apart from this compound, crystalline and amorphous water ice, hydrated magnesium sulfates ($MgSO_4.6H_2O$, $MgSO_4.7H_2O$), sodium-magnesium sulfates $Na_2Mg(SO_4)_2.4H_2O$, and ammonium sulfate $(NH_4)_2SO_4$ shows all a lower average and minimum RMS when included than when excluded. However, these differences in RMS vary significantly from one endmember to another. This result remains true when going from comb3 to comb4 and comb5. Magnetite (Fe_3O_4), sodium chloride (NaCl), sodium sulfate, magnesium chloride ($MgCl_2.4H_2O$ and $MgCl_2.6H_2O$), chlorate ($Mg(ClO_3)_2.6H_2O$), perchlorate ($Mg(ClO_4)_2.6H_2O$) and sodium perchlorate ($NaClO_4.2H_2O$) shows the opposite pattern, average and minimum RMS are lower when excluding them.

4.3.3. Improvement factor

The improvement factor was computed using Equation 16 for all combination cases and results are shown on Figures 8,9 and 10. As expected, the improvement factor behavior is consistent when going from 3 to 5 endmembers for each endmember, only a slight decrease is observed. This was again expected as adding more endmembers tends to produce better fits more easily (see Section 4.3.2) and therefore the spectral contribution of a single compound will appear lower from the 3 to the 5 endmembers case. This is true for all endmembers except for the ammonium sulfate $(NH_4)_2SO_4$) for which the improvement factor remains mostly the same and even stronger at certain wavelengths in the 5 endmember case. This clearly shows the spectral importance of this compound in the fitting procedure.

Apart from this compound, there is strong evidence of an important spectral contribution for the water ice, both crystalline and amorphous, and the SAO for which the improvement factor

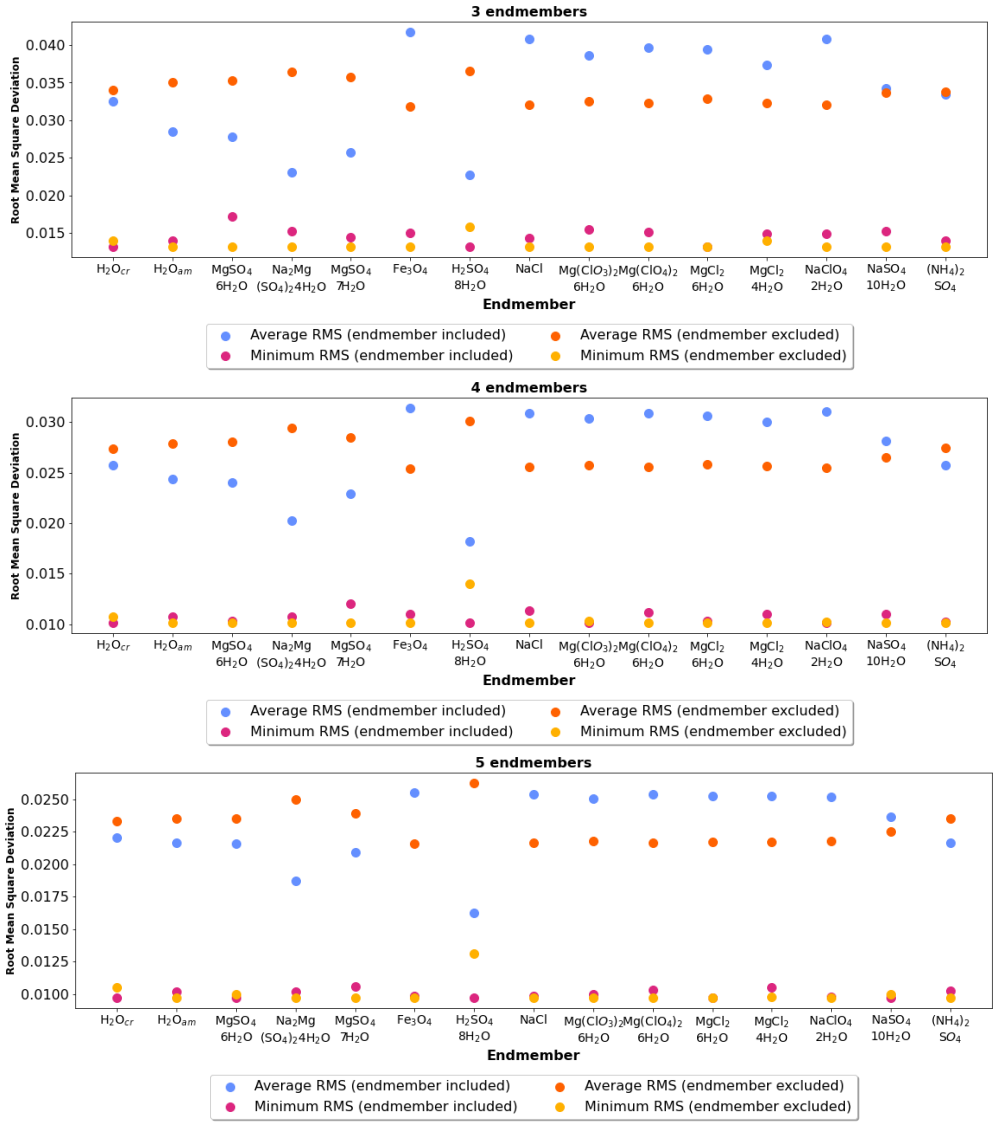

Figure 7: Comparison between the average and minimum RMS when the endmember is included in the combination (blue and purple) and when the endmember is excluded from the combination (orange and yellow). The best conditions occurs when the orange and yellow dots have a higher RMS value than the blue and purple ones.(top) : comb3 case, average and minimum RMS are computed over 91 out of 455 times when included and 364 out of 455 times when excluded. (middle) : comb4 case, average and minimum RMS are computed over 364 out of 1365 times when included and 1001 out of 1365 times when excluded. (bottom) : comb5 case , average and minimum RMS are computed over 1001 out of 3003 times when included and 2002 out of 3003 times when excluded. Note the differences in the y-axis values from comb3 to comb5: as more endmembers are considered in the mixture the average and minimum RMS are decreasing.

remains mostly above 1 on the spectral range. The SAO peaks between 1 and 1.5 μm where the improvement factor indicates that including it produces up to 4 times better fits (dividing the residuals by 4) than excluding it, especially at shorter wavelength. For water ice, results tend to show that on average including it seems to improve the fit. There are few wavelengths for which the improvement factor is slightly below 1 but overall it shows that excluding water ice does not improve the fit.

A notable result is the clear distinction between the hydrated sulfates Hexahydrite ($MgSO_4.6H_2O$), Epsomite ($MgSO_4.7H_2O$), Bloedite ($Na_2Mg(SO_4)_2.4H_2O$), and Mirabilite ($Na_2SO_4.10H_2O$) and the hydrated chlorine salts (chlorides, chlorates and perchlorate). The former show an important spectral contribution with an improvement factor almost always greater than 1 on the whole spectral range, except for Mirabilite for which the factor oscillate around 1. Conversely, the hydrated chlorine salts for which the general trend of the improvement factor is below 1, except for magnesium chloride hexahydrate ($MgCl_2.6H_2O$) for which values are above 1 on few spectral intervals. This observation remains true when comparing the hydrated sulfates and hydrated chlorine salts all the comb3, comb4 and comb5 cases. Finally, looking at the pure minerals such as magnetite (Fe_3O_4) and sodium chloride (NaCl), one can see no particular positive spectral contribution as the improvement factor remains below 1 on the whole spectral range. We note a similar behavior for these 2 endmembers and this is strongly related to their extinction coefficient k, which is mostly constant in this NIR region so they appear as dark impurities in the granular medium, lowering the reflectance. Since the magnetite is darker than the sodium chloride, its improvement factor is almost always below 1 and this implies that the model tends to reject the presence of such dark compound without particular spectral signature.

The analysis of the improvement factor points to conclusions similar to RMS analysis (see Section 4.3.2). This is not surprising since the RMS averages the quality of the fit over the whole spectral range while the improvement factor looks at the contribution at each wavelength. One would expect a strong correlation between the two. However, this allows us to look for potential biases in RMS analysis as an improvement factor of a compound that oscillates around 1 could produce similar RMS to a factor that appears very high on a small portion but generally below 1 elsewhere. Here, we can clearly emphasize the role of sulfated endmembers in the fitting procedure.

4.4. Optimistic SNR

Assuming an optimistic scenario in which the uncertainties in the data are small (2% of the reflectance value in the continuum at 1 μm), corresponding to a SNR of 50. We compute the RMS threshold beyond which the best fits are rejected as in Section 4.3. The value of the reflectance at 1 μm in the continuum is 0.58, using this we obtain a RMS threshold of 0.0116 (see Figures 4,5,6, left, blue vertical line).

A first notable result is that assuming such high SNR, all of the best-fits from the comb3 are above the RMS threshold and are therefore rejected. This implies that the model could not find a single combination to reproduce the data with such low uncertainty on the observation. When using comb4 and comb5 there are only a few combinations (respectively 21 and 153) for which the model is able to fit the data with a SNR of 50.

As our initial noise assumption in the Bayesian MCMC was not set at SNR = 50 but at 10% of the reflectance at each wavelength we cannot discuss here the full distribution of the posterior for each accepted best-fit. Instead, we use proxies based on the best-fit to analyze these successful combinations. However, before doing so, one would check first the consistency between a SNR of 5 and 50. To do so, we selected the lowest RMS best-fit from the comb5 case, which corresponds to a combination of crystalline water ice, hexahydrite $MgSO_4.6H_2O$, SAO

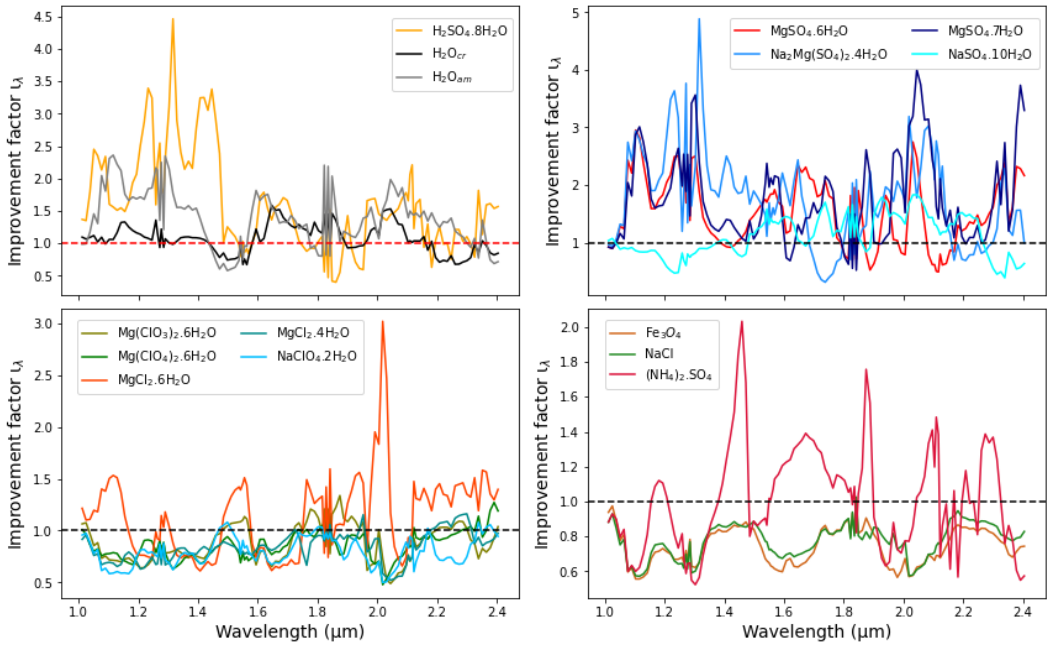

Figure 8: Improvement factor computed using Equation 16 for the comb3 case. (top left) : sulfuric acid octahydrate, crystalline and amorphous water ice. (top right) : magnesium (hexahydrite, epsomite), sodium (mirabillite) and magnesium-sodium (bloedite) hydrated sulfates. (bottom left) : magnesium chlorate, perchlorate, chloride and sodium perchlorate. (bottom right) : magnetite, sodium chloride and ammonium sulfate. Note the differences in the y-axis values of each subplot.

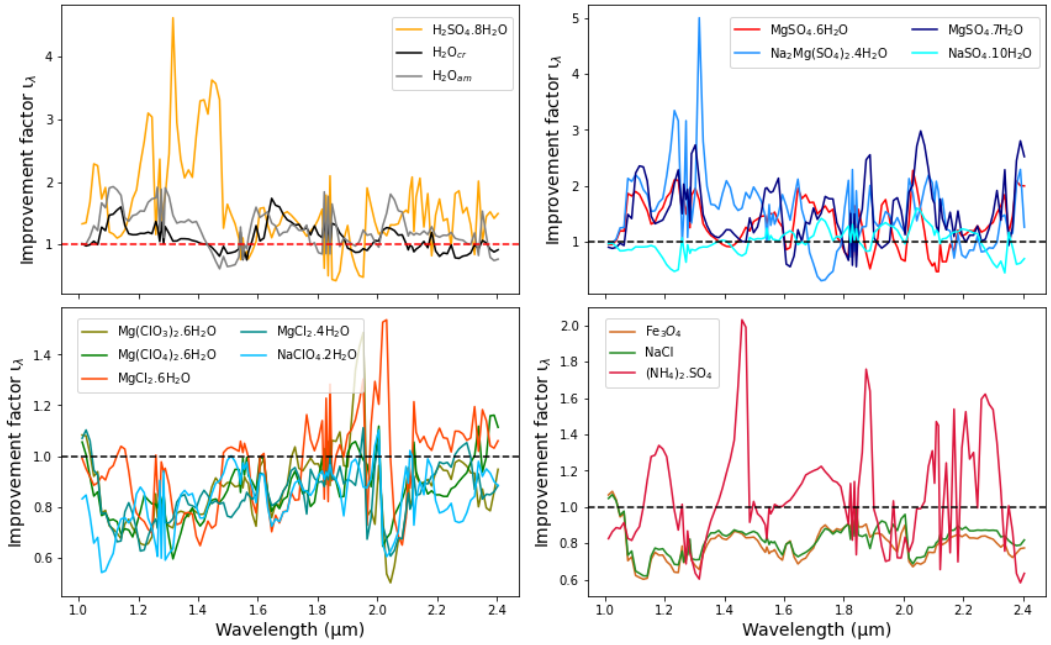

Figure 9: Same as Figure 8 but for the comb4 case. Note the differences in the y-axis values of each subplot.

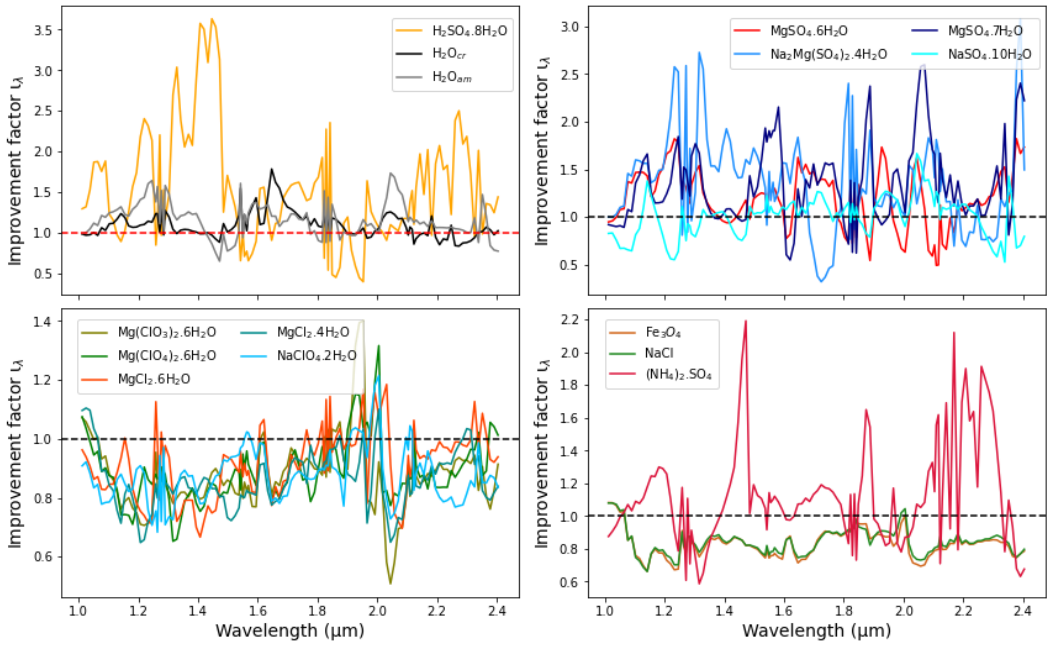

Figure 10: Same as Figure 8 but for the comb5 case. Note the differences in the y-axis values of each subplot.

$H_2SO_4.8H_2O$, chloride tetrahydrate $MgCl_2.4H_2O$ and Mirabilite $NaSO_4.10H_2O$ and we performed the same Bayesian inversion framework (same number of iterations, number of chains, burnin period, prior consideration) assuming only a 1% uncertainty on the data. Comparisons between the best-fit and the posterior distribution for both cases are shown on Figure 11.

Figure 11 indicates very consistent results with RMS of 0.0097 when assuming 10% uncertainty and 0.0095 when assuming 1% with a mean difference of the spectra lower than 3%. The pairwise posterior distribution also shows consistent results. As expected, the 1% uncertainty case gives more constraint on the fitting procedure so the posterior distribution appears tighter, the posterior density tend to 1 within narrower valleys compared to the 10% uncertainty case. Analyzing the best fit from 10% noise level and 1% noise level is thus equivalent.

4.4.1. Best-fit RMS

Here we will undertake the analysis of the best fit below the RMS threshold when assuming a SNR of 50. As previously stated in Section 4.4, there is no best-fit from the comb3 case below the RMS threshold. Figure 12 shows the endmembers distribution of the 21 and 153 retained combinations in the comb4 and comb5 cases, along with their corresponding best-fit and residuals.

A striking result is to note the very strong similarities between this collection of best-fits (Figure 12 right). Their shapes are very consistent from one combination to another. Looking at the residuals of the model fits one can see that small discrepancies near 1.18, 1.3 and 1.9 μm are visible but this may also be due to abnormal reflectance values in the data. No significant improvement is observed on the spectra between comb4 and comb5, and the minor discrepancies are located at the same wavelengths.

The endmember distribution (Figure 12 left) gives the number of times each endmember is used in the retained combinations below the RMS threshold corresponding to an SNR of 50 (see Figures 4, 5 and 6). Although the initial noise assumptions was set to 10% (equivalent to an SNR of 5) we showed for one combination of 5 endmembers that the best-fit is similar when assuming

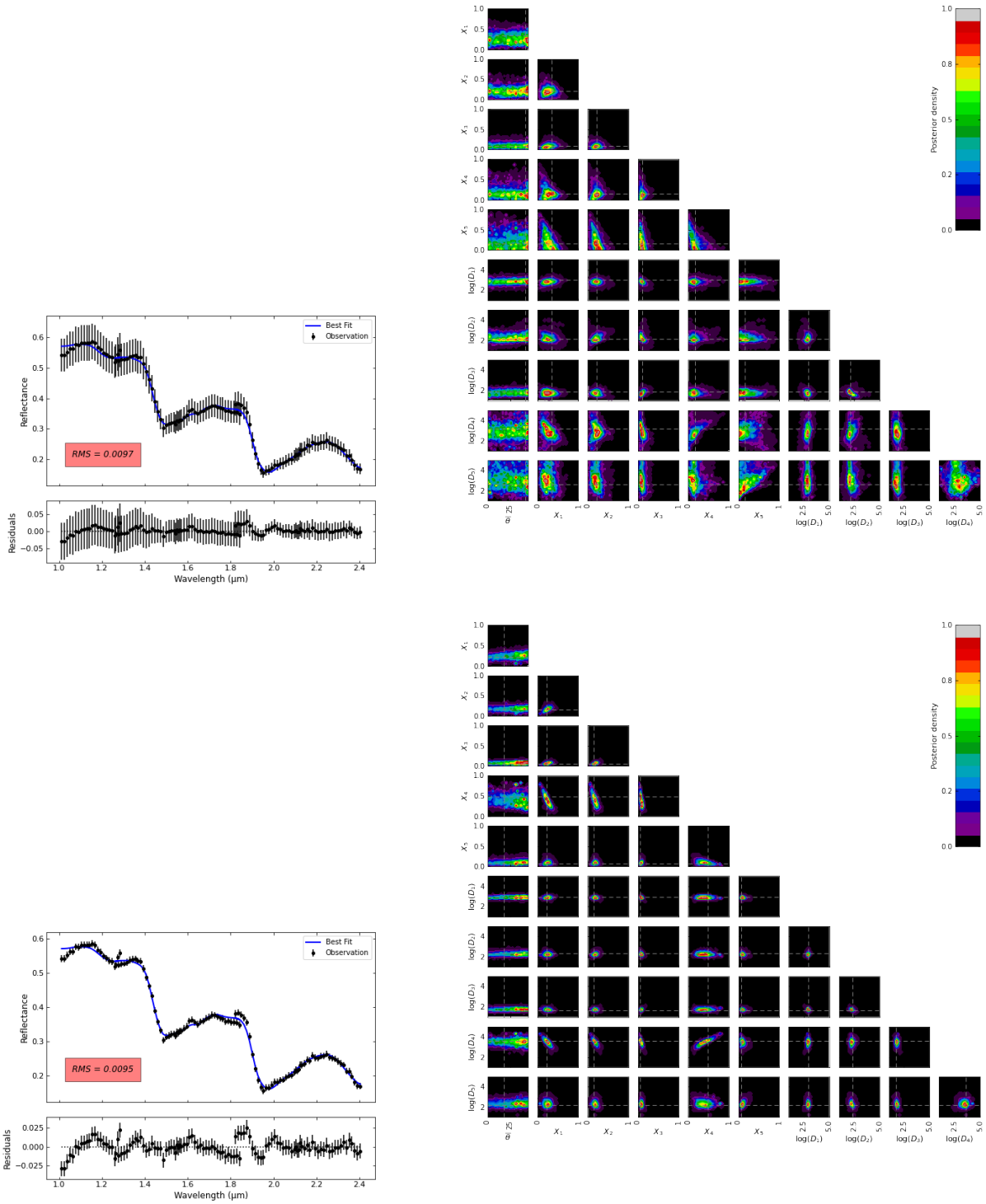

Figure 11: Best-fit with residuals (left) and posterior pairwise distributions (right) of two Bayesian MCMC inversions performed using 5 endmembers. $\bar{\theta}$ is the macroscopic roughness, X_i and D_i are the volumetric proportion and grain size of the crystalline water ice (1) hexahydrite (2), SAO (3), chloride tetrahydrate (4) and Mirabilite (5). Top: the uncertainty on the data is 10% (SNR of 5). Bottom: the uncertainty on the data is 1% (SNR of 50). Both best-fits are very similar, with a maximum difference of 2.87%

an SNR of 5 or 50 (see Figure 11). From this distribution it becomes clear that the inclusion of SAO is mandatory in this fitting procedure as it appears in all 21 and 153 combinations. A second important compound is the water ice. It appears either in crystalline (present in more than 60% of the best-fits) or amorphous (present in 40 to 50% of the best-fits) state. There is no combination of both crystalline and amorphous water ice in the 4 endmembers cases and only 20 combinations in the 5 endmembers case. The crystalline state seems to be found a little more often than the amorphous state, although the results seem to show that the distinction between the two possibilities is not trivial. Water ice and SAO are the fundamental endmembers to consider. An interesting result is also to notice that each endmember is present at least once in a combination, except for epsomite $MgSO_4.7H_2O$ in the 4 endmembers case. Overall, the endmember distribution in both cases is very similar and epsomite appears to be used 22 times in the 5 endmember case.

Since all the endmembers are retained at least once, it is very easy to understand why there are so many combinations retained in the 5 endmembers cases: adding a compound can only improve the fit and therefore the combinations are more numerous. Nevertheless, it allows to draw several important conclusions. First, some endmembers seem to be used more often than others: hexahydrite $MgSO_4.6H_2O$, bloedite $Na_2Mg(SO_4)_2.4H_2O$ and magnesium chlorate $Mg(ClO_3)_2.6H_2O$, the first two being really consistent with the strong evidence of SAO, being sulfated compounds, but still differ from other hydrated sulfates such as epsomite ($MgSO_4.7H_2O$) or mirabillite. Second, all other endmembers are evenly distributed, which may imply a similar spectral behavior allowing them to be replaced one by one without significantly affecting the quality of the fit. Although some endmembers have very similar optical constants because their chemical compositions are close, such as the hydrated sulfates or the chlorinated salts, others are very different from each other such as magnetite (Fe_3O_4) and magnesium chloride ($MgCl_2.4H_2O$ and $MgCl_2.6H_2O$). Substituting one such distinct compound for the other should change the quality of fit for a similar volumetric proportion and grain size. Of course we expect that abundances and grain size of these endmembers could drastically change from one best fit to another, but still this results imply that there are many successful combination that uses at least one of these endmembers to correctly reproduce the observation which makes surface characterization a highly non-trivial task.

4.4.2. Numerical abundances

We compare the numerical abundances using Equation 17 of each best-fit reaching SNR 50 and look at the minimum, maximum and average numerical abundance estimated for each endmember. We will only use the comb5 case because there are too few combinations for comb4, but we showed in Section 4.4.1 that the distribution of the comb4 and comb5 cases are comparable.

Numerical abundances are shown in Figure 13. A remarkable first observation is to note that there are combinations in which several endmembers have very high numerical abundances: $MgSO_4.6H_2O$ (81%), $Na_2Mg(SO_4)_2.4H_2O$ (92%), $MgSO_4.7H_2O$ (79%), $H_2SO_4.8H_2O$ (98%), $Mg(ClO_4)_2.6H_2O$ (97%), $MgCl_2.6H_2O$ (97%) and $NaSO_4.10H_2O$ (83%). This implies that the granular medium can be described in 7 different ways, each time dominated by one of these endmembers. Results are not distinguishable within the limit of our SNR. When looking at the SAO $H_2SO_4.8H_2O$, which is used in all 153 combinations, its numerical abundances may vary from 2% to 98% with an average abundance of 50% implying that many successful fits exist using a very small or very high contribution of this endmember. In contrast, results on water ice are surprising as each combination uses either crystalline or amorphous water ice but they are numerically very scanty where crystalline water ice has a minimum and maximum abundances of 2.10^{-9} and 4.10^{-3} with an average of $8.5.10^{-4}$ and amorphous water ice has a minimum and maximum abundances of 1.10^{-8} and 0.36 with an average of 0.015. This imply that while water ice seems mandatory, it appears diluted in a medium

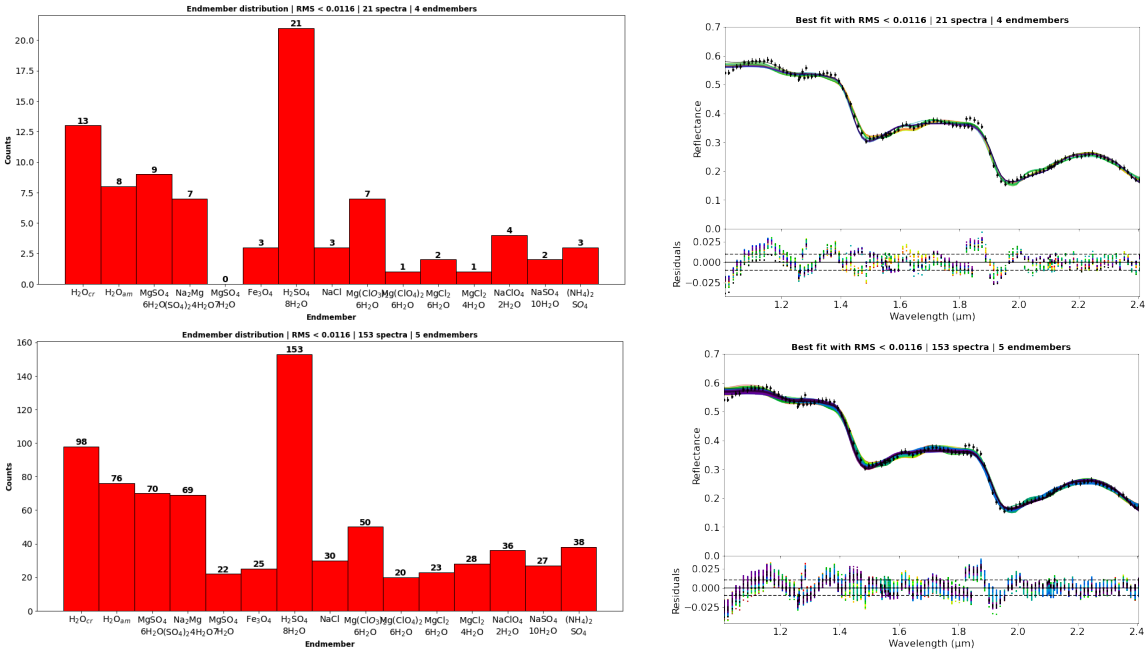

Figure 12: Left: Endmember presence of the selected combination for best-fits below the RMS threshold of 0.0116 (SNR of 50) for the comb4 (top panel) and comb5 (bottom panel) cases. Right: Corresponding best-fits and residuals for comb4 (21 spectra) and comb5 (153 spectra) cases. Each color represents a single combination. Dotted lines represent 1 sigma error.

largely dominated by other endmembers. When amorphous water ice is used, the model predicts on average higher numerical abundances than for crystalline water ice.

Apart from these three species there is no clear distinction between the endmembers. Except for SAO and hexahydrite ($MgSO_4.6H_2O$), all the minimum numerical abundances are below 1.10^{-6}. Average hydrated sulfates abundances are between 0.1 ($NaSO_4.10H_2O$) and 0.42 ($Na_2Mg(SO_4)_2.4H_2O$) which is higher than hydrated chlorine salts for which abundances vary between 1.10^{-4} ($NaClO_4.2H_2O$) and 0.21 ($Mg(ClO_3)_2.6H_2O$. Such result should be treated with caution, in general numerical abundances clearly shows that many combinations and therefore representations of the granular medium are acceptable when considering an SNR of 50. Although some endmembers appear mandatory as they are present in more combinations than others, their numerical proportion may vary drastically from one combination to another. An endmember with a low volumetric abundance but a large grain size leads to a low numerical abundance but the endmember can still control the shape of a spectrum. Therefore, a small endmember numerical abundance does not necessarily imply that its presence is unlikely, as evidenced by the results on water ice. Likewise, an endmember with a high volumetric abundance and a small grain size leads to a high numerical abundance but this does not necessarily imply that such compound has a high impact on the spectrum. With this in mind, one can still recognize that hydrated sulfates endmembers have on average higher abundances than hydrated chlorine salts.

5. Discussion

We define four criteria to interpret the numerous results on the exhaustive test of all combinations. When assuming a pessimistic SNR of 5 all tested combinations falls below the subsequent

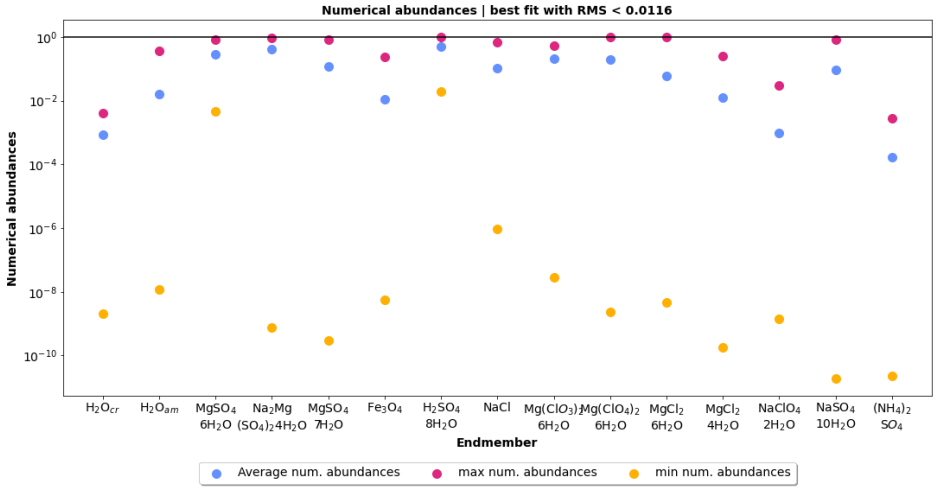

Figure 13: Numerical abundances of the selected best fit below the RMS threshold of 0.0116 (SNR of 50) for the 5 endmembers case. Comparison between the average (blue), maximum (purple) and minimum (yellow) numerical abundances for each endmember.

RMS threshold which makes it possible to compare all the cases tested. In order to characterize the contribution of each endmember we used the RMS estimated from Equation 15 and the improvement factor defined Equation 16. These two criteria provide first information on the relevance of certain endmembers. When assuming an optimistic SNR of 50, a smaller, but still significant, number of combinations are retained. These remaining combinations were analyzed via two more criteria, the distribution of their occurences and the numerical proportion with which they are associated. Our goal being to select the few relevant endmembers for future analysis of NIMS data we must integrate together the results of these 4 criteria. We thus propose to rate each endmember according to the results obtained for each criterion. We therefore propose the following notation :

1. RMS including/excluding endmember at SNR=5: 1 if the average and minimum RMS is always lower when the endmember is included, 0.5 if only the average RMS is lower when the endmember is included and 0 otherwise.
2. Improvement factor at SNR=5: 1 if on average the improvement factor is above the value of 1, 0.5 if close to unity (from 0.95 to 1.05) and 0 if below the value of 1.
3. Best-fit RMS at SNR=50: 1 if the endmember is always present, 0.5 if it is more represented than the average and 0 otherwise.
4. Numerical Abundances at SNR=50: 1 if the average numerical abundance is above 50%, 0.5 if between 10 and 50% and 0 if below 10%.

Summary of the results per criteria for the 15 endmembers are provided in Tables 2 and 3. From this synthesis we can identify the most relevant endmembers to use.

First, SAO stands out very clearly, the RMS is always the lowest when including it, its improvement factor clearly shows its high contribution on the spectrum, this endmember is the only one being used in every retained combinations assuming a SNR of 50 and its average numerical abundance is 50.7%. This clearly proves how mandatory is the SAO when trying to reproduce the NIMS data.

Then comes crystalline water ice, hexahydrite ($MgSO_4.6H_2O$) and bloedite ($Na_2Mg(SO_4)_2.4H_2O$) with similar average over the 4 criteria. Crystalline water ice is the second endmember for which the RMS is always lower when including it. Its improvement factor is above 1 over the majority

Criteria	H_2SO_4 $8H_2O$	H_2O (cr)	$MgSO_4$ $.6H_2O$	$Na_2Mg(SO_4)_2$ $.4H_2O$	H_2O (am)	$MgSO_4$ $7H_2O$	$(NH_4)_2$ SO_4
RMS (SNR 5)	1	1	0.5	0.5	0.5	0.5	0.5
Improvement factor (SNR 5)	1	1	1	1	1	1	1
Distribution (SNR 50)	1	0.5	0.5	0.5	0.5	0	0
Numerical Abundances (SNR 50)	1	0	0.5	0.5	0	0.5	0
Average	1	0.625	0.625	0.625	0.5	0.5	0.375

Table 2: Selection criteria: summary of results. From left to right: Sulfuric Acid Octahydrate, crystalline water ice, Hexahydrite, Bloedite, amorphous water ice, Epsomite and Mascagnite.

of the spectral range and it is the second most used endmembers in the retained combinations of a SNR 50. The only downside being its very low numerical abundance. Hexahydrite and bloedite also seem to be important, the RMS analysis is not as conclusive as for the first two endmembers but their improvement factor and distributions are similar to crystalline water ice while both showing a higher average numerical abundance.

Then are amorphous water ice and epsomite ($MgSO_4.7H_2O$), the first one being close to crystalline water ice but the RMS analysis shows that lower RMS is achieved when excluding it. Epsomite is comparable to hexahydrite and bloedite, due to its chemical composition similarity. However, even though the RMS analysis, improvement factor and numerical abundance is somehow similar to the two other hydrated sulfates, its occurences in the distribution for the SNR 50 is very low, making this endmember a less relevant choice.

An interesting result is to notice that ammonium sulfate mascagnite ($(NH_4)_2SO_4$) is better ranked than some hydrated sulfates and all chlorinated salts. This is mostly due to the RMS analysis, showing a lower average RMS when including it, but also its improvement factor is significantly better than all chlorinated endmembers. Among the last are the chlorinated salts, mirabillite and sodium chloride (NaCl) and magnetite (Fe_3O_4). Magnesium chlorate ($Mg(ClO_3)_2.6H_2O$) seems to be slighlty above due to higher occurence in the distribution for the SNR 50 as well as a high average numerical abundance.

Mirabillite, magnesium perchlorate ($Mg(ClO_4)_2.6H_2O$), magnesium chloride hexahydrate ($MgCl_2.6H_2O$) and sodium chloride are ranked similarly. The first one only shows an improvement factor close to unity which implies that integrating it does not significantly improve the fit, but does not deteriorate it. The others have an average numerical abundance above 10%.

The last are magnesium chloride tetrahydrate ($MgCl_2.4H_2O$), sodium perchlorate ($NaClO_4.2H_2O$) and magnetite. These 3 endmembers do not show a signs of significant contributions on a single criterion. This does not mean that such endmembers are improbable when trying to characterize Europa's surface, but rather that they do not particularly distinguish from others.

From that synthesis, one would recognize that at least SAO, crystalline water ice and hydrated sulfate such as hexahydrite ($MgSO_4.6H_2O$) or bloedite ($Na_2Mg(SO_4)_2.4H_2O$) are essential endmembers to consider when trying to reproduce a NIMS observation. Except for mirabillite, there is a clear evidence that hydrated sulfates show in general a more remarkable contribution than chlorinated salts. However, despite this finding, it remains difficult to discriminate between endmembers with similar chemical composition. So rather than choosing between all these endmembers, one may have to use a representative of a chemical set. With our approach and results, the ideal endmembers to consider would be : SAO, water ice (both crystalline and amorphous, although their distinction is not trivial) hexahydrite as the representative of the hydrated sulfates, magnesium chlorate ($Mg(ClO_3)_2.6H_2O$) as the representative of the chlorinated salts and the ammonium sulfate mascagnite ($(NH_4)_2SO_4$).

Criteria	Na_2SO_4 $10H_2O$	$Mg(ClO_3)_2$ $6H_2O$	$Mg(ClO_4)_2$ $6H_2O$	$MgCl_2$ $6H_2O$	NaCl	$MgCl_2$ $4H_2O$	$NaClO_4$ $2H_2O$	Fe_3O_4
RMS (SNR 5)	0	0	0	0	0	0	0	0
Improvement factor (SNR 5)	0.5	0	0	0	0	0	0	0
Distribution (SNR 50)	0	0.5	0	0	0	0	0	0
Numerical Abundances (SNR 50)	0.5	0.5	0.5	0.5	0.5	0	0	0
Average	0.25	0.25	0.125	0.125	0.125	0	0	0

Table 3: Selection criteria: summary of results. From left to right: Mirabilite, magnesium chlorate, magnesium perchlorate, magnesium chloride hexahydrate, sodium chloride, magnesium chloride tetrahydrate, sodium perchlorate and Magnetite.

6. Conclusion

To understand the processes responsible for the evolution of Europa's surface, one has to finely understand and characterize its microphysics. While future missions (Grasset et al., 2013; Phillips and Pappalardo, 2014) will provide extensive knowledge on the surface composition, our current best asset remains infrared spectroscopy.

We performed an extensive study of almost 5000 combinations of 15 endmembers and found that there is a significantly high number of them that produce similar fit to the data. Especially at SNR=5, all are acceptable. With SNR=50 only few % reach the target RMS. This finding forces us to be cautious when trying to fix a typical composition for the dark lineaments of Europa's trailing anti-Jovian hemipshere.

In addition, by using criteria and by prioritizing the endmembers according to the relevance of their contribution for each criterion, we show that it is not trivial to distinguish two endmembers with a close chemical composition, such as hydrated sulfates or chlorinated compounds. However, grouping criteria together clearly highlights the fact that sulfuric acid octahydrate and water ice are required, which is in complete agreement with previous studies of Europa's surface composition at these locations (Carlson et al., 2005; Ligier et al., 2016; Mishra et al., 2021a; King et al., 2022).

We also show that hydrated sulfates such as hexahydrite ($MgSO_4.6H_2O$) and bloedite ($Na_2Mg(SO_4)_2.4H_2O$) tend to improve more the fit than chlorinated salts. This does not necessarily imply that chlorinated endmembers do not exist on the surface, but differentiating between them will be difficult, if not impossible, with NIMS data and infrared spectroscopy at these wavelengths.

A major finding of this study is that it is not possible to use infrared spectroscopy in 1.0-2.5 μm range to differentiate chemically similar compounds such as hydrated sulfates or chlorinated salts, even by assuming a high SNR. There are many combinations for which the numerical abundance of the same endmember vary drastically which leads to a multitude of different representations of the same surface. It is therefore necessary to provide external constraints with different instruments. When this is the case, we would be able to better constrain the microphysics of the surface. Such constraint could be brought by the future JUICE (ESA) (Grasset et al., 2013) and Europa Clipper (NASA) (Phillips and Pappalardo, 2014) missions. Cross-comparison of NIMS data with data acquired by the space observatory, such as the JWST (Clampin, 2008), could also help by reducing the photometric uncertainty, improving the spectral resolution and increasing the spectral range to bring additional constraints.

When analysing NIMS data of Europa's surface to characterize its chemical composition and microphysical properties we recommend two distinct approaches. Either by using all potential endmembers together in a fitting procedure and interpret in terms of surface composition using a Bayesian approach to fully integrate the associated uncertainties. Since a very small number of endmembers seems necessary to fit the data, such approach takes the risk of overfitting the data

which may produce bias when interpreting results. Or by using one representative endmember per chemical set and study the chemical variation within one location rather than precisely determine the exact surface composition. This has the advantage of investigating the link between geological units and the physical processes at their origins by highlighting the dominance of certain chemical compounds. However, a fine microphysical characterization is then impossible as the abundances and grain sizes may vary if two endmembers with similar chemical composition were substituted.

Acknowledgements

We would like to thank the Galileo/NIMS teams for making their data available on NASA's PDS. We also acknowledge support from the "Institut National des Sciences de l'Univers" (INSU), the Centre National de la Recherche Scientifique (CNRS) and Centre National d'Etudes Spatiales (CNES) through the Programme National de Planétologie. This work is partly funded through the ESA co-funded PhD studentships programme (idea: I-2019-01294)

References

Andrieu, F., Schmidt, F., Douté, S., Chassefière, E., nov 2018. Ice state evolution during spring in richardson crater and mars. Icarus 315, 158–173.

Andrieu, F., Schmidt, F., Schmitt, B., Douté, S., Brissaud, O., sep 2015. Radiative transfer model for contaminated slabs: experimental validations. Applied Optics.

Belgacem, I., Schmidt, F., Jonniaux, G., mar 2020. Regional study of europa's photometry. Icarus 338, 113525.

Belgacem, I., Schmidt, F., Jonniaux, G., nov 2021. Regional study of ganymede's photometry. Icarus 369, 114631.

Carlson, R., Anderson, M., Mehlman, R., Johnson, R., oct 2005. Distribution of hydrate on europa: Further evidence for sulfuric acid hydrate. Icarus 177 (2), 461–471.

Carlson, R., Weissman, P., Smythe, W., and, J. M., may 1992. Near-infrared mapping spectrometer experiment on galileo. Space Science Reviews 60 (1-4).

Carlson, R. W., Johnson, R. E., Anderson, M. S., oct 1999. Sulfuric acid on europa and the radiolytic sulfur cycle. Science 286 (5437), 97–99.

Chandrasekhar, S., 1960. Radiative transfer. New York: Dover.

Clampin, M., jan 2008. The james webb space telescope (JWST). Advances in Space Research 41 (12), 1983–1991.

Cubillos, P., Harrington, J., Loredo, T. J., Lust, N. B., Blecic, J., Stemm, M., dec 2016. ON CORRELATED-NOISE ANALYSES APPLIED TO EXOPLANET LIGHT CURVES. The Astronomical Journal 153 (1), 3.

Dalton, J. B., nov 2007. Linear mixture modeling of europa's non-ice material based on cryogenic laboratory spectroscopy. Geophysical Research Letters 34 (21).

Dalton, J. B., Pitman, K. M., sep 2012. Low temperature optical constants of some hydrated sulfates relevant to planetary surfaces. Journal of Geophysical Research: Planets 117 (E9), n/a–n/a.

De Angelis, S., Tosi, F., Carli, C., Potin, S., Beck, P., Brissaud, O., Schmitt, B., Piccioni, G., Sanctis, M. D., Capaccioni, F., mar 2021. Temperature-dependent, VIS-NIR reflectance spectroscopy of sodium sulfates. Icarus 357, 114165.

Douté, S., Schmitt, B., dec 1998. A multilayer bidirectional reflectance model for the analysis of planetary surface hyperspectral images at visible and near-infrared wavelengths. Journal of Geophysical Research: Planets 103 (E13), 31367–31389.

Douté, S., Schmitt, B., Langevin, Y., Bibring, J.-P., Altieri, F., Bellucci, G., Gondet, B., Poulet, F., jan 2007. South pole of mars: Nature and composition of the icy terrains from mars express OMEGA observations. Planetary and Space Science 55 (1-2), 113–133.

Fastelli, M., Comodi, P., Schmitt, B., Beck, P., Poch, O., Sassi, P., Zucchini, A., aug 2022. Reflectance spectra (1–5 μm) at low temperatures and different grain sizes of ammonium-bearing minerals relevant for icy bodies. Icarus 382, 115055.

Fernando, J., Schmidt, F., Ceamanos, X., Pinet, P., Douté, S., Daydou, Y., mar 2013. Surface reflectance of mars observed by CRISM/MRO: 2. estimation of surface photometric properties in gusev crater and meridiani planum. Journal of Geophysical Research: Planets 118 (3), 534–559.

Fernando, J., Schmidt, F., Douté, S., sep 2016. Martian surface microtexture from orbital CRISM multi-angular observations: A new perspective for the characterization of the geological processes. Planetary and Space Science 128, 30–51.

Filacchione, G., Adriani, A., Mura, A., Tosi, F., Lunine, J. I., Raponi, A., Ciarniello, M., Grassi, D., Piccioni, G., Moriconi, M. L., Altieri, F., Plainaki, C., Sindoni, G., Noschese, R., Cicchetti, A., Bolton, S. J., Brooks, S., aug 2019. Serendipitous infrared observations of europa by juno/JIRAM. Icarus 328, 1–13.

Gelman, A., Rubin, D. B., nov 1992. Inference from iterative simulation using multiple sequences. Statistical Science 7 (4).

Grasset, O., Dougherty, M., Coustenis, A., Bunce, E., Erd, C., Titov, D., Blanc, M., Coates, A., Drossart, P., Fletcher, L., Hussmann, H., Jaumann, R., Krupp, N., Lebreton, J.-P., Prieto-Ballesteros, O., Tortora, P., Tosi, F., Hoolst, T. V., apr 2013. JUpiter ICy moons explorer (JUICE): An ESA mission to orbit ganymede and to characterise the jupiter system. Planetary and Space Science 78, 1–21.

Greeley, R., Sullivan, R., Klemaszewski, J., Homan, K., Head, J. W., Pappalardo, R. T., Veverka, J., Clark, B. E., Johnson, T. V., Klaasen, K. P., Belton, M., Moore, J., Asphaug, E., Carr, M. H., Neukum, G., Denk, T., Chapman, C. R., Pilcher, C. B., Geissler, P. E., Greenberg, R., Tufts, R., sep 1998. Europa: Initial galileo geological observations. Icarus 135 (1), 4–24.

Hanley, J., Dalton, J. B., Chevrier, V. F., Jamieson, C. S., Barrows, R. S., nov 2014. Reflectance spectra of hydrated chlorine salts: The effect of temperature with implications for europa. Journal of Geophysical Research: Planets 119 (11), 2370–2377.

Hansen, G. B., 2004. Amorphous and crystalline ice on the galilean satellites: A balance between thermal and radiolytic processes. Journal of Geophysical Research 109 (E1).

Hapke, B., jul 1984. Bidirectional reflectance spectroscopy 59 (1), 41–59.

Hapke, B., sep 1993. Theory of Reflectance and Emittance Spectroscopy. Cambridge University Press.

Hapke, B., nov 2012. Bidirectional reflectance spectroscopy 7 221 (2), 1079–1083.

Hapke, B., feb 2013. Comment on "a critical assessment of the hapke photometric model" by y. shkuratov et al. Journal of Quantitative Spectroscopy and Radiative Transfer 116, 184–190.

Harrington, J., Himes, M. D., Cubillos, P. E., Blecic, J., Rojo, P. M., Challener, R. C., Lust, N. B., Bowman, M. O., Blumenthal, S. D., Dobbs-Dixon, I., Foster, A. S. D., Foster, A. J., Green, M. R., Loredo, T. J., McIntyre, K. J., Stemm, M. M., Wright, D. C., apr 2022. An open-source bayesian atmospheric radiative transfer (BART) code. i. design, tests, and application to exoplanet HD 189733b. The Planetary Science Journal 3 (4), 80.

Henyey, L. C., Greenstein, J. L., jan 1941. Diffuse radiation in the galaxy 93, 70.

Kargel, J. S., dec 1992. Ammonia-water volcanism on icy satellites: Phase relations at 1 atmosphere. Icarus 100 (2), 556–574.

King, O., Fletcher, L. N., Ligier, N., mar 2022. Compositional mapping of europa using MCMC modeling of near-IR VLT/SPHERE and galileo/NIMS observations. The Planetary Science Journal 3 (3), 72.

Labarre, S., Ferrari, C., Jacquemoud, S., jul 2017. Surface roughness retrieval by inversion of the hapke model: A multiscale approach. Icarus 290, 63–80.

Ligier, N., Poulet, F., Carter, J., Brunetto, R., Gourgeot, F., may 2016. VLT/SINFONI OBSERVATIONS OF EUROPA: NEW INSIGHTS INTO THE SURFACE COMPOSITION. The Astronomical Journal 151 (6), 163.

McCord, T. B., Hansen, G. B., Fanale, F. P., Carlson, R. W., Matson, D. L., Johnson, T. V., Smythe, W. D., Crowley, J. K., Martin, P. D., Ocampo, A., Hibbitts, C. A., and, J. C. G., may 1998. Salts on europa's surface detected by galileo's near infrared mapping spectrometer. Science 280 (5367), 1242–1245.

Mishra, I., Lewis, N., Lunine, J., Hand, K. P., Helfenstein, P., Carlson, R. W., MacDonald, R. J., sep 2021a. A comprehensive revisit of select galileo/NIMS observations of europa. The Planetary Science Journal 2 (5), 183.

Mishra, I., Lewis, N., Lunine, J., Helfenstein, P., MacDonald, R. J., Filacchione, G., Ciarniello, M., mar 2021b. Bayesian analysis of juno/JIRAM's NIR observations of europa. Icarus 357, 114215.

Pappalardo, R. T., Belton, M. J. S., Breneman, H. H., Carr, M. H., Chapman, C. R., Collins, G. C., Denk, T., Fagents, S., Geissler, P. E., Giese, B., Greeley, R., Greenberg, R., Head, J. W., Helfenstein, P., Hoppa, G., Kadel, S. D., Klaasen, K. P., Klemaszewski, J. E., Magee, K., McEwen, A. S., Moore, J. M., Moore, W. B., Neukum, G., Phillips, C. B., Prockter, L. M.,

Schubert, G., Senske, D. A., Sullivan, R. J., Tufts, B. R., Turtle, E. P., Wagner, R., Williams, K. K., oct 1999. Does europa have a subsurface ocean? evaluation of the geological evidence. Journal of Geophysical Research: Planets 104 (E10), 24015–24055.

Phillips, C. B., Pappalardo, R. T., may 2014. Europa clipper mission concept: Exploring jupiter's ocean moon. Eos, Transactions American Geophysical Union 95 (20), 165–167.

Querry, M., 1987. Optical constants of minerals and other materials from the millimeter to the ultraviolet. Contractor Report CRDEC-CR-88009.

Roush, T. L., Teodoro, L. F., Blewett, D. T., Cahill, J. T., jun 2021. Optical constants and diffuse reflectance of opaque minerals: A modeling study using magnetite. Icarus 361, 114331.

Schmidt, F., Bourguignon, S., jan 2019. Efficiency of BRDF sampling and bias on the average photometric behavior. Icarus 317, 10–26.

Schmidt, F., Fernando, J., nov 2015. Realistic uncertainties on hapke model parameters from photometric measurement. Icarus 260, 73–93.

Schmitt, B., 2020. Near and mid-ir optical constants of crystalline h2o ice ih at 140-145k.

Schmitt, B., Bollard, P., Albert, D., Bonal, L., 2017. Sshade/ghosst: "grenoble astrophysics and planetology solid spectroscopy and thermodynamics" database.

Seeliger, H., 1884. Zur photometrie des saturnringes. Astronomische Nachrichten 109 (20), 305–314.

Shkuratov, Y., Kaydash, V., Korokhin, V., Velikodsky, Y., Petrov, D., Zubko, E., Stankevich, D., Videen, G., dec 2012. A critical assessment of the hapke photometric model. Journal of Quantitative Spectroscopy and Radiative Transfer 113 (18), 2431–2456.

Shkuratov, Y., Kaydash, V., Korokhin, V., Velikodsky, Y., Petrov, D., Zubko, E., Stankevich, D., Videen, G., feb 2013. Response to the comment by b. hapke on "a critical assessment of the hapke photometric model". Journal of Quantitative Spectroscopy and Radiative Transfer 116, 191–195.

Shkuratov, Y., Starukhina, L., Hoffmann, H., Arnold, G., feb 1999. A model of spectral albedo of particulate surfaces: Implications for optical properties of the moon. Icarus 137 (2), 235–246.

ter Braak, C. J. F., Vrugt, J. A., oct 2008. Differential evolution markov chain with snooker updater and fewer chains. Statistics and Computing 18 (4), 435–446.

Trotta, F., Schmitt, B., 2018. Mid-ir optical constants of amorpous h2o ia at 15k and crystalline h2o ih at 60k.

Trotta, R., 2017. Bayesian methods in cosmology.

Trumbo, S. K., Brown, M. E., Hand, K. P., nov 2020. Endogenic and exogenic contributions to visible-wavelength spectra of europa's trailing hemisphere. The Astronomical Journal 160 (6), 282.

Chapter 5

Conclusion

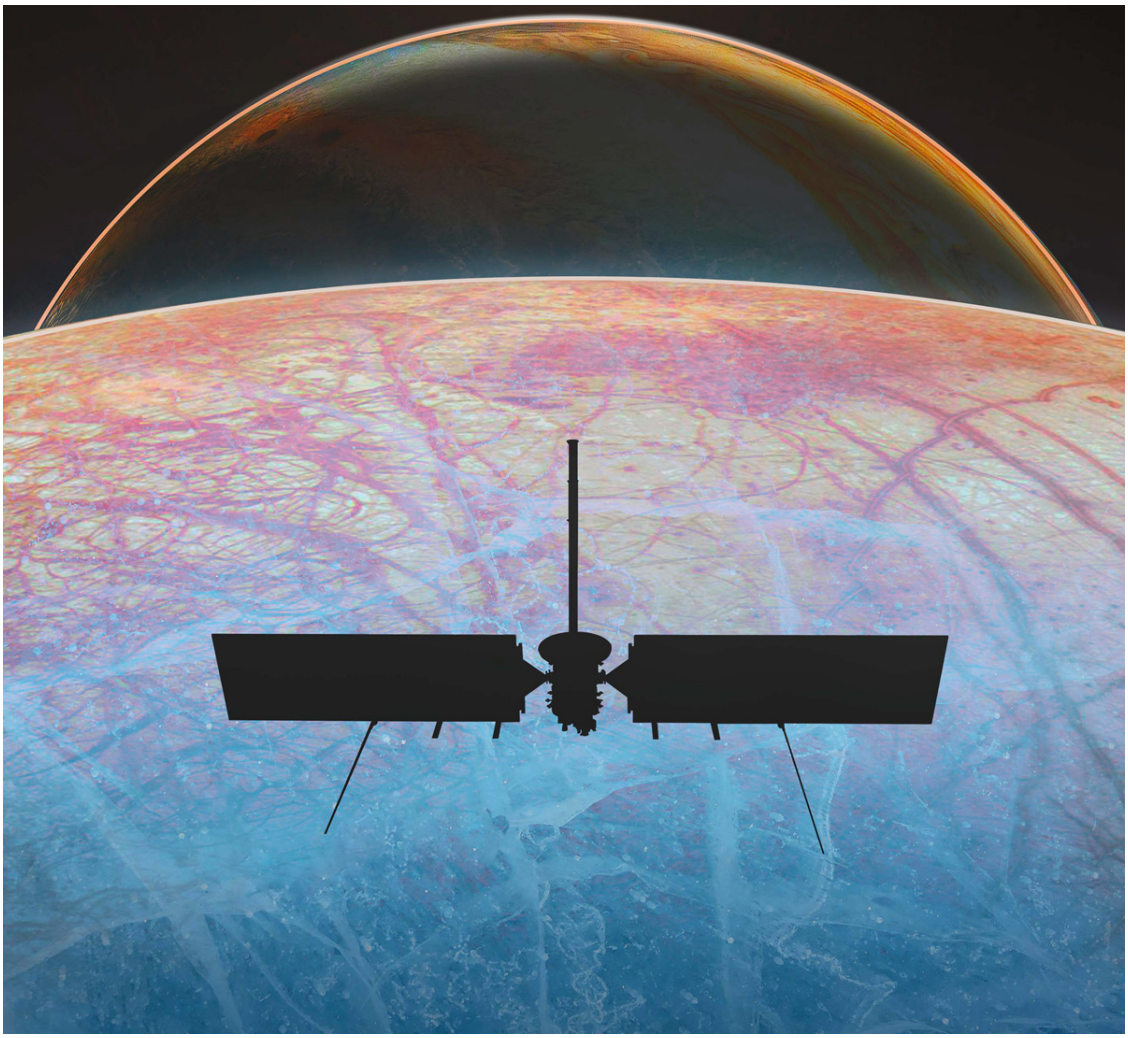

Illustration of the «journey to an ocean world» by the future NASA Europa Clipper mission. Credit: NASA/ Jet Propulsion Laboratory-Caltech

The objectives of the work presented in this part were to extend our knowledge of the microphysical properties of ice on the surface of Europa. The scientific context developed in chapter. 3 led to outstanding questions which we can summarize as follows: Can we select the best chemical compounds to characterize Europa's surface with Galileo/NIMS data? Are there other compounds not proposed so far to reproduce the data? What is the spatial correlation between the ice microphysics and the observed morphologies? Can we identified preferred observation targets for future mission?

These different issues are intimately related to each other and cannot be treated separately. The question concerning the selection of chemical species must thus be answered first. Then a ice microphysics characterization is possible through the analysis of several observations. By doing this we will finally be able to make a comparison between the different observations of similar geological structure, or of two different morphologies.

It is by following this research approach that we have conducted this work and therefore the chapter 4 is dedicated to the selection of the best chemical compounds for Europa. To do so, we used a typical spectrum of a dark lineaments within the trailing anti-jovian hemisphere showing highly distorted water ice bands. We have selected a list of 15 relevant chemical compounds. Most of them have been used by previous studies such as the sulfuric acid octahydrate, magnesium and sodium hydrated sulfates and chlorinates. We have added other compounds that were not previously included in such spectroscopic analysis, such as magnetite and ammonium sulfate. We use the Hapke model (Hapke, 2012) as a radiative transfer model to correctly simulate the light path within a granular medium and therefore we needed to use the optical properties of the selected compounds. Most of them were available through online database (SSHADE (Schmitt et al., 2017a)) or via corresponding publications ((Querry, 1987; Dalton and Pitman, 2012; Trotta and Schmitt, 2018; Schmitt, 2020)). For others, we used available reflectance spectra of granular material obtained in laboratory (Hanley et al., 2015; Fastelli et al., 2022)) to derive their refractive indices using an analytical radiative transfer model (Shkuratov et al., 1999). Using a robust bayesian inference framework (Cubillos et al., 2016) to properly account for the absolute calibration uncertainties of 10% (Carlson et al., 1992) we tested for the first time all combinations of 3, 4 and 5 endmembers among the 15 selected. The parameters we have estimated are the volume abundances, the grain size and the surface roughness. This approach has made it possible to test a very large number of different surface representations (more than 5000 tested combinations) for a single spectrum of Europa. Because the optical constants are not always available on the same spectral range, and because it was necessary to be able to test all mixtures in a similar way, we limited our study to the $1-2.5\ \mu$m range.

Our results demonstrated several crucial points. First, there is a very large number of different combinations which can produce similar fits, which are practically indistinguishable considering a pessimistic SNR of 10%. Considering a very optimistic scenario on the SNR of 1%, it appears that no combinations of 3 endmembers are able to correctly reproduce the data. There are respectively 21 and 153 combinations of 4 and 5 endmembers that evenly fit the data. Second, all selected compounds are used in at least one combination, even magnetite and ammonium sulfate. We used different criteria to try to rank the relevance of the compounds in the selection mixtures. This allowed us to evaluate the goodness of fit per endmember, the spectral contribution per endmember, the statistics on all acceptable fits and the corresponding representation of the medium in all acceptable fits (numerical abundances of each endmember). We thus show that except for water ice and sulfuric acid octahydrate (SAO), there are no other compounds that stand out. It all seems to be able to be used in combination with water ice and SAO, sometimes involving very different surface representations (volume abundances and grain size). This shows in particular that it is not possible to discern among these minor compounds with the NIMS data on this spectral range. And so we cannot precisely define the composition of the surface at the scale of a spectrum.

The conclusion drawn during this work have several implications. It is clear that the use of a realistic radiative transfer model is necessary to really understand the composition of the surface, which is not only a matter of volume abundance but also of grain size. We have seen that the same surface can be represented with two similar compounds having drastically different numerical abundances but similar volume abundances. To understand the processes occurring on Europa's surface, it is necessary to know

whether the observed area is composed of very small or very large grains of a certain chemical nature. Such information can only be obtained by combining a radiative transfer model with a bayesian approach to fully explore the parameter space of the solutions. However, in order to carry out such a microphysical study on Europa, external constraints must be brought as it is not possible to discriminate between a large variety of compounds with the NIMS data. Such constraints could come from other instruments, or from near-infrared reflectance data with a higher SNR and spectral resolution on a larger spectral range from future missions and observations.

Several perspectives are envisaged for this work. With the close flyby of Europa by the NASA/JUNO mission (on September 29, 2022) there is an opportunity to differentiate between different chemical species with the Juno's near-IR spectrometer (JIRAM). JIRAM is a spectro-imager operating on the $2-5$ μm range with a spectral resolution of 9 nm and a SNR significantly higher than NIMS. This combined with the high spatial resolution achieved during the flyby should provide important data to understand the surface composition.

In a similar way, future observations of Europa by the NIRSpec instrument of the James Webb Space Telescope will provide data at a very high spectral resolution with a very high SNR on a larger spectral range than JIRAM. Despite the lower spatial resolution, such data will also help to discriminate among the chemical species likely to be present on the surface. This would then allow to constrain the ideal mixture to use for future inversions of high spatial resolution observations made by the NIMS instrument, and thus characterize the ice microphysics.

Other perspectives of this work consist in the application of the methodology developed to other planetary objects. There are near-infrared data of other icy moons such as Ganymede from the Galileo/NIMS instrument and Enceladus from the Cassini/VIMS instrument. The radiative transfer model used in this work and the bayesian inference framework adapted to our problem is perfectly transposable to other data. Studying the microphysical properties of different surfaces is also a way to understand the impact of the processes involved. A cross comparison of different surface properties from a similar approach would be of great benefit for the planetary sciences community while waiting for data from future ESA/JUICE and NASA/EuropaClipper missions.

Part III

Mars: toward surface ice characterization with NOMAD-LNO

This part presents the work carried out toward a characterization of the ice microphysics on Mars. The scientific context and the outstanding questions are developed in chapter. 6. The NOMAD instrument on board ExoMars Trace Gas Orbiter is also presented in this chapter. To use the NOMAD data and study the surface ice properties a calibration method was required. In the chapter. 7 the construction of a reference synthetic solar spectrum to calibrate the NOMAD data is presented. Such spectrum was used to develop a calibration method that is described in chapter. 8. With the calibrated data, a first analysis was performed in chapter. 9 to investigate the ability to detect CO_2 ice with NOMAD. Conclusions and perspectives are given in chapter. 10.

Chapter 6

Context

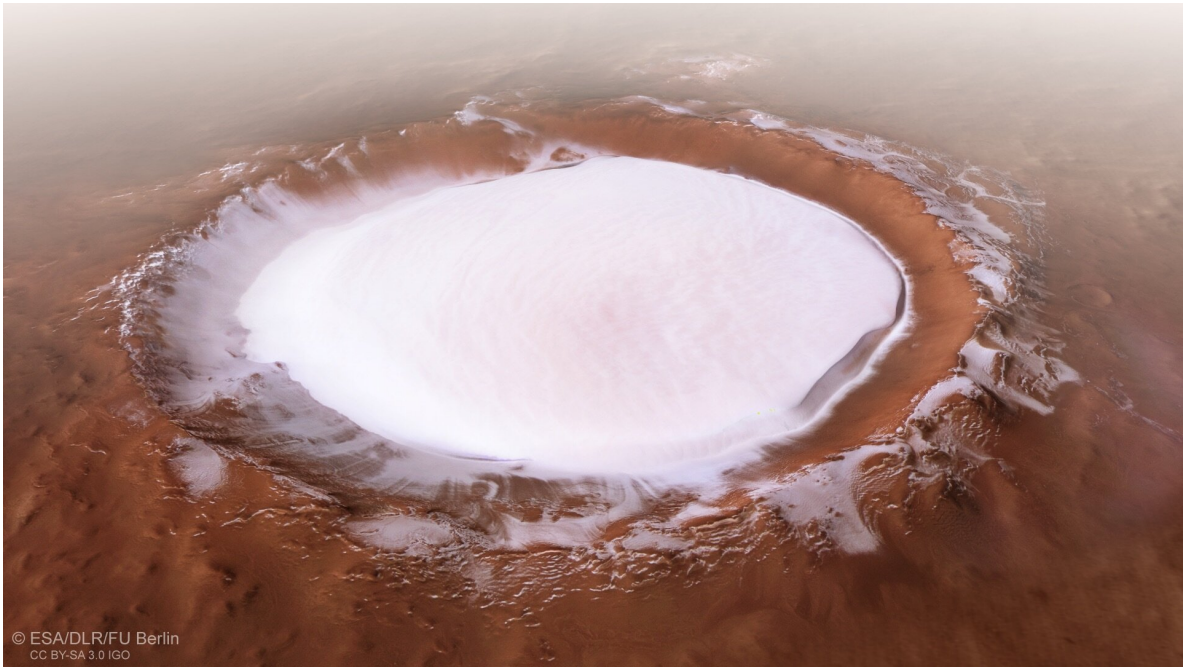

Evidence of water ice in the Korolev crater on Mars seen by ESA's Mars Express High Resolution Stereo Camera (HRSC). The crater is located in the northern lowlands of Mars (72°N), its diameter is about 82 km and the water ice thickness in the centre is estimated at about 1.8 km. Credit: ESA/DLR/FU Berlin

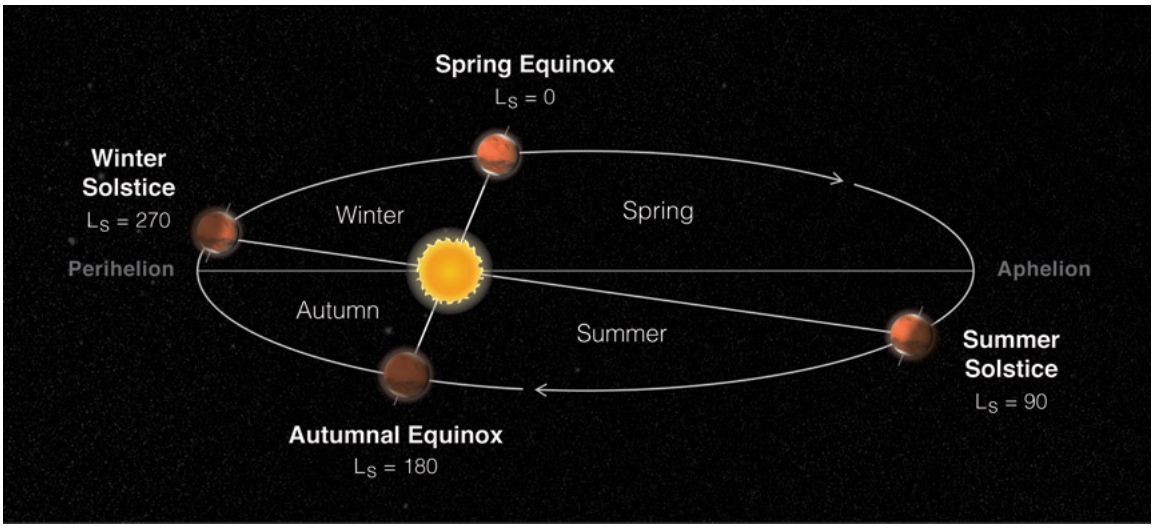

Figure 6.1: Orbit of Mars. Indicated seasons correspond to the boreal seasons. Date of the Martian year is identified by the Solar Longitude (L_S). Credit : NASA Ames Research Center

The observation of Mars goes back to the antiquity with the description of his retrograde movement in the sky by the Egyptian astronomer Senenmut 1500 years before our era. The red planet was then perceived differently from the other celestial bodies. Subsequently, the use of the astronomical telescope by Galileo (1610), Huygens (1659), Cassini (1666) and Herschel (1784) have lifted the veil on the mysteries of the planet regarding the inclination of its axis, its rotational and revolution period. Then, other observations highlighted the existence of dark spots near the equator and bright spots at the poles, raising many controversies in the scientific community regarding the surface morphology and Martian climate. Many questions remained until the first half of the twentieth century and it is finally the space age starting in the 1960's that clarified our understanding of the red planet. From the first flyby of Mars by the Soviet probe Mars 1 in 1963 to the landing of the Perseverance rover in 2021, a total of 46 space missions followed one another with a success rate of about 50%. Thus, the evolution of space and instrumental techniques allowed orbiter, lander and rover to load instruments more and more adapted to scientific questionings.

This chapter will make the inventory of the current knowledge on the Martian climate and the markers of its interaction with the surface according to the results of recent space missions. It will address current open questions regarding the study of Martian icy surfaces and will expose the aim of this PhD work. A second part is dedicated to the description of the NOMAD instrument that we will use.

6.1 Planet Mars

Mars is the fourth planet in the solar system orbiting at an average distance of 1.52 AU around the Sun. It is distinguished from the Earth by its weakest equatorial radius (3396 km against 6371 km for the Earth) and its orange tinge linked to the presence of ferric oxides on the large majority of the regolith (Poulet et al., 2007). On the other hand, it has a common orbital characteristic with the Earth which is the inclination of its axis with respect to the orbital plane (25.2° against 23.43° for the Earth) also conferring annual seasons cycle. Seasons are identified by the notion of Solar Longitude (L_S) which is the angle made by the Mars-Sun axis at a time of the year and the reference axis corresponding to the boreal spring equinox (see Fig.6.1) . Due to a strongest eccentricity of its orbit (0.0934 vs 0.0167 for the Earth), the seasons are more pronounced in the southern hemisphere, where winters are long and cold ($L_S = 90°$) and summer are short and hot ($L_S = 270°$). A martian day (commonly called Sol) last 24h39min35sec and a Martian year counts 669 Sol or 607 terrestrial days.

Surface of Mars presents a major dichotomy between the northern hemisphere, characterized by

smooth plains little cratered and therefore more recent, and the southern hemisphere composed of highlands strongly cratered, witnesses of much older events. There are two major morphologies : the presence of volcanic structure testifying to past magmatic events and the presence of two large impact basins, Hellas Planitia (42°S, 70°E) and Argyre Planitia (49°S, 326°E). These morphologies play a significant role on the atmospheric dynamics (see section 6.2) and conversely, the atmospheric alteration of mafic basalts from ancient volcanism makes the surface very dusty, rich in ferric oxides (Poulet et al., 2007). Finally, other observed morphologies show the past flow of liquid water on the surface (dendritic fluvial network, outflow channels) and are sometimes associated with the presence of hydrated minerals, such as phyllosillicates, identified using spectral criteria (Poulet et al., 2009) and in-situ measurements from rovers. These large morphological structures are thus to be related to the past climatic history of the planet and will not be detailed here because they are not the object of this work. On the other hand, the morphologies associated with recent climatic events are described in sec.6.3. Their understanding require to characterize first the atmosphere and its dynamic.

6.2 Martian climate

6.2.1 The atmosphere

The first information regarding the Martian atmosphere dates back to 1965, when the American spacecraft Mariner 4 approaches Mars within 10 000 km and made a first estimation of the surface pressure around 6 mbar (4 and 8 mbar respectively). It also confirmed the previous spectroscopic observations from the Earth having suggested that the atmosphere is mainly composed of CO_2 . Recent data also confirm these results. The surface pressure is between 3 and 12 mbar depending on the season and location. The atmosphere is composed of CO_2 (96%), argon (1.93%), dinitrogen (1.89%) and dioxygen (0.145%). Other trace gases such as carbon monoxide (700ppm), water vapour (300ppm) and nitric oxide (120ppm) were also detected. The scale height (vertical distance to travel to divide the pressure by a factor e) is comparable to that of the Earth with a value of 11.1 km (8.5 km on Earth). On the other hand, the Martian atmosphere is more tenuous and more extensive with a troposphere up to 45 km altitude, followed by a mesosphere (110 km) and a thermosphere/ionosphere (800 km). Finally, the atmosphere is heavily loaded with dust aerosols from the surface and transported through seasonal atmospheric circulation, facilitating the identification of atmospheric stratification 6.2 but greatly complicating the observation and study of the surface. The estimation of the aerosol concentration is needed to properly correct the atmospheric contribution in the spectroscopic analysis of the surface, however this physical quantity (often referred as the AOT for Aerosol Optical Thickness) is hard to assess considering the similarity between the atmospheric aerosols and the surface dust. The minimal and maximal temperatures recorded at the surface are respectively 140K (-133°C) and 273K (0°C) for a mean annual temperature of about 210K (-63°C). With such a low water vapour content and a much lower average temperature than on Earth, Mars justifies is title of “cold and dry desert”.

6.2.2 Atmospheric circulation

6.2.2.1 CO_2 cycle

Martian atmospheric circulation is mainly controlled by the CO_2 cycle (Leighton and Murray, 1966). Indeed, during the local winter, surface temperature reach the CO_2 condensation temperature (140K) allowing condensation on the surface of CO_2 ice. Since CO_2 is the main atmospheric component, this condensation of a fraction of the total atmospheric mass causes a pressure drop up to 30% of the total atmospheric pressure above the winter hemisphere. This phenomenon creates a latitudinal pressure gradient and leads to the formation of a single Hadley cell (Forget et al., 1999) whose ascending branch starts from the summer hemisphere (southern hemisphere during boreal winter and conversely during southern winter) by transporting the atmospheric components at high altitude to the winter hemisphere. Then, the air comes down and travels near the surface toward the summer hemisphere creating strong surface winds

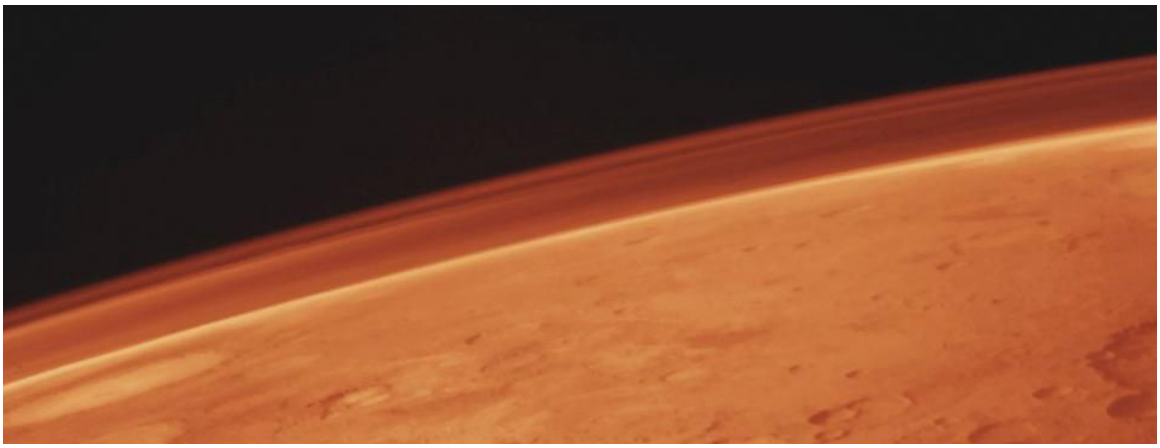

Figure 6.2: Mars limb image taken by the Viking 1 probe. The atmosphere is heavily loaded with dust, making it possible to distinguish its stratification. Credits : NASA/JPL.

that lift the regolith's dust into the atmosphere. During the spring temperature goes up and the CO_2 ice sublimates raising the atmospheric pressure and stopping Hadley's circulation until the next local winter. This Hadley cell changes direction around each equinox (Forget et al., 1999) and is directly related to annual variation of surface pressure, the atmosphere inflates and deflates twice a martian year (see Fig. 6.3).

This condensation/sublimation cycle is particularly visible on the polar ice caps (see Fig. 6.4) and it is also responsible for the formation of seasonal deposits (see Fig. 6.3) that can reach mid-latitudes of Mars (50°N and 45°S). Due to the longest duration of winter in the southern hemisphere, the south seasonal cap has a larger spatial extent than the northern one. During the local spring and summer, sublimation of CO_2 seasonal ice deposits uncover residual polar ice caps with significant differences :

- The northern residual polar ice cap is composed of almost pure water ice interspersed with more dusty layers over a thickness of about a kilometers (Phillips et al., 2008). This layer named North Polar Layered Deposits (NPLD) and covered by a layer of water ice with a thickness of up to one kilometer.
- The southern polar ice cap is composed of a ten meters thick CO_2 ice layer covering a 300 kilometers diameter surface (Kieffer, 1979) on top of a hundred meters layer of almost pure water ice, all resting on a stratified unit similar to the NPLD, the South Polar Layered Deposits (SPLD) whose diameter reaches more than 1000 km for a thickness up to 3.7 km. Unlike the NPLD, the SPLDs are not directly visible since they are mostly covered by a thick dust layer. In addition, this residual cap has the peculiarity of not being centered on the geographical South pole.

Residual ice caps and stratified north and south deposits are therefore important CO_2 and H_2O reservoirs for the martian atmosphere (Phillips et al., 2011). In addition, the presence of a surface CO_2 layer onto the southern residual cap acts as a cold trap for the water ice layer, preventing it from sublimating (Montmessin, 2004).

6.2.2.2 Water cycle

The main source of atmospheric water is the northern residual cap, during sublimation of the seasonal cap of CO_2 the residual cap of water ice get into contact with the atmosphere (Montmessin, 2004; Pottier et al., 2017). It can therefore sublimate during the boreal spring and the water vapour is transported by the atmospheric circulation imposed by the Hadley cell. This atmospheric water can then be adsorbed by the surface during its transport or condense in the atmosphere as a cloud near the equator by adiabatic cooling following orographic uplift or within the upstroke of the Hadley cell. The atmospheric circulation imposed by the cell implies there is no or very little water exchange between the two hemispheres and

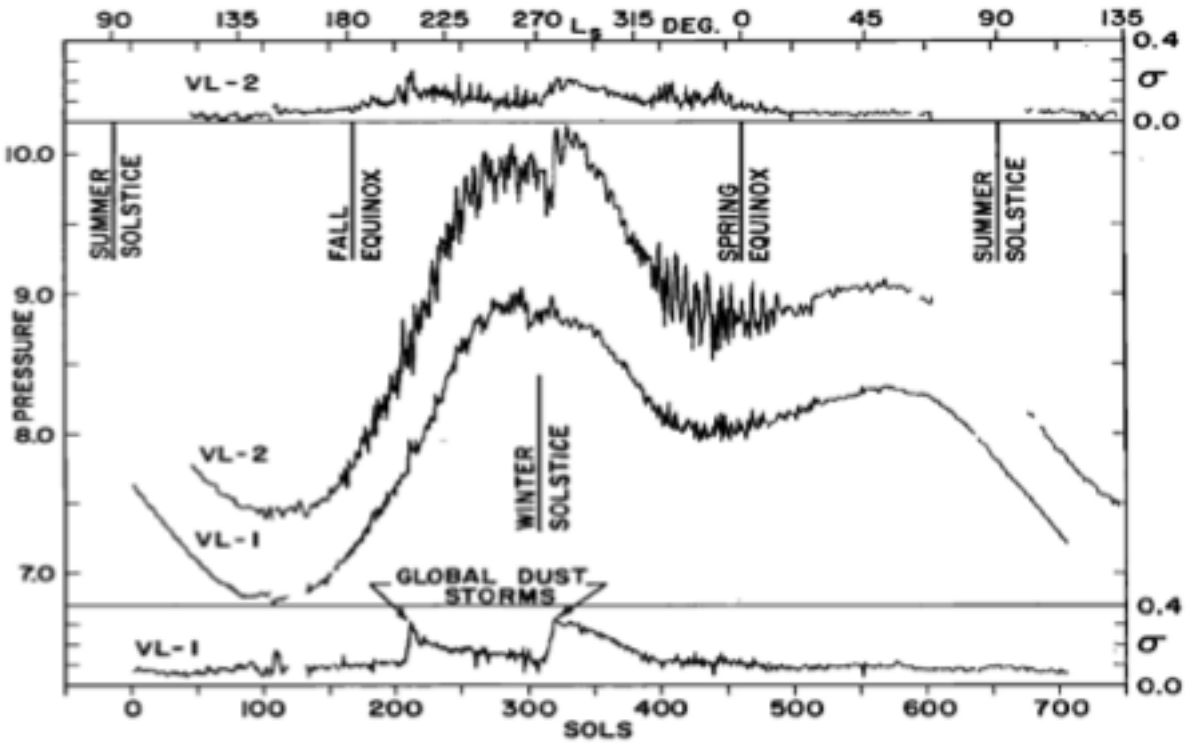

Figure 6.3: The annual surface pressure cycle measured by Viking landers 1 & 2. From (Hess et al., 1980)

the sublimated water vapour ends up being re-condensed on the northern residual cap. In opposition with the northern reservoir, the water ice layer of the southern residual cap provides little water to the martian atmosphere because it is covered by a residual layer of CO_2 ice preventing the sublimation of the water vapour. This cold trap mechanism explains the stability of the water layer in the southern hemisphere. The significant difference between the structure of both residual ice caps and the atmospheric circulation imposed by the large Hadley cell ensures there is few water exchange between the poles and the southern hemisphere, which remains on average drier than the northern one (Fig. 6.5, left).

Another important water ice reservoir is the martian sub-surface. This water may come from the adsorption of atmospheric water vapour coming from the hemispheric transport or the alteration of hydrated minerals in depth. As pressure and temperature conditions make it impossible for liquid water to be stable on the surface, this water is stored as a permafrost whose Phoenix lander has confirmed its presence a few centimeters below the surface. In addition, the neutron spectrometer on board Mars Odyssey (2001) confirmed the presence of a hydrogen-rich basement, expressed as a mass fraction of water-equivalent hydrogen (Feldman, 2004). The map resulting from this work shows a mass fraction varying between 2% (at the equator and the mid-latitudes) and 70% (at the poles) reinforcing the idea of an important water reservoir in sub-surface.

The water cycle is therefore mainly controlled by the CO_2 cycle, allowing its sublimation but also guaranteeing its condensation. However, the water cycle also influences the CO_2 cycle, especially during the re-condensation of water onto the CO_2 seasonal ice by cold trapping. This newly formed frost made of small grains whose albedo is very high which delays or prevents the sublimation of CO_2 ice (Appéré et al., 2011).

6.2.2.3 Dust cycle

As the water cycle, there is a dust cycle on Mars strongly constrained by the CO_2 cycle. In fact, besides the pressure variations caused by the CO_2 condensation at the surface, the insolation differences as a function of latitude create a latitudinal variation of temperature. Thus, the hot air masses rise within

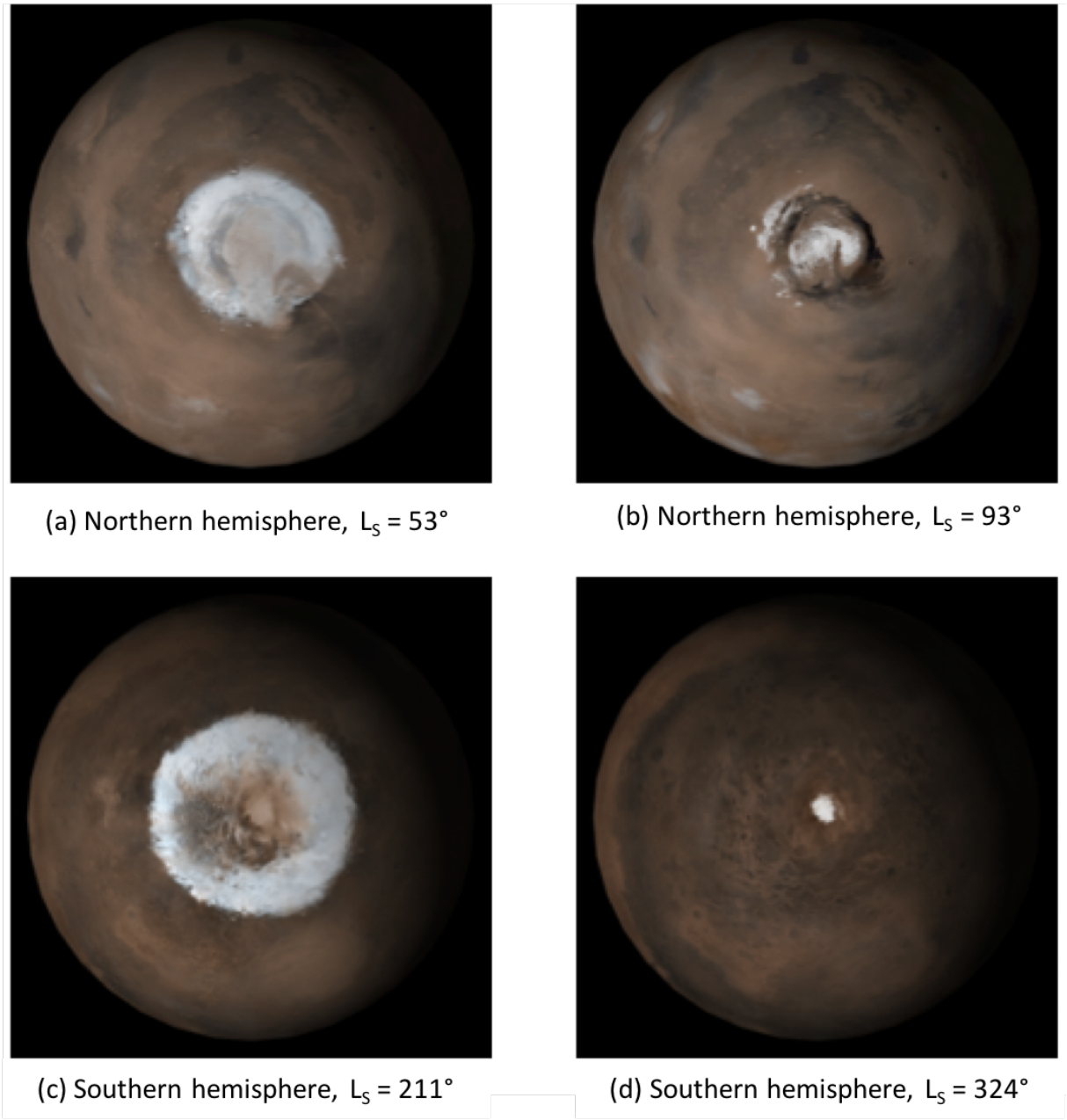

Figure 6.4: Variation of seasonal extensions of Mars polar caps, polar projection mosaic. (a) Northern hemisphere in the middle of the boreal spring, CO_2 deposits extend for thousands of kilometers. (b) Northern hemisphere at the summer boreal solstice, the seasonal ice disappeared and reveal the permanent ice cap. (c) Southern hemisphere in early austral spring. The darker region is the cryptic region. (d) Southern hemisphere in the middle of the austral summer, the seasonal ice disappears and discovers the permanent CO_2 ice cap. Credit : NASA/JPL/MSSS

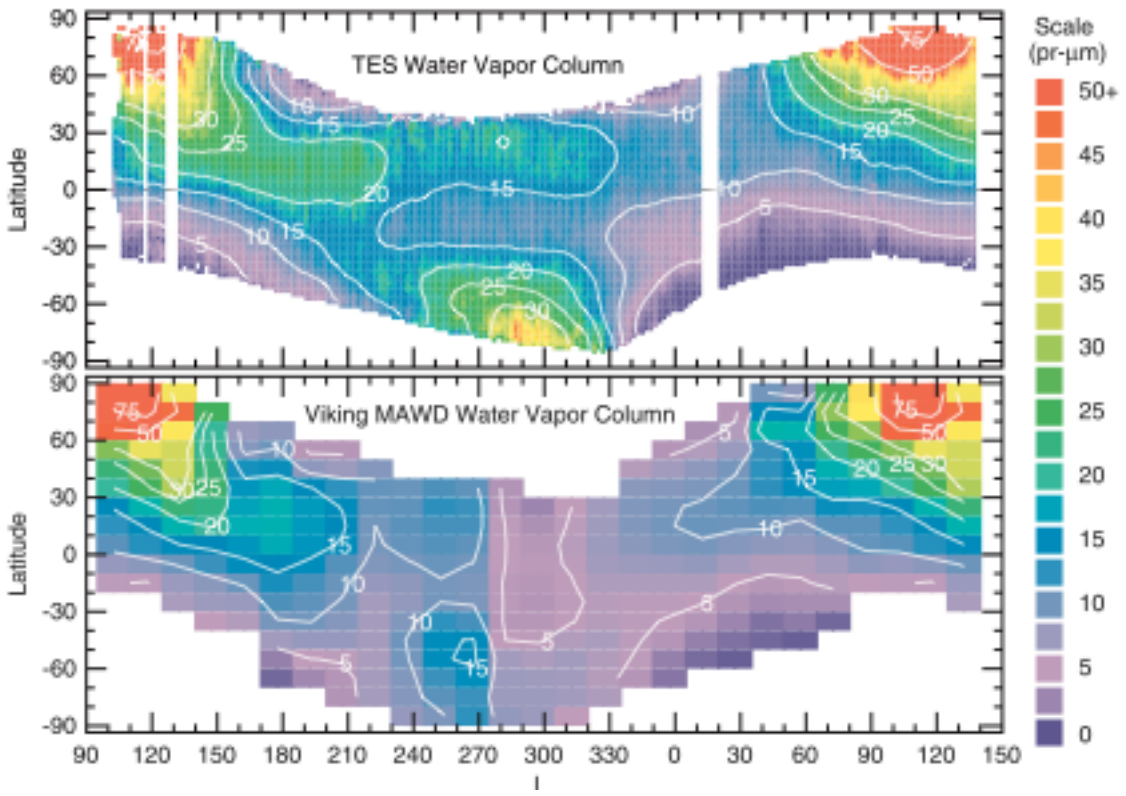

Figure 6.5: Left : Annual water transport cycle measured by TES spectrometer onboard MRO. Each value corresponds to a zonal average of the water vapour content of the atmospheric column, in precipitable millimeters. From (Smith, 2002).

the summer hemisphere and migrate to colder region (in the winter hemisphere) and cool down thereby participating in the establishment of the large convective Hadley cell (Spiga et al., 2013). The rotation of the planet causes a deviation of the convective cell (as on Earth) and generates a dominant eastward wind at high altitude. At lower elevations these winds are deflected by the air masses circulation from the winter to the summer hemisphere, taking a north-east direction during the boreal winter and a south-east direction during the austral winter. These winds are also reinforced by the thermal contrast between the surface and the atmosphere, which is greater at the poles with the CO_2 seasonal ice deposits. They also contribute to the erosion of the surface and to the transport of dust in the atmosphere. There are two major types of transport :

- Dust whirlwinds or "Dust devils" occur at small spatial scale and are formed when the hot surface air reaches a lower pressure zone. Hot air rises and is replaced by colder air whose surface friction promotes the vertical rotation of the air mass and its horizontal movement. This phenomenon can reach heights of several kilometers and is reinforced near dark surfaces experiencing greater sunlight because they contribute more directly to the heating of the surface air. Due to the orbital configuration of Mars, dust devils are more frequent in the southern hemisphere since the austral summer experience a greater sunshine. Finally, the roughness of the surface (topography) may also contribute to the variations of pressure and insolation which favours the triggering of dust devils.

- Regional storm events are connected to atmospheric circulation and a significant thermal contrast between the surface and the atmosphere. Winds created in the polar regions can therefore be very intense and tear off large amounts of dust on the surface, up to regional scales. This air-bone dust suspension has the main effect of warming the atmosphere and reducing the gap between minimum and maximum temperatures over a day. This is due to the optical properties of the dust, they strongly absorb the solar radiation in the visible spectral range and restores it as heat in the atmosphere. They are also great diffusers, decreasing radiation reaching the surface. This will therefore considerably increase the thermal contrast between the atmosphere and the surface and therefore enhance the atmospheric circulation. This feedback favours the duration of storms and can trigger a global storm across the entire Martian atmosphere.

Both mechanisms contribute significantly to the contribution of dust within the climate dynamics (Spiga et al., 2013). The characteristic time and the radiative impact of the phenomenon depend strongly on the particle size and their optical properties. This cycle is strongly correlated with the CO_2 and water cycle and their entanglements lead to the formation of seasonal deposits on the surface (6.3) whose formation mode, spatial and temporal evolution are still subject to debate within the scientific community. Another mechanism involving the dust transport into the atmosphere is the cold gas jet which is detailed in subsection 6.3.2.

6.3 Icy surfaces and ice-related morphologies

There are two groups of observable morphologies on the surface of Mars. The first one regards the ancient processes and reflects a past climate alternating between warm periods, propitious for the flow of liquid water (Carr, 1995), and cold periods favourable to the establishment of glacial morphology (Bouquety et al., 2019). This alternation would be related to significant variations of the obliquity (Laskar et al., 2004) and is most probably due to higher atmospheric pressure (close to 1 bar) than today (Wordsworth, 2016). The second group regards the current and active processes occurring in the seasons. It has been observed significant evolution of the surface with the first high spatial resolution images (25 cm per pixel for the HiRISE imager on board Mars Reconnaissance Orbiter) and allowed to identify the processes responsible for these morphologies. We thus distinguish :

- Glacial and periglacial landscapes : thermal contraction polygons and lobed ejecta craters. They reflect the presence of a water rich soil as a permafrost ;

- Active flows : gullies, Recurring Slope Linae (RSL) and flood, whose formation mechanisms are still debated ;
- Aeolian processes : migration of dunes and wrinkles with surface winds ;
- Seasonal deposits : dark spots, dark flows, gullies, dark polygons, spiders. These morphologies are directly related to the seasonal CO_2 condensation/sublimation cycle ;

These latter are the subject of this work and their understanding is still debated. These processes are related to the Martian climate dynamics and have no known terrestrial equivalents, making them very interesting. This work will focus on ice-related morphologies such as cold jets, dark spots and spiders who testify a close entanglement between the CO_2 , water and dust cycles.

6.3.1 The cryptic region

During winter, seasonal ice caps cover the entire poles and ice can extend up to 50° latitudes (Langevin et al., 2007). It is therefore necessary to distinguish seasonal ice cap that is totally covered by ice and the seasonal ice that can appear locally according to the local slope, the orientation of the surface with respect to the Sun and the thermophysical properties of the surface (Schmidt and Portyankina, 2018). Most CO_2 ice is formed when the insolation is minimal, which makes it difficult to observe with instruments using reflected sunlight. However, thermal spectrometers have been able to remove the doubt about the maximum extension of seasonal ice by identifying the regions where the surface is at the CO_2 condensation temperature (see Fig. 6.6) although these regions may appear dark (low albedo) in reflected sunlight during the day. Thus, a large area of the southern seasonal cap has been identified as darker, it is the cryptic region (Kieffer et al., 2006). The measured albedo is comparable to that of lower latitudes regolith and would involve two possibilities :

- The ice layer is transparent in a compact and polycrystalline form, revealing the underlying regolith ;
- The ice layer is covered by an optically fine dust that would be thermised by the CO_2 ice ;

There is currently no clear consensus on this subject although many models attempt to provide an answer. Both hypothesis are based on the optical properties of the materials and require various observations at both spatial and temporal scales, making it difficult to validate. In addition, many active processes occur on these icy surfaces (both polar caps and seasonal ice) during the sublimation of the ice but their concentrations remain higher in the cryptic region (Langevin et al., 2006; Kieffer et al., 2006; Andrieu et al., 2018).

6.3.2 Cold jets

During the spring, the sunlight becomes more important favouring the sublimation of the CO_2 seasonal ices. Their sublimation is mainly controlled by their albedo (Schmidt et al., 2009). During this period, icy surfaces are covered by dark spots (Fig. 6.7) whose spatial and temporal variability is still poorly constrained. Among the various mechanisms proposed, the cold gas jet (Piqueux, 2003; Kieffer et al., 2006)is today a consensus (Fig. 6.8). The model is based on the optical properties of the CO_2 ice, which is translucent to visible radiation and thus absorbs very little of the incident solar radiation, thus reaching the underlying regolith. The latter is very dark and therefore absorbs a significant proportion of the incident energy that is restored in the thermal infrared wavelengths where CO_2 ice is highly absorbent. The absorbed energy causes sublimation of the ice layer from below. The CO_2 gas is then trapped between the regolith and the compact ice layer. When the pressure within the layer reaches the breaking point of ice, the ice cracks and the gas escape rapidly with the regolith dust. Dust can be transported into the atmosphere or deposited on the surface as dark spots.

This model is supported by thermal, dynamic and mechanical studies showing its coherence with observations (Thomas et al., 2011). It has been shown that the solid greenhouse effect is possible within

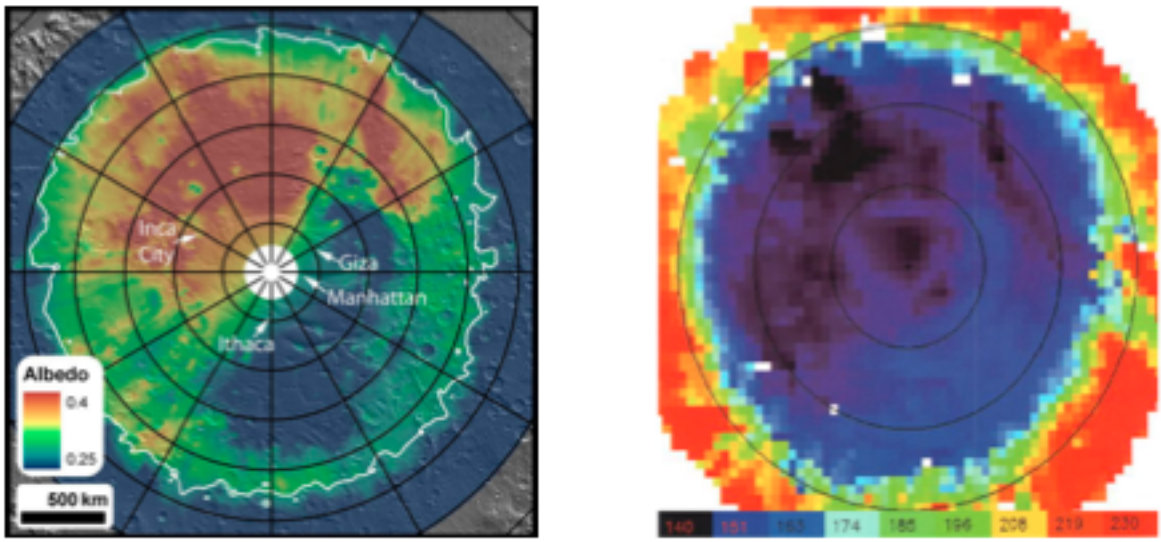

Figure 6.6: Left: Albedo map of the seasonal southern cap of Mars at the beginning of the austral winter (Ls = 220-225 °) from (Hansen et al., 2010). The seasonal deposit limit is shown in white. The cryptic region is the zone whose albedo is comparable to that of the regolith beyond the seasonal ice. Right: Surface temperature map of the same region at the same season from thermal emission spectra of TES (Thermal Infrared Spectrometer) instrument from (Kieffer, 2001). All of the seasonal deposits are at the CO_2 ice condensation temperature and confirm that the cryptic region is ice-covered.

water ice (Kaufmann et al., 2007). Moreover, this effect would be sufficient enough to initiate a basal sublimation of seasonal deposits in the late polar night (Portyankina et al., 2010). Thermal models also shown that this effect can occur very quickly after the end of the polar night (Pilorget et al., 2011). However, some problems remain :

- Not active jets were observed. All observations are made around noon local time to promote maximum sunlight while this phenomenon is assumed to occur as soon as the first solar rays hit the surface ;
- The model does not explain the spatial variability observed at local scales ;
- The activity declines during the spring while it should occurs as long as there are icy surfaces ;
- How can CO_2 ice be translucent ? (Andrieu et al., 2018)
- The role of impurities (water ice, dust) within the CO_2 ice layer is not taken into account ; Can they prevent geyser to occur ?
- Is there a link between theses processes and the dark flow activities ? (Pasquon et al., 2016; Portyankina et al., 2019)

If this cold gas jet phenomenon exists, then it plays a significant role in the atmospheric dynamic of Mars as a dust transport agent. It might be the most active geomorphological mechanism on Mars (Piqueux and Christensen, 2008) and a finer characterization is therefore necessary.

6.3.3 Spiders

An intriguing morphology is also present in polar regions, especially in the cryptic region, in the form of dendritic structures called “spiders”. These araneiforms are made of converging dendritic network trenches of metric depths and widths (Fig. 6.9, bottom). These structures can reach several hundred

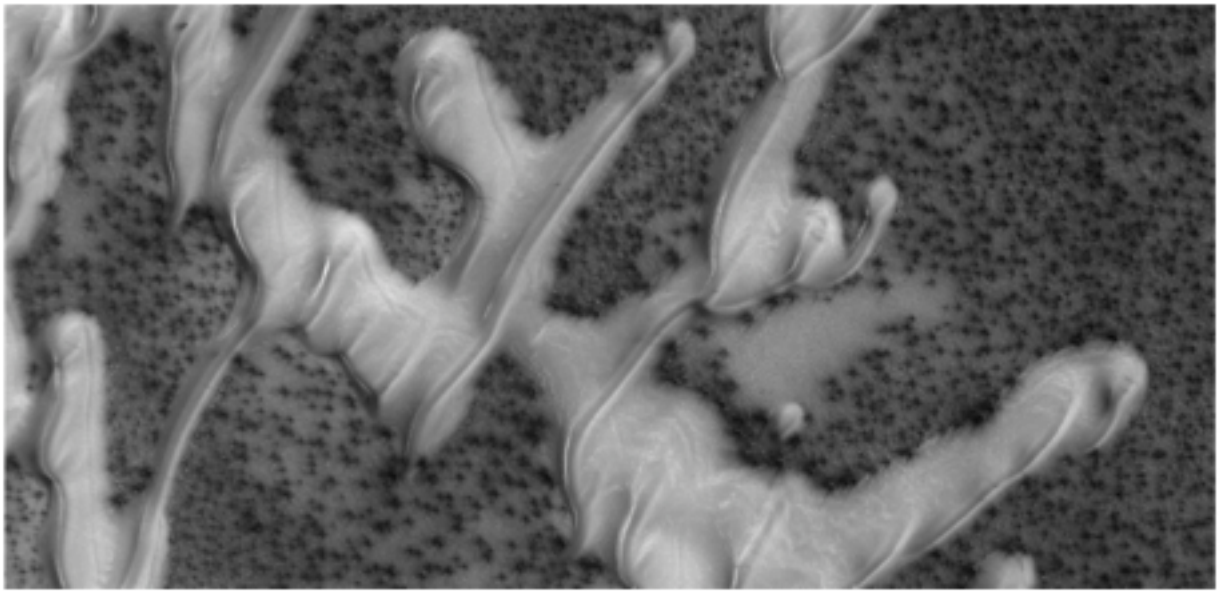

Figure 6.7: During the spring, the icy surfaces are covered with dark spots. It is the cold gas jet model which explain this phenomenon. This 7 km wide image is extracted from the HiRISE spectro-imager and it shows the presence of dunes (80 ° N, 123 ° E, Ls = 7.5 °) with no jet activity while the inter-dunes are covered by dark spots. Credit: NASA/JPL/University of Arizona.

meters in diameter and their presence is sometimes correlated with the presence of dark spots (Fig. 6.9, top). It was quickly proposed that they are carved by the cold jets activity after multiple repetition over the years. There is no clear consensus on this and spiders could be geologically old considering the low efficiency erosion process at those latitudes (Portyankina and Aye, 2018). It nevertheless denotes the existence of a violent mechanism, able of considerably changing the surface and left its imprint on very long times. A more violent jet mechanism could therefore be the cause. However, these structures are related to the seasonal ice evolution and need to be further investigated.

6.4 Outstanding questions

Active processes of Martian icy surfaces are still debated. High latitude cold jets could be the most effective erosion mechanism on Mars (Piqueux, 2003) and the many feedbacks between CO_2 water and dust cycle are still poorly constrained in the climate models. Also, CO_2 ice is suspected to be present near equatorial latitudes early in the morning, an quickly sublimates when the sun illuminates the surface, possibly triggering the cold jets mechanism. The ExoMars TGO mission is to first to provide data at various local times combined with a very high spectral resolution, allowing, for the first time, to access the surface properties early in the morning and late in the evening. A fine spectroscopic analysis of such data holds promise for understanding the processes governing the evolution of the Martian surfaces and climate.

To do so, it is first necessary to provide a radiative transfer model capable of quantitatively describing the light-matter interactions occurring within a CO_2 ice layer, and thus reproduce the more accurately the spectra obtained by the instruments. It is also necessary to be able to record data on variable temporal and spatial scales considering the quickness of those phenomenon. Such a radiative transfer model was recently developed by F. Andrieu (Andrieu et al., 2015) to simulate infrared reflectance spectra of a CO_2 ice sheet by varying the thickness of the ice, its compactness, its roughness and the characteristics of its impurities (composition, volume proportion, size). This model has been validated on laboratory measurements (Andrieu et al., 2016) and a rapid inversion method particularly suited for massive remote sensing data was developed (Andrieu et al., 2016). It has been shown that this approach is valid for Mars.

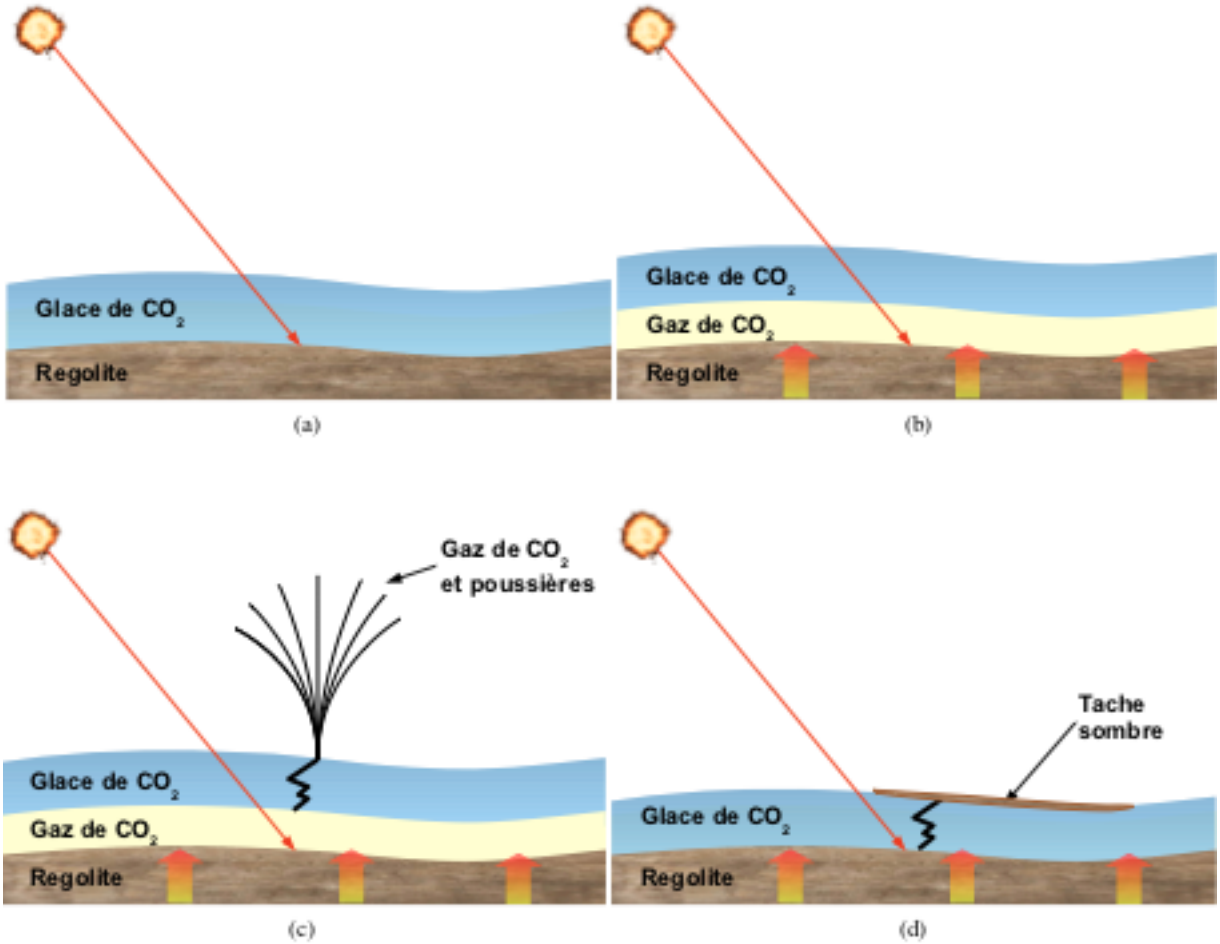

Figure 6.8: Cold gas jets model (cryoventing) proposed by H.G. Kieffer and formalized by S.Piqueux et al. (Piqueux, 2003; Kieffer et al., 2006). (a) CO_2 ice is transparent to solar radiation reaching the regolith. (b) The dark regolith absorbs this radiation, heats up, and restores it in the thermal infrared. The CO_2 ice absorbs this radiation and start sublimating from below. (c) The pressure within the layer increases and reaches the breaking point of the ice, the trapped gas escapes with the regolith dust. (d) These dusts are deposited over the ice layer as a dark spots.

The team confirmed that CO_2 is in translucent state in the Richardson crater (Andrieu et al., 2018) by analyzing the CRISM (Compact Reconnaissance Imaging Spectrometer for Mars) data, a spectro-imager in the visible-infrared (0.36 - 3.92 µm) wavelengths.

Thus, as a follow-up of this work, we would propose to use such radiative transfer model in an extensive analysis of the microphysical properties of the CO_2 ice at various location and local time on Mars using the data from the NOMAD/LNO (Limb and Nadir Occultation) near-infrared data on board the ExoMars TGO mission, described hereafter.

The LNO channel is a state of the art spectrometer at a very high spectral resolution and, at the time of this work, required a precise spectral and radiometric calibration to fully exploit the potential of the data. The LNO calibration constitutes the major part of the work carried out during this PhD, and will be developed in chapter 8. For that purpose, we needed a reference solar spectrum in the same spectral range. Since it wasn't available in the literature, our construction of a reference solar spectrum is described in chapter 7. The first attempt to extract spectroscopic information out of the calibrated dataset is developed in chapter 9.

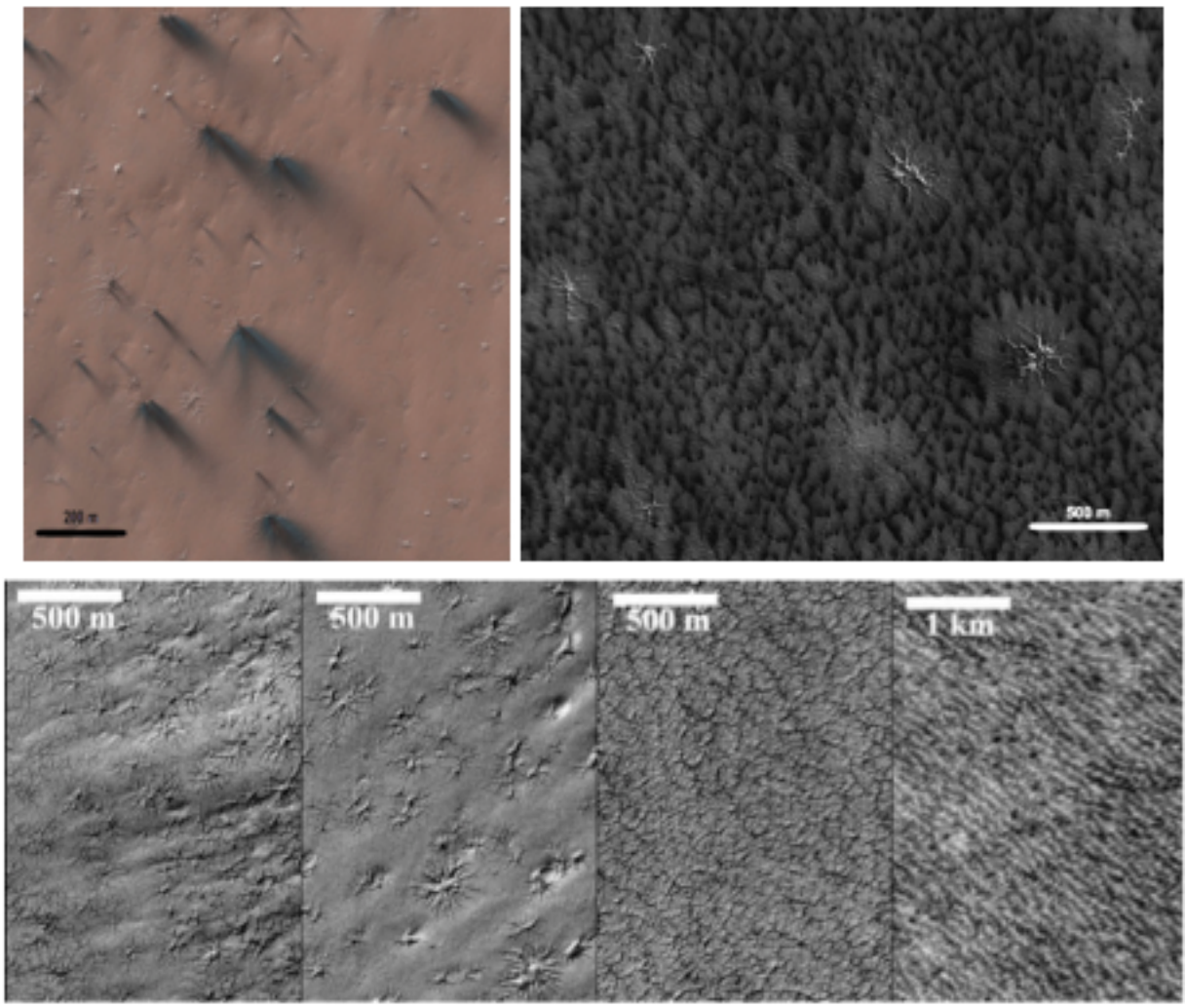

Figure 6.9: Top : The spiders are sometimes correlated with the cold jet activity (left) and sometimes no (right). Images took during the southern spring at high latitudes (85-87°S). Bottom : Several size and location of spiders on Mars, seen by the MOC camera (Piqueux, 2003).

6.5 The ExoMars-TGO mission

The ExoMars - Trace Gas Orbiter (TGO) is a space mission launched in 2016 by the European Space Agency (ESA) and the Russian Space Agency (Roscosmos). The satellite arrived in Mars orbit in 2017 and, after more than a year of airbone manoeuvring, it is now on a circular orbit traveled in 120 minutes at a 400 km altitude and tilted 74° regarding the martian equator. The first acquisition began in April 2018 and the nominal duration of the mission is 5 years. The scientific objectives of the mission were based on a controversial detection of methane by the OMEGA spectro-imager onboard Mars Express. This is why TGO is mainly intended to finely characterize the Martian atmosphere to detect a wide range of trace gases, including methane, their isotopes and their possible interactions with the surface. To do this, the mission embeds 4 instruments :

- Atmospheric Chemistry Suite (ACS) : Three infrared spectrometers (0.7 - 25 µm) to analyze the composition and structure of the Martian atmosphere but also to observe the sun in order to refine solar occultation data ;

- Color and Stereo Surface Imaging System (CaSSIS) : A high-resolution camera (5 m per pixel) capable of obtaining color and stereoscopic images over a wide swath. The imager will images the

surface to help understanding the geological and dynamical process governing potential sources and sink of trace gases ;

- Fine Resolution Epithermal Neutron Detector (FREND) : Neutron detector used to map the presence of hydrogen on the surface and subsurface of Mars ;

- Nadir and Occultation for MArs Discovery (NOMAD) : Three spectrometers covering a wide range of wavelengths (ultraviolet - infrared) to characterize the martian atmospheric components ;

In addition to the scientific objectives, the TGO spacecraft will serve as a telecommunication relay for the ExoMars 2020 rover. The high spectral and spatial resolution of the instruments should make it possible to refine the climate models and to characterize surface/atmosphere interactions. In addition, the TGO's particular orbit allows a global coverage of the planet and observations at various local time (4h-22h) thus allowing a characterization of the temporal variability on a daily scale, which is unprecedented.

6.6 Description of the NOMAD instrument

The NOMAD instrument (Nadir and Occultation for MArs Discovery) is a suite of three spectrometers led by the Belgian Institute for Space Aeronomy (BIRA-IASB) on board of the ESA/Roscosmos ExoMars Trace Gas Orbiter mission (Neefs et al., 2015). The ExoMars program consists of two missions designed to study the trace gases of the martian atmosphere but also to acquire information on potential on-going geological and biological processes on the surface of Mars (Vago et al., 2015). The three channels (spectrometers) works separately but are all controlled via a single main electronic interface (Neefs et al., 2015). Two channels (SO and LNO) are infrared spectrometers and are based upon the SOIR (Solar Occultation in the InfraRed) instruments aboard the Venus Express mission. The third channel is an ultraviolet and visible spectrometer (UVIS). Those channels are optimized for different observation modes (see figure 6.10).

The SO channel (Solar Occultation) has the same optical design as SOIR Vandaele et al. (2013), a compact high-resolution echelle grating spectrometer with an acousto-optic tunable filter (AOTF) working in the infrared domain from 2.3 μm to 4.3 μm (4250-2320 cm^{-1}) with a resolving power ($\lambda/\Delta\lambda$) of around 20000 (see tab 6.1).

The LNO (Limb and Nadir Occultation) channel is similar to the SO optical design but it has been optimized for the observation of weak IR light sources. The channel has a reduced wavelength range, from 2.3 μm to 3.8 μm (4250-2630 cm^{-1}), and a resolving power of around 10000 (see tab. 6.1). This work will focus on the use of this channel thus the design and the calibration will be detailed below.

The UVIS channel can operate in both solar occultation and nadir viewing geometries from 0.2 μm to 0.65 μm with a spectral resolution of approximately 1.5 nm.

With such high resolving power, NOMAD fits in with the science objective of the ExoMars program (which are detailed in (Vandaele et al., 2015, 2018)) but is also perfectly suited to study the state of icy surfaces. Moreover, the near-circular orbit varying between 380 and 430 km above the surface with an inclination of 74° allows to complete 12 orbits in one sol (one orbital period last approximately 2 hours long) which leads to the observation of the surface at various local times and allow a fine characterization of the icy surfaces temporal evolution.

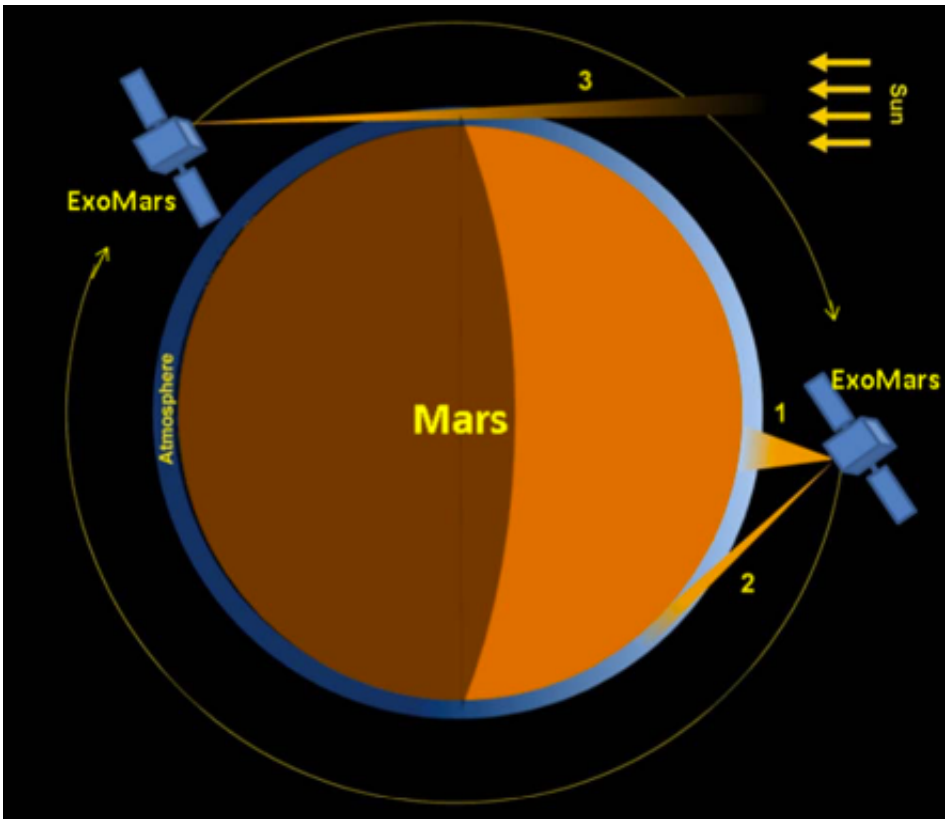

Figure 6.10: NOMAD observation modes : Nadir (1), Limb (2) and solar occultation (3). From (Neefs et al., 2015).

6.6.1 General description

The ExoMars TGO is a nadir tracking spacecraft, meaning that its -Y axis is always pointing perpendicular to the surface of Mars (Neefs et al., 2015). The LNO and UVIS have nadir lines of sight and are therefore always directed to Mars. The solar-pointing lines of sights are inclined with respect to the nadir direction by 67.07° in the -Y/-X plane through the use of periscopes (Neefs et al., 2015; Vandaele et al., 2018)(see figures 6.11 and 6.12). The TGO is therefore suited for nadir and limb observations (Neefs et al., 2015) and measures solar occultations when the solar lines of sight pass through the atmosphere before sunset and after sunrise. To optimize the signal, the LNO and SO field of view (FOV) must comprise the entire solar disc (Neefs et al., 2015) resulting in a rectangular FOV for both channels, hence the LNO channel is also able to perform solar occultations. However, since its primary role is to perform nadir and limb measurement, some modifications were implemented to increase the signal throughput and to reduce the thermal background of the instrument (Vandaele et al., 2018). This is why the highest wavelength limit of the detector sensitivity has been reduced and the length of the slit has been increased from 30 to 150 arcmin in the spatial direction and from 2 to 4 arcmin in the spectral direction. Since its entrance aperture diameter is bigger, all its optical elements are larger (Neefs et al., 2015), resulting in a larger accousto-optic tunable filter (AOTF) crystal, a more intense cooling, a longer integration time but also an appropriate pixel binning and spectra accumulation (Vandaele et al., 2018). This led to a significant change in the spectral and spatial resolution between both channels. A summary of the channels specifications is given table 6.1 (from (Neefs et al., 2015)).

6.6.2 Spectrometer design of the LNO infrared channel

The optical design of the LNO spectrometer is identical to that of SO and therefore very similar to SOIR, it is a combination of a high-dispersion echelle grating along with an AOTF and a cooled detector. The

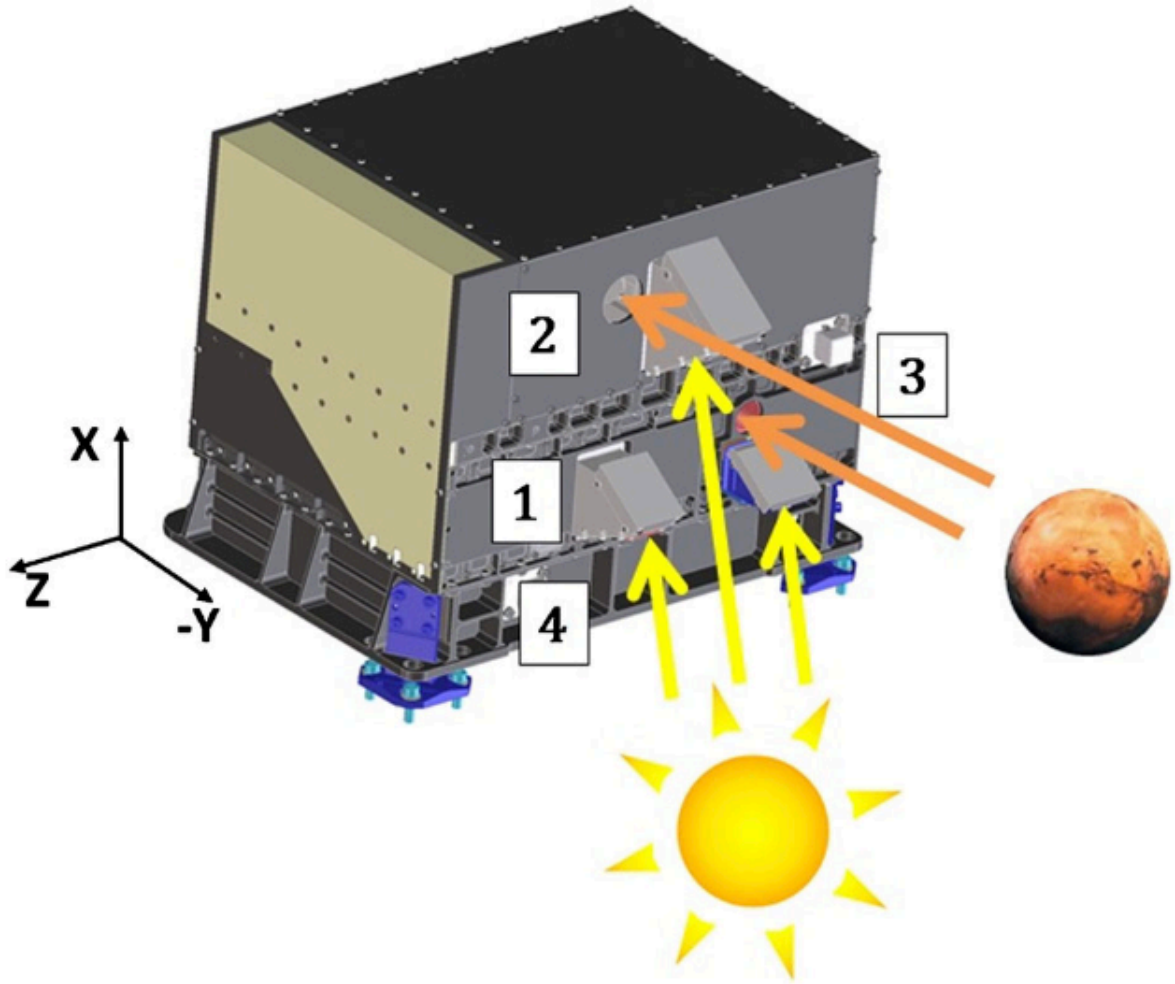

Figure 6.11: The NOMAD instrument with the nadir (orange) and solar (yellow) lines of sight for the SO (1), LNO (2) and UVIS (3) spectrometers. The electronics is located on the underside (4). From (Vandaele et al., 2018).

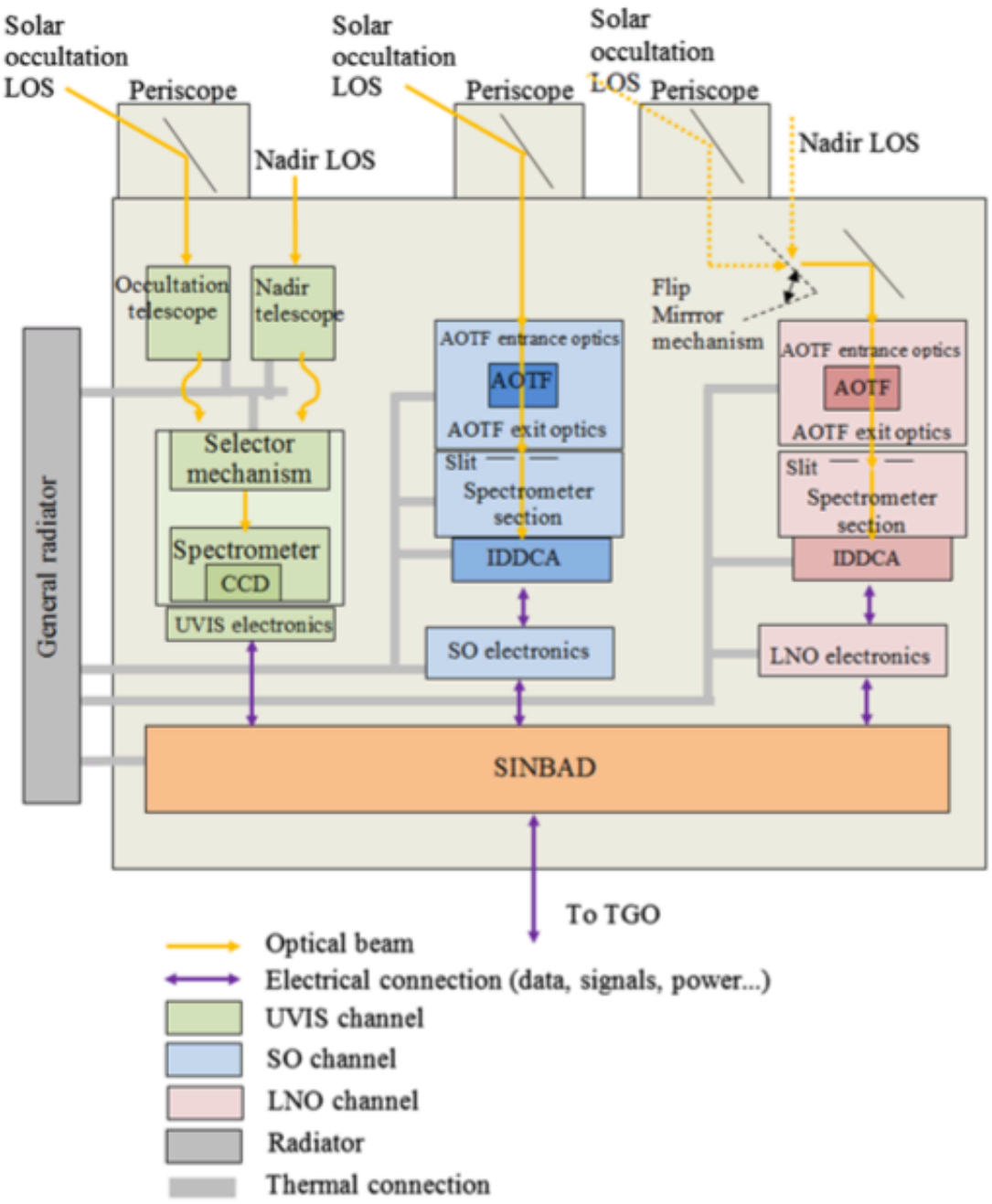

Figure 6.12: The NOMAD subsystems : three spectrometers connected to a central processor unit (SINBAD) which manage all electrical power and data connections between the spacecraft and the three channels. The general radiator with the thermal control system maintain the operational temperature range for the complete instrument through a series of temperature sensors distributed inside the instrument. From (Vandaele et al., 2018).

Characteristics	SO	LNO	Unit
Wavelength λ	$2.3-4.3$	$2.3-3.8$	μm
Wavenumber ν	$4250-2320$	$4250-2630$	cm^{-1}
Instrument Line Profile (ILP)	0.22	0.5	cm^{-1}
Pixel sampling (FWHM)	≥ 2	≥ 2	
Resolving power $\lambda/\Delta\lambda$	20000	10000	
Spectral Resolution	$0.15-0.22$	$0.3-0.5$	cm^{-1}
Slit width in object space	2	4	arcmin
Slit length in object space	30	150	arcmin
Field of view	2×30	4×150	arcmin
Spatial sampling	1	1	arcmin
SNR (over the complete spectral range)	≥ 900	≥ 400	
Optical bench mass	13.5	9.4	kg
Footprint (400 km orbit)		1×0.3	$arcmin^2$
Footprint (400 km orbit)		17.5×0.5	km^2
Detector	320×256	320×256	pixel
Detector temperature	88	88	K

Table 6.1: Summary of SO and LNO characteristics. From (Neefs et al., 2015; Vandaele et al., 2013, 2018).

main advantage of using an echelle grating is that the full height of the detector can be used to register spectral lines (Neefs et al., 2015), which greatly improves the SNR after column binning. The AOTF is placed as diffraction order sorting devices in front of the spectrometer section to avoid order's overlap at the output of the grating (Neefs et al., 2015). Such device also offer a "quick electronic driven random access to spectral orders" (Neefs et al., 2015) without moving any mechanical parts as well as an incident light shutter for the background measurement. The design is illustrated figure 6.13.

6.6.3 The acousto-optic tunable filter (AOTF)

The AOTF is an electro-optical device based on the Bragg diffraction, the interaction between acoustic and electromagnetic waves, in a birefringent crystal of Tellurium dioxide (TeO_2). Under the application of a radio-frequency (using a Transducer) the crystal vibrates and its internal structure is alternatively compressed and dilated through the crossing of the oscillating acoustic wave front. This results in a periodic modification of its optical properties, its refractive index, thus producing a diffraction of the incident light. The intensity of the diffraction is proportional to the amplitude of the acoustic signal applied to the crystal. In addition, changing the acoustic frequency applied to the crystal alters the periodicity of the refractive index variation and therefore the wavelength at which the light is diffracted. The AOTF crystal acts mainly as a filter for selecting the desired order of diffraction which will be transmitted to the diffraction grating. One of the main characteristic of an AOTF is that the FWHM of their spectral band (in wavenumber units) is, to a certain extent, constant over the wavelength range. This allows to match the AOTF passband with the free spectral range of the grating and therefore optimize the system. Part of the non-polarized light entering the crystal travels to the exit of the AOTF without diffraction (order 0) and a part is diffracted at a small angle to either side of the undiffracted beam (Neefs et al., 2015). NOMAD only uses the ordinary polarization of the incoming light (k_0). In the AOTF the polarization plane rotates so that the extraordinary polarization of the diffracted light beam (k_e^*) is transferred toward the spectrometer (Neefs et al., 2015) (see figure 6.14). Thus, if no radio frequency is applied to the crystal (AOTF off) then the spectrometer measures the thermal noise and the background noise also called "dark observation" which are used to correct the specific noises of the detector environment

The main characteristics of the AOTF used for the LNO channel are summarized table 6.2. For a

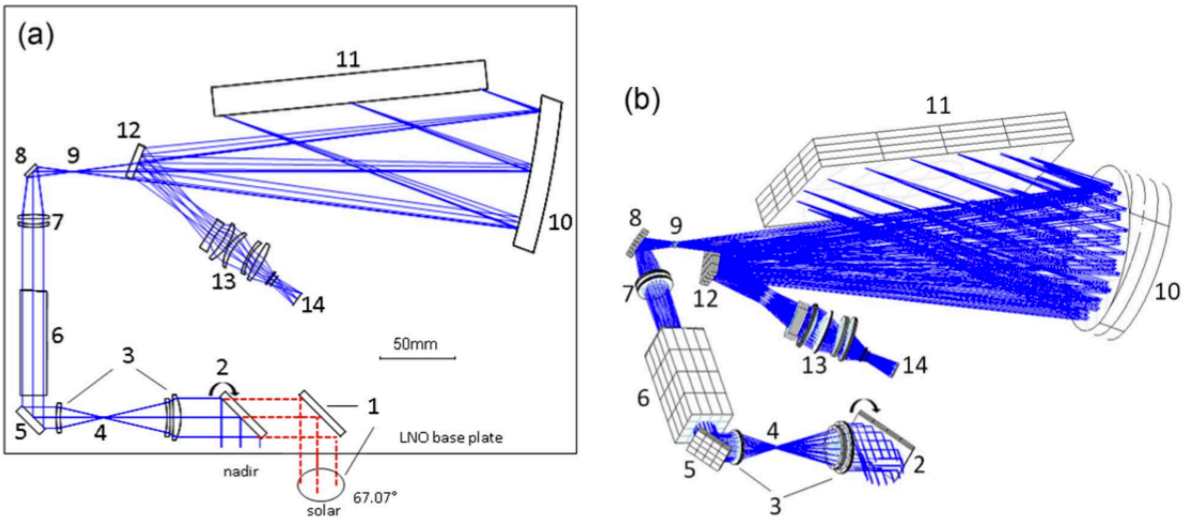

Figure 6.13: Optical design of the LNO channel : (a) 2D left and (b) 3D right. From (Neefs et al., 2015). The LNO channel has two entrance apertures, one for the solar entrance (1) using a periscope with two flat mirrors to tilt the beam by 67.07° and one for the nadir entrance (2) with a single flat flip mirror. Then, the front-end optics of the channel consist of the AOTF entrance optic (3) that match the incoming light beam to the acceptance angle of the AOTF. A diaphragm (4) is also used in the intermediate image plane of the entrance optic to limits the FOV of the system and therefore reduce scattering and ghost images but also to prevent overlap between order 1 and order 0 of the AOTF. A folding mirror (5) directs the light to the AOTF (6) that select diffraction orders to be measured toward the AOTF exit optics (7). Folding mirror (8) creates an image of the scene on the spectrometer entrance slit (9) , which defines the FOV of the spectrometer. Off-axis parabolic mirror (10) is used to collimate the light beam to the echelle grating (11). After dispersion of the light by the grating, the beam reaches again the parabolic mirror (10) that is used as an imaging lens along with the detector optics (13). A last folding mirror (12) project the beam on the detector (14).

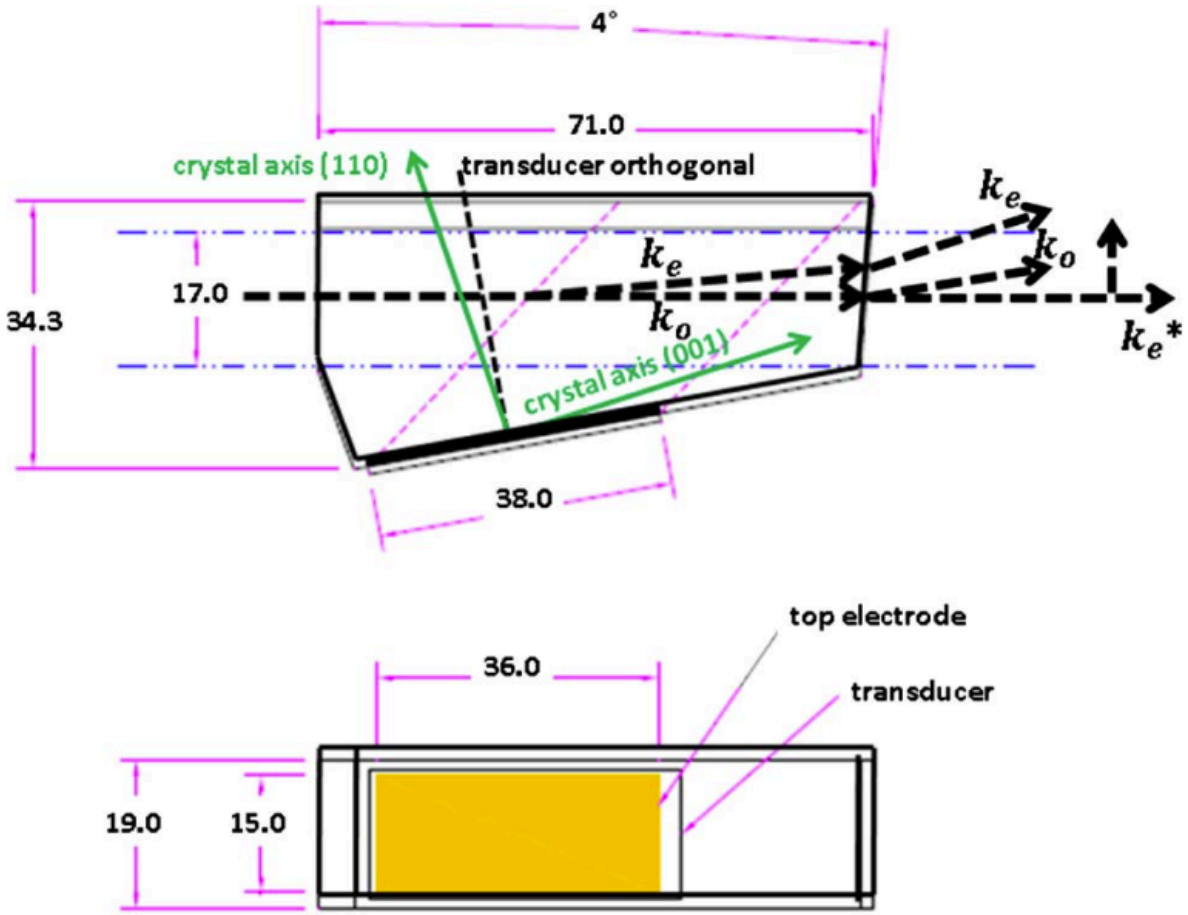

Figure 6.14: Layout of LNO AOTF with indication of system axes and beam polarization (k_0 and k_e are the incoming ordinary and extraordinary beams, k_e^* is the useful diffracted extraordinary beam), from (Neefs et al., 2015).

complete description of the LNO AOTF optics, see (Neefs et al., 2015). To properly account for the AOTF effect, two functions need to be introduced : the tuning and the transfer functions. The first one links the AOTF frequency to a wavenumber and allows to tune the filter. The second one illustrates the effect of the filter on the incoming light at a given radio-frequency.

6.6.3.1 The tuning function

The tuning function expresses the link between the radio frequency applied to the AOTF crystal and the wavenumber at which the maximum of the signal is transmitted by the crystal (Vandaele et al., 2013). For a fixed radio frequency (f_{AOTF}) the AOTF selects a narrow band of the incoming wavelength defined by the following relation :

$$f_{AOTF} = \frac{v_{speed}.\Delta n}{\lambda}.\sqrt{sin^4\theta_i + 2sin^2(2\theta_i)} \tag{6.1}$$

Where λ is the wavelength, θ_i is the incident angle, v_{speed} is the acoustic speed and Δn is the birefringence index of the crystal. The dependence of the birefringence with the wavelength follows (Mahieux, 2011) :

$$\Delta n = \frac{a}{\lambda - \lambda_c} + b \tag{6.2}$$

Parameters	Value	Unit
Spectral bandwidth (FWHM)	24 ± 1	cm^{-1}
Spectral range	2.2-3.9	μm
Radio frequency	15.197 - 31.389	MHz
Diffraction angle	5.2	$^\circ$
Diffraction efficiency	≥ 80	%
Side lobes suppression	4.5	% (of main lobe)

Table 6.2: AOTF characteristics for the LNO channel. From (Neefs et al., 2015)

For the TeO_2 we consider : $a = 7.156$ nm, $b = 0.1338$ et $\lambda_c = 262.9$ nm (from (Mahieux, 2011)). The AOTF tuning function is slightly temperature dependent.

6.6.3.2 The transfer function

The transfer function represents the fraction of incident light filtered by the crystal for a range of wavelength considered. The transmission within an AOTF filter is generally represented by a sinc-square function :

$$T_{AOTF}(\nu) = \left[sinc\left(0.886.\frac{\nu - \nu_0}{fwhm}\right)\right]^2 \tag{6.3}$$

Where ν is the wavenumber, ν_0 is the central wavenumber and $fwhm$ is the full width at half maximum of the function. The transfer function of an AOTF is temperature dependent and a simple sinc-square function is insufficient to account for the AOTF effect on the spectra. A more complex transfer function is often needed using lab calibration and in-flight characterization.

6.6.4 The echelle grating

A diffraction grating or echelle spectrometer is an optical device composed by a series of parallel slots spaced regularly to produce the diffraction of the incident light into different diffraction orders. Slit spacing controls the extent of the diffraction for a given wavelength. For the LNO spectrometer, a "blazed grating" is used, it is a particular grating whose grooves are tilted at a special angle, called the Blaze angle. This angle is generally chosen to optimize the efficiency of the diffraction for a given wavelength. the commonly adopted geometry is the so-called "Littrow configuration" (see figure 6.15, left) in which the Blaze angle is chosen so that the incident and diffraction angle are the same, and are equal to the Blaze angle. In such configuration, the grating equation is (Neefs et al., 2015):

$$m.\lambda_c = \frac{sin\alpha + sin\beta}{\sigma} = \frac{2sin\theta_B}{\sigma} \tag{6.4}$$

Where m is the diffraction order, α is the incident angle, β is the diffraction angle, θ_B is the Blaze angle and σ is the grating groove density (lines/mm). The LNO has a near-Littrow configuration (Neefs et al., 2015) to slightly separate the incident beam from the diffracted beam. Thus, the grating is tilted so that both beams make a small γ angle between the perpendicular plane to the grating surface and the grooves (see figure 6.15, right). It is also necessary to take into account a slight deviation angle i of the incident angle with respect to the Blaze angle in the perpendicular plane to the grooves. The grating equation becomes (Neefs et al., 2015):

$$m.\lambda_c = \frac{2sin\theta_B.cosi.cos\gamma}{\sigma} \tag{6.5}$$

The blaze grating characteristics of the LNO channel are summarized table 6.3. The grating efficiency is estimated at 85% in the center of the grating and falls to 40% on the edges.

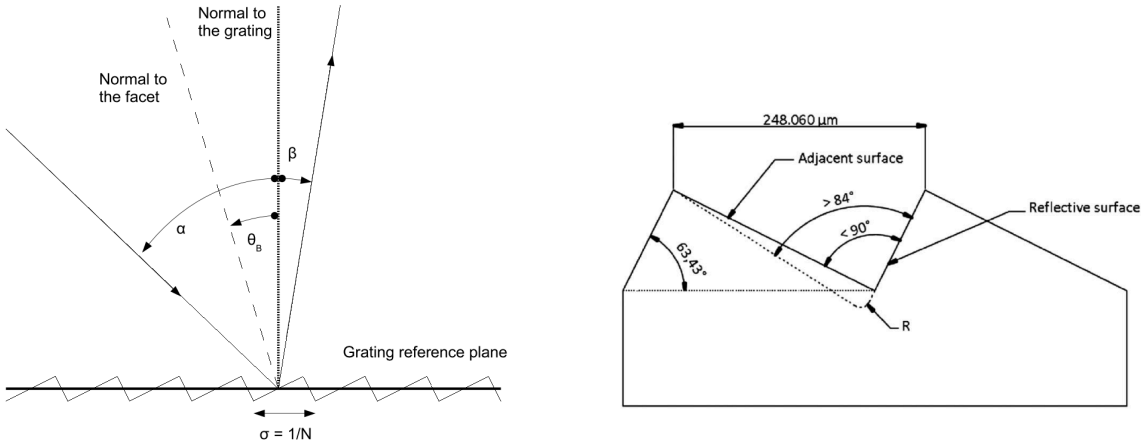

Figure 6.15: Left : Illustration of a diffraction grating in a near-Littrow configuration : the grooves are tilted according to the blaze angle (θ_B). The efficiency of the grating is maximum for an incident angle (α) equal to the Blaze angle, from (Mahieux, 2011). Right : Grating section with slightly over-tilted adjacent surfaces, from (Neefs et al., 2015).

Parameters	Value	Precision	Unit
Blaze angle θ_B	63.43	$\pm$0.1	°
Groove density σ (at 0°C)	4.033512		lines/mm
Number of grooves N	$\geq$ 765		
Groove spacing d	248.06	$\pm$0.001	μm
Off-Littrow angle γ	2.75	$\pm$0.0025	°
Off-Blaze angle i	0	$\pm$0.016	°

Table 6.3: Grating characteristics of the LNO channel, from (Neefs et al., 2015).

6.6.4.1 Free Spectral Range (FSR)

The grating configuration is such that the central wavelength λ_c of each order falls at the center of the detector. It is therefore necessary to introduce the "Free Spectral Range" (FSR) corresponding to the wavelength range for which there is no overlap by adjacent orders, is constant for an echelle spectrometer (Neefs et al., 2015) and is expressed :

$$FSR = \frac{1}{m.\lambda_c} = \frac{\sigma}{2sin\theta_B.cosi.cos\gamma} \tag{6.6}$$

The calculation gives a FSR of 22.56 cm^{-1} for the LNO channel (Neefs et al., 2015). Thus, it is possible to estimate the wavelengths corresponding to the edge of the FSR :

$$\lambda_0 = \lambda_c \pm \frac{FSR}{2} = \frac{2sin\theta_B.cosi.cos\gamma}{\sigma.(m \pm 1/2)} \tag{6.7}$$

The FSR of the NOMAD channel is slightly larger than the spectral span of the detector's sensitive area, so the edge of the FSR fall off the detector for orders $m < 130$ (Neefs et al., 2015). For higher order, the FSR falls entirely on the detector.

6.6.4.2 The grating Blaze function

The near-Littrow configuration ensures that the efficiency of the diffraction is maximum when the refracted angle is equal to the incident angle. Then, the efficiency decreases as the deviation between those angles increase. This effect is represented by the Blaze function BF (Pyo, 2003):

$$\frac{m.\lambda}{\sigma.cos\gamma} = sin\alpha + sin\beta \tag{6.8}$$

$$\alpha = \alpha_B + \theta_B \tag{6.9}$$

$$\alpha \geq \beta : BF = sinc[\frac{1}{\lambda}.\frac{\sigma.cos\gamma.cos\alpha}{cos\alpha_B}.(sin\alpha_B + sin(\beta - \theta_B))]^2 \tag{6.10}$$

$$\alpha < \beta : BF = \left(\frac{cos\beta}{cos\alpha}\right)^2 sinc[\frac{1}{\lambda}.\frac{\sigma.cos\gamma.cos\alpha}{cos\alpha_B}.(sin\alpha_B + sin(\beta - \theta_B))]^2 \tag{6.11}$$

Where α_B is the angle between the incident beam and the normal of the facet in the perpendicular plane to the grooves. The Blaze function intensity as a function of the diffraction orders for each spectral pixel of the detector has been estimated using the LNO channel parameters (see table 6.3) and is represented in figure 6.16.

6.6.5 The detector

The NOMAD detector is made of 256 rows in the spatial direction and 320 columns in the spectral direction. Every photovoltaic diodes (pixels) have a size of 30 x 30 μm and are individually coupled to the CMOS readout integrated circuit (Neefs et al., 2015). When a pixel of a CMOS type detector receives a photon, the latter is absorbed and generates a pair of electrons under the photoelectric effect. These electrons create an electric voltage which is converted into a digital number (ADU for Analog to Digital Unit) via an ADC (Analog to Digital Convertor), the measured intensity difference by a pixel depends on the number of bits of the ADC, ie. 14 for NOMAD. This means that each pixel of the detector is able to distinguish $2^{14} = 16384$ different intensities. Binning pixel helps to increase the amount of signal recorded by the detector. The gain of the spectrometer expresses the number of electrons converted into a digital number, expressed in electrons by ADU, thus the ADU represents the number of counted electron pairs. During an observation, every rows of the detector are illuminated, however, due to data

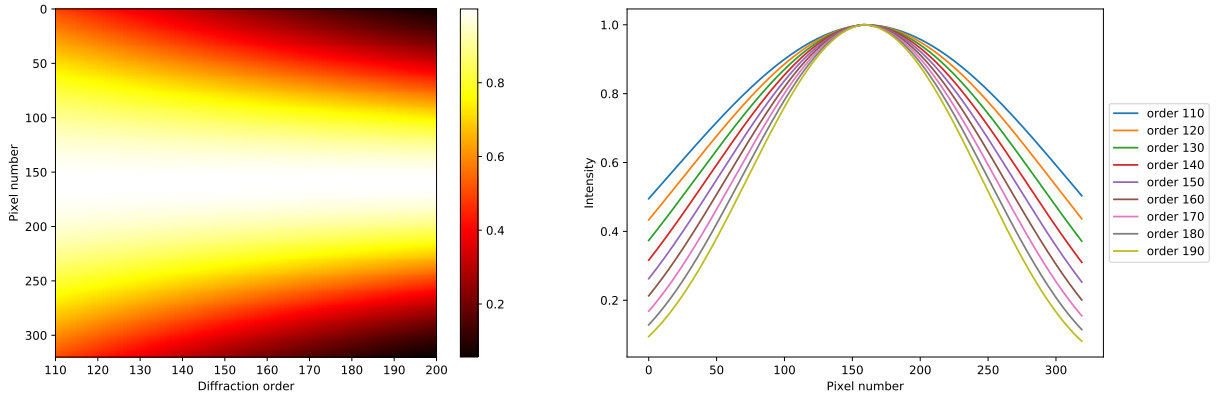

Figure 6.16: Left : Blaze function intensity as a function of the diffraction orders for even pixels of the detector, computed using equations 6.8,6.9,6.10 and 6.11. Right : Blaze function intensity for a few diffraction orders. The intensity is always maximum at the center of the detector but the full-width at half maximum of the functions decreases as the diffraction order increases.

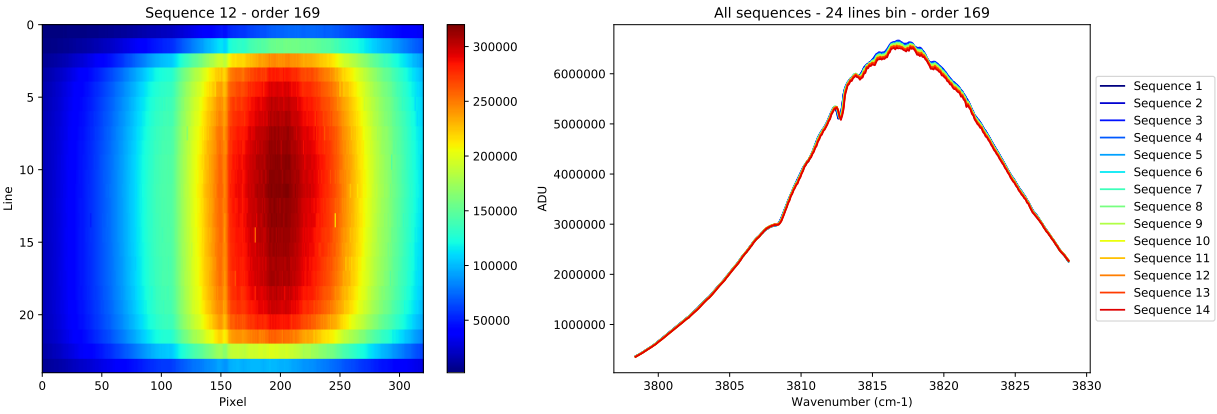

Figure 6.17: Left : A typical observation of the Sun (2018/07/02) of the diffraction order 169 for the 24 lines and 320 pixels by the LNO channel, expressed in Analog to Digital Unit (ADU). The ADU signal amounts to more than 300,000 due to the number of accumulation of the recorded spectra before transmitting to the Earth. Right : Same observation of the order 169 for all sequences after binning of the 24 lines. The ADU amounts to more than 6000,000 after the binning which considerably increases the signal. The small differences from one sequence to another also show the stability of the detector.

rate limitations only 24 detector lines can be processed by the spacecraft and transmitted to Earth (Neefs et al., 2015). This means that the LNO lines will be reduced to 24 “Superlines” through binning process. A typical results of a Sun observation by the LNO channel for any diffraction order after the binning is shown figure 6.17.

6.6.6 Observation mode

Before starting a Nadir observation, the detector needs to be cooled down to its operating temperature of approximately 90 K (Neefs et al., 2015) to ensure that the thermal noise of the environment is not measured by the spectrometer. The AOTF will select diffraction order to be observed, therefore, three types of observations are possible :

- Miniscan : Only a fraction of the entire spectral range is measured. The AOTF frequency slowly varies to observe the signal across a few diffraction order and the transition between them.
- Fullscan : The entire spectral range of the channel is measured. The AOTF input varies by large

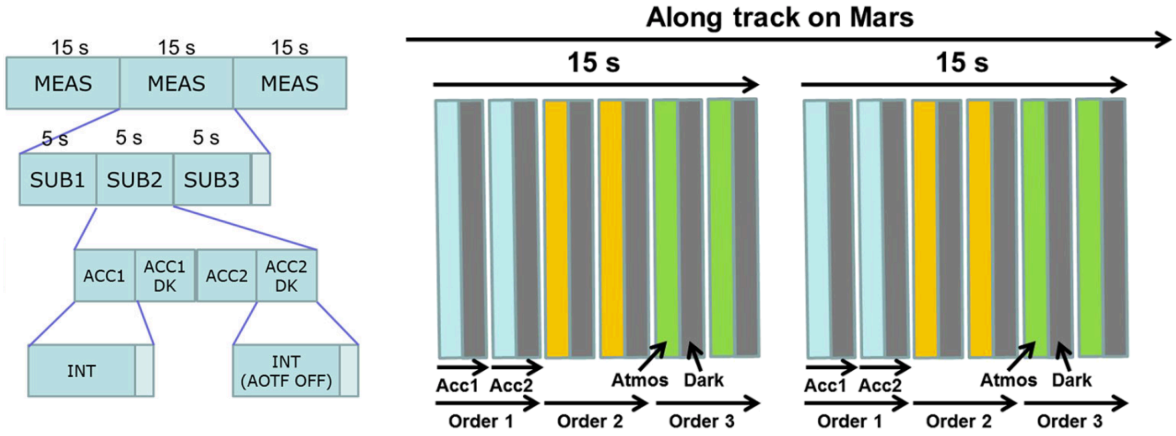

Figure 6.18: Typical nadir observation sequence of the LNO channel for three different configurations of the AOTF. The cycle is 15s leading to 5s per setting. For each setting, the measurement is composed of succession of two observations and two dark observations which are subtracted on board, from (Vandaele et al., 2018).

steps, covering one diffraction order at a time. These measurements help to quantify thermal effects on wavenumber calibration.

- Dedicated scan : special AOTF frequencies are observed in order to select the corresponding diffraction order (for instance only the one where methane absorption bands are present)

A typical observation sequence of the surface is illustrated figure 6.18. The observation cycle lasts 15 seconds (MEAS) and is decomposed into 3 periods of 5 seconds corresponding to a different configuration of the AOTF (SUB1, SUB2 and SUB3). Thus, for the same cycle, three diffraction orders can be measured. Each measurement (ACC1, ACC2) is completed by a measurement of a "Dark" (ACC1 DK) which is then subtracted from the spectrum directly on board. Only two measurements per order are shown here but it is possible to accumulate several as a function of the integration time and the configuration of the AOTF (Vandaele et al., 2018). If only one spectral domain is measured (Fullscan), then the 24 "superlines" will be transmitted. If the record includes multiple spectral subdomains (Mini scan), then an appropriate combination of lines should be used. For example, considering 6 spectral domains, then a combination of 6 gives 4 superlines per domain. The lines combination has an impact on the spatial resolution of the channel (Neefs et al., 2015).

6.6.7 The fullscan mode

During a fullscan observation, the whole spectral range of the LNO is covered (diffraction order 110 to 215) across multiple observation sequences. This helps to perform a complete calibration of the instrument but makes it difficult to estimate the AOTF transfer function shape, for which a miniscan is more appropriate (the input radio frequency is slowly varied across a fraction of the spectral range). The choice of using fullscan was made for two reasons : first there is no miniscan for all diffraction orders but only across a spectral range where strong atmospheric absorptions are present, second it is important to have an estimate of the instrumental responsivity over the whole diffraction orders range. Six fullscans were available : 2018/07/02, 2018/11/01, 2019/03/14, 2019/06/09, 2019/12/07 and 2020/01/05. A scheme of a fullscan observation is given figure 6.19. Typical fullscan observations are shown figure 6.20, the x-axis is the pixel number, the y-axis is the diffraction order (i.e. the AOTF frequency) and the z-axis shows the sensitivity of the detector (in ADU, colors in the graph). As a function of the pixel number,

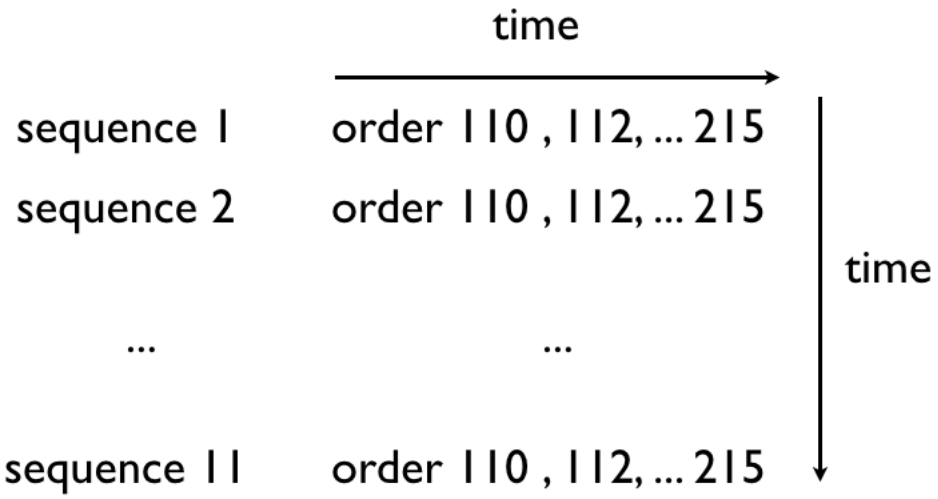

Figure 6.19: Typical scheme of a NOMAD fullscan observation : order 110 to 215 are successively measured forming a sequence, several sequences are repeated.

the sensitivity is best between 100 and 250 and very low between 1 and 100. This shape is related to the Blaze function as it reaches lower values on the edge of the detector (pixel number 1 and 320). As a function of the diffraction order, the sensitivity is good around order 130 and best between order 160 and 200 and this is related to the scientific goal of NOMAD, as it was designed to study the atmosphere (CO, CO_2 and H_2O between orders 163 and 192) and its traces gases (CH_4 between orders 130-136). One can see a decrease of the sensitivity between 2018/07/02 and 2019/03/14 as the maximum recorded ADU takes lower values which reflects the wear of the detector, for the same illumination condition (exposure time, binning, etc...). However, the overall shape of the fullscan remains the same across multiple solar observations.

6.6.8 Solar data

Observations used for the calibration come from full scan observations of the sun (see fig. 6.20) by the LNO channel. During these observations, integration time per acquisition was reduced to 2 ms to prevent detector saturation and 78 measurements were accumulated. Data correspond to the ADU signal measured by the detector and are stored inside a 4x4 matrix containing :

- The number of successive observations (sequence) ;
- The measured diffraction orders (110 to 215 for LNO);
- The 24 spatial “superlines” after the binning of the illuminated rows ;
- The wavenumbers sampled on the 320 spectral pixels ;

A typical example of a NOMAD solar observation of the order 190 by the 24 spatial lines of the detector is represented figure 6.21 (left). The maximum intensity is recorded by the central lines of the detector and the shape of the continuum may vary from one line to another. To account for such variations and to increase the signal-to-noise ratio, the 24 lines are summed together (see Fig. 6.21, right) for each observation sequences. Once made, the continuum is smoother and the solar lines (absorption bands) are easily identifiable. There is a small variation of the recorded intensity from one sequence to another but the variation are much smaller than the average intensity of the spectrum.

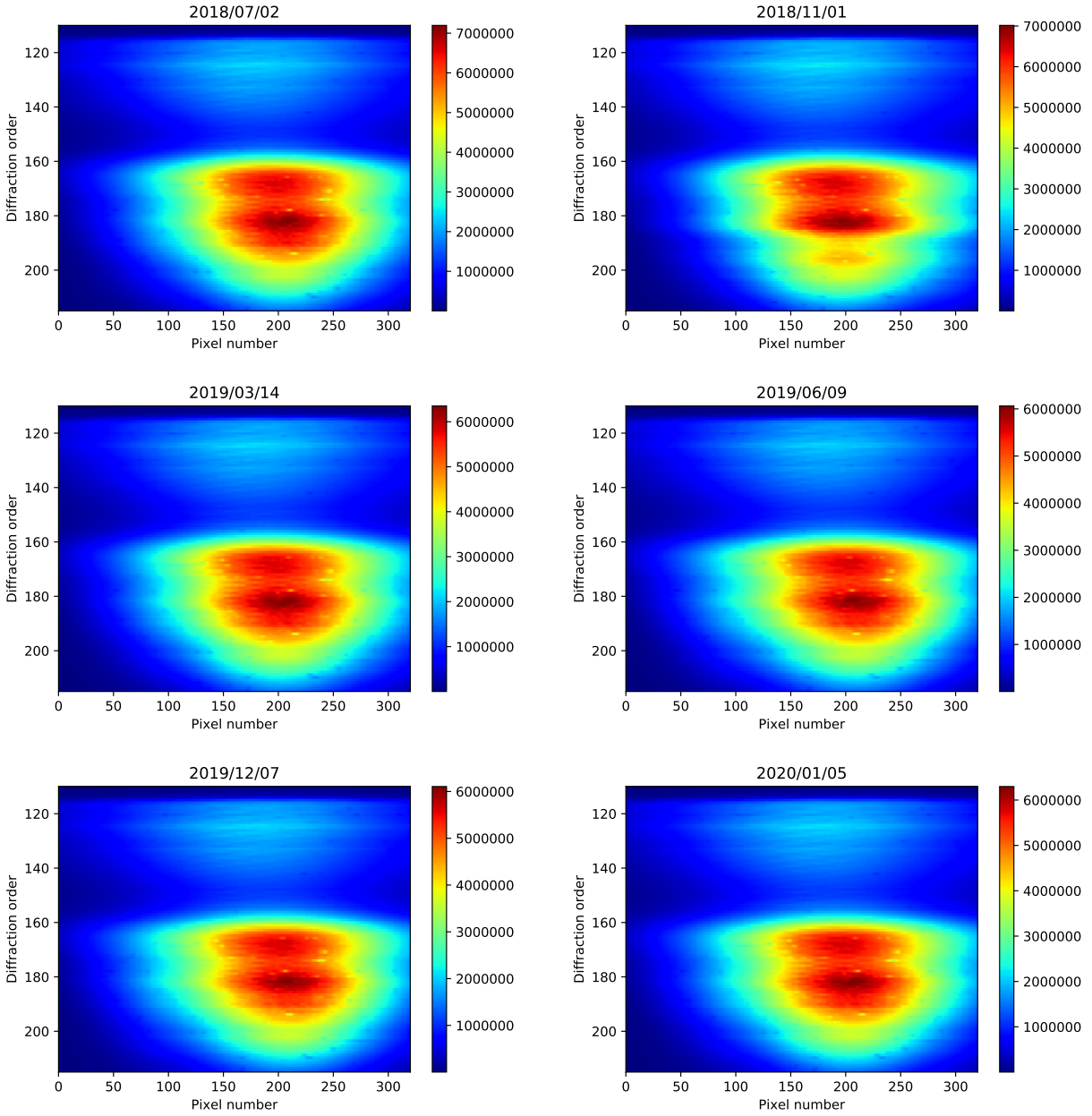

Figure 6.20: Example of one sequence of several LNO fullscan data obtained after binning of the 24 lines illuminated by the Sun, every line of the image represents a single spectrum at a particular diffraction order. The absorption due to solar lines is visible as spots. These fullscans also illustrate the relative sensitivity (in ADU) of the LNO channel as a function of the diffraction order and the pixel number. View from top.

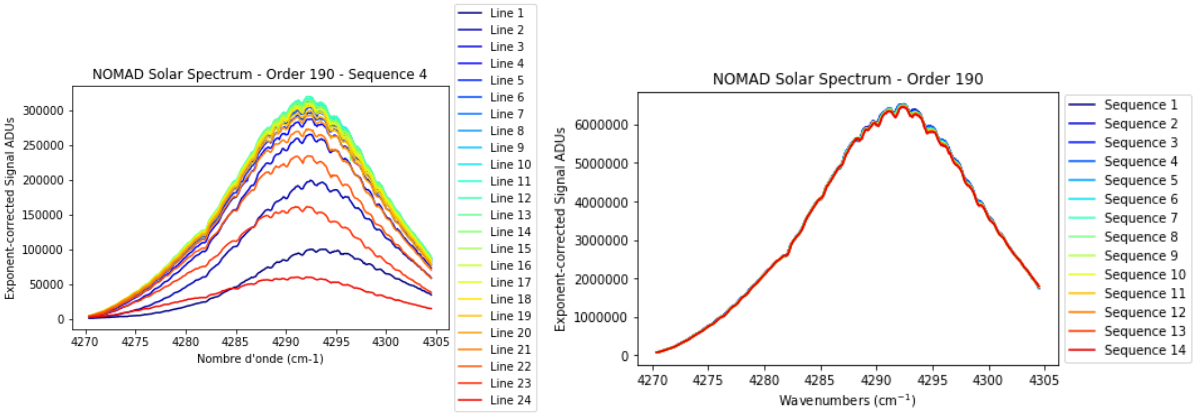

Figure 6.21: Left : Example of a NOMAD Solar spectrum observation : the fourth sequence of the order 190 for the 24 lines illuminated. The overall shape illustrates a bell continuum with multiple absorption bands (solar lines). The maximum intensity of the continuum does not coincide with the central wavenumber (pixels) and are recorded by the central lines (12 to 14) of the detector. From one line of the detector to another, the maximum intensity is not recorded at the same wavenumber (pixels) while the absorption band's position is unchanged. This shift in wavenumbers and the change in the shape of the continuum between the lines are related to NOMAD optical devices and must be taken into account when simulating a NOMAD solar observation. Right : Same observation after stacking the 24 lines for the 14 observations sequence. This raises the overall signal to noise ratio of the spectra (higher ADU signal) and gives the continuum a more consistent shape. Absorption bands are well located, only the total intensity slightly change from one sequence to another.

6.7 Conclusion

In this chapter, we introduced the scientific knowledge and the open questions related to the characterization of ice microphysics on Mars. Understanding seasonal processes involving CO_2 ice requires observations at different local solar times with a high spectral resolution and good spatial coverage. The NOMAD instrument on board the ExoMars Trace Gas Orbiter mission described in this chapter appears to be particularly relevant to address those questions. The mission is designed to observe the martian surface and atmosphere at very different local time and the high SNR and spectral resolution of the nadir channel of NOMAD (LNO) should make it possible to study surface ice. To use such data, it was first necessary to tackle the instrument calibration. The NOMAD-LNO spectrometer is a very complex instrument combining state of the art techniques to promote a very high spectral resolution. The calibration of LNO constitutes the major part of the work carried out during this PhD, and will be developed in chapter 8. For that purpose, we needed a reference spectrum of the Sun in the same spectral range with a high spectral resolution. Since such spectrum was not available in the literature, the construction of a reference solar spectrum is described in chapter 7. The first attempt to extract spectroscopic information out of the calibrated dataset is developed in chapter 9.

Chapter 7

Construction of a reference solar spectrum

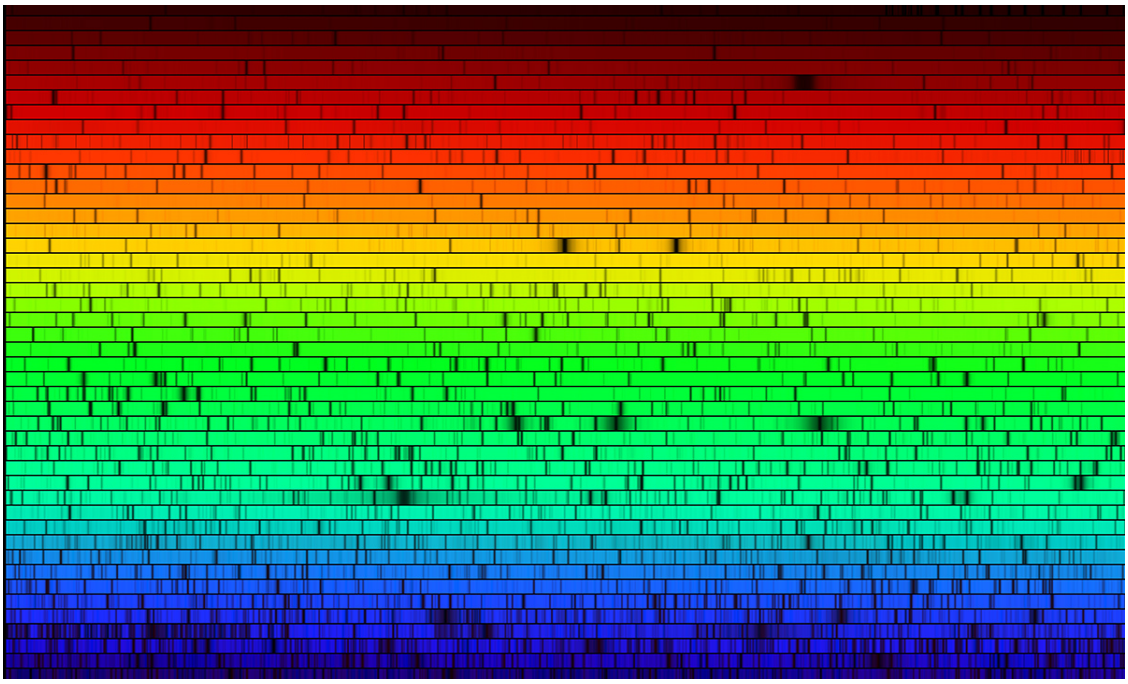

A high-resolution version of the spectrum of our Sun on the $400-700$ nm spectral range (visible domain) observed with the Fourier Transform Spectrometer at the McMath-Pierce Solar Facility at the National Solar Observatory on Kitt Peak (Tucson, Arizona, USA). The image is build to mimic an echelle spectrum, the wavelength increases from left to right along each strip, and from bottom to top. Each of the 50 slices covers 6 nm. The black lines dotting the spectrum are the absorption bands in the photosphere known as the Fraunhofer lines. Credit: N.A. Sharp, NOAO/NSO/Kitt Peak FTS/AURA/NSF

As previously shown by Fiorenza and Formisano (Fiorenza and Formisano, 2005), a measured photometrically calibrated solar radiance in the range 1.2-5 μm with a high spectral resolution (1 cm^{-1}) does not exist. Here we report an attempt to estimate such solar spectrum to perform radiometric calibration of the NOMAD instrument on board ExoMars-TGO using the combination of the Kurucz Solar spectrum (Chance and Kurucz, 2010) and the ACE-FTS infrared solar spectrum (Hase et al., 2010) to produce a calibrated solar radiance spectrum on the spectral range of the NOMAD-LNO channel (2.3 - 3.8 μm). The notions of spectral irradiance, spectral radiance and solid angles are covered and illustrated with examples. The final solar spectrum used for the LNO calibration is then presented.

7.1 Spectral irradiance

7.1.1 Definition

Please find here the important radiometric quantities definition regarding irradiance.

7.1.1.1 Irradiance

Irradiance (E) is the radiometric quantity defined as the power per unit area of electromagnetic radiation incident on a surface. The SI unit for irradiance is watts per square meter (W/m^2).

$$E = \frac{\partial \phi}{\partial A} \tag{7.1}$$

Where ϕ is the radiant flux (power) in W and A is the area in m^2.

7.1.1.2 Spectral irradiance

Spectral irradiance (E_λ) is the same quantity but expressed in unit of wavelength (per nm) in the spectrum :

$$E_\lambda = \frac{\partial E}{\partial \lambda} = \frac{\partial^2 \phi}{\partial \lambda \partial A} \tag{7.2}$$

Where λ is the wavelength (in nm).
Or the equivalent per wavenumber ν (in cm^{-1}):

$$E_\nu = \frac{\partial E}{\partial \nu} \tag{7.3}$$

7.1.1.3 Wavelength to wavenumber

The conversion factor between wavenumber and wavelength is:

$$\nu(cm^{-1}) = \frac{10000}{\lambda(\mu m)} \tag{7.4}$$

7.1.1.4 Irradiance in wavelength to wavenumber

The conversion between spectral irradiance in wavelength E_λ (in $W/m^2/\mu m$) and in wavenumber E_ν (in $W/m^2/cm^{-1}$) is:

$$E_\nu = E_\lambda \frac{\lambda(\mu m)^2}{10000} \tag{7.5}$$

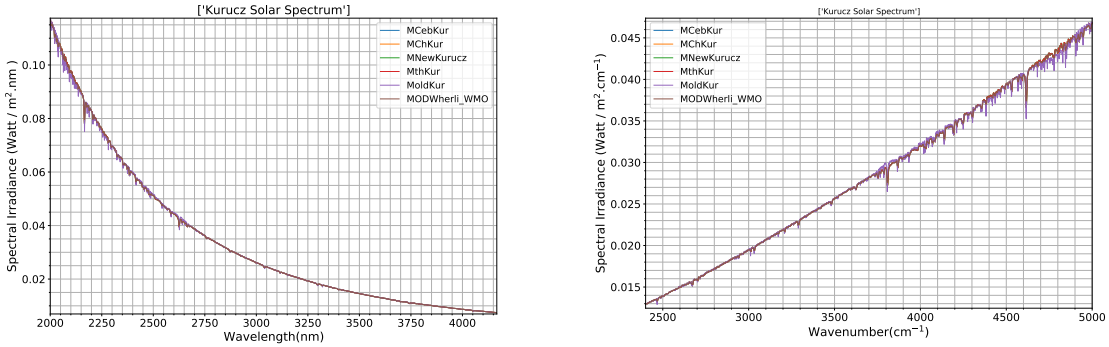

Figure 7.1: MODTRAN extraterrestrial solar spectrum in spectral irradiance on the 2.0-4.25 μm wavelength range (left) and on the 2400-5000 cm^{-1} wavenumber range (right). The spectra are : Cebula+Kurucz (MCebKur, blue), Chance+Kurucz (MChKur, orange), New Kurucz (MNewKur, green), Thullier+Kurucz (MthKur, red), Old Kurucz (MoldKur, purple) and Wherli 1985 (MODWherli_WMO, brown). Spectra are similar from one to another as only some solar lines intensities slightly vary.

7.1.1.5 Solid angle

In the case of small solid angle, one can define the solid angle Ω as the directions covered to observe a surface S at a distance D:

$$\Omega = \frac{S}{D^2} \tag{7.6}$$

7.1.1.6 Solid angle half aperture

In the case of a disk, the solid angle is conical and one can define the solid angle Ω as a function of its half aperture α:

$$\Omega = 2\pi \times (1 - \cos(\alpha)) \tag{7.7}$$

7.1.2 Solar spectral irradiance at Earth

We start by using spectral irradiance data from Chance and Kurucz (Chance and Kurucz, 2010) developed by combining high spectral resolution ground-based observation with lower spectral resolution balloon-based measurements. The resulting spectrum is available on the MODTRAN Extraterrestrial Spectra at 1 cm^{-1} wavenumber resolution. Figure 7.1 shown the different spectra of this database with the spectral irradiance units (W/m^2/nm) on the NOMAD-LNO spectral range (2.0-4.25 nm or 4250-2630 cm^{-1}). To validate theoretical values of spectral irradiance and spectral radiance we selected the 2 μm wavelength (5000 cm^{-1}), spectral range was extended for this purpose.

The spectrum New Kurucz was selected for the rest of the study as it is the most recent one. Figure 7.2 shows this spectra after conversion from (W/m^2/nm) to (W/m^2/μm) on the wavelength and wavenumber range. This gives the spectral irradiance of the Sun at Earth distance (1 AU) with a reference value of 117 (W/m^2/μm) at 2 μm (5000 cm^{-1}).

7.1.3 Solar spectral irradiance at Mars

The total power irradiated by the Sun (radiant flux) in all directions remains constant. The total area of the sphere at a distance of the planet increases with the square of the sun-planet distance. Thus, the irradiance and spectral irradiance of the Sun follows the inverse square law :

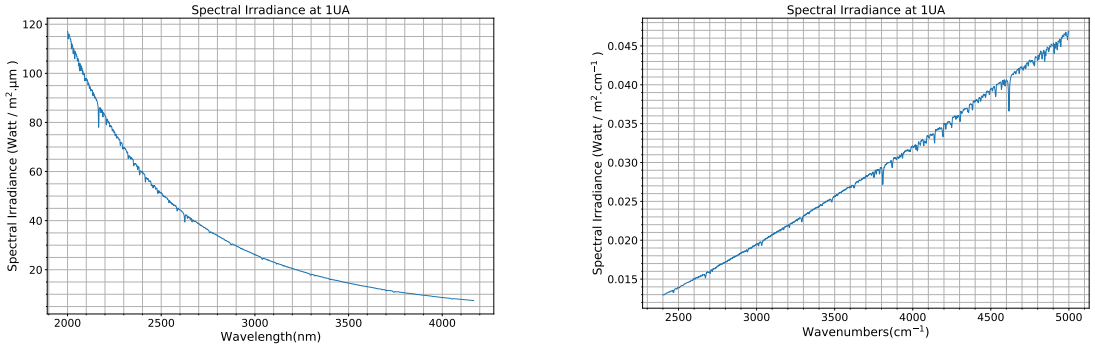

Figure 7.2: New Kurucz solar spectrum in spectral irradiance on the 2.0-4.25 μm wavelength range (left) and on the 2400-5000 cm^{-1} wavenumber range (right) at Earth distance from the Sun (1 AU).

$$E_{\lambda,D} = \frac{E_\lambda}{D^2} \tag{7.8}$$

Where E_λ is the spectral irradiance at Earth (1 AU) and D is the Sun-object distance in AU. Here we consider $D = 1.524$ UA, the mean distance of Mars from the Sun. Note that for a perfect radiometric calibration of an instrument in orbit around Mars, the spectral irradiance should vary as the Mars-Sun distance vary between 1.38 and 1.66 AU. At 2 μm (5000 cm^{-1}), the spectral irradiance is in average:

$$E_{2\mu\text{m},1.524AU} = \frac{117}{1.524^2} = 52\,\text{W/m}^2/\mu\text{m} \tag{7.9}$$

We can express it in W/cm^2/cm^{-1}, the most usual unit of spectral irradiance, given eq. 7.4 and 7.5:

$$E_{5000\text{cm}^{-1},1.524AU} = \frac{117}{1.524^2} \times (1 \times 10^{-4}) \times (\frac{2^2}{10000}) = 2.08 \times 10^{-6}\text{W/cm}^2/\text{cm}^{-1} \tag{7.10}$$

Figure 7.3 shows the spectral irradiance at Mars on the whole LNO spectral range.

7.2 Spectral radiance

7.2.1 Definition

The important radiometric quantities regarding radiance are defined hereafter. The difference with irradiance (see previous section) is that here the flux is also normalized by solid angle.

7.2.1.1 Radiance

Radiance (L_Ω) is the radiant flux received by a surface per unit solid angle $\partial\Omega_s$ per unit project area ∂A. The SI unit for radiance is watts per square meter per steradian (W/m^2/sr) :

$$L_\Omega = \frac{\partial^2\phi}{\partial\Omega_s.\partial A.\cos(\theta)} = \frac{\partial E}{\partial\Omega_s.\cos(\theta)} \tag{7.11}$$

Where ϕ is the radiant flux (power) in W, $A.\cos(\theta)$ is the projected area in m^2 (with θ the incidence/emergent angle) and Ω_s is the solid angle (see definition in Figure 1.3 of chap. 1), defined by :

$$\partial\Omega_s = \frac{\partial S.\cos(\theta_s)}{r^2} \tag{7.12}$$

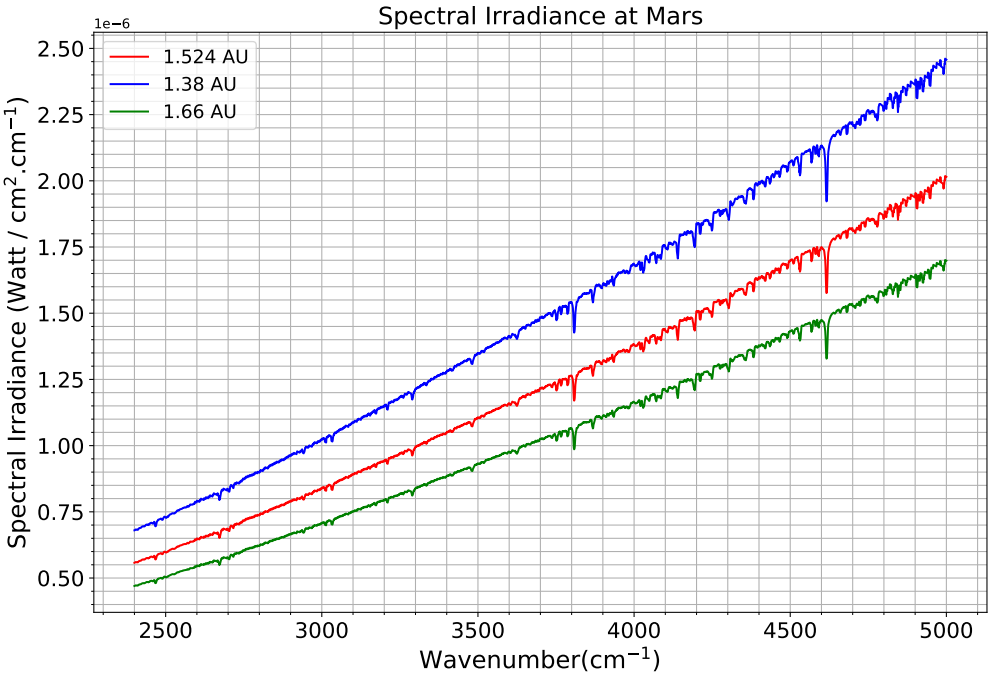

Figure 7.3: New Kurucz solar spectrum in standard spectral irradiance ($W/cm^2/cm^{-1}$) on the 2400-5000 cm^{-1} range at several Mars distance from the Sun : Perihelion (blue), Mean distance (red) and Aphelion (green).

Radiance is a function of viewing direction, depending on incidence angle θ through $\cos(\theta)$ and azimuth angle through $\frac{\partial\phi}{\partial\Omega_s}$. For a Lambertian surface, $\frac{\partial^2\phi}{\partial\Omega_s.\partial A}$ is proportional to $\cos(\theta)$ and L_Ω is isotropic. When estimating the radiance emitted by a source, ∂S refers to an area on the surface of the source and $\partial\Omega_s$ to the solid angle into which the light is emitted. When estimating the radiance received by a detector, ∂S refers to an area on the surface of the detector and $\partial\Omega_s$ to the solid angle subtended by the source as viewed from the detector.

7.2.1.2 Spectral radiance

Finally, spectral radiance is the same quantity but expressed per unit wavelength (per nm) in the spectrum, similarly to spectral irradiance :

$$L_{\Omega,\lambda} = \frac{\partial L_\Omega}{\partial\lambda} = \frac{\partial E_\lambda}{\partial\Omega_s.\cos(\theta)} \tag{7.13}$$

Spectral radiance SI units is watts per square meter per steradian per nanometer ($W/m^2/sr/nm$). The equivalent definition can be used for wavenumber $L_{\Omega,\nu}$.

7.2.1.3 *Etendue* or throughput of the detector

The throughput of the detector G (sometimes called etendue, or geometrical extent), characterizes how "spread out" the light is in area and angle in m^2/sr.

$$\partial^2 G = \partial\Omega_s.\partial S.\cos(\theta) \tag{7.14}$$

7.2.1.4 Conservation of radiance

As the light travels through an ideal optical system with refractive index $n = 1$, both the etendue and the radiant flux are conserved. Thus the radiance (and spectral radiance) is also conserved:

$$L_\Omega = \frac{\partial \phi}{\partial G} = L^*_\Omega \tag{7.15}$$

At first order, the Martian (spectral) radiance reaching the detector is thus identical to the Martian (spectral) radiance leaving Mars.

7.2.1.5 Lambertian surface (orthotropic)

A lambertian surface is a light source emitting radiation in a isotropic way. At first order a planet or the sun is orthotropic, meaning that it appears as a disk and we could not see any limb darkening. The radiance L_Ω is thus distributed over the whole half space and related to the total irradiance E.

$$L_\Omega = \frac{E}{\pi} \tag{7.16}$$

A facet of a surface (such a planet) is a secondary source, reflecting the incoming solar radiance I_0 (in $\mathrm{W/m^2}$)

$$L_\Omega = \frac{I_0}{\pi} A \cos(\theta) \tag{7.17}$$

with A, the albedo.

By extension, the same definition stands for spectral quantities, with the albedo also depending on wavelength $A(\lambda)$:

$$L_{\Omega,\lambda} = \frac{I_{0,\lambda}}{\pi} A(\lambda) \cos(\theta) \tag{7.18}$$

The equivalent definition can be used for wavenumber $L_{\Omega,\nu}$.

7.2.2 Solid angles in the Solar System

To compute spectral radiance at Mars from spectral irradiance data (see fig. 7.3), we start by estimating the solid angle of the Sun as seen from Earth (see eq. 7.6) :

$$\Omega_{Sun-Earth} = \frac{\pi . R^2_{Sun}}{D^2_{Sun-Earth}} \tag{7.19}$$

With $R_{Sun} = 696342$ km, the radius of the Sun and $D_{Sun-Earth} = 149597870$ km (1 AU) the distance of the Sun from Earth. We find $\Omega_{Sun-Earth} = 6.8 \times 10^{-5}$ steradian (sr).

Then, we estimate the solid angle of the Sun as seen from Mars using the mean distance between Mars and the Sun (1.524 AU) :

$$\Omega_{Sun-Mars} = \frac{\Omega_{Sun-Earth}}{1.524^2} \tag{7.20}$$

We find $\Omega_{Sun-Mars} = 3.0 \times 10^{-5}$ steradian (sr). We can also estimate the half-aperture α (in degree) of the solid angle of the Sun as seen from Mars:

$$\Omega_{Sun-Mars} = 2\pi \times (1 - \cos(\alpha)) \tag{7.21}$$

$$\alpha = \arccos(\frac{1 - \Omega_{Sun-Mars}}{2\pi}) \times \frac{180}{\pi} = 0.18^\circ \tag{7.22}$$

From then the spectral radiance at Mars can be computed. Two methods needs to be considered depending on whether we observe the Sun or Mars.

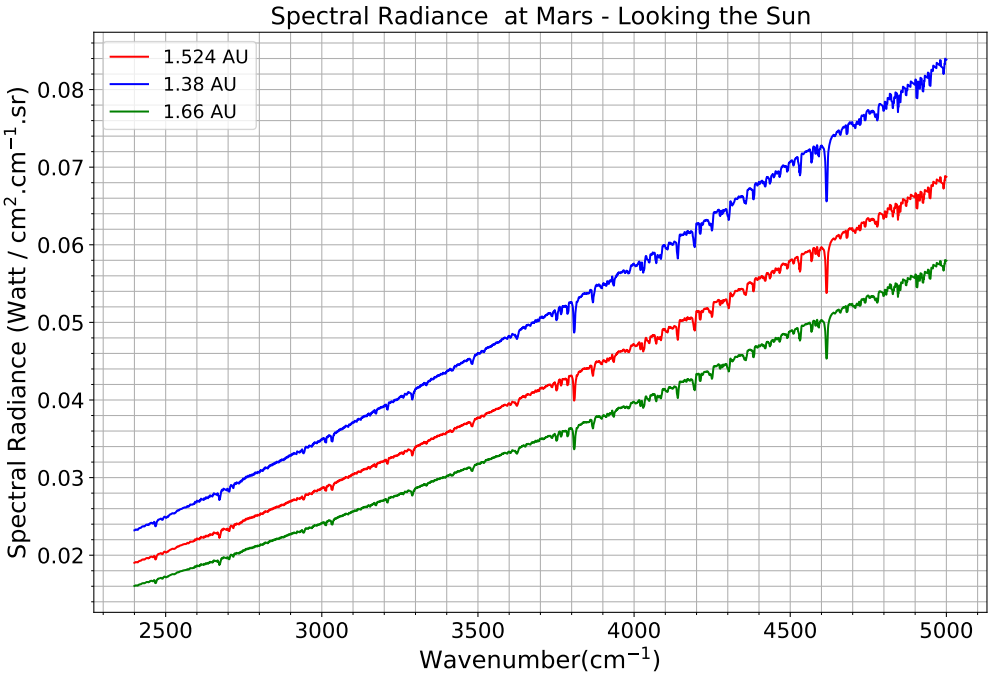

Figure 7.4: Spectral Radiance of the Sun when looking to the Sun on the 2400-5000 cm^{-1} range at several Mars distances from the Sun : Perihelion (blue), Mean distance (red) and Aphelion (green).

7.2.3 Solar radiance: looking at the Sun

When looking at the Sun from Mars, the energy is distributed only over the solid angle of the Sun (from eq. 7.13, with $\theta = 0$ since the detector is normal to the flux) :

$$L_{\Omega_{Sun-Mars},5000cm^{-1},1.524AU} = \frac{E_{5000cm^{-1},1.524AU}}{\Omega_{Sun-Mars}} \tag{7.23}$$

At 2 μm, we find $L_{\Omega_{Sun-Mars},5000cm^{-1},1.524AU} = 0.066$ W/cm^2/cm^{-1}/sr. Figure 7.4 illustrates the spectral radiance as seen from Mars looking at the Sun for different Mars-Sun distance over the spectral range of LNO. Please note that this radiance is reached only when the field of view of the detector is smaller than the sun (one can observe a piece of the sun and no deep sky). Please also note that we assume that the sun is an homogeneous and isotropic source.

7.2.4 Martian radiance

Assuming that Mars is a lambertian reflector, illuminated at incidence angle θ by the solar irradiance (see eq. 7.18) and by conservation of the radiance (see eq. 7.15), the martian radiance reaching the detector is:

$$L_{Mars,5000cm^{-1},1.524AU} = \frac{E_{5000cm^{-1},1.524AU}}{\pi}.A.\cos(\theta) \tag{7.24}$$

At 2 μm, for an incidence angle $\theta = 45°$, and an albedo of 0.4, we find $L_{Mars,5000cm^{-1},1.524AU} = 1.34 \times 10^{-7}$ W/cm^2/cm^{-1}/sr. Figure 7.5 shows the spectral radiance as seen from Mars when looking the planet for different Mars-Sun distance over the spectral range of LNO.

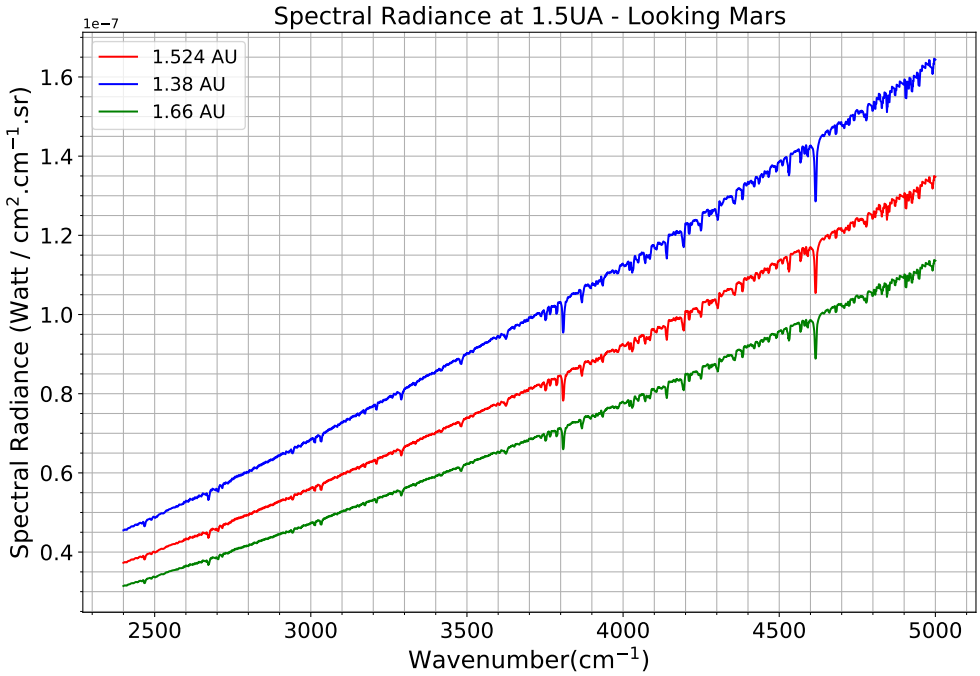

Figure 7.5: Spectral Radiance of the Sun when looking Mars on the 2400-5000 cm^{-1} range at several Mars distances from the Sun : Perihelion (blue), Mean distance (red) and Aphelion (green).

7.2.5 Radiance solar spectrum for the NOMAD/LNO calibration

The LNO channel is looking the surface of Mars at very high spectral resolution, which reinforces the need for a calibrated radiance solar spectrum with a higher spectral resolution than the data from the MODTRAN database. We have chosen the solar spectrum derived from the Fourier ACE spectrometer data on board SCISAT-1, operating on the spectral range 2-13 μm (750 - 4430 cm^{-1}) at a very high spectral resolution (0.02 cm^{-1}) (Hase et al., 2010). The processed data available are in transmittance $S_{transmittance}$ illustrated figure 7.6 (left) on the LNO spectral range. This transmittance spectrum ($S_{transmittance}$) was converted to spectral irradiance spectrum (in $W.cm^{-2}.cm^{-1}$) with a Planck's law considering a sun temperature of 5778K :

$$S_{radiance} = S_{transmittance}.F_{Planck} \tag{7.25}$$

$$F_{Planck}(\nu, T) = c_1.\nu^3.\frac{1}{exp(c_2.\frac{\nu}{T}) - 1} \tag{7.26}$$

Where ν is the wavenumber, T the sun temperature, $c_1 = 1,191042.10^{-5}$ $mW.m^{-2}.sr^{-1}.cm^{-1}$ and $c_2 = 1.4387753$ $K.cm^{-1}$.

Then, a fit with the spectral continuum of the *NewKurucz* (Chance and Kurucz, 2010) solar spectrum from the MODTRAN spectral database (the spectrum used previously for the spectral radiance computation) was made to account for small deviation of the continuum slope between the Planck's law and the actual sun blackbody spectrum. The obtained solar spectrum was also interpolated on the *NewKurucz* spectrum to extend the spectral range for the NOMAD data simulation. Finally, the spectrum was converted to spectral radiance ($W.cm^{-2}.cm^{-1}.sr^{-1}$) using equations from section 7.2.3, since LNO looks at the Sun when performing the radiometric calibration (see figure 7.6, right).

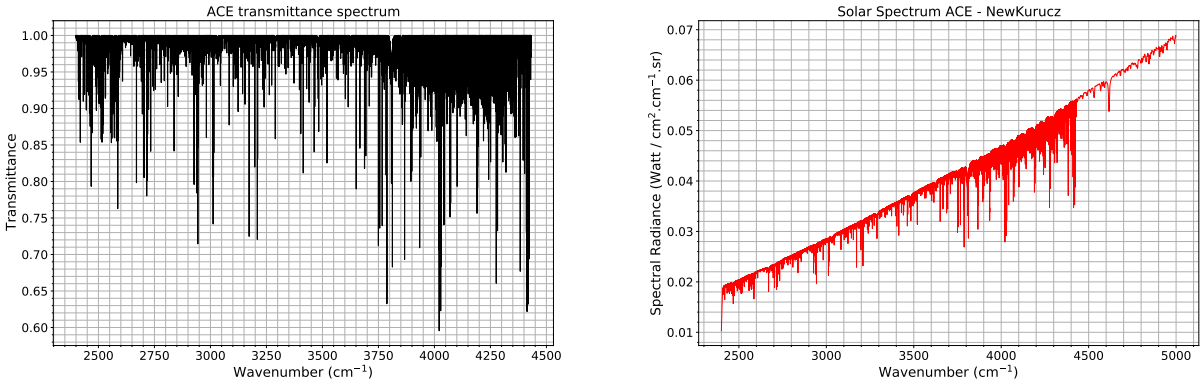

Figure 7.6: Left : ACE transmittance spectrum $S_{transmittance}$ used for the calibration at a very high spectral resolution (0.02 cm^{-1}). Right : ACE solar spectrum after interpolation on the *NewKurucz* solar spectrum continuum and conversion to spectral radiance values considering the mean Mars-Sun distance as explained in section 7.2.3.

7.3 Comparison with the Planetary Spectrum Generator (PSG) tool

Before using the calibrated spectra presented previously, a comparison with other independent data and model is necessary to validate the spectral radiance computation method when looking at Mars. We decided to use the *Planetary Spectrum Generator* (PSG) tool developed at NASA (Villanueva et al., 2018) which is an online radiative-transfer suite applicable to a broad range of planetary objects, such as Mars. It allows the estimation of a solar spectrum at Mars distance when looking at the Sun or at the surface at the desired geometry with the desired instrument (field of view, spectral range, spectral resolution...). Thus, the tool can be adjusted to match the LNO characteristics. The final products are spectrum at the desired radiance unit. This allows us to have a comparison of the spectral irradiance and spectral radiance values that we theoretically estimated for the LNO calibration.

Figure 7.7 displays this comparison for the spectral irradiance (left) and spectral radiance (right) radiometric units.

The spectral irradiance generated spectrum by PSG (figure 7.7, left) was made with an opening angle of the size of the Sun, but the result is the same for any field of view (FoV) greater than the size of the Sun at Mars distance since the irradiance units is collecting the whole energy flux.

The spectral radiance solar spectrum generated with PSG (figure 7.7, right) was made using a field of view (FoV) of the size of the object (the Sun), which is the case for the LNO channel. This works for any FoV smaller than the object as only the Sun illuminates the detector. The larger the opening, the more the flux is averaged with the background of the sky, which is dark.

In both cases, our theoretical consideration is in agreement with PSG. Our calculations is around 5% smaller than PSG, most probably due to a different solar temperature. We thus validate the approach.

One last case to test is the Martian radiance when assuming Mars is a Lambertian reflector (see section 7.2.4). To do so in PSG, we consider Mars without atmosphere, with an albedo of 0.4, an incidence angle of 0° (the Sun is behind the detector) and a distance to Sun of 1.48 AU. Figure 7.8 shows the comparison between PSG and our theoretical estimation of the radiance considering two scenarios in our calculation : an incidence angle of 0° and 45°. In both case, the order of magnitude of the spectral radiance we estimate is consistent with PSG, the small differences are related to a potential difference in the Sun's temperature in both models. One can see the impact of high incidence angle as the radiance significantly decreases with the incidence angle increasing (see 7.8).

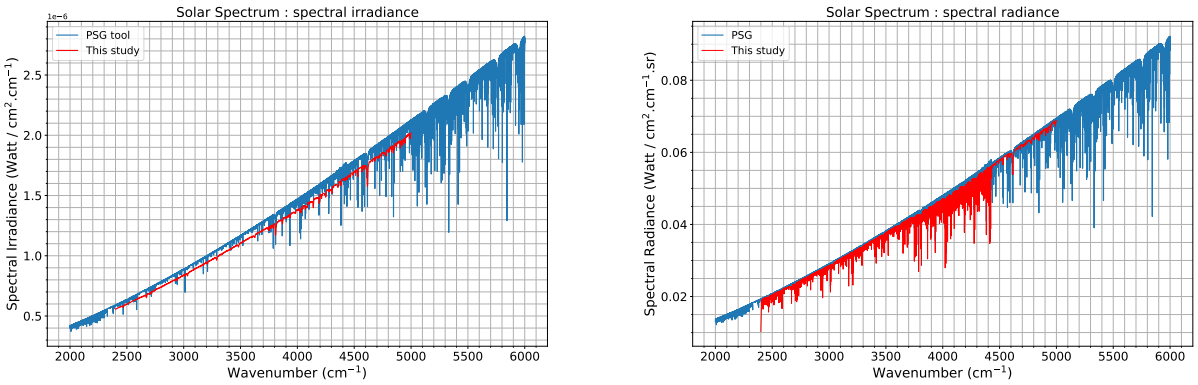

Figure 7.7: Comparison between the estimated solar spectrum at Mars in this study (red) against the solar spectrum estimated by PSG (blue). Left : solar spectrum in spectral irradiance unit. One can see a small difference between both spectra, the red one being always slightly weaker, but this can be related to a small variation of the Sun's temperature in both calculation. There is a good agreement between both our theoretical consideration (see section 7.1.3) and PSG with a value of 2.08×10^{-6} W/cm^2/cm^{-1} at 5000 cm^{-1}. Right : solar spectrum in spectral radiance units. Again, there is a small slope variation between both spectra but overall the spectral radiance values are consistent between the two with a spectral radiance value of 0.0694 W/cm^2/cm^{-1}/sr at 5000 cm^{-1} which is consistent with the values estimated (see section 7.2.3).

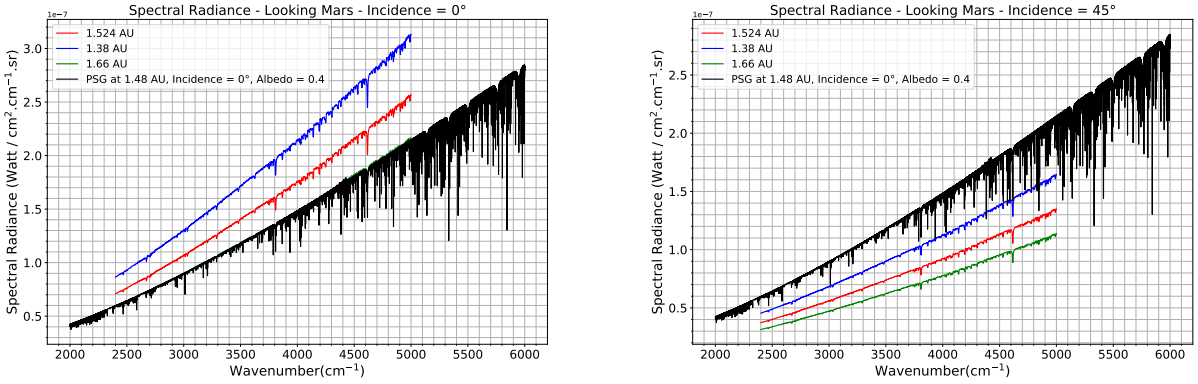

Figure 7.8: Comparison between the spectral radiance of Mars estimated in this study (color curves) for three Sun-Mars distance (perihelion, mean distance and aphelion) with an albedo of 0.4 and estimated by PSG (black curve) for a Mars-Sun distance of 1.48 AU with the same albedo. Left : The incidence angle is set to 0° to match PSG's parameters. One can see that with the same geometrical consideration, the spectral radiance estimated by PSG at 1.48 AU is similar to the one we estimate in this study at the aphelion (green curve). This small difference can be related to a difference in the Sun's temperature in both calculation. Right : when considering an incidence of 45° (except for PSG fixed at 0°, same as left plot), one can see a significant drop of the radiance as the radiance estimated by PSG at 1.48 AU is higher than the one we estimate for the perihelion (1.38 AU).

7.4 Conclusion

With the aim of providing a synthetic solar spectrum at the spectral resolution of the NOMAD/LNO channel, we report the construction of such solar spectrum using a combination of the Kurucz Solar spectrum (Chance and Kurucz, 2010), the ACE-FTS infrared solar spectrum (Hase et al., 2010) and theoretical considerations. We developed the successive steps to build a spectral radiance solar spectrum from initial irradiance data. A cross comparison with an online tool that uses radiative transfer considerations showed a good agreement with our theoretical solar spectrum. Such results will be used to perform the radiometric calibration of the NOMAD/LNO channel as developed in the next chapter.

Chapter 8

NOMAD-LNO calibration

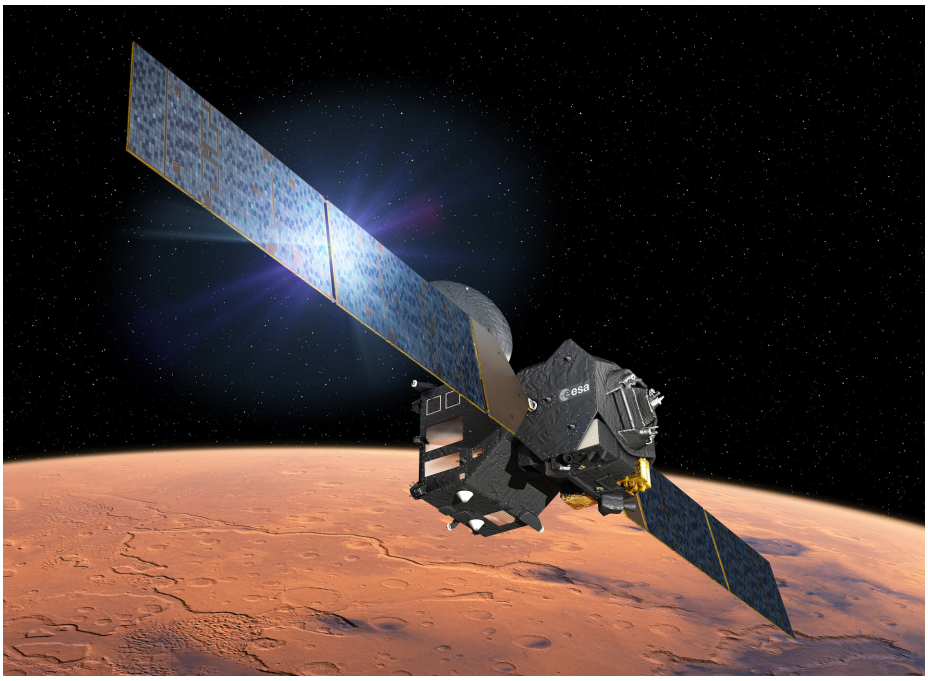

Illustration of the ExoMars Trace Gas Orbiter (TGO) at Mars. Launched in 2016 it is the first part of an international program led by ESA in cooperation with the Russian Space Agency (Roskosmos). The second part constitutes the ExoMars 2020 mission which includes the rover Rosalind Franklin. The TGO mission successfuly arrived at Mars in October 2016. 12 months of aerobraking using the martian atmosphere were necessary to reach the low orbit of the mission and the beginning of scientific observations.

This chapter presents the complete methodology that has been developed to perform the instrumental calibration of the NOMAD/LNO channel. The method is based on theoretical considerations on the shape of instrumental transfer functions and their application to a synthetic solar spectrum (see chap. 7). The method, results and model validation are presented in the following article:

G. Cruz Mermy, F. Schmidt, I.R. Thomas, F. Daerden, B. Ristic, M.R. Patel, J.-J. Lopez-Moreno, G. Bellucci, A.C. Vandaele, Calibration of NOMAD on ExoMars Trace Gas Orbiter : Part 3 - LNO validation and instrument stability, Planetary and Space Science, Volume 218, 2022, 105399, ISSN 0032-0633, https ://doi.org/10.1016/j.pss.2021.105399.

Calibration of NOMAD on ExoMars Trace Gas Orbiter: Part 3 - LNO validation and instrument stability

G. Cruz Mermy[1], F. Schmidt[1,2], I. R. Thomas[3], F. Daerden[3], B. Ristic[3], M. R. Patel[4,5], J.-J. Lopez-Moreno[6],G. Bellucci[7], A.C. Vandaele[3] and the NOMAD Team

[1]Université Paris Saclay, Géosciences Paris Saclay (GEOPS), 91405 Orsay, France

[2]Institut Universitaire de France (IUF)

[3]Royal Belgian Institute for Space Aeronomy (BIRA-IASB), Av. Circulaire 3, 1180 Brussels, Belgium

[4]The Open University, Walton Hall, Milton Keynes, MK7 6AA, U.K.

[5]STFC Rutherford Appleton Laboratory, Oxfordshire OX11 0QX, U.K

[6]Instituto de Astrofisica de Andalucia (IAA/CSIC), Granada, Spain

[7]Istituto di Astrofisica e Planetologia Spaziali (IAPS/INAF), Via del Fosso del Cavaliere, 00133 Rome, Italy

*corresponding author: guillaume.cruz-mermy@universite-paris-saclay.fr

Keywords. Space instrumentation; calibration; Mars; spectroscopy; surface; ExoMars

1. Introduction

The ExoMars program consists of two missions designed to study the trace gases of the martian atmosphere but also to acquire information on potential ongoing geological and biological processes on the surface of Mars (Vago et al., 2015). Since April 2018, the four instruments aboard the ESA/Roscosmos ExoMars Trace Gas Orbiter mission has acquired observations of both the atmosphere and surface of Mars. Among them the NOMAD instrument (Nadir and Occultation for MArs Discover), led by the Belgian Institute for Space Aeronomy (BIRA-IASB), is a suite of three spectrometers spanning the UV and IR spectral range: SO (Solar occultation), LNO (limb, nadir, and occultation) and UVIS (ultraviolet-visible). The three channels work separately but are all controlled via a single main electronic interface (Neefs et al., 2015). The two first channels are infrared spectrometers based upon the SOIR (Solar Occultation in the InfraRed) instrument aboard the Venus Express mission (Nevejans et al., 2006).

The LNO channel is a compact high-resolution echelle grating spectrometer with an acousto-optic tunable filter (AOTF) working in the infrared domain from 2.3 μm to 3.8 μm (4250-2630

cm^{-1}) with a resolving power ($\lambda/\Delta\lambda$) of around 10000, specially designed for nadir observation. With such high resolving power combined with the near-circular orbit of TGO permitting 12 orbits in one sol, promoting a global coverage of the planet, the NOMAD-LNO instrument is perfectly suited to study the martian surface and atmosphere.

The main objective of this article is to propose an original calibration procedure, adaptable for the full dataset of NOMAD-LNO. This calibration is complementary to the one proposed by Thomas et al. (2021) who developed a fully empricial method using in-flight data. In their paper the LNO ground calibration, occultation and nadir boresight pointing vectors, detector characterisation and illumination pattern are covered. A combination of several observation of the sun is used to derive instrument temperature effects such as the shape and intensity of a LNO spectrum. The radiometric calibration is done by assuming temporal stability of the instrument and directly using solar observation to calibrate nadir observation.

In this paper we will not assume temporal stability of the instrument. Our approach is thus able to investigate the temporal evolution of the instrumental sensitivity, which is expected to vary due to degradation by energetic particles. This approach will be based on an empirical continuum removal to take into account the departure between actual blaze function and its theoretical form. By construction, our approach is thus more robust but may fail to model some instrumental effect such as the temperature dependence of the blaze and AOTF transfer function on the raw continuum of an LNO spectrum. The main calibration of NOMAD-LNO is well described in Thomas et al. (2021). This complementary work aims to validate the calibration of LNO but also to give additional information about instrumental transfer function and instrumental line shape.

2. NOMAD LNO instrument

The optical design of the LNO spectrometer is identical to that of SO and therefore very similar to SOIR (Nevejans et al., 2006; Vandaele et al., 2013), it is a combination of a high-dispersion echelle grating along with an AOTF and a cooled detector. The main advantage of using an echelle grating is that the full height of the detector can be used to register spectral lines (Neefs et al., 2015), which greatly improves the SNR after column binning. In the spatial direction, the detector contains 256 rows of pixels and only 144 of the 150 illuminated spatial lines are read out (Thomas et al., 2021). The AOTF is placed as diffraction order sorting devices in front of the spectrometer section to avoid order overlap at the output of the grating (Neefs et al., 2015). More information regarding the LNO channel, its working principle, and technical details can be found in previous articles (Neefs et al., 2015; Thomas et al., 2016, 2021).

Before starting a nadir observation, the detector needs to be cooled to its operating temperature of approximately 90 K (Neefs et al., 2015) to ensure that the thermal noise of the environment is not measured by the spectrometer. The AOTF will select the diffraction order to be observed, therefore, three types of observations are possible :

- Miniscan: Only a fraction of the entire spectral range is measured. The AOTF frequency slowly varies to observe the signal across a few diffraction orders and the transition between them.
- Fullscan: The entire spectral range of the channel is measured. The AOTF input varies by large steps, covering one diffraction order at a time.
- Dedicated scan: special AOTF frequencies are observed to select the corresponding diffraction order (for instance only the one where methane absorption bands are present).

As well as the SO channel, LNO can operate looking toward the sun which allows measurement of the solar lines for precise in-flight calibration. The solar miniscans and fullscans are precious observation that provides complementary information on the instruments. Solar miniscans allow a precise determination of the AOTF transfer function shape and the Instrument Line Shape but each miniscan covers only a limited spectral range. A first in-flight calibration using miniscans has been proposed by Liuzzi et al. (2019). Fullscans are dedicated to spectral and photometric calibration as the whole spectral range is covered. In this work, the calibration model built for LNO is based on the solar fullscans observations.

3. Data

3.1. Solar fullscan

The NOMAD-LNO fullscans are solar observation made for calibration purposes. The instrument, normally in nadir position, is pointing toward the sun. The choice of using solar fullscans was made for two reasons. First, there are not enough miniscans to cover all diffraction orders with a significant amount of data while fullscans always cover the whole spectral range which allows testing the time dependence of the calibration. Second, it is important to estimate the instrumental sensitivity over the whole diffraction order range. As of June 2020, six solar calibrations have been performed on the following dates: 02/07/2018, 01/11/2018, 14/03/2019, 09/06/2019, 07/12/2019 and 05/01/2020. A typical fullscan observation is shown in figure 1. The x-axis is the pixel number (sometimes also called spectel), the y-axis is the diffraction order (i.e. the AOTF frequency) and the contours shows the sensitivity of the detector to incoming solar radiation (in ADU for Analog to Digital Units). As a function of the pixel number, the sensitivity is best between 100 and 250 and very low between 1 and 100. This shape is related to the Blaze function as it reaches lower values on the edge of the detector (pixel number 1 and 320). As a function of the diffraction order, the sensitivity is good around order 130 and best between order 160 and 200. This is related to the scientific goal of NOMAD, as it was designed to study the atmosphere (CO, CO_2, and H_2O between orders 163 and 192) and its traces gases (CH_4 between orders 130-136). Raw data (in ADU) are already dark subtracted directly onboard. Before using the fullscans as raw data for the calibration, a normalization needs to be done to account for the integration time t_{int}, the spectral resolution Δ_ν (varying across the spectral range), the number of accumulation NOA of recorded spectra, and the binning bin done before transmitting the data to Earth. The normalization equation follows :

$$S_{obs} = \frac{Counts(ADU)}{t_{int}.\Delta_\nu.NOA.bin} \tag{1}$$

Where Counts is the dark-subtracted raw spectrum across the 320 spectels. For the LNO fullscan, instrument parameters are:

- $t_{int} = 2$ ms
- $0.1469 \leq \Delta_\nu \leq 0.2649\ cm^{-1}$ between order 110 and 215 (Liuzzi et al., 2019)
- $NOA = 78$
- $bin = 24$ as the 24 central lines are illuminated by the sun and stacked to increase the signal for the calibration

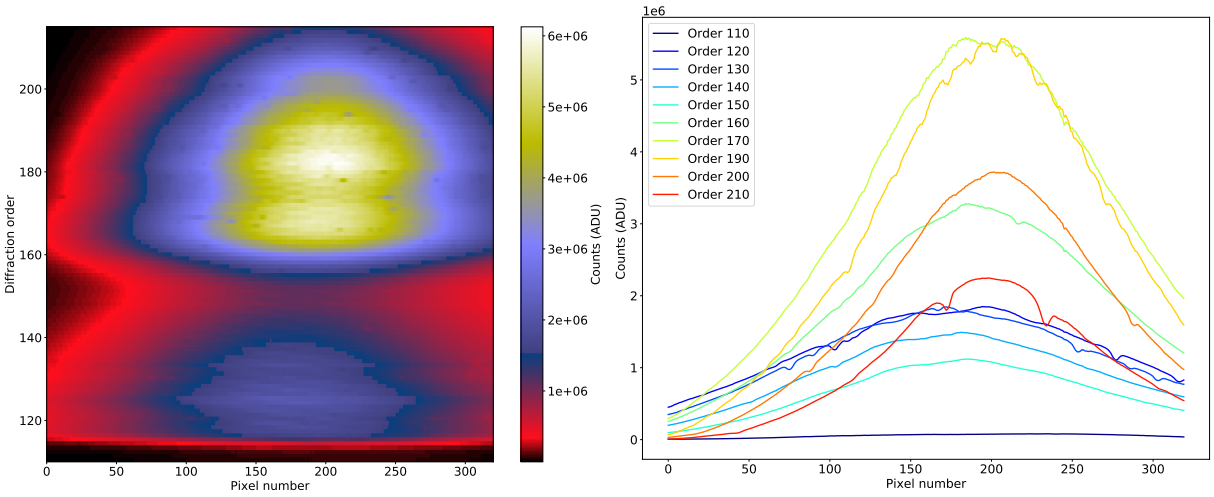

Figure 1: Example of a typical NOMAD-LNO solar fullscan (observation of 14/03/2019, sequence number 10 out of 15). Here the 24 central lines illuminated are summed to promote a better SNR. The left figure shows the complete fullscan across the whole LNO spectral range (order 110 to 215). Each line of the image represents a spectrum at a particular diffraction order sampled on the 320 spectral spectels of the detector (i.e the wavenumbers). The colors represent the intensity (expressed in ADU) measured by the detector and solar lines are visible as spots. The right figure shows a cross-section within the fullscan at particular diffraction orders. Here the characteristic "bell" shape of the continuum is clearly visible, the width and height of each spectrum is order-dependent and are related to the instrument-specific design (AOTF + blazed grating). Weak solar lines are also visible which illustrates the high spectral resolution of the instrument.

These parameters are constant for all LNO fullscans. The spectrum S_{obs} is considered the actual observation of the sun. Each sequence of a fullscan starts with the order 110 and ends with the order 215. This sequence is then repeated several times (between 14 and 34 times). Due to the very weak signal-to-noise ratio on the edge of the detector (spectels 1 to 50) only spectels 50 to 320 are considered for the calibration.

3.2. Construction of a reference synthetic solar spectrum for NOMAD

The sun is the best blackbody available for in-flight calibration because its spectrum is well defined and its time variations are minimal. The synthetic solar spectrum that we use to compare LNO solar observations is derived from the Fourier Atmospheric Chemistry Experiment (ACE) spectrometer data aboard SciSat-1, operating in the spectral range 2-13 μm (750 - 4430 cm^{-1}) at a very high spectral resolution (0.02 cm^{-1}) (Hase et al., 2010). The processed data available is a transmittance solar spectrum (called S_T hereafter) which was converted to spectral irradiance spectrum (in $W.cm^{-2}.(cm^{-1})^{-1}$) with a fit of the spectral continuum of the *NewKurucz* (Chance and Kurucz, 2010) solar spectrum S_{Kurucz} from the MODTRAN spectral database. To do so we first defined the continuum by a convolution with a median Gaussian filter $G(0)$ with a large standard deviation (σ) to avoid the contribution of solar lines:

$$S_{continuum} = S_{Kurucz} \star \mathcal{G}(0, \sigma) \tag{2}$$

Then, the solar continuum $S_{continuum}$ was interpolated in the wavenumbers sampling of the ACE spectrum to maintain the very high spectral resolution. The spectrum is then converted to spectral radiance (in $W.cm^{-2}.(cm^{-1})^{-1}.sr^{-1}$) by dividing the interpolated $S_{continuum}$ spectrum by the solid angle (in sr units) with which the sun is observed by LNO. In this case the sun is entirely

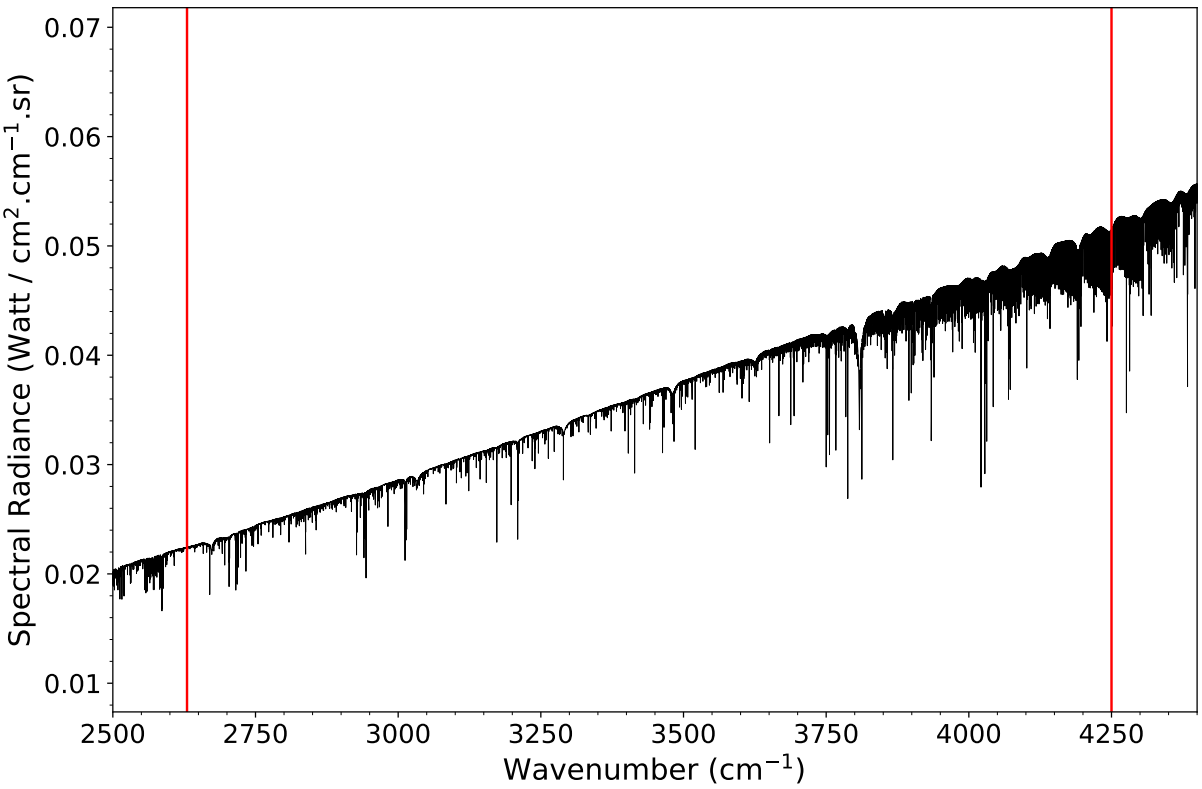

Figure 2: Solar spectrum (S_L) used in this study in spectral radiance and the mean distance Mars-Sun (1.524 AU). The very high spectral resolution of the Fourier ACE spectrometer allows the identification of weak solar lines, which is necessary for the calibration of LNO. The LNO spectral range is shown as red vertical lines.

resolved by the detector therefore the solid angle is simply the surface of the sun divided by the square of the Mars-Sun distance (in km). Here we considered the mean Mars-Sun distance (1.524 AU). We also integrate the Mars-Sun distance ($d_{\odot\sigma}$ (in AU) in $S_{continuum}$ since the *NewKurucz* solar spectrum was measured from Earth orbit at a distance of 1 AU. This leads to the final spectrum S_L:

$$S_L = S_{continuum}.S_T/d^2_{\odot\sigma} \tag{3}$$

3.3. NOMAD-LNO observation (nadir)

The science phase of the LNO channel started in March 2018. During one orbit (nadir-looking), one to six diffraction orders can be measured, for instance when 3 orders are measured the observation cycle lasts 15 seconds and is decomposed into 3 periods of 5 seconds corresponding to a different configuration of the AOTF (Vandaele et al., 2015, 2018). Thus, for the same cycle, three diffraction orders can be measured, each measurement is completed by a measurement of the "Dark" which is then subtracted directly on board (Vandaele et al., 2018). In April 2021, more than 12,810 files are available, each file corresponds to a particular diffraction order during one orbit. Not all diffraction orders are measured in each orbit and most of the time a combination of useful orders for a science objective are acquired together, such as orders 131-136 (CH_4), 146-150 (CO_2), 167-171 (H_2O), and 186-192 (CO) (Liuzzi et al., 2019; Vandaele et al., 2019). We decide here to illustrate our calibration with order 189 due to the significant amount of data and for its

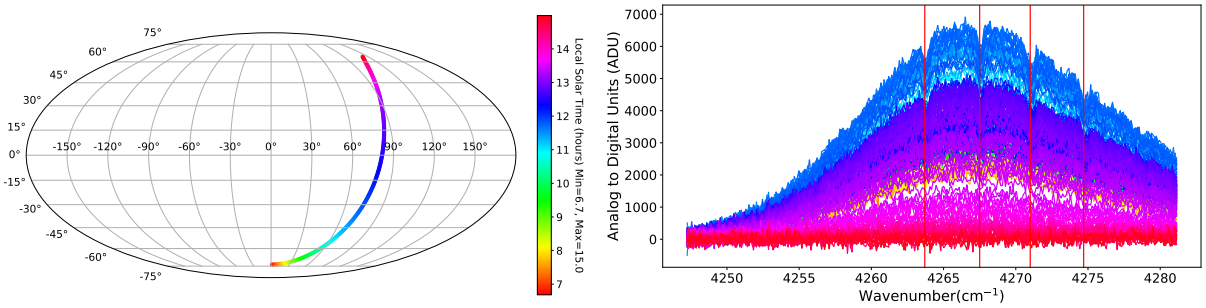

Figure 3: Order 189: groundtrack (left) and raw spectra (right) of 18/09/2018, the colors refer to local solar time. The low-altitude near-circular orbit of TGO allows observations at various local times. The characteristic 'bell" shape of LNO spectra is visible, especially when the signal is strong at noon local solar time (in blue). The atmospheric bands are also visible, here red vertical lines indicate the CO absorption bands.

scientific interest (Smith, 2021). Thus, for a particular order, the time necessary to obtain a global map coverage of the planet can be spread over a long time, typically one martian year. To exclude any temporal variation in the instrument that could bias the calibration and the reflectance map produced, it is important to test the time dependence of the instrument on the photometric sensitivity to look at the potential aging of the detector before calibrating data spanning several years. A typical LNO orbit is shown in figure 3 for order 189.

4. Method

The calibration aim was to build a model to estimate the spectral conversion (wavenumbers in cm^{-1} for each spectels of the detector) and the photometric sensitivity (conversion factor from ADU to spectral radiance). The model must be versatile enough to face the uncertainties of some instrumental functions, such as the AOTF transfer function and the grating blaze function.

The method used here is based on the usual comparison between a real solar observation and a simulated solar spectrum. The observations are LNO solar fullscans and we aim to simulate the same observation by accounting for the AOTF and grating effects. The comparison is done after spectra continuum correction to work out the baseline uncertainties. This approach is of particular importance for correct calibration of nadir data, for which there is no observation free of atmospheric absorption (Liuzzi et al., 2019). The calibration steps we perform are the following :

1. First-order spectral calibration: conversion of detector spectel number and diffraction order to wavenumber (Section 4.1)
2. Calibration inversion, by minimizing the residual between observation and simulation, following these steps:
   (a) Application of the grating blaze function and AOTF transfer function shape (Section 4.2.1)
   (b) Simulation of the Instrument Line Shape (ILS) (Section 4.2.2)
   (c) Integration of a residual wavenumber shift (Section 4.2.3)
   (d) Continuum removal to remove the shape imposed by the instrumental functions (Section 4.2.4)
   (e) Normalization and estimation of the sensitivity (Section 4.2.5)
   (f) Computation of the residue (Section 4.3)

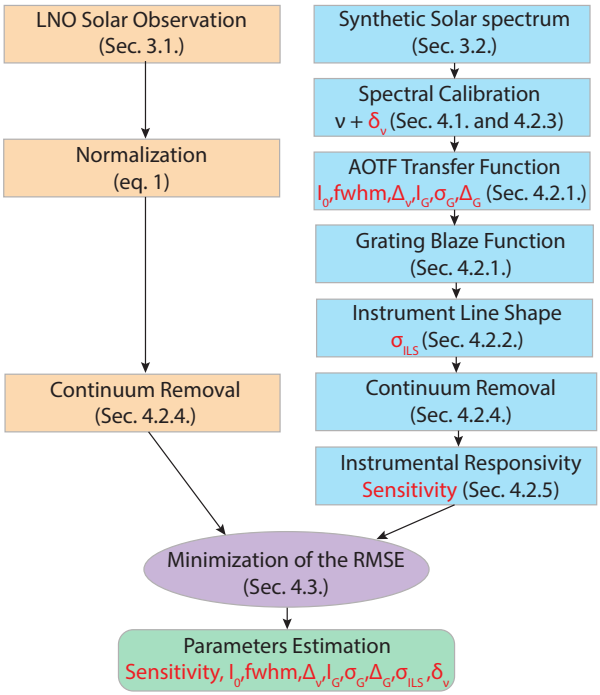

Figure 4: Flowchart summarizing the steps of the calibration model. The parameters estimated by the inversion are indicated in red.

3. By construction, the result of the minimization leads to the estimation of the instrumental sensitivity

An illustration of the calibration pipeline with the different corresponding sections is given figure 4.

4.1. Spectral calibration

The very first step to perform is to compute the spectral calibration which is based on the position of well-defined solar lines in the calibration spectra that can be used to match a line's frequency with the spectel number in which it falls (Liuzzi et al., 2019). The diffraction order number is related to the AOTF frequency and the aim is to get a relationship between the spectel number of the detector and the wavenumber, at a corresponding diffraction order. This relationship is modeled by a second-order polynomial :

$$\frac{\nu}{m} = F_0 + F_1.p + F_2.p^2 \tag{4}$$

Where ν is the wavenumber, m is the diffraction order and p is the spectel number (from 1 to 320). The coefficients F_0, F_1 and F_2 were obtained by Liuzzi et al. (2019) using Miniscan acquisitions and a total of 70 solar lines. The central spectel wavenumber of the considered order is noted ν_0 for spectel 160. The Free Spectral Range (FSR) is the wavelength range in which there is no overlap by adjacent orders. It can be computed using equation 4 at the spectel 160 (center of the detector) and gives a value of 22.545 cm^{-1} which is very close to what is reported in Neefs et al. (2015) with a value of 22.56 cm^{-1}. The FSR is expected to be a constant for echelle gratings (Neefs et al., 2015). To take into account small residual wavenumber shift, we introduced a parametrization described in section 4.2.3.

4.2. Photometric calibration

To simulate the instrumental effects, we need to take into account the instrumental transfer function T (here due to the grating and the AOTF), and the instrumental line shape ILS that blurred the signal in spectral domain. A simplified expression of the instrumental effects is:

$$S_{sim}(\nu) = (S_L(\nu).T(\nu)) \star ILS \tag{5}$$

Where $S_L(\nu)$ is the simulated solar spectrum described in section 3.2 and $T(\nu)$ is the instrumental transfer functions described hereafter. In the next sections, we will describe precisely the instrument model taken into account. We will emphasize for all functions the main parameter ν (representing the wavenumber) and the unknown parameters that our inversion scheme will estimate.

4.2.1. Instrumental transfer function

Grating blaze function. A diffraction grating or echelle spectrometer is an optical device which allows diffraction of the incident light into different diffraction orders. Slit spacing controls the extent of the diffraction for a given wavelength. For the LNO spectrometer, a "blazed grating" is used where the grooves are tilted in a special angle, called the "Blaze angle". This angle is generally chosen to optimize the efficiency of the diffraction for a given wavelength. The commonly adopted geometry is called "Littrow configuration" in which the Blaze angle is chosen so that the incident and diffraction angle are the same, and are equal to the Blaze angle. Moreover, the LNO has a near-Littrow configuration (Neefs et al., 2015) to slightly separate the incident beam from the diffracted beam. Thus, the grating is tilted so that both beams make a small γ angle between the perpendicular plane to the grating surface and the grooves. It is also necessary to take into account a slight deviation angle i of the incident angle with respect to the Blaze angle in the perpendicular plane to the grooves. The grating equation becomes (Neefs et al., 2015):

$$\frac{m}{\nu} = \frac{(\cos\alpha + \sin\beta).\cos i.\cos\gamma}{\sigma} = \frac{2\sin\theta_B.\cos i.\cos\gamma}{\sigma} \tag{6}$$

Where m is the diffraction order, α is the incident angle, β is the diffraction angle, θ_B is the Blaze angle, σ is the grating groove density (lines/mm), and ν is the wavenumber. The blaze grating characteristics of the LNO channel are summarized in table 1. The grating efficiency is estimated at 85% in the center of the grating and falls to 40% at the edges (Neefs et al., 2015). For each wavenumber within each order, we compute the diffraction angle β using equation 6. Then, we estimate the blazing efficiency for which we adopt the following relation :

$$T_{Blaze}(\nu) = C.\left[\mathrm{sinc}(\nu.\frac{\sigma.\cos\gamma.\cos\alpha}{\cos\alpha_B}.(\sin\alpha_B + \sin(\beta - \theta_B)))\right]^2 \tag{7}$$

Where $\alpha_B = \theta_B - \alpha$, the angle between the incident beam and the normal of the facet in the perpendicular plane to the grooves, and the grating geometric parameters $C = 1$ if $\alpha > \beta$ or $\left(\frac{\cos\beta}{\cos\alpha}\right)^2$if $\alpha < \beta$. The measured global shape of NOMAD spectra is partly determined by this $T_{Blaze}(\nu)$ function.

The LNO grating is made of an aluminum alloy (Neefs et al., 2015) and is therefore subject to compressions/expansions due to temperature changes. This would lead to groove density variations and shift the position of the function on the detector spectels. If the temperature within the spectrometer is known, then this effect can be taken into account considering the following formula describing the groove length σ. From a known groove length σ_1 at temperature T_1 it is possible to

Parameters	Value	Precision	Unit
Blaze angle θ_B	63.43	± 0.1	°
Groove density σ (at 0°C)	4.033512		lines/mm
Number of grooves N	≥ 765		
Groove spacing d	248.06	± 0.001	μm
Off-Littrow angle γ	2.75	± 0.0025	°
Off-Blaze angle i	0	± 0.016	°

Table 1: Grating characteristics of the LNO channel, from Neefs et al. (2015).

a	$-4.1272.10^{-3}$
b	$-3.0640.10^{-6}$
c	$8.7960.10^{-8}$
d	$1.0055.10^{-10}$
T_1	$24.5°C$
σ_1	248.06µm

Table 2: Reference groove spacing and temperature for the LNO channel from Marquardt et al. (2000).

estimate the groove length σ_2 at temperature T_2 using the thermal expansion equation (Marquardt et al., 2000):

$$\sigma_2 = \sigma_1 . \frac{(1 + (a + b.T_2 + c.T_2^2 + d.T_2^3))}{(1 + (a + b.T_1 + c.T_1^2 + d.T_1^3))} \tag{8}$$

Where a, b, c and d are instrument-specific coefficients for the LNO channels, T_2 is the given instrument temperature, T_1 is the design temperature and σ_1 is the reference groove spacing at design temperature (see table 1). Table 2 summarizes their value. Because the blaze function mainly controls the position of a NOMAD raw spectrum on the 320 pixels, especially the position of maximum intensity, and since the temperature of the grating is not perfectly known, our strategy was to perform a rough estimation: we average all data from the same fullscan for each order and perform a regression to estimate the temperature to use for each order. The residual discrepancies between blaze function and real data are removed by continuum removal.

AOTF transfer function shape. The AOTF is an electro-optical device based on the Bragg diffraction, the interaction between acoustic and electromagnetic waves, in a birefringent crystal of Tellurium dioxide (TeO_2). Under the application of a radio-frequency (using a Transducer) the crystal vibrates and its internal structure is alternatively compressed and dilated through the crossing of the oscillating acoustic wavefront. This results in a periodic modification of its optical properties, its refractive index, thus producing diffraction of the incident light. The intensity of the diffraction is proportional to the amplitude of the acoustic signal applied to the crystal. In addition, changing the acoustic frequency applied to the crystal alters the periodicity of the refractive index variation and therefore the wavelength at which the light is diffracted. The AOTF crystal acts mainly as a filter for selecting the desired order of diffraction which will be transmitted to the diffraction grating. Thus, if no radiofrequency is applied to the crystal (AOTF off) then the spectrometer measures the thermal noise and the background noise also called "dark observation" which are used to correct the specific noises of the detector environment. The main characteristics of the AOTF used for the LNO channel are well described in Neefs et al. (2015). The AOTF transfer function

shape is usually modeled by a sinc-square function. However, several tests showed that this model does not accurately represent the NOMAD-LNO AOTF (Liuzzi et al., 2019). This may be due to the contributions from adjacent orders which are not negligible and can be related to two main reasons :

- The AOTF input radiofrequency is not centered on the AOTF transfer function with respect to the observed order, so the AOTF admits throughput of adjacent orders.
- The Free Spectral Range of the grating is smaller than the detector's sensitive area causing invasion from adjacent orders.

To properly account for this effect, we tested several models that would increase the contribution from adjacent orders in the AOTF transfer function shape (using multiple sinc-square, using one sinc-square per order or adding a linear function to add a background contribution). The most promising model turns out to be the use of a Gaussian function along with the usual sinc-square function which is similar to what is reported in Liuzzi et al. (2019). The AOTF transfer function shape follows :

$$T_{sinc}(\nu, I_0, fwhm, \Delta_\nu) = I_0.\left[\mathrm{sinc}\left(0.886.\frac{\nu-\nu_0-\Delta_\nu}{fwhm}\right)\right]^2 \tag{9}$$

$$T_{gauss}(\nu, I_G, \sigma_G, \Delta_G) = I_G.\exp\left[\frac{(\nu-\nu_0-\Delta_G)^2}{\sigma_G^2}\right] \tag{10}$$

$$T_{AOTF}(\nu, I_0, fwhm, \Delta_\nu, I_G, \sigma_G, \Delta_G) = T_{sinc} + T_{gauss} \tag{11}$$

Where $fwhm$ is the full width at half maximum of the sinc-square function, Δ_ν is the sinc-square shift in wavenumber from the central wavenumber of the considered order ν_0, I_0 the sinc-square amplitude, I_G the Gaussian amplitude, σ_G the Gaussian standard deviation and Δ_G the shift in wavenumber of the Gaussian function. These are the six free parameters to estimate related to the AOTF. Adding a Gaussian function lowers the contribution of the transfer function side lobes, which were related to the sinc-square function, but widens the shape of the main lobe and prevents the function to reach zero intensity between the main lobe and the first side lobe. This allows the increase of the contribution from the first nearby order. The main lobe is still centered on the central order which guarantees that most of the filtered signal is related to this order.

Final expression. The simulated solar spectrum is therefore constrained by the shape and intensity of the AOTF transfer function and the grating blaze function. The contribution from one order depends on the product of both functions at one particular wavenumber (i.e., on a spectel number). Contribution from adjacent orders is summed on the 320 spectral detector spectels which samples the wavenumber of the central order. The expression of a simulated solar observation by LNO is shown in equation 12.

$$S_{sim}^{instru}(\nu, I_0, fwhm, \Delta_\nu, I_G, \sigma_G, \Delta_G) = \sum_{m-\Delta m}^{m+\Delta m} S_L.(T_{Blaze}.T_{AOTF}) \tag{12}$$

The calibration proposed here was made considering 3 adjacent orders ($\Delta m = 3$) following the work of Liuzzi et al. (2019) who has shown that using 3 adjacent orders amounts to considering more than 99% of the total flux for the LNO channel. The absolute amplitude of the blaze and

AOTF transmittance are estimated jointly as a general instrument sensitivity (see section 4.2.5). T_{Blaze} and T_{AOTF} are usually normalized.

4.2.2. Instrument Line Shape (ILS)

The simulated solar spectrum (S_{sim}^{instru}) is first convolved to the Instrumental Line Shape (ILS), modeled here by a centered Gaussian function $\mathcal{G}(0, \sigma_\nu)$ defined by a standard deviation (σ_ν) similar to what is reported in Liuzzi et al., 2019 (Liuzzi et al., 2019). This result in a smoothed spectrum S_{sim}^{smooth} defined as:

$$S_{sim}^{smooth}(\nu, \sigma_\nu) = S_{sim}^{instru}(\nu) \star \mathcal{G}(0, \sigma_\nu) \tag{13}$$

This step is crucial to simulated realistic solar lines shape and to characterize the actual wavenumber resolution of the instrument. Also, as the initial solar spectrum (S_L) used for the calibration has a much higher spectral resolution than NOMAD, the convolution allows the simulated spectrum to match the theoretical spectral resolution of the observation. To compute the spectral resolution as a function of the diffraction order, we first compute the AOTF driver frequency to AOTF central wavenumber following the tuning relation :

$$\nu_0 = G_0 + A.G_1 + A^2.G_2 \tag{14}$$

where ν_0 is the central wavenumber and A is the AOTF frequency. The coefficients G_0, G_1 , and G_2 were determined by Liuzzi et al. (2019) using miniscans. Then, we compute the spectral resolution at the desired diffraction order :

$$sr = sr_0 + \nu_0.sr_1 + \nu_0^2.sr_2 \tag{15}$$

The coefficients sr_0, sr_1 and sr_2 are empirical values obtained by Liuzzi et al. (2019) using miniscans. The spectral resolution is order-dependent and is estimated with the central wavenumber (ν_0) of each order. This value is used as initialization and we treat σ_ν as a free parameter.

4.2.3. Residual wavenumber shift

The spectral calibration (see section 4.1) is not perfectly constant over time and solar lines are slightly shifted from one observation to another. Despite a first rough estimation of the temperature of the grating blaze function some residual shift may persist due to small variation of the blaze function within the same order. Since the temperature of the grating is not known such an effect must be taken into account for precise calibration. Our approach is to estimate the shift for each observation to possibly improve the formulation of eq. 4. We introduce a residual shift in wavenumber (δ_ν) between the observation (S_{obs}) and simulation (S_{sim}^{smooth}), the simulated spectra was resampled on the observed wavenumber with the linear resampling method:

$$S_{sim}^{smooth,resamp}(\nu) = S_{sim}^{smooth}(\nu + \delta_\nu) \tag{16}$$

with the wavenumber shift (δ_ν) set as a free parameter.

4.2.4. Continuum removal

The justification of this continuum removal step is done section 5. We propose to use the continuum estimation noted $\mathfrak{C}$, using the following approach :

$$S_{sim}^{smooth,resamp,flat}(\nu) = \frac{S_{sim}^{smooth,resamp}(\nu)}{\mathfrak{C}(S_{sim}^{smooth,resamp}(\nu))}.\overline{S_L} \tag{17}$$

$$S_{obs}^{flat}(\nu) = \frac{S_{obs}(\nu)}{\mathfrak{C}(S_{obs}(\nu))}.\overline{(S_{obs})} \tag{18}$$

Where $\overline{S_L}$ is the mean solar radiance taken from the input solar spectrum at the desired order and $\overline{(S_{obs})}$ is the mean of the normalized observation recorded by the detector for the desired order and sequence. Both means are computed with spectels 50 to 320. We used the function $\mathfrak{C}$ following the Asymmetric Least Squares smoothing (Eilers et al., 2005) with the following parameters:

- Smoothness $\lambda = 1.10^2$;
- Asymmetry $p = 0.99$;
- Number of iterations : 10 ;

4.2.5. Sensitivity

The sensitivity of the instrument is computed using the following equation :

$$Sensitivity = \frac{\left\| \overline{S_{sim}^{smooth,resamp,flat}}(W.cm^{-2}.(cm^{-1})^{-1}.sr^{-1}) \right\|}{\left\| \overline{S_{obs}^{flat}}(ADU.(cm^{-1})^{-1}.s^{-1}) \right\|} \tag{19}$$

Where $\overline{S_{obs}^{flat}}$ is the mean of the normalized observation after continuum correction as stated in equation 18 and $\overline{S_{sim}^{smooth,resamp,flat}}$ the mean of simulated spectra after the continuum correction. The two means are estimated for spectels 50 to 320. We choose to take the mean instead of the intensity at the center of the detector because it is a more robust indicator than the value of a single spectel which is subject to noise. The sensitivity simply expresses the mean radiance per counts per second of the 270 considered spectels. Once the sensitivity is known, the observation data can be calibrated into spectral radiance following:

$$S_{obs}^{flat,cal}(W.cm^{-2}.(cm^{-1})^{-1}.sr^{-1}) = Sensitivity.S_{obs}^{flat}(ADU.(cm^{-1})^{-1}.s^{-1}) \tag{20}$$

With S_{obs}^{flat} the normalized observation after continuum correction.

4.3. Calibration inversion

The aim is to retrieve the best parameters to simulate S_{sim} for each spectrum of each sequence of all solar fullscan. The goal is to compute the sensitivity (photometric calibration) but also to look at the potential correlation between the estimated free parameters and instrumental parameters such as temperature.

Since the AOTF parameters, the wavenumber shift, and the actual wavenumber resolution are not known and subject to change from one observation to another, we decided to estimate them by a fitting procedure. Except for the Gaussian and sinc-square functions intensities (the sum of which must be equal to 1, such that a filter is defined) all six other parameters are expressed in wavenumbers units (cm^{-1}) which makes it possible to assume the range in which we expect these parameters to fall. This is why we choose a bound-constrained minimization with the L-BFGS-B algorithm (Byrd et al., 1995; Zhu et al., 1997). The minimization equation follows:

$$\min_{I_0,fwhm,\Delta_\nu,I_G,\sigma_G,\Delta_G,\delta_\nu,\sigma_{ILS}} \left(\left\| S_{sim}^{smooth,resamp,flat}(I_0, fwhm, \Delta_\nu, I_G, \sigma_G, \Delta_G, \delta_\nu, \sigma_{ILS}) - S_{obs}^{flat,cal} \right\| \right) \tag{21}$$

Parameter	Initialization	Range	Units
I_0	0.5	0.1 - 1.0	
fwhm	18	12.0 - 20.0	cm^{-1}
Δ_ν	0.1	-10.0 - 10.0	cm^{-1}
I_G	0.5	0.1 - 1.0	
σ_G	12	10.0 - 15.0	cm^{-1}
Δ_G	0.1	0.1 - 1.0	cm^{-1}
σ_ν	eq. 15	0.1 - 1.0	cm^{-1}
δ_ν	0.1	-2.0 - 2.0	cm^{-1}

Table 3: Summary of the initialization and boundaries used for the calibration inversion.

The remaining residue between the spectra is estimated with the Root Mean Square Error (RMSE):

$$RMSE = \sqrt{\frac{\sum \left(S_{sim}^{smooth,resamp,flat} - S_{obs}^{flat,cal} \right)^2}{N}} \tag{22}$$

With N, the number of considered spectels, here 270 as the first 50 spectels are removed due to low SNR. The relative RMSE (rel_{RMSE}) can be defined as follow :

$$rel_{RMSE} = \frac{RMSE}{\overline{S_{sim}^{smooth,resamp,flat}}} \tag{23}$$

with $\overline{S_{sim}^{smooth,resamp,flat}}$, the mean of the simulation spectra. This gives the relative error (in %) between the observation and the simulation. The inversion stops when the norm of the projected gradient of the RMSE is less or equal to 10^{-8} with a step size of 10^{-5} for each parameter.

A total of 8 free parameters were retrieved for each spectrum of all sequences and all fullscans. The minimization step needs an initialization of these parameters to look for the best fit. The initialization is crucial for a non-convex problem (which is the case here, since the problem is non-linear), that is why we tested several cases and finally reach a good optimum using the set of parameters for the initialization described in table 3.

5. Justification of the continuum removal

All modeled effects are not able to perfectly fit both the overall shape of the spectra and the absorption lines of the observation as shown in figure 5. In this figure, we applied the calibration procedure with/without the continuum removal (Fig. 5 A and B). One can see that without the continuum removal, the fitting procedure is dominated by the large-scale feature and unfortunately not coherent with detailed solar line shape. Such results imply that in the present state of instrument knowledge, it is not possible to take into account a precise instrumental transfer function for both shape and solar lines.

In order to check the consistency, we tried an alternative approach assuming perfectly known spectral calibration (Fig. 5 C). This may not be achievable in actual data analysis and would requires another pre-processing step of spectral calibration. Results show that the reconstruction is acceptable contrarily to the case without continuum removal (Fig. 5 B). Both continuum and solar lines can be reasonably well fitted, but the best reconstruction is for the fully blind case

(inversion of the spectral calibration with continuum removal) (Fig. 5 A). As one of the main advantages of LNO being its very high spectral resolution, one would emphasize the spectral line reconstruction instead of the continuum shape.

Here three strategies are possible. The first approach is to improve the characterization of the instrument, in particular by trying to handle the temperature dependence of the AOTF and grating blaze function shape. Due to the small amount of in-flight solar data acquisition, this strategy may be difficult, in particular to distinguish temperature dependence and temporal dependence (due to the degradation of the detector in space for instance). In addition, an improvement of the instrumental characterization using a spare ground instrument always rise the question of its representativity.

A second approach would be purely empirical (on in-flight data only, no reference solar spectrum). By assuming negligible temporal variability, Thomas et al. (2021) propose a fully empirical calibration, by estimating a comprehensive transfer function (including instrumental transfer function, sensitivity, and solar spectrum) and its temperature dependence, interpolated from actual data. This strategy, based on observation only, may be biased due to the noise in the data (despite an SNR $>$ 1000) and possible temporal variability. Nevertheless, this approach has the advantage to keep the large scale spectral features.

A third approach, proposed in the present article (see section 4.2.4), is to solve the problem by removing the continuum, focusing on small-scale spectral features, but possibly erasing large-scale spectral feature. This approach takes advantage, as previously mentioned, that the instrumental transfer function is normalized, and thus filtering would not change the level. In addition, the potential alteration of the large-scale feature would be identical for simulated and observed spectra, and thus would produce no bias, as also performed on NOMAD-SO channel (Villanueva et al., 2021; Knutsen et al., 2021).

The main advantage of such an approach is that it allows to keep the spectral radiance level (which is of primary importance for absolute photometric calibration) and produce flat continuum spectra. The validity of this approach can be measured by the root-mean-square error (RMSE) that should be low in comparison to the signal, but also by the coherence of the sensitivity measurement (consecutive measurement should be somehow similar). We propose hereafter to follow this strategy, which has the advantage to avoid any assumption of the temporal stability of the NOMAD instrument.

6. Results

Fit of order 189. An interesting way to check the validity of the model is to compare observations and simulations at the spectrum scale. Figure 6 shows such comparison for order 189 on the whole of a fullscan (here 14/03/2019), as an example. Here the spectra are flat due to the continuum removal step which allows apprehending only the level of the spectrum and the position of the bands. The 13 observation sequences are shown in a shade of gray while the optimized simulation after the inversion is shown in colors. The residue between the observation and the simulation is also indicated. Both the main and weak solar lines are well reproduced and the small discrepancies are within the continuum and related to very weak solar lines. As the position and depth of the line are mainly controlled by the AOTF transfer function, with the secondary lobes of the transfer function being responsible for the leakage of adjacent orders on the central order (here 189). This contribution is expected to significantly increase the intensity of such solar lines, especially if they are located on the edges of the order, as they can be duplicated. Order 189 displays such potentiality with two main solar lines on both edges of the detector. One can see that the

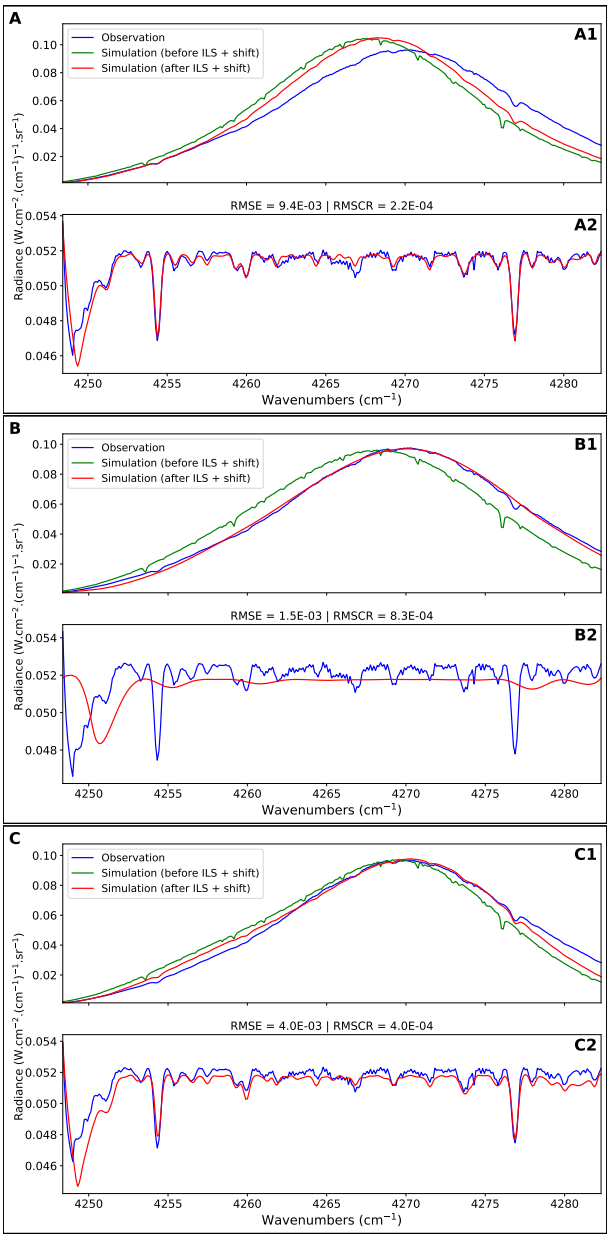

Figure 5: (A) Estimation of the inversion with continuum removal using the minimization equation 21. Note that the first 50 spectels on the left (up to 4253.5 cm^{-1}) are not included in the inversion due to low signal to noise ratio. (A1) Comparison between an observation ($S_{obs}(\nu)$, in blue) and two types of calibration inversion: before integration of the wavenumber shift and ILS ($S_{sim}^{instru}(\nu)$, in green) and after ($S_{sim}^{smooth,resamp}(\nu)$, in red). The RMSE indicates the quality of the fit. (A2) Comparison between an observation (S_{obs}^{flat}, in blue) and the simulation ($S_{sim}^{smooth,resamp,flat}(\nu)$, in red) both after continuum removal. The RMSCR (RMSE after continuum removal) indicates the quality of the fit. (B) Same as (A) without continuum removal. (C) same as (A) without continuum removal but with spectral calibration assumed to be perfectly known. For the (B2) and (C2) plots we compute the continuum removal on the results of the inversion (continuum removal was not included in the inversion).

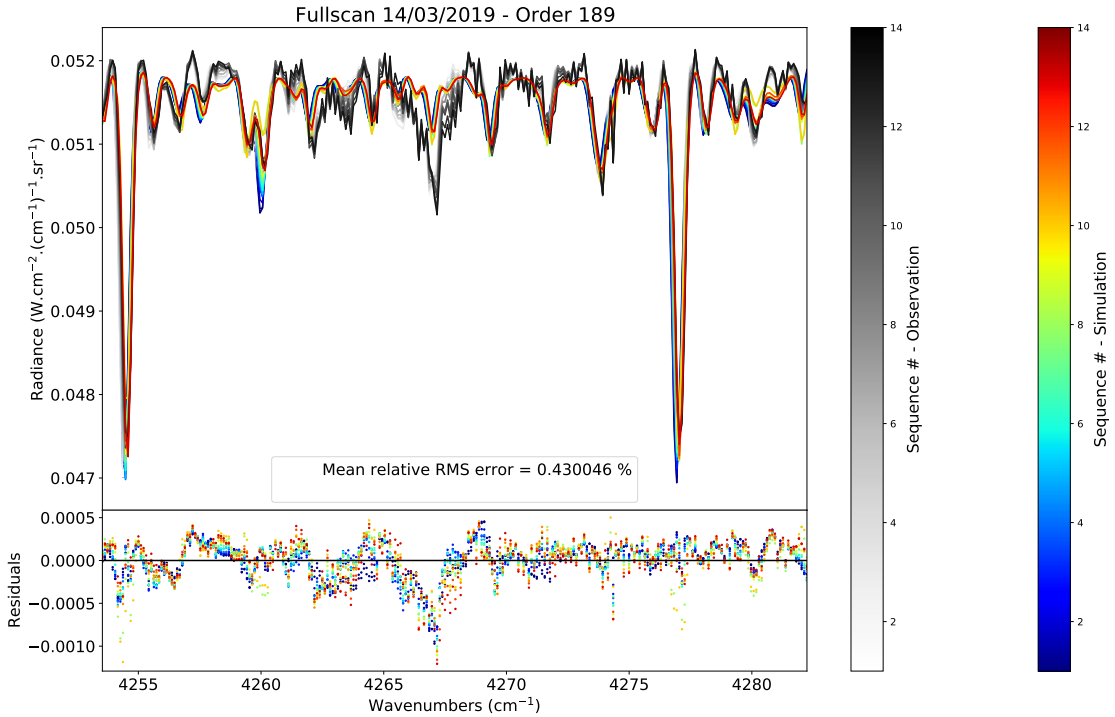

Figure 6: Fullscan of 14/03/2019, comparison between all observation sequences of order 189 (in shades of gray) and the respective optimized simulation (in colors). One can see that the main solar lines are well reproduced and the small discrepancies are only located within the continuum, near the weak solar lines. The mean relative RMS error of the 13 sequences is 0.43%.

model perfectly accounts for this contribution since the simulation match very well the observation (relative RMS = 0.43%), no matter the observation sequence.

RMSE. Here we illustrate the overall results of the calibration model. First, the RMSE can be used for all observations as it is the quality criterion of the approach. Figure 7 shows the relative RMSE based on equation 23 for diffraction orders 110 to 200. The large majority of the points are below 1% error except for extreme orders (100-110 and 198-200) for which the SNR can be very low. We can also notice that the fullscan showing the widest dispersion is that of 01/11/2018 for which the temperature during the observation was abnormally high, leading to noisier spectra and therefore greater difficulty in obtaining a correct fit. The relative RMSE appears more dispersed for orders 150 to 190 compared to orders 120 to 150. This can be explained by the fact that high orders have stronger solar lines, which implies more information in the spectra to model the AOTF resulting in a larger standard deviation of the RMSE. However, if we exclude outliers above 1% , the average value of the relative RMSE between orders 150-190 is comparable to that of orders 120-150. This low RMSE for most of the orders (around 0.5%) tends to validate the spectrum-to-spectrum calibration method using a continuum removal approach.

Sensitivity. The main objective of the model is to establish the conversion factor from the measured ADU by the detector to spectral radiance. This step is done using equation 19 on all spectra of all fullscan so that we can look at the potential variations of this factor during the mission. Figure 8 shows the sensitivity curves of the LNO channel, which was estimated using equation 19. As we estimate the mean *Sensitivity* on 270 spectels, it expresses the mean radiance per counts per

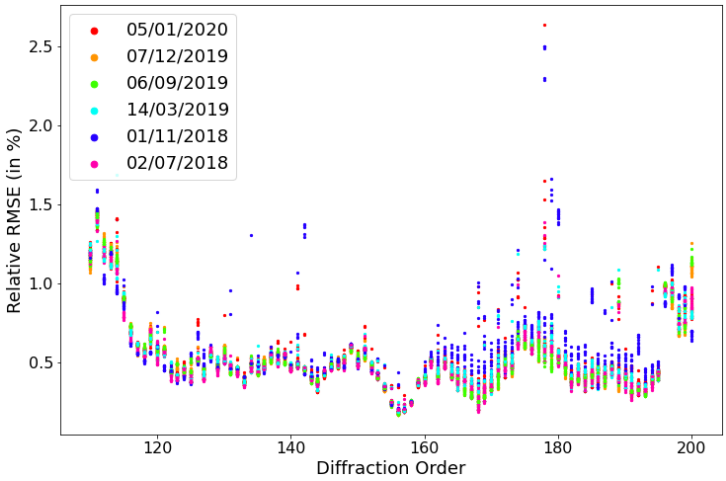

Figure 7: Relative RMS error rel_{RMSE} between the simulation and the observation for diffraction orders 110 to 200 and the 6 solar fullscans. Each point represents a single spectrum of a fullscan sequence.

second of this 270 spectels. The shape of the curves is very similar to what was obtained during ground calibration before the mission: orders 120 to 135 and 165 to 190 have a higher sensitivities (Thomas, 2020). This is related to the initial design of the instrument whose purpose was a precise atmospheric characterization and these orders match the spectral range in which CO, H_2O and CH_4 have significant absorption. In addition, a drastic fall of the sensitivity near order 150 was expected and is correctly reproduced. The significant drop of the sensitivity for extreme orders illustrates well how the SNR can be low for these orders, and therefore the reasons for a higher RMSE (noisy observation are harder to fit). An exception is made for orders around 150 as the sensitivity is quite low but the RMSE of these orders is also the lowest. This is related to the fact that these orders have very few solar lines which imply an easier fit of an almost flat continuum. Nevertheless, from one fullscan to another the shape is constant but the intensity slightly changes. The first two fullscans (02/07/2018 in purple and 01/11/2011 in navy blue) display lower sensitivities while fullscans of 06/09/2019 (in green) and 07/12/2019 (in orange) show the highest values. These differences can be explained in many ways and one of the advantages of this calibration method is to be able to test the dependence of the sensitivity such as a function of time, of the Mars-Sun distance, or the temperature. Hereafter we will demonstrate that the temperature dependence is the dominant factor.

With such variation of the instrumental sensitivity (Fig. 8), one would look if there is any correlation with other parameters. This step was made using both the nominal and redundant temperature T sensors of the LNO that monitors the temperature within the spectrometer every 2 minutes. Here we show the correlation with the nominal sensor. The temporal resolution of the temperature sensor is 2 minutes, which is too high compared to the time between two consecutive LNO observations. Temperature data were thus interpolated to match the timestamp of each fullscan. Figure 9 shows the sensitivity as a function of the temperature. Here all diffraction orders of the six fullscans are shown along with the linear regression (dotted line). The gap between the points illustrates the temperature variation between the fullscans. Within one sequence, one can see a slope that seems to be consistent between all orders showing that sensitivity decline when temperature increases. Looking at all sequences together, the relationship seems linear and we fit a line for each diffraction order:

$$Sensitivity = a.T + b \tag{24}$$

With T the temperature. The adjusted a and b values are available in public archive[1]. By postulating that the temperature is mainly responsible for the sensitivity change of the detector, and correcting these variations with a linear fit we can show that there is no sign of a correlation with time (aging of the detector) in the instrumental response of the detector (see figure 10) which was not obvious in the first place.

Regarding the absolute uncertainty of the sensitivity retrieved here, and hence on the radiance derived from the calibration. All the steps introduced in the calibration pipeline (ILS, spectral shift, AOTF parameters and continuum correction) respect the energy conservation. Thus, according to equation 19, the main source of uncertainty come from the number of counts (S_{obs}^{flat} in $ADU.(cm^{-1})^{-1}.s^{-1}$) of the LNO observation of the sun and from the synthetic solar spectrum ($S_{sim}^{mooth,resamp,flat}$ in spectral radiance). The LNO observation are normalized according to equation 1 and we can assume that the uncertainty on the integration time, number of accumulation, spectral resolution and binning factor is negligible. According to Thomas et al. (2021), a typical LNO spectrum of 3000 ±500 counts would have an SNR of about 25 ±5, which gives an absolute error between 0.6% and 1%. Also, the maximum expected systematic error is 4% (Thomas et al., 2021). The uncertainty on $S_{sim}^{mooth,resamp,flat}$ is related to the initial solar spectrum, according to Chance and Kurucz (2010), the absolute accuracy of the solar spectrum is of 3.5-4%. This leads to a maximum absolute uncertainty on the radiance less than 10%. Although the maximum error may be high, the systematic error of LNO is not often expected to be 4%.

AOTF. Among all the inverted parameters six of them account for the AOTF transfer function shape. They are crucial because they account for the contribution of the main and adjacent orders which define the intensity of solar lines. An example of the transfer function retrieved after the inversion is given in figure 11 for one observation of order 189. In this case, the estimated AOTF transfer function is slightly asymmetrical, promoting a higher contribution of order 190 compared to order 188. The "bell" shape of an LNO spectrum is partly controlled by the blaze function but the AOTF sidelobes are also affecting the spectra by widening or shrinking the flanks of the continuum. To reproduce all the potential shapes of an LNO spectrum, which vary from one order to another it is necessary to integrate variations in intensity, width and offsets of the AOTF transfer function.

In the example shown figure 11 the AOTF inverted parameters to reconstruct the final spectrum are:

- $I_0 = 0.74$ ±0.3
- $fwhm = 17.41$ cm^{-1} ±0.86
- $\Delta_\nu = 2.34$ cm^{-1} ±0.53
- $I_G = 0.71$ ±0.57
- $\sigma_G = 12.86$ cm^{-1} ±0.77
- $\Delta_G = 2.33$ cm^{-1} ±0.59

[1] https://doi.org/10.14768/2d7688ba-2e5f-473c-8e03-763e93f4bd6b

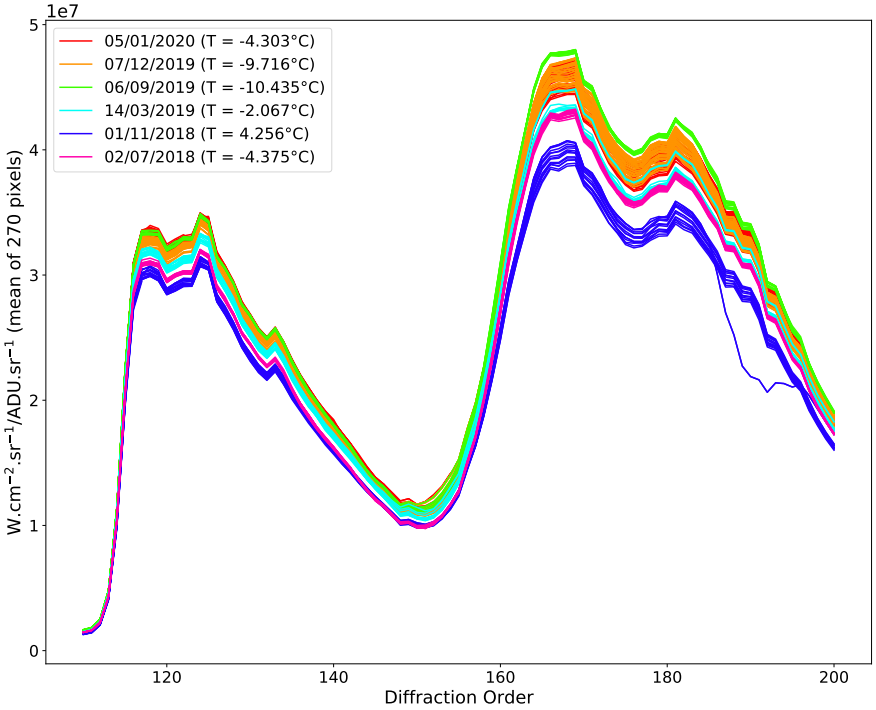

Figure 8: Radiance to counts conversion (*Sensitivity*) for diffraction orders 110 to 200 retrieved for the 6 LNO solar fullscan using equation 19. The mean temperature during the fullscan is indicated. This illustrates the sensitivity curves of the LNO channel. The shape is very consistent from one sequence to another but also between the fullscans, with two main peaks of sensitivity around orders 125 and 170 and a lower sensitivity for the extreme orders and around orders 150.

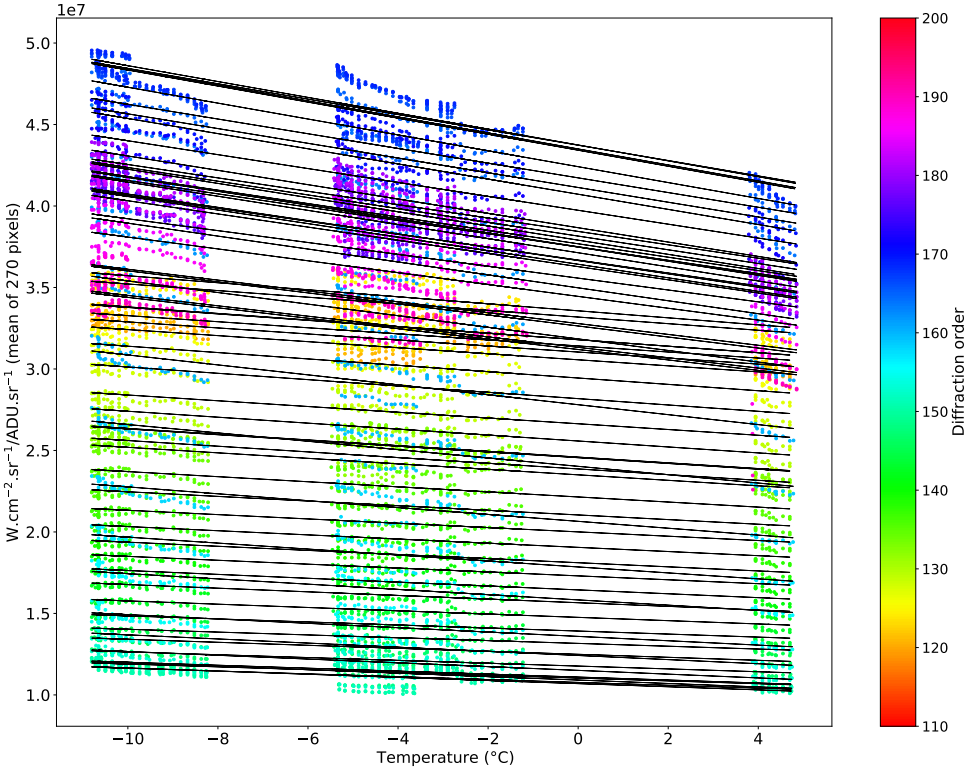

Figure 9: Sensitivity as a function of the instrumental temperature (nominal sensor). The colors refer to diffraction order and the dotted line shows the linear regression per order.

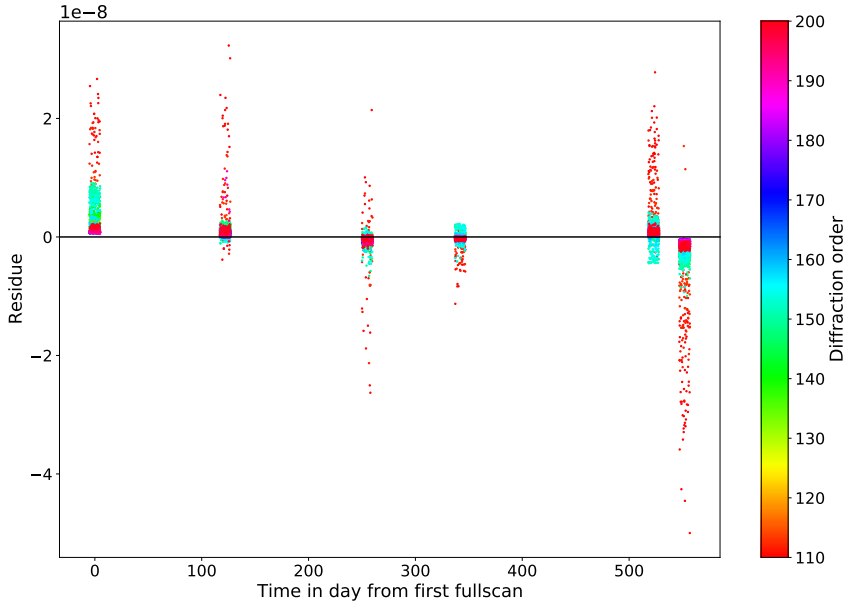

Figure 10: Residue after temperature correction of the sensitivity using eq. 24 as a function of time (in day) from first fullscan. The results are artificially spread horizontally for clarity. Despite few outliers near order 110 (in red) for which the sensitivity is very low, the residues indicate that there is no correlation of the sensitivity with time and therefore no aging of the detector to the first order.

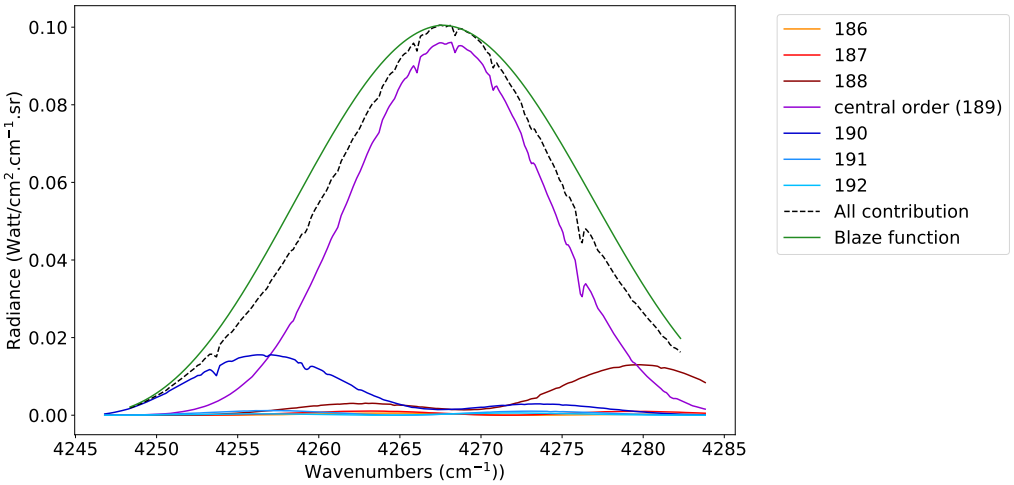

Figure 11: AOTF transfer function: contribution from the main order (189 in purple) and 3 adjacents orders. The sum of all contributions that define the final spectrum is shown in black dashed line and the Blaze function of the central order is shown in green. The main lobe of the AOTF transfer function accounts for the contribution of the central order while the sidelobes control the shape and intensity of adjacent orders which are summed onto the wavenumbers of the central order. The shape of the final spectrum is therefore constrained by the product of the Blaze function and the AOTF transfer function.

We tested several temperature and temporal dependence and did not find any obvious correlation. These parameters define the shape of the AOTF and can therefore be strongly correlated together. This is particularly noticeable on the spectral shift of the sinc-square (Δ_ν) and the gaussian (Δ_G) whose values and uncertainties are similar. A shift of one can thus be compensated by the other, but the best fit is estimated for a similar offset of the two. This observation is the same for the intensities of the two filters (I_0 and I_G) whose uncertainties are relatively large. However, the width of the filters ($fwhm$ and σ_G) is well constrained and the values obtained are similar to what is obtained by Liuzzi et al. (2019).

Spectral calibration and ILS. Figure 12 shows the actual spectral resolution of the instrument σ_ν retrieved by the algorithm for all available data as a function of the diffraction order. A comparison with the theoretical spectral resolution computed using eq. 15 is provided. We found that σ_ν is slightly higher (mostly around 0.05) than expected but still follows the theoretical trend. Some points are way off the trend and are often related to orders with lower sensitivity and thus more noise, so the convolution requires a much wider ILS to get a proper fit. This is illustrated with the fullscan of 01/11/2018 (navy blue points), which corresponds to the highest temperature and lowest sensitivity (see fig. 9, navy blue curves)

The wavenumber shift δ_ν account for potential deviation from the theoretical spectral calibration (see eq. 4). Figure 13 (top panel) shows the retrieved shift as a function of the diffraction order for the 6 fullscans. When expressed in pixel, the shift appears constant with the diffraction order. Nevertheless, the shifting intensity is different from one fullscan to another. We tested a temperature dependence of the wavenumber shift δ_ν in figure 13 (bottom panel) using orders 130 to 190 and found a slope of about 0.75 pixels per degree which is consistent with what Liuzzi et al. (2019) and Thomas et al. (2021) reported with values of 0.71 and 0.83 pixels per degree.

The wavenumber shift and ILS analysis emphasize that our approach works well for diffraction orders with multiple well-defined solar lines because the continuum removal approach allows assigning a greater weight to the variations brought by the solar lines and therefore to the AOTF parameters. The quality of the fit is higher for orders with the number of strong solar lines. Also, such orders have often higher sensitivities which promote a better estimation of the wavenumber shift and the spectral resolution.

7. Calibration pipeline

With such an approach any nadir observation can be calibrated to spectral radiance, the pipeline to calibrate a raw nadir spectrum is as follows: first, the raw spectrum is normalized following equation 1 with the spectral resolution (eq. 15). Second, we remove the continuum using eq. 18 to get a flat spectrum. Then, knowing the temperature at the time of the measurement from housekeeping and using coefficients a and b from eq. 24, we apply the sensitivity factor to convert the normalized ADU to spectral radiance (see Eq. 20). This product can be used to create reflectance map such as the one reported in Thomas et al. (2021) applying the following equation:

$$R = \pi . \frac{I}{F} \tag{25}$$

With I the spectral radiance and $F = S_L . \pi . \cos(\theta_i)$ the spectral irradiance received by the surface (see section 3.2) accounting for the incident angle θ_i and the distance of the sun at the time of the observation. A typical reflectance map obtained via our approach is shown in figure 14 for order 189 using data spread over mostly 3 years. A comparison with the reflectance obtained

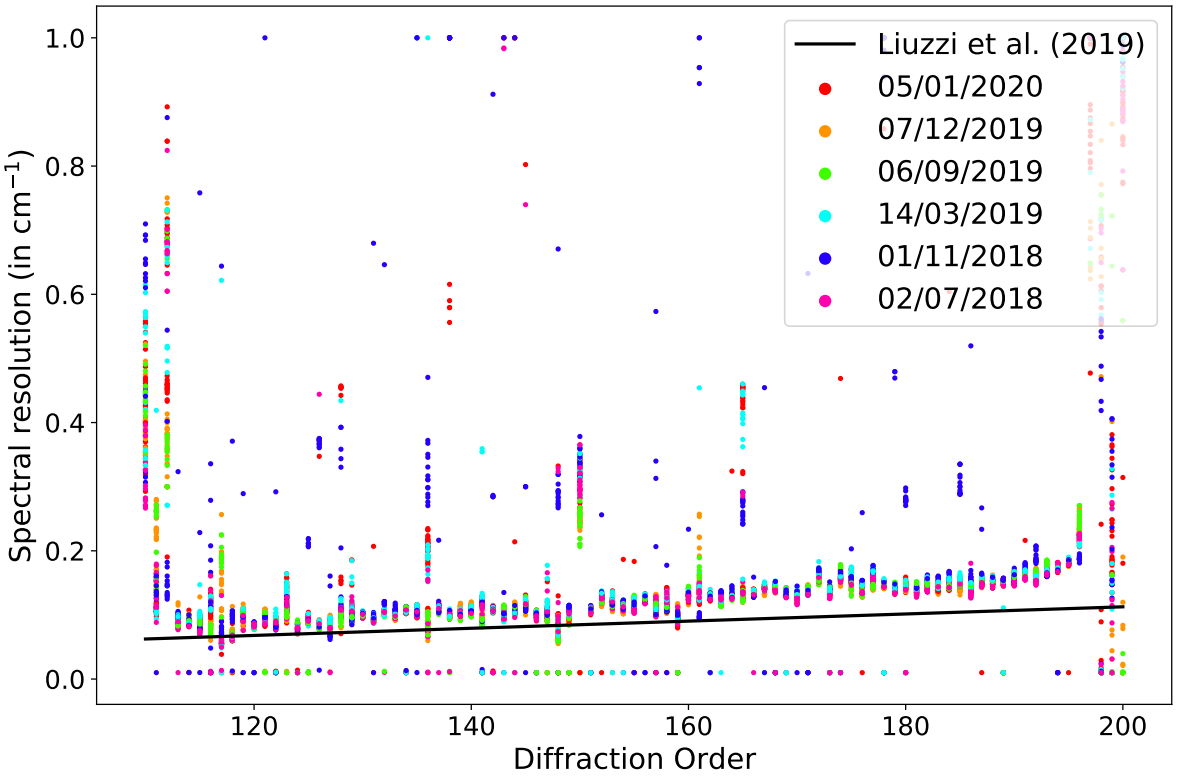

Figure 12: Actual ILS spectral resolution σ_ν retrieved from the calibration inversion. Each point corresponds to a single spectrum, the color refers to the 6 fullscans used. The empirical spectral resolution computed using eq. 15 (Liuzzi et al., 2019)) is shown as a black line. For a clearer comparison, data from Liuzzi et al. (2019) were converted from a Gaussian FWHM to a Gaussian standard deviation considering $FWHM = 2\sqrt{2\ln 2}\sigma$

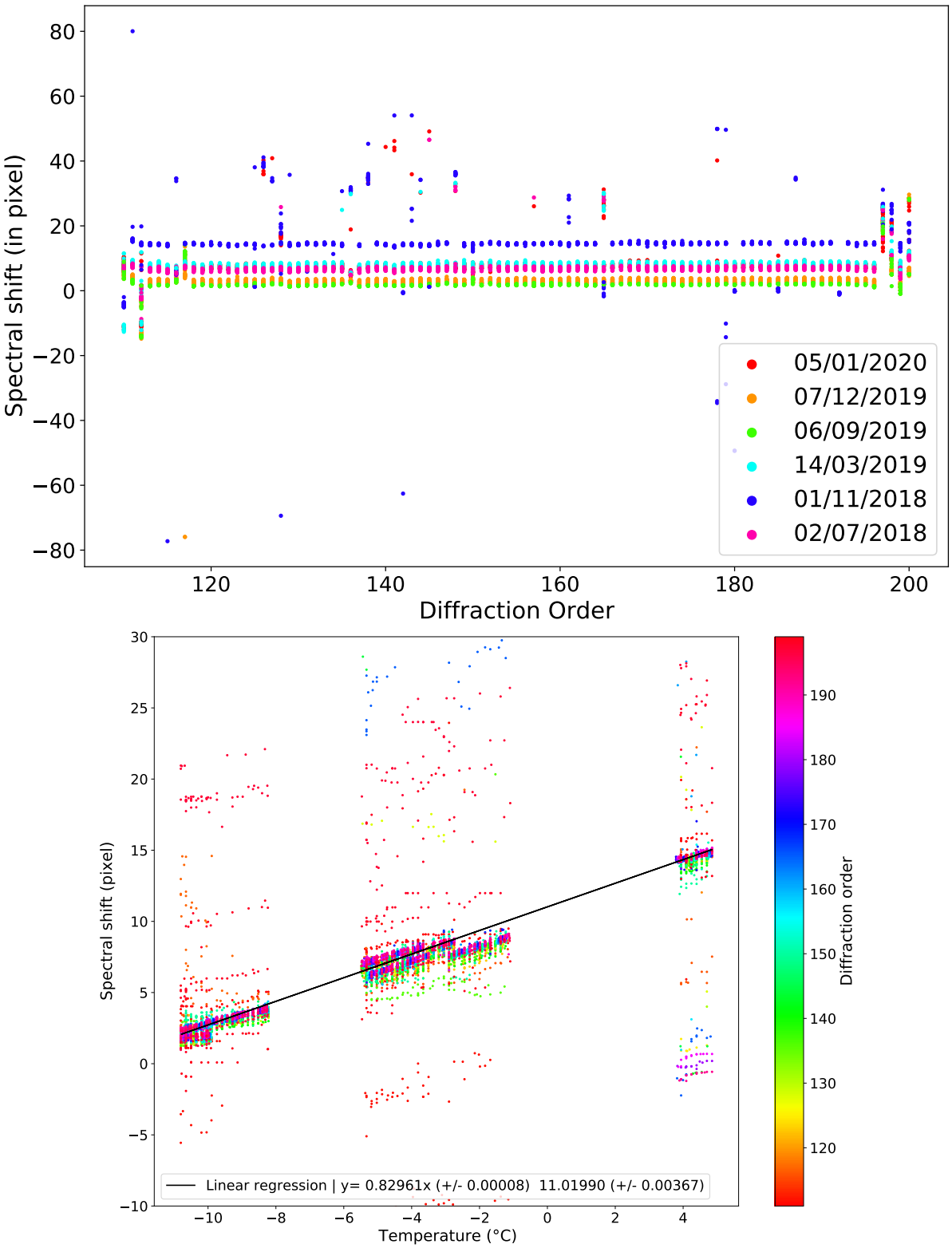

Figure 13: Wavenumber shift δ_ν (in pixel units) retrieved from the calibration inversion. Top image show the spectal shift as a function of the diffraction order, colors refer to the fullscan. Bottom image shows the shift as a function of temperature. The color refers to the diffraction order.

following the method of Thomas et al. (2021) is also shown (fig. 14, bottom panel). The two calibrations provide very similar results with a linear coefficient of 1.024 and -0.017 (correlation coefficient of 0.987) despite different approaches. This result shows that both calibrations are in agreement mostly within 3% and that our approach underestimates (resp. overestimates) the one from Thomas et al., 2011 for reflectance < 0.2 (resp. > 0.2).

8. Conclusion

We propose an alternative calibration method for the LNO data using reference solar spectra with the advantage of being able to investigate the correlations between the instrumental sensitivity and the temperature of the instrument. By having done this, we can understand the potential temporal variations of the instrument due to its aging. The method is based on the adjustment of a synthetic spectrum to the solar data acquired with NOMAD-LNO fullscan operation mode, which allows a calibration over the whole spectral range of the instrument (different orders), using an analytical model that simulate the instrumental effects. To realize this calibration, we propose to focus on the level and the fine solar bands shape and remove the continuum. This strategy allows to correct of unknowns in the instrumental AOTF/blaze functions but could possibly remove the large spectral feature of the order. However, by performing the same continuum removal to the synthetic data, it is possible to compare synthetic and observation data without bias (Villanueva et al., 2021; Knutsen et al., 2021).

In addition, this method makes it possible to test the correlations between sensitivity and instrumental parameters (AOTF shape, ILS, wavenumber shift), such as temperature and time. By doing this, we show that there is at first degree a linear relationship between the temperature and the sensitivity. By removing this effect, we demonstrated that there is no sign of temporal change in the sensitivity, which validates the calibration method proposed by Thomas et al. (2021). If any temporal variations of the detector occur in the future, our method should be able to capture them.

Finally, with such a model, one can calibrate any nadir observation to spectral radiance and reflectance data. The calibrated data show a very strong correlation with the approach proposed by Thomas et al. (2021) mostly within 3%. The two approaches are therefore complementary and coherent.

Acknowledgements. The NOMAD experiment is led by the Royal Belgian Institute for Space Aeronomy (IASB-BIRA), assisted by Co-PI teams from Spain (IAA-CSIC), Italy (INAF-IAPS), and the United Kingdom (Open University). We would like to thank everyone involved in the ExoMars project. Funding: This project acknowledges funding by the Belgian Science Policy Office (BELSPO), with the financial and contractual coordination by the ESA Prodex Office (PEA 4000103401, 4000121493), by Spanish Ministry of Science and Innovation (MCIU) and by European funds under grants PGC2018-101836-B-I00 and ESP2017-87143-R (MINECO/FEDER), as well as by UK Space Agency through grants ST/V002295/1, ST/V005332/1 and ST/S00145X/1 and Italian Space Agency through grant 2018-2-HH.0. This work was supported by the Belgian Fonds de la Recherche Scientifique – FNRS under grant number 30442502 (ET_HOME). The IAA/CSIC team acknowledges financial support from the State Agency for Research of the Spanish MCIU through the "Center of Excellence Severo Ochoa" award for the Instituto de AstrofÃsica de AndalucÃa (SEV-2017-0709). US investigators were supported by the National Aeronautics and Space Administration. Canadian investigators were supported by the Canadian Space Agency. We acknowledge support from the "Institut National des Sciences de l'Univers" (INSU), the "Centre

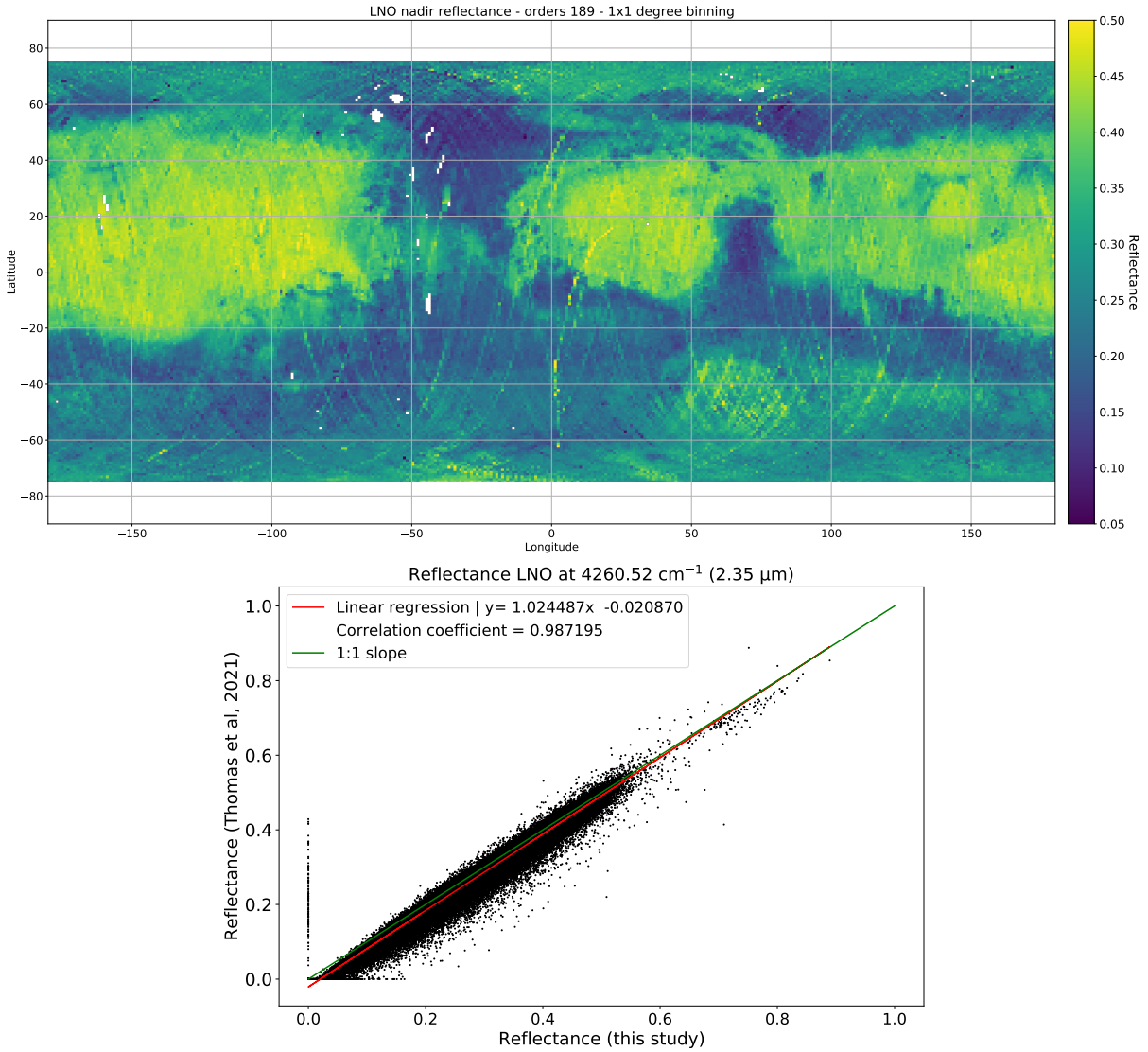

Figure 14: Reflectance of order 189 at 4260.52 cm^{-1} using 1230 orbits from 29/03/2018 to 19/10/2021. Data with incident angle higher than 80° were removed to promote a better SNR. Also, to reduce albedo variation due to seasonal effects at high latitude we only considered data between latitude 75° N and 75° S. The top image shows a map binned onto a 1°x1° grid using 134,738 spectra. Bottom shows a comparison between the reflectance estimate in this study and the reflectance obtained using the approach of Thomas et al. (2021) for the same order.

National de la Recherche Scientifique" (CNRS) and "Centre National d'Etudes Spatiales" (CNES) through the "Programme National de Planétologie". This work is partly funded through the ESA co-funded PhD studentships programme (idea: I-2019-01294).

References

Byrd, R.H., Lu, P., Nocedal, J., Zhu, C., 1995. A limited memory algorithm for bound constrained optimization. SIAM Journal on Scientific Computing 16, 1190–1208. doi:10.1137/0916069.

Chance, K., Kurucz, R., 2010. An improved high-resolution solar reference spectrum for earth's atmosphere measurements in the ultraviolet and visible and and near infrared. Journal of Quantitative Spectroscopy and Radiative Transfer 111, 1289–1295. doi:10.1016/j.jqsrt.2010.01.036.

Eilers, Paul, Boelens, Hans, 2005. Baseline corection with asymmetric least squares smoothing.

Hase, F., Wallace, L., McLeod, S.D., Harrison, J.J., Bernath, P.F., 2010. The ACE-FTS atlas of the infrared solar spectrum. Journal of Quantitative Spectroscopy and Radiative Transfer 111, 521–528. doi:10.1016/j.jqsrt.2009.10.020.

Knutsen, E.W., Villanueva, G.L., Liuzzi, G., Crismani, M.M., Mumma, M.J., Smith, M.D., Vandaele, A.C., Aoki, S., Thomas, I.R., Daerden, F., Viscardy, S., Erwin, J.T., Trompet, L., Neary, L., Ristic, B., Lopez-Valverde, M.A., Lopez-Moreno, J.J., Patel, M.R., Karatekin, O., Bellucci, G., 2021. Comprehensive investigation of mars methane and organics with ExoMars/NOMAD. Icarus 357, 114266. doi:10.1016/j.icarus.2020.114266.

Liuzzi, G., Villanueva, G.L., Mumma, M.J., Smith, M.D., Daerden, F., Ristic, B., Thomas, I., Vandaele, A.C., Patel, M.R., Lopez-Moreno, J.J., Bellucci, G., 2019. Methane on mars: New insights into the sensitivity of CH4 with the NOMAD/ExoMars spectrometer through its first in-flight calibration. Icarus 321, 671–690. doi:10.1016/j.icarus.2018.09.021.

Marquardt, E., Le, J., Radebaugh, R., 2000. Cryogenic material properties database. 11th International Cryocooler Conference .

Neefs, E., Vandaele, A.C., Drummond, R., Thomas, I.R., Berkenbosch, S., Clairquin, R., Delanoye, S., Ristic, B., Maes, J., Bonnewijn, S., Pieck, G., Equeter, E., Depiesse, C., Daerden, F., Ransbeeck, E.V., Nevejans, D., Rodriguez-Gómez, J., López-Moreno, J.J., Sanz, R., Morales, R., Candini, G.P., Pastor-Morales, M.C., del Moral, B.A., Jeronimo-Zafra, J.M., Gómez-López, J.M., Alonso-Rodrigo, G., Pérez-Grande, I., Cubas, J., Gomez-Sanjuan, A.M., Navarro-Medina, F., Thibert, T., Patel, M.R., Bellucci, G., Vos, L.D., Lesschaeve, S., Vooren, N.V., Moelans, W., Aballea, L., Glorieux, S., Baeke, A., Kendall, D., Neef, J.D., Soenen, A., Puech, P.Y., Ward, J., Jamoye, J.F., Diez, D., Vicario-Arroyo, A., Jankowski, M., 2015. NOMAD spectrometer on the ExoMars trace gas orbiter mission: part 1—design and manufacturing and testing of the infrared channels. Applied Optics 54, 8494. doi:10.1364/ao.54.008494.

Nevejans, D., Neefs, E., Ransbeeck, E.V., Berkenbosch, S., Clairquin, R., Vos, L.D., Moelans, W., Glorieux, S., Baeke, A., Korablev, O., Vinogradov, I., Kalinnikov, Y., Bach, B., Dubois, J.P., Villard, E., 2006. Compact high-resolution spaceborne echelle grating spectrometer with acousto-optical tunable filter based order sorting for the infrared domain from 2.2 to 4.3 μm. Applied Optics 45, 5191. doi:10.1364/ao.45.005191.

Smith, M., 2021. Nomad nadir-geometry retrievals of co in the mars atmosphere. doi:10.17632/PX89DK6CK9.1.

Thomas, I., 2020. Nomad experiment to archive interface control document. URL: ftp://npsa01.esac.esa.int/pub/mirror/ExoMars2016/em16_tgo_nmd/document/EAICDhttps://nomad.aeronomie.be/ProjectDir/data/nomad_hdf5_datasets.pdf.

Thomas, I., Aoki, S., Trompet, L., Robert, S., Depiesse, C., Willame, Y., Cruz-Mermy, G., Schmidt, F., Erwin, J., Vandaele, A., Daerden, F., Mahieux, A., Neefs, E., Ristic, B., Hetey, L., Patel, M., Moreno, J.L., Bellucci, G., , the NOMAD Team, 2021. Calibration of nomad onboard the exomars trace gas orbiter: Part 2 - the lno channel. Submitted .

Thomas, I.R., Vandaele, A., Robert, S., Neefs, E., Drummond, R., Daerden, F., Delanoye, S., Ristic, B., Berkenbosch, S., Clairquin, R., Maes, J., Bonnewijn, S., Depiesse, C., Mahieux, A., Trompet, L., Neary, L., Willame, Y., Wilquet, V., Nevejans, D., Aballea, L., Moelans, W., Vos, L.D., Lesschaeve, S., Vooren, N.V., Lopez-Moreno, J.J., Patel, M.R., Bellucci, G., the NOMAD Team, 2016. Optical and radiometric models of the NOMAD instrument part II: the infrared channels - SO and LNO. Optics Express 24, 3790. doi:10.1364/oe.24.003790.

Vago, J., Witasse, O., Svedhem, H., Baglioni, P., Haldemann, A., Gianfiglio, G., Blancquaert, T., McCoy, D., de Groot, R., 2015. ESA ExoMars program: The next step in exploring mars. Solar System Research 49, 518–528. doi:10.1134/s0038094615070199.

Vandaele, A., Neefs, E., Drummond, R., Thomas, I., Daerden, F., Lopez-Moreno, J.J., Rodriguez, J., Patel, M., Bellucci, G., Allen, M., Altieri, F., Bolsée, D., Clancy, T., Delanoye, S., Depiesse, C., Cloutis, E., Fedorova, A., Formisano, V., Funke, B., Fussen, D., Geminale, A., Gérard, J.C., Giuranna, M., Ignatiev, N., Kaminski, J., Karatekin, O., Lefèvre, F., López-Puertas, M., López-Valverde, M., Mahieux, A., McConnell, J., Mumma, M., Neary, L., Renotte, E., Ristic, B., Robert, S., Smith, M., Trokhimovsky, S., Auwera, J.V., Villanueva, G., Whiteway, J., Wilquet, V., Wolff, M., 2015. Science objectives and performances of NOMAD and a spectrometer suite for the ExoMars TGO mission. Planetary and Space Science 119, 233–249. doi:10.1016/j.pss.2015.10.003.

Vandaele, A.C., , Korablev, O., Daerden, F., Aoki, S., Thomas, I.R., Altieri, F., López-Valverde, M., Villanueva, G., Liuzzi, G., Smith, M.D., Erwin, J.T., Trompet, L., Fedorova, A.A., Montmessin, F., Trokhimovskiy, A., Belyaev, D.A., Ignatiev, N.I., Luginin, M., Olsen, K.S., Baggio, L., Alday, J., Bertaux, J.L., Betsis, D., Bolsée, D., Clancy, R.T., Cloutis, E., Depiesse, C., Funke, B., Garcia-Comas, M., Gérard, J.C., Giuranna, M., Gonzalez-Galindo, F., Grigoriev, A.V., Ivanov, Y.S., Kaminski, J., Karatekin, O., Lefèvre, F., Lewis, S., López-Puertas, M., Mahieux, A., Maslov, I., Mason, J., Mumma, M.J., Neary, L., Neefs, E., Patrakeev, A., Patsaev, D., Ristic, B., Robert, S., Schmidt, F., Shakun, A., Teanby, N.A., Viscardy, S., Willame, Y., Whiteway, J., Wilquet, V., Wolff, M.J., Bellucci, G., Patel, M.R., López-Moreno, J.J., Forget, F., Wilson, C.F., Svedhem, H., Vago, J.L., and, D.R., 2019. Martian dust storm impact on atmospheric h2o and d/h observed by ExoMars trace gas orbiter. Nature 568, 521–525. doi:10.1038/s41586-019-1097-3.

Vandaele, A.C., , Lopez-Moreno, J.J., Patel, M.R., Bellucci, G., Daerden, F., Ristic, B., Robert, S., Thomas, I.R., Wilquet, V., Allen, M., Alonso-Rodrigo, G., Altieri, F., Aoki, S., Bolsée, D., Clancy, T., Cloutis, E., Depiesse, C., Drummond, R., Fedorova, A., Formisano, V., Funke, B., González-Galindo, F., Geminale, A., Gérard, J.C., Giuranna, M., Hetey, L., Ignatiev, N., Kaminski, J., Karatekin, O., Kasaba, Y., Leese, M., Lefèvre, F., Lewis, S.R., López-Puertas, M., López-Valverde, M., Mahieux, A., Mason, J., McConnell, J., Mumma, M., Neary, L., Neefs,

E., Renotte, E., Rodriguez-Gomez, J., Sindoni, G., Smith, M., Stiepen, A., Trokhimovsky, A., Auwera, J.V., Villanueva, G., Viscardy, S., Whiteway, J., Willame, Y., Wolff, M., 2018. NOMAD and an integrated suite of three spectrometers for the ExoMars trace gas mission: Technical description and science objectives and expected performance. Space Science Reviews 214. doi:10.1007/s11214-018-0517-2.

Vandaele, A.C., Mahieux, A., Robert, S., Berkenbosch, S., Clairquin, R., Drummond, R., Letocart, V., Neefs, E., Ristic, B., Wilquet, V., Colomer, F., Belyaev, D., Bertaux, J.L., 2013. Improved calibration of SOIR/venus express spectra. Optics Express 21, 21148. doi:10.1364/oe.21.021148.

Villanueva, G.L., Liuzzi, G., Crismani, M.M.J., Aoki, S., Vandaele, A.C., Daerden, F., Smith, M.D., Mumma, M.J., Knutsen, E.W., Neary, L., Viscardy, S., Thomas, I.R., Lopez-Valverde, M.A., Ristic, B., Patel, M.R., Holmes, J.A., Bellucci, G., and, J.J.L.M., 2021. Water heavily fractionated as it ascends on mars as revealed by ExoMars/NOMAD. Science Advances 7, eabc8843. doi:10.1126/sciadv.abc8843.

Zhu, C., Byrd, R.H., Lu, P., Nocedal, J., 1997. Algorithm 778: L-BFGS-b: Fortran subroutines for large-scale bound-constrained optimization. ACM Transactions on Mathematical Software 23, 550–560. doi:10.1145/279232.279236.

Chapter 9

CO_2 ice detection with NOMAD/LNO

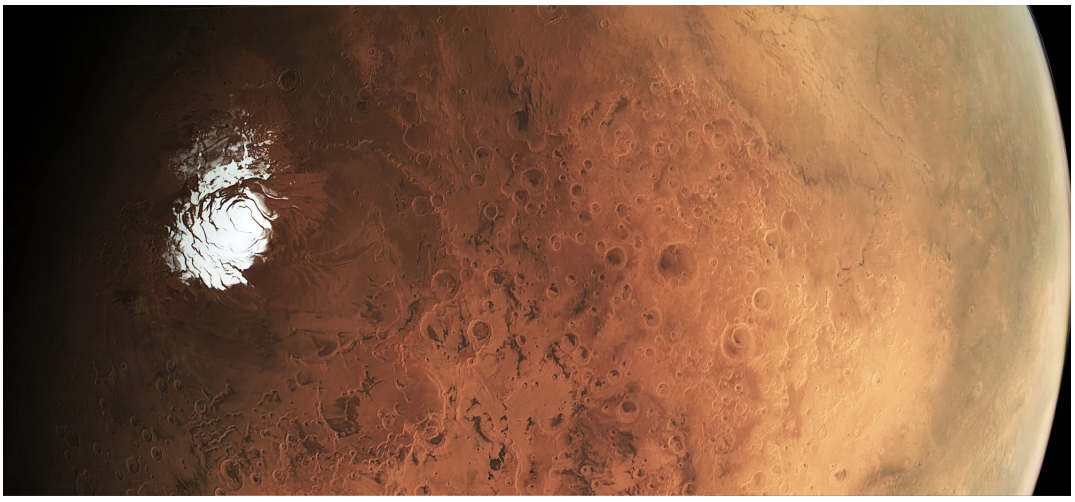

The residual south polar cap of Mars during local Summer. The cap is mostly made up of CO_2 ice and is not perfectly centered on the south pole. Credit: ESA/DLR/FU Berlin/CC BY-SA

This chapter presents an analysis of NOMAD/LNO data in order to detect spectroscopic signals associated with CO_2 ices on the surface. The aim is to demonstrate the possibility of using these data to undertake further microphysical characterization but also to understand the potential limits imposed by the instruments. During an orbit around Mars, the LNO channel only observes some parts of the total spectral range, called diffraction orders (see chapter 6). Thus, from one orbit to another the same orders are not necessarily observed. This implies that it is sometimes necessary to wait for a very long time before obtaining sufficient spatial and temporal coverage to carry out specific investigations. For instance, one might want to use data of the same geographical area at different time of the martian seasons, which is not necessarily possible during the same Martian year for a specific diffraction order. With the start of the mission in 2018 a very large number of nadir data are now usable and now make it possible to account for the ability of LNO to detect surface ice. We will begin by presenting the best diffraction orders for detecting surface ice from theoretical simulations (section 9.1). Then, the calibration steps allowing to transform the raw data to reflectance spectra and the comparison with an independent calibration method will be presented (section 9.2). Finally, we will show spectra and maps associated with the presence of CO_2 surface ice (section 9.3).

9.1 Selection of the best diffraction orders

The NOMAD/LNO channel is similar to the Solar Occultation channel and was therefore designed for observation of atmospheric absorption bands, often very narrow and numerous within the same order. Using this instrument to detect surface ice spectroscopic signal (whose wider absorption bands are sometimes spread over several orders) requires combining several criteria together.

Some of these criteria are related to instrumental calibration and the specific design of the instrument. For instance, the instrumental sensitivity is not constant through the whole spectral range and therefore some diffraction orders will have a very low signal-to-noise ratio (SNR) and therefore a signal coming from the surface will not be usable. Also, it has been shown during the calibration procedure that the first 50 spectels of the detector are very noisy and therefore cannot be used, this limits CO_2 ice detection to orders covering a single absorption band and that this one does not appear in the first 50 spectels. Additionally the use of an AOTF involves the risk that the signal from adjacent orders leaks onto the observed order. This artefact can artificially create a new ghost absorption band or reinforce artificially a pre-existing absorption band. Details about instrumental effects and sensitivities can be found in the previous chapter dedicated to the instrumental calibration.

Finally, an important consideration for observing the surface is to select orders little or not affected by atmospheric absorption from gases. Indeed, spectral ranges where the atmosphere absorbs a lot will greatly reduce the signal from the surface and requires a dedicated atmospheric correction. It is therefore preferable to avoid such a correction for a first analysis of the data by choosing orders with a high atmospheric transmittance.

Note that, even if all these criteria are met, it remains an important atmospheric contribution on Mars: aerosols. They play a major role in the martian atmosphere and it is not easy to correct them because it requires an accurate estimate of their quantities at the time of observation, which can be hard to retrieve. For the remainder of this analysis we will ignore this contribution as a first quicklook and we will come back to this during the outlook. From these considerations, three diffraction orders are distinguished for the study of CO_2 ice: orders 189, 193 and 194.

To estimate atmospheric contributions by gases we used the Planetary Spectrum Generator (PSG) tools (Villanueva et al., 2018) to simulate spectra at the LNO spectral resolution with the channel characteristics but without accounting for the AOTF and blazed grating effects (mostly implying no contribution from adjacent orders). We consider a vertical profile from the Mars Climate Database (MCD) and included the main chemical species present in the martian atmosphere: CO_2, N_2, O_2, CO, H_2O, O_3 and CH_4. Results are shown figs. 9.1, 9.2 and 9.3 (left). In all three cases, the atmosphere is almost fully transparent with only minor and small absorption bands dropping the transmittance to 20% at most for order 189 but only 0.4% and 1% for orders 193 and 194.

The surface reflectance of a CO_2 ice was estimated with a radiative transfer model (Andrieu et al., 2015) for all diffraction orders. The model is an adaptation of the Hapke model in which the surface is made of a CO_2 ice slab overcoming a semi-infinite granular medium representing the martian regolith. The model used the optical constants of the CO_2 ice (Quirico and Schmitt, 2018) and the martian dust empirically derived from observations made with the Compact Reconnaissance Imaging Spectrometer (CRISM) (Andrieu et al., 2018). Results are shown figs 9.1, 9.2 and 9.3 (right) for a CO_2 ice slab of varying thickness. The identified bands are the well-known 2.35 μm (4256 cm^{-1}) for order 189 and 2.29 μm (4363 cm^{-1}) for orders 193 and 194. The same band is observed for the last two orders as this wavenumbers are covered by both orders. So, contribution by adjacent orders may reinforce the strength of the band. A narrower bands is also expected in order 193 at 4347 cm^{-1} (2.3 μm) making this order very relevant for CO_2 ice detection. At these wavelengths, the CO_2 ice is usually very bright within the continuum, the reflectance mostly drops within the bands. The band depth increases with the increasing thickness of the slab. The very high resolution of LNO allows an order to fully resolves these narrow bands, so the reflectance of the continuum quickly drops too with the increasing thickness as the result of the widening of the band.

These 3 orders are the only one allowing a combination of a high sensitivity of the instrument at these wavelengths, an almost fully transparent atmosphere and a CO_2 ice absorption features. While the same band is observed twice in orders 193 and 194 we have to rule out order 194 because the band falls perfectly within the first 50 spectels of the detector, which have a very low SNR. The following will focus on the use of orders 189 and 193.

9.2 Validation of LNO reflectance spectra

This section will developed the stages of conversions from nadir raw data measured by LNO radiance and reflectance spectra. Examples adapted to orders 189 and 193 will serve as illustrations. These conversions are based on the calibration steps (see previous chapter for a more detailed description) that have been developed in this study. Currently, two complementary calibration methods exist for the LNO channel, based on different assumptions and approaches.

The first one was proposed by (Thomas et al., 2022) is based on direct calibration of nadir data from multiple solar observations by LNO assuming a temporal stability of the instrument. The instrumental effects related to the combination of the AOTF and the grating and producing complex shapes in the continuum of a LNO spectrum were associated to temperature variations within the detector. As multiple solar observations at different temperature exist, an interpolation between these different spectra as a function of temperature is used to directly calibrate a nadir observation. The strength of this approach is that it offers a realistic view of the data without erasing any existing features (such as surface contribution) and uses data to calibrate data. The weaknesses are that it relies on a strong assumption of the temporal stability of the instrument, but also consider that all instrumental effects are related to temperature. If other of these effects occur they are not taken into account, possibly producing bias in the continuum of a spectrum. This calibration will be named the 'BIRA' method.

The second approach proposed by (Cruz-Mermy et al., 2022) uses theoretical considerations (see chapter 8). It combines a synthetic solar spectrum made at the spectral resolution of LNO (see chapter 7) with a model simulating the instrumental effects of the AOTF and grating to properly account for the contribution of adjacent orders. The final spectra are corrected for the continuum to remove the remaining instrumental effects poorly constrained. An inversion procedure of this model using a gradient-descend minimization approach allowed to fully reconstruct the instrumental parameters (AOTF) and effects such as the pixel shifts as a function of temperature and the spectral resolution of each orders. An estimate of the instrumental sensitivity shows a strong correlation with temperature. Correcting for this effect revealed that the instrumental is stable through time, thus validating the BIRA method (Thomas et al., 2022). The strength of this approach holds in an estimation of the instrumental effects and the possibility of detecting future variations of the instrumental sensitivity. Furthermore, the continuum correction guarantees a realistic estimate of the radiometric level and allows a clear identification of narrow absorp-

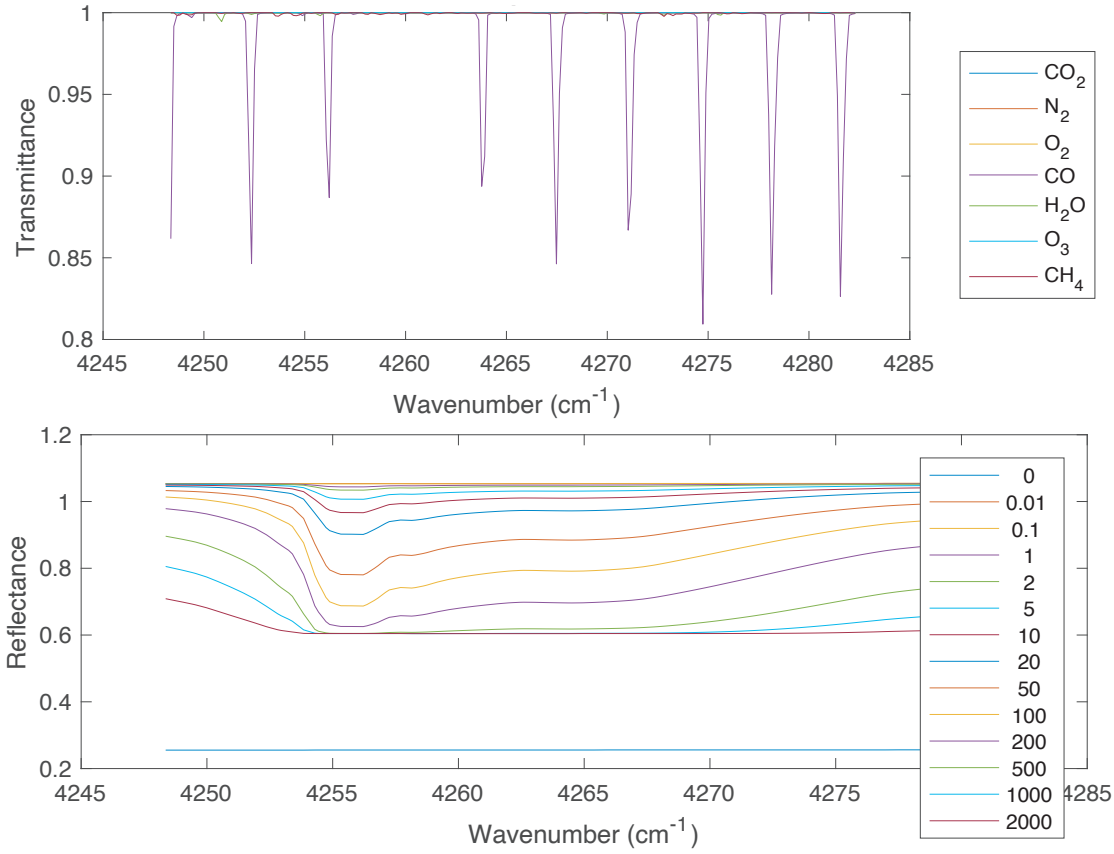

Figure 9.1: Theoretical simulations of order 189. (top):Transmittance spectra of the martian atmosphere derived from PSG (Villanueva et al., 2018) using the LNO channel characteristics and the vertical profile from the Mars Climate Database. The atmosphere is mostly transparent at this spectral range as there is only small CO bands dropping transmittance by 20% at most. There are windows in which no absorption are expected so most of the signal would come from the surface and the aerosols. (bottom): Direct model simulation (Andrieu et al., 2015): reflectance of a CO_2 ice slab as a function of the thickness. One can see major absorption features dropping the reflectance in both orders with the band being centered around 4256 cm^{-1}.

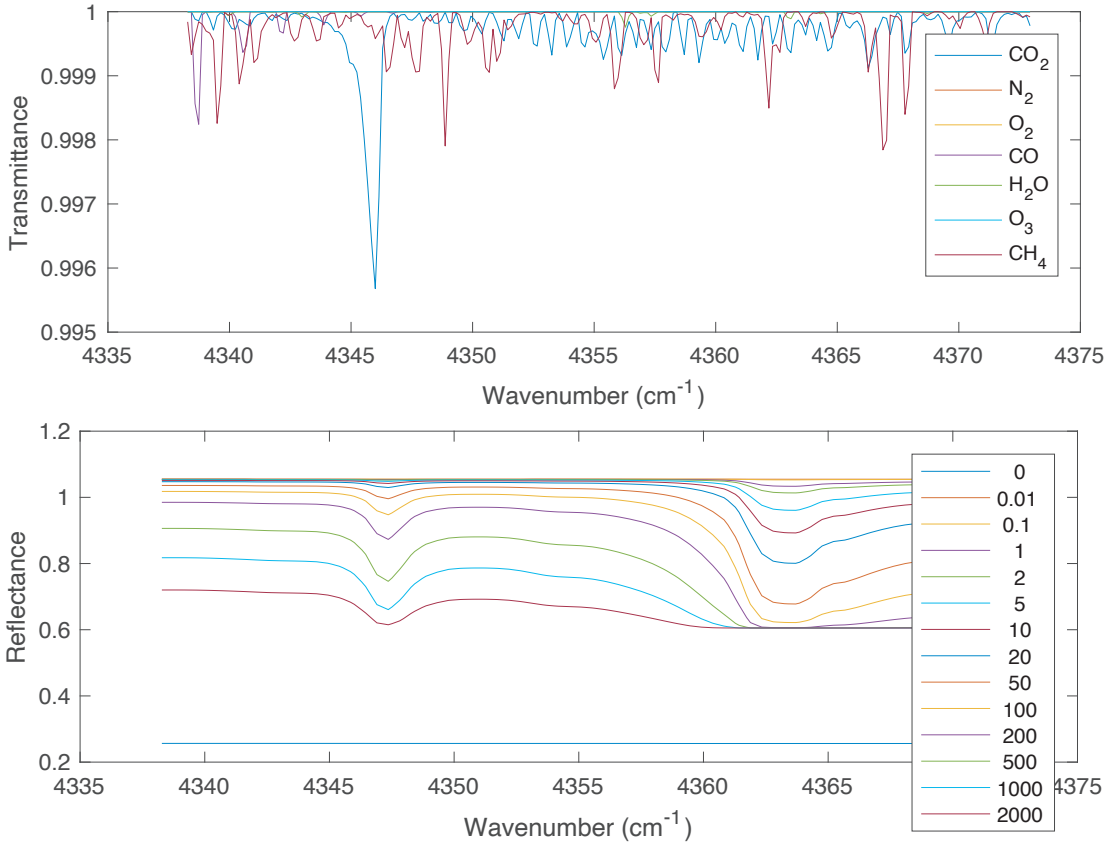

Figure 9.2: Theoretical simulations of order 193. (top):Transmittance spectra of the martian atmosphere derived from PSG (Villanueva et al., 2018) using the LNO channel characteristics and the vertical profile from the Mars Climate Database. The atmosphere is mostly transparent at this spectral range with only few absorption bands dropping the transmittance to 0.04% at most. There are windows in which no absorption are expected so most of the signal would come from the surface and the aerosols. (bottom): Direct model simulation (Andrieu et al., 2015): reflectance of a CO_2 ice slab as a function of the thickness. One can see major absorption features dropping the reflectance in both orders with the band being centered around 4363 cm^{-1}.

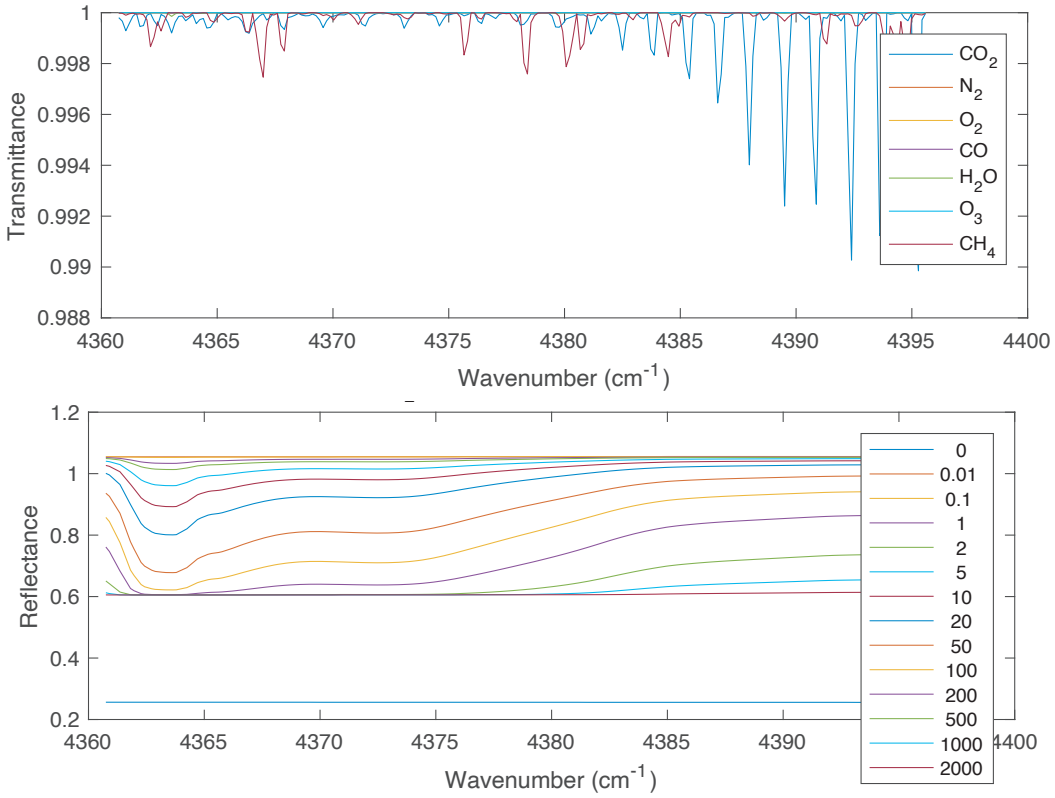

Figure 9.3: Theoretical simulations of order 194. (top):Transmittance spectra of the martian atmosphere derived from PSG (Villanueva et al., 2018) using the LNO channel characteristics and the vertical profile from the Mars Climate Database. The atmosphere is mostly transparent at this spectral range with only few absorption bands dropping the transmittance to 1% at most. (bottom): Direct model simulation (Andrieu et al., 2015): reflectance of a CO_2 ice slab as a function of the thickness. One can see major absorption features dropping the reflectance with the band being centered around 4363 cm^{-1}. It is the same band than order 193 but located on the left side of the spectra.

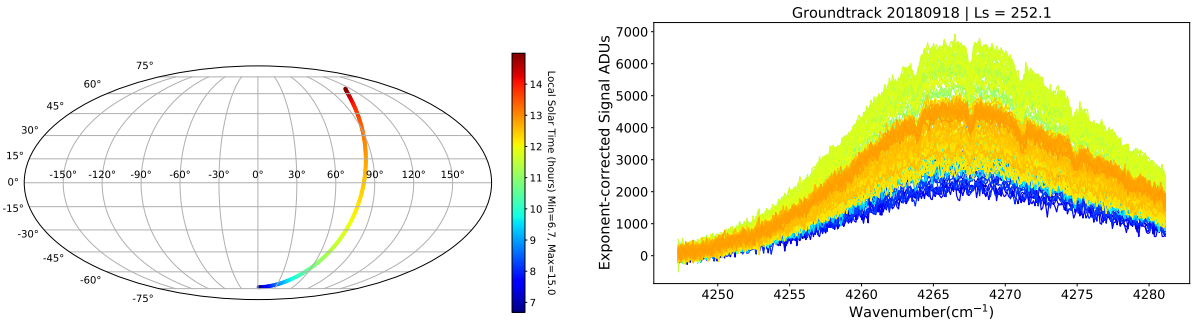

Figure 9.4: Order 189 : ground-track of the observation 20180907_143527_1p0a_LNO_1_DP_189 on a Mollweide projection (left) and raw data S_{ADU} (right). The color refers to the Local Solar Time (see colorbar). The characteristic bell-shape of a NOMAD raw spectrum is clearly visible as the ADU goes up to reach a maximum between wavenumbers 4265 cm^{-1} and 4270 cm^{-1}. The ADU also increase with the Local Solar Time (LST), reaching its maximum for LST = 12 which corresponds to midday (highest solar elevation) then gradually decreases. The atmospheric lines (CO lines) are also clearly appearing, specially when the ADU is maximal.

tion bands, which is well suited for atmospheric retrievals. In contrast, the weak points are that such approach is SNR dependent as orders with very low sensitivities are poorly reconstructed, which leads to a poor estimation of instrumental parameters. Moreover, the continuum correction steps take the risk of erasing large scale spectral features such as a slope in the continuum or a large absorption bands, making the BIRA method more suited to surface studies. This approach will be referred as the 'GEOPS' method.

The conversion from digital numbers recorded by LNO to reflectance will be cover using the GEOPS method. A comparison between the two methods will be made to highlight the cross compatibility of these approaches.

9.2.1 Raw data

Raw data are spectra transmitted to Earth after dark subtraction. They are expressed in Analog to Digital Unit (ADU) hereafter.

9.2.1.1 Order 189

There are 1,668 orbits of order 189 between 2018/03/29 and 2022/08/07, i.e.: $L_S = 150$ (end of Northern hemisphere Summer) of Mars Year 34 (MY34) to $L_S = 280$ (end of Northern hemisphere Winter) of Mars Year 36 (MY36). This accounts for a total of 3,336,000 spectra covering the latitude range of $-76.4°$S to 76.2°N. A typical example of spectra recorded during one orbit is shown figure 9.4 (ground-track of 2018/09/07 from observation 20180907_143527_1p0a_LNO_1_DP_189).

9.2.1.2 Order 193

Observation of order 193 started on 2019/11/04 and there are 560 orbits recorded until 2022/08/02. The observation begin with $L_S = 101$ of MY35 (Northern Hemisphere summer) and reach $L_S = 277$ of MY36 (Northern Hemisphere winter) which account for an amount of 1,012,000 spectra covering the latitude range of $-76.7°$S to 76.3°N. An example of a ground-track and the associated spectra recorder is shown figure 9.5 (ground-track of 2020/05/08 from observation 20200508_204800_1p0a_LNO_1_DF_193).

9.2.2 Conversion to spectral radiance

The normalization procedure is applied on all available spectra of order 189 and 193. The raw data units S_{ADU} represents the signal − dark as a result of onboard acquisition. Raw data units S_{ADU} needs to be

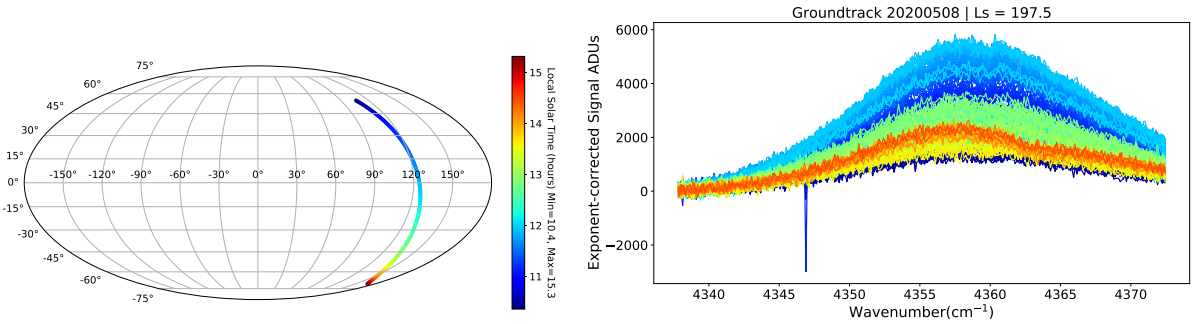

Figure 9.5: Order 193 : ground-track of the orbit 2020/05/08 (observation 20200508_204800_1p0a_LNO_1_DF_193) on a Mollweide projection (left) and raw data S_{ADU} (right). The color refers to the Local Solar Time (see colorbar). The characteristic bell-shape of a NOMAD raw spectrum is clearly visible as the ADU goes up to reach a maximum between wavenumbers 4355 cm^{-1} and 4363 cm^{-1}. The ADU also increases with the Local Solar Time (LST), reaching its maximum for LST = 12 which corresponds to midday (highest solar elevation) then gradually decreases. One cannot observe nearly any atmospheric line in this order, as expected.

treated to account for observation parameters such as :

- the binning (*Bins*) account for the number of illuminated rows during the observation, this number is constant for the LNO channel and we consider $Bins = 223 - 80 = 143$ with 80 and 223 being respectively the first and last detector's rows illuminated.
- the number of accumulation of recorded spectra (*NOA*). During an acquisition sequence, both light and dark frame are recorded and the subtraction is performed onboard. Only this difference is downloaded on Earth in S_{ADU}. Please note that in the BIRA procedure one single sequence of both light and frame measurement is considered with NOA=1, while in GEOPS the NOA=2. Thus, there is a factor 2 in S_{norm} and $Responsivity$ between GEOPS and BIRA's approaches. This difference by a factor of 2 is canceled-out when tacking into account the responsivity (Eq. 9.5).
- the integration time (Int_{time}). The time of an acquisition sequence in ms.
- the spectral resolution ($Spec_{res}$). The average spectral resolution of a spectel in the considered order in cm^{-1}. Please note that the $Responsivity$ must be computed with the same $Spec_{res}$. Exactly as the factor of 2 in NOA, $Spec_{res}$ factor cancels out when the data is calibrated (Eq. 9.5).

The normalize raw data unit S_{norm} is computed with the following equation:

$$S_{norm} = \frac{S_{ADU}}{(Bins \times NOA \times Int_{time} \times Spec_{res})} \tag{9.1}$$

From one orbit to another, the NOA varies between 8 and 28, the integration time Int_{time} between 195 ms and 220 ms and the spectral resolution is mostly constant with a mean value at 0.2508 cm^{-1} for order 189 and 0.2562 cm^{-1} for order 193. An example of normalized spectra is shown figure 9.6 for both orders (same orbit as for figure 9.4 and 9.5).

Raw data are converted to spectral radiance using the radiometric calibration factor estimated during the calibration procedure (Cruz-Mermy et al., 2022). We first used a continuum removal to correct for the bell shape. This step is not necessary in principle when the blaze function is well known. We find that for LNO, the discrepancies between ideal blaze function and real one are too different. Instead, we propose a purely empirical approach of continuum removal. This differs from the BIRA's approach.

We use the Asymmetric Least Squares smoothing algorithm (Eilers et al., 2005) for the continuum estimation $\mathscr{C}$ in order to estimate the baseline spectra with the following parameters : smoothness $\lambda = 1.10^3$, asymmetry $p = 0.9$ and 10 iterations.

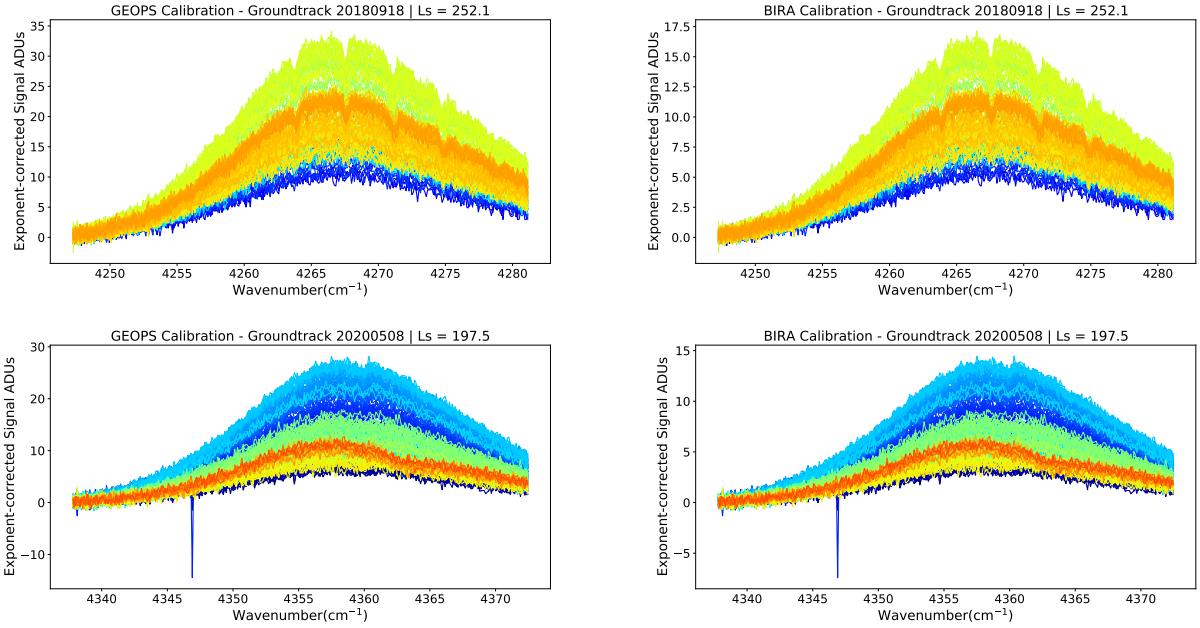

Figure 9.6: Normalized raw data S_{norm} for order 189 (top, ground-track of 2018/09/07) and 193 (bottom, ground-track of 2020/05/08) : comparison between GEOPS (left) and BIRA (without tacking into account the spectral resolution) (right) calibration procedure (see raw data figure 9.4 and 9.5). There is a factor of $2 \times Spec_{res} \approx 0.5$ between the two normalization as expected. This factor will be canceled out when applying the radiometric calibration. Except this factor, the spectra are very similar.

$$S_{baseline} = \mathscr{C}\left(S_{norm}\right) \tag{9.2}$$

The flatten spectra is computed by:

$$S'_{flat} = \frac{S_{norm}}{S_{baseline}} \tag{9.3}$$

The level of the initial spectra S_{norm} is kept by:

$$S_{flat} = S'_{flat} \times \overline{S_{baseline}} \tag{9.4}$$

With $\overline{S_{baseline}}$ denoting the average level of the baseline.

This operation is similar to the baseline removal applied on solar calibration measurements (Cruz-Mermy et al., 2022). An example of the spectra obtained after the continuum removal procedure is shown in figure 9.7 (left).

From then, the radiometric calibration factor (*Responsivity*), estimated by our calibration procedure from solar measurements, is applied to all spectra to get the spectral radiance (in $\mathrm{W/m^2/cm^{-1}/sr^{-1}}$):

$$S_{rad} = S_{flat} \times Responsivity \tag{9.5}$$

With *Responsivity* in $\frac{\mathrm{W.cm^2.cm^{-1}.sr^{-1}}}{\mathrm{ADU}}$. It is important to note that *Responsivity* was estimate from several solar calibration measurements by LNO at different time of the mission (see chapter 8). This allowed us to express the *Responsivity* as a function of temperature and calibrate a nadir based on the sensor temperatures, using the appropriate factor. An example of radiance spectra are shown figure 9.7 (right).

The final step is to account for the solar incident angle α across the ground-track to correct for the geometry of the observation and estimate the true radiance of the spectra:

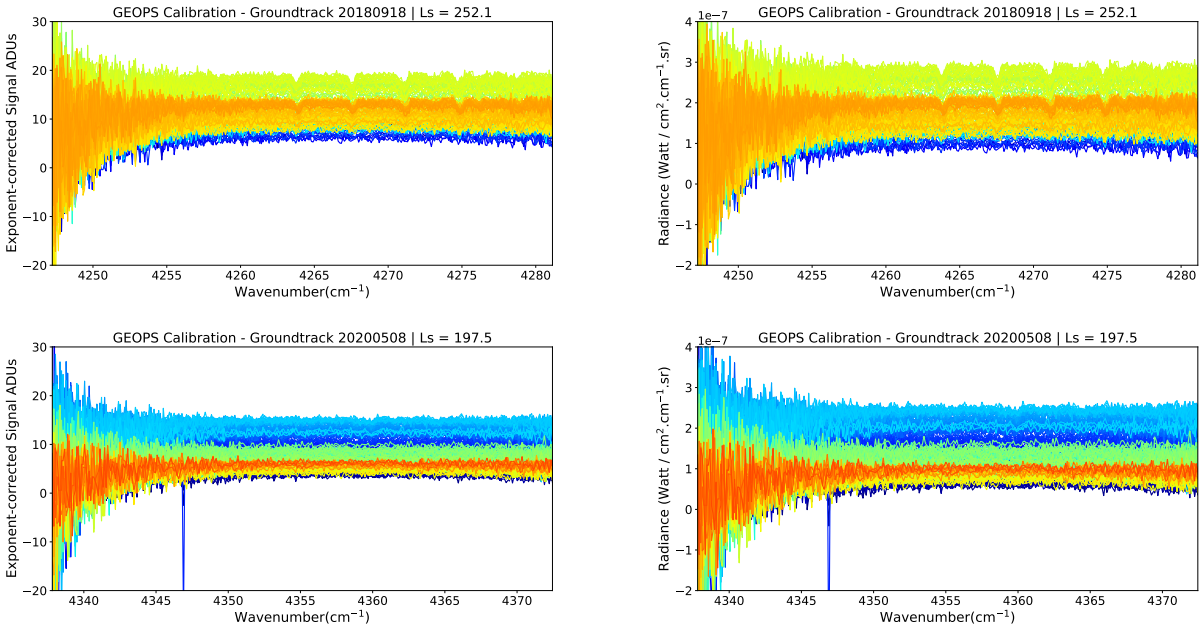

Figure 9.7: Calibration procedure : normalized spectra after the continuum removal operation (left) and conversion to spectral radiance (right) using the radiometric calibration factor determined by solar calibration measurements for order 189 (top) and 193 (bottom). One can see negative values on the left side (the first 50 spectels) of the detector related to very low signal due to the bell-shape imposed by the blaze function and thus negative dark subtraction. Despite the first 50 spectels the continuum is flat and the atmospheric lines are still well defined when present (order 189). The maximum radiance corresponds to spectra taken at LST close to midday, which is consistent with the raw data. The order of magnitude of the spectral radiance (~ 10^{-7} W/m^2/cm^{-1}/sr^{-1}) is also consistent with what was expected by the theoretical calculations of the spectral radiance reaching Mars.

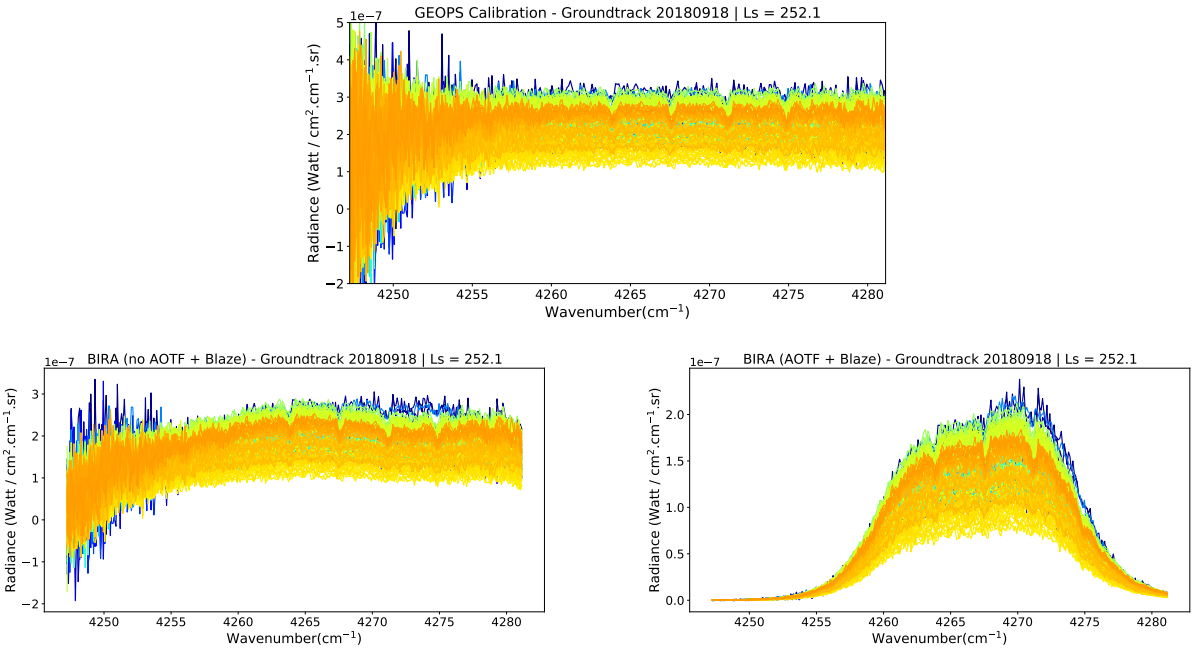

Figure 9.8: Radiance spectra of order 189 for the 2018/09/07 orbit after correcting for the cosine of the incident angle. Top : GEOPS calibration procedure. Bottom : BIRA's calibration. (Bottom left) Radiance calibrated from laboratory blackbody measurements without using the AOTF or the blaze function. The counts-to-radiance conversion is derived from a Planck function at the temperature of the blackbody and wavenumber of the pixel. One can see variations of the continuum that are not realistic but the order of magnitude of the radiance is consistent with the GEOPS radiometric calibration with values around 2×10^{-7} W/m^2/cm^{-1}/sr^{-1}. (Bottom right) Radiance calculated from laboratory blackbody measurements, which uses the AOTF and blaze functions to calculate the full radiance hitting each pixel to derive the counts-to-radiance conversion. One can see the overall shape similar to the raw data with the edges of the spectra having very low radiance values. The maximum radiance is reached on the center of the detector with values around 2×10^{-7} W/m^2/cm^{-1}/sr^{-1}. The radiance spectra estimated with the GEOPS method has higher radiance values and this can be related to a difference between the Sun's temperature during solar calibration measurements and the temperature of the blackbody used at BIRA.

$$S_{final} = \frac{S_{rad}}{\cos(\alpha)} \tag{9.6}$$

Figure 9.8 shows example of a fully radiance calibrated spectra and a comparison with calibrated radiance spectra coming from BIRA's calibration method.

9.2.3 Conversion to reflectance

With calibrated radiance data, one would estimate the reflectance R (free of atmospheric corrections) to check the consistency of the calibrations between BIRA and GEOPS. The reflectance is estimated following equation 9.7 by dividing S_{final} the measured spectral radiance corrected for the cosine of the incident angle by F the spectral irradiance of the Sun reaching Mars corrected for the Mars-Sun distance at the time of the observation:.

$$R = \pi . \frac{I}{F} = \pi . \frac{S_{final}}{F} \tag{9.7}$$

Where S_{final} is the spectral radiance in W/m^2/cm^{-1}/sr^{-1} and F the spectral irradiance in W/m^2/cm^{-1}, so the reflectance R is actually in sr^{-1} unit. Reflectance is calculated on the 320 spectels (wavenumbers)

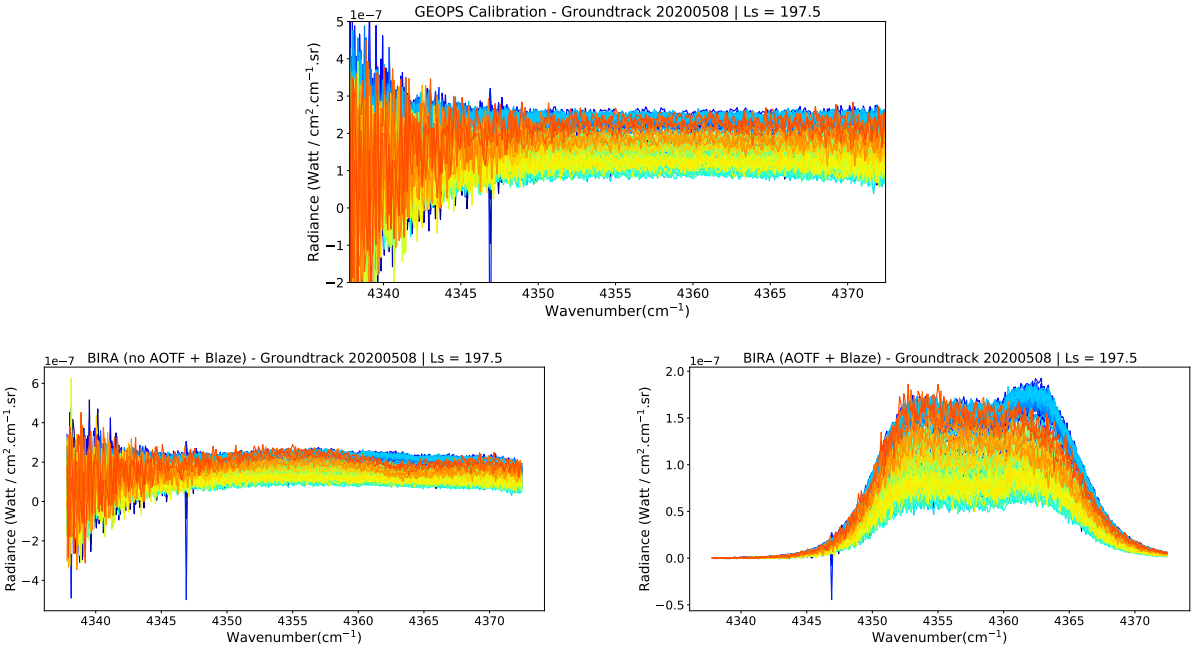

Figure 9.9: Radiance spectra of order 193 for the 2020/05/08 orbit after correcting for the cosine of the incident angle. Top : GEOPS calibration procedure. Bottom : BIRA's calibration. (Bottom left) Radiance calibrated from laboratory blackbody measurements without using the AOTF or the blaze function. The counts-to-radiance conversion is derived from a Planck function at the temperature of the blackbody and wavenumber of the pixel. One can see variations of the continuum that are not realistic but the order of magnitude of the radiance is consistent with the GEOPS radiometric calibration with values around 2×10^{-7} W/m^2/cm^{-1}/sr^{-1}. (Bottom right) Radiance calculated from laboratory blackbody measurements, which uses the AOTF and blaze functions to calculate the full radiance hitting each pixel to derive the counts-to-radiance conversion. One can see the overall shape is similar to the raw data with the edges of the spectra having very low radiance values. The maximum radiance is reach on the center of the detector with values between 1×10^{-7} and 2×10^{-7} W/m^2/cm^{-1}/sr^{-1}. The radiance spectra estimated with the GEOPS method has higher radiance values and this can be related to a difference between the Sun's temperature during solar calibration measurements and the temperature of the blackbody used at BIRA.

of each spectra of all orbits.

9.2.4 Comparison with BIRA

To provide an interesting validation, we compared our product with the NOMAD data calibrated at BIRA. Figures 9.10 shows such comparison for all reflectance spectra at one particular wavenumber of order 189 and 193 while figure 9.11 shows the comparison on the scale of few spectra, over the entire spectral range of the order.

Overall, the comparison rises the following points:

- BIRA and GEOPS calibration are consistent at first order. There is only 2% departure between both calibration approaches for order 189, which is reduced to 1% for order 193.
- The BIRA's calibration of order 189 and 193 seems to be affected by a significant continuum effect, most probably coming from a blaze function discrepancy between expected and real one, this is clearly evidenced fig. 9.11 showing 10 spectra of the same orbit calibrated with both methods for the two orders. In both cases spectra were taken at latitudes close to equatorial at noon local solar time (LST), areas in which no CO_2 ice should not be present. This feature must be related to an instrumental effect not properly accounted in the BIRA's method. This is all the more certain because the deflections take place at the same spectels position (120 to 320) in both orders. It also seems to affect the continuum level as it appears slightly lower in BIRA's method on the whole spectral range in both orders.
- The GEOPS' method is not affected, by construction, by this continuum effect. The negative side of this purely ab initio approach is that is may cancel out large scale absorption features as clearly evidenced with order 193 (fig. 9.9, bottom left) in which a deflection feature appears in some spectra from BIRA's calibration (in orange) corresponding to a potential signature of CO_2 ice as the color corresponds to the observation of high latitudes of the southern hemisphere during local spring (see fig. 9.5, left). Such feature is initially present in raw data (fig. 9.5, right) but erased by the continuum correction step of the GEOPS method (fig. 9.7, bottom). Note that the instrumental effects in BIRA's approach evidenced in fig. 9.11 can strengthen the expected CO_2 ice band if located at the same wavenumbers.

9.2.5 Comparison with TES

To compare our results with a reference albedo map of Mars, we selected the MGS TES Global Bolometric Albedo map (Christensen et al., 2001) that uses the VISIR channel data (visible/near-IR from 0.3 to 2.9 μm) reduced to Lambert albedo and gridded at 8 pixels/degree (see figure 9.12). This map represents the surface reflectance corrected from the atmosphere (gas and aerosols) and seasonal deposits.

As the NOMAD data are not corrected for the atmospheric contributions, we expect higher reflectance values than TES because at the wavenumbers of orders 189 and 193 the atmosphere is mostly non absorbing but diffusing (see figs 9.4 and 9.5).

The theoretical effect of aerosols contribution will be estimated in section 9.2.5.2 whereas the next section will be dedicated to the TES vs NOMAD/LNO (using our GEOPS' calibration) comparison.

9.2.5.1 Surface maps

Only the aerosols scattering should increase the reflectance top-of-atmosphere. However, the large-scale variations should be reproduced and we expect a high positive correlation between the maps. In this section we will compare the resulting surface maps.

Order 189 corresponds to the spectral range 4247 - 4281 cm^{-1} (2.335 - 2.354 μm). We estimate the reflectance at wavenumbers in which there is no absorption features to ensure that most of the signal comes from the surface and the aerosols scattering. Figure 9.13 shows the results of the reflectance we

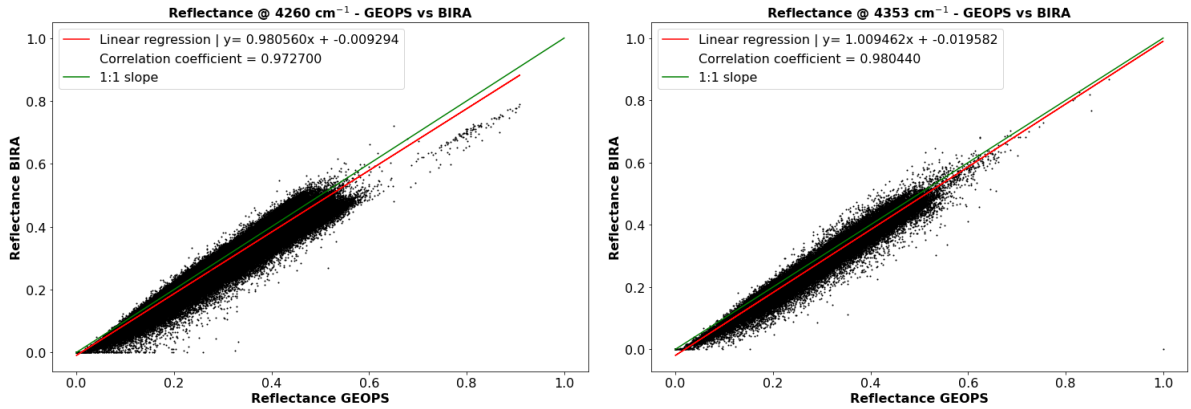

Figure 9.10: Scatter plot between the reflectance from the GEOPS calibration method against the reflectance from BIRA's calibration method. The linear regression is shown in red and the 1/1 correlation slope in green. (Left) order 189 at 4260 cm^{-1}, the correlation is positive with an excellent correlation coefficient of 0.97, the BIRA reflectance is 0.98 time lower than GEOPS following the slope of the linear regression. (Right) order 193 at 4353 cm^{-1}, the positive correlation coefficient (0.98) indicates an excellent correlation between the two datasets than for order 189. The BIRA reflectance is 1.001 time higher than GEOPS. Overall there is a very good agreement between BIRA and GEOPS on both orders, which reflect a consistent calibration.

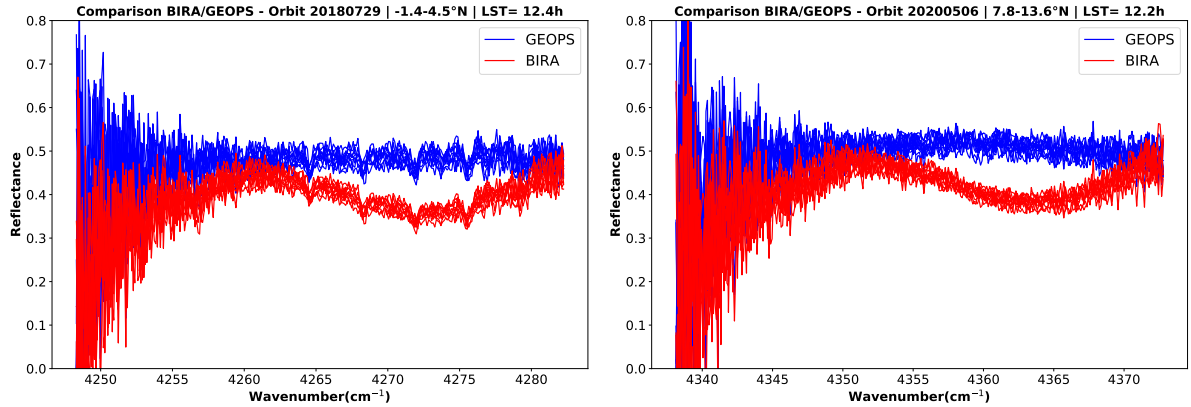

Figure 9.11: Reflectance estimated from BIRA (red) and from GEOPS (blue) on the whole spectral range of order 189 (left) and 193 (right). In both case there is a good agreement between the two on the major part of the spectra but there is a deflection in the BIRA's continuum occurring on the same spectel range (120-320) for both orders while the continuum of GEOPS is flat on the whole spectral range. Those variances are most probably due to a misestimation of the blaze function in the BIRA's approach.

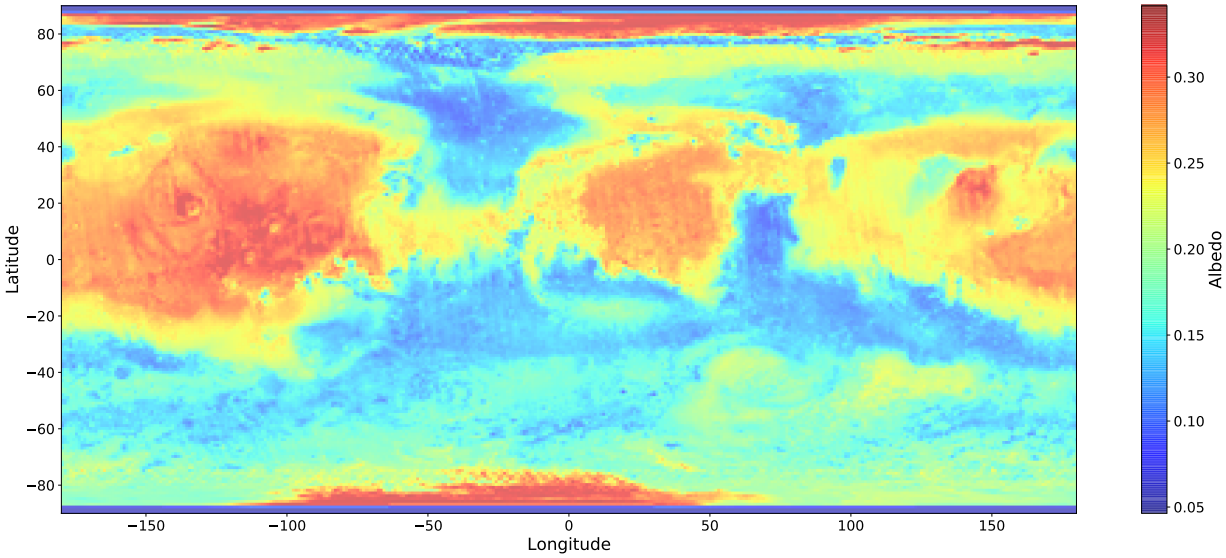

Figure 9.12: MGS TES Global Bolometric Albedo map reduced to Lambert albedo, in the broadband 3448-33330 cm^{-1} (0.3 to 2.9 μm) gridded at 8 pixels/degree. Pixel resolution is 7,410 meters per pixel (m) minimum at the equator(Christensen et al., 2001).

estimate at 4260 cm^{-1}. Since there are latitude/longitude pairs observed multiple times, we estimate the mean reflectance within a square of 1° longitude by 1° latitude. The overall reflectance we estimate is higher than TES but the large scale variations are well reproduced. The latitude/solar longitude map (see figure 9.14) corrected from the seasonal effect, showing higher reflectance during local spring (southern hemisphere) and autumn (northern hemisphere). The maximal extent of the polar cap is visible as the reflectance takes higher values up to latitude of -60°S at $L_S = 200$. To compute the correlation between the two dataset, we remove NOMAD data below -60° South latitude to avoid seasonal effects such as the extension of the polar cap during winter, that would increase the reflectance. Looking at the scatter plot (figure 9.20) one can see that there is a strong correlation between NOMAD and TES (correlation coefficient at 0.83) but the reflectance of NOMAD is about 1.46 time higher than TES. Since there is no correction for the aerosols scattering in the NOMAD data, we expect the reflectance to be higher.

Order 193 represents the 4337 - 4372 cm^{-1} (2.287 - 2.305 μm) spectral range. The reflectance is estimated on all the spectral range but the reflectance map generated (see figure 9.15) is at wavenumber 4354 cm^{-1} at which there is almost no absorption from the atmosphere, so the signal comes from the aerosol scattering and the surface. The map is at spatial resolution of 1° per pixel, in the same way as for order 189. Since there are multiple latitude/longitude coordinates observed several times we take the mean of all reflectance at the coordinate. Again the reflectance is higher than the TES albedo, mostly due to aerosols scattering. The large scale variations are consistent with TES : the northern mid-latitude having higher albedo than the southern mid-latitude and both polar regions display higher albedo. Seasonal deposits effects are not corrected which explains some differences at high latitude. When looking at the reflectance on a latitude/solar longitude map (see figure 9.16) , one can see that high latitudes reflectances are more consistent, being higher during the southern hemisphere spring ($L_S = 200$) which corresponds the maximal extent of the south polar cap. The correlation between TES and GEOPS reflectance (see figure 9.21) is positive with a correlation coefficient of 0.84. The slope of the linear regression shows that GEOPS albedo is 1.6 higher than TES so the positive correlation is more representative of good agreement in large scale variation.

9.2.5.2 Theoretical effect of aerosols contribution

Radiative transfer models can be used to compute the reflectance top-of-atmosphere (TOA), knowing the surface and atmospheric properties. The discrete ordinate method DISORT (Stamnes et al., 1988)

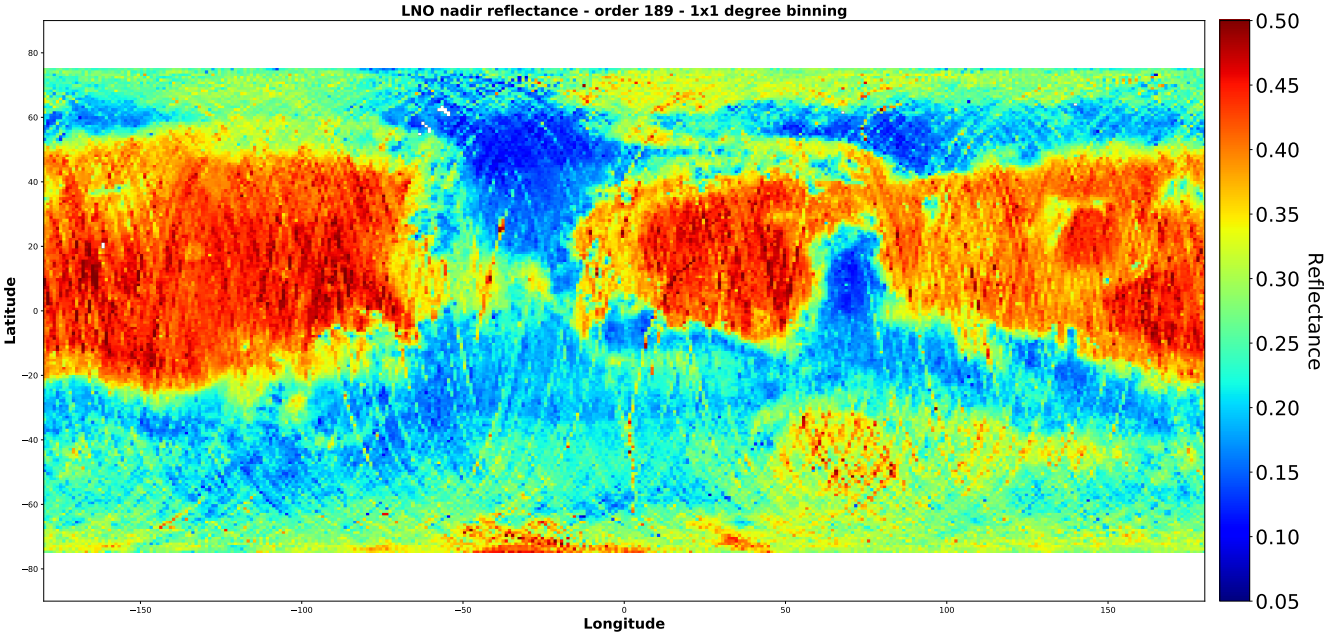

Figure 9.13: Latitude/Longitude reflectance map of order 189 at 4260 cm^{-1}, without atmospheric corrections. One can see that large scale variation are coherent with TES (Fig. 9.12): higher reflectance values in the northern mid-latitude than the southern, except for Hellas Basin in which the reflectance is high. The high latitude reflectance seems to be higher than expected in several places but this is mostly related to the aerosol scattering. Locally it can also be related to seasonal effect such as the extension of the polar caps during the winter, increasing the reflectance.

(see sec. 1.2.2) was used in various modelization of the radiative transfer in the martian atmosphere. The SHDOM code (Evans, 1998) is also a widely used model but it has been shown that Monte-Carlo methods are faster and more accurate for simulation in which there are few modelled radiative quantities. Finally, Monte-Carlo approaches are also possible (Vincendon et al., 2007) in various geometries but at a high computational cost. In the following, we will use the DISORT model to estimate the effects of the aerosols on a reflectance spectrum measured top-of-atmosphere .

Aerosols optical properties The main approach to characterize the aerosols properties is to combine different acquisition to create a typical martian emission phase function (reflectance as a function of emission angle). Then an analysis using a radiative transfer model (tacking into account single and multiple scattering) allows to retrieve scattering properties of aerosols and surface albedos. This approach has been proposed for IRTM (Clancy and Lee, 1991), TES (Clancy, 2003), OMEGA (Vincendon et al., 2007) or CRISM (Wolff et al., 2009). Another approach was made by considering only the aerosol single scattering albedo and not the absorption (Erard et al., 1994) but this way is mainly valid for "low integrated optical thicknesses from the Sun to the surface, then to the instrument" (Vincendon et al., 2007). (Vincendon et al., 2007) proposed a parametrization of the aerosols using single scattering albedo and optical thickness as a function of wavelength. In the following, we will use and describe this model.

Aerosols Parametrization In 2007, *Vincendon et al* (Vincendon et al., 2007) reported an approach to recover surface reflectance spectra and evaluate the optical depth of aerosols in the near-IR. They used their own radiative transfer model based on a Monte Carlo approach (Vincendon et al., 2007). The choice of the approach is justified as they considered few inputs and the surface since no atmospheric layers are considered here. The main parameters are :

- the optical depth τ at normal incidence,

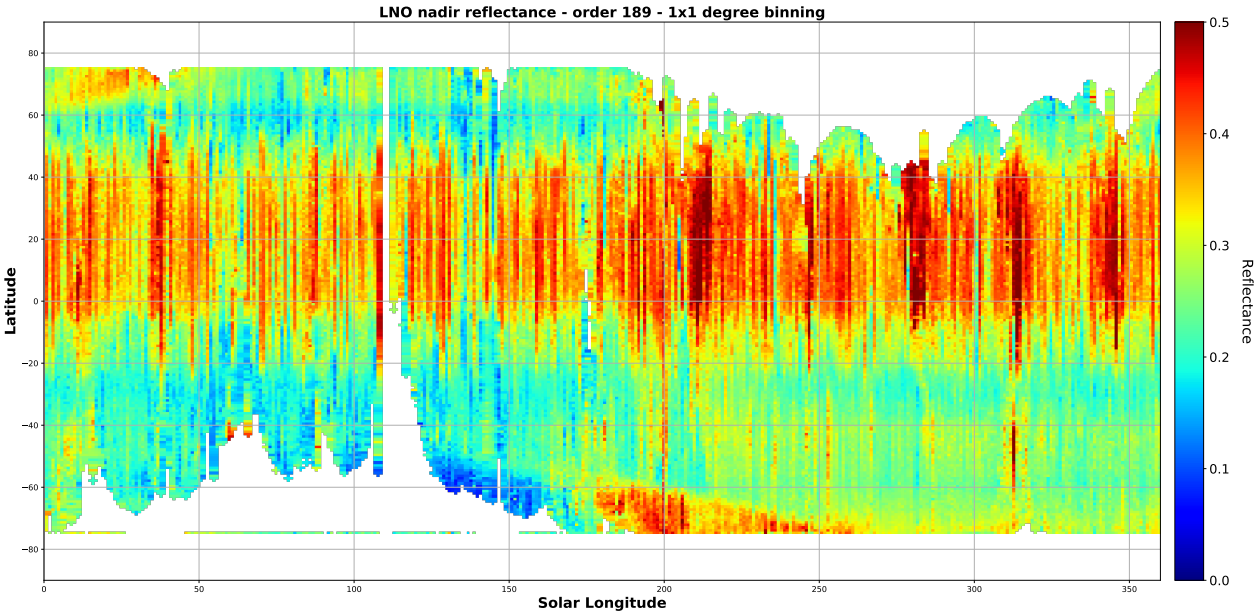

Figure 9.14: Latitude/Solar Longitude reflectance map of order 189 at 4260 cm^{-1}, without atmospheric corrections. Each points represent a square of 1° of latitude by 1° of solar longitude and the reflectance is estimated by taking the mean of all reflectance values that fall within each box. One can see that northern mid-latitude values are always higher which is consistent with the latitude/longitude map (see figure 9.13). The solar longitude expresses the seasonal variation. It starts at $L_s = 0$ (Northern spring equinox, Southern autumn equinox) so the southern latitudes are not covered by NOMAD as the signal from the permanently shadowed surface is too weak. When the southern spring start ($L_s = 150$), the southern hemisphere is more and more illuminated by the Sun so the ground-track coverage shift from North to South and one can see the reflectance increases in the southern high latitude which may corresponds to the southern polar cap which reaches it's maximum around $L_S = 200$ then slowly decreases. During this time, the northern hemisphere is not covered by NOMAD as it is local winter. Higher reflectance values are also observed in the southern mid-latitude (-40°S to -60°S) which is consistent with the latitude/longitude reflectance map.

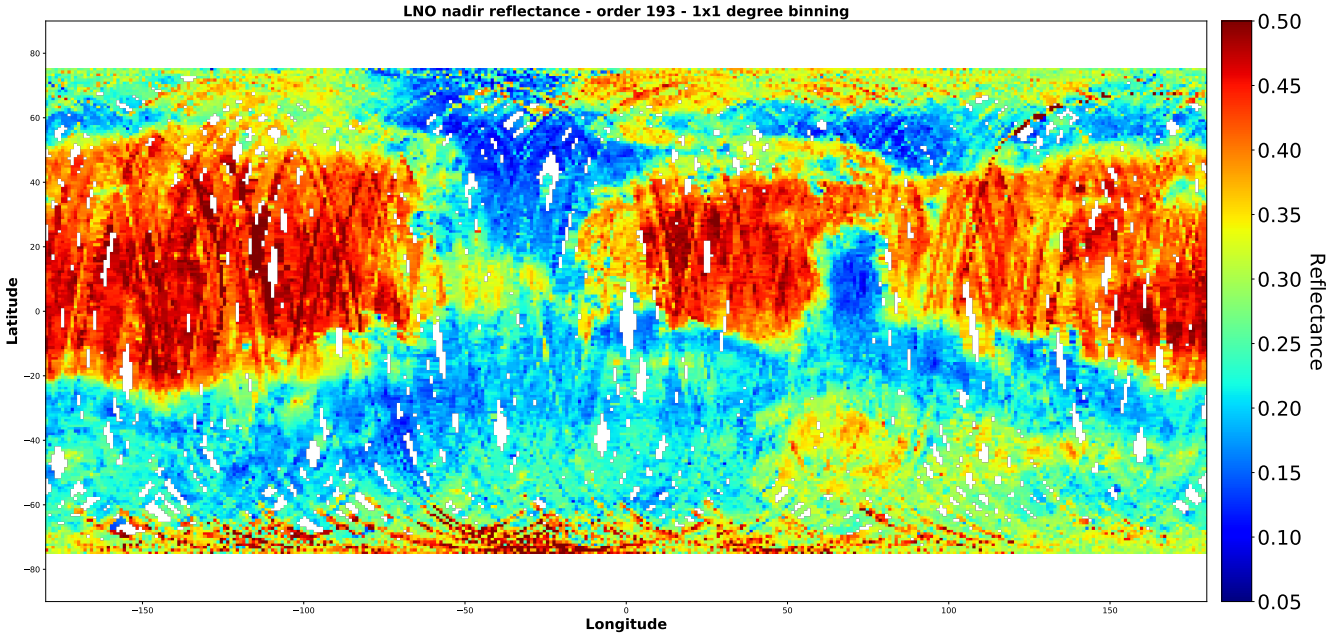

Figure 9.15: Latitude/Longitude reflectance map of order 193 at 4354 cm^{-1} based on equation 9.7, without atmospheric corrections. Same as Fig. 9.15 but for order 193..

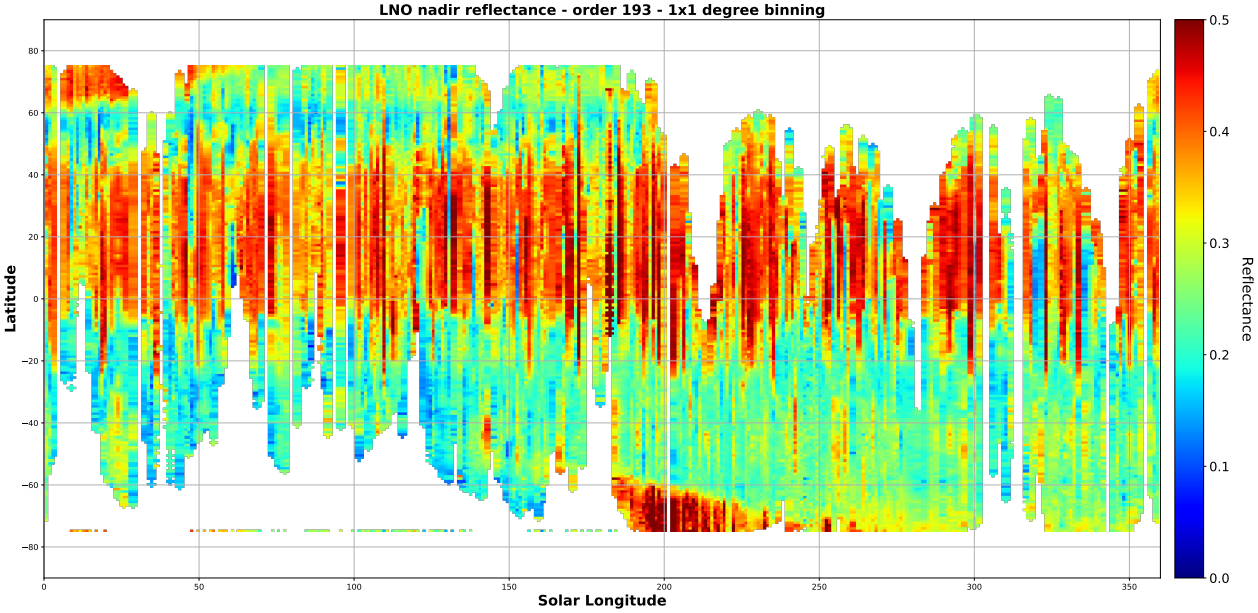

Figure 9.16: Latitude/Solar Longitude reflectance map of order 193 at 4354 cm^{-1}, without atmospheric corrections. Same as Fig. 9.14 but for order 193.

- the phase function,
- the single scattering albedo ω of the aerosols,
- the surface albedo A,
- geometry : solar incidence angle θ_0, emergence angle θ and azimuth angle φ.

With this approach, they were able to retrieve the single scattering albedo ω of the aerosols assuming a Henyey-Greenstein phase function with a constant value of the asymmetry parameter $g = 0.63$ on the 1-2.5 μm spectral range. This value of g is consistent with the 0.64 to 0.67 values obtained by (Clancy, 2003) using TES. The choice of the phase function is also consistent with (Ockert-Bell et al., 1997) in their study of the atmospheric dust optical properties.

For a given particle phase function, the reflectance of an aerosols layer with infinite optical depth depends only on the single scattering albedo ω of aerosols (Vincendon et al., 2007). This parameter defines the fraction of photons absorbed for each interaction with aerosols. Assuming that atmospheric dust is spectrally similar to bright regions, (Ockert-Bell et al., 1997) conclude that ω varies slowly around 0.955 in the 1-2.5 μm spectral range. Using OMEGA observations of a dust storm, (Vincendon et al., 2007) obtained a reflectance factor of about 0.45 at 1 μm, which is consistent with the highest albedo observed by OMEGA in the near-IR. This led to an estimation of $\omega(\lambda)$ ranging between 0.971 and 0.976 in the 1-2.5 μm wavelength range. The single scattering albedo as a function of wavelength $\omega(\lambda)$ retrieved by (Vincendon et al., 2007) is shown figure 9.17. Theses values of $\omega(\lambda)$ along with the Henyey-Greenstein phase function and the asymmetry parameters $g = 0.63$ will be used later in the DISORT model.

Since the dust optical depth is not constant with wavelength, we used the estimation of $\tau_0(\lambda)$ made by (Vincendon et al., 2007) using OMEGA observations (see figure 9.18, red curve) and a linear combination of models of (Clancy, 2003) that best fits the observation. The values of $\tau_0(1\mu m) = 0.38$ was choose as a reference (τ_0) to estimate the variation of $\tau(\lambda)$ following the formula :

$$\tau(\lambda) = \frac{\tau_0(\lambda)}{\tau_0(1\mu m)} \tag{9.8}$$

The resulting $\tau(\lambda)$ is shown figure 9.18 (black curve).

Effects of the aerosols With the DISORT model and the aerosols parametrization one can compute the theoretical reflectance top-of-atmosphere (TOA) as a function of the surface reflectance and the aerosols optical thickness (AOT), for a given geometry of observation at a given wavelength. Such computation was made and is illustrated fig. 9.19 for an incidence angle of 40°, an emission angle of 0° (nadir viewing point, such as the NOMAD-LNO channel) and azimuthal angle of 0° at a wavelength of 2.31 μm. Such wavelength was chosen because it is close to the two orders studied in this work (189 and 193) and whose wavelengths used for the reflectance maps shown in sec. 9.2.5.1 are respectively 2.29 and 2.34 μm. From this result we can note that with an increase of the AOT a bright surface (reflectance between 0 and 0.5) will appear darker while a dark surface (reflectance above 0.5) will appear brighter. The pivot point distinguishing these two regimes is around a reflectance of 0.5. We also note that for an extremely high AOT, the TOA reflectance is always 0.5, regardless of the surface reflectance. This clearly illustrates the effects of the aerosols in the martian atmosphere and shows why we should be careful when comparing the calibrated NOMAD data and the TES data, the latter being the only one corrected for the aerosols contribution.

The comparison between TES and NOMAD for orders 189 and 193 are shown figs. 9.20 and 9.21. To do this we had to reduce the initial high resolution of TES (8 pixels per degree) to match the NOMAD resolution (1 pixel per degree) and took the average reflectance of the corresponding TES pixels, producing a first bias. In these graphs, the TES reflectance act as the true surface reflectance while the NOMAD reflectance is the corresponding reflectance top-of-atmosphere. We can first note that the NOMAD reflectance is globally higher than the TES reflectance. This is in complete agreement with the expected

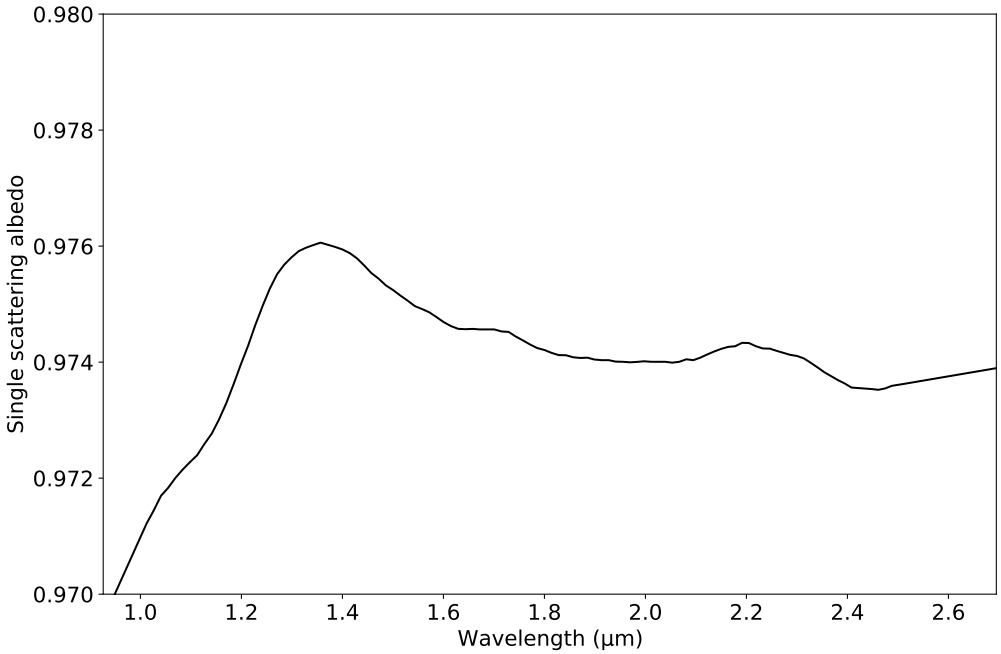

Figure 9.17: Dust single scattering albedo as a function of wavelength $\omega(\lambda)$ retrieved by (Vincendon et al., 2007) with a Monte-Carlo approach using OMEGA observation of a dust storm. They assumed a single-lobed Henyey-Greenstein phase function with $g = 0.63$.

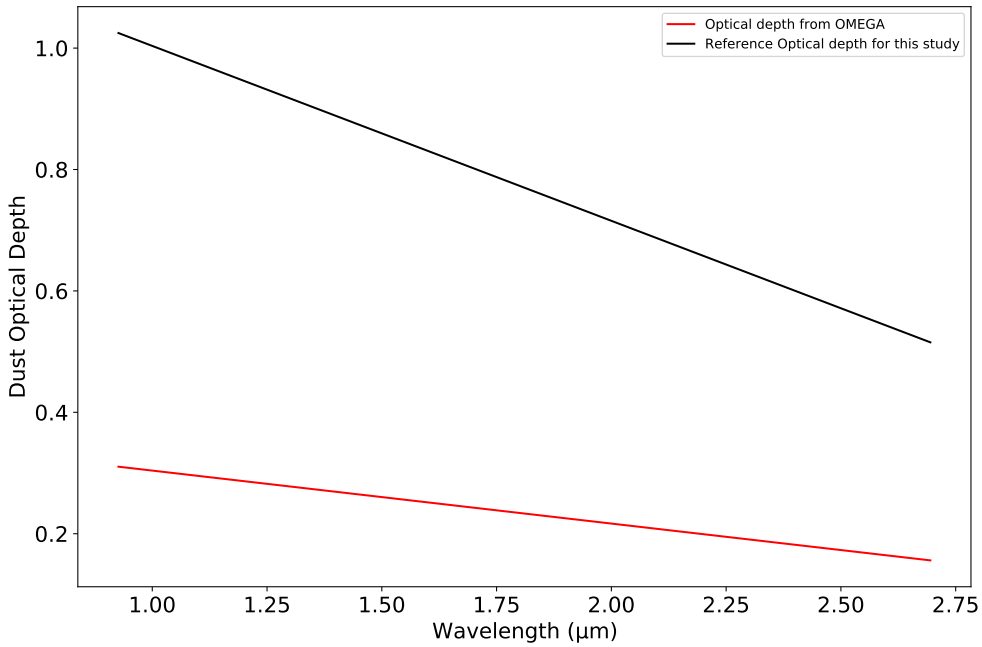

Figure 9.18: Dust optical depth of the layer (τ) as a function of wavelength. The red line are optical depth retrieved by OMEGA in (Vincendon et al., 2007). The value of $\tau(1\mu m) = 0.38$ is used as a reference for this study. The black line is the optical depth used in this study based on equation 9.8.

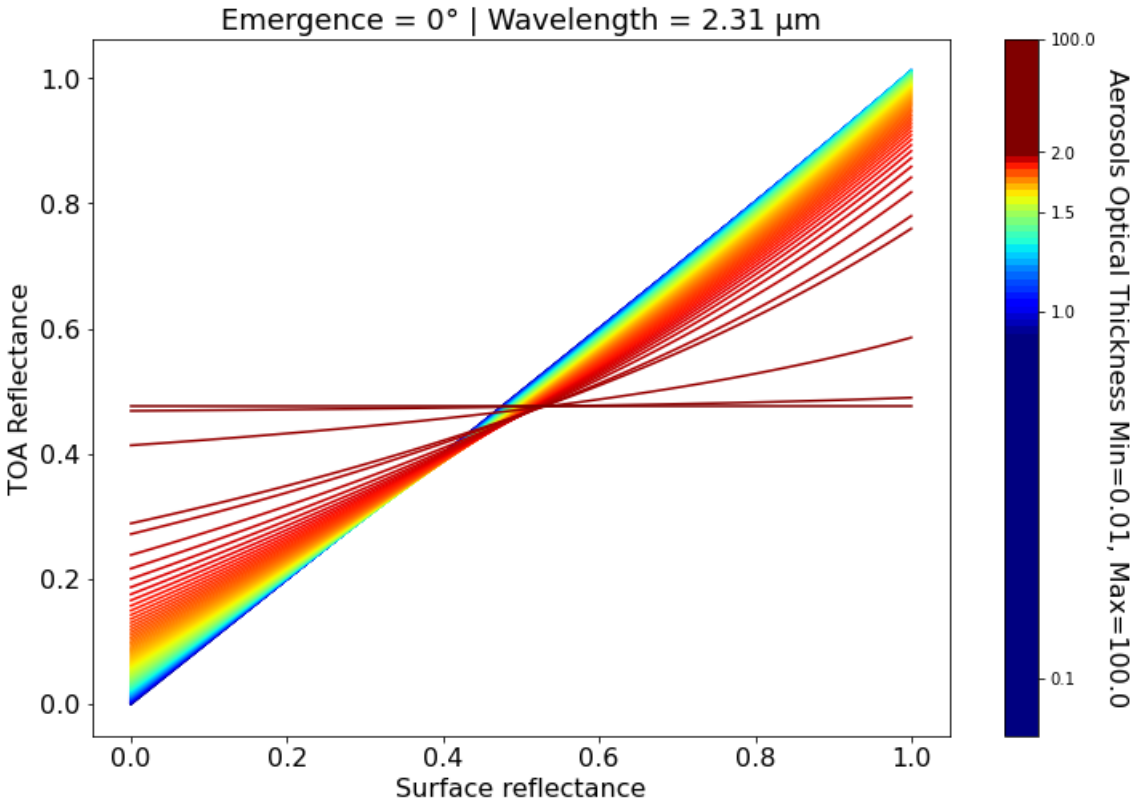

Figure 9.19: Reflectance top-of-atmopshere as a function of the surface reflectance for varying aerosols optical thickness (in color). The incidence angle is 40°, the emission is 0° (nadir viewing geometry) and the wavelength is 2.31 μm.

theoretical effects of the aerosols as illustrated fig. 9.19, the TES reflectance being below 0.5, this brightening of a dark surface is reproduce. However we can see that this brightening effect seems to be stronger for higher values of the TES reflectance, which is not in agreement with the expected effects. This effect should be lower as the surface reflectance approaches 0.5. This can be related to several reasons, first the TES reflectance map is made from the broadband 0.3 to 2.9 μm range and whose spatial resolution has been reduced. The NOMAD reflectance maps are made at a particular wavelength (2.29 and 2.34 μm) whose reflectance value is averaged within the same pixel observed several times. Since the data used cover more than one Martian year, some areas may see their reflectance vary due to different AOT during the observation. For these reasons, a more detailed comparison is not feasible.

9.2.6 Discussion

The comparison with the TES is helpful because it is a well calibrated product based on the combination of multiple images, it is therefore an excellent candidate to ensure that the major trends are reproduced, and thus to validate part of the radiometric calibration. However, this comparison is tricky for major reasons :

- The produced reflectance maps are made based on the reflectance at one particular wavenumber, even if order 189 and 193 falls within the spectral range with which the TES map was made (0.3 to 2.9 μm) there maybe large scale absorption / slopes in this spectral range, making direct comparison with NOMAD difficult.

- The TES map is corrected for the atmosphere (both gases and aerosols) which lower the albedo as the aerosols scattering tends to increase the reflectance of a dark surface as seen in sec. 9.2.5.2.

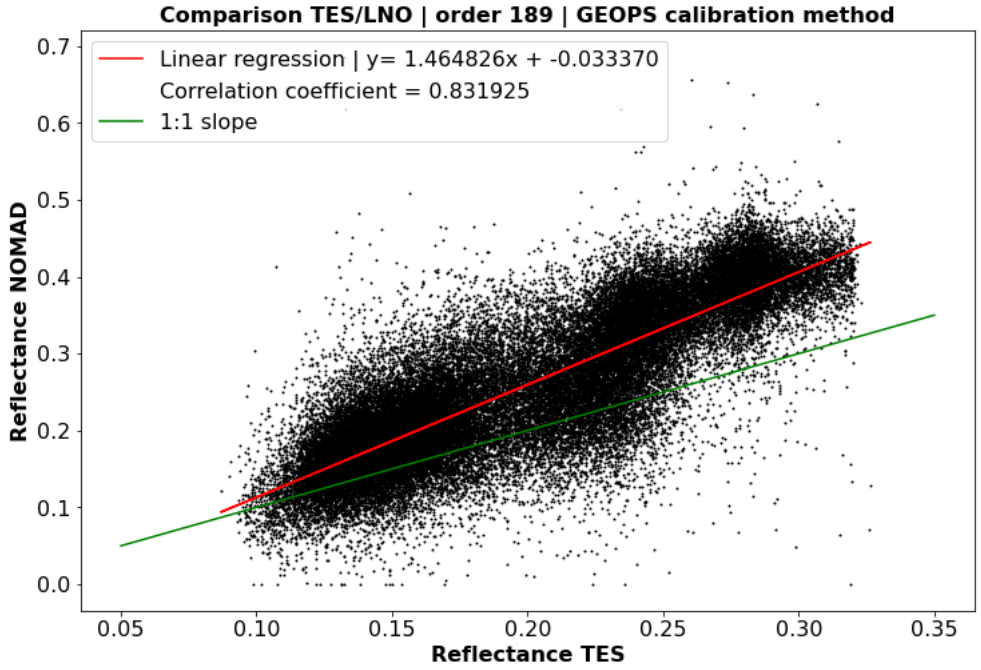

Figure 9.20: TES albedo versus reflectance of NOMAD for order 189 at 4260 cm^{-1}. The correlation coefficient (0.83) shows that there is a positive correlation between TES and NOMAD which confirms that large-scale variations are reproduced. The slope of the linear regression shows that NOMAD reflectance is about 1.5 time higher than TES, as expected by aerosols scattering. The 1:1 slope is shown in green.

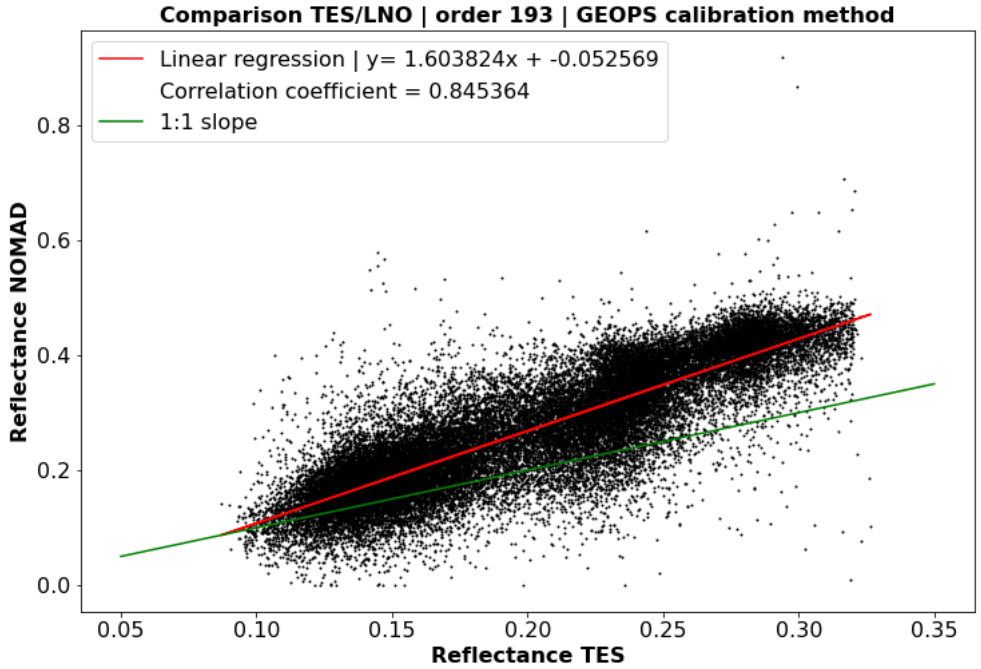

Figure 9.21: TES albedo versus reflectance of NOMAD for order 193 at 4354 cm^{-1}. The correlation coefficient is positive (0.84), despite a small dispersion, there is a trend which indicates that large scale variations are reproduced. The slope of the linear regression shows that NOMAD reflectance is about 1.6 time higher than TES, mostly due to aerosols scattering. The 1:1 slope is shown in green.

This scattering is expected to be very efficient at the wavenumbers of orders 189 and 193 (around 2.3 μm).

- The spatial resolution of TES, originally at 8 pixels/degree was degraded to match the 1 pixel/degree at which the NOMAD map are made, which can erase local variations and degrade the quality of the fit.
- The TES map is corrected for seasonal deposit variations, such as the extension of seasonal winter polar cap in both hemisphere, while the NOMAD data has not enough coverage yet to correct for such seasonal effects. Higher albedo values estimate with NOMAD are expected.

9.3 Surface CO_2 ice detection with LNO

As the atmospheric transmittance is high in both 189 and 193 orders, one would expect to see absorption features of the surface CO_2 ice during winter in the high latitude spectra whose SNR is high enough. Such investigation was undertaken on both order to look at the band depth through several parameters such as the latitude, the solar longitude and the local solar time to create maps but also at the scale of a spectrum or a collection of spectra from the same orbit. In this section, we will only consider data calibrated with the BIRA method (Thomas et al., 2022) as we showed above that the GEOPS method may completely erase large-scale features such as CO_2ice absorption features.

9.3.1 Band Depth

To estimate the band depth (B_d) the following formula was used :

$$B_d = 1 - \frac{R_{band}}{R_{continuum}} \tag{9.9}$$

Where R_{band} is the reflectance at the center of the band (ν_{band}) and $R_{continuum}$ the reflectance of the continuum not affected by the absorption ($\nu_{continuum}$). Since both orders 189 and 193 have a major CO_2 ice band this formula can be applied on all reflectance data previously shown to identify potential CO_2 ice signature in the data. The band reflectance (R_{band}) is taken at wavenumber 4256 cm^{-1} for order 189 and 4363 cm^{-1} for order 193 in agreement with the direct model simulation (see figs 9.1 and 9.2, right). The continuum reflectance ($R_{continuum}$) is taken at wavenumber 4260 cm^{-1} for order 189 and 4353 cm^{-1} for order 193 on a flat part of the reflectance, outside of the band and near the center of the order to ensure a better SNR. We do not include data with an incident angle above 80° to avoid data with very low SNR, which mainly concerns observations at very high latitudes.

Results are shown below : latitude/longitude maps (figs.9.22 and 9.23), latitude/solar longitude maps (figs.9.24 and 9.25) and latitude/local solar time maps(figs. 9.26 and 9.27). Maps are usually made with a spatial resolution of 1 pixel/degree and by taking the mean of all band depths that falls within the same coordinate, except for the latitude/local solar time maps for which the map is gridded on a 1 pixel/degree of latitude and 1 pixel/2.5 min of local solar time. Description and interpretations of the obtained maps can be found in the legend of corresponding figures.

The main conclusions are as follows:

- Although calibration artefacts may be present in the reflectance data, the strong similarities between the maps of order 189 and 193 tends to show the ability of LNO to detect CO_2 surface ice.
- The band-depth is very often stronger in order 193 which makes it possible to identify more regions where CO_2 ice is likely to be present, even if it is difficult to decide between possible CO_2 ice clouds, real surface ice or spectral continuum artefacts.
- The Latitude/Solar longitude and Latitude/Local Solar Time maps are consistent with the implementation of seasonal polar caps in both the northern and southern hemisphere.

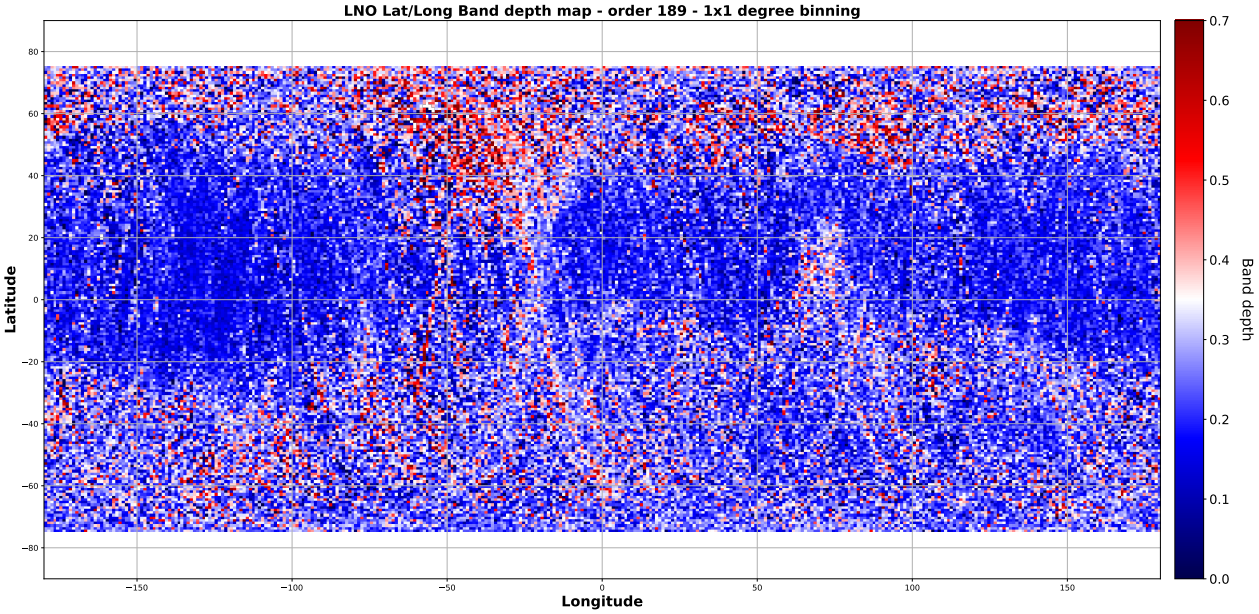

Figure 9.22: Latitude/Longitude band depth map of order 189 at 4256 cm^{-1}. The spatial resolution is 1 pixel/degree. As expected, higher band depth values are mostly present in both southern and northern higher latitude (below -40°S and above 40°N). One can see that there is a lot of intersecting orbit and therefore a lot of coordinate pairs observed several times, by considering the mean band depth per pixel we reduce / erase the potential presence of deeper band. This is why the latitude/longitude map does not allow interpretation of spatial distribution as it requires to account for seasonal variations. However it allows to simply identify the potential presence of CO_2 ice at several locations.

- The Latitude/Local Solar Time maps shows potential evidences of CO_2 ice or frost early in the morning and late in the afternoon near equatorial latitudes.

9.3.2 CO_2 ice at LNO spectral resolution

The band depth maps revealed the presence of the CO_2 ice at several locations : both at high north and south latitudes, during local winter, and at particular local solar time such as early in the morning and late during the day. Knowing the time and space parameters at which the CO_2 ice is potentially detected, one would look at the scale of one spectrum or a collection of a few spectra to check the shape of the CO_2 ice band when present. From the reflectance maps and band depth maps, the CO_2 ice may be found at :

- Latitude below -60°S and above 60°N during local winter and spring, at any local solar time.
- Both southern and northern mid-latitude, at early and late local solar time.

To promote the detection of CO_2 ice, we also selected spectra whose SNR is high enough to minimize effects of the noise on the band. Figure 9.28 and 9.29 show examples of spectra from several orbit with which CO_2 ice is detected in both orders 189 and 193. Even though the atmospheric contribution from gases are negligible, this is not the case for aerosols and these can lead to significant changes in the spectra's shape and absolute level (as evidenced by the comparison with TES, see sec. 9.2.5). Thus, one have to be cautious when analyzing these spectra because bias may exist. A detailed analysis would require a correction of the aerosols radiative effects.

Order 189 shows a CO_2 ice absorption bands at 4256 cm^{-1} close to the very noise first spectels. The band stands out as it is slightly deeper and wider than the CO atmospheric lines within the continuum between 4260 and 4275 cm^{-1}. The continuum is slightly bent reinforcing the boundary between the

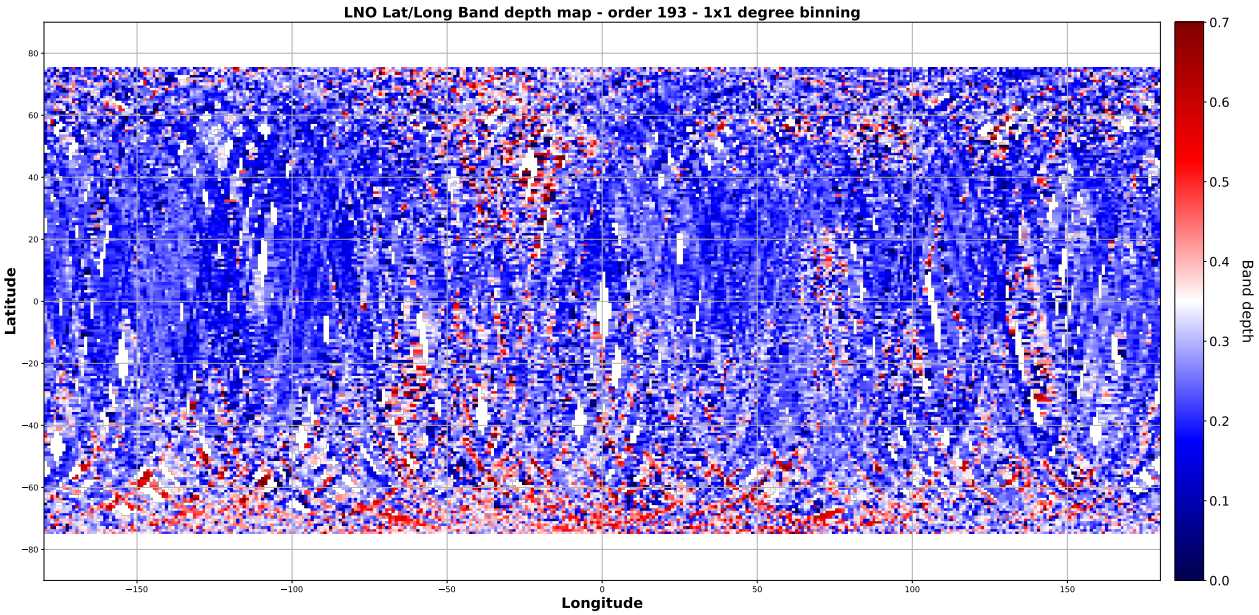

Figure 9.23: Latitude/Longitude band depth map of order 193 at 4363 cm^{-1}. The spatial resolution is 1 pixel/degree. Similarly to order 189 (figure 9.22), the few high band depth values are mostly present on higher latitude. Higher band depths are also found at lower latitudes and could be related to either CO_2 ice clouds, surface ices at early local time or an instrumental effects from the calibration.

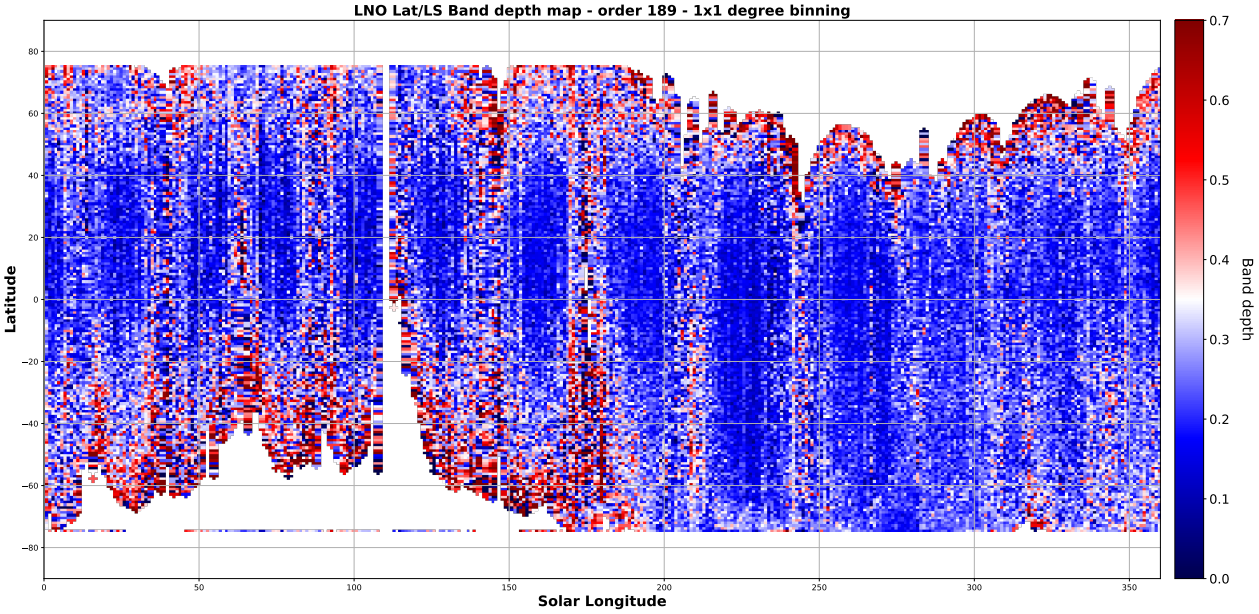

Figure 9.24: Latitude/Solar Longitude band depth map of order 189 at 4256 cm^{-1}. The spatial resolution is 1 pixel/degree of latitude and solar longitude. Again, each coordinate is assigned the mean of all band depth from spectra falling within the same pixel. Since the solar longitude express the seasonal variation, higher band depth values should always be present at the same coordinate. One can see a significant increase of the band depth at southern high latitude between L_S =150 and L_S =200 which is consistent with the reflectance increase at the same location (see 9.14), most probably related to the seasonal south polar cap. High band depth values are also present several time at equatorial/mid-latitudes which are harder to interpret (clouds, local CO_2 ice condensation, or simply noise and/or calibration artefacts). The high latitude of the northern hemisphere display often high band depth values, all across solar longitude, but the seasonal northern polar cap is not as well identified as the southern one.

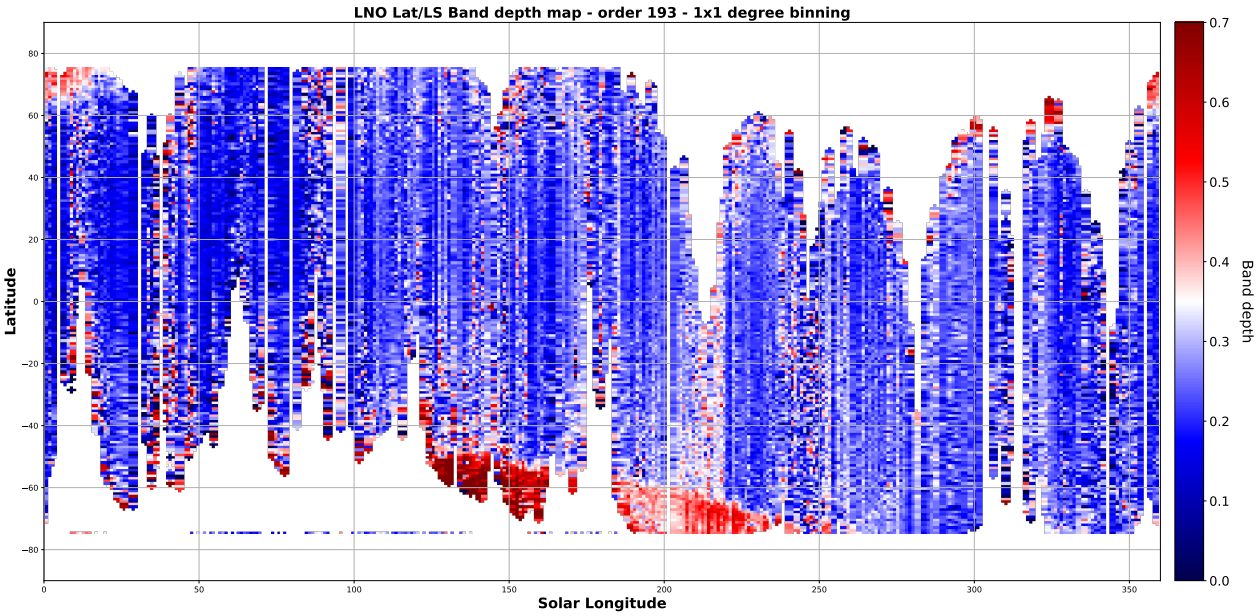

Figure 9.25: Latitude/Solar Longitude band depth map of order 193 at 4363 cm^{-1}. Same as Fig. 9.24 but for order 193. The seasonal coverage is lower than for order 189, however one can see band depth taking higher values between -60°S and -80°S from $L_S = 140$ to $L_S = 160$ which is the end of local winter and the beginning of local spring, so those values are most probably related to the south polar cape extent, in agreement with the reflectance map of order 189 (see figure 9.16). The northern hemisphere displays high band depth values, similar to order 189 at the same solar longitude. There are also numerous higher values at southern mid-latitude to the equator, especially around $L_S = 250$ that are more difficult to interpret (CO_2ice clouds, surface ices at early local time or instrumental effects from the calibration).

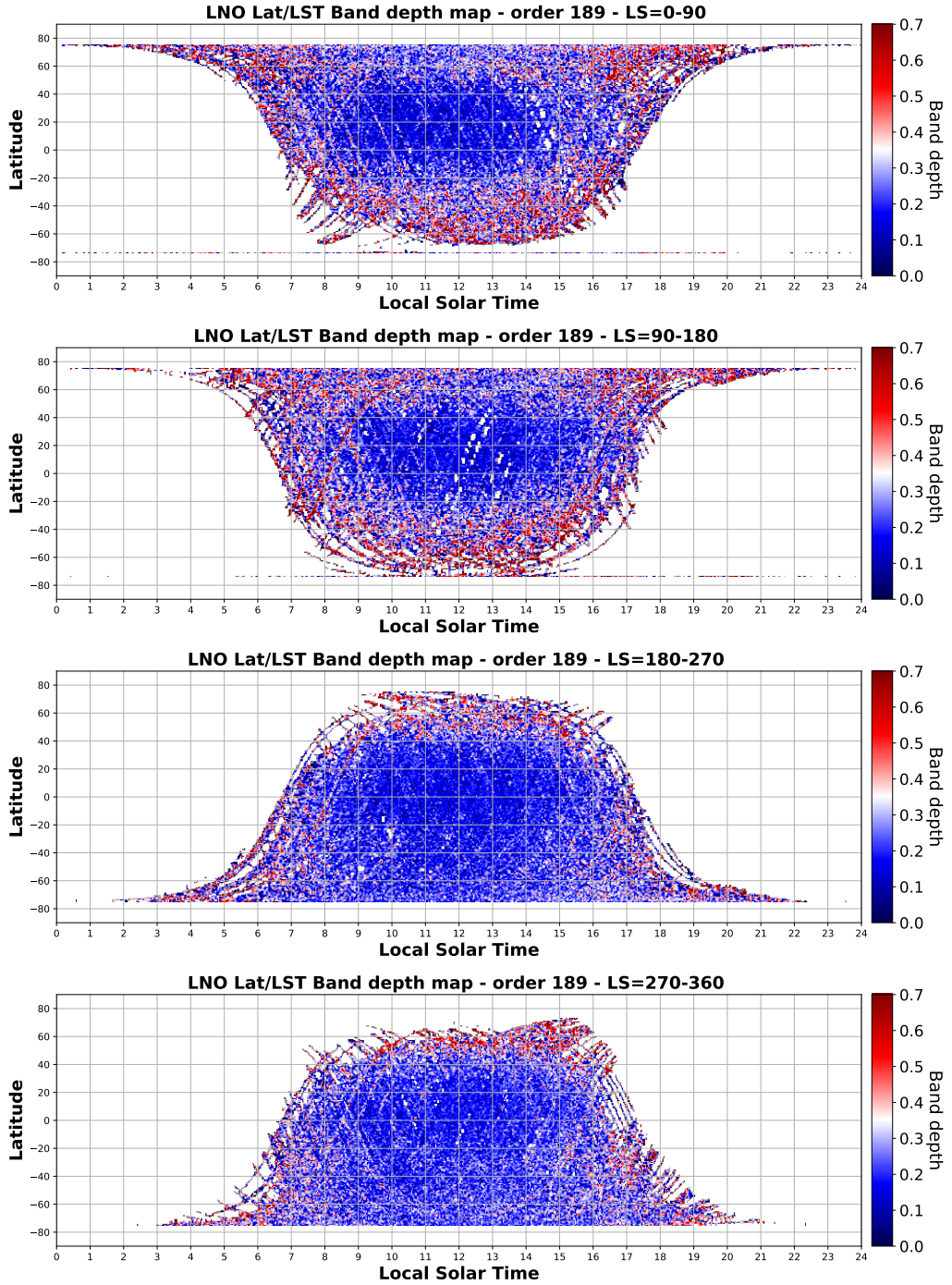

Figure 9.26: Latitude/Local Solar Time (LST) band depth map of order 189 at 4256 cm^{-1} for various seasons gridded on a 1 pixel/degree of latitude and 1 pixel/2.5 min of local solar time. The solar longitude (LS) increases from top to bottom. When LS is between $0-90$ (Northern hemisphere spring equinox to summer solstice), higher band depth are seen in the northern hemisphere high latitudes (above 50°N) at early and late local time but also in the southern hemisphere high latitudes during all day, corresponding to the formation of the south polar caps during local winter. A similar band depth map is obtained for LS between $90-180$ (Northern hemisphere summer solstice to autumn equinox) with even more band depths values of 0.5 corresponding to a higher extent of the southern seasonal CO_2 ice polar caps during spring. Moving to LS between $180-270$ and $270-360$ corresponding to the Northern hemisphere autumn equinox to spring equinox, the recession of the southern polar caps is clearly visible as the band depth values reach 0 at high latitudes. The northern polar caps is not visible either because of the winter polar nights preventing dayside observations.

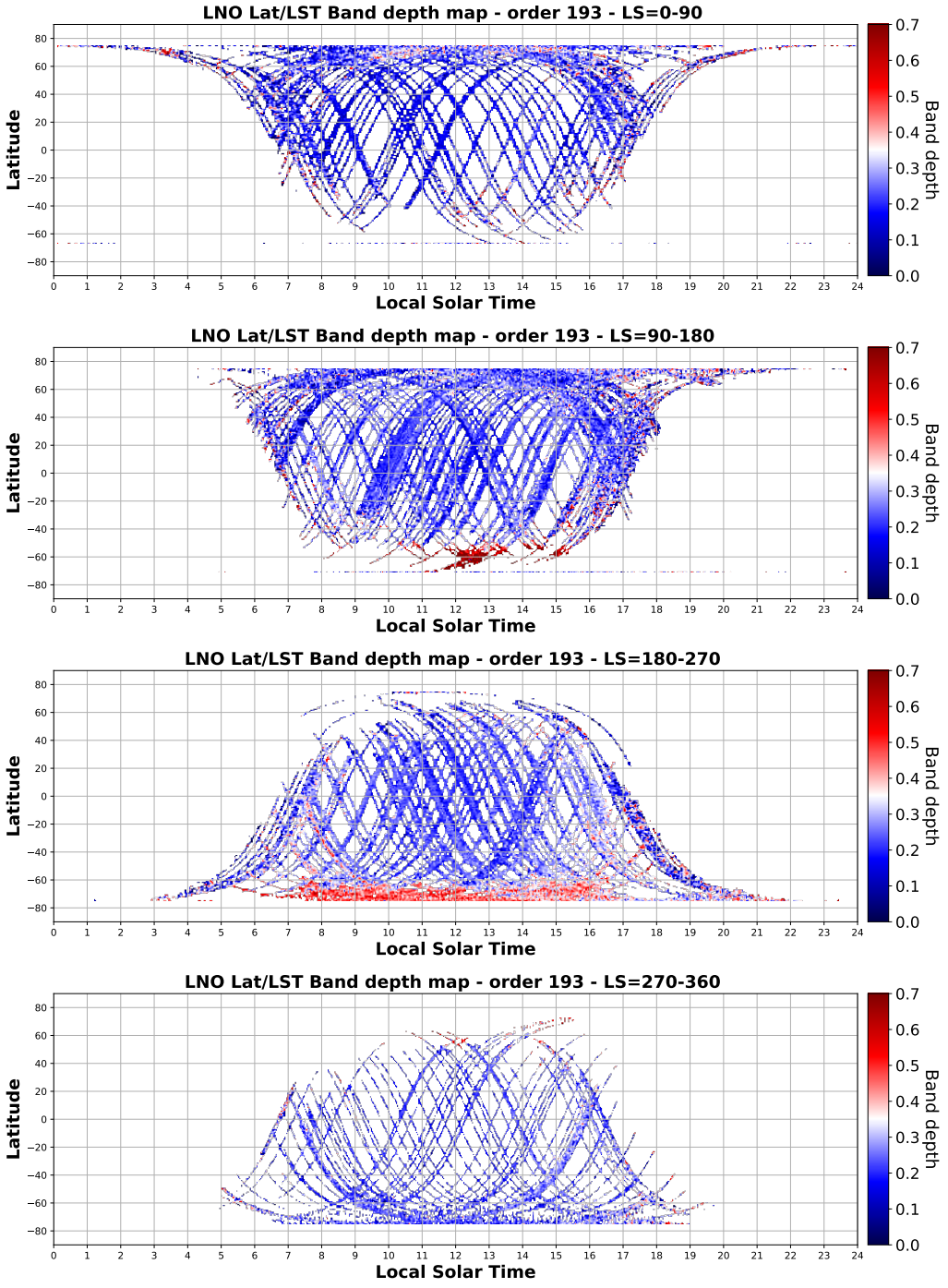

Figure 9.27: Latitude/Local Solar Time (LST) band depth map of order 193 at 4363 cm^{-1}. Same as Fig.9.26 but for order 193. Interpretations are similar to those made for order 189 (see fig.9.26) confirming the CO_2 ice detection. The band depth within this order is however much higher than for order 189, which can either be a real spectroscopic feature or a reinforcement of the band depth via calibration artefact in the continuum. This could explain some higher band depths values near equatorial latitudes. Nevertheless, the fact that most of the higher band depth locations are well explained by the presence of surface CO_2 ice and that the majority of equatorial observations shows a very weak or even absent band testifies in a favor of a real spectroscopic signature.

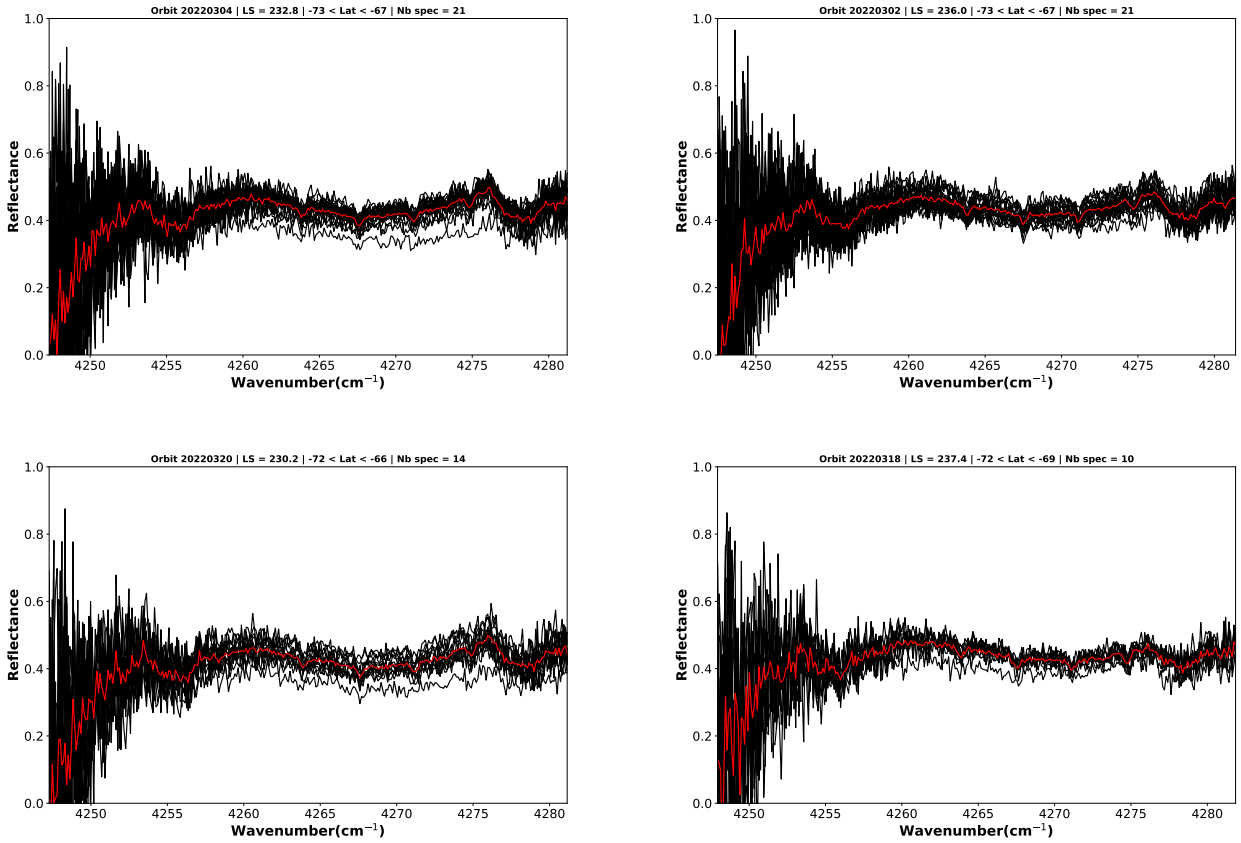

Figure 9.28: Order 189 : all spectra at high latitude (below 60°) of orbit 2022/03/04, 2022/03/02, 2022/03/20, and 2022/03/18 (black) and mean spectrum (red). Those high latitude spectra display a specific CO_2 ice band at 4256 cm^{-1}. The band is close to the first 50 noisy pixels so it is sometimes hard to identify and its depth is comparable to the noise variation. This explains why the band depth map of order 189 (see figure 9.24) is nosier than for order 193 (see figure 9.25). Also, the band is duplicated on the right side of the spectra due to contribution by adjacent orders from the AOTF. This allows a confirmation of the detection but can also serve for a fine spectroscopic analysis made in parallel on the two bands.

band and its shoulders. An interesting features is that the band appears duplicated on the right side of the spectra, at 4277 cm^{-1} due to the contribution by adjacent orders from the AOTF. This is a good proxy to confirm the detection of the CO_2 ice and could also be used to perform spectroscopic analysis if the original band on the left side is to noisy.

Order 193 shows a very deep and wide band at 4360 cm^{-1}, possibly intensified by a deflection within the continuum and contribution by adjacent orders. The shoulder is clearly distinguished by its higher reflectance separating the band from the noisy spectels on the left. This feature is much more pronounced than for order 189 making this order an excellent candidate for CO_2 ice microphysical characterizations. It also explains well the differences between the band depth maps showed in section. 9.3.1.

9.4 Conclusion

Using a combination of criteria such as the instrumental sensitivity, the atmospheric contribution by gases and direct model simulation of CO_2 ice spectra at the spectral resolution of LNO, we selected three potential diffraction orders to undertake a quicklook analysis of the nadir data with the aim of highlighting the capability of LNO to detect CO_2 surface ice. Orders 189 and 193 appeared to be the

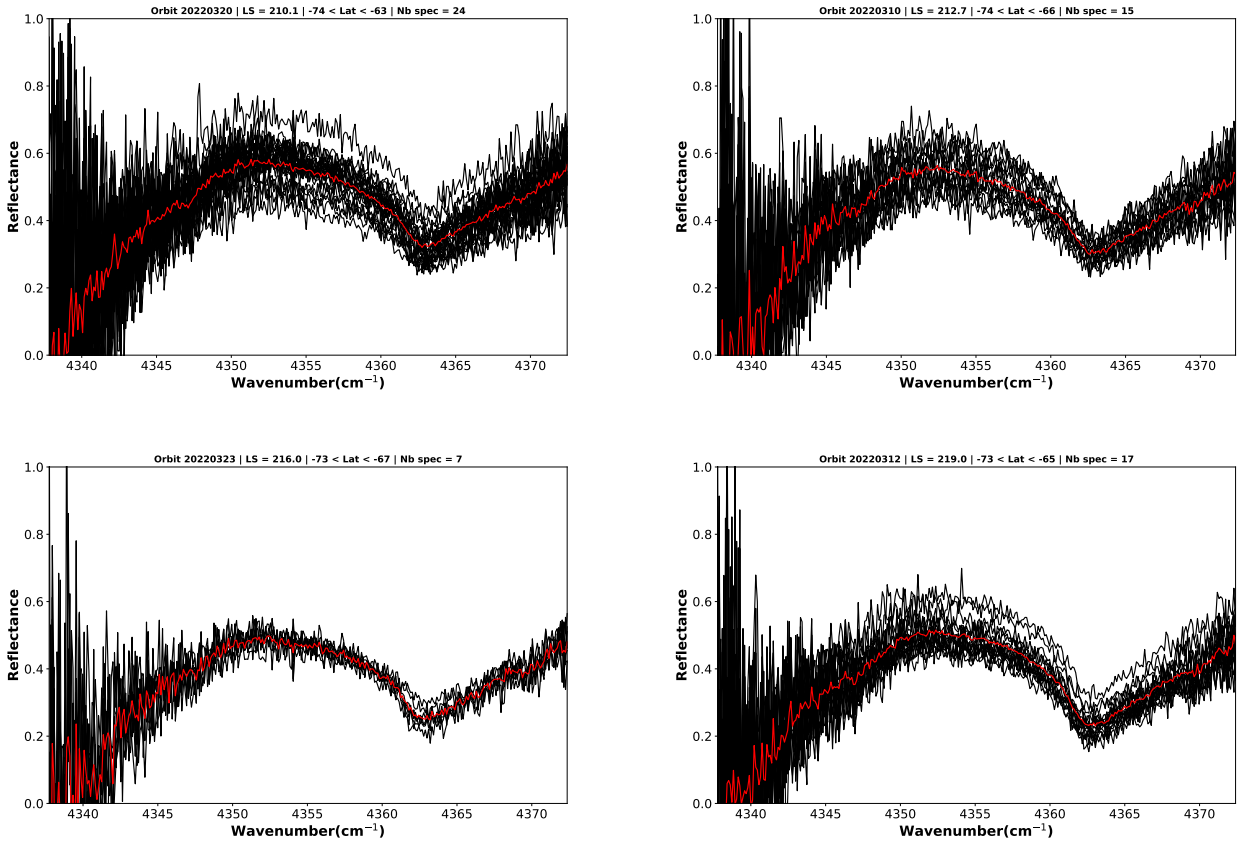

Figure 9.29: Order 193 : all spectra at high latitude (below 60°) of orbit 2022/03/20, 2022/03/10, 2022/03/23, and 2022/03/12 (black) and mean spectrum (red). Those high latitude spectra display a specific CO_2 ice band 4363 cm^{-1}. The band is much more visible than for order 189, as it is located closer to the center of the detector, with higher SNR. Order 193 seems more appropriate to use for the CO_2 ice detection due to the higher amplitude of the band at this wavenumber.

most promising for future investigations of microphysical properties because the atmosphere is mostly transparent at these wavelengths and the CO_2 ice shows significant absorptions.

Two calibration procedures were proposed for the LNO channel, based on different assumptions and approaches. The one proposed by BIRA (Thomas et al., 2022) is well suited for surface studies as the method keep the continuum of a raw spectra but may be biased by unaccounted instrumental effects. The other method proposed by us, (Cruz-Mermy et al., 2022), called GEOPS, includes a continuum correction and is thus more suited for atmospheric analysis but erases any large-scale features possibly coming from the surface. A comparison between the two methods was made on all reflectance spectra available at the time of this work and reveal a strong agreement between the two datasets.

A comparison with the MGS TES Global Bolometric Albedo map (Christensen et al., 2001) coming from a different instrument revealed a consistency in large-scale variation of the reflectance between LNO and TES. The comparison is tricky and is quickly limited by the fact that TES data had to be unresolved to match the LNO spatial resolution. Also, the TES product is made from reflectance values in the broadband 3448-33330 cm^{-1} (0.3 to 2.9 μm) region while LNO spectral range covers a very small part of the TES range. Finally, TES is corrected for both gases and aerosols, while the gases contribution are expected to be negligible for these orders, the aerosols contribution is clearly highlighted as LNO reflectances are mostly higher than TES. This implies to be cautious when first analyzing NOMAD data as bias may be present, but the large-scale correlation with TES shows LNO data reliability.

Using a simple band-depth computation, we showed that both orders 189 and 193 can be used to detect CO_2 ice absorption at locations consistent with the presence of seasonal polar caps at high altitudes, but also potential clouds near equatorial latitudes during the day and possibly CO_2 frost at early and late local solar time at mid-latitudes. Looking at specific observations at the scale of several spectra taken within multiples orbits during southern local spring at latitudes below $-60°$S, we clearly identified the CO_2 ice spectroscopic features in both orders. Such observation must be investigated further through finer microphysical characterization after a dedicated atmospheric correction.

Although order 193 seems more appropriate for characterizing surface ice with a deeper and wider absorption band, there are currently three times more observations of order 189, promoting a better spatial and temporal coverage. Both orders should be used together when its possible to enhance the detection and estimation of surface ice properties. Either when the two orders are observed at the same time, or by using close orbits with similar solar longitude and local solar time.

Perspectives includes the use of orders 189 and 193 nadir data with a realistic radiative transfer (Andrieu et al., 2015) to undertake investigations of the microphysical properties of surface ices, such as the thickness of the CO_2ice slab, the volume proportion and grain size of impurities composing it, such as water ice or martian dust, or the surface roughness.

Chapter 10

Conclusion

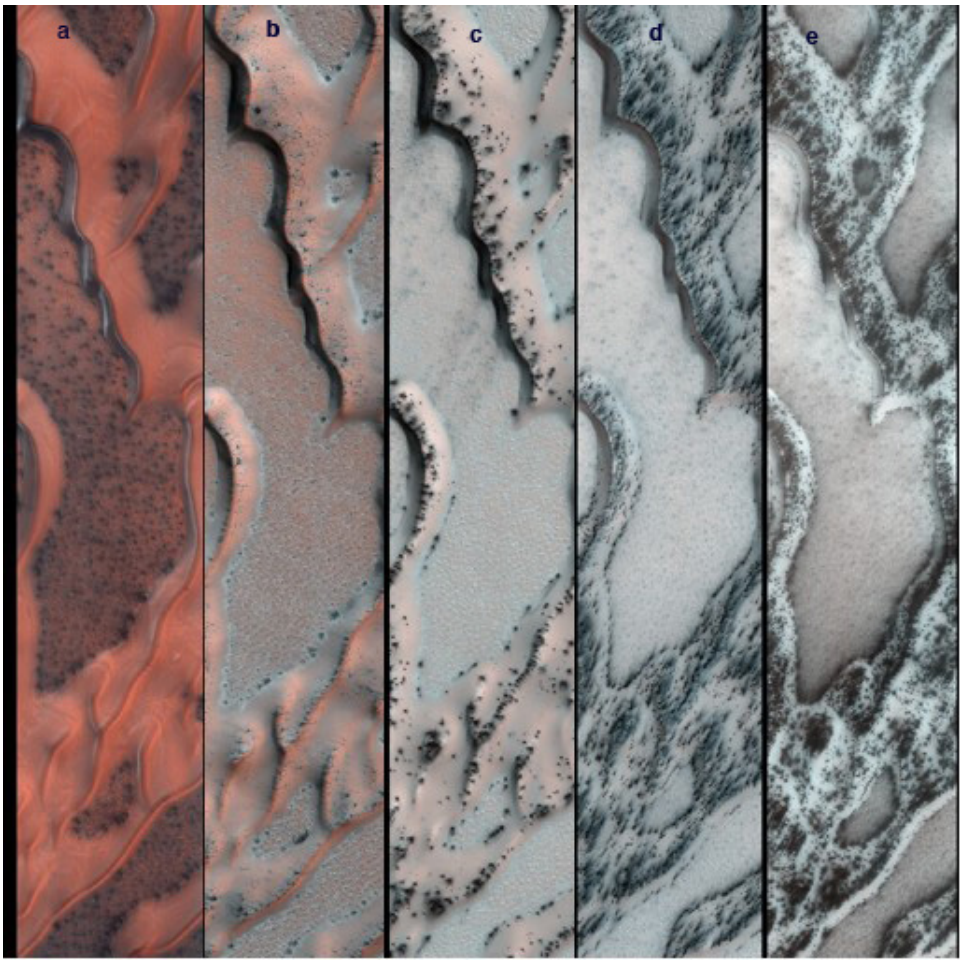

«Seasonal changes on Far-Northern Mars». The High Resolution Imaging Science Experiments (HiRISE) camera on board NASA's Mars Reconnaissance Orbiter snapped this series of false-color images of sand dunes in the north polar region of Mars (N80, E122) in 2013. The area covered is about 1.3 kilometers wide. In early spring (panel A) the ground is covered by a seasonal layer of CO_2 ice and dark spots are visible between the dunes. As spring progresses (panel B to E) dark deposits are mostly localized on dunes. This is interpreted as the results of ice cracks releasing pressurized gas trapped below the ice layer and carrying sand and dust to the top of the ice layer. The deposits are dropped in fan-shaped downhill and downwind. Credit: NASA/JPL-Caltech/Univ. of Arizona

In this part we have covered the work undertaken to characterize the ice microphysics on Mars. We have seen that some morphologies involving seasonal ice such as spiders could be explained by a fine microphysical characterisation of the ice at various local time. Near-infrared data from the nadir channel of the NOMAD instrument (LNO) on board ExoMars Trace Gas Orbiter mission can allow such characterization with observations at a wide variety of local solar times. Moreover, the very high spectral resolution makes it possible to collect data of the martian surface on a very narrow spectral range, allowing to resolve specific absorption bands and thus promoting a fine microphysical characterisation. As the first acquisitions coincide with the beginning of this PhD research project a calibration of the data was required before they can be used.

Two calibration methods were envisaged, the first one proposed by (Thomas et al., 2022) directly uses the observation of the Sun by LNO to calibrate the nadir data. Such approach works well when assuming that the instrument is stable through time because it is fast and efficient. An advantage is that we do not lose any spectral informations but we can not explain some residual instrumental effects that may affect the spectrum. A second approach is to use a theoretical synthetic solar spectrum and simulate the instrumental effect. A comparison with the LNO observations of the Sun gives the instrumental sensitivity and the conversion factor to convert digital numbers to spectral radiance and reflectance. This approach was used in this work. To do so, a synthetic solar spectrum at high spectral resolution on the same spectral range than LNO was required. The construction of such spectrum was described chapter. 7. Using this product, a calibration method was developed (see chapter. 8) and used to calibrate nadir observations. The two approaches show consistent results in terms of reflectance obtained, thus validating the results obtained.

Some diffraction orders were investigated for their ability to detect CO_2 ice on Mars. Orders 189 and 193 seem to be the most relevant because of the very high transmittance of the atmosphere at these wavelengths but also because they fully resolve a thin absorption band. Reflectance and band depth maps as a function of latitude, longitude, solar longitude and local solar time have highlighted the detection of CO_2 ice at expected locations, such as the high latitudes during local spring, but also other potential detections at lower latitudes and very extreme local times. However it is not possible to confirm such detection or precise the origin of the ice signature (surface ice, clouds or instrumental artefact) at the dawn of this first analysis. Moreover, a proper correction of the aerosols must be applied before analyzing any nadir data, especially for a precise microphysical characterization using radiative transfer models. To do so, one has to have an estimation of the aerosols optical thickness at the time of the observations, which is difficult to obtained so far.

Several perspectives are considered for this work. A key first step will be to correct the effects of the aerosols. A very good opportunity lies in the UVIS instrument, the third spectrometer of the NOMAD suite. UVIS observes the martian surface in the ultraviolet to visible wavelengths and can provide an estimate of the AOT since many observations are made at the same time as LNO. Then, an estimate of the equivalent AOT in the specific near-infrared wavelengths will have to be realized. Once such correction is applicable, any nadir observations of orders 189 and 193 could be used to investigate the ice microphysics. In a similar way as developed in part. II, a realistic radiative transfer combined with a bayesian approach will give the ice thickness, the volume abundance and grain size of the impurities and the surface roughness. With such results at varying location in space and time (on a seasonal but also daily scale) it will be possible to follow the evolution of ice properties and to better understand the processes involved.

General conclusion

In this PhD research project we have undertaken a work of characterization of the ice properties present on planetary surfaces of Europa and Mars. To do so we have used physical models that rigorously describe the interactions between light and the materials involved. This choice is guided by the fact that the investigated ices show significantly varying optical properties at near-infrared wavelengths, which allows to derive the microphysical properties of the surface (abundance, grain size, roughness). In addition, many data from space missions are available in this golden age.

In part I we covered the notions of radiative transfer in icy surfaces and we present examples of well-known models that have been frequently used in planetary sciences. We detailed the model used in this work, the Hapke model, and illustrated how to compute reflectance spectrum with it. A major concept behind this work is the inversion of a physical model. As opposed to the forward problem, the inverse problem is to find the best set of parameters to accurately reproduce the data from a model. We presented some examples of inversion methods used in planetary sciences and compared examples of inversion performed on a typical data used in this study. This part constitutes the development of the tools and methods which are then applied in the following parts.

In part II we conducted a microphysical study of the ice on Europa. We have set out the scientific context to define key questions regarding Europa's surface. Using the near-infrared Galileo/NIMS data we have investigated the composition of Europa's surface using a typical spectrum of the trailing Anti-Jovian hemisphere using a radiative transfer model and a bayesian inference approach. We have shown in particular that it is not possible to accurately constrain the composition of Europa with the NIMS data and that external constraints are required before starting a fine microphysical characterization of the surface.

In part III we presented the work done for a characterization of martian icy surfaces. We covered the scientific background and presented the ExoMars Trace Gas Orbiter mission and the nadir channel data of the NOMAD instrument on which we base our work. An instrumental calibration was required and is presented. A first analysis from the calibrated data have shown the ability of NOMAD to detect CO_2 surface ice.

Specific perspectives are presented in part II and III for future works. More general perspectives of this work are possible. The results obtained during this PhD research project have shown that it is mandatory to use a realistic radiative transfer model that accurately integrates the nonlinear effects of the light path within a planetary regolith to undertake investigation of the ice microphysics. Some parameters are strongly correlated and the solutions can be multiple for a single parameter. This is also why a robust inversion technique should be preferred, at the cost of a computation time that can be long. The approach used here is perfectly applicable to any near-infrared data of an icy surface, and therefore the prospects for investigations are very numerous (Mars, the Jovian icy moons, Enceladus and other icy moons of Saturn, Pluto). This approach will further benefit from future datasets with higher spatial and/or spectral resolution (NASA/EuropaClipper, ESA/JUICE, JWST/NIRSpec) and this work is therefore only the beginning of a long project to characterize the ices of the solar system.

Bibliography

Anderson, J. D., Lau, E. L., Sjogren, W. L., Schubert, G., Moore, W. B., dec 1996. Gravitational constraints on the internal structure of ganymede. Nature 384 (6609), 541–543.

Anderson, J. D., Schubert, G., Jacobson, R. A., Lau, E. L., Moore, W. B., Sjogren, W. L., jun 1998a. Distribution of rock, metals, and ices in callisto. Science 280 (5369), 1573–1576.

Anderson, J. D., Schubert, G., Jacobson, R. A., Lau, E. L., Moore, W. B., Sjogren, W. L., sep 1998b. Europa's differentiated internal structure: Inferences from four galileo encounters. Science 281 (5385), 2019–2022.

Andrieu, F., Schmidt, F., Douté, S., Chassefière, E., nov 2018. Ice state evolution during spring in richardson crater and mars. Icarus 315, 158–173.

Andrieu, F., Schmidt, F., Schmitt, B., Douté, S., Brissaud, O., sep 2015. Radiative transfer model for contaminated slabs: experimental validations. Applied Optics.

Andrieu, F., Schmidt, F., Schmitt, B., Douté, S., Brissaud, O., sep 2016. Retrieving the characteristics of slab ice covering snow by remote sensing. The Cryosphere 10 (5), 2113–2128.

Appéré, T., Schmitt, B., Langevin, Y., Douté, S., Pommerol, A., Forget, F., Spiga, A., Gondet, B., Bibring, J.-P., may 2011. Winter and spring evolution of northern seasonal deposits on mars from OMEGA on mars express. Journal of Geophysical Research 116 (E5).

B. Schmitt, C. De Berg, M. F., Jan. 1995. Solar System Ices. Springer Netherlands.
URL https://www.ebook.de/de/product/6700422/solar_system_ices.html

Barr, A. C., Canup, R. M., nov 2008. Constraints on gas giant satellite formation from the interior states of partially differentiated satellites. Icarus 198 (1), 163–177.

Belgacem, I., Schmidt, F., Jonniaux, G., mar 2020. Regional study of europa's photometry. Icarus 338, 113525.

Belgacem, I., Schmidt, F., Jonniaux, G., nov 2021. Regional study of ganymede's photometry. Icarus 369, 114631.

Belton, M. J., Team, G. I., jan 2000. Results of the galileo solid state imaging (SSI) experiment. Advances in Space Research 26 (10), 1641–1647.

Berdis, J. R., Gudipati, M. S., Murphy, J. R., Chanover, N. J., may 2020. Europa's surface water ice crystallinity: Discrepancy between observations and thermophysical and particle flux modeling. Icarus 341, 113660.

Bouquety, A., Sejourne, A., Costard, F., Mercier, D., Bouley, S., jun 2019. Morphometric evidence of a 3 and6 ga glacial valleys and glacial cirques in martian highlands: South of terra sabaea. Geomorphology 334, 91–111.

Braak, C. J. F. T., sep 2006. A markov chain monte carlo version of the genetic algorithm differential evolution: easy bayesian computing for real parameter spaces. Statistics and Computing 16 (3), 239–249.

Brown, M. E., Hand, K. P., mar 2013. SALTS AND RADIATION PRODUCTS ON THE SURFACE OF EUROPA. The Astronomical Journal 145 (4), 110.

Brown, M. E., Hill, R. E., mar 1996. Discovery of an extended sodium atmosphere around europa. Nature 380 (6571), 229–231.

Brown, R. H., Cruikshank, D. P., Tokunaga, A. T., Smith, R. G., Clark, R. N., may 1988. Search for volatiles on icy satellites. Icarus 74 (2), 262–271.

Burchell, M., Cole, M., Ratcliff, P., aug 1996. Light flash and ionization from hypervelocity impacts on ice. Icarus 122 (2), 359–365.

Byrd, R. H., Lu, P., Nocedal, J., Zhu, C., sep 1995. A limited memory algorithm for bound constrained optimization. SIAM Journal on Scientific Computing 16 (5), 1190–1208.

Calvin, W. M., Clark, R. N., Brown, R. H., Spencer, J. R., 1995. Spectra of the icy galilean satellites from 0.2 to 5 μm: A compilation, new observations, and a recent summary. Journal of Geophysical Research 100 (E9), 19041.

Carlson, R., Anderson, M., Johnson, R., Schulman, M., Yavrouian, A., jun 2002. Sulfuric acid production on europa: The radiolysis of sulfur in water ice. Icarus 157 (2), 456–463.

Carlson, R., Anderson, M., Mehlman, R., Johnson, R., oct 2005. Distribution of hydrate on europa: Further evidence for sulfuric acid hydrate. Icarus 177 (2), 461–471.

Carlson, R., Weissman, P., Smythe, W., and, J. M., may 1992. Near-infrared mapping spectrometer experiment on galileo. Space Science Reviews 60 (1-4).

Carlson, R. W., Anderson, M. S., Johnson, R. E., Smythe, W. D., Hendrix, A. R., Barth, C. A., Soderblom, L. A., Hansen, G. B., McCord, T. B., Dalton, J. B., Clark, R. N., Shirley, J. H., Ocampo, A. C., Matson, D. L., mar 1999a. Hydrogen peroxide on the surface of europa. Science 283 (5410), 2062–2064.

Carlson, R. W., Johnson, R. E., Anderson, M. S., oct 1999b. Sulfuric acid on europa and the radiolytic sulfur cycle. Science 286 (5437), 97–99.

Carlson, R. W., Smythe, W. D., Lopes-Gautier, R. M. C., Davies, A. G., Kamp, L. W., Mosher, J. A., Soderblom, L. A., Leader, F. E., Mehlman, R., Clark, R. N., Fanale, F. P., oct 1997. The distribution of sulfur dioxide and other infrared absorbers on the surface of io. Geophysical Research Letters 24 (20), 2479–2482.

Carr, M., Apr. 1995. The martian drainage system and the origin of valley networks and fretted channels. Journal of Geophysical Research 100.

Carr, M. H., Belton, M. J. S., Chapman, C. R., Davies, M. E., Geissler, P., Greenberg, R., McEwen, A. S., Tufts, B. R., Greeley, R., Sullivan, R., Head, J. W., Pappalardo, R. T., Klaasen, K. P., Johnson, T. V., Kaufman, J., Senske, D., Moore, J., Neukum, G., Schubert, G., Burns, J. A., Thomas, P., Veverka, J., jan 1998. Evidence for a subsurface ocean on europa. Nature 391 (6665), 363–365.

Cassen, P., Reynolds, R. T., Peale, S. J., sep 1979. Is there liquid water on europa? Geophysical Research Letters 6 (9), 731–734.

Chance, K., Kurucz, R., jun 2010. An improved high-resolution solar reference spectrum for earth's atmosphere measurements in the ultraviolet and visible and and near infrared. Journal of Quantitative Spectroscopy and Radiative Transfer 111 (9), 1289–1295.

Chandrasekhar, S., 1960. Radiative transfer. New York: Dover.

Chang, P. C., Walker, J., Hopcraft, K., dec 2005. Ray tracing in absorbing media 96 (3-4), 327–341.

Christensen, P. R., Bandfield, J. L., Hamilton, V. E., Ruff, S. W., Kieffer, H. H., Titus, T. N., Malin, M. C., Morris, R. V., Lane, M. D., Clark, R. L., Jakosky, B. M., Mellon, M. T., Pearl, J. C., Conrath, B. J., Smith, M. D., Clancy, R. T., Kuzmin, R. O., Roush, T., Mehall, G. L., Gorelick, N., Bender, K., Murray, K., Dason, S., Greene, E., Silverman, S., Greenfield, M., oct 2001. Mars global surveyor thermal emission spectrometer experiment: Investigation description and surface science results. Journal of Geophysical Research: Planets 106 (E10), 23823–23871.

Clampin, M., jan 2008. The james webb space telescope (JWST). Advances in Space Research 41 (12), 1983–1991.

Clancy, R. T., 2003. Mars aerosol studies with the MGS TES emission phase function observations: Optical depths and particle sizes and and ice cloud types versus latitude and solar longitude. Journal of Geophysical Research 108 (E9).

Clancy, R. T., Lee, S. W., sep 1991. A new look at dust and clouds in the mars atmosphere: analysis of emission-phase-function sequences from global viking IRTM observations. Icarus 93 (1), 135–158.

Clark, R. N., nov 1980. Ganymede, europa, callisto, and saturn's rings: Compositional analysis from reflectance spectroscopy. Icarus 44 (2), 388–409.

Clark, R. N., Carlson, R., Grundy, W., Noll, K., apr 2012. Observed ices in the solar system. In: The Science of Solar System Ices. Springer New York, pp. 3–46.

Collins, G. C., Head, J. W., Pappalardo, R. T., Spaun, N. A., jan 2000. Evaluation of models for the formation of chaotic terrain on europa. Journal of Geophysical Research: Planets 105 (E1), 1709–1716.

Comodi, P., Fastelli, M., Maturilli, A., Balic-Zunic, T., Zucchini, A., feb 2021. Emissivity and reflectance spectra at different temperatures of hydrated and anhydrous sulphates: A contribution to investigate the composition and dynamic of icy planetary bodies. Icarus 355, 114132.

Cooper, J., jan 2001. Energetic ion and electron irradiation of the icy galilean satellites. Icarus 149 (1), 133–159.

Craft, K. L., Patterson, G. W., Lowell, R. P., Germanovich, L., aug 2016. Fracturing and flow: Investigations on the formation of shallow water sills on europa. Icarus 274, 297–313.

Cruz-Mermy, G., Schmidt, F., Andrieu, F., Cornet, T., Belgacem, I., Altobelli, N., apr 2023. Selection of chemical species for europa's surface using galileo/NIMS. Icarus 394, 115379.

Cruz-Mermy, G., Schmidt, F., Thomas, I., Daerden, F., Ristic, B., Patel, M., Lopez-Moreno, J.-J., Bellucci, G., Vandaele, A., sep 2022. Calibration of NOMAD on ExoMars trace gas orbiter: Part 3 - LNO validation and instrument stability. Planetary and Space Science 218, 105399.

Cubillos, P., Harrington, J., Loredo, T. J., Lust, N. B., Blecic, J., Stemm, M., dec 2016. ON CORRELATED-NOISE ANALYSES APPLIED TO EXOPLANET LIGHT CURVES. The Astronomical Journal 153 (1), 3.

Culberg, R., Schroeder, D. M., Steinbrügge, G., apr 2022. Double ridge formation over shallow water sills on jupiter's moon europa. Nature Communications 13 (1).

Dalton, J., Prieto-Ballesteros, O., Kargel, J., Jamieson, C., Jolivet, J., Quinn, R., oct 2005. Spectral comparison of heavily hydrated salts with disrupted terrains on europa. Icarus 177 (2), 472–490.

Dalton, J. B., nov 2007. Linear mixture modeling of europa's non-ice material based on cryogenic laboratory spectroscopy. Geophysical Research Letters 34 (21).

Dalton, J. B., Pitman, K. M., sep 2012. Low temperature optical constants of some hydrated sulfates relevant to planetary surfaces. Journal of Geophysical Research: Planets 117 (E9), n/a–n/a.

de Pater, I., Lissauer, J. J., dec 2014. Planetary Sciences. Cambridge University Press.

Domingue, D., Hapke, B., sep 1992. Disk-resolved photometric analysis of european terrains. Icarus 99 (1), 70–81.

Domingue, D., Hapke, B., Lockwood, G., Thompson, D., mar 1991. Europa's phase curve: Implications for surface structure. Icarus 90 (1), 30–42.

Douté, S., Lopes, R., Kamp, L. W., Carlson, R., Schmitt, B., may 2004. Geology and activity around volcanoes on io from the analysis of NIMS spectral images. Icarus 169 (1), 175–196.

Douté, S., Schmitt, B., Langevin, Y., Bibring, J.-P., Altieri, F., Bellucci, G., Gondet, B., Poulet, F., jan 2007. South pole of mars: Nature and composition of the icy terrains from mars express OMEGA observations. Planetary and Space Science 55 (1-2), 113–133.

Eichhorn, K., Grün, E., jun 1993. High-velocity impacts of dust particles in low-temperature water ice. Planetary and Space Science 41 (6), 429–433.

Eilers, Paul, Boelens, Hans, Nov. 2005. Baseline corection with asymmetric least squares smoothing.

Erard, S., Mustard, J., Murchie, S., Bibring, J.-P., Cerroni, P., Coradini, A., oct 1994. Martian aerosols: Near-infrared spectral properties and effects on the observation of the surface. Icarus 111 (2), 317–337.

Evans, K. F., feb 1998. The spherical harmonics discrete ordinate method for three-dimensional atmospheric radiative transfer. Journal of the Atmospheric Sciences 55 (3), 429–446.

Fagents, S. A., dec 2003. Considerations for effusive cryovolcanism on europa: The post-galileo perspective. Journal of Geophysical Research: Planets 108 (E12).

Fanale, F. P., Li, Y.-H., Carlo, E. D., Farley, C., Sharma, S. K., Horton, K., Granahan, J. C., jul 2001. An experimental estimate of europa's "ocean" composition independent of galileo orbital remote sensing. Journal of Geophysical Research: Planets 106 (E7), 14595–14600.

Fastelli, M., Comodi, P., Schmitt, B., Beck, P., Poch, O., Sassi, P., Zucchini, A., aug 2022. Reflectance spectra (1–5 μm) at low temperatures and different grain sizes of ammonium-bearing minerals relevant for icy bodies. Icarus 382, 115055.

Feldman, W. C., 2004. Global distribution of near-surface hydrogen on mars. Journal of Geophysical Research 109 (E9).

Fernando, J., Schmidt, F., Ceamanos, X., Pinet, P., Douté, S., Daydou, Y., mar 2013. Surface reflectance of mars observed by CRISM/MRO: 2. estimation of surface photometric properties in gusev crater and meridiani planum. Journal of Geophysical Research: Planets 118 (3), 534–559.

Fernando, J., Schmidt, F., Douté, S., sep 2016. Martian surface microtexture from orbital CRISM multi-angular observations: A new perspective for the characterization of the geological processes. Planetary and Space Science 128, 30–51.

Figueredo, P. H., 2002. Geology and origin of europa's “mitten” feature (murias chaos). Journal of Geophysical Research 107 (E5).

Fiorenza, C., Formisano, V., aug 2005. A solar spectrum for PFS data analysis. Planetary and Space Science 53 (10), 1009–1016.

Forget, F., Hourdin, F., Fournier, R., Hourdin, C., Talagrand, O., Collins, M., Lewis, S. R., Read, P. L., Huot, J.-P., oct 1999. Improved general circulation models of the martian atmosphere from the surface to above 80 km. Journal of Geophysical Research: Planets 104 (E10), 24155–24175.

Gabasova, L., 2021. Composition of the surface of pluto by spectro-imagery. new horizons mission. Ph.D. thesis, Université Grenoble Alpes.

Gaidos, E. J., Nimmo, F., jun 2000. Tectonics and water on europa. Nature 405 (6787), 637–637.

Geissler, P., 2015. Cryovolcanism in the outer solar system. In: The Encyclopedia of Volcanoes. Elsevier, pp. 763–776.

Geissler, P., Greenberg, R., Hoppa, G., McEwen, A., Tufts, R., Phillips, C., Clark, B., Ockert-Bell, M., Helfenstein, P., Burns, J., Veverka, J., Sullivan, R., Greeley, R., Pappalardo, R., Head, J., Belton, M., Denk, T., sep 1998. Evolution of lineaments on europa: Clues from galileo multispectral imaging observations. Icarus 135 (1), 107–126.

Gelman, A., Rubin, D. B., nov 1992. Inference from iterative simulation using multiple sequences. Statistical Science 7 (4).

Grasset, O., Dougherty, M., Coustenis, A., Bunce, E., Erd, C., Titov, D., Blanc, M., Coates, A., Drossart, P., Fletcher, L., Hussmann, H., Jaumann, R., Krupp, N., Lebreton, J.-P., Prieto-Ballesteros, O., Tortora, P., Tosi, F., Hoolst, T. V., apr 2013. JUpiter ICy moons explorer (JUICE): An ESA mission to orbit ganymede and to characterise the jupiter system. Planetary and Space Science 78, 1–21.

Greeley, R., Figueredo, P. H., Williams, D. A., Chuang, F. C., Klemaszewski, J. E., Kadel, S. D., Prockter, L. M., Pappalardo, R. T., Head, J. W., Collins, G. C., Spaun, N. A., Sullivan, R. J., Moore, J. M., Senske, D. A., Tufts, B. R., Johnson, T. V., Belton, M. J. S., Tanaka, K. L., sep 2000. Geologic mapping of europa. Journal of Geophysical Research: Planets 105 (E9), 22559–22578.

Greeley, R., Sullivan, R., Klemaszewski, J., Homan, K., Head, J. W., Pappalardo, R. T., Veverka, J., Clark, B. E., Johnson, T. V., Klaasen, K. P., Belton, M., Moore, J., Asphaug, E., Carr, M. H., Neukum, G., Denk, T., Chapman, C. R., Pilcher, C. B., Geissler, P. E., Greenberg, R., Tufts, R., sep 1998. Europa: Initial galileo geological observations. Icarus 135 (1), 4–24.

Greenberg, R., oct 1999. Chaos on europa. Icarus 141 (2), 263–286.

Greenberg, R., Geissler, P., Hoppa, G., Tufts, B., Durda, D. D., Pappalardo, R., Head, J. W., Greeley, R., Sullivan, R., Carr, M. H., sep 1998. Tectonic processes on europa: Tidal stresses, mechanical response, and visible features. Icarus 135 (1), 64–78.

Grynko, Y., Shkuratov, Y., may 2003. Scattering matrix calculated in geometric optics approximation for semitransparent particles faceted with various shapes 78 (3-4), 319–340.

Grynko, Y., Shkuratov, Y., jul 2007. Ray tracing sumulation of light scattering by spherical clusters consisting of particles with different shapes 106 (1-3), 56–62.

Guillot, T., Stevenson, D. J., Hubbard, W. B., Saumon, D., 2004. The interior of Jupiter.

Hall, D. T., Strobel, D. F., Feldman, P. D., McGrath, M. A., Weaver, H. A., feb 1995. Detection of an oxygen atmosphere on jupiter's moon europa. Nature 373 (6516), 677–679.

Hand, K. P., Berisford, D., Daimaru, T., Foster, J., Hofmann, A. E., Furst, B., dec 2019. Penitente formation is unlikely on europa. Nature Geoscience 13 (1), 17–19.

Hand, K. P., Brown, M. E., mar 2013. Keck ii observations of hemispherical differences in h2o2 on europa. Astrophysical Journal Letters 766 (2), L21.

Hand, K. P., Carlson, R. W., may 2015. Europa's surface color suggests an ocean rich with sodium chloride. Geophysical Research Letters 42 (9), 3174–3178.

Hand, K. P., Carlson, R. W., Chyba, C. F., dec 2007. Energy, chemical disequilibrium, and geological constraints on europa. Astrobiology 7 (6), 1006–1022.

Hand, K. P., Chyba, C. F., Carlson, R. W., Cooper, J. F., jun 2006. Clathrate hydrates of oxidants in the ice shell of europa. Astrobiology 6 (3), 463–482.

Hanley, J., Chevrier, V. F., Barrows, R. S., Swaffer, C., Altheide, T. S., aug 2015. Near- and mid-infrared reflectance spectra of hydrated oxychlorine salts with implications for mars. Journal of Geophysical Research: Planets 120 (8), 1415–1426.

Hanley, J., Dalton, J. B., Chevrier, V. F., Jamieson, C. S., Barrows, R. S., nov 2014. Reflectance spectra of hydrated chlorine salts: The effect of temperature with implications for europa. Journal of Geophysical Research: Planets 119 (11), 2370–2377.

Hansen, C., Thomas, N., Portyankina, G., McEwen, A., Becker, T., Byrne, S., Herkenhoff, K., Kieffer, H., Mellon, M., jan 2010. HiRISE observations of gas sublimation-driven activity in mars' southern polar regions: I. erosion of the surface. Icarus 205 (1), 283–295.

Hansen, G. B., 2004. Amorphous and crystalline ice on the galilean satellites: A balance between thermal and radiolytic processes. Journal of Geophysical Research 109 (E1).

Hapke, B., apr 1981. Bidirectional reflectance spectroscopy: 1. theory 86 (B4), 3039–3054.

Hapke, B., jul 1984. Bidirectional reflectance spectroscopy 59 (1), 41–59.

Hapke, B., aug 1986. Bidirectional reflectance spectroscopy 67 (2), 264–280.

Hapke, B., sep 1993. Theory of Reflectance and Emittance Spectroscopy. Cambridge University Press.

Hapke, B., jun 2002. Bidirectional reflectance spectroscopy 157 (2), 523–534.

Hapke, B., nov 2012. Bidirectional reflectance spectroscopy 7 221 (2), 1079–1083.

Hapke, B., feb 2013. Comment on "a critical assessment of the hapke photometric model" by y. shkuratov et al. Journal of Quantitative Spectroscopy and Radiative Transfer 116, 184–190.

Hapke, B., Nelson, R., Smythe, W., may 1998. The opposition effect of the moon: Coherent BackscatterandShadow hiding 133 (1), 89–97.

Harmon, J. K., Slade, M. A., oct 1992. Radar mapping of mercury: Full-disk images and polar anomalies. Science 258 (5082), 640–643.

Harrington, J., Himes, M. D., Cubillos, P. E., Blecic, J., Rojo, P. M., Challener, R. C., Lust, N. B., Bowman, M. O., Blumenthal, S. D., Dobbs-Dixon, I., Foster, A. S. D., Foster, A. J., Green, M. R., Loredo, T. J., McIntyre, K. J., Stemm, M. M., Wright, D. C., apr 2022. An open-source bayesian atmospheric radiative transfer (BART) code. i. design, tests, and application to exoplanet HD 189733b. The Planetary Science Journal 3 (4), 80.

Harris, D. L., 1961. Photometry and colorimetry of planets and satellites. In: Kuiper, G. P., Middlehurst, B. M. (Eds.), Planets and Satellites. https://doi.org/10.1016/0019-1035(80)90033-0, p. 272.
URL https://ui.adsabs.harvard.edu/abs/1961plsa.book..272H

Hase, F., Wallace, L., McLeod, S. D., Harrison, J. J., Bernath, P. F., mar 2010. The ACE-FTS atlas of the infrared solar spectrum. Journal of Quantitative Spectroscopy and Radiative Transfer 111 (4), 521–528.

Hastings, W. K., apr 1970. Monte carlo sampling methods using markov chains and their applications. Biometrika 57 (1), 97–109.

Head, J. W., Pappalardo, R. T., nov 1999. Brine mobilization during lithospheric heating on europa: Implications for formation of chaos terrain, lenticula texture, and color variations. Journal of Geophysical Research: Planets 104 (E11), 27143–27155.

Henyey, L. C., Greenstein, J. L., jan 1941. Diffuse radiation in the galaxy 93, 70.

Hess, S. L., Ryan, J. A., Tillman, J. E., Henry, R. M., Leovy, C. B., mar 1980. The annual cycle of pressure on mars measured by viking landers 1 and 2. Geophysical Research Letters 7 (3), 197–200.

Hobley, D. E. J., Moore, J. M., Howard, A. D., Umurhan, O. M., oct 2018. Formation of metre-scale bladed roughness on europa's surface by ablation of ice. Nature Geoscience 11 (12), 901–904.

Hoppa, G. V., Tufts, B. R., Greenberg, R., Geissler, P. E., sep 1999. Formation of cycloidal features on europa. Science 285 (5435), 1899–1902.

Hussmann, H., Spohn, T., oct 2004. Thermal-orbital evolution of io and europa. Icarus 171 (2), 391–410.

Jaccard, C., 1976. P. v. hobbs ice physics. oxford, clarendon press, 1974. xvii, 837 p. £29. Journal of Glaciology 17 (75), 155–156.

Kargel, J. S., dec 1991. Brine volcanism and the interior structures of asteroids and icy satellites. Icarus 94 (2), 368–390.

Kargel, J. S., dec 1992. Ammonia-water volcanism on icy satellites: Phase relations at 1 atmosphere. Icarus 100 (2), 556–574.

Kargel, J. S., Kaye, J. Z., Head, J. W., Marion, G. M., Sassen, R., Crowley, J. K., Ballesteros, O. P., Grant, S. A., Hogenboom, D. L., nov 2000. Europa's crust and ocean: Origin, composition, and the prospects for life. Icarus 148 (1), 226–265.

Kaufmann, E., Komle, N., Kargl, G., jan 2007. Laboratory simulation and theoretical modelling of the solid-state greenhouse effect. Advances in Space Research 39 (3), 370–374.

Khurana, K. K., Kivelson, M. G., Stevenson, D. J., Schubert, G., Russell, C. T., Walker, R. J., Polanskey, C., oct 1998. Induced magnetic fields as evidence for subsurface oceans in europa and callisto. Nature 395 (6704), 777–780.

Kieffer, H., nov 2001. TES mapping of mars' north seasonal cap. Icarus 154 (1), 162–180.

Kieffer, H. H., 1979. Mars south polar spring and summer temperatures: A residual CO2frost. Journal of Geophysical Research 84 (B14), 8263.

Kieffer, H. H., Christensen, P. R., Titus, T. N., aug 2006. CO2 jets formed by sublimation beneath translucent slab ice in mars' seasonal south polar ice cap. Nature 442 (7104), 793–796.

King, O., Fletcher, L. N., Ligier, N., mar 2022. Compositional mapping of europa using MCMC modeling of near-IR VLT/SPHERE and galileo/NIMS observations. The Planetary Science Journal 3 (3), 72.

Kissel, J., Krueger, F. R., jan 1987. Ion formation by impact of fast dust particles and comparison with related techniques. Applied Physics A Solids and Surfaces 42 (1), 69–85.

Kivelson, M., Khurana, K., Volwerk, M., jun 2002. The permanent and inductive magnetic moments of ganymede. Icarus 157 (2), 507–522.

Kubelka, P., may 1948. New contributions to the optics of intensely light-scattering materials part i 38 (5), 448.

Kuiper, G. P., Nov. 1957. Infrared observations of planets and satellites. The Astronomical Journal 62, 245–245.
URL https://ui.adsabs.harvard.edu/abs/1957AJ.....62..245K

Küppers, M., Schneider, N. M., feb 2000. Discovery of chlorine in the io torus. Geophysical Research Letters 27 (4), 513–516.

Lane, A. L., Nelson, R. M., Matson, D. L., jul 1981. Evidence for sulphur implantation in europa's UV absorption band. Nature 292 (5818), 38–39.

Langevin, Y., Bibring, J.-P., Montmessin, F., Forget, F., Vincendon, M., Douté, S., Poulet, F., Gondet, B., jul 2007. Observations of the south seasonal cap of mars during recession in 2004-2006 by the OMEGA visible/near-infrared imaging spectrometer on board mars express. Journal of Geophysical Research: Planets 112 (E8).

Langevin, Y., Douté, S., Vincendon, M., Poulet, F., Bibring, J.-P., Gondet, B., Schmitt, B., Forget, F., aug 2006. No signature of clear CO2 ice from the 'cryptic' regions in mars' south seasonal polar cap. Nature 442 (7104), 790–792.

Lapotre, M. G. A., Ehlmann, B. L., Minson, S. E., may 2017. A probabilistic approach to remote compositional analysis of planetary surfaces. Journal of Geophysical Research: Planets 122 (5), 983–1009.

Laskar, J., Correia, A., Gastineau, M., Joutel, F., Levrard, B., Robutel, P., aug 2004. Long term evolution and chaotic diffusion of the insolation quantities of mars. Icarus 170 (2), 343–364.

Leblanc, F., Johnson, R., Brown, M., sep 2002. Europa's sodium atmosphere: An ocean source? Icarus 159 (1), 132–144.

Leighton, R., Murray, B., Jul. 1966. Behavior of carbon dioxide and other volatiles on mars. Science 153.

Leonard, E., D.A., P., D.A., S., G.C., C., 2018. The europa global geologic map. Planetary Geologic Mappers Annual Meeting.

Lesage, E., Massol, H., Howell, S. M., Schmidt, F., jul 2022. Simulation of freezing cryomagma reservoirs in viscoelastic ice shells. The Planetary Science Journal 3 (7), 170.

Lesage, E., Massol, H., Schmidt, F., jan 2020. Cryomagma ascent on europa. Icarus 335, 113369.

Lesage, E., Schmidt, F., Andrieu, F., Massol, H., jun 2021. Constraints on effusive cryovolcanic eruptions on europa using topography obtained from galileo images. Icarus 361, 114373.

Ligier, N., Poulet, F., Carter, J., Brunetto, R., Gourgeot, F., may 2016. VLT/SINFONI OBSERVATIONS OF EUROPA: NEW INSIGHTS INTO THE SURFACE COMPOSITION. The Astronomical Journal 151 (6), 163.

Liuzzi, G., Villanueva, G. L., Mumma, M. J., Smith, M. D., Daerden, F., Ristic, B., Thomas, I., Vandaele, A. C., Patel, M. R., Lopez-Moreno, J.-J., Bellucci, G., mar 2019. Methane on mars: New insights into the sensitivity of CH4 with the NOMAD/ExoMars spectrometer through its first in-flight calibration. Icarus 321, 671–690.

Lloyd, S., mar 1982. Least squares quantization in PCM. IEEE Transactions on Information Theory 28 (2), 129–137.

Lucarini, V., Peiponen, K.-E., Saarinen, J. J., Vartiainen, E. M., Apr. 2005. Kramers-Kronig Relations in Optical Materials Research. Springer Berlin Heidelberg.

Lucchita, B. K., Soderblom, L., 1982. The Geology of Europa. University of Arizona Press, Tucson.

Lyons, L., Nov. 2007. A particle physicist's perspective on astrostatistics. In: Babu, G. J., Feigelson, E. D. (Eds.), Statistical Challenges in Modern Astronomy IV. Vol. 371 of Astronomical Society of the Pacific Conference Series. p. 361.
URL https://ui.adsabs.harvard.edu/abs/2007ASPC..371..361L

Mahieux, A., 2011. Inversion of the infrared spectra recorded by the soir instrument on board venus express. Ph.D. thesis, Université Libre de Bruxelle - Faculté des Sciences Appliquées - Laboratoire de Chimie quantique et Photophysique.

Manga, M., Michaut, C., apr 2017. Formation of lenticulae on europa by saucer-shaped sills. Icarus 286, 261–269.

Mastrapa, R. M., Sandford, S. A., Roush, T. L., Cruikshank, D. P., Ore, C. M. D., jul 2009. Optical constant of amorphous and crystalline h2o ice: 2.5-22 μm (4000-455 cm–1) optical constant of h2o-ice 701 (2), 1347–1356.

McCord, T. B., Hansen, G. B., Fanale, F. P., Carlson, R. W., Matson, D. L., Johnson, T. V., Smythe, W. D., Crowley, J. K., Martin, P. D., Ocampo, A., Hibbitts, C. A., and, J. C. G., may 1998. Salts on europa's surface detected by galileo's near infrared mapping spectrometer. Science 280 (5367), 1242–1245.

McCord, T. B., Hansen, G. B., Matson, D. L., Johnson, T. V., Crowley, J. K., Fanale, F. P., Carlson, R. W., Smythe, W. D., Martin, P. D., Hibbitts, C. A., Granahan, J. C., Ocampo, A., may 1999. Hydrated salt minerals on europa's surface from the galileo near-infrared mapping spectrometer (NIMS) investigation. Journal of Geophysical Research: Planets 104 (E5), 11827–11851.

McCord, T. B., Orlando, T. M., Teeter, G., Hansen, G. B., Sieger, M. T., Petrik, N. G., Keulen, L. V., feb 2001. Thermal and radiation stability of the hydrated salt minerals epsomite, mirabilite, and natron under europa environmental conditions. Journal of Geophysical Research: Planets 106 (E2), 3311–3319.

McEwen, A. S., mar 1988. Global color and albedo variations on io. Icarus 73 (3), 385–426.

McKinnon, W. B., apr 1999. Convective instability in europa's floating ice shell. Geophysical Research Letters 26 (7), 951–954.

Meador, W. E., Weaver, W. R., 1975. A photometric function for diffuse reflection by particulate materials. NASA Tech, Note D-7903.

Metropolis, N., Rosenbluth, A. W., Rosenbluth, M. N., Teller, A. H., Teller, E., jun 1953. Equation of state calculations by fast computing machines. The Journal of Chemical Physics 21 (6), 1087–1092.

Minnaert, M., may 1941. The reciprocity principle in lunar photometry 93, 403.

Mishra, I., Lewis, N., Lunine, J., Hand, K. P., Helfenstein, P., Carlson, R. W., MacDonald, R. J., sep 2021a. A comprehensive revisit of select galileo/NIMS observations of europa. The Planetary Science Journal 2 (5), 183.

Mishra, I., Lewis, N., Lunine, J., Helfenstein, P., MacDonald, R. J., Filacchione, G., Ciarniello, M., mar 2021b. Bayesian analysis of juno/JIRAM's NIR observations of europa. Icarus 357, 114215.

Miyamoto, H., Mitri, G., Showman, A. P., Dohm, J. M., oct 2005. Putative ice flows on europa: Geometric patterns and relation to topography collectively constrain material properties and effusion rates. Icarus 177 (2), 413–424.

Montmessin, F., 2004. Origin and role of water ice clouds in the martian water cycle as inferred from a general circulation model. Journal of Geophysical Research 109 (E10).

Moore, J., may 2001. Impact features on europa: Results of the galileo europa mission (GEM). Icarus 151 (1), 93–111.

Mosegaard, K., Tarantola, A., jul 1995. Monte carlo sampling of solutions to inverse problems. Journal of Geophysical Research: Solid Earth 100 (B7), 12431–12447.

Neefs, E., Vandaele, A. C., Drummond, R., Thomas, I. R., Berkenbosch, S., Clairquin, R., Delanoye, S., Ristic, B., Maes, J., Bonnewijn, S., Pieck, G., Equeter, E., Depiesse, C., Daerden, F., Ransbeeck, E. V., Nevejans, D., Rodriguez-Gómez, J., López-Moreno, J.-J., Sanz, R., Morales, R., Candini, G. P., Pastor-Morales, M. C., del Moral, B. A., Jeronimo-Zafra, J.-M., Gómez-López, J. M., Alonso-Rodrigo, G., Pérez-Grande, I., Cubas, J., Gomez-Sanjuan, A. M., Navarro-Medina, F., Thibert, T., Patel, M. R., Bellucci, G., Vos, L. D., Lesschaeve, S., Vooren, N. V., Moelans, W., Aballea, L., Glorieux, S., Baeke, A., Kendall, D., Neef, J. D., Soenen, A., Puech, P.-Y., Ward, J., Jamoye, J.-F., Diez, D., Vicario-Arroyo, A., Jankowski, M., sep 2015. NOMAD spectrometer on the ExoMars trace gas orbiter mission: part 1—design and manufacturing and testing of the infrared channels. Applied Optics 54 (28), 8494.

Ockert-Bell, M. E., Bell, J. F., Pollack, J. B., McKay, C. P., Forget, F., apr 1997. Absorption and scattering properties of the martian dust in the solar wavelengths. Journal of Geophysical Research: Planets 102 (E4), 9039–9050.

Pappalardo, R. T., jan 2010. Seeking europa's ocean. Proceedings of the International Astronomical Union 6 (S269), 101–114.

Pappalardo, R. T., Belton, M. J. S., Breneman, H. H., Carr, M. H., Chapman, C. R., Collins, G. C., Denk, T., Fagents, S., Geissler, P. E., Giese, B., Greeley, R., Greenberg, R., Head, J. W., Helfenstein, P., Hoppa, G., Kadel, S. D., Klaasen, K. P., Klemaszewski, J. E., Magee, K., McEwen, A. S., Moore, J. M., Moore, W. B., Neukum, G., Phillips, C. B., Prockter, L. M., Schubert, G., Senske, D. A., Sullivan, R. J., Tufts, B. R., Turtle, E. P., Wagner, R., Williams, K. K., oct 1999. Does europa have a subsurface ocean? evaluation of the geological evidence. Journal of Geophysical Research: Planets 104 (E10), 24015–24055.

Pappalardo, R. T., Head, J. W., Greeley, R., Sullivan, R. J., Pilcher, C., Schubert, G., Moore, W. B., Carr, M. H., Moore, J. M., Belton, M. J. S., Goldsby, D. L., jan 1998. Geological evidence for solid-state convection in europa's ice shell. Nature 391 (6665), 365–368.

Pappalardo, R. T., W., H. J., D., S. N., R., G., J., S. R., the Galileo SSI Team, 1998b. Classification of europan ridges and troughs and possible genetic sequence. Lunar Planet Sci. Conf.

Paranicas, C., Carlson, R. W., Johnson, R. E., feb 2001. Electron bombardment of europa. Geophysical Research Letters 28 (4), 673–676.

Pasquon, K., Gargani, J., Massé, M., Conway, S. J., aug 2016. Present-day formation and seasonal evolution of linear dune gullies on mars. Icarus 274, 195–210.

Phillips, C. B., Pappalardo, R. T., may 2014. Europa clipper mission concept: Exploring jupiter's ocean moon. Eos, Transactions American Geophysical Union 95 (20), 165–167.

Phillips, R. J., Davis, B. J., Tanaka, K. L., Byrne, S., Mellon, M. T., Putzig, N. E., Haberle, R. M., Kahre, M. A., Campbell, B. A., Carter, L. M., Smith, I. B., Holt, J. W., Smrekar, S. E., Nunes, D. C., Plaut, J. J., Egan, A. F., Titus, T. N., Seu, R., apr 2011. Massive CO2 ice deposits sequestered in the south polar layered deposits of mars. Science 332 (6031), 838–841.

Phillips, R. J., Zuber, M. T., Smrekar, S. E., Mellon, M. T., Head, J. W., Tanaka, K. L., Putzig, N. E., Milkovich, S. M., Campbell, B. A., Plaut, J. J., Safaeinili, A., Seu, R., Biccari, D., Carter, L. M., Picardi, G., Orosei, R., Mohit, P. S., Heggy, E., Zurek, R. W., Egan, A. F., Giacomoni, E., Russo, F., Cutigni, M., Pettinelli, E., Holt, J. W., Leuschen, C. J., Marinangeli, L., may 2008. Mars north polar deposits: Stratigraphy and age and and geodynamical response. Science 320 (5880), 1182–1185.

Pilorget, C., Forget, F., Millour, E., Vincendon, M., Madeleine, J., may 2011. Dark spots and cold jets in the polar regions of mars: New clues from a thermal model of surface CO2 ice. Icarus 213 (1), 131–149.

Pilorget, C., Vincendon, M., Poulet, F., dec 2013. A radiative transfer model to simulate light scattering in a compact granular medium using a monte-carlo approach: Validation and first applications 118 (12), 2488–2501.

Piqueux, S., 2003. Sublimation of mars's southern seasonal CO2ice cap and the formation of spiders. Journal of Geophysical Research 108 (E8).

Piqueux, S., Christensen, P. R., jun 2008. North and south subice gas flow and venting of the seasonal caps of mars: A major geomorphological agent. Journal of Geophysical Research 113 (E6).

Portyankina, G., Aye, K.-M., 2018. Co2-driven geomorphological processes : landscape evolution. In: Dynamic Mars. Elsevier.

Portyankina, G., Markiewicz, W. J., Thomas, N., Hansen, C. J., Milazzo, M., jan 2010. HiRISE observations of gas sublimation-driven activity in mars' southern polar regions: III. models of processes involving translucent ice. Icarus 205 (1), 311–320.

Portyankina, G., Merrison, J., Iversen, J., Yoldi, Z., Hansen, C., Aye, K.-M., Pommerol, A., Thomas, N., apr 2019. Laboratory investigations of the physical state of CO2 ice in a simulated martian environment. Icarus 322, 210–220.

Pospieszalska, M., Johnson, R., mar 1989. Magnetospheric ion bombardment profiles of satellites: Europa and dione. Icarus 78 (1), 1–13.

Pottier, A., Forget, F., Montmessin, F., Navarro, T., Spiga, A., Millour, E., Szantai, A., Madeleine, J.-B., jul 2017. Unraveling the martian water cycle with high-resolution global climate simulations. Icarus 291, 82–106.

Poulet, F., Gomez, C., Bibring, J.-P., Langevin, Y., Gondet, B., Pinet, P., Belluci, G., Mustard, J., jul 2007. Martian surface mineralogy from observatoire pour la minéralogie and l'eau and les glaces et l'activité on board the mars express spacecraft (OMEGA/MEx): Global mineral maps. Journal of Geophysical Research: Planets 112 (E8).

Poulet, F., Mangold, N., Platevoet, B., Bardintzeff, J.-M., Sautter, V., Mustard, J., Bibring, J.-P., Pinet, P., Langevin, Y., Gondet, B., Aléon-Toppani, A., may 2009. Quantitative compositional analysis of martian mafic regions using the MEx/OMEGA reflectance data. Icarus 201 (1), 84–101.

Prockter, L. M., 2005. Ice in the solar system. Johns Hopkins Apl Technical Digest https://doi.org/10.1126/science.258.5082.640 26, 175–188.

Pyo, T.-S., 2003. Blaze function and the groove shadowing effect.
URL https://www.naoj.org/staff/pyo/IRCS_and_Reduction/node12.html

Querry, M., 1987. Optical constants of minerals and other materials from the millimeter to the ultraviolet. Contractor Report CRDEC-CR-88009.

Quick, L. C., Barnouin, O. S., Prockter, L. M., Patterson, G. W., sep 2013. Constraints on the detection of cryovolcanic plumes on europa. Planetary and Space Science 86, 1–9.

Quick, L. C., Glaze, L. S., Baloga, S. M., mar 2017. Cryovolcanic emplacement of domes on europa. Icarus 284, 477–488.

Quick, L. C., Marsh, B. D., jun 2015. Constraining the thickness of europa's water–ice shell: Insights from tidal dissipation and conductive cooling. Icarus 253, 16–24.

Quick, L. C., Marsh, B. D., jun 2016. Heat transfer of ascending cryomagma on europa. Journal of Volcanology and Geothermal Research 319, 66–77.

Quirico, E., Schmitt, B., 2018. Near-ir optical constants of crystalline co2 ice at 179 k completed with 28k data.

Rathbun, J. A., Musser, G. S., Squyres, S. W., nov 1998. Ice diapirs on europa: Implications for liquid water. Geophysical Research Letters 25 (22), 4157–4160.

Reynolds, R. T., Cassen, P. M., feb 1979. On the internal structure of the major satellites of the outer planets. Geophysical Research Letters 6 (2), 121–124.

Robert T. Pappalardo, W. B. M., Jul. 2009. Europa. UNIV OF ARIZONA PR.
URL https://www.ebook.de/de/product/8203996/europa.html

Roth, L., oct 2021. A stable h2o atmosphere on europa's trailing hemisphere from HST images. Geophysical Research Letters 48 (20).

Roth, L., Saur, J., Retherford, K. D., Strobel, D. F., Feldman, P. D., McGrath, M. A., Nimmo, F., jan 2014. Transient water vapor at europa's south pole. Science 343 (6167), 171–174.

Schmidt, F., Bourguignon, S., jan 2019. Efficiency of BRDF sampling and bias on the average photometric behavior. Icarus 317, 10–26.

Schmidt, F., Douté, S., Schmitt, B., Vincendon, M., Bibring, J.-P., Langevin, Y., apr 2009. Albedo control of seasonal south polar cap recession on mars. Icarus 200 (2), 374–394.

Schmidt, F., Fernando, J., nov 2015. Realistic uncertainties on hapke model parameters from photometric measurement. Icarus 260, 73–93.

Schmidt, F., Portyankina, G., 2018. The exotic processes driving ephemeral seasonal surface change on mars. In: Dynamic Mars. Elsevier, pp. 157–186.

Schmitt, B., 2020. Near and mid-ir optical constants of crystalline h2o ice ih at 140-145k.

Schmitt, B., Bollard, P., Albert, D., Bonal, L., 2017a. Sshade/ghosst: "grenoble astrophysics and planetology solid spectroscopy and thermodynamics" database.

Schmitt, B., Bollard, P., Albert, D., Garenne, A., Gorbacheva, M., Bonal, L., Volcke, P., and, t. S. P. C., 2017b. Sshade: "solid spectroscopy hosting architecture of databases and expertise".

Schmitt, B., Quirico, E., Trotta, F., Grundy, W. M., 1998. Optical properties of ices from UV to infrared. In: Astrophysics and Space Science Library. Springer Netherlands, pp. 199–240.

Shepard, M. K., 2017. Planetary reflectance and basic scattering laws. Cambridge University Press, pp. 131–169.

Shirley, J. H., Jamieson, C. S., Dalton, J. B., aug 2016. Europa's surface composition from near-infrared observations: A comparison of results from linear mixture modeling and radiative transfer modeling. Earth and Space Science 3 (8), 326–344.

Shkuratov, Y., Bondarenko, S., Kaydash, V., Videen, G., Muñoz, O., Volten, H., jul 2007. Photometry and polarimetry of particulate surfaces and aerosol particles over a wide range of phase angles 106 (1-3), 487–508.

Shkuratov, Y., Kaydash, V., Korokhin, V., Velikodsky, Y., Petrov, D., Zubko, E., Stankevich, D., Videen, G., feb 2013. Response to the comment by b. hapke on "a critical assessment of the hapke photometric model". Journal of Quantitative Spectroscopy and Radiative Transfer 116, 191–195.

Shkuratov, Y., Petrov, D., Videen, G., nov 2003. Classical photometry of prefractal surfaces 20 (11), 2081.

Shkuratov, Y., Starukhina, L., Hoffmann, H., Arnold, G., feb 1999. A model of spectral albedo of particulate surfaces: Implications for optical properties of the moon. Icarus 137 (2), 235–246.

Shkuratov, Y. G., Stankevich, D. G., Petrov, D. V., Pinet, P. C., Cord, A. M., Daydou, Y. H., Chevrel, S. D., jan 2005. Interpreting photometry of regolith-like surfaces with different topographies: shadowing and multiple scattering 173 (1), 3–15.

Smith, M. D., nov 2002. The annual cycle of water vapor on mars as observed by the thermal emission spectrometer. Journal of Geophysical Research: Planets 107 (E11), 25–1–25–19.

Snieder, R., Trampert, J., 2003. Linear and nonlinear inverse problems. In: Geomatic Method for the Analysis of Data in the Earth Sciences. Springer Berlin Heidelberg, pp. 93–164.

Sotin, C., Head, J. W., Tobie, G., apr 2002. Europa: Tidal heating of upwelling thermal plumes and the origin of lenticulae and chaos melting. Geophysical Research Letters 29 (8), 74–1–74–4.

Spencer, J. R., feb 1987. Thermal segregation of water ice on the galilean satellites. Icarus 69 (2), 297–313.

Spencer, J. R., Calvin, W. M., dec 2002. Condensed o2 on europa and callisto. The Astronomical Journal 124 (6), 3400–3403.
URL https://arxiv.org/abs/1701.01467

Spiga, A., Faure, J., Madeleine, J.-B., Määttänen, A., Forget, F., apr 2013. Rocket dust storms and detached dust layers in the martian atmosphere. Journal of Geophysical Research: Planets 118 (4), 746–767.

Stamnes, K., Tsay, S.-C., Wiscombe, W., Jayaweera, K., jun 1988. Numerically stable algorithm for discrete-ordinate-method radiative transfer in multiple scattering and emitting layered media. Applied Optics 27 (12), 2502.

Stephan, K., Hibbitts, C., Hoffmann, H., Jaumann, R., mar 2008. Reduction of instrument-dependent noise in hyperspectral image data using the principal component analysis: Applications to galileo NIMS data. Planetary and Space Science 56 (3-4), 406–419.

Sullivan, R., Greeley, R., Homan, K., Klemaszewski, J., Belton, M. J. S., Carr, M. H., Chapman, C. R., Tufts, R., Head, J. W., Pappalardo, R., Moore, J., Thomas, P., the Galileo Imaging Team, jan 1998. Episodic plate separation and fracture infill on the surface of europa. Nature 391 (6665), 371–373.

Tan, S., Sekine, Y., Kuzuhara, M., mar 2022. Spatially resolved observations of europa's surface with subaru/IRCS at 1.0–1.8 μm: Upper limits to the abundances of hydrated cl-bearing salts. The Planetary Science Journal 3 (3), 70.

Tarantola, A., Jan. 2005. Inverse Problem Theory and Methods for Model Parameter Estimation. CAMBRIDGE.
URL http://www.ipgp.fr/~tarantola/Files/Professional/Books/InverseProblemTheory.pdf

Tarantola, A., Valette, B., 1982. Generalized nonlinear inverse problems solved using the least squares criterion. Reviews of Geophysics 20 (2), 219.

ter Braak, C. J. F., Vrugt, J. A., oct 2008. Differential evolution markov chain with snooker updater and fewer chains. Statistics and Computing 18 (4), 435–446.

Thomas, I. R., Aoki, S., Trompet, L., Robert, S., Depiesse, C., Willame, Y., Cruz-Mermy, G., Schmidt, F., Erwin, J. T., Vandaele, A. C., Daerden, F., Mahieux, A., Neefs, E., Ristic, B., Hetey, L., Berkenbosch, S., Clairquin, R., Beeckman, B., Patel, M. R., Lopez-Moreno, J. J., Bellucci, G., sep 2022. Calibration of NOMAD on ESA's ExoMars trace gas orbiter: Part 2 – the limb, nadir and occultation (LNO) channel. Planetary and Space Science 218, 105410.

Thomas, N., Portyankina, G., Hansen, C., Pommerol, A., mar 2011. HiRISE observations of gas sublimation-driven activity in mars' southern polar regions: IV. fluid dynamics models of CO2 jets. Icarus 212 (1), 66–85.

Tobie, G., 2003. Tidally heated convection: Constraints on europa's ice shell thickness. Journal of Geophysical Research 108 (E11).

Tobie, G., Mocquet, A., Sotin, C., oct 2005. Tidal dissipation within large icy satellites: Applications to europa and titan. Icarus 177 (2), 534–549.

Trotta, F., Schmitt, B., 2018. Mid-ir optical constants of amorpous h2o ia at 15k and crystalline h2o ih at 60k.

Trotta, R., 2017. Bayesian methods in cosmology.

Trumbo, S. K., Brown, M. E., Hand, K. P., aug 2019. H2o2 within chaos terrain on europa's leading hemisphere. The Astronomical Journal 158 (3), 127.

Trumbo, S. K., Brown, M. E., Hand, K. P., nov 2020. Endogenic and exogenic contributions to visible-wavelength spectra of europa's trailing hemisphere. The Astronomical Journal 160 (6), 282.

Twersky, V., feb 1962. Multiple scattering of waves and optical phenomena 52 (2), 145.

Vago, J., Witasse, O., Svedhem, H., Baglioni, P., Haldemann, A., Gianfiglio, G., Blancquaert, T., McCoy, D., de Groot, R., dec 2015. ESA ExoMars program: The next step in exploring mars. Solar System Research 49 (7), 518–528.

Vance, S. D., Panning, M. P., Stähler, S., Cammarano, F., Bills, B. G., Tobie, G., Kamata, S., Kedar, S., Sotin, C., Pike, W. T., Lorenz, R., Huang, H.-H., Jackson, J. M., Banerdt, B., jan 2018. Geophysical investigations of habitability in ice-covered ocean worlds. Journal of Geophysical Research: Planets 123 (1), 180–205.

Vandaele, A., Neefs, E., Drummond, R., Thomas, I., Daerden, F., Lopez-Moreno, J.-J., Rodriguez, J., Patel, M., Bellucci, G., Allen, M., Altieri, F., Bolsée, D., Clancy, T., Delanoye, S., Depiesse, C., Cloutis, E., Fedorova, A., Formisano, V., Funke, B., Fussen, D., Geminale, A., Gérard, J.-C., Giuranna, M., Ignatiev, N., Kaminski, J., Karatekin, O., Lefèvre, F., López-Puertas, M., López-Valverde, M., Mahieux, A., McConnell, J., Mumma, M., Neary, L., Renotte, E., Ristic, B., Robert, S., Smith, M., Trokhimovsky, S., Auwera, J. V., Villanueva, G., Whiteway, J., Wilquet, V., Wolff, M., dec 2015. Science objectives and performances of NOMAD and a spectrometer suite for the ExoMars TGO mission. Planetary and Space Science 119, 233–249.

Vandaele, A. C., , Lopez-Moreno, J.-J., Patel, M. R., Bellucci, G., Daerden, F., Ristic, B., Robert, S., Thomas, I. R., Wilquet, V., Allen, M., Alonso-Rodrigo, G., Altieri, F., Aoki, S., Bolsée, D., Clancy, T., Cloutis, E., Depiesse, C., Drummond, R., Fedorova, A., Formisano, V., Funke, B., González-Galindo, F., Geminale, A., Gérard, J.-C., Giuranna, M., Hetey, L., Ignatiev, N., Kaminski, J., Karatekin, O., Kasaba, Y., Leese, M., Lefèvre, F., Lewis, S. R., López-Puertas, M., López-Valverde, M., Mahieux, A., Mason, J., McConnell, J., Mumma, M., Neary, L., Neefs, E., Renotte, E., Rodriguez-Gomez, J., Sindoni, G., Smith, M., Stiepen, A., Trokhimovsky, A., Auwera, J. V., Villanueva, G., Viscardy, S., Whiteway, J., Willame, Y., Wolff, M., jun 2018. NOMAD and an integrated suite of three spectrometers for the ExoMars trace gas mission: Technical description and science objectives and expected performance. Space Science Reviews 214 (5).

Vandaele, A. C., Mahieux, A., Robert, S., Berkenbosch, S., Clairquin, R., Drummond, R., Letocart, V., Neefs, E., Ristic, B., Wilquet, V., Colomer, F., Belyaev, D., Bertaux, J.-L., sep 2013. Improved calibration of SOIR/venus express spectra. Optics Express 21 (18), 21148.

Villanueva, G., Smith, M., Protopapa, S., Faggi, S., Mandell, A., sep 2018. Planetary spectrum generator: An accurate online radiative transfer suite for atmospheres and comets and small bodies and exoplanets. Journal of Quantitative Spectroscopy and Radiative Transfer 217, 86–104.

Vincendon, M., Langevin, Y., Poulet, F., Bibring, J.-P., Gondet, B., jul 2007. Recovery of surface reflectance spectra and evaluation of the optical depth of aerosols in the near-IR using a monte carlo approach: Application to the OMEGA observations of high-latitude regions of mars. Journal of Geophysical Research: Planets 112 (E8).

Wahr, J., Selvans, Z. A., Mullen, M. E., Barr, A. C., Collins, G. C., Selvans, M. M., Pappalardo, R. T., mar 2009. Modeling stresses on satellites due to nonsynchronous rotation and orbital eccentricity using gravitational potential theory. Icarus 200 (1), 188–206.

Wendel, J., oct 2017. Geologic map of europa highlights targets for future exploration. Eos.

Wolff, M. J., Smith, M. D., Clancy, R. T., Arvidson, R., Kahre, M., Seelos, F., Murchie, S., Savijärvi, H., jun 2009. Wavelength dependence of dust aerosol single scattering albedo as observed by the compact reconnaissance imaging spectrometer. Journal of Geophysical Research 114.

Wordsworth, R. D., jun 2016. The climate of early mars. Annual Review of Earth and Planetary Sciences 44 (1), 381–408.

Zahnle, K., sep 2001. Differential cratering of synchronously rotating satellites by ecliptic comets. Icarus 153 (1), 111–129.

Zhu, C., Byrd, R. H., Lu, P., Nocedal, J., dec 1997. Algorithm 778: L-BFGS-b: Fortran subroutines for large-scale bound-constrained optimization. ACM Transactions on Mathematical Software 23 (4), 550–560.

Zolotov, M. Y., Shock, E. L., dec 2001. Composition and stability of salts on the surface of europa and their oceanic origin. Journal of Geophysical Research: Planets 106 (E12), 32815–32827.

List of Figures

List of Tables

Acronyms

- ACE - Atmospheric Chemistry Experiment
- ACS - Atmospheric Chemistry Suite
- ADC - Analog to Digital Convertor
- ADU - Analog to Digital Unit
- AOT - Aerosols Optical Thickness
- AOTF - Acousto Optic Tunable Filter
- AU - Astronomical Units
- BIRA-IASB - Royal Belgian Institute for Space Aeronomy
- CaSSIS - Color and Stereo Surface Imaging System
- CGAS - Cooled Array Grating Spectrometer
- CMOS - Complementary Metal-Oxide-Semiconductor
- CRISM - Compact Reconnaissance Imaging Spectrometer for Mars
- DEMC - Differential Evolution Markov Chain
- DISORT - DIScrete Ordinate Radiative Transfer
- ESA - European Space Agency
- FOV - Field Of View
- FREND - Fine Resolution Epithermal Neutron Detector
- FSR - Free Spectral Range
- FTS - Fourier Transform Spectrometer
- FWHM - Full Width at Half Maximum
- GEOPS - GEOsciences Paris Saclay
- HiRISE - High Resolution Imaging Science Experiment
- HRSC - High Resolution Stereo Camera
- HST - Hubble Space Telescope
- ILS - Instrument Line Shape
- IRTF - InfraRed Telescope Facility
- IRTM - InfraRed Thermal Mapper
- IRCS - InfraRed Camera and Spectrograph
- ISS - Imaging Science System
- JIRAM - Jovian InfraRed Auroral Mapper

- JUICE - JUpiter ICy moons Explorer
- JWST - James Webb Space Telescope
- L-BFGS-B - Limited-memory Broyden-Fletcher-Goldfarb-Shanno (version B) algorithm
- LNO - Limb and Nadir Occultation
- LORRI - LOng Range Reconnaissance Imager
- LST - Local Solar Time
- MAJIS - Moons And Jupiter Imaging Spectrometer
- MAP - Maximum A Posteriori probability
- mc3 - Multi-Core Markov-Chain Monte Carlo
- MCMC - Markov Chain Monte Carlo
- MGS - Mars Global Surveyor
- MISE - Mapping Imaging Spectrometer for Europa
- MODTRAN - MODerate resolution atmopsheric TRANsmission
- MRO - Mars Reconnaissance Orbiter
- NASA - National Aeronautics and Space Administration
- NIMS - Near Infrared Mapping Spectrometer
- NIR - Near InfraRed (wavelengths)
- NIRCam - Near Infrared Camera
- NIRSpec - Near-Infrared Spectrograph
- NOA - Number Of Accumulation
- NOMAD - Nadir and Occultation for MArs Discovery
- NPLD - North Polar Layer Deposits
- OMEGA - Observatoire pour la Minéralogie, l'Eau, les Glaces et l'Activité
- PDF - Probability Density Function
- PSF - Point Spread Function
- PSG - Planetary Spectrum Generator
- RAM - Random Access Memory
- RMS - Root Mean Square deviation
- RSL - Recurring Slope Linae
- SHDOM - Spherical Harmonic Discrete Ordinate Method
- SNR - Signal-to-Noise Ratio
- SO - Solar Occultation

- SOIR - Solar Occultation in the InfraRed
- SPLD - South Polar Layer Deposits
- SSI - Solid State Imaging experiment
- STIS - Space Telescope Imaging Spectrograph
- TOA - Top-Of-Atmopshere
- TES - Thermal Emission Spectrometer
- TGO - Trace Gas Orbiter
- UV - UltraViolet (wavelengths)
- UVIS - Ultraviolet and VISible